Introduction to Graphene-Based Nanomaterials

Graphene is one of the most intensively studied materials and has unusual electrical, mechanical, and thermal properties which provide almost unlimited potential applications. This book provides an introduction to the electrical and transport properties of graphene and other two-dimensional nanomaterials, covering *abinitio* to multiscale methods. Updated from the first edition, this book contains added chapters on other two-dimensional materials, spin-related phenomena, and an improved overview of Berry phase effects. Other topics include powerful order-N electronic structure, transport calculations, AC transport, and multiscale transport methodologies. Chapters are complemented with concrete examples and case studies, questions and exercises, detailed appendices, and computational codes. This book is a valuable resource for graduate students and researchers working in physics, or materials science or engineering, who are interested in the field of graphene-and two-dimensional nanomaterials.

Luis E. F. Foa Torres is a condensed matter physicist and Associate Professor of Physics at the University of Chile. Previous positions include Research Scientist at the National Council for Scientific and Technical Research (CONICET) in Argentina, and fellow of the Alexander von Humboldt Foundation in Dresden, Germany. His research is focused on quantum transport, two-dimensional materials, topological insulators, and the physics of driven systems. He was awarded the International Centre for Theoretical Physics (ICTP) Prize in 2018.

Stephan Roche is a Catalan Institution for Research and Advanced Studies (ICREA) Research Professor working at the Catalan Institute of Nanoscience and Nanotechnology (ICN2) and at the Barcelona Institute of Science and Technology (BIST). He leads the Theoretical and Computational Nanoscience group which focuses on the understanding of quantum transport phenomena from the molecular to the mesoscopic scales with particular focus on spin dynamics in topological (and Dirac) matter. In 2009, he was awarded the prestigious Friedrich Wilhelm Bessel Prize from the Alexander von Humboldt Foundation (Germany). He serves as deputy leader of the Spintronics Work Package in the Graphene Flagship consortium.

Jean-Christophe Charlier is Full Professor at the École Polytechnique de Louvain and Senior Researcher at the Institute of Condensed Matter and Nanosciences of the University of Louvain (UCLouvain) in Belgium. His main scientific interests are centered on theoretical condensed matter physics and nanosciences, covering the areas of electronic, structural, and dynamical properties and quantum transport in nanostructures using first-principles theories and computational physics. In 2016, he was awarded the chair of Francqui Research Professor at UCLouvain from the Francqui-Stichting Foundation (Belgium).

Introduction to Graphene-Based Nanomaterials

From Electronic Structure to Quantum Transport

Second Edition

LUIS E. F. FOA TORRES
University of Chile

STEPHAN ROCHE
Barcelona Institute of Science and Technology

JEAN-CHRISTOPHE CHARLIER
University of Louvain

CAMBRIDGE
UNIVERSITY PRESS

CAMBRIDGE
UNIVERSITY PRESS

University Printing House, Cambridge CB2 8BS, United Kingdom

One Liberty Plaza, 20th Floor, New York, NY 10006, USA

477 Williamstown Road, Port Melbourne, VIC 3207, Australia

314–321, 3rd Floor, Plot 3, Splendor Forum, Jasola District Centre, New Delhi – 110025, India

79 Anson Road, #06–04/06, Singapore 079906

Cambridge University Press is part of the University of Cambridge.

It furthers the University's mission by disseminating knowledge in the pursuit of education, learning, and research at the highest international levels of excellence.

www.cambridge.org
Information on this title: www.cambridge.org/9781108476997
DOI: 10.1017/9781108664462

First edition published 2014
Second edition published 2020

Printed in the United Kingdom by TJ International Ltd, Padstow Cornwall

A catalogue record for this publication is available from the British Library.

ISBN 978-1-108-47699-7 Hardback

Contents

Preface to the Second Edition

We are delighted to give a second birth to this book on the presentation of electronic and transport properties of graphene-related materials five years after its first edition. Over these years, research in the area of graphene and two-dimensional materials has evolved. The changes are well reflected by the name of the 2017 Solvay Workshop dedicated to this field: *From physics of graphene to graphene for physics*. Indeed today, rather than studying graphene's properties, we are using it mostly as a platform for unveiling new physics. Furthermore, with each newly discovered two-dimensional material a similar path emerges, from studying their properties to using them as a brave new playground for exciting physics. At the same time, we are witnessing a very interesting return to three-dimensional systems, this time based on the stacking of two-dimensional structures which allows for more tailor-made properties.

In this new edition we decided to expand different aspects that were either missing or too succint in the previous edition. This includes, the new family of two-dimensional materials Berry phases and quantum Hall effects, and spintronics. We have reduced a few chapters that did not age very well to make space for this more exciting new material. As with the first edition we keep being committed to offering problems and solutions through our website, besides those provided in the book.

Please do not hesitate to contact us if you have questions or comments. In this sense, when choosing whom to contact it might be useful to keep in mind the distribution of our contributions to the book, which take advantage of our complementary expertise: Jean-Christophe wrote of the parts dealing with *ab initio* and new two-dimensional materials (Chapters 1, 3, 10, Appendices A and B, and parts of Chapter 2 and Appendix C), Stephan was in charge of spintronics, disorder effects, and transport (Chapters 6, 8, Appendix D, and parts of Chapters 2, 4, 5, and 7), Luis took care of the transport, quantum Hall effects, and AC transport parts (Chapters 4, 7, and 9 and parts of Chapters 2, 5, and Appendix C).

We would like to thank again our colleagues and coworkers for their help and inspiring our work. Besides those already acknowledged in our first preface, here we would like to also thank those newcomers to our family: Matías Berdakin, David Beljonne, Felix Casanova, Aurélie Champagne, José Chesta, Samuel Dechamps, José Hugo García, Rocío González, Benoît Hackens, Hafid Khalfoun, Víctor Manuel Martínez Álvarez, Joaquín Medina, Viet-Hung Nguyen, Álvaro Núñez, Esteban Rodríguez, Pierre Seneor, Christoph Stampfer, Benoît Van Troeye, and Marc Vila.

We thank our home institutions for supporting our research, as well as the Alexander von Humboldt Foundation (SR and LEFFT), the Abdus Salam International Centre for Theoretical Physics (LEFFT), and the Francqui-Stichting Foundation of Belgium (JCC). Finally, we are indebted to our respective wives (Sandra Rieger, Encarni Carrasco Perea, and Mireille Toth-Budai) and our children (Hector and Gabriel Roche, and Ilona, Elise, and Mathilde Charlier) for their warm enthusiasm and continuous support during all these years of time-consuming work.

We hope that you find this second edition to be a useful companion for starting in this field and perhaps even for your day-to-day research.

And we wish you an exciting journey in Flatland and beyond!

Preface to the First Edition

Once deemed impossible to exist in nature, graphene, *the first truly two-dimensional nanomaterial ever discovered*, has rocketed to stardom since being first isolated in 2004 by Nobel Laureates Konstantin Novoselov and Andre K. Geim of the University of Manchester. Graphene is a single layer of carbon atoms arranged in a flat honeycomb lattice. Researchers in high energy physics, condensed matter physics, chemistry, biology, and engineering, together with funding agencies and companies from diverse industrial sectors, have all been captivated by graphene and related carbon-based materials such as carbon nanotubes and graphene nanoribbons, owing to their fascinating physical properties, potential applications, and market perspectives.

But what makes graphene so interesting? Basically, graphene has redefined the limits of what a material can do: it boasts record thermal conductivity and the highest current density at room temperature ever measured (a million times that of copper!); it is the strongest material known (a hundred times stronger than steel!) yet is highly mechanically flexible; it is the least permeable material known (not even helium atoms can pass through it!); the best transparent conductive film; the thinnest material known; and the list goes on.

A sheet of graphene can be quickly obtained by exfoliating graphite (the material that the tip of your pencil is made of) using sticky tape. Graphene can readily be observed and characterized using standard laboratory methods, and can be mass-produced either by chemical vapor deposition (CVD) or by epitaxy on silicon carbide substrates. Driven by these intriguing properties, graphene research is blossoming at an unprecedented pace and marks the point of convergence of many fields. However, given this rapid development, there is a scarcity of tutorial material to explain the basics of graphene while describing the state of the art in the field. Such materials are needed to consolidate the graphene research community and foster further progress.

The dearth of up-to-date textbooks on the electronic and transport properties of graphene is especially dramatic: the last major work of reference in this area – written by Riichiro Saito, Gene Dresselhaus, and Mildred Dresselhaus – was published in 1998. Seeking to answer the prayers of many colleagues who have had to struggle in a nascent field characterized by a huge body of research papers but very little introductory material, we decided to write this book. It is the fruit of our collective research experience, dating from the early days of research on graphene and related materials, up through the past decade, when each of us developed different computational tools and

theoretical approaches to understanding the complex electronic and transport properties in realistic models of these materials.

We have written *Introduction to Graphene-Based Nanomaterials: From Electronic Structure to Quantum Transport* for everyone doing (or wishing to do) research on the electronic structure and transport properties of graphene-related systems. Assuming basic knowledge of solid-state physics, this book offers a detailed introduction to some of the most useful methods for simulating these properties. Furthermore, we have made additional resources (computational codes, a forum, etc.) available to our readers at cambridge.org/foatorres, and at the book website (*introductiontographene.org*), where additional exercises as well as corrections to the book text (which will surely appear) will be posted.

Graphene and related materials pertain to a larger family that encompasses all kinds of two-dimensional materials, from boron nitride lattices, to transition-metal dichalcogenides (MoS_2, WS_2), to the silicon analogue of graphene, silicene, a recently discovered zero-gap semiconductor. Researchers are beginning to explore the third dimension by shuffling two-dimensional materials and by fabricating three-dimensional heterostructures (BN/graphene, BN/MoS_2/graphene, etc.) with unprecedented properties.

Interestingly, low-energy excitations in two-dimensional graphene (and in one-dimensional metallic carbon nanotubes), known as massless Dirac fermions, also develop at the surface of topological insulators (such as Bi_2Se_3, Bi_2Te_3, etc.), which are bulk insulators. Topological insulators thus share commonalities with graphene, such as Berry's phase-driven quantum phenomena (Klein tunneling, weak antilocalization, etc.), and exhibit other features such as spin-momentum locking that offer different and ground-breaking perspectives for spintronics. Therefore, we believe that our presentation of the fundamentals of electronic and transport properties in graphene and related materials should prove useful to a growing community of scientists, as they touch on advanced concepts in condensed matter physics, materials science, and nanoscience and nanotechnology.

The book starts with an introduction to the electronic structures and basic concepts in transport in low-dimensional materials, and then proceeds to describe the specific transport phenomena unique to graphene-related materials. Transport concepts are then presented through simple disorder models, which in some cases enable comparison with analytical treatments. Additionally, the development of multiscale quantum transport methodologies (either within the Landauer–Büttiker or Kubo–Greenwood formalisms) is introduced in a straightforward way, showing the various options for tackling defects and impurities in graphene materials with more structural and chemical complexity: from combined *ab initio* with tight-binding models to transport calculations fully based on first principles. To facilitate reading, the essential technical aspects concerning the formalism of Green functions, as well as transport implementation and order-N transport schemes are described in dedicated appendices.

This book encompasses years of scientific research, research that has enabled us to establish certain foundations in the field, a work made possible by the efforts of

collaborators, including many postdoctoral and doctoral students. We are particularly indebted to Jean-Joseph Adjizian, Hakim Amara, Rémi Avriller, Blanca Biel, Andrés Botello-Méndez, Victoria Bracamonte, Hernán Calvo, Jessica Campos-Delgado, Damien Connétable, Alessandro Cresti, Eduardo Cruz-Silva, Aron Cummings, Virginia Dal Lago, Xavier Declerck, Simon Dubois, Nicolas-Guillermo Ferrer Sanchez, Lucas Ingaramo, Gabriela Lacconi, Sylvain Latil, Nicolas Leconte, Aurélien Lherbier, Alejandro Lopez-Bezanilla, Thibaud Louvet, Yann-Michel Niquet, Daijiro Nozaki, César Núñez, Hanako Okuno, Frank Ortmann, Andreï Palnichenko, Pablo Pérez-Piskunow, Juan Pablo Ramos, Claudia Rocha, Xavier Rocquefelte, Luis Rosales, Haldun Sevincli, Eric Suárez Morell, Florent Tournus, François Triozon, Silvia Urreta, Gregory Van Lier, Dinh Van Tuan, François Varchon, Wu Li, Zeila Zanolli, and Bing Zheng.

We would also like to express our sincere gratitude to the following inspiring individuals with whom we have worked over the past decade: Pulickel Ajayan, Tsuneya Ando, Marcelo Apel, Adrian Bachtold, Carlos Balseiro, Florian Banhart, Robert Baptist, Christophe Bichara, Xavier Blase, Roberto Car, Antonio Castro-Neto, Mairbek Chshiev, Gianaurelio Cuniberti, Silvano De Franceschi, Hongjie Dai, Alessandro De Vita, Millie and Gene Dresselhaus, François Ducastelle, Reinhold Egger, Peter Eklund, Morinobu Endo, Walter Escoffier, Chris Ewels, Andrea Ferrari, Albert Fert, Takeo Fujiwara, Xavier Gonze, Andrea Latgé, Caio Lewenkopf, Annick Loiseau, Jose-Maria Gómez Rodriguez, Nicole Grobert, Paco Guinea, Luc Henrard, Eduardo Hernández, Jean-Paul Issi, Ado Jorio, Philip Kim, Jani Kotakoski, Vladimir Kravtsov, Philippe Lambin, Sergio Makler, Ernesto Medina, Vincent Meunier, Natalio Mingo, Costas Moulopoulos, Joel Moser, Yann-Michel Niquet, Kentaro Nomura, Kostya Novoselov, Pablo Ordejón, Pedro Orellana, Mónica Pacheco, Michael Payne, Horacio Pastawski, Marcos Pimenta, Bertrand Raquet, Gian-Marco Rignanese, Angel Rubio, Riichiro Saito, Bobby Sumpter, Mauricio and Humberto Terrones, Gonzalo Usaj, and Sergio Valenzuela.

We thank our home institutions for supporting our research, as well as the Alexander von Humboldt Foundation (SR and LEFFT) and the Abdus Salam International Centre for Theoretical Physics (LEFFT). Finally, we are indebted to our respective wives (Sandra Rieger, Encarni Carrasco Perea, and Mireille Toth-Budai) and our children (Hector and Gabriel Roche, and Ilona, Elise, and Mathilde Charlier) for their warm enthusiasm and continuous support during all these years of time-consuming work.

We hope that you find this book to be a useful companion for starting in this field and perhaps even for your day-to-day research. We recommend that you start by reading Chapter 1 and then follow the advice in *Guide to the book* (Section 1.3).

And we wish you an exciting journey in Flatland!. . .

1 Introduction to Carbon-Based Nanostructures

Carbon is a truly unique chemical element. It can form a broad variety of architectures in all dimensions, both at the macroscopic and nanoscopic scales. During the last 20+ years, brave new forms of carbon have been unveiled. The family of carbon-based materials now extends from C_{60} to carbon nanotubes, and from old diamond and graphite to graphene. The properties of the new members of this carbon family are so impressive that they may even redefine our era. This chapter provides a brief overview of these carbon structures.

1.1 Carbon Structures and Hybridizations

Carbon is one of the most versatile elements in the periodic table in terms of the number of compounds created from it, mainly due to the types of bonds it may form (single, double, and triple bonds) and the number of different atoms it can join in bonding. When we look at its ground state (lowest energy) electronic configuration ($1s^2 2s^2 2p^2$), carbon is found to possess two core electrons ($1s$) that are not available for chemical bonding and four valence electrons ($2s$ and $2p$) that can participate in bond formation (Fig. 1.1(a)). Since two unpaired $2p$ electrons are present, carbon should normally form only two bonds in its ground state.

However, carbon should maximize the number of bonds formed because chemical bond formation will induce a decrease of system energy. Consequently, carbon will rearrange the configuration of the valence electrons. Such a rearrangement process is called *hybridization*, where only $2s$ and $2p$ electrons are affected. Indeed, one $2s$ electron will be promoted into an empty $2p$ orbital, thus forming an excited state (Fig. 1.1(b)). Carbon will thus hybridize from this excited state, being able to form at most four bonds.

One possible hybridization scheme consists in mixing the four atomic orbitals (one $2s$ orbital + three $2p$ orbitals), leading to the formation of four sp^3 hybrid orbitals, each filled with only one electron (Fig. 1.1(c)). In order to minimize repulsion, these four hybrid orbitals optimize their position in space, leading to a tetrahedral geometry where four σ bonds are formed with carbon neighbors, each at an angle of 109.5° to each other. Methane (CH_4) is the typical molecule that satisfies this specific bonding arrangement. Diamond is the three-dimensional carbon allotropic form where the

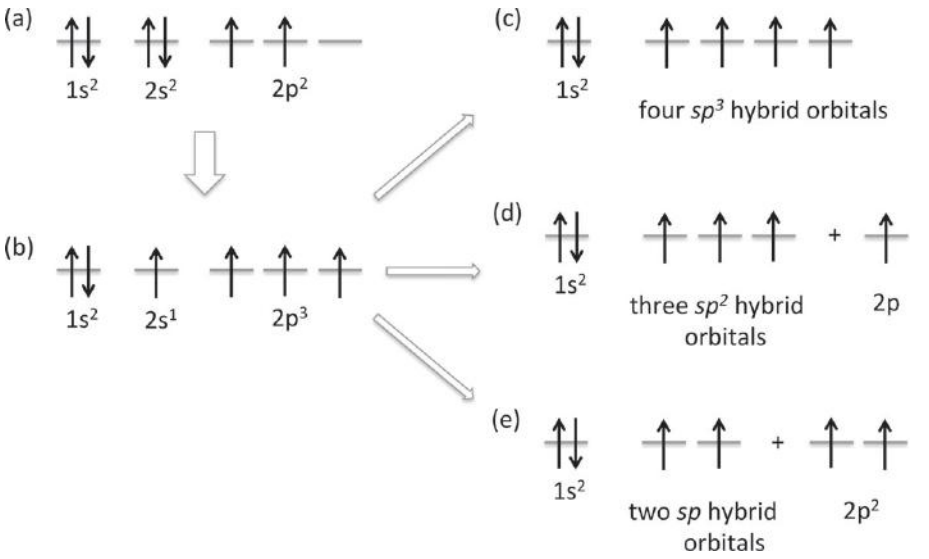

Figure 1.1 Electronic configurations of carbon: (a) ground state; (b) excited state; (c) sp^3 hybridization; (d) sp^2 hybridization; and (e) sp hybridization.

atoms are arranged in a variation of the face-centered cubic crystal structure called a diamond lattice (Fig. 1.2(a)). In diamond, all carbon atoms are in the sp^3 hybridization and are connected by σ bonds (due to the overlapping between two hybrid orbitals, each containing one electron) to four nearest neighbors with a bond length of 1.56 Å. Diamond (from the ancient Greek $\alpha\delta\alpha\mu\alpha\sigma$ – *adámas* "unbreakable") is renowned as a material with extreme mechanical properties originating from the strong sp^3 covalent bonding between its atoms. In particular, diamond exhibits one of the highest hardness values, has an extremely high thermal conductivity, is an electrical insulator with a bandgap of ∼5.5 eV, and is transparent to visible light (Hemstreet et al. 1970).

Another possible hybridization scheme consists in mixing three atomic orbitals among the four (one 2*s* orbital + two 2*p* orbitals), leading to the formation of three sp^2 hybrid orbitals, each filled with only one electron (Fig. 1.1(d)). Again, the three sp^2 hybrid orbitals will arrange themselves in order to be as far apart as possible, leading to a trigonal planar geometry where the angle between each orbital is 120°. The remaining *p*-type orbital will not mix and will be perpendicular to this plane. In such a configuration, the three sp^2 hybrid orbitals will form σ bonds with the three nearest neighbors and the side-by-side overlap of the unmixed pure *p* orbitals will form π bonds between the carbon atoms, accounting for the carbon–carbon double bond. Ethylene (C_2H_4) and aromatic molecules like benzene (C_6H_6) are typical examples of sp^2 hybridization.

Graphite is a three-dimensional crystal made of stacked layers consisting of sp^2 hybridized carbon atoms (Fig. 1.2(b)); each carbon atom is connected to another three making an angle of 120° with a bond length of 1.42 Å. This anisotropic structure

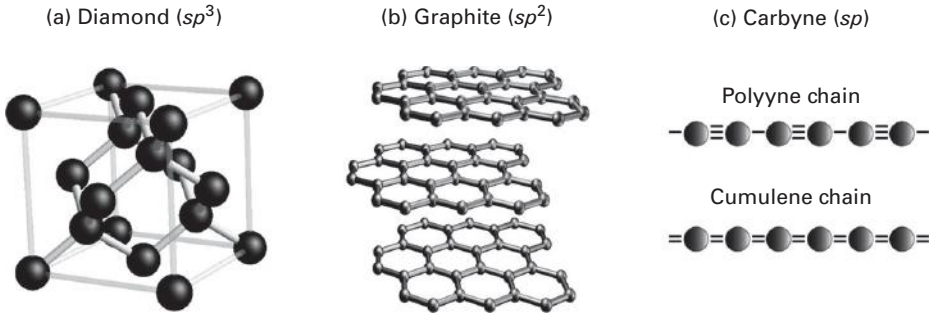

Figure 1.2 Carbon structures exhibiting different hybridizations: (a) diamond (sp^3); (b) graphite (sp^2); and (c) carbyne (sp).

clearly illustrates the presence of strong σ covalent bonds between carbon atoms in the plane, while the π bonds provide the weak interaction between adjacent layers in the graphitic structure. Graphite (from the ancient Greek $\gamma\rho\alpha\phi\omega$ – *graphó* "to write") is well known for its use in pencils because of its ability to mark surfaces as a writing material, due to nearly perfect cleavage between basal planes related to the anisotropy of bonding. Under standard conditions (ordinary temperatures and pressures), the stable form of carbon is *graphite*. Unlike diamond, graphite is a popular lubricant, an electrical (semi-metal) and thermal conductor, and reflects visible light. *Natural* graphite occurs in two crystal structures: Bernal (hexagonal) (Bernal 1924) and rhombohedral (Lipson & Stokes 1942) structures that are characterized by different stackings of the basal planes, $\ldots ABABAB \ldots$ and $\ldots ABCABC \ldots$, respectively. The hexagonal and rhombohedal structures belong to the $P6_3/mmc$ (D^4_{6h}) and $R\bar{3}m$ (D^5_{3d}) space groups, respectively. Samples usually contain no more than 5–15% rhombohedral structure intermixed with Bernal form, and sometimes, disordered graphite (Lipson & Stokes 1942). These disordered graphitic forms, such as pregraphitic carbon or turbostratic graphite, are mainly composed of randomly oriented basal carbon sheets. However, pure graphite crystals can be found naturally and can also be artificially synthesized by thermolytic processes, such as the production of highly oriented pyrolytic graphite (HOPG) (Moore 1974).

The last possible hybridization consists in mixing two atomic orbitals (one $2s$ orbital + one $2p$ orbital) of the four, leading to the formation of two *sp* hybrid orbitals, each filled with only one electron (Fig. 1.1(e)). The geometry that results is linear with an angle between the *sp* orbitals of 180°. The two remaining *p*-type orbitals, which are not mixed, are perpendicular to each other. In such a configuration, the two *sp* hybrid orbitals will form σ bonds with the two nearest neighbors and the side-by-side overlap of the two unmixed pure *p* orbitals will form π bonds between the carbon atoms, accounting for the carbon–carbon triple bond (which is thus composed of one σ bond and two π bonds). Acetylene (H−C≡C−H) is the typical linear molecule that satisfies this specific bonding arrangement. Carbon also has the ability to form one-dimensional chains, called carbynes (Fig. 1.2(c)), that are traditionally classified as *cumulene* (monoatomic chains

with double bonds, $\cdots{=}C{=}C{=}\cdots$) or *polyyne* (dimerized chains with alternating single and triple bonds, $\cdots{-}C{\equiv}C{-}\cdots$). While sp^2 and sp^3 carbon-based structures have been widely characterized, the synthesis of carbynes has been a challenge for decades due to the high reactivity of chain ends and a strong tendency to interchain crosslinking (Heimann et al. 1999). Linear carbon chains consisting of a few tens of atoms were first synthesized via chemical methods (Cataldo 2005) by stabilizing the chain ends with nonreactive terminal groups (Kavan & Kastner 1994; Lagow et al. 1995). However, these systems consist of a mixture of carbon and other chemical elements, and the synthesis of carbynes in a pure carbon environment has only recently been achieved via supersonic cluster beam deposition (Ravagnan et al. 2002, 2007) and via electronic irradiation of a single graphite basal plane (graphene) inside a transmission electron microscope (Jin et al. 2009; Meyer et al. 2008).

1.2 Carbon Nanostructures

Carbon nanomaterials also reveal a rich polymorphism of various allotropes exhibiting each possible dimensionality: fullerene molecule (0D), nanotubes (1D), graphite platelets and graphene ribbons (2D), and nano-diamond (3D) are selected examples (Terrones et al. 2010). Because of this extraordinary versatility of nanomaterials exhibiting different physical and chemical properties, carbon nanostructures are playing an important role in nanoscience and nanotechnology.

Carbon nanoscience started with the discovery of C_{60} Buckminsterfullerene (Kroto et al. 1985). This cage-like molecule of 7 Å diameter contains 60 carbons atoms laid out on a sphere (Fig. 1.3(a)). The structure of the C_{60} Buckminsterfullerene consists of a truncated icosahedron with 60 vertices and 32 faces (20 hexagons and 12 pentagons where no pentagons share a vertex) with a carbon atom at the vertex of each polygon and a bond along each polygon edge (Fig. 1.3(a)). Each carbon atom in the structure is bonded covalently with three others ($sp^{2+\delta}$ hybridization; δ is due to the curvature) with an average bond length of 1.46 Å within the five-member rings (single bond) and 1.4 Å for the bond connecting five-member rings (the bond fusing six-member rings). The number of carbon atoms in each fullerene cage can vary. Indeed, fullerene molecules are generally represented by the formula C_n, where n denotes the number of carbon atoms present in the cage. Anyway, the C_{60} nano-soccer ball (or *buckyball*) is the most stable and well-characterized member of the fullerene family. The name of these C_n molecules was derived from the name of the noted inventor and architect Buckminster Fuller since C_n resembles his trademark geodesic domes. The C_{60} molecule is still dominating fullerene research and stimulating the creativity and imagination of scientists, and has paved the way for a whole new chemistry and physics of nanocarbons (Dresselhaus et al. 1996).

Soon after, in 1988, graphitic onions – of which the first electron microscope images were reported by Sumio Iijima in 1980 (Harris 1999) – were suggested to

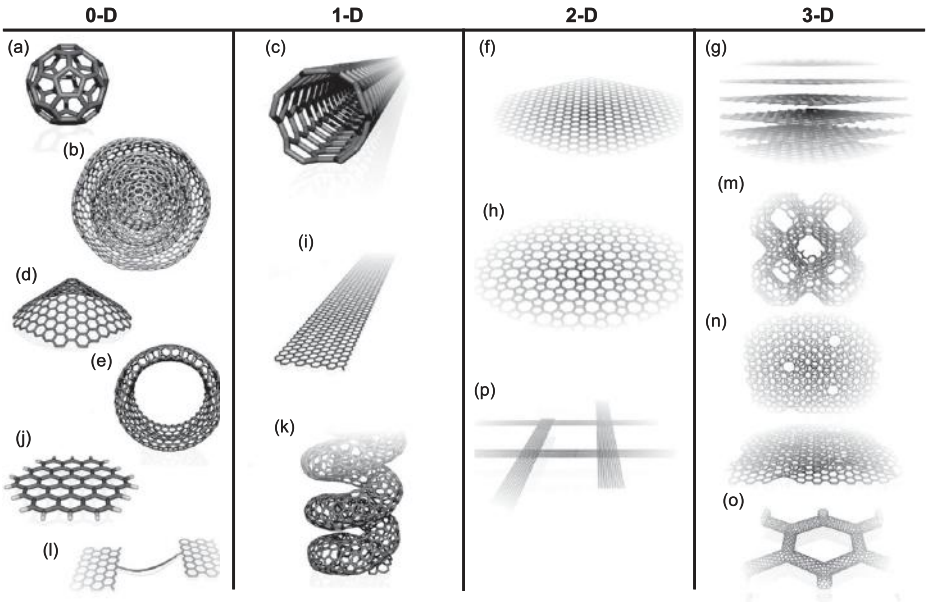

Figure 1.3 Atomistic models of various sp^2-like hybridized carbon nanostructures exhibiting different dimensionalities, 0D, 1D, 2D, and 3D: (a) C_{60}: Buckminsterfullerene; (b) nested giant fullerenes or graphitic onions; (c) carbon nanotube; (d) nanocones or nanohorns; (e) nanotoroids; (f) graphene surface; (g) 3D graphite crystal; (h) Haeckelite surface; (i) graphene nanoribbons; (j) graphene clusters; (k) helicoidal carbon nanotube; (l) short carbon chains; (m) 3D Schwarzite crystals; (n) carbon nanofoams (interconnected graphene surfaces with channels); (o) 3D nanotube networks, and (p) nanoribbon 2D networks. Reproduced from Terrones et al. (2010)

be nested icosahedral fullerenes (C60@C240@C540@C960…) (Kroto & McKay 1988) containing only pentagonal and hexagonal carbon rings (Fig. 1.3(b)). In 1992, the reconstruction of polyhedral graphitic particles into almost spherical carbon onions (nested giant fullerenes) was demonstrated by Daniel Ugarte (1992) using high-energy electron irradiation inside a high-resolution transmission electron microscope (HRTEM). By analogy, the formation of C_{60} has also been very recently observed *in situ* by creating local defects in graphene upon electron irradiation in a HRTEM (Chuvilin et al. 2010). These carbon onions are quasi-spherical nanoparticles consisting of fullerene-like carbon layers enclosed by concentric graphitic shells, thus exhibiting electronic and mechanical properties different from any other carbon nanostructures due to their highly symmetric structure.

In 1976, the "ultimate" carbon fibers (later known as a multiwall carbon nanotubes), produced by a modified chemical vapor deposition (CVD) method usually used to produce conventional carbon fibers, were observed using TEM (Oberlin et al. 1976). However, the emergence of carbon nanotubes (CNTs) really came in 1991 after the C_{60} discovery. Indeed, "graphite microtubules," multiwall nanotubes (MWNTs) produced via an arc discharge between two graphite electrodes in an inert atmosphere

(same method for producing fullerenes), were first characterized using HRTEM (Iijima 1991), thus confirming that their atomic structures consisted of nested graphene nanotubes terminated by fullerene-like caps. A couple of years later, in 1993, single-wall carbon nanotubes – SWNTs, Fig. 1.3(c) – were synthesized using the same carbon arc technique in conjunction with metal catalysts (Bethune et al. 1993; Iijima & Ichihashi 1993). CNTs are allotropic forms of carbon characterized by a long and hollow cylindrical-shaped nanostructure with a length-to-diameter ratio that may reach 10^8 (Zheng et al. 2004), which is significantly larger than for any other one-dimensional material. Carbon nanotubes are frequently considered as members of the fullerene family, since their ends may be capped with a buckyball hemisphere. The cylinder walls are formed by one-atom-thick sheets of carbon rolled up at specific and discrete *chiral* angles. Both the nanotube diameter and this rolling angle lead to specific properties; for example, a SWNT may behave as a metal or a semiconductor depending on its geometry (Saito et al. 1998), as described in detail in Chapter 2. Due to long-range weak interactions (van der Waals and π-stacking), individual nanotubes naturally align into *ropes* or *bundles* (Thess et al. 1996). These carbon nanotubes exhibit unusual properties which are extremely valuable for nanotechnology, electronics, mechanics, optics, and other fields of materials science. In particular, owing to their extraordinary mechanical properties, electrical and thermal conductivity, carbon nanotubes find applications as additives (primarily carbon fiber) in composite materials, as for instance, in baseball bats, golf clubs, or car parts (Dresselhaus et al. 2001).

After these consecutive discoveries of the fullerenes and carbon nanotubes, other graphitic-like nanostructures were successfully produced, observed, and accurately characterized using various experimental techniques. The topologies associated with these new carbon nanostructures include nanocones (Fig. 1.3(d)) (Krishnan et al. 1997), nanopeapods (Smith et al. 1998), nanohorns (Fig. 1.3(d)) (Iijima et al. 1999), and carbon rings or toroids (Fig. 1.3(e)) (Liu et al. 1997).

The fundamental building block in all these carbon nanostructures (except for sp^3 nanodiamond) relies on the theoretical concept of the two-dimensional crystalline allotrope of carbon called *graphene* (Fig. 1.3(f)). Indeed, graphene is the name given to the ideally perfect infinite one-atom-thick planar sheet of sp^2-bonded carbon atoms, densely packed in a honeycomb crystal lattice (Boehm et al. 1962). This ideal two-dimensional solid has thus been widely employed as a useful theoretical concept to describe the properties of many carbon-based materials, including graphite (where a large number of graphene sheets are stacked; see Fig. 1.3(g)) (Wallace 1947), nanotubes (where graphene sheets are rolled up into nanometer-sized cylinders; see Fig. 1.3(c)), large fullerenes (where graphene sheets, according to Euler's theorem, contain at least 12 pentagons displaying a spherical shape; see Fig. 1.3(a–b)), and ribbons (where graphene is cut into strips; see Fig. 1.3(i)) (Li et al. 2008). Actually, planar graphene itself was presumed not to exist in the free state, being unstable with respect to the formation of curved structures such as soot, fullerenes, and nanotubes. However, in 2004, graphene samples were synthesized either by mechanical exfoliation (repeated peeling or micromechanical cleavage, known as the "scotch tape method") of bulk

graphite (highly oriented pyrolytic graphite) (Novoselov et al. 2004, 2005) or by epitaxial growth through thermal decomposition of SiC (Berger et al. 2006). The relatively easy production of graphene using the scotch tape method and the transfer facility of a single atomic layer of carbon from the *c*-face of graphite to a substrate suitable for the measurement of its electrical properties have led to a renewed interest in what was considered to be a prototypical, yet theoretical, two-dimensional system. Graphene displays unusual electronic properties arising from confinement of electrons in two dimensions and peculiar geometrical symmetries. Indeed, old theoretical studies of graphene (Wallace 1947) reveal that the specific linear electronic band dispersion near the Brillouin zone corners (Dirac point) gives rise to electrons and holes that propagate as if they were massless Dirac fermions, with a velocity of the order of a few hundredths of the velocity of light. Charge excitations close to the Fermi level can thus be formally described as massless relativistic particles obeying a Dirac equation, whereas a new degree of freedom reflecting inherent symmetries (sublattice degeneracy) appears in the electronic states: the *pseudospin*. Because of the resulting pseudospin symmetry, electronic states turn out to be particularly insensitive to external sources of elastic disorder (topological and electrostatic defects) and, as a result, charge mobilities in graphene layers as large as 10^5 cm^2 V^{-1} s^{-1} have been reported close to the Dirac point (Novoselov et al. 2004). In addition, in suspended graphene, the minimum conductivity at the Dirac point approaches a universal (geometry independent) value of $4e^2/h$ at low temperature (Du et al. 2008). Low-temperature electron mobility approaching 2×10^5 cm^2 V^{-1} s^{-1} has been measured for carrier density below 5×10^9 cm^{-2}. Such values cannot be attained in conventional semiconductors such as silicon or germanium. In addition, graphene has been demonstrated to exhibit anomalous quantum transport properties such as an integer quantum Hall effect (Novoselov et al. 2005; Zhang et al. 2005), and also one of the most exotic and counterintuitive consequences of quantum electrodynamics: the unimpeded penetration of relativistic particles through high and wide potential barriers, known as the Klein paradox (Katsnelson et al. 2006). These discoveries have stirred a lot of interest in the scientific community as well as in the international media. The excitement behind this discovery has two main driving forces: basic science and technological implications (Geim & Novoselov 2007). Because of its high electronic mobility, structural flexibility, and capability of being tuned from *p*-type to *n*-type doping by the application of a gate voltage, graphene is considered a potential breakthrough in terms of carbon-based nanoelectronics.

All these outstanding properties of the graphene sheet have heavily stimulated the discovery of new, closely-related planar carbon-based nanostructures with sp^2 hybridization, such as bilayer graphene, trilayer graphene, few-layer graphene, and graphene nanoribbons; these nanostructures that have subsequently emerged, each having novel and unusual properties that are different from those of both graphene and graphite. Whenever these structures exhibit $\ldots ABABAB \ldots$ or $\ldots ABCABC \ldots$ stackings, they are considered as graphitic stacks. In fact, this distinction is made because it has been demonstrated that the properties of graphene can be recovered in systems with several sp^2-hybridized carbon layers when stacking disorder is introduced.

Theoretical works have also suggested the possibility of stable, flat sp^2-hybridized carbon sheets containing pentagons, heptagons, and hexagons, termed pentaheptites (2D sheets containing heptagons and pentagons only) (Crespi et al. 1996) or Haeckelites (2D crystals containing pentagons, heptagons and/or hexagons, see Fig. 1.3(h)) (Terrones et al. 2000). These planar structures are intrinsically metallic and could exist in damaged or irradiated graphene. However, further experiments are needed in order to both produce and identify them successfully.

When infinite perfect graphene crystals become finite, borders and boundaries appear, implying the presence of carbon atoms that exhibit a coordination below three at the edges. Among these graphene-based nanostructures are nanoribbons (Fig. 1.3(i)) and nanoclusters (Fig. 1.3(j)). In general, a graphene nanoribbon (GNR) is defined as a 1D sp^2-hybridized carbon crystal with boundaries, which possesses a large aspect ratio (Fig. 1.3(i)). Edge terminations could be armchair, or zigzag, or even a combination of both. The graphene cluster concept arises when the dimensionality is lost and no periodicity is present (Fig. 1.3(j)). Finally, long carbon chains either with alternating single–triple or with double bonds (Fig. 1.2(c)) are also considered as a 1D nanosystem as already briefly described in the previous section.

Finally, Schwarzites are hypothetical graphitic (sp^2 hybridization) three-dimensional crystals obtained by embedding non-hexagonal carbon rings (Fig. 1.3(m)), thus spanning two different space groups in which the most symmetrical cases belong to cubic Bravais lattices (Terrones & Terrones 2003). These 3D carbon-based nanostructures can be visualized as nanoporous carbon (Fig. 1.3(n)), exhibiting nanochannels. From a theoretical point of view, these nanoporous carbon materials have been suggested to have outstanding performance in the storage of hydrogen due to their large surface area (Kowalczyk et al. 2007). Another type of 3D array of nanocarbons consists of nanotube networks (Fig. 1.3(o)), which have been predicted to exhibit outstanding mechanical and electronic properties, besides having a large surface area (e.g., 3600 m^2/g) (Romo-Herrera et al. 2006). Interestingly, these types of random 3D nanotube networks have been produced using CVD approaches (Lepro et al. 2007) and further theoretical and experimental studies are still required in order to achieve crystalline 3D networks.

The series of events described above and dedicated to the most important discoveries in carbon nanoscience clearly demonstrate that carbon is a fascinating element and is able to form various morphologies at the nanoscale, possessing different physicochemical properties, some of them yet unknown. In the following sections, we will concentrate on novel one- and two-dimensional sp^2-like carbon nanostructures. But before starting your trip, we recommend that you read *Guide to the Book* below.

1.3 Guide to the Book

This book deals with the electronic and transport properties of some of the most promising new forms of carbon ever introduced before. Chapter 2 starts by introducing the electronic properties of both pristine and defected carbon nanostructures, and

also overviews the salient electronic features under magnetic fields (Aharonov–Bohm phenomenon and Landau levels). The emphasis is on tight-binding models, though widely used effective low-energy models are also introduced. When possible, the results are commented on in the light of *ab initio* simulations. Chapter 3 overviews the electronic properties of the most important representatives of the 2D materials family other than graphene (*h*-BN, TMDs, Phosphorene, Borophene, Silicene, Germanene, Stanene, MXenes, ...), including also some review related to novel electronic and optoelectronic properties in van der Waals heterostructures.

The rest of the book is mostly dedicated to the electronic transport properties of graphene-related materials. Chapter 4 offers a general overview of the tools used later on, namely, Landauer–Büttiker and Kubo–Greenwood formalisms, together with the commonly used semiclassical Boltzmann transport equation, which presents severe limitations for the exploration of the quantum transport at the Dirac point. Most of the technical details (or tricks!) concerning the numerical implementations of such transport methods are given in dedicated appendices. The first illustrations of transport properties in disordered graphene materials are given in Chapter 5, with a starting discussion concerning the limits of ballistic transport and the peculiar Klein tunneling mechanism. The role of disorder is further discussed broadly in Chapter 6 through the use of the legendary Anderson disorder model, which is the first approach for studying the main transport length scales and conduction regimes. Weak and strong localization phenomena (including weak antilocalization) are presented and related to the nature of disorder (short- versus long-range potential). Various forms of structural disorders are then studied including monovacancies, and polycrystalline and amorphous graphene, showing how irregularities affect mean free paths and localization lengths, eventually turning the materials to a strong Anderson insulator.

Chapter 7 covers different aspects of Berry phases, magnetic field effects, and the quantum Hall regime. The chapter ends with a presentation of Haldane's model for a quantum Hall effect without Landau levels. Chapter 8 gives an overview of spintronics in two-dimensional materials. This chapter presents some debate and open issues, as perceived by the authors, and these issues should generate a great amount of research in the next decade. In particular, graphene spintronics offers fascinating possibilities of revolutionary information processing using the spin degree of freedom. Progress toward spin gating and spin manipulation, however, demands attention and effort in revisiting the way spin diffusion and spin relaxation mechanisms are described in graphene, as these are likely to genuinely differ from conventional relaxation effects described in metals and small-gap semiconductors.

Chapter 9 gives a brief overview of quantum transport beyond DC conditions, Floquet theory for time-periodic Hamiltonians, and a succinct review of the literature on AC transport in carbon-based nanostructures. This is currently a very active field, which connects to graphene photonics and plasmonics. Many developments are expected within the next few years, and theoretical study certainly needs to be further extended. The material provided here will be very useful for those researchers interested in the field.

Ab initio and multiscale transport methodologies are discussed in Chapter 10. To achieve accurate transport calculations on very-large-size disordered systems, a combination of *ab initio* approach and order-*N* transport algorithms is crucial. The presentation will provide a simple description of various possible hybrid methodologies for investigating the complex transport fingerprints of chemically or structurally disordered carbon nanotubes of graphene-based materials. Some targeted functionalities such as chemical sensing will then be discussed in detail for chemically functionalized nanotubes. Sensing is often viewed as a major application for such low-dimensional carbon-based materials. The possibilities but also limitations of these numerical approaches are illustrated in this chapter.

Some of these chapters are essentially tutorials (Chapters 1–5, 7, and 9 and Appendices A–D), offering enough material for introductory lectures at the master degree level. Others are intended to give an overview of most foundational literature in the respective fields or to shine some light on leading-edge research (Chapters 6, 8, and 10). The choice of topics, presentation, and illustrations is unavoidably biased toward the authors' own experiences, and despite the attempts to properly acknowledge the foundational papers, many citations are certainly missing. We will try to amend this in later editions.

All chapters contain a very short list of suggested material for further reading. The core tutorial chapters of this book contain lists of problems with varying levels of difficulty. Many of them are computational exercises where a *learning by doing* spirit is encouraged. Along this line, many solutions, additional exercises, and miscellaneous material, as well as computational codes, are made available online at the website:

www.introductiontographene.org
www.cambridge.org/foatorres

The symbol on the right will indicate that additional material is available online. The authors intend that an updated list of typos and errors will also be available there. This will be the authors' contact point with their ultimate inspiration for this enterprise: you and your fellow readers.

Finally, the interdisciplinarity of the potential readers of this book makes it impossible (and probably pointless) to develop a book that all readers can read linearly from beginning to end. This is why the authors suggest tailoring it to your own experience and objectives. Before starting, it is recommended that you get your own *Table of Instructions* from the authors' website.

1.4 Further Reading

- Readers may enjoy the personal accounts given in Dresselhaus (2011) and Geim (2011), where the flavor of the story behind the development of these materials is given.

2 Electronic Properties of Carbon-Based Nanostructures

2.1 Introduction

As described in Chapter 1, the sp^2 carbon-based family exhibits a great variety of allotropes, from the low-dimensional fullerenes, nanotubes, and graphene ribbons to two-dimensional monolayer graphene, or stacked graphene multilayers. Two-dimensional monolayer graphene stands as the building block, since all the other forms can be derived from it. Graphene nanoribbons can be seen as quasi-one-dimensional structures, with one lateral dimension short enough to trigger quantum confinement effects. Carbon nanotubes can be geometrically constructed by folding graphene nanoribbons into cylinders, and graphite results from the stacking of a very large number of weakly bonded graphene monolayers.

The isolation of a single graphene monolayer by mechanical exfoliation (repeated peeling or micromechanical cleavage) starting from bulk graphite has been actually quite a surprise, since it was previously believed to be thermodynamically unstable (Novoselov et al. 2004; Novoselov, Jiang et al. 2005). At the same time, the route for controlling the growth of graphene multilayers on top of silicon carbide by thermal decomposition was reported, and this eventually led to fabrication of single graphene monolayers of varying quality depending on the surface termination (silicon or carbon termination) (Berger et al. 2006). Basic electronic properties of graphene actually have been well known since the seminal work by Wallace in the late 1940s (Wallace 1947), such as the electron–hole symmetry of the band structure and the specific linear electronic band dispersion near the Brillouin zone corners (Dirac point), but it was after the discovery of carbon nanotubes by Iijima from NEC (Iijima 1991) that the exploration of electronic properties of graphene-based materials was revisited. (For a review, see Charlier et al. (2007).)

This chapter introduces the main electronic features of monolayer graphene and few-layer graphene together with their low-dimensional versions (carbon nanotubes and graphene nanoribbons). Section 2.2 starts with an overview of the electronic properties of graphene described using a simple nearest-neighbor *tight-binding* model, together with an extended derivation of the effective description of low-energy excitations as massless Dirac fermions. The description beyond the linear approximation is then discussed by introducing trigonal warping deformation or extending the *tight-binding* model to third-nearest-neighbor coupling.

This is followed by the improved description provided by *first-principles* calculations within density functional theory (DFT) and beyond using *many-body perturbation theory within the GW approximation*, which leads to a renormalized Fermi velocity close to the Dirac point. Then we focus on the specificities of graphene nanoribbons (GNRs), with a description of the formation of confinement-induced energy gaps which increase linearly with reducing the lateral size. These GNR structures are shown to share some commonalities with their folded versions, since carbon nanotubes (CNTs) are often pictured as the geometrical result of rolling up a graphene ribbon. Carbon nanotubes are found to be either metallic or semiconducting depending on their helical symmetry. Metallic (armchair) nanotubes are actually the best existing one-dimensional ballistic conductors, almost insensitive to the Peierls dimerization mechanism, and exhibiting quantized conductance when appropriately connected to metals such as palladium. The energy gaps in semiconducting tubes downscale linearly with the tube diameter and eventually close for the limit of very large diameter (in accordance with the zero-gap limit of a graphene monolayer). Finally, note that there is currently great interest in analyzing the effects of chemical doping and structural defects in graphene-based materials, given the possibility to tailor the electronic properties and add novel functionalities to the related devices, to improve or complement the silicon-based CMOS (complementary metal-oxide-semiconductor) technologies.

2.2 Electronic Properties of Graphene

2.2.1 *Tight-Binding* Description of Graphene

In two-dimensional graphene, carbon atoms are periodically arranged in an infinite honeycomb lattice (Fig. 2.1(a)). Such an atomic structure is defined by two types of bonds within the sp^2 hybridization, as described in Chapter 1. From the four valence orbitals of the carbon atom (the $2s$, $2p_x$, $2p_y$, and $2p_z$ orbitals, where z is the direction perpendicular to the sheet), the (s, p_x, p_y) orbitals combine to form the inplane σ (bonding or occupied) and σ^* (antibonding or unoccupied) orbitals. Such orbitals are even with respect to the planar symmetry. The σ bonds are strongly covalent bonds determining the energetic stability and the elastic properties of graphene (Fig. 2.1(a)). The remaining p_z orbital, pointing out of the graphene sheet as shown in Fig. 2.1(a), is odd with respect to the planar symmetry and decoupled from the σ states. From the lateral interaction with neighboring p_z orbitals (called the $pp\pi$ interaction), localized π (bonding) and π^* (antibonding) orbitals are formed (Wallace 1947). Graphite consists of a stack of many graphene layers. The unit cell in graphite can be primarily defined using two graphene layers translated from each other by a C–C distance ($a_{cc} = 1.42$ Å). The three-dimensional structure of graphite is maintained by the weak interlayer van der Waals interaction between π bonds of adjacent layers which generate a weak but finite out-of-plane delocalization (Charlier et al. 1994b).

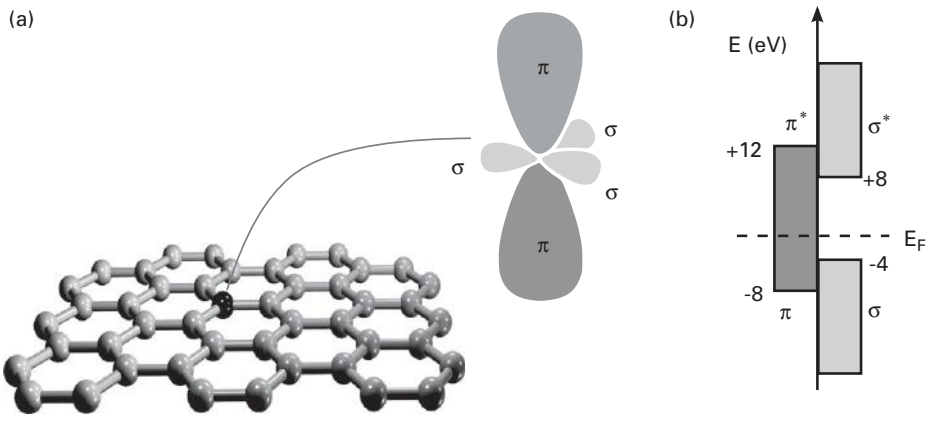

Figure 2.1 The carbon valence orbitals: (a) the three σ orbitals in graphene, and the π orbital perpendicular to the sheet. The σ bonds in the carbon hexagonal network strongly connect the carbon atoms and are responsible for the binding energy and the structural properties of the graphene sheet. The π bonds are perpendicular to the surface of the sheet. The corresponding bonding and antibonding σ bands are separated by a large energy gap of $\sim$12 eV; while (b) the bonding and antibonding π states lie in the vicinity of the Fermi level (E_F). Consequently, the σ bonds are frequently neglected for prediction of the electronic properties of graphene around the Fermi energy.

The bonding and antibonding σ bands are actually strongly separated in energy ($>$12 eV at γ), and therefore their contribution to electronic properties is commonly disregarded (Fig. 2.1(b)). The two remaining π bands completely describe the low-energy electronic excitations in both graphene (Wallace 1947) and graphite (Charlier et al. 1991). The bonding π and antibonding π^* orbitals produce valence and conduction bands (Fig. 2.1(b)), which cross at the charge neutrality points (Fermi level of undoped graphene) at vertices of the hexagonal Brillouin zone.

Carbon atoms in a graphene plane are located at the vertices of a hexagonal lattice. This graphene network can be regarded as a triangular Bravais lattice with two atoms per unit cell (A and B) and basis vectors ($\mathbf{a}_1, \mathbf{a}_2$):

$$\mathbf{a}_1 = a\left(\frac{\sqrt{3}}{2}, \frac{1}{2}\right), \quad \mathbf{a}_2 = a\left(\frac{\sqrt{3}}{2}, -\frac{1}{2}\right). \tag{2.1}$$

Note that $a = \sqrt{3}a_{cc}$, where $a_{cc} = 1.42$ Å is the carbon–carbon distance in graphene. In Fig. 2.2(a), A-type and B-type atoms are represented by full and empty dots respectively. From this figure we see that each A- or B-type atom is surrounded by three atoms of the opposite type.

Through the use of the condition $\mathbf{a}_i \cdot \mathbf{b}_j = 2\pi\delta_{ij}$, the reciprocal lattice vectors ($\mathbf{b}_1, \mathbf{b}_2$) can be obtained,

$$\mathbf{b}_1 = b\left(\frac{1}{2}, \frac{\sqrt{3}}{2}\right), \quad \mathbf{b}_2 = b\left(\frac{1}{2}, -\frac{\sqrt{3}}{2}\right), \tag{2.2}$$

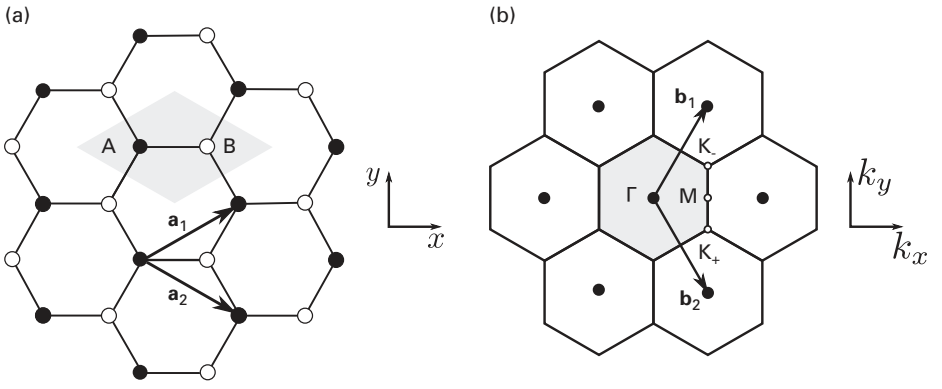

Figure 2.2 (a) Showing the basis vectors $\mathbf{a}_1$ and $\mathbf{a}_2$ in the hexagonal network of graphene. This network is a triangular Bravais lattice with a two-atom basis: A (full dots) and B (empty dots). (b) The reciprocal lattice points corresponding to the triangular Bravais lattice (full dots) as well as the associated basis vectors $\mathbf{b}_1$ and $\mathbf{b}_2$. The unit cell/Brillouin zone are shown shaded in gray in (a) and (b). Highly symmetric points labeled with Γ (zone center), K_+, K_-, and M are also indicated in (b).

with $b = 4\pi/(3a_{cc}) = 4\pi/a\sqrt{3}$. These vectors are shown in Fig. 2.2(b) together with the first Brillouin zone (shaded gray). This hexagonal-shaped Brillouin zone[1] is built as the Wigner–Seitz cell of the reciprocal lattice. Out of its six corners, two of them are inequivalent. (The others can be written as one of these two plus a reciprocal lattice vector.) These two special points are denoted with K_+ and K_-. Another high symmetry point is the one labeled with M in Fig. 2.2(b). They are given by

$$\mathbf{K}_+ = \frac{4\pi}{3a}\left(\frac{\sqrt{3}}{2}, -\frac{1}{2}\right), \quad \mathbf{K}_- = \frac{4\pi}{3a}\left(\frac{\sqrt{3}}{2}, \frac{1}{2}\right), \quad \mathbf{M} = \frac{2\pi}{\sqrt{3}a}(1, 0)\,. \tag{2.3}$$

When the carbon atoms are placed onto the graphene hexagonal network (Fig. 2.2(a)), the electronic wavefunctions from different atoms overlap. However, because of symmetry, the overlap between the p_z orbitals and the s or the p_x and p_y electrons is strictly zero. Therefore, the p_z electrons that form the π bonds in graphene can be treated independently from the other valence electrons. Within this π-band approximation, the A atom (or B atom) is uniquely defined by one orbital per atom site $p_z(\mathbf{r} - \mathbf{r}_A)$ (or $p_z(\mathbf{r} - \mathbf{r}_B)$).

To derive the electronic spectrum of the total Hamiltonian, the corresponding Schrödinger equation has to be solved. According to Bloch's theorem, the eigenfunctions evaluated at two given Bravais lattice points $\mathbf{R}_i$ and $\mathbf{R}_j$ differ from each other

[1] Note that the hexagonal shape of the Brillouin zone is a consequence of the triangular Bravais lattice. It is by no means connected with the two-atom basis, which does not enter into the definition of the Brillouin zone.

in just a phase factor, $\exp(\mathrm{i}\mathbf{k}\cdot(\mathbf{R}_i-\mathbf{R}_j))$. Because of the two-atom basis, the Bloch *ansatz* for the eigenfunctions is a linear combination of Bloch sums[2] on each sublattice:

$$\Psi(\mathbf{k},\mathbf{r}) = c_A(\mathbf{k})\tilde{p}_z^A(\mathbf{k},\mathbf{r}) + c_B(\mathbf{k})\tilde{p}_z^B(\mathbf{k},\mathbf{r}), \tag{2.4}$$

where

$$\tilde{p}_z^A(\mathbf{k},\mathbf{r}) = \frac{1}{\sqrt{N_{\text{cells}}}}\sum_j \mathrm{e}^{\mathrm{i}\mathbf{k}\cdot\mathbf{R}_j} p_z(\mathbf{r}-\mathbf{r}_A-\mathbf{R}_j), \tag{2.5}$$

$$\tilde{p}_z^B(\mathbf{k},\mathbf{r}) = \frac{1}{\sqrt{N_{\text{cells}}}}\sum_j \mathrm{e}^{\mathrm{i}\mathbf{k}\cdot\mathbf{R}_j} p_z(\mathbf{r}-\mathbf{r}_B-\mathbf{R}_j), \tag{2.6}$$

where $\mathbf{k}$ is the electron wavevector, N_{cells} the number of unit cells in the graphene sheet, and $\mathbf{R}_j$ is a Bravais lattice point. In the following, we will neglect the overlap $s = \langle p_z^A | p_z^B\rangle$ between neighboring p_z orbitals. Then, the Bloch sums form an orthonormal set:

$$\langle \tilde{p}_z^\alpha(\mathbf{k}) \mid \tilde{p}_z^\beta(\mathbf{k}')\rangle = \delta_{\mathbf{k},\mathbf{k}'}\delta_{\alpha,\beta}, \tag{2.7}$$

where $\alpha,\beta = A,B$. Using these orthogonality relations in the Schrödinger equation, $\mathcal{H}\Psi(\mathbf{k},\mathbf{r}) = E\Psi(\mathbf{k},\mathbf{r})$, one obtains a 2×2 eigenvalue problem,

$$\begin{pmatrix} \mathcal{H}_{AA}(\mathbf{k}) & \mathcal{H}_{AB}(\mathbf{k}) \\ \mathcal{H}_{BA}(\mathbf{k}) & \mathcal{H}_{BB}(\mathbf{k}) \end{pmatrix} \begin{pmatrix} c_A(\mathbf{k}) \\ c_B(\mathbf{k}) \end{pmatrix} = E(\mathbf{k}) \begin{pmatrix} c_A(\mathbf{k}) \\ c_B(\mathbf{k}) \end{pmatrix}. \tag{2.8}$$

The matrix elements of the Hamiltonian are given by

$$\mathcal{H}_{AA}(\mathbf{k}) = \frac{1}{N_{\text{cells}}}\sum_{i,j} \mathrm{e}^{\mathrm{i}\mathbf{k}\cdot(\mathbf{R}_j-\mathbf{R}_i)} \langle p_z^{A,\mathbf{R}_i} \mid \mathcal{H} \mid p_z^{A,\mathbf{R}_j}\rangle, \tag{2.9}$$

$$\mathcal{H}_{AB}(\mathbf{k}) = \frac{1}{N_{\text{cells}}}\sum_{i,j} \mathrm{e}^{\mathrm{i}\mathbf{k}\cdot(\mathbf{R}_j-\mathbf{R}_i)} \langle p_z^{A,\mathbf{R}_i} \mid \mathcal{H} \mid p_z^{B,\mathbf{R}_j}\rangle, \tag{2.10}$$

with $\mathcal{H}_{AA} = \mathcal{H}_{BB}$ and $\mathcal{H}_{AB} = \mathcal{H}_{BA}^*$, and introducing the notation $p_z^{A,\boldsymbol{\tau}} = p_z(\mathbf{r}-\mathbf{r}_A-\boldsymbol{\tau})$ and $p_z^{B,\boldsymbol{\tau}} = p_z(\mathbf{r}-\mathbf{r}_B-\boldsymbol{\tau})$. After simple manipulations, and by restricting the interactions to first-nearest-neighbors only, one gets:

$$\begin{aligned}\mathcal{H}_{AB}(\mathbf{k}) &= \langle p_z^{A,0}|\mathcal{H}|p_z^{B,0}\rangle + \mathrm{e}^{-\mathrm{i}\mathbf{k}\cdot\mathbf{a}_1}\langle p_z^{A,0}|\mathcal{H}|p_z^{B,-\mathbf{a}_1}\rangle + \mathrm{e}^{-\mathrm{i}\mathbf{k}\cdot\mathbf{a}_2}\langle p_z^{A,0}|\mathcal{H}|p_z^{B,-\mathbf{a}_2}\rangle \\ &= -\gamma_0\alpha(\mathbf{k}),\end{aligned} \tag{2.11}$$

where γ_0 stands for the transfer integral between first neighbor π orbitals (typical values for γ_0 are 2.9–3.1 eV (Charlier et al. 1991; Dresselhaus et al. 2000)), and the function $\alpha(\mathbf{k})$ is given by

$$\alpha(\mathbf{k}) = (1 + \mathrm{e}^{-\mathrm{i}\mathbf{k}\cdot\mathbf{a}_1} + \mathrm{e}^{-\mathrm{i}\mathbf{k}\cdot\mathbf{a}_2}). \tag{2.12}$$

[2] Alternatively, one may proceed by writing the Hamiltonian and the eigenfunctions in matrix form, as shown in the supplementary material on the authors' website.

Taking $\langle p_z^{A,0}|\mathcal{H}|p_z^{A,0}\rangle = \langle p_z^{B,0}|\mathcal{H}|p_z^{B,0}\rangle = 0$ as the energy reference, we can write $\mathcal{H}(\mathbf{k})$ as

$$\mathcal{H}(\mathbf{k}) = \begin{pmatrix} 0 & -\gamma_0\alpha(\mathbf{k}) \\ -\gamma_0\alpha(\mathbf{k})^* & 0 \end{pmatrix}. \tag{2.13}$$

This 2×2 Hamiltonian is very appealing and may also be written in terms of Pauli matrices as in Haldane (1988), thereby emphasizing the analogy with a spin Hamiltonian.[3] Section 2.2.2 derives in detail the consequences of the A/B bipartite lattice structure on the (pseudo)-spinor symmetry of (four-component) electronic eigenstates. The energy dispersion relations are easily obtained from the diagonalization of $\mathcal{H}(\mathbf{k})$ given by Eq. (2.13):

$$E_\pm(\mathbf{k}) = \pm\gamma_0|\alpha(\mathbf{k})| \tag{2.14}$$

$$= \pm\gamma_0\sqrt{3 + 2\cos(\mathbf{k}\cdot\mathbf{a}_1) + 2\cos(\mathbf{k}\cdot\mathbf{a}_2) + 2\cos(\mathbf{k}\cdot(\mathbf{a}_2 - \mathbf{a}_1))}, \tag{2.15}$$

which can be further expanded as

$$E_\pm(k_x, k_y) = \pm\gamma_0\sqrt{1 + 4\cos\frac{\sqrt{3}k_x a}{2}\cos\frac{k_y a}{2} + 4\cos^2\frac{k_y a}{2}}. \tag{2.16}$$

The wavevectors $\mathbf{k} = (k_x, k_y)$ are chosen within the first hexagonal Brillouin zone (BZ). Clearly, the zeros of $\alpha(\mathbf{k})$ correspond to the crossing of the bands with the $+$ and $-$ signs. One can verify that $\alpha(\mathbf{k} = \mathbf{K}_+) = \alpha(\mathbf{k} = \mathbf{K}_-) = 0$, and therefore the crossings occur at the points $\mathbf{K}_+$ and $\mathbf{K}_-$. Furthermore, with a single p_z electron per atom in the π–π^* model (the three other s, p_x, p_y electrons fill the low-lying σ band), the $(-)$ band (negative energy branch) in Eq. (2.16) is fully occupied, while the $(+)$ branch is empty, at least for electrically neutral graphene. Thus, the Fermi level E_F (or charge neutrality point) is the zero-energy reference in Fig. 2.3 and the Fermi surface is composed of the set of K_+ and K_- points. Graphene displays a metallic (zero-gap) character. However, as the Fermi surface is of zero dimension (since it is reduced to a discrete and finite set of points), the term semimetallic or zero-gap semiconductor is usually employed. Expanding Eq. (2.16) for $\mathbf{k}$ in the vicinity of $\mathbf{K}_+$ (or $\mathbf{K}_-$), $\mathbf{k} = \mathbf{K}_+ + \delta\mathbf{k}$ ($\mathbf{k} = \mathbf{K}_- + \delta\mathbf{k}$), yields a linear dispersion for the π and π^* bands near these six corners of the 2D hexagonal Brillouin zone,

$$E_\pm(\delta\mathbf{k}) = \pm\hbar v_F|\delta\mathbf{k}|, \tag{2.17}$$

[3] Writing the Hamiltonian in terms of Pauli matrices allows us to also classify the terms according to their symmetries. A particularly important one is electron–hole symmetry. The Hamiltonian is said to have electron–hole symmetry if there is a transformation $\mathcal{P}$, such that $\mathcal{P}^\dagger\mathcal{H}\mathcal{P} = -\mathcal{H}$. This guarantees that if Ψ is an eigenstate of $\mathcal{H}$ with a positive energy E (electron function), then $\mathcal{P}\Psi$ is also an eigenstate with energy $-E$ (hole function) and the spectrum is symmetric with respect to $E = 0$. For a Hamiltonian as the one here, a term proportional to σ_z (such as a staggering potential which breaks A–B symmetry) opens a gap but preserves electron–hole symmetry.

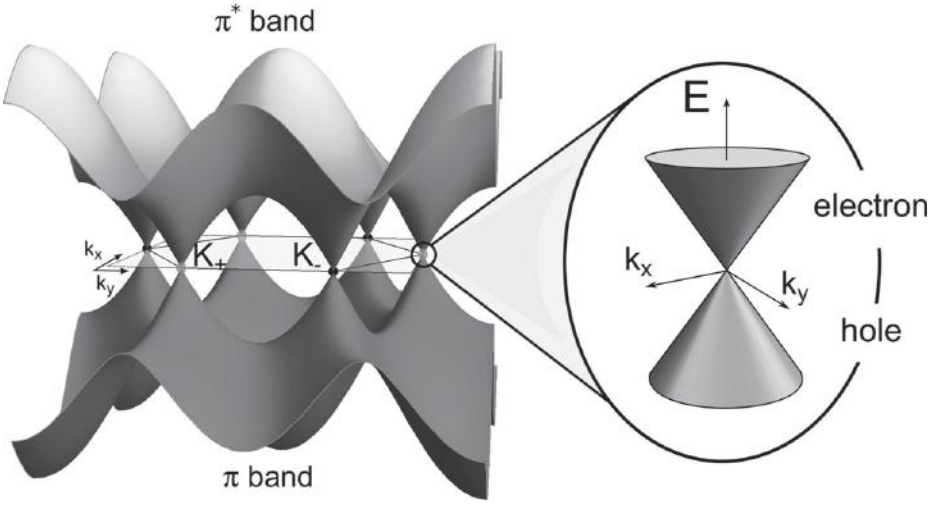

Figure 2.3 Graphene π and π^* electronic bands. In this simple approach, the π and π^* bands are symmetric with respect to the valence and conduction bands. The linear dispersion relation close to the K_+ (light gray dots) and K_- (black dots) points of the first 2D Brillouin zone gives rise to the "Dirac cones" as shown on the right. Note that close to these cones k_x and k_y are used to denote the shift from the corresponding K point.

where

$$v_F = \frac{\sqrt{3}\gamma_0 a}{2\hbar} \tag{2.18}$$

is the electronic group velocity. Graphene is thus highly peculiar for this linear energy–momentum relation and electron–hole symmetry. The electronic properties in the vicinity of these corners of the 2D Brillouin zone mimic those of *massless* Dirac fermions (developed in Section 2.2.2) forming "Dirac cones" as illustrated in Fig. 2.3. The six points where the Dirac cones touch are referred to as the Dirac points. The electronic group velocities close to those points are quite high at $\sim 8.5 \times 10^5$ m/s, and within the massless Dirac fermions analogy, represent an effective "speed of light."

This simple orthogonal *tight-binding* model (Wallace 1947) yields π and π^* zone-center Γ energies, which are symmetric ($\pm\gamma_0$) with respect to E_F. In fact, the antibonding (unoccupied) π^* bands are located at a higher energy if the overlap integral S is not set to zero (as illustrated in Fig. 2.1(b)). A better (but more complicated) $\pi - \pi^*$ parameterization could lead to analogous results (Reich et al. 2002), as well as more accurate first-principles calculations. In the following, after a presentation of the effective massless Dirac fermion model, we comment on the effects beyond nearest-neighbor interactions and the so-called trigonal warping correction.

2.2.2 Effective Description Close to the Dirac Point and Massless Dirac Fermions

By expanding Eq. (2.13) for the Hamiltonian around K_+ and K_- (the two inequivalent corners of the Brillouin zone) we get an approximation close to those points. To keep a compact notation in what follows, $\mathbf{k}$ measures the deviations from those points. A linear expansion then gives

$$\mathcal{H}_{K_+} = \hbar v_F \begin{pmatrix} 0 & k_x - ik_y \\ k_x + ik_y & 0 \end{pmatrix} = v_F(p_x\sigma_x + p_y\sigma_y), \tag{2.19}$$

where $p_{x(y)} = \hbar k_{x(y)}$ and the Pauli matrices are defined as usual:

$$\sigma_x = \begin{pmatrix} 0 & 1 \\ 1 & 0 \end{pmatrix}, \ \sigma_y = \begin{pmatrix} 0 & -i \\ i & 0 \end{pmatrix}, \ \sigma_z = \begin{pmatrix} 1 & 0 \\ 0 & -1 \end{pmatrix}. \tag{2.20}$$

The effective Hamiltonian can also be written in the more compact form:

$$\mathcal{H}_{K_+} = v_F \hat{\boldsymbol{\sigma}} \cdot \mathbf{p}, \tag{2.21}$$

where $\hat{\boldsymbol{\sigma}} = (\sigma_x, \sigma_y, \sigma_z)$. For the inequivalent K point, the transposed Hamiltonian is given as:

$$\mathcal{H}_{K_-} = \mathcal{H}^t_{K_+}. \tag{2.22}$$

Substituting $\mathbf{p}$ by the corresponding operator $\hat{\mathbf{p}} = -\mathrm{i}\hbar\hat{\nabla}$ in Eq. (2.21) – this is equivalent to the $\boldsymbol{k} \cdot \boldsymbol{p}$ or effective mass approximation (Ajiki 1993; DiVicenzo & Mele 1984) – a form equivalent to the Dirac–Weyl Hamiltonian in two dimensions is obtained, which in quantum electrodynamics follows from the Dirac equation by setting the rest mass of the particle to zero. Therefore, the low-energy excitations mimic those of massless Dirac particles of spin 1/2 (such as a massless neutrino), with velocity of light c, and inherent chirality as explained below. However, in contrast to relativistic Dirac particles, low-energy excitations of graphene have a Fermi velocity v_F about 300 times smaller than the light velocity, whereas the Pauli matrices appearing in the low-energy effective description operate on the sublattice degrees of freedom instead of spin, hence the term *pseudospin*. The low-energy quasiparticles in graphene are often referred to as massless Dirac fermions.

One of the most interesting properties of the Dirac–Weyl equation is its helical or chiral nature[4] which is a direct consequence of the Hamiltonian being proportional to the helicity operator, which here for the case of the Hamiltonian in Eq. (2.21) is defined as

$$\hat{h} = \hat{\boldsymbol{\sigma}} \cdot \frac{\mathbf{p}}{|\mathbf{p}|}. \tag{2.23}$$

The quantity $\hat{h}$ is essentially the projection of the sublattice pseudospin operator $\hat{\sigma}$ on the momentum direction. Interestingly, since $\hat{h}$ commutes with the Hamiltonian, the projection of the pseudospin is a well-defined conserved quantity, which can be either positive or negative, corresponding to pseudospin and momentum being *parallel* or

[4] For massless particles the terms Dirac equation and Weyl equation are used interchangeably.

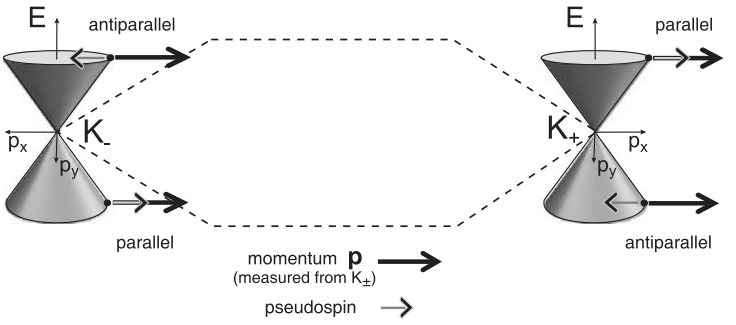

Figure 2.4 The two inequivalent Dirac cones at K_+ and K_- points of the first Brillouin zone, together with direction of the pseudospin parallel or antiparallel to the momentum $\mathbf{p}$ of selected energies in conduction and valence bands.

antiparallel to each other (see Fig. 2.4). At the K_- point, the Hamiltonian is proportional to $\hat{\sigma}^t \cdot \mathbf{p}$ and involves the *left-handed* Pauli matrices $\hat{\sigma}^t$ (in contrast to the right-handed matrices $\hat{\sigma}$). Therefore, one says that chirality is inverted when passing from K_+ to K_- as represented in Fig. 2.4.

To explore this in more detail, let us rewrite once more the Hamiltonian as

$$\mathcal{H}_\xi(\mathbf{p}) = v_F|\mathbf{p}| \begin{pmatrix} 0 & \mathrm{e}^{-\mathrm{i}\xi\theta_p} \\ \mathrm{e}^{+\mathrm{i}\xi\theta_p} & 0 \end{pmatrix}, \tag{2.24}$$

where $p_x + \mathrm{i}p_y = \sqrt{p_x^2 + p_y^2}\mathrm{e}^{\mathrm{i}\theta_p}$, $\theta_p = \arctan(p_y/p_x)$, and ξ can take the values $\xi = +1$ which corresponds to K_+ and $\xi = -1$ which corresponds to K_-. Then, one can verify that this Hamiltonian is diagonalized by the unitary operator

$$\mathcal{U}_\xi = \frac{1}{\sqrt{2}} \begin{pmatrix} -\mathrm{e}^{-\mathrm{i}\xi\theta_p} & \mathrm{e}^{-\mathrm{i}\xi\theta_p} \\ 1 & 1 \end{pmatrix}. \tag{2.25}$$

Indeed,

$$\mathcal{U}_\xi^\dagger(\mathbf{p})\mathcal{H}_\xi(\mathbf{p})\mathcal{U}_\xi(\mathbf{p}) = v_F \begin{pmatrix} -|\mathbf{p}| & 0 \\ 0 & |\mathbf{p}| \end{pmatrix} = -v_F|\mathbf{p}|\sigma_z, \tag{2.26}$$

which makes explicit the linear energy dispersion $E_\pm(\mathbf{p}) = \pm v_F|\mathbf{p}|$ and the electron–hole symmetry.[5] On the other hand, the eigenstates of Eq. (2.24) can be written as

$$|\Psi_{\xi,s}\rangle = \frac{1}{\sqrt{2}} \begin{pmatrix} 1 \\ s\mathrm{e}^{+\mathrm{i}\xi\theta_p} \end{pmatrix}. \tag{2.27}$$

The index $s = \pm 1$ is the band index ($s = +1$ for the conduction band and $s = -1$ for the valence band) and ξ the valley index as stated before ($\xi = +1$ (K_+), $\xi = -1$ (K_-)). Using this explicit form for the eigenstates, we can directly verify that they are

[5] Also, by comparison with the relativistic expression, $E(p) = \pm\sqrt{p^2v_F^2 + m^{*2}c^4}$ enforces a zero effective mass.

also eigenstates of the appropriate helicity operator (also called chirality operator) with eigenvalues ± 1.

Around K_+ ($\xi = +1$), the pseudospin of eigenstates in the conduction band is parallel to the momentum and antiparallel for eigenstates in the valence band. The chirality in this case is simply the band index. The property around K_- ($\xi = -1$) is reversed as illustrated in Fig. 2.4. This peculiarity has a strong influence in many of the most intriguing properties of graphene. For example, for an electron to backscatter (i.e., changing $\mathbf{p}$ to $-\mathbf{p}$) it needs to reverse its pseudospin. But as the pseudospin direction is locked to that of momentum, backscattering is not possible if the Hamiltonian is not perturbed by a term which flips the pseudospin. (This is also termed *absence of backscattering* (Ando et al. 1998).)

Although we are dealing all the time with both valleys separately, it is important to keep in mind that the full structure of the eigenstates is described by a four-component spinor wavefunction, $(|\Psi_{K_+,A}\rangle, |\Psi_{K_+,B}\rangle, |\Psi_{K_-,A}\rangle, |\Psi_{K_-,B}\rangle)^t$. The full Hamiltonian of ideal graphene is given by

$$\hat{\mathcal{H}} = v_F \begin{pmatrix} 0 & \pi^\dagger & 0 & 0 \\ \pi & 0 & 0 & 0 \\ 0 & 0 & 0 & \pi \\ 0 & 0 & \pi^\dagger & 0 \end{pmatrix}, \tag{2.28}$$

with $\pi = p_x + \mathrm{i}p_y$ and $\pi^\dagger = p_x - \mathrm{i}p_y$. Although for this ideal case, the states at both k points are decoupled, one should be aware that any perturbation which is not smooth at the atomic scale (e.g., due to impurities) will couple them.

One notes that this peculiar electronic band structure of graphene yields a specific behavior of the total density of states which can be written

$$\rho(E) = \int \frac{dk_x dk_y}{(2\pi)^2} \delta(E - \varepsilon_k) = \frac{2|E|}{(\pi \hbar^2 v_F^2)}, \tag{2.29}$$

while the carrier density is given by

$$n(E) = \frac{sgn(E)(E^2)}{(\pi \hbar^2 v_F^2)}. \tag{2.30}$$

2.2.3 Electronic Properties of Graphene beyond the Linear Approximation

The description of quasiparticles as massless Dirac fermions is accurate for low-energy excitations. However, it may be necessary to refine the model by including the deformation of the electronic band structure, which is particularly important for higher energies (trigonal warping). This can be captured by a development of the electronic dispersion up to second order in momentum shift with respect to the $K_\pm$ points. Finally, in very clean graphene, electron–electron interaction can induce some low-energy renormalization of the electronic bands and wavepacket velocity. All these effects are briefly reviewed in the following sections.

Trigonal Warping Corrections

It is important to know that deviations from the linear dispersion of the energy bands away from the Fermi level are designated as *trigonal warping*. Indeed, when expanding the full band structure close to one of the Dirac points ($\mathbf{k} = \mathbf{K}_\pm + \mathbf{p}/\hbar$ with $\mathbf{p}/\hbar \ll |\mathbf{K}_\pm|$), the energy dispersion is given by

$$E_\pm(p) \simeq \pm v_F|\mathbf{p}| + \mathcal{O}\left[\left(\frac{p}{\hbar K_\pm}\right)^2\right], \tag{2.31}$$

where $\mathbf{p}$ is the momentum measured relatively to the Dirac point and $v_F = \sqrt{3}\gamma_0 a/2\hbar$, the Fermi velocity. The expansion of the spectrum around the Dirac point up to the second order in p, and including second-nearest-neighbor interaction ($\gamma_0^{(2)}$) gives

$$E_\pm(\mathbf{p}) \simeq 3\gamma_0^{(2)} \pm v_F|\mathbf{p}| - \left(\frac{9\gamma_0^{(2)}a^2}{4} \pm \frac{3\gamma_0 a^2}{8}\sin(3\theta_p)\right)|\mathbf{p}|^2, \tag{2.32}$$

where $\theta_p = \arctan(p_x/p_y)$ is the angle in momentum space. Note that the presence of $\gamma_0^{(2)}$ shifts the position of the Dirac point in energy, thus breaking the electron–hole symmetry. Consequently, up to order $(p/\hbar K_\pm)^2$, the dispersion depends on the p direction in momentum space and has a threefold symmetry. This is the so-called trigonal warping of the electronic spectrum (Ando et al. 1998; Dresselhaus & Dresselhaus 2002). (See also Problem 2.10.)

Effects beyond Nearest Neighbors and Comparison with First-Principles Calculations

Most *tight-binding* (TB) studies use a first-nearest-neighbors π–π^* scheme to describe graphene's electronic properties. However, when compared to *ab initio* calculations, this simplified TB approach predicts the electronic energies correctly in a limited energy range. A better, but more complicated, π–π^* parameterization has been proposed in the literature for both graphene (Reich et al. 2002) and few-layer graphene (Grüneis et al. 2008).

When interactions are included up to the third-nearest-neighbors (3rd nn), the resulting two centers third nearest-neighbors nn π–π^* orthogonal TB model turns out to be much more efficient (Lherbier et al. 2012), accurately describing first-principles results over the entire Brillouin zone. In contrast to the 1st nn π–π^* model, which produces a totally symmetric band structure, the 3rd nn TB model recovers the asymmetry between valence and conduction van Hove singularities, and the agreement with *ab initio* band structures is quite satisfactory, as illustrated in Fig. 2.5. The 3rd nn parameters of the TB model used to construct these band structures (Fig. 2.5) are only composed of a single on-site energy term ε_{p_z} and three hopping terms $\gamma_0^{(1)} = \gamma_0$, $\gamma_0^{(2)}$, and $\gamma_0^{(3)}$ corresponding to 1st, 2nd, and 3rd nn interactions, respectively. The pristine graphene Hamiltonian then reads as

$$H = \sum_i \varepsilon_{p_z}|\phi_i\rangle\langle\phi_i| + \sum_{i,\langle j,k,l\rangle}\left(\gamma_0^{(1)}|\phi_j\rangle\langle\phi_i| + \gamma_0^{(2)}|\phi_k\rangle\langle\phi_i| + \gamma_0^{(3)}|\phi_l\rangle\langle\phi_i| + h.c.\right), \tag{2.33}$$

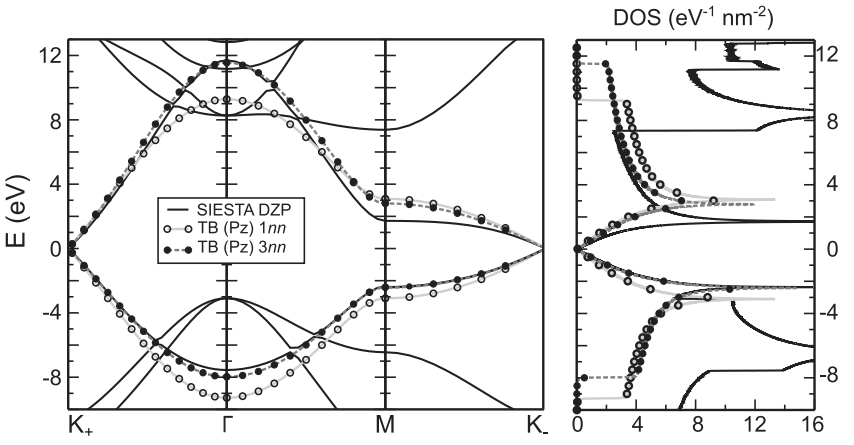

Figure 2.5 Electronic band structures and density of states (DOS) computed using the SIESTA code with a double-ζ polarized (DZP) basis set (full lines) along K–Γ–M–K path for a 1×1 supercell (unit cell). The TB band structures for a first nearest-neighbors model (1nn, lines with open circle symbols) and for a third nearest-neighbors model (3nn, lines with filled circle symbols) are also plotted. Fermi energy is set to zero. (Adapted with permission from Lherbier et al. (2012). Copyright (2012) by the American Physical Society)

with $\varepsilon_{p_z} = 0.6\,\text{eV}$, and $\gamma_0^{(1)} = -3.1\,\text{eV}$, $\gamma_0^{(2)} = 0.2\,\text{eV}$, and $\gamma_0^{(3)} = -0.16\,\text{eV}$. The sum on index i runs over all carbon p_z orbitals. The sums over j, k, l indexes run over all p_z orbitals corresponding respectively to 1st, 2nd, and 3rd nearest neighbors of the ith p_z orbital. In Fig. 2.5, the TB band structure (lines with symbols) is superimposed on the *ab initio* band structure (full lines). A good agreement is obtained, especially for the valence bands. The conduction band side seems to be a little bit less accurate but this is uniquely due to the inability of the pristine graphene TB model to reproduce the conduction band along the K–M branch.

The *ab initio* electronic bands of graphene (Charlier et al. 2007) along the high-symmetry $M-\Gamma-K$ directions are presented in Fig. 2.6.[6] Its space group ($P3m$) contains a mirror symmetry plane, allowing symmetric σ and antisymmetric π states to be distinguishable. In a 2D crystal, a parallel mirror symmetry operation separates the eigenstates for the whole Brillouin zone, and not only along some high-symmetry axis. The π and π^* bands cross at the vertices of the hexagonal Brillouin zone (vertices labeled by their momentum vector usually denoted by K_+ and K_- as mentioned above). *Ab initio* calculations confirm that the π and π^* bands are quasilinear (linear very close to K_+ or K_- and near the Fermi energy), in contrast with the quadratic energy–momentum relation obeyed by electrons at band edges in conventional semiconductors. When several interacting graphene planes are stacked as in few-layer graphite (nGLs) or in the perfect graphite crystal, the former antisymmetric π bands are split owing to

[6] Note that in plots like the one in Fig. 2.6, the dispersion does not depend on the K point (K_+ or K_-) selected for the path in the Brillouin zone (horizontal axis in that figure). Therefore, it is usual to call this point generically K. Notwithstanding, one must remember that pseudospin is different on each valley.

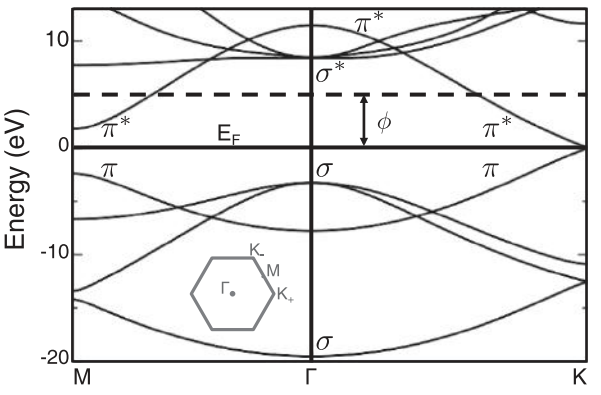

Figure 2.6 Electronic band structure of graphene. The bonding σ and the antibonding σ^* bands are separated by a large energy gap. The bonding π (highest valence band) and the antibonding π^* (lowest conduction band) cross at the K_+ (and K_-) points of the Brillouin zone. The Fermi energy (E_F) is set to zero and ϕ indicates the work function. Above the vacuum level (dashed horizontal line), the states of the continuum are difficult to describe and merge with the σ^* bands. The 2D hexagonal Brillouin zone is illustrated in the inset with the high-symmetry points Γ, M, K_+, and K_-. (Adapted with permission from Charlier et al. (2007). Copyright (2007) by the American Physical Society)

bonding or antibonding patterns, whereas the σ bands are much less affected by the stacking, as explained in the next section.

Interaction-Driven Distortions at the Dirac Point

Although *ab initio* DFT calculations confirm the *tight-binding* linear dispersion picture, the estimation of the Fermi velocity v_F was found to be smaller by 15–20% than the experimental value (Calandra & Mauri 2007). Consequently, the role of electron–electron self-energy effects in the quasiparticle (QP) band structures and the Fermi velocity has been clarified (Siegel et al. 2011, Trevisanutto et al. 2008). With respect to the density-functional theory within the local-density approximation (Fig. 2.7(a)), the Fermi velocity is renormalized with an increase of 17%, such that it corrects the DFT underestimation and leads to a value of 1.12×10^6 m/s (Trevisanutto et al. 2008), in good agreement with accurate magnetotransport measurement of 1.1×10^6 m/s (Zhang et al. 2005). Furthermore, the nearly linear DFT band dispersion in GW is considerably distorted. Close to the Dirac point, the self-energy results in an unusually negative GW bandgap correction and the appearance of a kink in the band structure (Fig. 2.7(b)), which is due to a coupling with the π plasmon at ∼5 eV and the low-energy $\pi \rightarrow \pi^*$ single-particle excitations.

By measuring the cyclotron mass in suspended graphene with carrier concentrations which varied by three orders of magnitude, Elias et al. (2011) showed departures from linear behavior due to electron–electron interactions (with increasing v_F near the Dirac point). Interestingly, no gap was found even at energies as close as 0.1 meV to the Dirac point and no new interaction-driven phases were observed. This suggests that if there is a gap in graphene, it is not larger than 0.1 meV.

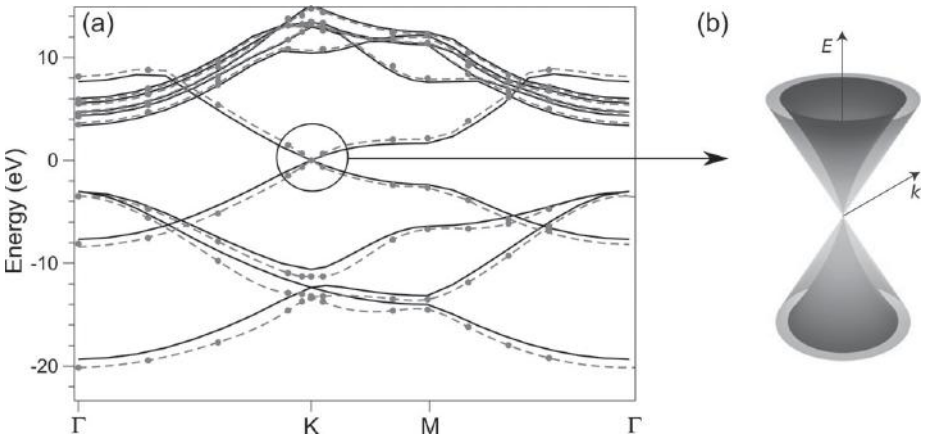

Figure 2.7 Many-body effects in graphene: (a) electronic band structures calculated within both DFT-LDA (solid lines) and GW (circles and dashed lines) approaches; (b) reshaping of the Dirac cone due to the interaction-driven renormalization (increase) of the Fermi velocity at low momenta. The outer cone represents the linear Dirac spectrum without many-body effects. ((a) Reproduced from Trevisanutto et al. (2008). Copyright (2008) by the American Physical Society. (b) Reprinted with permission from Macmillan Publishers Ltd: *Nature Physics* (Elias et al. 2011), copyright (2011))

Consequently, the quasiparticle properties of graphene are modified by the presence of long-range Coulomb interactions. Their effects are especially pronounced when the Fermi energy is close to the Dirac point, and can result in strong renormalization of the Dirac band structure (the Fermi velocity v_F) and a reconstruction of the Dirac cone structure near the charge neutrality point. Consequently, many electronic characteristics and transport phenomena are strongly affected by these many-body effects that are sensitive to the value of the Coulomb interaction constant in graphene.

In the preceding pages, the electronic properties of two-dimensional graphene have been described using either an effectively massless Dirac fermion model in the vicinity of the charge neutrality point or using a *tight-binding* approach within the nearest-neighbors approximation. Refinements of the electronic band structure have been obtained by going beyond the linear approximation, including trigonal warping effects, extending the *tight-binding* model to third nearest neighbors, or by performing full first-principles calculations, including GW corrections. Actually, both DFT and GW simulations confirm the low-energy linear energy dispersion close to the charge neutrality point, although renormalized Fermi velocity is obtained owing to many-body effects (long-range Coulomb interactions) at the Dirac point. In Section 2.3, the effect of the stacking on the electronic properties of few-layer graphene is highlighted.

2.3 Electronic Properties of Few-Layer Graphene

Bulk 3D graphites are semi-metallic materials, which exhibit very peculiar electronic properties. Indeed, the first semi-empirical models for Bernal (or *ABAB*-stacking)

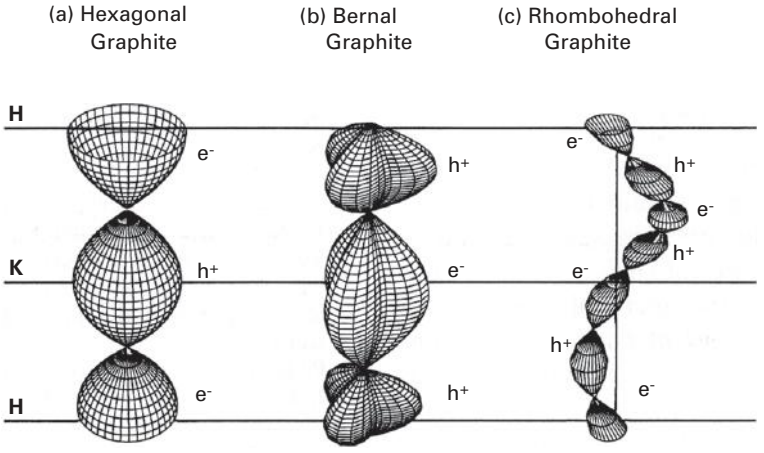

Figure 2.8 Electronic properties of graphite(s) with various stacking: Fermi surfaces of (a) simple hexagonal graphite (*AAA*-stacking), (b) Bernal graphite (*ABAB*-stacking), and (c) rhombohedral graphite (*ABC*-stacking). The three Fermi surfaces are centered on the vertical $H-K-H$ edge of the 3D Brillouin zone. Electron and hole pockets are labeled using e^- and h^+, respectively. (Reprinted from Charlier et al. (1994a), copyright (1994), with permission from Elsevier)

(McClure 1957; Slonczewski & Weiss 1958) and rhombohedral (or *ABC*-stacking) graphites (Haering 1958; McClure 1969) have demonstrated that the shape of the Fermi surface, and consequently the nature of the charge carriers, are strongly dependent upon the geometry of the stacking between layers. The Fermi surfaces of these two graphite structures are represented in Fig. 2.8, and compared to the "ideal" simple hexagonal case (*AAA*-stacking) where all graphene planes are piled up exactly on top of each other. Fermi surfaces are located along the $H-K-H$ edge of the 3D Brillouin zones and exhibit a complex shape due to the coexistence of holes and electrons at the charge neutrality point (Charlier et al. 1991, 1992, 1994a).

Analogously, since few-layer graphenes are intermediate quasi-2D crystals between bulk graphite(s) and graphene, their electronic structures will be reminiscent of both of them. The weak interlayer interaction that creates the band dispersion out of the basal plane in graphite(s) is now responsible for the band mixing between isolated graphene bands occurring in few-layer graphene. Since coexistence of carriers is only possible when different bands are present in the same energy range, the number of layers and the dependence of geometry of the interlayer interaction are key parameters influencing the transport properties in these quasi-2D graphene-based systems.

In bilayer graphene (*AB*-stacking), due to symmetry reasons, the $P\bar{3}m1$ group does not contain the horizontal mirror plane. Consequently, the valence band and conduction band only exhibit two contact points since they are not degenerated, except along the high-symmetry axes, thus avoiding any deep domain of coexistence of electrons and holes (Fig. 2.9(a)). The close-up of the overlapping region clearly demonstrates the loss of the linear dispersion of the kinetic energy of the charge carriers ($E \propto k$) previously obtained for graphene (Latil & Henrard 2006; Varchon et al. 2007). Indeed, the band

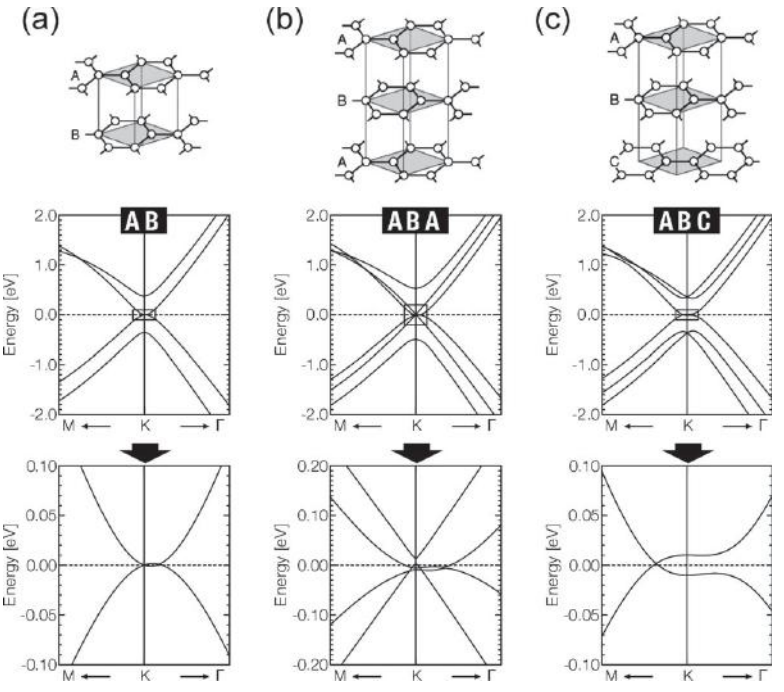

Figure 2.9 Electronic properties of few-layer graphene: band structures in the vicinity of *K*, and near the Fermi level (zero energy), for: (a) bilayer graphene (*ABC*-stacking); (b) trilayer graphene (*ABA*-stacking); and (c) trilayer graphene (*ABC*-stacking). (Adapted with permission from Latil & Henrard (2006). Copyright (2006) by the American Physical Society)

structures of the bilayer system present a parabolic shape ($E \propto k^2$) along the high-symmetry axes. In addition, both band extrema are actually saddle points (delimiting a pseudogap $\varepsilon_{\text{psg}} \sim 3\,\text{meV}$), and the real overlap between the two touching points (*K* itself and one point along the $K - \Gamma$ axis) is $\delta\varepsilon \sim 1\,\text{meV}$ (Latil & Henrard 2006). Unfortunately, this domain of coexistence is far too narrow to be visible experimentally. Nevertheless, the important feature that is preserved is the absence of a bandgap since the upper valence band touches the lower conduction band at the *K* point of the Brillouin zone. However, theoretically a significant bandgap could be induced by lowering the symmetry of the system through the application of a perpendicular electric field (Castro et al. 2007). Indeed, a bilayer graphene-based material has been produced experimentally, exhibiting an electrically tunable bandgap, a phenomenon of great significance for both basic physics and its applications (Mak et al. 2009).

Regarding the trigonal warping corrections discussed before for monolayer graphene, we note that this effect turns out to be strong only close to the charge neutrality point in this case. *Tight-binding* models developed for graphite can be easily extended to the bilayer structure, which presents *AB*-stacking as in 3D bulk graphite. The set of hopping parameters for graphene has to be completed with $\gamma_1 \simeq 0.4\,\text{eV}$ (hopping energy between A_1 and A_2 atoms from the two layers), $\gamma_4 \simeq 0.04\,\text{eV}$ (hopping energy between A_1 (A_2)

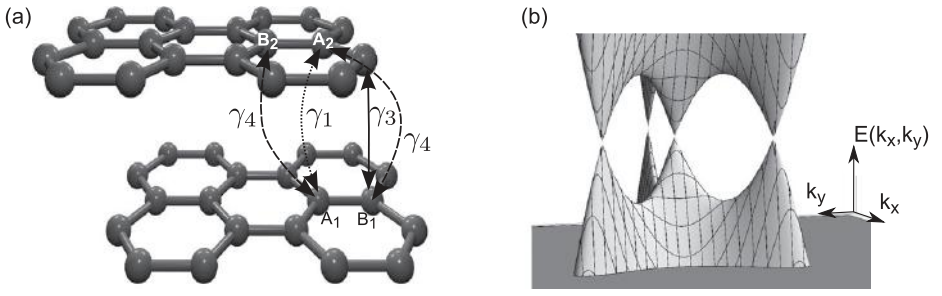

Figure 2.10 (a) Model of bilayer graphene where the hopping parameters connecting different layers mentioned in the text are indicated. (b) The dispersion relation of bilayer graphene very close to the charge neutrality point splits into four pockets when γ_3 is considered. (This contrasts dramatically with the parabolic dispersion that it is found when this term is ignored.)

and B_2 (B_1) atoms from the two layers), and $\gamma_3 \simeq 0.3$ eV (hopping interaction between B_1 and B_2; see Fig. 2.10(a). The hopping γ_4 leads to a k-dependent coupling between the sublattices. The same role is played by the inequivalence between sublattices within a layer. However, in this approximation, the γ_3 hopping term qualitatively changes the spectrum at low energies since it introduces a trigonal distortion, or warping, of the bands. Unlike the one introduced by a large momentum in Eq. (2.32), such trigonal warping drastically modifies the parabolic dispersions at the Dirac point at low energies ($\varepsilon < 5$ meV). The electron–hole symmetry is preserved but instead of two bands touching at $k = 0$, three sets of Dirac-like linear bands are obtained. The Dirac point is thus split in four pockets (see Fig. 2.10(b)), one Dirac point remaining at $\varepsilon = 0$ and $k = 0$, while the three other Dirac points, also at $\varepsilon = 0$, lie at three equivalent points with a finite momentum (McCann & Falko 2006; McCann et al. 2007) (see also Problem 2.11).

From the *AB* bilayer, trilayer graphene is constructed with an additional layer, keeping either the Bernal *ABA*-stacking pattern (Fig. 2.9(b)) or the rhombohedral *ABC*-stacking pattern (Fig. 2.9(c)). Indeed, when adding this third layer, electronic properties change, and two different situations arise depending on how this extra layer is stacked on the others.

The first possibility involves stacking the third layer so that it mirrors the first layer (Fig. 2.9(b)). Also referred to as Bernal or *ABA*-stacking, this arrangement has an electrical structure of overlapping linear and quadratic bands. The band structure of the *ABA* trilayer is characterized by band crossings in the vicinity of the Fermi level (Fig. 2.9(b)). The $P\bar{6}m2$ space group of the *ABA* trilayer contains the horizontal mirror symmetry, allowing the separation of the antisymmetric states and the symmetric ones. Moreover, the two symmetric bands exhibit a quasilinear dispersion (*massless fermions*); however, unlike monolayer graphene, a gap opens due to the nonequivalence of carbon atoms in the same layer ($\varepsilon_{\text{gap}} \sim 12$ meV). The band overlap between the top of the quasi-massless holes band and the electrons band is predicted to be of the order of a few meV (Latil & Henrard 2006).

The second possibility, known as rhombohedral or *ABC*-stacking, involves displacing the third layer with respect to the second layer in the same direction again as the second with respect to the first. As the first precursor of the "rhombohedral family," the electronic structure of *ABC* trilayer graphene has cubic dispersion ($E \propto k^3$). This means that for low carrier concentrations (which correspond to low momentum states) the relative kinetic energy of the particles in rhombohedral graphene's cubic bands will be less than that in bilayer graphene's quadratic bands, which is again less than monolayer graphene's linear bands. The band structure of the *ABC* trilayer ($P\bar{3}m1$ space group) exhibits a single crossing point between valence and conduction bands, located along the *K*–*M* axis (Fig. 2.9(c)). Consequently, any coexistence of charge carriers is strictly forbidden in this specific stacking. However, a graphene *quasi-massless* dispersion is preserved and bounded by a pseudogap $\varepsilon_{\text{psg}} \sim 18$ meV. The group velocities vary from $1.9–2.6 \times 10^5$ m/s (Latil & Henrard 2006).

But what happens when the number of layers is increased? *N* layers of graphene have approximately $2^{(N-2)}$ possible arrangements (Yacoby 2011). One of these arrangements is the natural extension of the *ABC*-stacked trilayer that consists of a multilayer with cyclic arrangement given by *ABCABCA*, and so on. The dispersion of such multilayers is predicted to have even lower kinetic energy ($E \propto k^N$). The reason that such electronic behavior has not yet been seen in graphite, the macroscopic form of multilayer graphene, is because natural graphite usually exhibits Bernal stacking where such effects would be absent. However, if effective ways of growing artificial few-layer graphene with rhombohedral stacking are found, *ABC* trilayer graphene might be a new playground to tailor the electronic properties of few-layer graphene-based nanostructures.

Moreover, *ab initio* calculations on bilayer and trilayer graphene (Latil et al. 2007) suggest that the massless fermion behavior, a typical signature of single-layer graphene, is preserved in incommensurate multilayered graphitic systems. Indeed, the linear dispersion is conserved in turbostratic multilayer systems despite the presence of adjacent layers (Fig. 2.11), thus predicting the presence of Dirac carriers in disoriented few-layer graphene. More generally, the electronic properties (and consequently the optical, vibrational, and transport properties) of a given FLG film are found to be controlled mainly by the misorientation of the successive layers rather than their number (Latil et al. 2007). Recent experiments have shown that a rotation among the different graphene layers can generate van Hove singularities which, interestingly, can be brought arbitrarily close to the Fermi energy when the angle of rotation is changed (Li, Luican et al. 2010), thereby opening promising opportunities for tuning the role of interactions in the material.[7]

To add even more excitement to this area, recent experiments and simulations in bilayer graphene (Kim et al. 2013) show that even tiny imperfections (stacking and twist

[7] The problem of rotated or twisted graphene layers is fascinating and many questions are still open. For example, from which rotation angle does a twisted bilayer behave as a monolayer? In Suárez Morell et al. (2010) it was suggested that this transition occurs at a finite angle of 1.5° (the magic angle) when decoupling is achieved. These issues have now resurfaced after the discovery of superconductivity in twisted bilayer graphene (Cao et al. 2018).

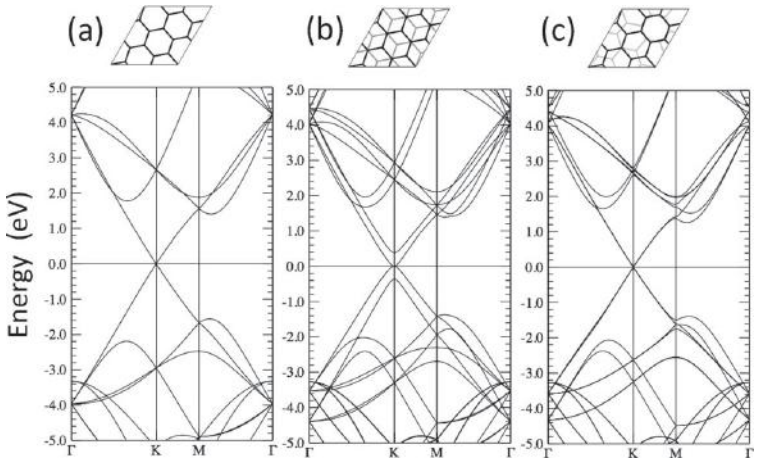

Figure 2.11 Electronic properties of single and bilayer graphenes: band structures of (a) single-layer; (b) Bernal bilayer; and (c) turbostratic bilayer in the vicinity of *K* point of the Brillouin zone and the Fermi energy. The corresponding supercells are also represented. (Adapted with permission from Latil et al. (2007). Copyright (2007) by the American Physical Society)

angle) can dramatically change the electronic structure. The ARPES data presented in Kim et al. (2013) show the coexistence of massive and massless Dirac fermions due to a distribution of twists as small as 0.1°.

In conclusion, the electronic properties of few-layer graphene (FLG) are quite complex and present exotic electronic states. Indeed, depending on the stacking geometry and on the number of layers, an FLG can be either metallic (with single or mixed carriers) or an extremely narrow-gap semiconducting 2D system.

In the next two sections, confinement effects will be described when the graphene sheet is cut in strips as for graphene nanoribbons or rolled up in cylinders such as carbon nanotubes. The remarkable properties of graphene derived close to the K_+ and K_- points are found to remain valid for 1D systems such as metallic nanotubes and wide armchair nanoribbons. However, other symmetries result in semiconducting systems with varying gaps. Semiconducting nanotubes and ribbons with increasing diameter (or width) show a linear downscaling of their associated energy gaps. By using proper boundary conditions, the electronic band structure of both types of system can be analytically derived, as illustrated in the following.

2.4 Electronic Properties of Graphene Nanoribbons

As mentioned above, the combination of high charge-carrier mobilities and long coherent lengths makes graphene an outstanding material for nanoscale electronics. However, this wonder material has an Achilles heel. The electric conduction cannot

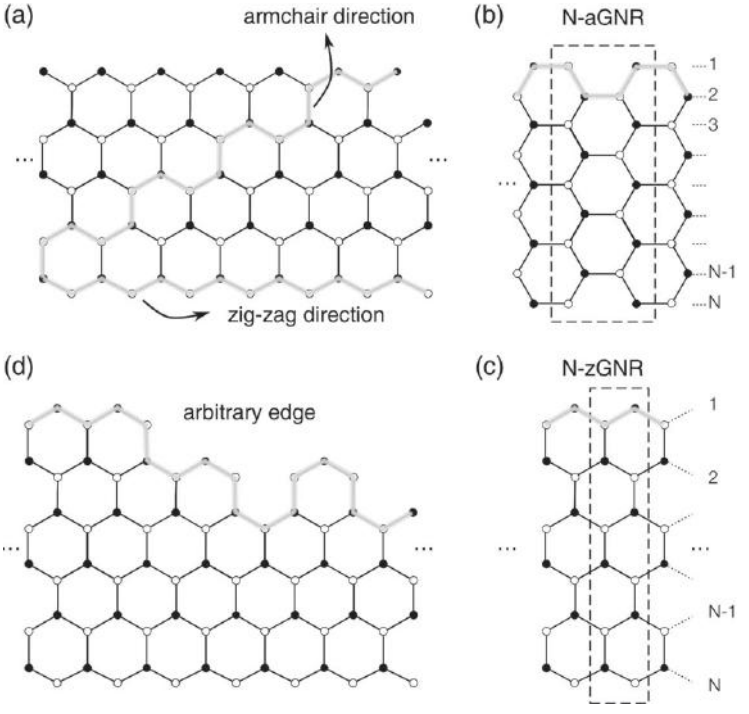

Figure 2.12 (a) Honeycomb lattice of graphene showing both armchair and zigzag directions. Ribbons with *armchair* and *zigzag* edges are shown in the schemes in (b) and (c), respectively, where the shape of the edges at the top of each scheme is highlighted with a gray shadow. Their corresponding 1D unit cells are marked with dashed boxes. A ribbon with a more general edge shape is shown in (d).

be turned off by, for example, changing a gate voltage as is usual in field-effect transistors. The ability to "turn off" graphene is crucial for achieving the control of the current flow needed in active electronic devices. Therefore, opening a bandgap in graphene is an important problem and many different creative ways of doing it have been proposed.[8] One possible solution is to use narrow strips of graphene, also called graphene nanoribbons (GNRs).

Graphene nanoribbons can be obtained by cutting a graphene sheet as shown in Fig. 2.12. If a certain direction is followed when cutting, two typical shapes are basically possible: the armchair edge (Fig. 2.12(b)) and the zigzag edge (Fig. 2.12(c)), with both edges having a difference of 30° between them. More complex shapes other than these two "ideal" cases are a combination of armchair- and zigzag-shaped pieces (Enoki et al. 2007; Kobayashi et al. 2005). This last case is commonly found in experiments where obtaining atomically precise ribbons is difficult. This may jeopardize the achievement

[8] Alternatives in the bulk material include growing epitaxial graphene on a SiC substrate (Zhou et al. 2007). In that case the interaction with the substrate breaks the symmetry between the A and B sublattices, thereby opening a bandgap of about 0.26 eV. In bulk bilayer graphene, a gap can be opened by applying an electric field perpendicular to its surface (Zhang, Tang et al. 2009).

of clean bandgaps even for ribbons a few nanometers wide. Fortunately, strategies involving top-down[9] and bottom-up[10] approaches have allowed for important progress. Furthermore, unzipping carbon nanotubes, which could be termed a theorist's dream, has also been experimentally demonstrated (Jiao, Wang et al. 2010; Roche 2011; Shimizu et al. 2011; Wang et al. 2011).

The atomic structure of nanoribbons with armchair and zigzag edges is represented in Fig. 2.12(b) and 2.12(c), along with their corresponding unit cells. Here, we follow previous conventions (Abanin et al. 2006; Brey & Fertig 2006; Ezawa 2006; Kawai et al. 2000; Lee, Son et al. 2005; Miyamoto et al. 1999; Nakada et al. 1996; Okada & Oshiyama 2001; Sasaki et al. 2006; Son et al. 2006a; 2006b; Wakabayashi et al., 1999), and GNRs with armchair (zigzag) edges on both sides are classified by the number of dimer lines (zigzag lines) across the ribbon width. We will denote with *N*-aGNR and *N*-zGNR such armchair and zigzag GNRs, respectively, with *N* being respectively the number of dimer and zigzag lines. In addition, if not otherwise stated, in the following, the dangling bonds on the edge sites of GNRs will be assumed to be terminated by hydrogen atoms, although dangling bonds would not make any contribution to the electronic states near the Fermi level. Of course, these ideally shaped edges do not correspond to the experimental observations (Girit et al. 2009; Liu, Suenaga et al. 2009; Ritter & Lyding 2009), where GNRs currently have a high degree of edge roughness. A more complex edge is illustrated in Fig. 2.12(d). Topological aspects of this edge disorder will be presented in the sections dedicated to the study of quantum transport in disordered GNRs.

The edges in graphene nanoribbons confine the electronic wavefunctions along the direction perpendicular to the ribbon axis. Their electronic properties can be obtained by imposing the appropriate boundary conditions on the Schrödinger's equation within the simple *single-band tight-binding approximation* based on π-states of graphene (Ezawa 2006; Nakada et al. 1996; Wakabayashi et al. 1999) or on the two-dimensional Dirac's equation with an effective speed of light ($\sim 10^6$ m/s) (Abanin et al. 2006; Brey & Fertig 2006; Sasaki et al. 2006).

As we will see below, the presence of edges introduces new states not present in bulk 2D graphene (Nakada et al. 1996). These states appear because of the hard boundary conditions at the edges. Indeed, if instead of a vanishing wavefunction at the edges, one considers periodic boundary conditions – this is essentially the zone-folding approximation for carbon nanotubes introduced later in Section 2.5 – , one finds that the wavevector along the direction perpendicular to the ribbon axis k_{perp} is quantized, thereby defining a set of "cutting" lines in the Brillouin zone. Within this approximation, the band structure results from cutting the dispersion for bulk graphene along those lines.

[9] See, for example, Han et al. (2007), Chen et al. (2007), Li, Wang et al. (2008), Tapaszto et al. (2008), Datta et al. (2008), Ci et al. (2008), Jiao et al. (2009), Kosynkin et al. (2009), Jiao, Wang et al. (2010), Roche (2011), Shimizu et al. (2011), Wang et al. (2011).

[10] See Campos-Delgado et al. (2008), Sprinkle et al. (2010), Cai et al. (2010), Kato & Hatakeyama (2012). In the last study, the authors demonstrated GNR devices with a transport gap of $\sim$60 meV and high on/off ratios ($>10^4$).

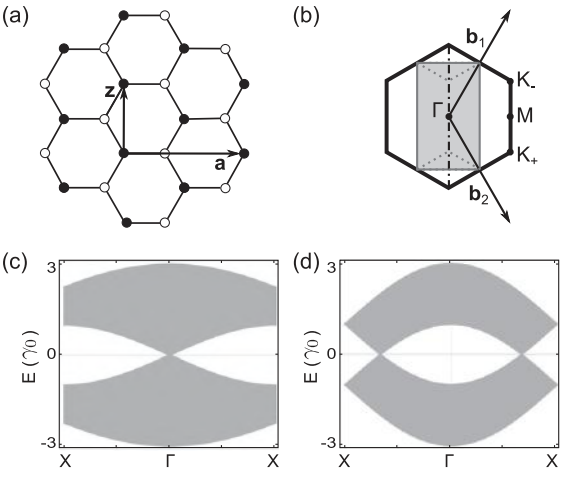

Figure 2.13 (a) A four-atom unit cell used in the zone-folding procedure. (b) The corresponding Brillouin zone is shaded gray together with the unit vectors and the Brillouin zone of bulk graphene. Depending on the ribbon termination, K_+ and K_- can be folded at $\pm 2\pi/(3a)$ along the vertical axis (zigzag ribbons) or onto the Γ point (armchair ribbons). (c) and (d) The projections of graphene's bulk dispersion onto the armchair and zigzag directions, respectively.

Figure 2.13 illustrates the basic picture of the zone-folding scheme: starting from a four-atom unit cell (Fig. 2.13(a)), one gets the corresponding Brillouin zone (gray rectangle in Fig. 2.13(b)). It is easy to see that for this Brillouin zone, the K points for zigzag ribbons fold at $\pm 2\pi/(3a)$ along the vertical axis. For armchair ribbons, the K points fold directly onto the Γ point. Projecting the bulk dispersion of graphene on each of the zigzag and armchair directions gives the shaded areas in Fig. 2.13(c) and (d), respectively. While this approximation may give the correct overall shape of the band structure and even the states at the "bulk" of the ribbon (which can be formed by superposition of states with k_{perp} and $-k_{\text{perp}}$), it fails dramatically for low energies, where it misses edge states. We note that edge states are generically present in all nanoribbons, even those with irregular edges, except the armchair ones (Akhmerov 2011).

The specific edge symmetry of zigzag and armchair nanoribbons is shown in Fig. 2.12. When the Dirac equation is used, appropriate boundary conditions need to be applied at the edges (vanishing wavefunction). For zigzag nanoribbons, given that one edge is formed entirely of A-type atoms while the other edge contains only B-type atoms, the boundary conditions can be imposed separately on each sublattice (Brey & Fertig 2006). For armchair graphene nanoribbons, this is no longer the case (Brey & Fertig 2006). Here, we take a different path, and consider armchair and zigzag graphene nanoribbons within a *tight-binding* model following Cresti et al. (2008) and Dubois et al. (2009).

2.4.1 Electronic Properties of Armchair Nanoribbons (aGNRs)

By analogy with what has been done previously for graphene, the *tight-binding* Hamiltonian of the ribbons can be written as

$$\mathcal{H} = \sum_i \varepsilon_i \hat{c}_i^\dagger \hat{c}_i - \sum_{i,j} \gamma_{ij} \hat{c}_i^\dagger \hat{c}_j, \tag{2.34}$$

where ε_i represent the onsite energies, which can be chosen as the reference energies ($\varepsilon_i = \varepsilon = 0$), γ_{ij} are the transfer integrals between the jth and ith π orbitals, and $\hat{c}_i^\dagger$ ($\hat{c}_i$) is an operator, which creates (annihilates) an electron at the orbital localized around site i. Within the first-nearest-neighbor approximation, $\gamma_{ij} = \gamma_0$ for i, j neighboring sites and zero otherwise. (This is equivalent to assuming that the ribbon edges are passivated in such a way that bulk graphene is reproduced.)

Thanks to the periodicity along the axis of the aGNR, the $\hat{c}_i$ and $\hat{c}_i^\dagger$ operators may be expressed as Bloch sums,

$$\hat{c}_i = \frac{1}{\sqrt{N}} \sum_k \mathrm{e}^{\mathrm{i}kR_i} \hat{c}_k(i), \tag{2.35}$$

where R_i is the position of the ith site and $\hat{c}_k(i)$ is one of the $\left\{\hat{c}_k^{1A}, \hat{c}_k^{1B}, \hat{c}_k^{2A}, \hat{c}_k^{2B}, \ldots, \hat{c}_k^{NB}\right\}$ operators, named by reference to the unit cell sites $\{1_A, 1_B, \ldots, N_A, N_B\}$ as represented in Fig. 2.12(b).

Inserting Eq. (2.35) into Eq. (2.34), the *tight-binding* Hamiltonian of *armchair* GNRs can be expressed in terms of the basis set $\left\{\hat{c}_k^{1A}, \hat{c}_k^{1B}, \hat{c}_k^{2A}, \hat{c}_k^{2B}, \ldots, \hat{c}_k^{NB}\right\}$,

$$\mathcal{H} = \sum_{k \in BZ} \mathcal{H}_k \,, \tag{2.36}$$

with

$$\mathcal{H}_k = \gamma_0 \hat{\phi}_k^\dagger \begin{pmatrix} 0 & \mathrm{e}^{\mathrm{i}k\frac{a}{2}} & 0 & 1 & 0 & 0 & \cdots \\ \mathrm{e}^{-\mathrm{i}k\frac{a}{2}} & 0 & 1 & 0 & 0 & 0 & \cdots \\ 0 & 1 & 0 & \mathrm{e}^{\mathrm{i}k\frac{a}{2}} & 0 & 1 & \cdots \\ 1 & 0 & \mathrm{e}^{-\mathrm{i}k\frac{a}{2}} & 0 & 1 & 0 & \cdots \\ 0 & 0 & 0 & 1 & 0 & \mathrm{e}^{\mathrm{i}k\frac{a}{2}} & \cdots \\ 0 & 0 & 1 & 0 & \mathrm{e}^{-\mathrm{i}k\frac{a}{2}} & 0 & \cdots \\ \cdots & \cdots & \cdots & \cdots & \cdots & \cdots & \cdots \end{pmatrix} \hat{\phi}_k, \tag{2.37}$$

where

$$\hat{\phi}_k = \left[\hat{c}_k^{1A}, \hat{c}_k^{1B}, \hat{c}_k^{2A}, \hat{c}_k^{2B}, \ldots, \hat{c}_k^{NA}, \hat{c}_k^{NB}\right]^T. \tag{2.38}$$

Through diagonalizing the Hamiltonian of Eq. (2.37), the band structure is obtained. Figure 2.14 shows the results for three different nanoribbons (15-aGNR, 16-aGNR, and 17-aGNR). We note that the typical Dirac-like linear dispersion or the direct gap

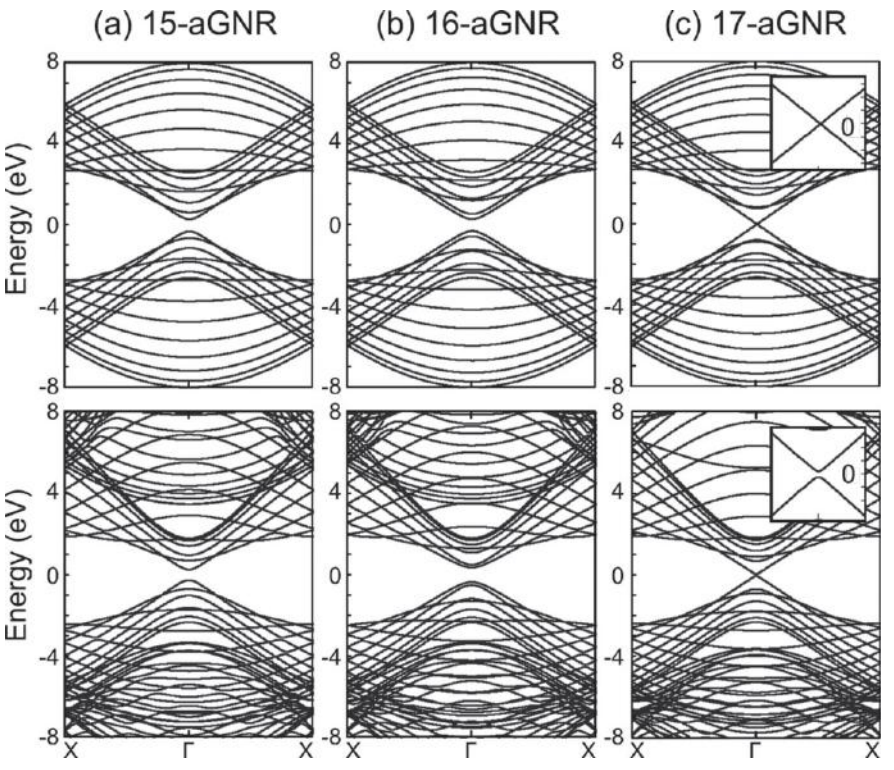

Figure 2.14 Energy band structures of three armchair nanoribbons (N-aGNRs) of various widths ($N = 15, 16, 17$). The *tight-binding* band structures (top) computed using a constant hopping energy ($\gamma_0 = 2.7$ eV) between nearest neighbors are compared to *ab initio* band structures (bottom). Reproduced from Dubois (2009)

always appears at $k = 0$ for the *armchair* configuration, a fact that can also be predicted by using the zone-folding approximation. (An alternative approach based on a mode decomposition in *real* space is presented in Section 5.2.2.)

From these results, we can see that some ribbons exhibit semiconducting behavior while others are metallic. An analytical calculation (Cresti et al. 2008) of the eigenvalues of the *tight-binding* Hamiltonian at $k = 0$ shows that the energy gap (Δ_N) is width dependent:

$$\Delta_N = \begin{cases} \Delta_{3\ell} = |\gamma_0| \left(4\cos\frac{\pi\ell}{3\ell+1} - 2\right), \\ \Delta_{3\ell+1} = |\gamma_0| \left(2 - 4\cos\frac{\pi(\ell+1)}{3\ell+2}\right), \\ \Delta_{3\ell+2} = 0, \end{cases} \tag{2.39}$$

with $\Delta_{3\ell} > \Delta_{3\ell+1} > \Delta_{3\ell+2} = 0$, where N (related to the ribbon width) and ℓ are integers.

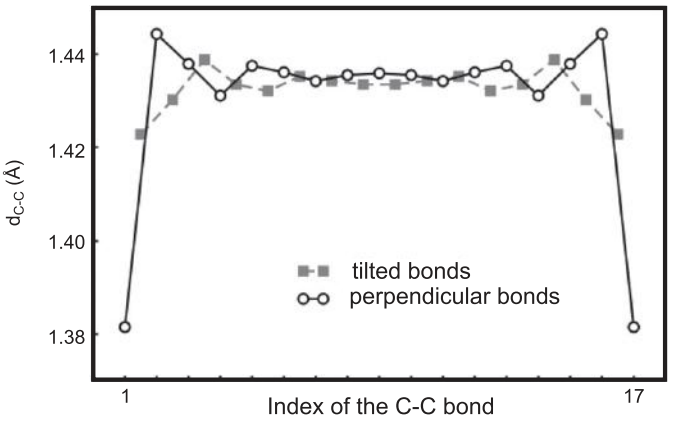

Figure 2.15 Evolution of the carbon–carbon bond length (d_{C-C}) across the 17-aGNR ribbon width, computed using *ab initio* structural optimization techniques. Both the length of the carbon–carbon parallel (empty circles) and tilted (filled squares) bonds with respect to the ribbon axis are illustrated. Reproduced from Dubois (2009).

Therefore, the *tight-binding* model predicts that N-aGNRs are metallic for every $N = 3\ell + 2$ (where ℓ is a positive integer), and semiconducting otherwise.[11]

More precise DFT calculations, however, reveal that even for the $3\ell + 2$-GNRs, there is a small gap at $k = 0$. According to DFT, all armchair ribbons remain semiconducting (Son et al. 2006a, 2006b) with gaps which decrease as the width of the aGNR increases, reaching the zero-gap value of graphene for infinite ribbon width. For a $\sim$5 nm wide ribbon with metallic behavior as predicted by the *tight-binding* model, the *ab initio* bandgap has a magnitude of only $\sim$0.05 eV.

The origin of this gap opening can be attributed to edge effects (Son et al. 2006a) not taken into account in the simple *tight-binding* model. Indeed, the edge carbon atoms of the aGNR are passivated by hydrogen atoms, some foreign atoms, or molecules in general. Therefore, one may generally expect the σ bonds between hydrogen and carbon as well as the onsite energies of the carbons at the edges and their bonding distances to be different from those in the middle of the ribbon. The bonding distances between carbons at the edges decrease from 1.44 Å (Fig. 2.15) leading to an increase of $\sim$15% in the hopping integral between π orbitals. This explains the emergence of a bandgap for all the aGNRs (Dubois 2009; Son et al. 2006a). By introducing these modified onsite and hopping energies within an improved nearest-neighbors *tight-binding* model, one obtains an improved agreement with the DFT band structure.

Finally, it has to be noted that the *ab initio* energy gaps are further increased when the electron–electron correlations are taken into account by means of GW corrections (Yang et al. 2007). DFT-LDA and quasiparticle bandgaps for armchair GNRs of

[11] An alternative to the path described above is described in Section 5.2.2, where a mode decomposition in real space, obtained by straightforward parallelization of the *tight-binding* Hamiltonian for GNRs and carbon nanotubes, is introduced. This scheme is useful especially when carrying out transport calculations, and therefore is introduced later on when the text deals with ballistic transport in carbon nanostructures.

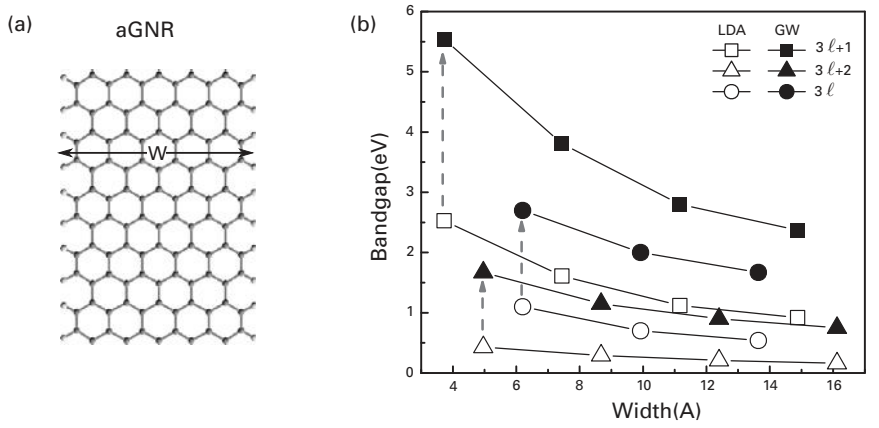

Figure 2.16 (a) Ball-stick model for an 11-aGNR, which exhibits 11 C–C dimer lines making up its width w. Hydrogen atoms (light-colored balls on the left and right edges) are used to passivate the edge σ-dangling bonds. (b) Width-dependence of aGNRs bandgaps. The three families of aGNRs are represented by different symbols. The values of the same family of aGNRs are connected by solid lines as a visual guide. The open symbols are LDA bandgaps while the solid symbols are the corresponding quasiparticle bandgaps. Dashed arrows are used to indicate the self-energy correction for the smallest width ribbon of each of the three aGNRs families. (Adapted with permission from Yang et al. (2007). Copyright (2007) by the American Physical Society. By courtesy of Li Yang)

various width are compared in Fig. 2.16. In agreement with DFT-LDA calculations, the quasiparticle band structure has a direct bandgap at the zone center for all investigated aGNRs. In addition, the bandgaps of the three families of N-aGNRs, which are classified according to whether $N = 3\ell + 1$, $3\ell + 2$, or 3ℓ (N being the number of dimer chains as explained earlier in Fig. 2.12(b), and ℓ being an integer), present qualitatively the same hierarchy as those obtained in DFT-LDA ($E_g^{3\ell+1} > E_g^{3\ell} > E_g^{3\ell+2} \neq 0$). Although including electron–electron interaction, the energy gaps are also found to decrease as the widths of the aGNR increase, reaching the zero-gap value of graphene for the infinite width.

2.4.2 Electronic Properties of Zigzag Nanoribbons (zGNRs)

Taking into account a periodicity along the ribbon length, one rewrites the Hamiltonian as a Bloch sum ($\mathcal{H} = \sum_{k \in BZ} \mathcal{H}_k$). For zGNRs, $\mathcal{H}_k$ finally reads

$$\mathcal{H}_k = \gamma_0 \hat{\phi}_k^{\dagger} \begin{pmatrix} 0 & 2\cos(\frac{ka}{2}) & 0 & 0 & 0 & \cdots \\ 2\cos(\frac{ka}{2}) & 0 & 1 & 0 & 0 & \cdots \\ 0 & 1 & 0 & 2\cos(\frac{ka}{2}) & 0 & \cdots \\ 0 & 0 & 2\cos(\frac{ka}{2}) & 0 & 1 & \cdots \\ 0 & 0 & 0 & 1 & 0 & \cdots \\ \cdots & \cdots & \cdots & \cdots & \cdots & \cdots \end{pmatrix} \hat{\phi}_k, \qquad (2.40)$$

where $\hat{\phi}_k = \left[\hat{c}_k^{1A}, \hat{c}_k^{1B}, \hat{c}_k^{2A}, \hat{c}_k^{2B}, \ldots, \hat{c}_k^{NA}, \hat{c}_k^{NB}\right]^t$.

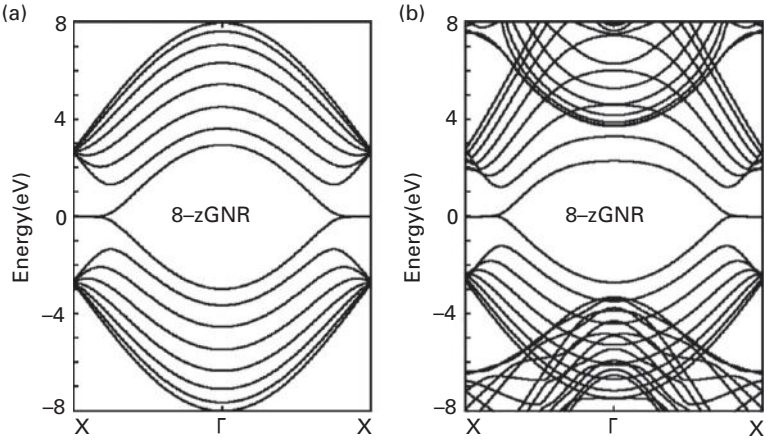

Figure 2.17 Band structure of zigzag nanoribbons (8-zGNR): (a) *tight-binding* band structures using a constant nearest-neighbors hopping energy ($\gamma_0 = -2.7$ eV); (b) *ab initio* band structures. Reproduced from Dubois (2009)

Through diagonalizing of the Hamiltonian of Eq. (2.40), the band structure shown in Fig. 2.17 is obtained. One notes that a dispersion relation reminiscent of the Dirac cones develops around $k = \pm 2\pi/(3a)$. Another salient feature is the formation of a sharp peak in the density of states at E_F, resulting from the formation of partially flat and degenerate bands with zero energy (between the Dirac points and the border of the Brillouin zone ($2\pi/(3a) \leq |k| \leq \pi/a$)), and which represents the highest valence and lowest conduction bands.

First-principles calculations of the electronic structure confirm that the zero-energy states are mainly confined along the ribbon edges, but progressively spread along the ribbon lateral dimension as the wavevector is shifted from π/a to $2\pi/(3a)$ (see Fig. 2.17(b)). A slight dispersion of those states (which is width dependent) develops due to the overlap between opposite edge states and the formation of bonding and antibonding states. Actually, simple calculations show that an edge shape with three or four zigzag sites per sequence is enough to form the edge state (Nakada et al. 1996). The presence of such remarkably confined electronic edge states has been confirmed by scanning tunneling microscopy (STM) and scanning tunneling spectroscopy (STS) measurements (Kobayashi et al. 2005).

In contrast with the aGNR case, the modification of the carbon–carbon bonding distance at the edges is not found to affect the low-energy electronic structures (Fig. 2.18). The partially flat bands at the Fermi energy are actually "topologically protected," and thus insensitive to the precise hopping energy across the ribbon width.

The peculiar edge states of zGNRs are, furthermore, evidence of some local magnetic ordering, although the ribbon as a whole has a nonmagnetic ground state, with ferromagnetic ordering at each zigzag edge and antiparallel spin orientation between the two edges (Fig. 2.19(a)) (Lee, Son et al. 2005; Okada & Oshiyama 2001; Son et al. 2006a; 2006b; Wakabayashi et al. 1999). One notes, however, that the difference in

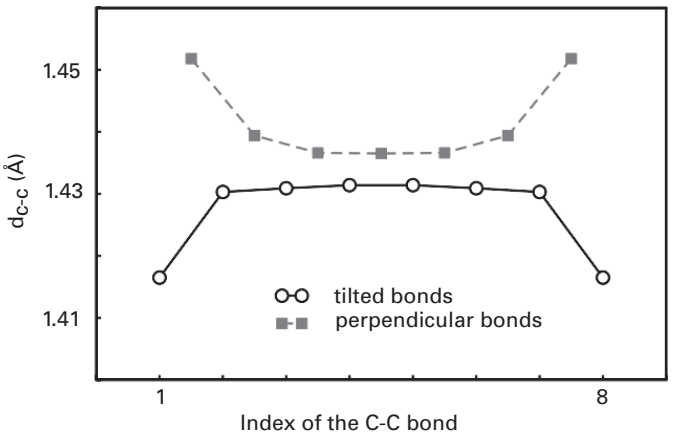

Figure 2.18 Evolution of the carbon–carbon bond length (d_{C-C}) across the 8-zGNR ribbon width, obtained after *ab initio* structural optimization. Both the length of the carbon–carbon parallel (empty circles) and tilted (filled squares) bonds with respect to the ribbon axis are shown. Reproduced from Dubois (2009)

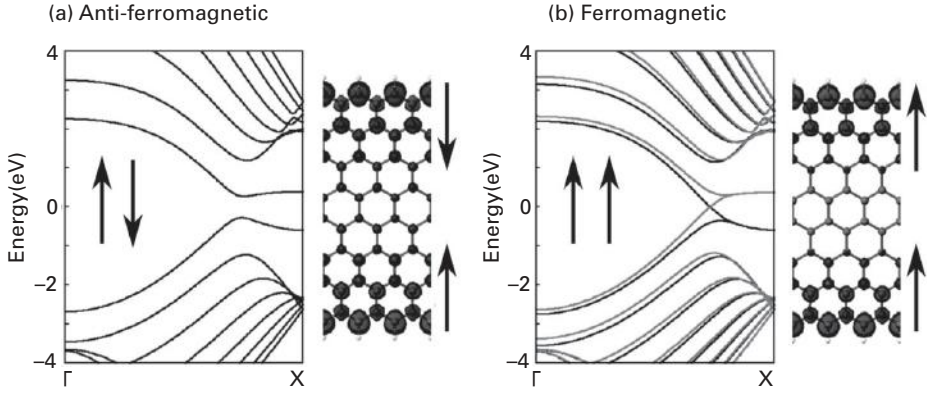

Figure 2.19 Spin-polarized electronic structure of the 8-zGNR: (a) ↑↓ configuration (ground state): a ferromagnetic order along its axis and antiparallel coupling between the edges; (b) ↑↑ configuration: a ferromagnetic order along its axis and parallel coupling between the edges. In each panel, the energy band structure (left) and the spin-polarized electronic densities ($\rho_\uparrow - \rho_\downarrow$, right) of the iso-surfaces are computed within the spin-dependent DFT framework. Adapted from Dubois (2009)

total energy per edge atom between non-spin-polarized and spin-polarized edge states is only of the order of a few tens of meV (Son et al. 2006a). Additionally, zGNRs exhibit a Curie-like temperature dependence of the Pauli paramagnetic susceptibility, and a crossover is predicted from high-temperature diamagnetic to low-temperature paramagnetic behavior in the magnetic susceptibility (Wakabayashi et al. 1999).

The electronic ground state of the pristine 8-zGNR shows some antiparallel (↑↓) spin orientations between the edges (Fig. 2.19(a)), leading to a semiconducting band

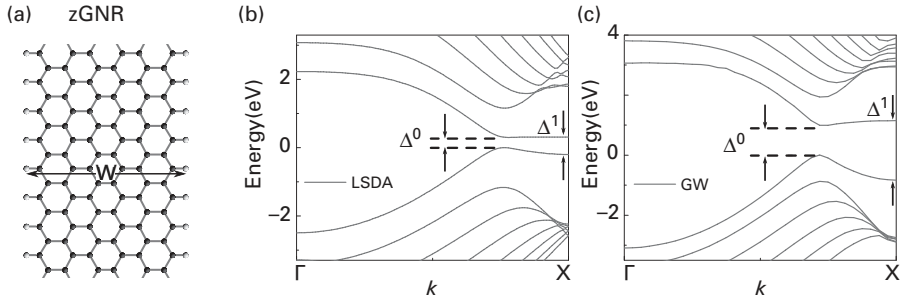

Figure 2.20 (a) Ball-stick model for a 12-zGNR which exhibits 12 zigzag chains along the ribbon axis. Hydrogen atoms (light-colored balls on the left and right edges) are used to passivate the edge σ-dangling bonds. (b and c) Calculated band structure (and energy gap) of a 12-zGNR within the LSDA (b) and GW (c) approximations. The up and down spin states are degenerated for all the bands in the $\uparrow\downarrow$ ground state configuration, and the top of the valence band is set at zero. The symbols Δ^0 and Δ^1 denote the direct bandgap and the energy gap at the zone boundary. (Adapted with permission from Yang et al. (2007). Copyright (2007) by the American Physical Society)

structure (0.5 eV bandgap) with full spin degeneracy. Besides, the magnetic configuration with parallel ($\uparrow\uparrow$) spin orientations between the edges (Fig. 2.19(b)) is metastable (11 meV/edge-atom higher in energy). This configuration displays a metallic behavior, as the $\pi^*_\uparrow$ and $\pi_\downarrow$ bands cross at the Fermi energy with the formation of a total magnetic moment of 0.51 μ_B (per edge atom).

Through performance of spin-polarized calculations, the energy gap formation in zGNRs can be rationalized by the magnetic ordering-induced staggered sublattice potentials (Kane and Mele 2005b). This is unique to the edge symmetry since opposite spin states are forced to lie on different sublattices. Since the strength of the staggered potentials in the middle of the ribbon decreases with the ribbon width, the bandgaps of zigzag GNRs are consequently inversely proportional to their width. The band structure of zGNRs is slightly modified when accounting for the GW correction (Yang et al. 2007). The self-energy corrections are found to enlarge the energy gaps for all zGNRs and slightly increase the band dispersion of edge states (Fig. 2.20).

In contrast to the bandgap (Δ^0) located around three-fourths of the way to the Brillouin zone edge (Fig. 2.20), the zGNR energy gap at the zone boundary (Δ^1) is width-insensitive because of its dominant edge-state character (Yang et al. 2007). The dependence of the GW correction on the wave vector slightly affects the band dispersion of zGNRs (Fig. 2.20(b–c)). The GW correction is calculated to be about 1 eV for Δ^0 for a ribbon width between 1–2.5 nm (Yang et al. 2007). Since the Δ^1 gap is width independent, the corresponding GW correction remains in the order of 1.5 eV.

To conclude, we have seen the fundamental role played by edge symmetries, for determining the precise values and the width dependence of energy bandgaps in both *armchair* and *zigzag* GNRs. The enhanced electron–electron interaction in these quasi-one-dimensional systems yield to significant self-energy correction in both *armchair*

and *zigzag* GNRs. The states near the bandgap of zGNRs are sensitive to the wavevector, giving rise to a larger band width and smaller effective mass (Yang et al. 2007). The computed bandgaps lie in the range 1–3 eV for GNRs with widths from 3 to 1 nm.

2.5 Electronic Properties of Carbon Nanotubes

2.5.1 Structural Parameters of CNTs

In 1991, helped by state-of-the-art transmission microscopy, Sumio Iijima from NEC laboratories in Japan discovered and first characterized *Helical microtubules of graphitic carbon* (Iijima 1991). The microtubules were made of concentric cylindrical shells with a spacing between them of about 3.4 Å, the same as usually found in conventional graphite materials. Their diameter ranged from a few nanometers for the inner shells to several hundred nanometers for the outer shells and they constituted what today we call carbon nanotubes. A few years later, arc discharge methods with transition metal catalysts were used to successfully synthesize carbon nanotubes made of a *single* graphene layer rolled into a hollow cylinder (Bethune et al. 1993; Iijima & Ichihashi 1993). In contrast to the multiwall carbon nanotubes (MWNTs) obtained earlier, these structures, called single-wall carbon nanotubes (SWNTs), had diameters of about 1 nm and an impressively perfect crystalline structure. They were considered the "ultimate" carbon-based 1D systems.

As shown in Fig. 2.21, the structure of single-wall carbon nanotubes is that of a rolled graphene strip (Saito et al. 1998). Their structure can be specified by the chiral

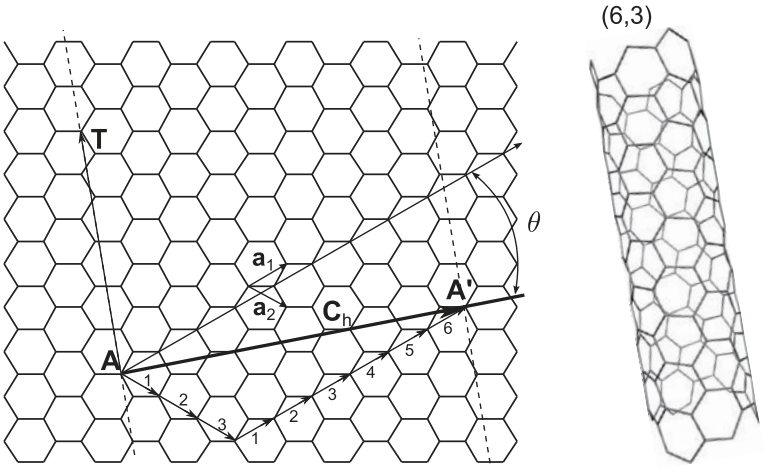

Figure 2.21 The graphene network. The lattice vectors are indicated by $\mathbf{a}_1$ and $\mathbf{a}_2$. In this example the chiral vector is $\mathbf{C}_h = 6\mathbf{a}_1 + 3\mathbf{a}_2$. The direction perpendicular to $\mathbf{C}_h$ is the tube axis (dashed lines) where the translational vector $\mathbf{T}$ is indicated. The angle between $\mathbf{C}_h$ and the $\mathbf{a}_1$ "zigzag" direction of the graphene lattice defines the chiral angle θ. The resulting $(6, 3)$ nanotube is shown on the right. The unit cell for this nanotube is a rectangle bounded by $\mathbf{C}_h$ and $\mathbf{T}$.

vector ($\mathbf{C}_h$) that connects two equivalent sites (A and A′ in Fig. 2.21) on a graphene sheet. Therefore, the chiral vector can be specified by two integer numbers (n and m), $\mathbf{C}_h = n\mathbf{a}_1 + m\mathbf{a}_2$, and represents the relative position of the pair of atoms on the graphene network which form a tube when rolled. The (n, m) pair uniquely labels SWNTs.

Since the chiral vector $\mathbf{C}_h$ defines the circumference of the tube, its diameter can be estimated as $d_t = |\mathbf{C}_h|/\pi = \frac{a}{\pi}\sqrt{n^2 + nm + m^2}$, where a is the lattice constant of the honeycomb network ($a = \sqrt{3} \times a_{cc}$ and $a_{cc} \simeq 1.42$ Å , the C–C bond length). The chiral vector $\mathbf{C}_h$ uniquely defines a particular (n, m) tube, as well as its chiral angle θ which is the angle between $\mathbf{C}_h$ and $\mathbf{a}_1$ ("zigzag" direction of the graphene sheet, see Fig. 2.21).

The chiral angle θ can be calculated from

$$\cos\theta = \frac{\mathbf{C}_h \cdot \mathbf{a}_1}{|\mathbf{C}_h||\mathbf{a}_1|} = (2n + m)/(2\sqrt{n^2 + nm + m^2}), \tag{2.41}$$

and lies in the range $0 \leq \mid \theta \mid \leq 30^\circ$, because of the hexagonal symmetry of the graphene lattice. Nanotubes of the type $(n, 0)$ ($\theta = 0^\circ$) are called *zigzag* tubes, because they exhibit a zigzag pattern along the circumference. Such tubes display carbon–carbon bonds parallel to the nanotube axis. On the other hand, nanotubes of the type (n, n) ($\theta = 30^\circ$) are called *armchair* tubes because they exhibit an armchair pattern along the circumference. Such tubes display carbon–carbon bonds perpendicular to the nanotube axis. Both zigzag and armchair nanotubes are achiral tubes, in contrast with general ($n, m \neq n \neq 0$) chiral tubes (compare, for example, the structure of the tubes shown in Fig. 2.22(a)).

Besides the tube diameter, the chiral vector also determines the unit cell. The translational period t along the tube axis is given by the smallest graphene lattice vector $\mathbf{T}$ perpendicular to $\mathbf{C}_h$. The translational vector $\mathbf{T}$ can be written as a linear combination of the basis vectors $\mathbf{a}_1$ and $\mathbf{a}_2$ as $\mathbf{T} = t_1\mathbf{a}_1 + t_2\mathbf{a}_2$. Using the orthogonality relation $\mathbf{C}_h \cdot \mathbf{T} = 0$, one obtains $t_1 = (2m + n)/N_R$ and $t_2 = -(2n + m)/N_R$, where N_R is the greatest common divisor of $(2m + n)$ and $(2n + m)$. The length of the translational vector is given by $t = |\mathbf{T}| = \sqrt{3}a\sqrt{n^2 + nm + m^2}/N_R$. The nanotube unit cell is thus a cylindrical surface with height t and diameter d_t. The number of carbon atoms per unit cell is $N_C = 4(n^2 + nm + m^2)/N_R$. All this information is condensed in Table 2.1.

2.5.2 Electronic Structure of CNTs within the Zone-Folding Approximation

Now that we have completely defined the structure of the nanotubes (diameter, chirality, unit cell, etc.) from the pair (n, m), let us turn to their electronic properties. We start from the single-band *tight-binding* model of graphene in a nearest-neighbor approximation as introduced before. Simplicity is a big advantage of this approximation, which, together with a zone folding approach, allows for the prediction of the electronic properties (Hamada et al. 1992; Saito et al. 1992a). As made clear in the next paragraphs, the zone folding neglects curvature effects, thereby giving a good approximation for tubes of large enough radii ($d_t > 1$ nm). The zone-folding approach considers a nanotube as

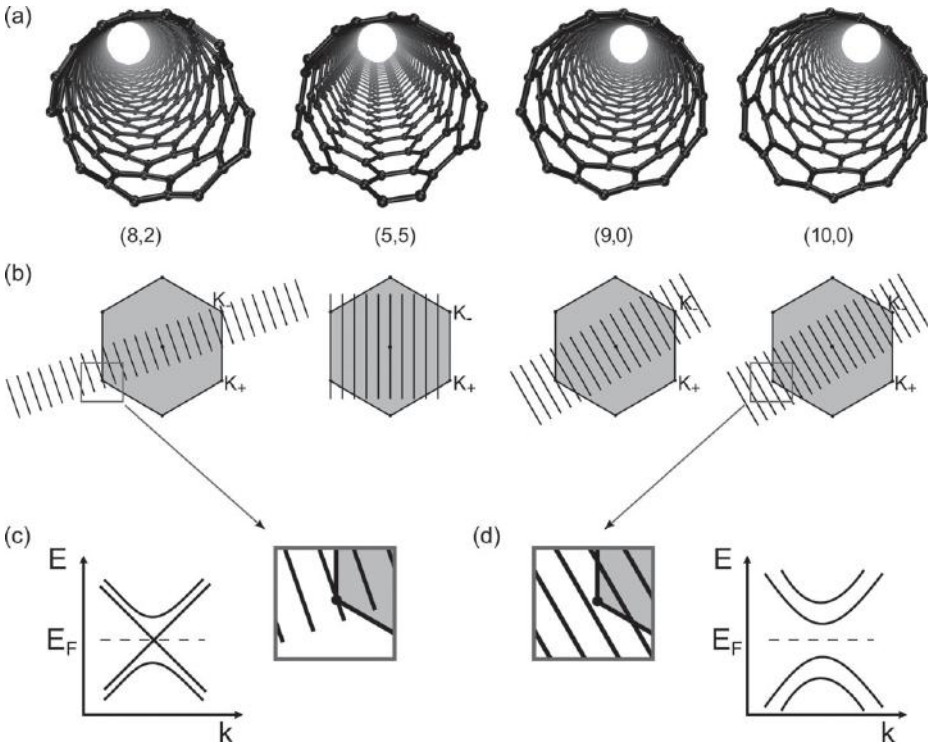

Figure 2.22 (a) Atomic structures of (8, 2) chiral nanotubes, (5, 5) armchair, (9, 0), and (10, 0) zigzag. (b) Allowed *k*-vectors for the same nanotubes mapped onto the graphene Brillouin zone. The areas within the gray rectangles in (b) are zoomed for better visualization in (c) and (d). For metallic nanotubes, the allowed *k*-vectors include the *K* point of the graphene Brillouin zone as shown in (c). The corresponding dispersion relations are linear and exhibit a metallic behavior. In contrast, for semiconducting nanotubes, the *K* point is not an allowed vector and there is an energy gap, as shown in (d). A sketch with the dispersion relations for these two cases is also shown in (c) and (d).

a piece of graphene sheet with periodic boundary conditions along the circumferential direction. This can be expressed by the condition

$$\Psi_{\mathbf{k}}(\mathbf{r} + \mathbf{C}_h) = \mathrm{e}^{\mathrm{i}\mathbf{k}\cdot\mathbf{C}_h}\Psi_{\mathbf{k}}(\mathbf{r}) = \Psi_{\mathbf{k}}(\mathbf{r}), \tag{2.42}$$

where vectors $\mathbf{r}$ and $\mathbf{C}_h$ lie on the nanotube surface. The first equality in the last equation is a result of applying Bloch's theorem. These boundary conditions impose a quantization of the allowed wavevectors "around" the nanotube circumference, $\mathbf{k} \cdot \mathbf{C}_h = 2\pi q$ (q integer). In contrast, the wavevectors along the nanotube axis remain continuous.[12] Therefore, when plotting the allowed wavevectors in reciprocal space, we are left with a set of parallel lines whose direction and spacing depend on the indices (n, m) (see the

[12] Strictly speaking, this is true for infinite nanotubes. However, for typical nanotube sizes, the discrete nature of the states may become evident at low enough temperatures.

Table 2.1 Structural parameters for (n, m) carbon nanotubes. (Adapted with permission from Charlier et al. (2007). Copyright (2007) by the American Physical Society.)

Symbol	*Name*	*Formula/value*
a	Graphene lattice constant	$a = \sqrt{3} \times a_{cc} \simeq 2.46$ Å
		$a_{cc} \simeq 1.42$ Å
$\mathbf{a}_1, \mathbf{a}_2$	Graphene basis vectors	$\left(\frac{\sqrt{3}}{2}; \frac{1}{2}\right) a, \left(\frac{\sqrt{3}}{2}; -\frac{1}{2}\right) a$
$\mathbf{b}_1, \mathbf{b}_2$	Graphene reciprocal lattice vectors	$\left(\frac{1}{\sqrt{3}}; 1\right) \frac{2\pi}{a}, \left(\frac{1}{\sqrt{3}}; -1\right) \frac{2\pi}{a}$
$\mathbf{C}_h$	Chiral vector	$\mathbf{C}_h = n\mathbf{a}_1 + m\mathbf{a}_2 \equiv (n, m)$
		$(0 \leq \mid m \mid \leq n)$
d_t	Tube diameter	$d_t = \frac{\mid \mathbf{C}_h \mid}{\pi} = \frac{a}{\pi}\sqrt{n^2 + nm + m^2}$
θ	Chiral angle	$0 \leq \mid \theta \mid \leq \frac{\pi}{6}$
		$\sin\theta = \frac{\sqrt{3}m}{2\sqrt{n^2+nm+m^2}}$
		$\cos\theta = \frac{2n+m}{2\sqrt{n^2+nm+m^2}}$
		$\tan\theta = \frac{\sqrt{3}m}{2n+m}$
$\mathbf{T}$	Translational vector	$\mathbf{T} = t_1\mathbf{a}_1 + t_2\mathbf{a}_2 \equiv (t_1, t_2)$
		$\gcd(t_1, t_2) = 1^{(*)}$
		$t_1 = \frac{2m+n}{N_R}, t_2 = -\frac{2n+m}{N_R}$
		$N_R = \gcd(2m + n, 2n + m)^{(*)}$
N_C	Number of C atoms per unit cell	$N_C = \frac{4(n^2+nm+m^2)}{N_R}$

In this table, n, m, t_1, t_2 are integers.
$^{(*)}$ $\gcd(n, m)$ denotes the greatest common divisor of the two integers n and m.

scheme in Fig. 2.22(b)). The dispersion for each allowed wavevector in the circumferential direction is then obtained by cutting the dispersion relation of 2D graphene along these cutting lines. Superposition of these curves gives the electronic structure of the (n, m) nanotube.

Given graphene's peculiar dispersion relation, a nanotube will be metallic whenever one of the cutting lines crosses the $\mathbf{K}$ (either $\mathbf{K}_+$ or $\mathbf{K}_-$) point. Based on this fact, a rule for metallicity follows from imposing that $\mathbf{K}$ is an allowed wavevector for the given (n, m) nanotube, i.e., $\exp(i\mathbf{K} \cdot \mathbf{C}_h) = 1$. Using $\mathbf{K} = |\mathbf{K}|\mathbf{a}_2/a$ with $|\mathbf{K}| = 4\pi/(3a)$, we find that $n + 2m$ must be a multiple of 3 or, in other terms, $n + 2m \equiv 0 \pmod 3$. Since $3m \equiv 0 \pmod 3$ for any m, it follows that $n - m \equiv 0 \pmod 3$. *Therefore, a nanotube defined by the* (n, m) *indices will be metallic if* $n - m = 3\ell$*, with* ℓ *an integer, or semiconducting if* $n - m = 3\ell \pm 1$.

As a result of the previous rule, most nanotubes are semiconductors and only a fraction (one-third) are metallic. Furthermore, (n, n) armchair nanotubes are always metallic, whereas $(n, 0)$ zigzag nanotubes are metallic whenever n is a multiple of 3. For metallic nanotubes, in the vicinity of E_F ($\mathbf{k} = \mathbf{K} + \delta\mathbf{k}$), the dispersion relation is

$$E_{\pm}(\delta\mathbf{k}) \simeq \pm\frac{\sqrt{3}a}{2}\gamma_0|\delta\mathbf{k}|, \tag{2.43}$$

presenting a linear energy–momentum relation (Fig. 2.22(c)).

For semiconducting nanotubes, the K point is not included and the conduction and valence bands emerge from states with k vectors located on the allowed line(s) closest to the K point (see Fig. 2.22(d)). Choosing (n, m) such that $n - m = 3\ell \pm 1$ gives a gap opening at the Fermi level with a magnitude that can be estimated by (see Problem 2.8)

$$\Delta E_g^1 = \frac{2\pi a\gamma_0}{\sqrt{3}|\mathbf{C}_h|} = \frac{2a_{cc}\gamma_0}{d_t}. \tag{2.44}$$

The value of ΔE_g^1 decreases with the inverse of the tube diameter d_t ($d_t = |\mathbf{C}_h|/\pi$) (White & Mintmire 1998).[13] In the large-diameter limit, one gets a zero-gap semiconductor, as is expected since graphene is recovered. For a realistic $(17, 0)$ tube with a diameter of 1.4 nm, one gets $\Delta E_g^1 \simeq 0.59$ eV.

An instructive exercise is to determine the Brillouin zone of a carbon nanotube, a task that we leave for Problem 2.7. Given that nanotubes are essentially one-dimensional, their Brillouin zone is one-dimensional as well. The zone edges are denoted with X and X', with $X' = -X$ due to time-reversal symmetry. The case of band folding for a $(5, 5)$ armchair nanotube is shown in Fig. 2.23 within a band-folding scheme. Note that the K points are folded at a distance of $\pm 2\pi/(3a)$ from the Γ point, whereas for zigzag nanotubes they are folded onto the Γ point itself.

In Fig. 2.24(a), the dispersion relations $E(k)$ for an $(8, 2)$ chiral nanotube are illustrated. Since $n-m$ is a multiple of 3, this nanotube exhibits metallic behavior with a band crossing at $k = \pm 2\pi/3\mathbf{T}$. Other chiral nanotubes, like the $(9, 6)$ (not shown), display a zero energy gap at $k = 0$. The DOS of chiral nanotubes (see Fig. 2.24(a)) displays van Hove singularities as for the achiral tubes (Charlier & Lambin 1998) shown in the other panels.

The electronic band structure of an armchair $(5, 5)$ carbon nanotube is presented in Fig. 2.24(b). Six bands for the conduction states, and an equal number for the valence, are observable. However, four of them are degenerate, leading to ten electronic levels in each case, consistent with the ten hexagons around the circumference of the $(5, 5)$ nanotube. For all armchair nanotubes, the energy bands exhibit a large degeneracy at the zone boundary, where $k = \pm\pi/a$ (X point), so that Eq. (2.16) becomes $E(k = \pm\pi/a) = \pm\gamma_0$. This comes from the absence of dispersion along the segments connecting the

[13] This $1/d_t$ dependence of the gap on the diameter relies on the assumption of a linear dispersion of the bands around E_F (White & Mintmire 1998). Away from E_F, the dispersion deviates from linear, an effect called trigonal warping (Saito et al. 2000), which induces a dependence of the bandgap not only on the diameter, but also on the (n, m) indices.

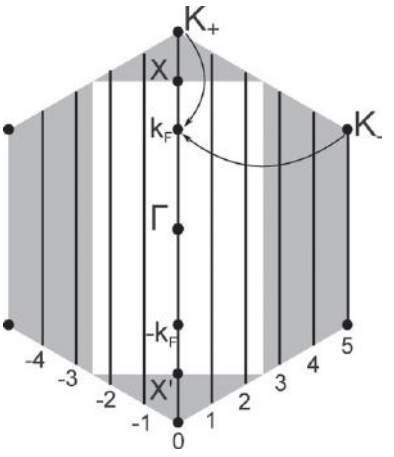

Figure 2.23 Brillouin zone for graphene (gray-shaded hexagon) together with the Brillouin zone (white rectangle) for a four-atom unit cell with lattice vectors $\mathbf{T} = \mathbf{a}_1 - \mathbf{a}_2$ (translational vector for armchair tubes) and $\mathbf{a}_1 + \mathbf{a}_2$ (equal to $\mathbf{C}_h/n$ for armchair tubes). The allowed k vectors for a $(5, 5)$ nanotube lie on the black lines depicted in the figure. To compute the $(5, 5)$ band structure, fold the corners of the hexagonal Brillouin zone onto the rectangular cell (white) and superimpose the bands calculated for bulk graphene along the black lines of length $2\pi/|\mathbf{T}|$.

neighboring centers of the BZ sides (the M points), an effect that yields the so-called trigonal warping of the bands as already discussed. The valence and conduction bands for armchair nanotubes cross at $k = k_F = \pm 2\pi/(3a)$, a point that is located at two-thirds of ΓX (Fig. 2.24(b)). This means that the original K vertices of the original graphene hexagonal BZ are folded at two-thirds of the ΓX line (or its inversion symmetry image). As discussed previously, the $(5, 5)$ armchair nanotube is thus a zero-gap semiconductor, which will exhibit metallic conduction at finite temperatures since only infinitesimal excitations are needed to promote carriers into the conduction bands.

The density of states (DOS) $\Delta N/\Delta E$ represents the number of available states ΔN for a given energy interval ΔE ($\Delta E \to 0$). This DOS is a quantity that can be measured experimentally under some approximations. The shape of the density of states is known to depend dramatically on dimensionality. In 1D, as shown below, the density of states diverges as the inverse of the square root of the energy ($1/\sqrt{E}$) close to band extrema. These "spikes" in the DOS are called van Hove singularities (vHs) and manifest confinement properties in the directions perpendicular to the tube axis. As carbon nanotubes are one-dimensional, their corresponding DOS exhibits such a spiky behavior at energies close to band edges (see Fig. 2.24). For all metallic nanotubes, the density of states per unit length along the nanotube axis is a constant at the Fermi energy (E_F), and can be expressed analytically (Mintmire & White 1998):

$$\rho(\varepsilon_F) = 2\sqrt{3}a_{cc}/(\pi\gamma_0|\mathbf{C}_h|). \tag{2.45}$$

The calculated 1D dispersion relations $E(k)$ for the $(9, 0)$ and the $(10, 0)$ zigzag nanotubes are illustrated in Fig. 2.24(c,d), respectively. As expected, the $(9, 0)$ tube

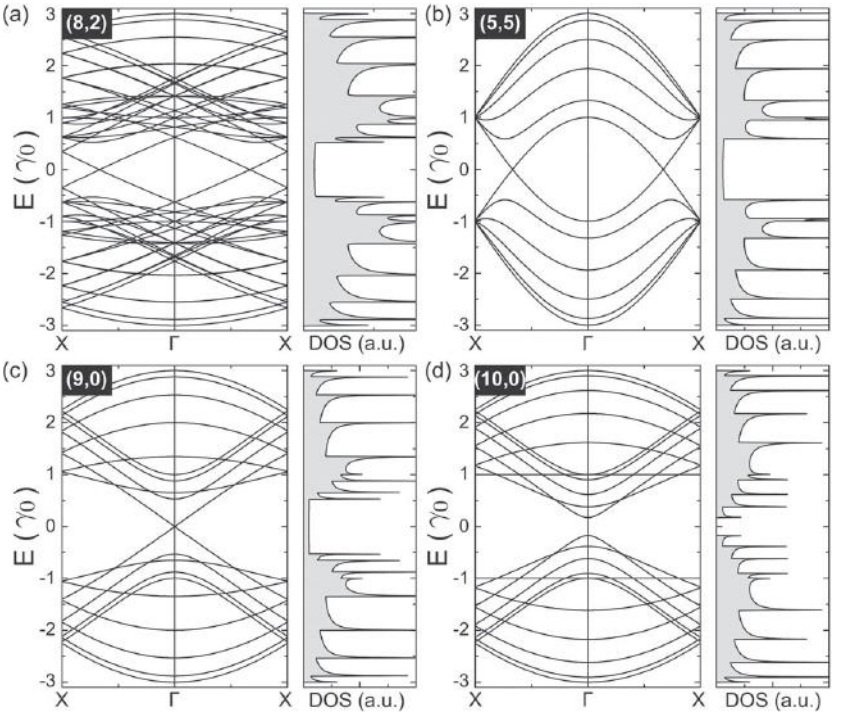

Figure 2.24 Band structure and density of states for (a) an $(8, 2)$ chiral nanotube; (b) a $(5, 5)$ armchair nanotube; (c) a $(9, 0)$ zigzag nanotube; and (d) a $(10, 0)$ zigzag nanotube within the zone-folding model. The 1D energy dispersion relations are presented in the $[-3\gamma_0; 3\gamma_0]$ energy interval in units of γ_0, the nearest-neighbor C–C *tight-binding* hopping parameter ($\sim$2.9 eV). The energy bands are plotted along the $X - \Gamma - X$ direction. The Fermi level is located at zero energy.

is metallic, with the Fermi surface located at Γ, whereas the $(10, 0)$ nanotube exhibits a finite energy gap at Γ. In particular, in the case of the $(10, 0)$ nanotube, there is a dispersionless energy band at $E/\gamma_0 = \pm 1$, which gives a singularity in the DOS at these particular energies. For a general $(n, 0)$ zigzag nanotube, when n is a multiple of 3, the energy gap at $k = 0$ (Γ point) becomes zero. However, when n is *not* a multiple of 3, an energy gap opens at Γ. The corresponding densities of states have a zero value at the Fermi energy for the semiconducting nanotube, and a small nonzero value for the metallic one.

Note that the k values for the band crossing at E_F in metallic nanotubes are $k = \pm 2\pi/3|\mathbf{T}|$ or $k = 0$ for armchair or zigzag tubes, respectively. These k values are also the locations of the bandgaps for the semiconducting zigzag nanotubes. The same k values also denote the positions of the energy gaps (including zero energy gaps) for the general case of chiral nanotubes.

In semiconducting zigzag or chiral nanotubes, the bandgap (as expressed in Eq. (2.44)) is independent of the chiral angle and varies inversely with the nanotube diameter: $\Delta E_g^1 = 2\gamma_0 a_{cc}/d_t$ (in the linear bands approximation). Density of states measurements by scanning tunneling spectroscopy (STS) provide a powerful tool for

probing the electronic structure of carbon nanotubes. It can be shown, indeed, that under some assumptions, the voltage–current derivative dI/dV is proportional to the DOS. Some experiments (Odom et al. 1998; Wilder et al. 1998) confirmed that the energy bandgap of semiconducting tubes is roughly proportional to $1/d_t$, and that about one-third of nanotubes are conducting, while the other two-thirds are semiconducting. Resonances in the DOS have also been observed experimentally (Odom et al. 1998; Wilder et al. 1998) on both metallic and semiconducting nanotubes whose diameters and chiral angles were determined using a scanning tunneling microscope (STM) (Venema et al. 1999). Several other experimental techniques such as resonant Raman scattering (Jorio et al. 2001), optical absorption, and emission measurements (Bachilo et al. 2002; Lefebvre et al. 2003; O'Connell et al. 2002) have also confirmed this structure in van Hove singularities of the electronic densities of states in single-wall carbon nanotubes.

2.5.3 Curvature Effects: Beyond the Zone-Folding Model

In the previous section, the electronic properties of CNTs are directly deduced from confinement of the electrons around the tube circumference through the restriction of the allowed k Bloch vectors, which neglects any curvature effects. However, such curvature effects become increasingly important as the nanotube diameter is further reduced. To account for the cylindrical geometry, one considers that carbon atoms are placed onto a cylindrical wall, which implies that (I) the C–C bonds perpendicular and parallel to the axis become different, so that the $\mathbf{a}_1$ and $\mathbf{a}_2$ have different lengths; (II) as a result, the formation of an angle for the two p_z orbitals located on bonds renormalize the hopping terms γ_0 between a given carbon atom with its three neighbors; (III) the broken planar symmetry induces a mixing between π and σ, forming hybrid orbitals that exhibit partial sp^2 and sp^3 character, all effects which are neglected in the zone-folding model of graphene.

Here, we briefly summarize the effect of finite curvature on the electronic properties of nanotubes. The aforementioned modifications indexed (I) and (II) change the conditions at which occupied and unoccupied bands are crossing (at k_F), which shifts this Fermi vector k_F away from the Brillouin zone corners (K point) of the graphene sheet (Kane & Mele 1997). Taking curvature into account for *armchair* nanotubes shifts the Fermi wavevector along an allowed line of the graphene Brillouin zone. However, for symmetry reasons, the metallic nature of *armchair* tubes remains insensitive to finite curvature. In contrast, for *non-armchair* metallic nanotubes, k_F is found to shift away from the K point perpendicular to the allowed k-lines, which produces the formation of a small bandgap at E_F (see Fig. 2.25).

Thus, in the presence of curvature effects, the sole zero bandgap tubes are the (n, n) *armchair* nanotubes, whereas (n, m) tubes with $n - m = 3\ell$ (ℓ is a nonzero integer) all fall into the category of tiny-gap semiconductors. *Armchair* tubes are usually labeled "type I" metallic tubes, while the others are of "type II." Remaining nanotubes belong to the intermediate-gap semiconductors (with gaps a few tenths of an eV). Tiny-gap

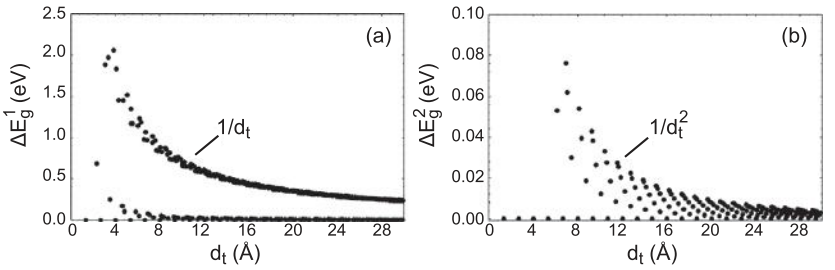

Figure 2.25 Magnitude of both primary (ΔE_g^1) and secondary (ΔE_g^2) gaps in carbon nanotubes with radii less than 15 Å . The primary gap (ΔE_g^1) scales as $1/d_t$: (a) the secondary gap (ΔE_g^2 or curvature induced gap) scales as $1/d_t^2$; (b) the dots at $\Delta E_g^1 = \Delta E_g^2 = 0$ correspond to the *armchair* nanotubes which always preserve their metallic character. (Adapted with permission from Kane & Mele (1997). Copyright (1997) by the American Physical Society)

semiconducting nanotubes also present a secondary gap induced by curvature, which depends on the tube diameter (as $1/d_t^2$) and chiral angle (Kane & Mele 1997). The secondary gap in quasi-metallic *zigzag* nanotubes (chiral angle $= 0$) is found to be

$$\Delta E_g^2 = \frac{3\gamma_0 a_{cc}^2}{4d_t^2}, \tag{2.46}$$

which is vanishingly small so that one generally considers that all the $n - m = 3\ell$ tubes are metallic at room temperature (see Fig. 2.25). Measurements of the density of states using scanning tunneling spectroscopy have nicely confirmed the predicted $1/d_t^2$ dependence for three zigzag nanotubes (Ouyang et al. 2001b), together with the true metallic nature of armchair nanotubes. The band-folding picture based on the single-band *tight-binding* approach is therefore highly reasonable for large enough tube diameter (above 1 nm) (Hamada et al. 1992; Mintmire et al. 1992; Saito et al. 1992a).

2.5.4 Small-Diameter Nanotubes: Beyond the *Tight-Binding* Approach

The effect of curvature is significant for very small tube diameter, when σ and π states are strongly rehybridized (effect (III)). The zone-folding picture ceases to be correct, demanding that *ab initio* calculations be achieved (Blase et al. 1994) (Fig. 2.26). Strongly modified low-lying conduction band states are introduced into the bandgap of insulating tubes because of hybridization of the σ^* and π^* states, which reduces the energy gaps of some nanotubes by more than 50%. For example, the $(6, 0)$ tube, predicted to be a semimetal in the band-folding scheme, becomes a true metal within LDA, with a density of states at the Fermi level equal to 0.07 state/eV atom (Fig. 2.26(b) and (c)). The $\sigma^* - \pi^*$ hybridization is confirmed by drawing the charge density associated with the states around the Fermi level, as shown in Fig. 2.26(a). Such states are no longer antisymmetric with respect to the tube wall, with a charge spilling out of the tube. Nanotubes with diameters above 1 nm evidence no $\sigma - \pi$ rehybridization.

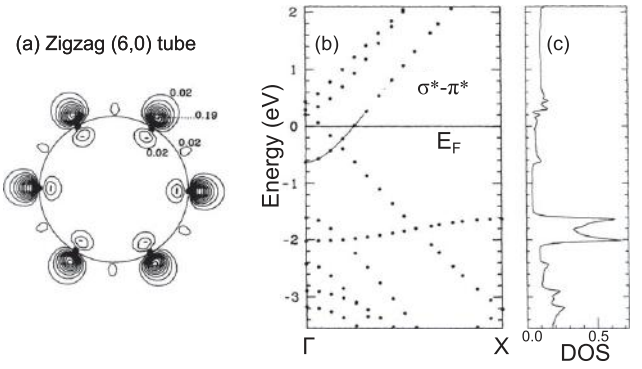

Figure 2.26 Electronic structure of a *zigzag* $(6, 0)$ nanotube. Contour plot of the charge density for state (a) at Γ. The contours are in a plane perpendicular to the axis of the tube containing six carbon atoms. The numbers cited are in units of $e/(a.u.)^3$. The circle represents a cross section of the cylinder on which the atoms lie. Electronic band structure (b) and density of states (c). The energies are in eV, the reference zero energy is at the Fermi level, and the DOS is in states/eV atom. The new band ($\sigma^* - \pi^*$) around the center of the Brillouin zone is traced as a visual guide. (Reproduced with permission from Blase et al. (1994). Copyright (1994) by the American Physical Society)

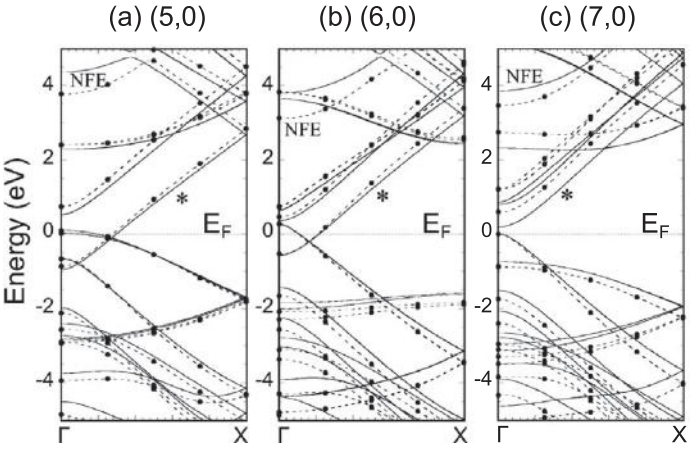

Figure 2.27 Electronic band structure of *zigzag*: (a) $(5, 0)$; (b) $(6, 0)$; and (c) $(7, 0)$ nanotubes. *Ab initio* (DFT-LDA) results (solid line) are compared to GW calculations (circles) for each relaxed geometry. Energy is measured from the Fermi level. Dashed lines are visual guides. (Adapted with permission from Miyake & Saito (2003). Copyright (2003) by the American Physical Society)

Electronic properties of small-diameter nanotubes have also been explored within the GW approximation, which makes it possible to account for many-body corrections (Miyake & Saito 2003). The GW calculations found that the energy of the $\sigma^* - \pi^*$ state is reduced with decaying diameter (as drawn by a * in Fig. 2.27), which strongly affects the $1/d$ law as soon as $d_t \sim 0.8\,\text{nm}$. For instance, the gap of the

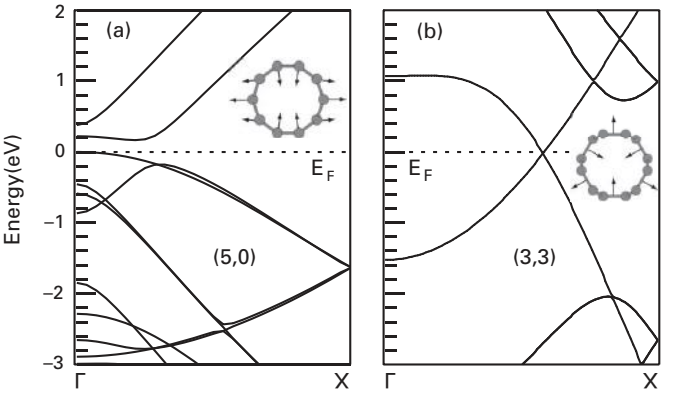

Figure 2.28 Band structures of (a) the distorted D_{2h} *zigzag* $(5,0)$ nanotube and (b) the *armchair* $(3,3)$ tube. The zero of energy has been set to the top of the valence bands and at the Fermi level, respectively. Inset are symbolic representations of the out-of-plane acoustical and optical modes at Γ for the phonon bands driving the Peierls instability in the (a) $(5,0)$ and (b) $(3,3)$ tubes, respectively. (Adapted with permission from Connétable et al. (2005). Copyright (2005) by the American Physical Society)

$(7,0)$ tube becomes 0.6 eV (Fig. 2.27(c)). Such a considerable many-body correction is actually compensated for by a lattice relaxation (Miyake & Saito 2003). The lowered state crosses the Fermi level in the $(5,0)$ and $(6,0)$ tubes which both become metallic (Fig. 2.27(a–b)). Therefore GW corrections are not strongly renormalizing the DFT results, which are reasonably good for varying tube diameters.

The analysis of optical spectra of both semiconducting and metallic tubes crucially needs to account for electron–hole interaction effects, which become prominent in small-diameter single-walled carbon nanotubes, but require *ab initio* calculations (Spataru et al. 2004). Finally, note that ultrasmall tube diameters (diameter of about 4 Å) have been obtained by performing tube growth inside $AlPO_4$-5 zeolite channels (with inner diameter of about 7.3 Å) (Wang et al. 2000). Some specific (but controversial) superconductivity has been reported in such ultrasmall tubes (Tang et al. 2001) which, given their reported diameter distribution around 4 Å, limits the possible geometries to the $(3,3)$, $(4,2)$, and $(5,0)$ nanotubes.

Such ultrasmall tubes have been studied using *ab initio* simulations by Connetable and coworkers (Connétable et al. 2005), who reported that the $(5,0)$ tube (predicted as a semiconductor in band-folding representation) becomes metallic with two bands (one doubly degenerate) crossing the Fermi level (yielding two different k_F), a curvature effect related to the Peierls distortion (Fig. 2.28(a)). In these calculations, the armchair $(3,3)$ remains semi-metallic, but with a $\pi - \pi^*$ band crossing at E_F that is displaced from its ideal $\frac{2}{3}\ \Gamma X$ position (Fig. 2.28(b)). To conclude, the zone-folding model is certainly valid as long as the tube diameter remains larger than 1 nm. When this condition is not satisfied, the single-band *tight-binding* approach can be misleading, requiring recourse to more accurate calculations, either through a sophisticated *tight-binding* approach, *ab initio* DFT-LDA, or even GW approximation depending on the tube being studied.

2.5.5 Nanotubes in Bundles

In the previous sections, only a special achiral subset of carbon tubes known as *armchair* nanotubes was predicted to exhibit true metallic behavior. These single-wall (n, n) nanotubes are the only real 1D cylindrical conductors with only two open conduction channels (energy subbands in a laterally confined system that cross the Fermi level). Hence, with increasing length, their conduction electrons ultimately become localized owing to residual disorder in the tube, which is inevitably produced by interactions between the tube and its environment. However, theoretical calculations (White & Mintmire 1998) have demonstrated that, unlike normal metallic wires, conduction electrons in *armchair* nanotubes experience an effective disorder averaged over the tube's circumference, leading to electron mean free paths that increase with nanotube diameter. This increase should result in exceptional ballistic transport properties and localization lengths of 10 μm or more for tubes with the diameters that are typically produced experimentally. These transport properties of *armchair* nanotubes are described in detail in Chapter 4.

Although the close-packing of individual nanotubes into ropes does not significantly change their electronic properties, *ab initio* calculations predicted that broken symmetry of the (10, 10) tube caused by the interactions between tubes in a rope induces a pseudogap of about 0.1 eV at the Fermi level (Delaney et al. 1998) (Fig. 2.29). Consequently, this pseudogap strongly modifies many of the fundamental electronic properties of the *armchair* tubes, explaining in particular a semimetallic-like temperature dependence of the electrical conductivity, as well as the presence of a finite gap in the infrared absorption spectrum for bundles of nanotubes.

As mentioned earlier, the electronic properties of isolated (n, n) *armchair* nanotubes are dictated by their geometrical structures, which impose the crossing of the two linear π–π^* bands at the Fermi energy (Fig. 2.29(a)). These two linear bands give rise to constant density of states near the Fermi level and to true metallic behavior. The atomic structure of an isolated (n, n) nanotube exhibits n mirror planes containing the tube axis. The π-bonding state is *even* (the wavefunction has no sign change) while the

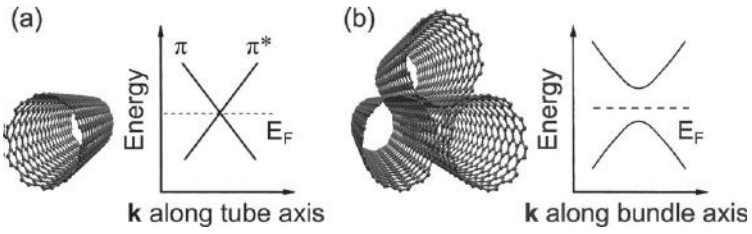

Figure 2.29 Energy band structures for (a) an isolated (10, 10) nanotube and (b) a bundle of (10, 10) nanotubes. The two diagrams show (a) the crossing of the two linear π–π^* bands for the isolated tube (π^*) character and (b) the bandgap opening due to the breaking of the mirror symmetry. E_F is the Fermi energy and k is the wavevector. (Adapted by permission from Macmillan Publishers Ltd: *Nature*, Delaney et al. (1998), copyright (1998))

π-antibonding state is *odd* (sign change) under these symmetry operations. The band crossing is thus allowed and the *armchair* nanotube is metallic, as illustrated schematically in Fig. 2.29(a). Note that it is precisely this symmetry of the isolated (n, n) tube that induces the intrinsic metallic behavior of the tube and its extraordinary ballistic conduction (White et al. 1998). Breaking this symmetry, however, completely alters this picture. If the tubes in the rope are separated enough to eliminate any nanotube interactions, the band structure will remain unchanged. However, the inter-tube distances in the bundle are small enough that each nanotube can feel the potential due to all neighboring tubes (Delaney et al. 1998). As a consequence of this perturbation, the Hamiltonian at any point k where the two π–π^* bands used to cross becomes

$$H_k = \begin{pmatrix} \varepsilon_0 + \delta_{11} & \delta_{12} \\ \delta_{21} & \varepsilon_0 + \delta_{22} \end{pmatrix},$$

where ε_0 is the unperturbed energy. The diagonal matrix elements δ_{11} and δ_{22} merely act to shift the energy and location in k-space of the band crossing. The off-diagonal elements (δ_{12} and δ_{21}) represent the quantum-mechanical level repulsion, thus opening a gap as illustrated schematically in Fig. 2.29(b). If the vertical line through k has high symmetry, the off-diagonal matrix elements may still be zero and a crossing may persist. However, at a general k point, the inter-tube interactions will dramatically change the physics of the ropes. If the symmetry of the nanotube is not broken in the bundle – i.e., for $(6, 6)$ armchair nanotubes – the crossing is preserved (Charlier et al. 1995). These inter-tube interactions, which break the rotational symmetry of *armchair* (n, n) tubes due to the local environment, have been measured experimentally using low-temperature scanning tunneling spectroscopy (Ouyang et al. 2001b), thus confirming that the magnitude of the pseudogap depends inversely on nanotube radius.

2.5.6 Multiwall Nanotubes

Another mechanism based on the multi-shell concept may tailor the electronic properties of nanotubes. Indeed, the weak interaction between the concentric shells in a multiwall nanotube may induce significant modifications of the electronic properties of the pristine individual nanotubes (Kwon & Tománek 1998; Lambin et al. 1994). The interwall coupling, already mentioned as opening a pseudogap in a bundle of single-wall nanotubes due to symmetry lowering, may periodically open and close four such pseudogaps near the Fermi energy (E_F) in a metallic double-wall nanotube during its rotation normal to the nanotube axis. Indeed, Fig. 2.30 illustrates the intriguing interplay between geometry and electronic structure during the rotation of the inside $(5, 5)$ armchair nanotube in the outside $(10, 10)$ nanotube, with the nanotubes sharing a common axis.

The individual $(5, 5)$ and $(10, 10)$ tubes are both metallic and present the conventional "graphitic" interwall separation of 3.4 Å when nested. To determine the electronic properties of the double-wall nanotube, a *tight-binding* technique with parameters extracted from *ab initio* calculations for simpler structures has been used (Kwon & Tománek 1998; Lambin et al. 1994). Due to the relatively high symmetry of the coaxial

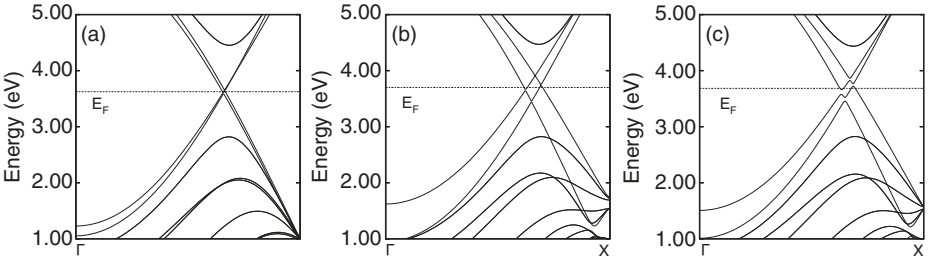

Figure 2.30 Energy band structures of a double-wall nanotube consisting of two aligned coaxial *armchair* nanotubes: (5, 5)@(10, 10). Near degenerate bands with no gap characterize the (5, 5)@(10, 10) double-wall nanotube without inter-tube interaction (a). In the presence of inter-tube interaction, depending on the mutual tube orientation, the (5, 5)@(10, 10) system may exhibit zero gap (b) in the most symmetric (point group symmetry: D_{5h}), or four pseudogaps (c) in a less symmetric and stable configuration (point group symmetry: C_5). (Adapted with permission from Kwon & Tománek (1998). Copyright (1998) by the American Physical Society. By courtesy of Young-Kyun Kwon)

system consisting of a D_{5d} (5, 5) nanotube nested inside the D_{10h} (10, 10) nanotube, the dependence of the inter-tube interaction on the tube orientation presents an 18° periodicity. In the absence of inter-tube interaction, the band structure of each isolated tube is preserved and characterized by two crossing linear π–π^* bands near E_F, one for the "left" and one for the "right" moving electrons. The band structures of a pair of decoupled (5, 5) and (10, 10) coaxial nanotubes are illustrated in Fig. 2.30(a) as a mere superposition of the individual band structures. Switching on the inter-tube interaction in the (5, 5)@(10, 10) double-wall tube removes the near degeneracy of the bands near E_F as well (see Fig. 2.30(b,c)). In the most stable orientation, the double-wall system is still characterized by the D_{5d} symmetry of the inner tube. The four bands cross, with a very small change in the slope (Fig. 2.30(b)). While the same argument also applies to a least stable configuration, markedly different behavior is found at any other tube orientation that lowers the symmetry, giving rise to four band crossings (Fig. 2.30(c)). This translates into four pseudogaps in the density of states near E_F (Kwon & Tománek 1998). At the Fermi level, the density of states of double-wall nanotubes is thus affected by the mutual orientation of the two constituent nanotubes since the positions of the four pseudogaps depend significantly on it. The opening and closing of pseudogaps during the liberation motion of the double-wall tube is a unique property that cannot be observed in single-wall nanotube ropes (Kwon & Tománek 1998). Finally, self-consistent charge density and potential profiles for double-wall nanotubes, considering various chiralities, have been obtained (Miyamoto et al. 2001), and demonstrate that the atomic structure of the inner tube modifies the charge density associated with states near E_F, even outside the outer tube, so that it could even be probed experimentally using an STM. A significant amount of charge, originating mainly from the π electron system of the tubes is transferred mainly into a new interwall state, related to the interlayer state in graphite (Miyamoto et al. 2001).

2.6 Defects and Disorder in Graphene-Based Nanostructures

In the first section of the this chapter, the fascinating electronic properties of graphene are described, suggesting the latter to be a material of choice for future nano -electronics. Indeed, graphene exhibits an extremely high stability, huge carrier mobilities, and a thermal conductivity predicted to be nearly twice that of diamond. Graphene also presents a high response to perpendicular electric fields, making it possible to tune the type and concentration of charge carriers. Its high carrier mobilities and long phase coherence length (Miao et al. 2007) suggest potential applications in integrated circuits, high-mobility transistors, or single-molecule gas sensors. Eventually, graphene can also be patterned using existing lithographic techniques and can meet many requirements for the process and design of nanoelectronic devices.

However, the lack of an electronic (or transport) gap in pristine graphene is an issue that has to be overcome in order to achieve a high I_{on}/I_{off} current ratio in graphene-based field-effect devices (Xia, Farmer et al. 2010). In this context, controlled engineering of defects in sp^2 carbon-based materials has become a topic of great excitement (Krasheninnikov & Banhart 2007). Indeed, the electronic (and transport) properties of carbon nanotubes (Charlier et al. 2007) and graphene-based nanomaterials (Cresti et al. 2008; Suenaga et al. 2007) can be considerably enriched by chemical modifications, including substitution and molecular doping (Latil et al. 2004; Lherbier, Blase et al. 2008) as well as functionalization. Another approach to tuning the electronic properties of graphene consists of using ion or electron-beam irradiation in order to introduce structural point defects (e.g., vacancies, Stone–Wales defects, adatoms, etc.) in sp^2 carbon-based nanostructures. Indeed, convincing room-temperature signatures of an Anderson regime in irradiated carbon nanotubes (Gómez-Navarro et al. 2005) and graphene (Nakaharaim et al. 2013) or low-T saturating conductivities in graphene samples (Chen et al. 2009) have been reported. Consequently, it is crucial to understand the influence of defects on the electronic properties of graphene-based nanostructures not only in order to conquer their detrimental effects, but also because controlled defect introduction may be used to tune the carbon nanosystem properties in a desired direction (e.g., gas sensor, etc.)

In the following, a few important defects in sp^2 carbon nanostructures are illustrated, and their specific effects on the electronic properties of the host material are discussed.

2.6.1 Structural Point Defects in Graphene

Structural point defects exist in various geometrical forms in graphene and more generally in all sp^2 carbon-based nanomaterials (Banhart et al. 2011; Kotakoski et al. 2011). For example, the Stone–Wales (SW) defect is a well-known and common planar defect in sp^2 carbon nanostructures, which consists of a 90° rotation of a carbon–carbon bond (Stone & Wales 1986). This topological transformation yields to the formation of two heptagons connected with two pentagons (Fig. 2.31(a,b) and Fig. 2.32(a)).

Vacancies are missing carbon atoms in the honeycomb lattice and can be created by irradiating graphene with ions such as Ar^+ for instance. By removing one C atom from

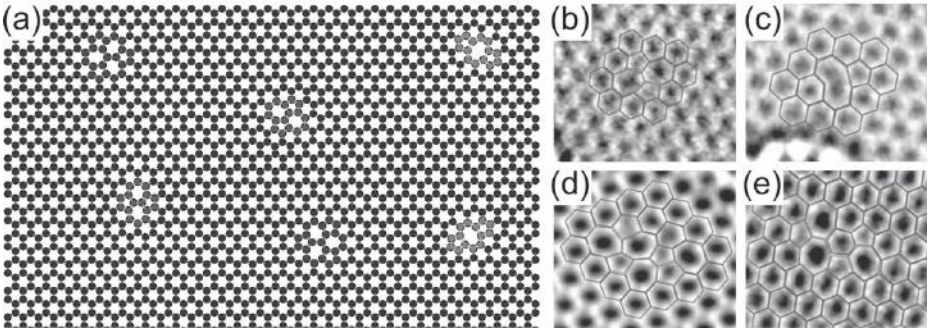

Figure 2.31 Structural point defects in graphene: (a) model for various realistic defects randomly oriented and distributed in graphene. HRTEM images of defects observed in graphene : (b) Stone–Wales; (c) vacancy; (d,e) more complex topologies containing pentagon–heptagon pairs. ((a) Adapted from Lherbier et al. (2012). Copyright (2008) American Physical Society. (b–e) Adapted with permission from Meyer et al. (2008). Copyright (2008) American Chemical Society)

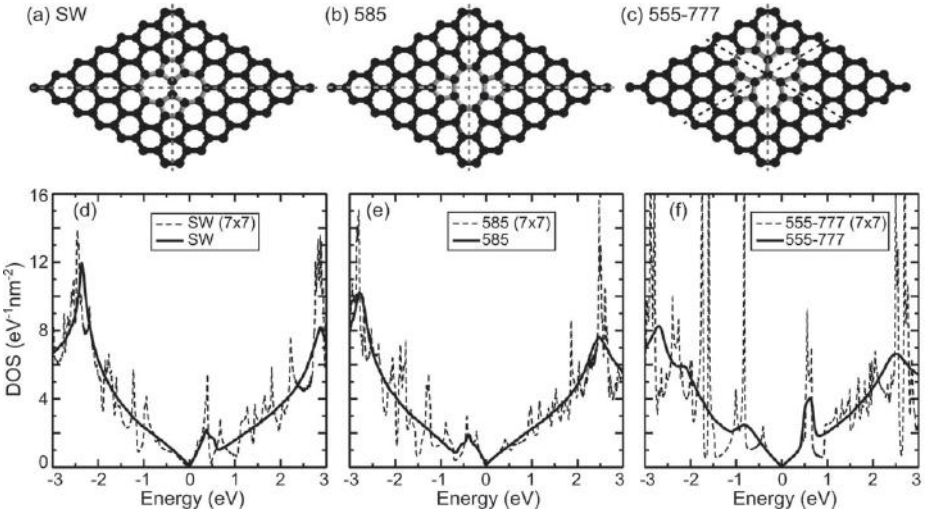

Figure 2.32 Topological defects in graphene and their corresponding effects on its electronic properties. Model of the three structural defects: (a) Stone–Wales; (b) 585; and (c) 555-777 divacancies. Symmetry axes are drawn in dashed lines, *tight-binding* densities of states for a single defect in a 7×7 graphene supercell (dashed lines indicate concentration of $\sim 1\%$) and for a large plane of graphene containing randomly distributed and oriented divacancies (thick lines indicate concentration of 1%) for the defects illustrated above: (d) Stone–Wales; (e) 585; and (f) 555-777 divacancies. (Adapted with permission from Lherbier et al. (2012). Copyright (2008) American Physical Society)

the graphene plane, three C atoms are left with an unsaturated bond. When the system is relaxed, this monovacancy undergoes a Jahn–Teller distortion: two of the unsaturated carbon atoms form a weak covalent bond, resulting in a pentagonal rearrangement (Fig. 2.31(c)). The third unsaturated carbon atom moves radially out of the plane, mod-

ifying the initial D_{3h} symmetry of the hexagonal network into the favored C_s symmetry (Amara et al. 2007). The monovacancy is a magnetic defect since the localized orbitals of the unsaturated carbon atom exhibit a net local magnetic moment (Lehtinen, Foster, Ayuela et al. 2004; Lehtinen, Foster, Ma et al. 2004), which could explain the issue of induced magnetization in some carbon nanomaterials (Yazyev, 2008, 2010; Yazyev & Helm, 2007). However, these single vacancies migrate easily in the graphene plane and are stabilized when they recombine with another, thus reconstructing into various divacancy defects (Kim et al. 2011; Krasheninnikov & Banhart 2007; Lee, Son et al. 2005).

For example, the reconstruction can lead to formation of two pentagons and one octagon (so-called 585, Fig. 2.32(b)), or also to three pentagons and three heptagons (so-called 555-777, Fig. 2.32(c)). According to *ab initio* calculations, the formation energy of the 555-777 divacancy is smaller than that of the 585 divacancy by about 0.9 eV (Lherbier et al. 2012). Such a stabilization of the 555-777 divacancy with regards to the 585 divacancy in graphene contrasts with the case of carbon nanotubes (Lee, Son et al. 2005). A third kind of divacancy has also been reported (Banhart et al. 2011; Meyer et al. 2008), exhibiting a larger extension and involving four pentagons, one hexagon, and four heptagons (so-called 5555-6-7777, not illustrated here). In contrast with monovacancies that cannot be considered as reversible geometrical modifications of the ideal graphene plane, divacancies and Stone–Wales defects belong to the class of topological defects. One also notes that the 585 divacancy as well as the SW defect possesses a D_{2h} symmetry since two orthogonal symmetry axes can be defined (Fig. 2.32(a, b)), whereas the 555-777 divacancy possesses a D_{3h} symmetry (Fig. 2.32(c)). Observation of these three structural point defects has already been reported in graphene by means of STM experiments (Suenaga et al. 2007; Ugeda et al. 2012) or transmission electron microscopy (TEM) images (Meyer, Kisielowski et al.(2008) 2008) and their influence on transport properties has also deserved in-depth inspection (Lherbier et al. 2011).

In order to investigate the effect of these structural defects on graphene, two center 3rd nearest-neighbors π–π^* orthogonal *tight-binding* models for both pristine and defective graphene can be computed using *ab initio* calculations. To extract optimized TB parameters, a set of points $E(k)$ is chosen in the *ab initio* band structure and used as constraints in a fit procedure (Lherbier et al. 2012). These TB parameters are usually fitted to reproduce as accurately as possible the full band structure (as described previously). An alternative strategy can also be applied when the *ab initio* Hamiltonian is expressed in a localized orbitals basis set. Indeed, the TB parameters can thus be directly *extracted* by performing successive operations on this *ab initio* Hamiltonian. In particular, the basis set has to be reduced to a single p_z orbital.

Local TB parameters corresponding to a given disorder potential are obtained using the same fitting technique as for the pristine graphene. For the impurity potential, only onsite modifications are considered, but the new arrangement of neighbors for carbon atoms in the core of the defects is carefully taken into account. For the SW defect, the rotation of the carbon–carbon bond leads to a modification of first, second, and third-

nearest neighbors for carbon atoms in the vicinity of the rotated bond. The validity of the TB parameterization for the defects is checked by comparing the *ab initio* and the TB band structures for a 7×7 supercell containing a single defect. In Fig. 2.32, the TB band structure (lines with symbols) is superimposed on the *ab initio* band structure (full lines). A good agreement is obtained, especially for the valence bands. The conduction band side seems to be less accurate but this is uniquely due to the inability of the pristine graphene TB model to reproduce a conduction band along a *K*–*M* branch.

The density of states of random distribution of structural point defects in the honeycomb lattice (large graphene planes) can then be estimated, revealing the salient features that persist after taking into account the randomness character of the disorder. Figure 2.32(d–f) presents the total DOS of large graphene samples containing 1% of SW, 585, and 555-777 divacancies, computed using the recursion method (see Appendix D), and compared with the total DOS calculated for a 7×7 supercell containing a single defect (more or less the same concentration, $\sim$1%). A first observation is that the DOS of random disordered systems is much smoother than the one corresponding to a single defect in a supercell. In the random disorder case, most of the peaks have disappeared except those close to the Dirac point (set to zero). The broadening due to the distribution disorder is more efficient in energy regions containing several bands. Close to the Dirac point, the number of bands is smaller, which preserves the defect-induced resonances. Secondly, the position of resonance energy peaks is consistent with the *ab initio* supercell band structures obtained for defective graphene (Lherbier et al. 2012). The DOS of randomly disordered graphene suggests that the electron transport in an energy region around $E = 0.35$ eV should be mainly damaged by SW defects, whereas hole transport should be altered around $E = -0.35$ eV for 585 divacancies, and finally that 555-777 divacancies exhibit several resonance energies around $E = 0.6, -0.8, -2.1$ eV, which should also lead to reduced transport performances. Such an in-depth analysis of the transport properties of graphene containing a random distribution of structural point defects is presented in Chapter 7.

2.6.2 Grain Boundaries and Extended Defects in Graphene

Single-atom-thick graphene sheets are presently produced by chemical vapor deposition (Li et al. 2009) on macroscopic scales (up to meters (Bae et al. 2010)), making their polycrystallinity almost unavoidable. This polycrystalline nature of graphene samples at micrometer length scales induces the presence of intrinsic topological defects of polycrystalline materials, such as grain boundaries and dislocations. Theoretically, graphene grain boundaries are predicted to inevitably affect all kinds of physical properties of graphene, but these drastic modifications strongly depend on their atomic arrangement. Using atomic-resolution imaging, experimentalists have been able to determine the location and identity of every atom at a grain boundary, discovering that different grains stitch together predominantly through pentagon–heptagon pairs (Huang et al. 2011) (see Fig. 2.33(a,b)). By correlating grain imaging with scanning probe and transport

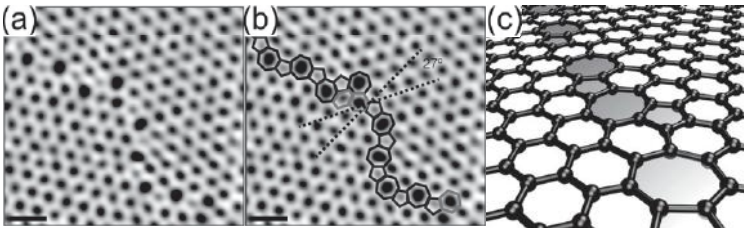

Figure 2.33 Atomic-resolution STEM images of polycrystalline graphene: (a) two grains (bottom left, top right) intersect with a 27° relative rotation. An aperiodic line of defects stitches the two grains together (scale bars 5 Å). This grain boundary is composed of pentagons, heptagons, and distorted hexagons as outlined in (b). (c) Model of the atomic structure of a tilt grain boundary in graphene separating two crystalline domains. ((a) and (b) Adapted with permission from Macmillan Publishers Ltd: *Nature* from Huang et al. (2011), copyright (2011). (c) By courtesy of Oleg Yazyev)

measurements, these grain boundaries were found to severely weaken the mechanical strength of graphene, but they do not so drastically alter their electrical properties.

From a theoretical point of view, grain boundaries (GB) with large-angle symmetric configurations were found to be energetically favorable using *ab initio* calculations (Yazyev & Louie, 2010a, 2010b) (see Fig. 2.33(c)). Drastic stabilization of small-angle configuration GBs via out-of-plane deformation has also been predicted (Yazyev & Louie 2010b), which is a remarkable feature of graphene as a truly two-dimensional material. Grain boundaries are expected to markedly alter electronic transport in graphene. Indeed, charge-carrier transport across periodic grain boundaries is primarily governed by a simple momentum conservation law (Yazyev & Louie 2010a). Two distinct transport behaviors have been predicted – either perfect reflection or high transparency for low-energy charge carriers, depending on the grain boundary atomic structure (see Fig. 2.33(c)). Furthermore, engineering of periodic grain boundaries with tunable transport gaps has also been suggested (Yazyev & Louie 2010a), allowing for controlling charge currents without the need to introduce bulk bandgaps in graphene. Tailoring electronic properties and quantum transport by means of grain boundary engineering may pave a new road toward practical digital electronic devices based on graphene at a truly nanometer scale.

The controlled engineering of extended defects represents a viable approach to creation and nanoscale control of one-dimensional charge distributions with widths of several atoms. When graphene is grown on two non-equivalent threefold hollow sites of Ni(111) substrate, termed fcc (face-centered cubic) and hcp (hexagonal close-packed) sites (Fig. 2.34(a)), a one-dimensional extended line of defects can be formed without any unsaturated dangling bonds by restructuring the two graphene half-lattices that are translated by a fractional unit cell vector $1/3(a_1 + a_2)$ (where a_1 and a_2 are the two graphene unit cell vectors) (Lahiri et al. 2010). (See Fig. 2.34(a).) The two graphene domains can be joined at their boundary so that every carbon has a threefold coordination, forming a one-dimensional topological defect consisting of a pair of pentagons and one octagon periodically repeated along the dislocation line (Fig. 2.34(b)).

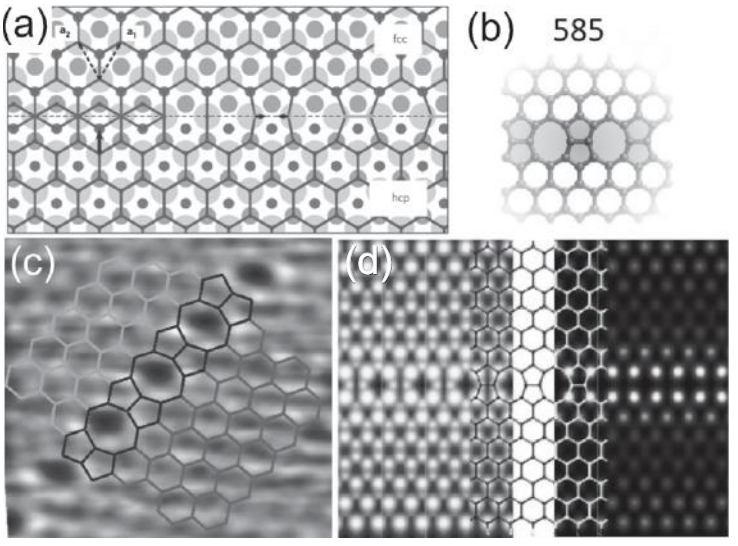

Figure 2.34 Extended one-dimensional defect in graphene. (a) Structural model and schematic formation: the two half-lattices can be joined along the $a_1 - a_2$ direction (indicated by the dashed line) by restructuring the graphene lattice. The domain boundary can be constructed as illustrated, by joining two carbon atoms – indicated by the two arrows – along the domain boundary line. This reconstructed domain boundary forms a periodic structure consisting of octagonal and pentagonal carbon rings. The underlying Ni(111) structure illustrates how the extended defect is formed by anchoring two graphene sheets to a Ni(111) substrate at slightly different adsorption sites. If one graphene domain has every second carbon atom located over an fcc-hollow site (upper part) and the other domain over a hcp-hollow site (lower part), then the two domains are translated by $1/3(a_1 + a_2)$ relative to one another. The light, medium, and dark gray spheres correspond to Ni atoms in the 1st, 2nd, and 3rd layers, respectively. (b) Schematic model based on the periodic repetition of a 585 (pentagon–octagon–pentagon) defect. (c) Experimental STM images. (d) *Ab initio* STM images simulated at constant current (left) and constant height (right) for the extended 585 one-dimensional extended line with the superimposed defect model. ((a) and (c) Reprinted by permission from Macmillan Publishers Ltd: *Nat. Nanotech.*, Lahiri et al. (2010), copyright 2010. (b) and (d) From Botello-Mendez et al. (2011). Adapted by permission of The Royal Society of Chemistry)

The atomic locations identified from scanning tunneling microscopy (Fig. 2.34(c)) confirm that the defect is composed of one octagon surrounded by a pair of pentagons and a period of twice the unit cell vector of graphene along the defect line has been measured (Lahiri et al. 2010). Although STM constitutes an excellent experimental tool for identifying defects in graphene (Amara et al. 2007), the interpretation of the images can sometimes be extremely complicated. Therefore, in order to overcome the problem of defect identification, simulated images have been calculated from the *ab initio* local density of states of an extended line of 585 defects embedded in GNRs using the Tersoff–Hamann approximation (Botello-Mendez et al. 2011) (Fig. 2.34(d)). LDOS are computed between 0.2–0.3 eV with respect to the Fermi energy in order to account for an n-type doping substrate (i.e., Ni in the experiment). It is noteworthy that the

ab initio STM image for the extended line of 585 defects (Fig. 2.34(d)) exhibits a quite good agreement with the experimental one (Fig. 2.34(c)).

Various architectures of an extended line of defects – embedded in graphene, and exhibiting pentagonal, heptagonal, and octagonal rings of carbon – were explored using first-principles simulations (Botello-Mendez et al. 2011). Three different stable atomic configurations were predicted to arise from the reconstruction of periodic divacancies.

Indeed, different divacancy defects with various orientations relative to the zigzag direction of graphene could be formed (Fig. 2.35). The first option is to remove carbon dimers oriented perpendicularly to the zigzag chains (Fig. 2.35(a)). Intuitively, it is expected that after geometrical relaxation, the structure would be composed of

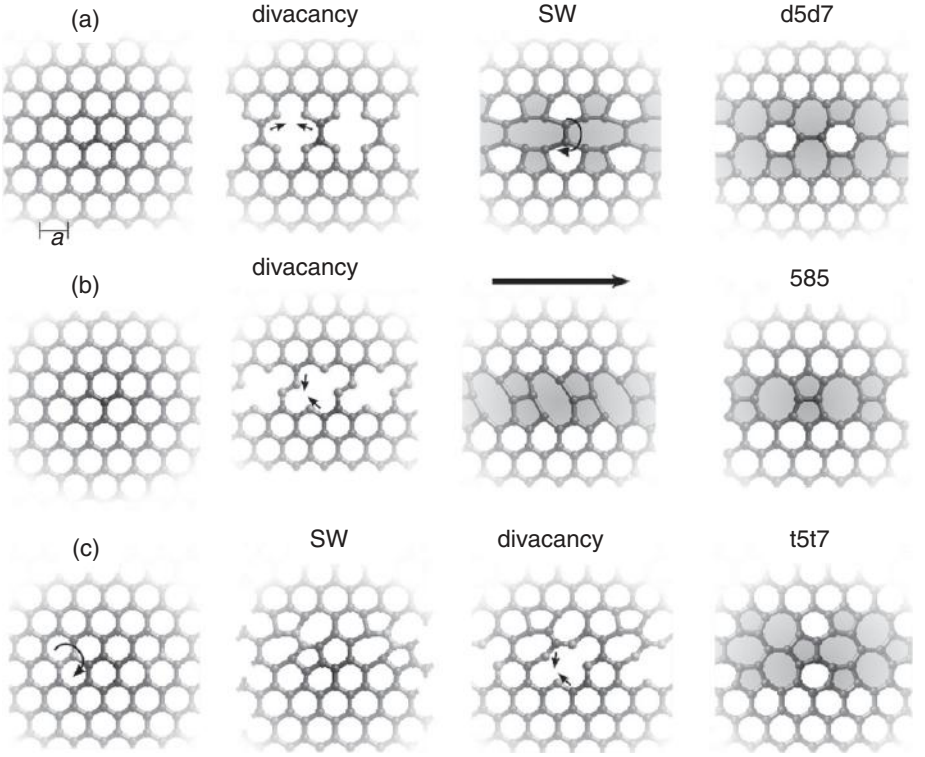

Figure 2.35 Formation of extended lines of defects in graphene through the reconstruction of divacancies. Lines of defects are formed after the removal of carbon dimers, either (a) perpendicular or (b) with a 30° deviation from the zigzag direction. These extended arrays of defects are called (a) d5d7 (double-5 double-7 structure) and (b) 585 (pentagon–octagon–pentagon structure), respectively. Further displacement of one graphene side by $\frac{1}{2}a$ (black arrow in b) is required to relax the 585 grain boundary as observed in Lahiri et al. (2010). An extended array of defects composed of a series of three pentagons and three heptagons (t5t7 – triple-5 triple-7 structure) is also topologically possible when the divacancy reconstruction occurs along with a SW transformation (c). (Images from Botello-Mendez et al. (2011). Adapted by permission of The Royal Society of Chemistry)

two pentagons separated by an octagon, also perpendicular to the zigzag orientation. However, the energy needed to achieve such a large strain prevents the octagons from being formed. Instead, a C–C bond rotation (as in a Stone–Wales defect) is needed to relieve the strain, as illustrated by the d5d7 structure in Fig. 2.35(a). The second option consists in removing the carbon dimers tilted 30° from the zigzag orientation of graphene, resulting in an alternated series of octagons and two pentagons sharing a same side, as represented by the 585 structure in Fig. 2.35(b).

A less strained 585 structure could be obtained by displacing one of the two graphene domains connected to the grain boundary by $\frac{1}{2}a$, where a is the lattice parameter of graphene. Such a grain boundary structure is the one observed during the epitaxial growth of graphene (Lahiri et al. 2010) (Fig. 2.34(c)). An alternative array of defects could be reconstructed from divacancies by means of a SW transformation, thus leading to a triple-pentagon triple-heptagon (t5t7) structure as depicted in Fig. 2.35(c). Such a defect shape has already been suggested as a stable topology for the reconstruction of an isolated divacancy in graphene (Amorim et al. 2007).

The energetic stability and the ground-state properties of these lines of defects arising from the reconstruction of divacancies have also been investigated using the DFT formalism (Botello-Mendez et al. 2011). LDA calculations predict that the most stable reconstruction of an array of divacancies is a line of t5t7 defects (Fig. 2.35(c)), whereas the GGA calculations predict that the most stable reconstruction is the 585 array of defects (Fig. 2.35(b)). Such a discrepancy can be easily explained by the fact that LDA calculations tend to underestimate the lattice parameters of graphene, while GGA calculations tend to overestimate these values. It is also noteworthy that the experimental observation of the 585 reconstruction is constrained by the specific synthesis conditions (Lahiri et al. 2010). However, in a top-down approach, e.g., vacancy creation through irradiation, the reconstruction would be either with the t5t7 or d5d7 line of defects, and would be most probably driven by the kinetics and interaction with the substrate.

In order to verify the potential advantages of these 1D arrays of defects in nano-electronics, electronic band structure calculations have been performed (Botello-Mendez et al. 2011; Lahiri et al. 2010). The presence of 5- and 7-member rings embedded into the sp^2-hybridized carbon network is found to induce an unexpected always-metallic behavior (Terrones, Terrones, Banhart et al. 2000). Indeed, an almost flat band, similar to that of zigzag-edged GNR, is present close to the Fermi energy (Fig. 2.36(a)), resulting in a spike in the DOS at the Fermi level. The corresponding electronic states from the band close to the Fermi level produce a local doping in a narrow stripe along the line defect, thus creating a perfect one-dimensional metallic wire embedded in the perfect graphene sheet. Such a well-defined atomic structure of a nanowire embedded in an atomically perfect graphene sheet can help to address, in a practical way, the formation of well-controlled contacts at the atomic level, as required for the future development of molecular electronics.

In the case of the extended line of t5t7 defects, extra conduction channels are induced (Botello-Mendez et al. 2011) and localized states could enhance the chemical

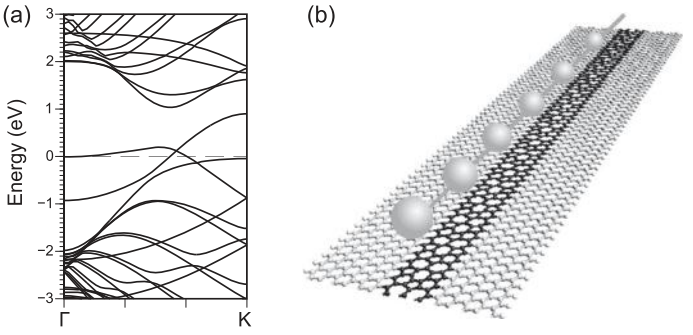

Figure 2.36 *Ab initio* electronic band structure of the 585 extended one-dimensional defect (a), exhibiting a flat band close to the Fermi level in the first half of the Brillouin zone. (b) Model illustrating the enhancement of chemical reactivity along the extended line of t5t7 defects allowing new molecular-sensing self-assembling possibilities. ((a) Reprinted by permission from Macmillan Publishers Ltd: *Nat. Nanotech*., Lahiri et al. (2010), copyright 2010. Image (b) by and courtesy of Andrés (Botello-Mendez et al. 2011))

reactivity of graphene. This extended defect opens the possibility of arranging molecules or atoms in a linear fashion, thus behaving as a 1D template (Fig. 2.36(b)). Such quasi-one-dimensional carbon-based metallic wires could have a big impact on the future development of smaller functional devices and may form building blocks for atomic-scale, all-carbon electronics.

2.6.3 Structural Defects at Graphene Edges

As illustrated in the previous sections, the atomic structure of the edges is responsible to a large extent for the electronic properties of graphene nanoribbons. In many nanoscale materials, the surfaces and the edges fix the symmetry inside the "bulk" and determine the corresponding low-energy electronic structure. In GNRs, the edges also turn out to rule the appearance of flat π bands at the Fermi level and ferromagnetic ordering of π electrons along the ribbon axis. In aiming at future applications of graphene in electronic and/or spintronic devices, the precise control of the edges is crucial.

Although the physics of the graphene edges has been intensively investigated in the literature, only very few works consider the possibility for the edge to relax toward geometries other than the standard mono-hydrogenated zigzag and armchair patterns (Koskinen et al. 2008; Wassmann et al. 2008). In addition, experimental studies of the graphene edge are even scarcer due to the difficulty in resolving the terminations atomically the without perturbing their intrinsic structures (Girit et al. 2009; Meyer et al. 2008). Such a lack of edge characterization continues to prevent a deep understanding of many experimental results. Indeed, despite theoretical calculations that predict nearly flat bands around the Fermi level for the zigzag edges, the experimental measurements reveal semiconducting behavior for all tested GNRs. Besides, the measured transport properties of graphene ribbons seem to be independent of their crystallographic orientation (Han et al. 2007; Li, Muller et al. 2008; Wang et al. 2008). Many reasons

related to sample preparation (e.g., presence of adsorbates, substrate effects, etc.) or to the appearance of mobility gaps induced by edge disorder have been put forward to explain this disagreement between theory and experiments. Presently, the graphene edge structure remains a widely debated issue (Dubois 2009).

2.6.4 Defects in Carbon Nanotubes

In the previous sections, only the geometrical aspect and the local environment of carbon nanotubes have been investigated. As in graphene, the intrinsic honeycomb network of carbon nanotubes is probably not as perfect and ideal as previously considered. Indeed, defects like pentagons, heptagons, vacancies, or dopants could certainly also be found, thus modifying dramatically the electronic properties of these 1D nanosystems. Introducing defects in the carbon network is thus an interesting way to tailor the intrinsic properties of the tube, in order to propose novel potential applications in nanoelectronics.

Thanks to the sensitivity of the metallic/semiconducting character of carbon nanotubes to their chirality, they can be used to form all-carbon metal–semiconductor, semiconductor–semiconductor, or metal–metal junctions. These junctions have great potential for applications since they are of nanoscale dimensions and made entirely of carbon. In constructing this kind of on-tube junction, the key is to seamlessly join together two half-tubes of different helicity, indexhelicity@helicity (*see also chirality*) , without too much cost in energy or disruption in structure. The introduction of pentagon–heptagon pair defects into the hexagonal network of a single-wall carbon nanotube has been shown to change the helicity of the carbon nanotube and fundamentally alter its electronic structure (Charlier et al. 1996; Chico et al. 1996; Dunlap 1994; Lambin et al. 1995; Saito et al. 1996). Both the existence of such atomic-level structures and the measurement of their respective electronic properties have already been resolved experimentally (Ouyang et al. 2001a; Yao et al. 1999).

The defects, however, must induce zero net curvature to prevent the tube from flaring or closing. The smallest topological defect with minimal local curvature (hence less energy cost) and zero net curvature is a pentagon–heptagon pair. When the pentagon is attached to the heptagon, as in the aniline structure, it only creates topological changes (but no net disclination), which can be treated as a single local defect. Such a pair will create only a small local deformation in the width of the nanotube, and may also generate a small change in the helicity, depending on its orientation in the hexagonal network. Figure 2.37 depicts the connection, using a single 5–7 pair, between two nanotubes exhibiting different electronic properties. As mentioned above, the $(8, 0)$ nanotube has a 1.2 eV gap in the *tight-binding* approximation, and the $(7, 1)$ tube is a metal (although a small curvature-induced gap is present close to the Fermi energy).

Joining a semiconducting nanotube to a metallic one, using a pentagon–heptagon 5–7 pair incorporated in the hexagonal network, can thus be proposed as the basis of a nanodiode (or molecular diode) for nanoelectronics. The system illustrated in Fig. 2.37 forms a quasi-1D semiconductor–metal junction, since within the band-folding picture

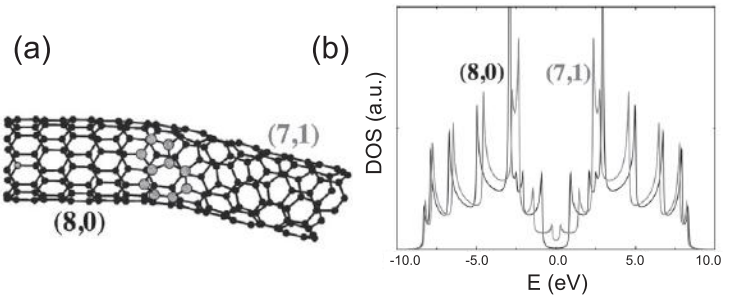

Figure 2.37 (a) Atomic structure of an $(8, 0)/(7, 1)$ intramolecular carbon nanotube junction. The large light-gray balls denote the atoms forming the heptagon–pentagon pair. (b) The electron density of states related to the two perfect $(8, 0)$ and $(7, 1)$ nanotubes is illustrated with thick black and thin gray lines, respectively. (Adapted with permission from Chico et al. (1996). Copyright (1996) American Physical Society. By courtesy of Leonor Chico)

the $(7, 1)$ half-tube is metallic and the $(8, 0)$ half-tube is semiconducting. This led to the prediction that these defective nanotubes would behave as the desired nanoscale metal–semiconductor Schottky barriers, semiconductor heterojunctions, or metal–metal junctions with novel properties, and that they could act as building blocks in future nanoelectronic devices.

The beam of a transmission electron microscope can be used to irradiate nanostructures locally. Covalently connected crossed single-wall carbon nanotubes can thus be created using electron beam welding at elevated temperatures (Terrones, Terrones, Banhart et al. 2000; Terrones et al. 2002). These molecular junctions of various geometries ("X,""Y," and "T") are found to be stable after the irradiation process. To study the relevance of some of these nanostructures, various models of ideal molecular junctions can be generated. The presence of heptagons is found to play a key role in the topology of nanotube-based molecular junctions. Figure 2.38 depicts an ideal "X" nanotube connection, where a $(5, 5)$ armchair nanotube intersects a $(11, 0)$ zigzag tube. In order to create a smooth topology at the molecular junctions, six heptagons are introduced at each crossing point (Terrones et al. 2002).

The local densities of states of the metallic $(5, 5)$ nanotube and the (semiconducting) $(11, 0)$ nanotube are illustrated in Fig. 2.38. The LDOS of the regions where the two nanotubes cross reveals an enhancement of the electronic states at the Fermi level. It is also notable that the presence of localized donor states in the conduction band (as indicated by arrows) is caused by the presence of heptagons. The novel small peak on the valence band (also shown by an arrow), close to the Fermi energy, can probably be attributed to the high curvature of the graphitic system (Terrones et al. 2002). The van Hove singularities present in the LDOS of the two achiral nanotubes are dramatically less pronounced in the junction region (Fig. 2.38), thus illustrating a clear loss of the one-dimensional character. Local density of states of CNT-based junction models suggests their importance in electronic device applications and paves the way towards

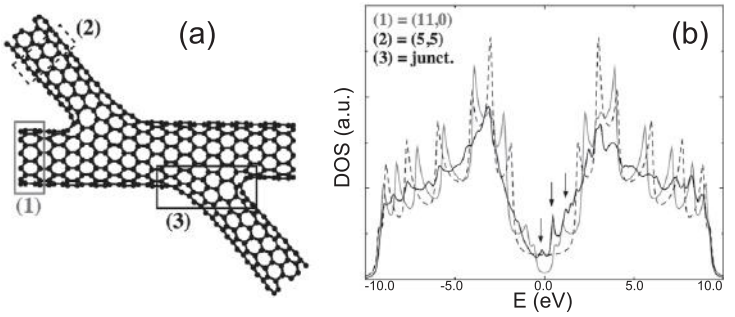

Figure 2.38 Atomic structure (a) and electronic properties (b) of an ideal X-junction, created by intersecting an (5, 5) tube with an (11, 0) tube. (b) shows the one-dimensional electronic densities of states of a semiconducting (11, 0) nanotube (light curve), a metallic (5, 5) nanotube (dashed curve) and the average over the intersecting region of the molecular junction (black curve). The Fermi level is positioned at the zero energy. Localized states due to the presence of defects are indicated by arrows. (Adapted with permission from Terrones et al. (2002). Copyright (2002) by the American Physical Society)

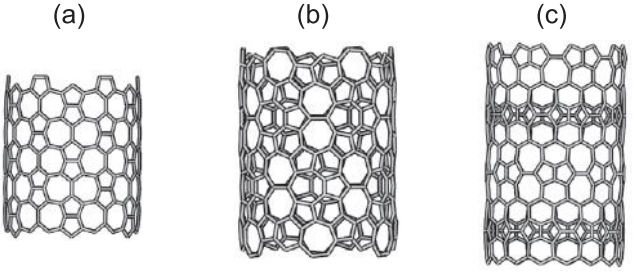

Figure 2.39 Nonchiral Haeckelite nanotubes of similar diameter (1.4 nm): (a) nanotube segment containing only heptagons and pentagons paired symmetrically; (b) nanotube segment exhibiting repetitive units of three agglomerated heptagons, surrounded by alternating pentagons and hexagons; (c) nanotube segment containing pentalene and heptalene units bound together and surrounded by six-membered rings. (Adapted with permission from Terrones, Terrones, Hernández et al. 2000. Copyright (2000) by the American Physical Society)

controlled fabrication of nanotube-based molecular junctions and network architectures exhibiting exciting electronic and mechanical behavior.

To close this subsection, we note that following the previous idea of introducing pentagons and heptagons into hexagonal networks, a novel class of perfect crystals – consisting of layered sp^2-like carbon and containing periodic arrangements of pentagons, heptagons, and hexagons – has been suggested theoretically (Terrones, Terrones, Hernández et al. 2000). These sheets are rolled up so as to generate single-wall nanotubes (Fig. 2.39), which resemble locally the radiolaria drawings of Ernst Haeckel (1862).

These ideally defective tubes exhibit intriguing electronic properties: calculations of local density of states of Haeckelite tubes reveal an important enhancement of

electronic states close to the charge neutrality point, independent of orientation, tube diameter, and chirality. Considering the possible metallic properties of Hackelites, these new nanostructures should offer different advantages compared to carbon nanotubes in applications (i.e., no helicity selection for electronic interconnect applications). Our calculations also reveal that these Haeckelite structures are more stable than C_{60}, and present cohesive energies of the order of 0.3–0.4 eV/atom with respect to graphene, allowing the potential synthesis of this new class of nanotubes. Although these ideal topologies have never been synthesized, the carbon coiled nanostructures have been explained by rolling up strips mainly made of heptagons, pentagons, and hexagons, with a predominance of nonhexagonal rings (Biró et al. 2002).

2.7 Further Reading and Problems

- General suggested references on carbon nanotubes include Saito et al. (1998) and Charlier et al. (2007).
- For a very detailed review on the low-energy ($\mathbf{k}\cdot\mathbf{p}$) approximation applied to graphene and carbon nanotubes, see Marconcini & Macucci (2011).
- A very detailed account of the boundary conditions in a terminated graphene network is presented in Akhmerov (2011). Furthermore, a very nice presentation on graphene zigzag edge states can be found in Wimmer (2009).

Problems

2.1 *Non-orthogonal tight-binding scheme and graphene dispersion.* Follow Section 2.2.1 and re-derive the dispersion relation for graphene without neglecting the overlap $s = \langle p_z^A | p_z^B \rangle$ between neighboring p_z orbitals. Compare the results obtained with and without the approximation.

2.2 *Electronic structure of graphene and boron nitride: the $\pi-\pi^*$ model.* Using a simple *tight-binding* approach (one π orbital per atom in a honeycomb lattice), the following TB Hamiltonian can be constructed:

$$H = \begin{pmatrix} \varepsilon_A & \gamma_0 f(k) \\ \gamma_0 f^*(k) & \varepsilon_B \end{pmatrix},$$

where ε_A and ε_B are the two onsite energies of the two corresponding atoms present in the unit cell, γ_0 is the hopping integral, and $f(k)$ is the sum of the nearest-neighbor phase factors and is equal to $e^{ik_x a/\sqrt{3}} + 2e^{-ik_x a/2\sqrt{3}} \cos(k_y a/2)$ (Wallace 1947).

Solve the eigenvalue problem when $\varepsilon_A = \varepsilon_B$ (graphene) and when $\varepsilon_A \neq \varepsilon_B$ (boron nitride sheet, Bernal graphite, etc.).

2.3 *Electronic structure of graphene: a tight-binding study.* Most *tight-binding* studies use a first-nearest-neighbors $\pi-\pi^*$ model to describe the electronic properties of graphene. However, such an approximation produces a perfectly symmetric band

structure (cf. previous exercise). In order to recover the existing asymmetry between valence (π) and conduction (π^*) bands, a third-nearest-neighbors $\pi-\pi^*$ model has to be used. Such a TB model is composed of a single onsite term ε_{p_z} and three hopping terms $\gamma_0^{(1)}$, $\gamma_0^{(2)}$, and $\gamma_0^{(3)}$ corresponding to the interaction between first-, second-, and third-nearest neighbors, respectively. The corresponding Hamiltonian can thus be expressed as follows:

$$H = \sum_i \varepsilon_{p_z} |\phi_i\rangle\langle\phi_i| + \sum_{i,<j,k,l>} \left(\gamma_0^{(1)} |\phi_j\rangle\langle\phi_i| + \gamma_0^{(2)} |\phi_k\rangle\langle\phi_i| + \gamma_0^{(3)} |\phi_l\rangle\langle\phi_i| + h.c.\right),$$

with $\varepsilon_{p_z} = 0.6$ eV, $\gamma_0^{(1)} = -3.1$ eV, $\gamma_0^{(2)} = 0.2$ eV, and $\gamma_0^{(3)} = -0.16$ eV. The sums on index i run over all carbon p_z orbitals. The sums over j, k, l indices run over all p_z orbitals corresponding, respectively, to first-, second-, and third-nearest neighbors of the ith p_z orbital. (For more detailed information, see Lherbier et al. (2012).)

Compare the electronic band structures of graphene along high symmetry lines using both the first-nearest-neighbors and the third-nearest-neighbors $\pi-\pi^*$ models.

2.4 *Electron–hole symmetry in bipartite lattices.* Consider a generic bipartite lattice, i.e., one that can be divided into two lattices where all the sites of one lattice have nearest neighbors that belong to the other.

(a) Arrange the basis vectors spanning the Hilbert space in such a way that all the orbitals corresponding to sublattice A come first. By assuming that only hoppings connecting sites of different sublattices are allowed, write a generic form for the Hamiltonian in block-matrix form.

(b) Use the previously obtained form of the Hamiltonian to show that if E is an eigenvalue of the Schrödinger equation, then $-E$ is also an eigenvalue and that therefore there is particle–hole symmetry.

(c) Consider a graphene network with a line defect as shown in Fig. 2.34(b). Say if the bipartite nature of the graphene lattice is preserved by this defect. What can you conclude on the electron–hole symmetry of the system with the defect?

2.5 *Electron–hole symmetry in finite systems.* As noted in Section 2.2.1, the Hamiltonian is said to have electron–hole symmetry if there is a transformation, $\mathcal{P}$, such that $\mathcal{P}^\dagger \mathcal{H} \mathcal{P} = -\mathcal{H}$. This implies that if Ψ is an eigenstate of $\mathcal{H}$ with a positive energy E (electron function), then $\mathcal{P}\Psi$ is also an eigenstate with energy $-E$. For the case of a finite size system such as a ribbon, the transformation must also be compatible with the boundary conditions. Can you mention one transformation that satisfies both requirements, independently of the edge termination? (For further reading, see Akhmerov & Beenakker (2008).)

2.6 *Edge states of zigzag graphene nanoribbons.*

(a) Consider a semi-infinite graphene sheet with a zigzag edge. Within a simple π orbitals Hamiltonian show that there is a normalizable solution for $E = 0$ which corresponds to a state localized at the edges. How does the decay length of this edge state (in the direction perpendicular to the edge) depend on the k vector?

(b) Repeat the previous point for a zigzag graphene nanoribbon of finite width.
(c) Find an alternative solution to the previous two points by starting from the effective Dirac Hamiltonian and by imposing appropriate boundary conditions.

2.7 *Structural parameters and Brillouin zone of carbon nanotubes.*
(a) Demonstrate the expressions for the structural parameters of CNTs given in Table 2.1.
(b) Consider (5, 5) and (6, 3) nanotubes. Determine their structural parameters, reciprocal basis vectors and their Brillouin zones.

2.8 *Zone-folding approximation for carbon nanotubes.*
(a) Re-derive by your own method the rule for metallicity of an SWNT within the zone-folding approximation.
(b) Analyze the case of semiconducting nanotubes and derive an expression for their bandgap (Eq. 2.44).
(c) Choose a set of four different nanotubes (including zigzag, armchair, and chiral), determine their structural parameters, and draw the associated cutting lines in reciprocal space. Are they metallic or semiconducting?

2.9 *Ratio of metallic to semiconducting carbon nanotubes.* Within the zone-folding approximation, one-third of carbon nanotubes are metallic. To demonstrate this statement:
(a) Determine the number of all the possible nanotubes up to (n, n), N.
(b) Determine the ratio between the total number of metallic nanotubes up to (n, n), N_m, and N. Assuming a random distribution of chiralities and large enough n, this gives the ratio of metallic to semiconducting nanotubes.

2.10 *Flat bands in carbon nanotubes and trigonal warping corrections.* If you examined carefully the dispersion relation for a (10, 0) nanotube in Fig. 2.24, you might have noticed the appearance of flatbands located at $\pm\gamma_0$. Here, we examine this in more detail.
(a) Plot the dispersion relation of bulk graphene (3D plot of $E(k_x, k_y)$) and visualize the constant energy lines.
(b) Plot graphene's isoenergy lines in k-space for different values of E from zero up to a few eV. Observe how these lines deviate from circles as the energy is shifted away from the Dirac point and try to conclude why these flat bands appear only for some CNTs.

2.11 *Bilayer graphene and trigonal warping effects.* In this exercise, we consider an effective Hamiltonian for bilayer graphene with Bernal stacking. The unit cell contains two inequivalent sites labeled as $A1, B1$ on the top layer and $A2, B2$ on the bottom layer. Their arrangement is such that atom $B1$ is on top of atom $A2$. Following (McCann, Kechedzhi et al. 2006), By indexing the wavefunctions $\Psi = (\psi_{A1}, \psi_{B2}, \psi_{A2}, \psi_{B1})^T$ for the K_+ valley and $\Psi = (\psi_{B2}, \psi_{A1}, \psi_{B1}, \psi_{A2})^T$ for the K_- valley, one can write a low-energy effective Hamiltonian as

$$\mathcal{H}(\mathbf{k}) = \xi \begin{pmatrix} 0 & v_3\pi & 0 & v\pi^\dagger \\ v_3\pi^\dagger & 0 & v\pi & 0 \\ 0 & v\pi^\dagger & 0 & \xi\gamma_1 \\ v\pi & 0 & \xi\gamma_1 & 0 \end{pmatrix},$$

where $\xi = 1(-1)$ for valley $K_+(K_-)$, $\pi = p_x + \mathrm{i}p_y$, $v = (\sqrt{3}/2)a\gamma_0/\hbar$, $v_3 = (\sqrt{3}/2)a\gamma_3/\hbar$, and a is the graphene lattice constant. The hopping parameters take the values $\gamma_0 = 3.16\,\mathrm{eV}$, $\gamma_1 = 0.39\,\mathrm{eV}$, and $\gamma_3 = 0.315\,\mathrm{eV}$.

(a) Calculate and plot the energy dispersion for this model of bilayer graphene with and without the parameter γ_3. The hopping parameter γ_3 is responsible for the trigonal warping effects commented on in Section 2.2.3.

(b) Repeat the previous exercise for the density of states. In which energy range can trigonal warping be neglected?

(c) What would happen if you broke the symmetry between the two graphene sheets?

** Additional exercises and solutions are available at our website.

3 The New Family of Two-Dimensional Materials and van der Waals Heterostructures

3.1 Introduction

Purely two-dimensional (2D) crystals are a subclass of nanomaterials that exhibit interesting physical characteristics due to the quantum confinement of their electrons. Graphene was the first to be isolated by exfoliating single layers from a graphite crystal using Scotch Tape technique (Novoselov, Geim et al. 2005). This original and efficient method was also applied to other materials with layered structures (Novoselov et al. 2005), creating a new family of atomically thin crystals. At present, the existence and the stability under ambient conditions of more than a few dozens of different 2D crystals have been reported, including hexagonal boron nitride (*h*-BN), transition metal dichalcogenides (MoS_2, $MoSe_2$, WS_2, WSe_2, $NbSe_2$, etc.), thin oxide layers (TiO_2, MoO_3, WO_3, etc.), silicene, germanene, phosphorene, borophene, arsenene, stanene, etc. These novel 2D systems also exhibit exotic properties suggesting new possible applications. For instance, in the context of electronic applications, research aims to develop devices built entirely out of ultrathin, flexible, and transparent 2D materials. The energy bandgap is one of the most important properties in any electronic material and can range from zero (in metals) to several electron-volts (in insulators). In order to develop the widest possible range of electronic devices, the largest range of bandgap energies should be available, which is the case in the 2D family where the bandgap values available range from zero (in graphene, metallic dichalcogenides, etc.) to more than 5 eV (*h*-BN), passing through 0.1–1 eV (in silicene, germanene, etc.) and 1–2 eV (in phosphorene, semiconducting dichalcogenides, etc.). Furthermore, depending on their specific electronic band structures, these 2D materials should be useful in a variety of settings, from infrared optoelectronics to high-mobility transport. Indeed, unlike their multilayered counterparts that exhibit an indirect bandgap, the bandgap of these 2D crystals is frequently found to be direct, a significant benefit for optoelectronic applications (Churchill and Jarillo-Herrero 2014) (see Fig. 3.1).

Looking beyond 2D, these isolated atomic monolayers can also be stacked on top of each others (Geim & Grigorieva 2013), creating layer-by-layer meta-materials characterized by weak interplanar van der Waals (vdW) interactions. Although limited to the stacking of only a few elemental monolayers, several vdW superlattices have recently been fabricated experimentally with perfect precision in the direction perpendicular to the plane (Haigh et al. 2012; Withers et al. 2015). These novel

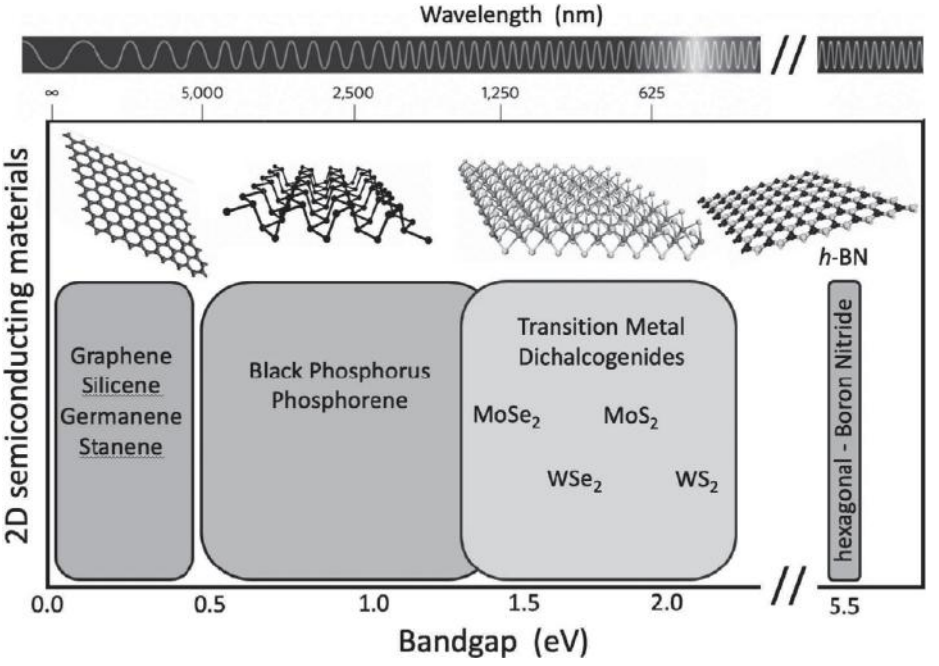

Figure 3.1 Comparison of the bandgap values for different 2D material families used for nanoelectronics and optoelectronics applications. The crystal structure is also displayed to highlight the similarities and differences between the different families. The range of values for each material can be achieved through a variety of means. For example, it is expected that variations in an applied perpendicular electric field, film thickness (number of layers), or straining or alloying could modify the bandgap value. (Adapted by permission from Macmillan Publishers Ltd: *Nature Nanotechnology*, Churchill and Jarillo-Herrero, copyright (2014) and *Nature Photonics*, Castellanos-Gomez, copyright (2016))

vdW superlattices also reveal unusual properties and new phenomena. Indeed, several experiments have clearly overruled the possibility of considering the properties of the resulting material as the superposition of the properties of its components. For example, when a MoS_2–WSe_2 staggered gap junction (separated by a few *h*-BN layers) is excited with a laser energy lower than the larger bandgap, electron–hole separation is surprisingly observed with the two charge carriers being collected in different layers, indicating that an exciton state with electrons and holes in different layers could be the excitonic ground state (Fang et al. 2014; Hong et al. 2014). Consequently, new synergetic properties, which cannot be trivially extrapolated are expected to arise in these novel vdW materials. In addition, these fascinating properties can be tuned on demand by modifying both the type of 2D crystals involved in the stack and the chosen sequence. The recent interest in vdW superlattices is based on this possibility of tuning their properties leading to promising potential in different domains of applications, such as electromechanics (flexible and transparent electronics), optoelectronics (solar cells, light-emitting diodes), spintronics, energy storage (lithium-ion batteries,

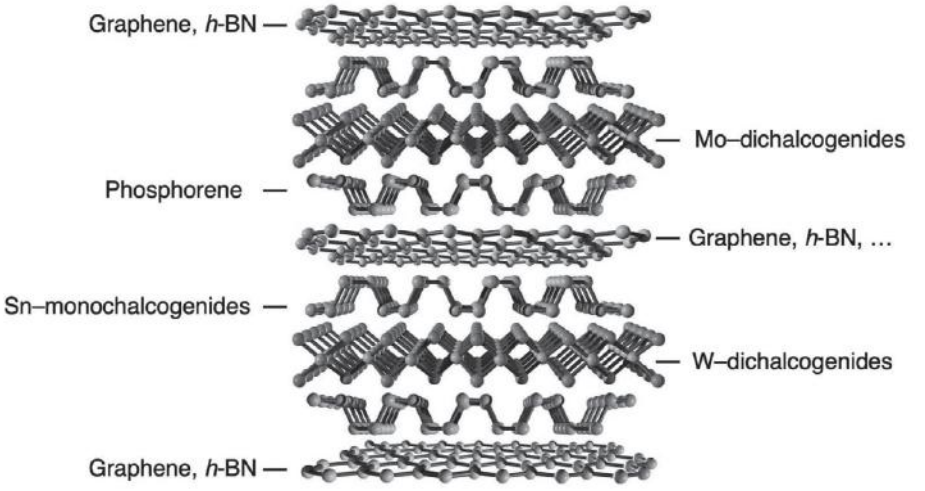

Figure 3.2 Schematic of a van der Waals heterostructure, which is composed by direct stacking of various individual 2D atomic layers in order to control the intrinsic properties of the complete atomic assembly.

hydrogen storage), thermoelectrics, etc. (Fogler et al. 2014; Furchi et al. 2014; Georgiou et al. 2013; Lee et al. 2014). Although the experimental fabrication of a desired vdW superlattice is still a challenging issue, this research field will remain active for quite a long time thanks to the virtually almost infinite numbers of possible combinations of 2D layers to create new vdW systems with promising properties that can be accurately predicted using state-of-the-art quantum simulations (see Fig. 3.2).

The goal of the present chapter consists in overviewing the electronic properties of the most important representatives of the 2D materials family, including also some review of some novel electronic and optoelectronic properties in van der Waals heterostructures.

3.2 Hexagonal Boron Nitride Monolayer

In the bulk phase, *h*-BN is a layered, wide band-gap semiconductor ($E_g > 6$ eV) (Watanabe et al. 2009) whose exceptional optical properties (intense luminescence signal) have recently attracted a growing interest (Bourrellier et al. 2016; Jacob 2014). From a structural point of view, boron nitride and graphene monolayers are very similar (see Fig. 3.3(a)). Boron and nitrogen are neighbors of carbon in the periodic table of elements, having respectively five and seven as atomic number. The boron–nitrogen bond distance (1.45 Å) is slightly greater than the carbon–carbon one in graphene (1.42 Å). The two hexagonal sublattices are obvious in *h*-BN since boron atoms are present on one sublattice and nitrogen on the other (see Fig. 3.3(a)).

Following the same approach as for graphene, the electronic properties of *h*-BN can be explained using a similar tight-binding model. Indeed, considering a single p_z orbital

per site and neglecting every interaction further away than nearest-neighbor ones, the solution for the energy of graphene can be expressed as:

$$E = \frac{1}{2N}\left[\mathcal{H}_{AA} + \mathcal{H}_{BB} \pm \sqrt{(\mathcal{H}_{AA} - \mathcal{H}_{BB})^2 + 4|\mathcal{H}_{AB}|^2}\right] \tag{3.1}$$

where N is the number of unit cells in the crystal. This expression can be easily simplified when $\mathcal{H}_{AA}$ is equal to $\mathcal{H}_{BB}$ by symmetry: $E = \frac{1}{N}\left[\mathcal{H}_{AA} \pm |\mathcal{H}_{AB}|\right]$.

However, this simplification made for graphene when $\mathcal{H}_{AA}$ and $\mathcal{H}_{BB}$ are identical is no longer valid for *h*-BN. Therefore, the previous expression for the energy becomes

$$E = \frac{1}{N}\left[E_m \pm \frac{1}{2}\sqrt{E_g^2 + 4|\mathcal{H}_{AB}|^2}\right] \tag{3.2}$$

where $E_m = (\mathcal{H}_{AA} + \mathcal{H}_{BB})/2$ and $E_g = |\mathcal{H}_{AA} - \mathcal{H}_{BB}|$ is the bandgap.

Consequently, in order for the conduction and valence bands to meet at one point, the expression under the square root has to cancel, which is impossible since $|\mathcal{H}_{AB}|^2$ remains always positive or equal to zero. Therefore, the simple fact that two different species compose *h*-BN instead of a single one (as in graphene) leads to the opening of a bandgap (see Fig. 3.3(b)). As mentioned in the Chapter 2, one way to open a gap in graphene is to break its lattice symmetry, making A and B sublattices unequivalent. In Fig. 3.3(b), the bandgap of *h*-BN is found to be direct while indirect in the bulk, as also confirmed recently with a detailed account of its origin by comparing the effect of different stacking sequences (Sponza et al. 2018). Using DFT techniques, this bandgap is estimated to be 4.7 eV, which is clearly underestimated compare to experimental values (6 eV) due to strong approximations used in the *ab intio* calculation as first explained by many-body corrections in quasiparticle band structure for *h*-BN (Blase et al. 1995). Finally, the inclusion of the electron–hole interaction is crucial for the correct description of the momentum-dependent dispersion of the excitations, allowing complete explanation of the optoelectronic properties of *h*-BN (Sponza et al. 2018).

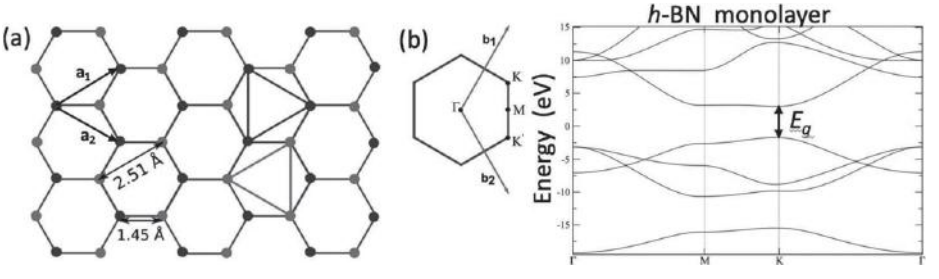

Figure 3.3 Boron nitride hexagonal lattice (a) where dark and light gray dots stands for nitrogen and boron, respectively. Direct lattice vectors (black arrows), interatomic distances, as well as the two hexagonal sublattices (dark and light gray triangles) are represented. The corresponding Brillouin zone (b) illustrating the reciprocal lattice vectors; the high-symmetry k points Γ, M, K; and K′; and the *ab intio* electronic band structure of *h*-BN along specific high-symmetry lines are also presented.

Bulk or few-layers *h*-BN are also extraordinary substrates for graphene because their atomically smooth surface is relatively free of dangling bonds and charge traps (Dean et al. 2010). Thanks to the lattice constant of hexagonal boron nitride, which is similar to that of graphite and its large electrical bandgap, graphene devices on *h*-BN substrates exhibit mobilities and carrier inhomogeneities that are almost an order of magnitude better than devices on conventional SiO_2. Indeed, mobilities measured for graphene on SiO_2 are of the order of $\sim$10,000 $cm^2\ V^{-1}\ s^{-1}$ (Tan et al. 2007) while they are of $\sim$100,000 $cm^2\ V^{-1}\ s^{-1}$ (Bolotin et al. 2008) for suspended graphene (at room temperature). However, the electronic quality of CVD graphene has been demonstrated to critically depend on the transfer method, and a dry transfer technique for graphene crystals that yields devices encapsulated in hexagonal boron nitride(*h*-BN) has been proposed leading to carrier mobilities up to $\sim$350,000 $cm^2\ V^{-1}\ s^{-1}$ (at room temperature) (Banszerus et al. 2015). Consequently, it is mandatory to lay graphene on an extremely flat substrate and to protect its surface from processing-related contaminations to obtain high-performance graphene-based electronic devices.

Also, graphene on *h*-BN can be considered as the first model for vdW heterostructure (Geim & Grigorieva 2013) as the superlattice potential, which is induced by lattice mismatch and crystal orientation, gives rise to various novel quantum phenomena, such as the Hofstadter's butterfly and the fractal quantum effect in Moiré superlattices (Dean et al. 2013; Ponomarenko et al. 2013). In particular, for graphene placed on *h*-BN, the specific difference between their lattice constants and crystallographic misalignment generate a hexagonal periodic structure known as a Moiré pattern (Fig. 3.4(a)). The resulting periodic perturbation, usually referred to as a superlattice, acts on graphene's charge carriers and leads to multiple minibands (Wallbank et al. 2013) and the generation of secondary Dirac-like spectra (Fig. 3.4(b)). These newly generated secondary Dirac cones appear as pronounced peaks in resistivity, and are crucial for understanding intriguing phenomena such as quantum Hall effects as a function of charge carrier density in this system (Ponomarenko et al. 2013). Consequently, graphene-*h*-BN superlattices provide a way of studying the rich physics expected in incommensurable quantum systems, and illustrate the possibility of controllably modifying the electronic spectra of two-dimensional atomic crystals by varying their crystallographic alignment within vdW heterostuctures.

For example, twisted bilayer graphene rotated by exactly 30° has been grown up to a millimeter scale on a silicon carbide surface while maintaining the specific rotation angle, thus creating a two-dimensional quasicrystal without translational symmetry (Ahn et al. 2018). Multiple Dirac cones replicated with the 12-fold rotational symmetry have been observed in angle-resolved photoemission spectra, revealing anomalous strong interlayer coupling with quasiperiodicity (Ahn et al. 2018). This specific bilayer graphene system offers a new type of quasicrystal, which unites the dodecagonal quasicrystalline nature and graphene's relativistic properties. Indeed, the corresponding electronic spectrum consists of resonant states labeled by 12-fold quantized angular momentum, together with the extended relativistic states.

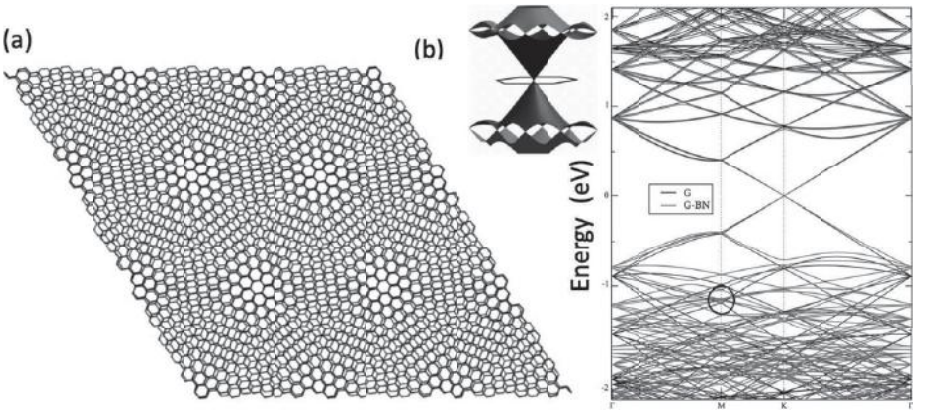

Figure 3.4 Graphene-hexagonal boron nitride bilayers. (a) Moiré pattern induced by the stacking of these two-hexagonal networks presenting a small lattice mismatch. (b) *Ab initio* electronic band structures of graphene (G) and graphene on *h*-BN, (G-BN) illustrating the presence of secondary Dirac cones (i.e., black circle) in both conduction and valence bands, as evidenced in the schematic graphene spectrum at the edge the superlattice Brillouin zone (black hexagon). (The scheme in (b) is reproduced with permission from Wallbank et al. (2013). Copyright (2013) by the American Physical Society)

The resulting quasi-band structure is composed of the nearly flat bands with spiky peaks in the density of states, where the wave functions exhibit characteristic patterns, which fit to the fractal inflations of the quasicrystal tiling (Moon et al. 2019).

Unconventional superconductivity (which cannot be explained by weak electron-phonon interactions) has also been observed in a two-dimensional superlattice created by stacking two sheets of graphene that are twisted relative to each other by a small angle of $\sim 1.1^\circ$ (Cao, Fatemi, Fang et al. 2018). For such a magic twist angle, the electronic band structure of this twisted bilayer graphene exhibits flat bands near zero Fermi energy, resulting in correlated insulating states at half-filling (Cao, Fatemi, Demir et al. 2018). Applying hydrostatic pressure increases the coupling between the layers and can thus be used to tune the phase diagram of twisted bilayer graphene, shifting the superconducting transition to higher angles and somewhat higher temperatures (Yankowitz et al. 2019). Several theoretical models are presently trying to explain this recently detected unconventional superconducting phase in twisted graphene bilayers based on topological superconductivity (Xu & Balents 2018), phonon-mediated superconductivity (Wu et al. 2018), or even complex correlation effects and charge density waves (Isobe et al. 2018; Peltonen et al. 2018; Po et al. 2018). However, the emergence of these flat bands have recently been demonstrated not to be just a matter of engineering material properties but directly related to the flatness of the lowest Landau level (Tarnopolsky et al. 2019). Consequently, this unconventional superconductivity observed in twisted bilayer graphene with small magic angle (Cao, Fatemi, Fang et al. 2018) has probably deep hidden connections to quantum Hall effect and could possibly occur in other van der Waals layered systems.

3.3 Two-Dimensional Transition Metal Dichalcogenides

In analogy to graphite and hexagonal boron–nitride, transition metal chalcogenides (TMDs) are layered materials in their bulk form with weak interlayer van der Waals interactions. Used for its catalytic properties and for dry lubrication, one of the most well-known TMD, bulk MoS_2, is known to be an indirect gap semiconductor (gap $\sim$1.3 eV) (Wilson & Yoffe 1969). In 2005, mechanical cleavage using the "Scotch-tape technique" was applied to bulk MoS_2 to fabricate a monolayer, demonstrating the stability of this 2D crystal at ambient conditions, thus opening up the possibility of investigating a novel and wide range of new semiconducting 2D crystals based on TMD materials (Novoselov, Jiang et al. 2005). These atomically thin transition metal dichalcogenides exhibit remarkable physical properties resulting from their reduced dimensionality and crystal symmetry and which could be of value for a broad range of applications (Wang et al. 2018). Indeed, the atomic structure of a hexagonal TMD monolayer of the type MX_2 (see Fig. 3.5(a)) is constituted by a layer of M atoms (where M is a transition metal atom such as Mo, W, etc.) sandwiched between two layers of X atoms (where X is a chalcogen atom such as S, Se, Te, etc.).

In bulk semiconducting TMDs, the indirect bandgap corresponds to the transition between the valence band maximum at the center of the hexagonal Brillouin zone (Γ point) and the conduction band minimum situated nearly halfway along the $\Gamma - K$ direction (Ribeiro-Soares et al. 2014). The spin–orbit interaction in TMDs is much stronger than in graphene due to the presence of relatively heavy elements and the involvement of the transition metal d orbitals. In 2010, it was found that by decreasing the thickness of few-layered MoS_2, the band structure of the material changed to finally become a direct gap semiconductor when thinned to a monolayer (Mak et al. 2010; Splendiani et al. 2010). The same trend applies to other monolayers of TMDs; a direct bandgap is also measured (and predicted theoretically) for $MoSe_2$, WS_2, and WSe_2 (Fig. 3.5(c–f)) where the corresponding band extrema are located at the finite momentum K^+ and K^- points of the hexagonal Brillouin zone (Fig. 3.5(b)). In summary, with respect to the electronic structure, TMDs are indirect bandgap semiconductors in their bulk form, but when thinned down to the limit of a single monolayer, the bandgap becomes direct, giving rise to interband transitions in the visible to near-infrared spectral range, thus leading to interesting optoelectronic properties. In contrast to the bulk phase, the TMD monolayer crystal structure has no inversion center, which allows to access a new degree of freedom of charge carriers, namely the K-valley index. In addition, the strong spin–orbit coupling in TMD monolayers leads to a spin–orbit splitting of hundreds meV in the valence band and a few to tens of meV in the conduction band (see Fig. 3.5(c–f)), which allows the control of the electron spin. Consequently, a 2D crystal lattice with broken inversion symmetry combined with strong spin–orbit interactions in TMD leads to a unique combination of the spin and valley degrees of freedom, thus paving the way for a new research field named "*Valleytronics*."

As mentioned earlier, the presence of a direct gap in the 2D form is particularly interesting for potential device applications because of the associated possibility

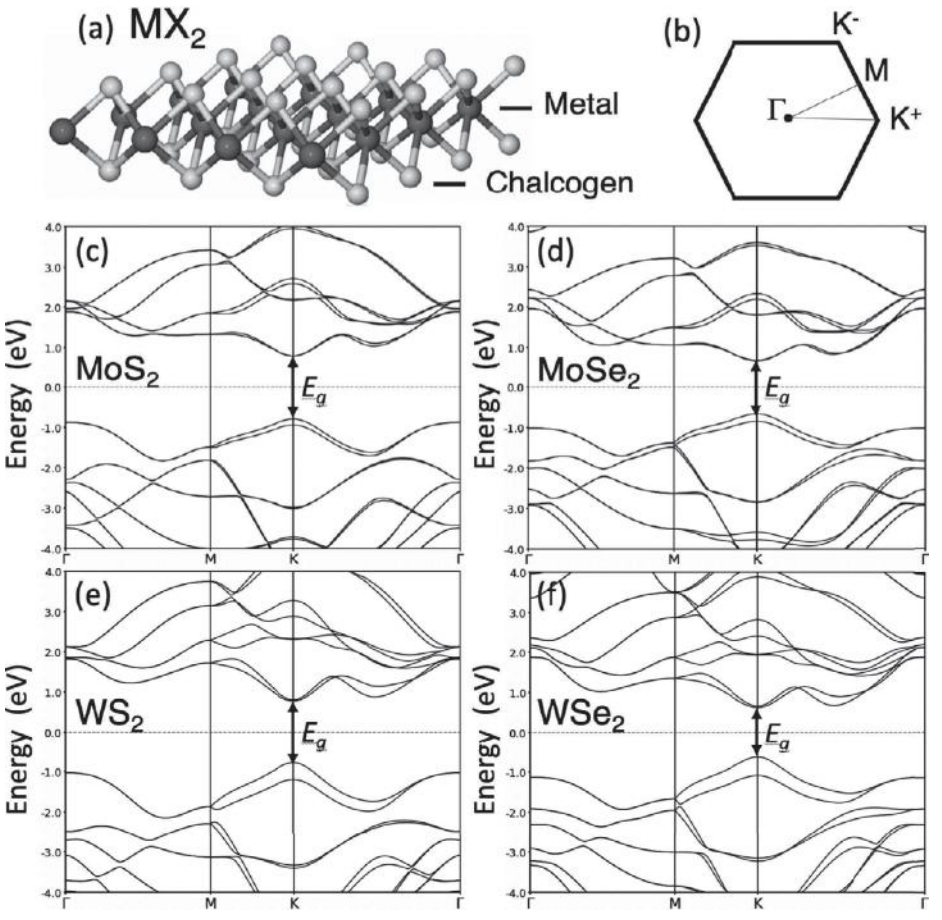

Figure 3.5 Monolayer transition metal dichalcogenide crystal structure – MX_2 (a) with $M =$ Mo, W and $X =$ S, Se and (b) the corresponding hexagonal Brillouin zone. The transition metal atoms (M) appear in dark gray, the chalcogen atoms (X) in light gray. *Ab initio* electronic band structures calculated for (c) MoS_2, (d) $MoSe_2$, (e) WS_2, and (f) WSe_2, and showing the underestimated DFT direct bandgap E_g at the K points (K^+ or K^-) and the spin–orbit splitting in both valence and conduction bands.

for efficient light emission. In the literature, the energy states close to the K points located at the edges of the first Brillouin zone are typically referred to as K^+ and K^- valleys (see Fig. 3.6(a)), whereas the term valley is generally used to designate band extremum in momentum space (Xiao et al. 2012). The specific optical properties of TMD monolayers are summarized in Fig. 3.6(b). Indeed, the absorption of polarized photons ($\sigma+$) generates carriers in the K^+ valley of the reciprocal space, while similarly, the absorption of polarized photons ($\sigma-$) generates carriers in the K^- valley. The chiral optical selection rules for interband transitions in the $K^\pm$ valleys can be deduced from symmetry arguments (Wang et al. 2018), but are beyond the scope of the present chapter.

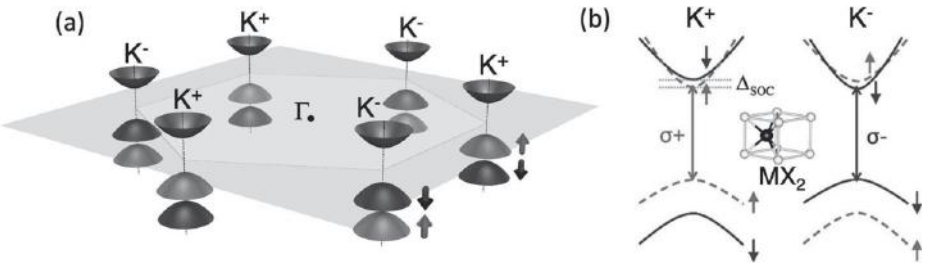

Figure 3.6 Schematic drawing of the band edges located at the *K*-points in semiconducting TMD monolayers (MX_2). (a) Spin–orbit coupling (Δ_{SOC}) leads to an effective locking of spin and valley indices. (b) Valley and spin optical transition selection rules. Solid (dashed) curves denote bands with spin down (up) quantized along the out-of-plane direction. ((a) is adapted with permission from Xiao et al. (2012). Copyright (2012) by the American Physical Society. (b) is adapted with permission from Wang et al. (2018). Copyright (2018) by the American Physical Society)

In addition to the 2D character of the TMD monolayers, weak dielectric screening from the environment yield a significant enhancement of the Coulomb interaction. This effect results in the formation of bound electron–hole pairs (*bright* and *dark* excitons), which dominate the optical and spin properties of this family of 2D materials (Wang et al. 2018). The spin–orbit coupling gives rise to the two valence subbands and, accordingly, to two types of excitons, *A* and *B*, which involve holes from the upper and lower energy spin states, respectively. At the conduction band minimum, a smaller, but still significant spin splitting (Δ_{SOC}) is also observed (see Fig. 3.6(b)). Both the value of the bandgap and these energy splittings due to the spin–orbit interaction strongly depend on the nature of the MX_2 material.

In conclusion, the family of semiconducting TMDs is an especially promising platform for fundamental studies of 2D systems, with potential applications in optoelectronics and valleytronics due to their direct bandgap in the monolayer limit and highly efficient light-matter coupling. In addition to their optical properties, TMDs attract also attention because of their electronic properties (Jariwala et al. 2014) as semiconductors, they can be used to fabricate new devices, such as atomically flat transistors (Radisavljevic et al. 2011), light-emitting diodes (Ross et al. 2014; Splendiani et al. 2010), and other optoelectronic devices such as ultrasensitive photodetectors (Lopez-Sanchez et al. 2013).

Monolayer TMD heterojunctions, including vertical and lateral $p-n$ junctions, have also attracted considerable attention due to their potential applications in electronics and optoelectronics. Lattice-misfit strain in atomically abrupt lateral heterojunctions, such as MoS_2-WSe_2, offers a new band-engineering strategy for tailoring their electronic properties (Zhang et al. 2018). Large-scale, spatially controlled synthesis of heterostructures made of single-layer semiconducting MoS_2 contacting conductive graphene have been reported (Zhao et al. 2016). These chemically assembled atomic transistors exhibit high transconductance (10 μS), on-off ratio ($\sim 10^6$), and mobility ($\sim 17\ cm^2\ V^{-1}\ s^{-1}$).

However, when MoS_2 layers are fully encapsulated within *h*-BN and electrically contacted in a multi-terminal geometry using gate-tunable graphene electrodes, electronic mobilities reaching 34,000 $cm^2\ V^{-1}\ s^{-1}$ have been measured at low temperature, confirming that charge carriers are mostly scattered by extrinsic interfacial impurities rather than bulk defects (Cui et al. 2015). In addition, a large enhancement in the spin–orbit coupling of graphene has been predicted when interfacing it with semiconducting TMDs (Gmitra & Fabian 2015). Anisotropic spin dynamics in bilayer heterostructures comprising graphene and MoS_2 or WS_2 have been demonstrated (Benítez et al. 2018), leading spin lifetime to vary over one order of magnitude depending on the spin orientation, being largest when the spins point out of the graphene plane. These findings provide a rich platform to explore coupled spin-valley phenomena and offer novel spin manipulation strategies based on spin relaxation anisotropy in 2D materials.

3.4 Other Two-Dimensional Materials

Over the past few years, the quest for novel 2D materials has been extremely intense, allowing the prediction and the successful synthesis of several new atomically thin layers in various systems. For example, silicene and germanene – the nearest cousins of graphene – have been synthesized and present interesting electronic structures (Cahangirov et al. 2009). In these 2D materials, the strong spin–orbit couplings can open an energy gap in the Brillouin zone, giving silicene and germanene an advantage over graphene in real applications. In early 2014, the existence of 2D blue phosphorene (Zhu & Tománek 2014), and two other new 2D phases of phosphorus (Guan et al. 2014) have been predicted. In 2015, stanene was also synthesized, and its topological aspects have been investigated (Zhu et al. 2015). The same year, atomically thin 2D boron polymorphs were synthesized on a silver surface (Mannix et al. 2015), revealing highly anisotropic metal characteristics. The goal of the present section consists in reviewing the main characteristics and advantages of all these new 2D materials regarding their electronic properties, and for their high potential for practical applications in the field of nanoelectronics.

3.4.1 Phosphorene

At room temperature, the most stable allotropic crystalline form of phosphorus is called black phosphorus (Morita 1986). Its name originates from its dark appearance, directly arising from its small electronic bandgap of $\sim$0.3 eV (Ehlen et al. 2016). In analogy with graphite which is an $\ldots ABAB \ldots$ stack of weakly bonded graphene sheets, the crystalline structure of black phosphorus consists of phosphorus layers stacked on top of each other and bound to the others by weakly-dispersive van der Waals forces (Klimeš & Michaelides 2012). A single monolayer of black phosphorus is called phosphorene (Liu et al. 2014), and exhibits unique properties in the 2D world, such as highly anisotropic electrical, thermal, mechanical, and optical properties; a direct electronic gap between

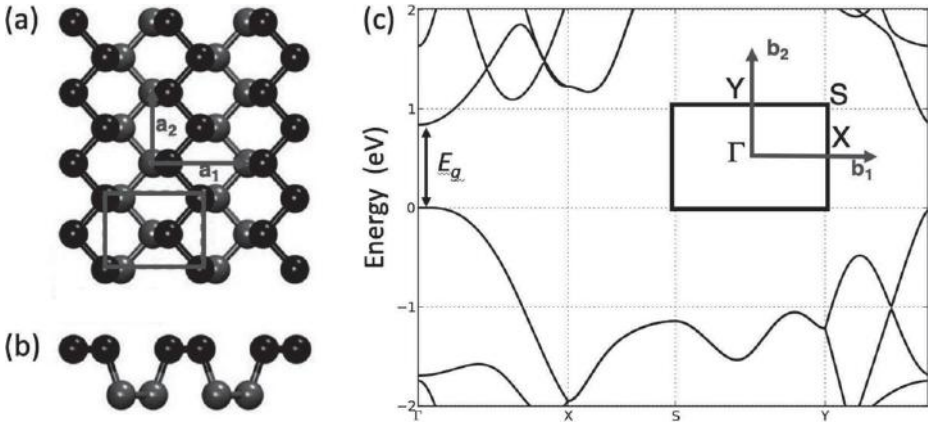

Figure 3.7 Phosphorene crystal structure (a) top and (b) side views. Phosphorus atoms appear in gray or black depending on their relative position in the monolayer (lower or upper planes). The a_1 and a_2 axes represent the *armchair* and *zigzag* directions in Phosphorene, respectively. (c) *Ab initio* electronic band structures along high-symmetry lines of the corresponding Brillouin zone, illustrating the direct bandgap (E_g) at the Γ point.

0.5 and 1.5 eV; photo-induced oxidation; and high carrier mobility (Castellanos-Gomez 2015; Favron et al. 2015). Since there are five electrons on the 3*d* orbitals of each phosphorus atom, sp^3-like hybridization is present within the phosphorene structure, causing the phosphorus atoms to be arranged in a puckered honeycomb lattice formation (see Fig. 3.7(a–b)).

Regarding its electronic properties, phosphorene is a direct bandgap semiconductor (Fig. 3.7(c)). However, this black phosphorus material exhibits a thickness-dependent direct bandgap that changes to 1.9 eV in a monolayer from 0.3 eV in the bulk, following the following rule: $E_g = E_{bulk} + 1.6\ \text{eV}/N^{1.4}$, where N is the number of layers in the system (Cai et al. 2014). Such increase in the bandgap value in monolayer phosphorene is proposed to be due to the absence of interlayer hybridization near the top of the valence and bottom of the conduction band (Liu et al. 2014).

Although it is one of the latest newcomers in the family of 2D materials, phosphorene presents potential applications in electronics and optoelectronics thanks to its high electronic mobility and its nonzero direct electronic bandgap (Castellanos-Gomez 2015). Field-effect transistors based on few-layer black phosphorus crystal with thickness down to a few nanometers have been fabricated (Li et al. 2014), exhibiting charge carrier mobility of the order of $\sim$1000 $\text{cm}^2\ \text{V}^{-1}\ \text{s}^{-1}$. However, phosphorene is unstable in ambient conditions: it oxidizes in the presence of light and air, limiting its applications up to now (Favron et al. 2015). In order to preserve its chemical integrity and its intrinsic properties, encapsulating phosphorene, for example with other 2D materials, has been proposed. Indeed, *h*-BN-encapsulation preserves the main electronic properties of the phosphorene monolayer, while *h*-BN spacers can be used to counteract the bandgap reduction in stacked black phosphorus (Constantinescu & Hine 2016).

However, phosphorene is exceptionally sensitive to environmental screening. For example, *h*-BN-encapsulation reduces the exciton binding energy in the monolayer by as much as 70% and completely eliminates the presence of a bound exciton in four-layer black phosphorus (Qiu et al. 2017). Consequently, from an optoelectronic point of view, the encapsulation does not affect the optical gap, which remains nearly unchanged, but the nature of the excited states and the qualitative features of the absorption spectrum are dramatically modified.

Further, a phosphorene–graphene hybrid material has been proposed as a high-capacity anode (Sun et al. 2015) for sodium-ion batteries (which are an alternative to lithium-ion batteries because sodium sources do not present the geopolitical issues that lithium sources might). This hybrid material made out of a few phosphorene layers sandwiched between graphene layers shows a specific capacity of 2440 mAh/g which can be explained by a dual mechanism of intercalation of sodium ions along the ridges of the phosphorene layers, followed by the formation of a Na_3P alloy (Sun et al. 2015). The presence of graphene layers in the hybrid material works as a mechanical backbone and an electrical highway, ensuring that a suitable elastic buffer space accommodates the anisotropic expansion of phosphorene layers for stable cycling operation. A recent theoretical work also demonstrates the importance of in-plane contraction induced by interlayer interactions in graphene–phosphorene heterostructures (Van Troeye et al. 2018).

3.4.2 Borophene

Boron is the lightest element (lowest Z) to form extended covalent network. However, the trivalent outer shell of boron usually forms highly delocalized bonds, where electrons are shared among three (or more) atoms, leading to 16 reported 3D bulk allotropes (Sergeeva et al. 2014), including the well-known phase composed of B_{12} icosahedral clusters (Oganov et al. 2009). Consequently, the synthesis of 2D materials with no analogous bulk layered allotropes is a quite difficult task (Mannix et al. 2018). Nevertheless, the synthesis of borophene monolayers via controlled atomic deposition of boron atoms on a silver surface has been reported (Feng et al. 2016, Mannix et al. 2015). Various 2D phases were observed, depending mainly on the deposition rate and the temperature, attesting the predicted large polymorphism of borophene. Many of these boron monolayers contain hexagonal holes (*hh*) stabilizing the planar structure. According to Penev et al. (2012), the fundamental ground state is obtained for an hexagonal hole concentration $x = 0.1 - 0.15$ in $B_{1-x}\ hh_x$. Consequently, $B_1\ hh_0$ is thus the densest boron limit, which corresponds to a dense buckled monolayer of boron atoms arranged in two interpenetrating rectangular sublattices (see Fig. 3.8(a–c), or equivalently the buckled closed-packed triangular lattice), which was presumably one of the phases recently synthesized (Mannix et al. 2015). The lattice parameters of the rectangular unit cell of borophene are displayed in Fig. 3.8(a–b), i.e., ($a = 1.62$ Å; $b = 2.87$ Å) with a buckling height of ∼0.9 Å between bottom and top boron atoms in order to enhance the energetic stability (Lherbier et al. 2016; Zhou et al. 2014).

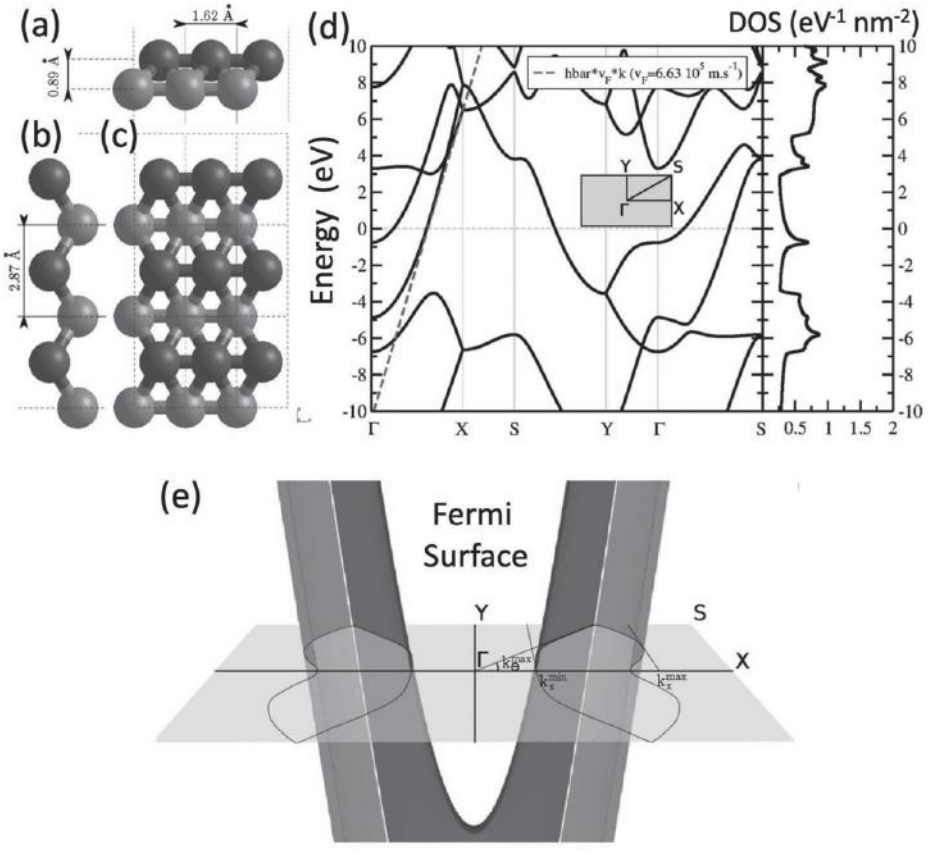

Figure 3.8 Borophene crystal structure, (a–b) side and (c) top views. The unit cell contains two boron atoms (depicted as dark and light gray spheres, respectively) and is delimited by solid lines while the repeated cells are delimited by dashed lines. (d) *Ab initio* electronic band structure and density of states (DOS) with zero energy aligned to the Fermi level (E_F). The Brillouin zone is shown in the inset. The highest group velocity (6.6×10^5 m/s) for a band crossing the Fermi level is highlighted by a dashed line starting at Γ. (e) 3D plot of the two electronic bands (only for positive k_y) crossing the Fermi level (symbolized by the semi-transparent plane) in an energy window [−1 eV; +1 eV]. Adapted from Lherbier et al. (2016)

The electronic band structure (Fig. 3.8(d)) exhibits a strongly anisotropic metallic character as the bands are found to be highly dispersive in the k_x direction ($\Gamma - X$ and $Y-S$) with relatively high group velocity of 6.6×10^5 m/s, while it appears that no bands cross the Fermi level in the k_y direction ($\Gamma - Y$ and $X-S$) as reported previously (Mannix et al. 2015). Notwithstanding, one also notes that dispersion occurs along the oblique $\Gamma - S$ path. This reveals that bands can actually cross the Fermi level parallel to the k_y direction in some region of the 2D Brillouin zone.

The full anisotropy of the electronic structure of borophene can be revealed by carefully inspecting the Fermi surface (which in 2D actually reduces to a Fermi line) as

represented in Fig. 3.8(e). While electronic bands always cross the Fermi level for any line parallel to k_x, this is not the case for lines parallel to k_y. Therefore, the electronic transport will occur only for selective wave vectors **k** whose k_x component belongs to the allowed region (see Fig. 3.8(e)), defining a maximal angle ($k_\theta^{\max}$) for the wave vectors $k = (k_x, k_y) \equiv (k_r, k_\theta)$.

Borophene was found to exhibit extremely low optical conductivities due to the absence of interband transitions up to 3 eV (Lherbier et al. 2016). Anisotropy was also reported for the theoretical optical conductivity showing that for an electric field oriented along the main conductive direction, the material stays optically inactive up to 6.5 eV. Although the exact value depends on disorder, the optical transmittances are predicted to possibly reach 100% in the visible range, making borophene more transparent than graphene (Lherbier et al. 2016).

The recent synthesis of borophene has clearly demonstrated the huge polymorphism in 2D for boron, providing unprecedented diversity in a mono-elemental 2D system with potential applications in electronics, chemical functionalization, and material synthesis (Mannix et al. 2018). The unique mechanical and optical properties with anisotropic metallicity of borophene are expected to be particularly useful when integrated into heterostructures with other 2D materials (Jariwala et al. 2017). Incorporation of borophene in vertically stacked heterostructures could also yield numerous benefits in nanoelectronics by providing metal-semiconductor junctions (i.e., atomically thin Schottky diodes, tunneling transistors, etc.). Moreover, the optical and plasmonic properties predicted for borophene (Huang et al. 2017; Lherbier et al. 2016) could provide a new metallic 2D layer to investigate lightmatter interactions in vertical vdW heterostructures. Finally, in analogy to phosphorene, sandwiching borophene between other 2D layers (i.e., *h*-BN) would induce protection from air exposure while simultaneously preserving its intrinsic properties as for high-performance graphene-based devices (Dean et al. 2010).

3.4.3 Silicene, Germanene, and Stanene

In group IV of the periodic table, elements other than carbon can also form elemental 2D materials similar to graphene, based on silicon (silicene) (Feng et al. 2012; Vogt et al. 2012), germanium (germanene) (Dvila et al. 2014), and tin (stanene) atoms (Zhu et al. 2015). Although these 2D allotropic forms of silicon, germanium, and tin are characterized by a hexagonal honeycomb structure similar to that of graphene, the latter are not flat, but rather adopt a periodically buckled topology (Grazianetti et al. 2016) (see Fig. 3.9(a–c)). The larger bond length in silicene (∼2.3 Å) compared with graphene (∼1.42 Å) prevents the silicon atoms from forming strong π bonds. Consequently, the ideally flat hexagonal structure distorts in order to bring silicon atoms closer together to enable a stronger overlap of their π-bonding p_z orbitals, resulting in a buckling (mixed sp^2-sp^3 hybridization), which stabilizes such a puckered hexagonal arrangement. This vertical buckling distance δ between the top and bottom atoms of the puckered hexagonal crystal structure (Fig. 3.9(c)) is correlated to the

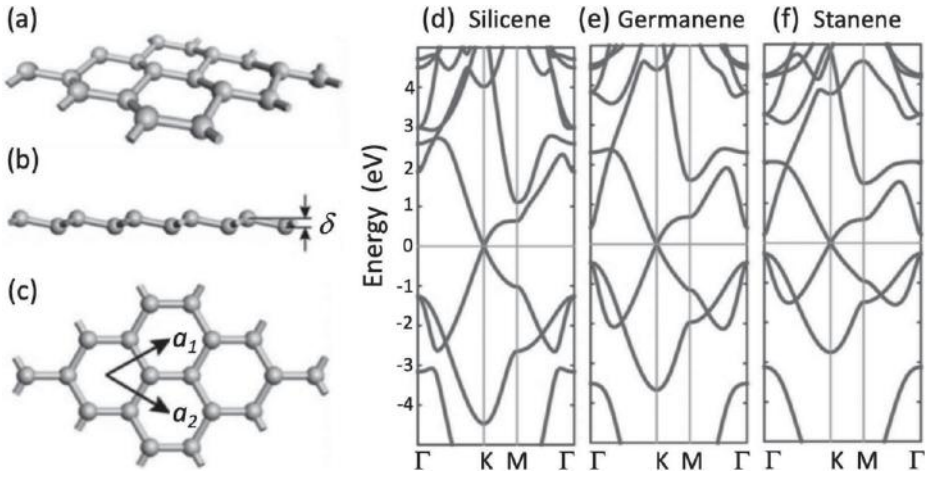

Figure 3.9 Crystal structure of silicene, germanene, and stanene (a), side (b), and top (c) views. The unit cell contains two atoms (like in graphene), but the honeycomb lattice is buckled by a distance δ in the out-of-plane direction depending on the nature of the group IV element. (d–f) *Ab initio* electronic band structure with zero energy aligned to the Fermi level. Energy bandgaps are too small to be visible (see text). Adapted from Zhang et al. (2017)

bond angle between the framework atoms and the hybridization of the atomic orbitals. Consequently, the δ value increases from 0 Å in graphene to 0.45 Å in silicene, 0.7 Å in germanene, and 0.85 Å in free-standing stanene, thus inducing an associated decrease of the bond angle, from 120° (pure sp^2 hybridization of C atoms) to 110° (almost pure sp^3 hybridization of Sn atoms) (Molle et al. 2017).

In addition to this structural buckling, the spin–orbit coupling is larger in silicon and germanium and even more in tin with respect to carbon, leading to electronic band structures that are slightly different from graphene (Fig. 3.9(d–f)). Indeed, when SOC is not taken into account, silicene, germanene, and stanene are predicted to be zero-gap semiconductors with linear dispersions near the K and K' Dirac points and Fermi velocities roughly half of that for graphene (6×10^5 m/s). However, when SOC is switched on, silicene, germanene, and stanene exhibit a semiconducting behavior (Molle et al. 2017) with bandgaps of the order of ∼1.5–2 meV, ∼25–30 meV, and ∼0.1 meV, respectively.

As a result of their buckled character, these 2D semiconductors can potentially serve as a nanotechnology platform with multiple physical features for fundamental research and applications such as on-demand or reconfigurable devices for electronic, photonic, thermal, energy, mechanical, chemical, and sensor nanosystems (Molle et al. 2017). However, these narrow-bandgap 2D semiconductors have been so far only epitaxially grown on metallic surfaces in ultrahigh vacuum (Dvila et al. 2014; Feng et al. 2012; Vogt et al. 2012; Zhu et al. 2015), and their limited environmental stability prevent the investigation of their intrinsic properties. Moreover, the metallic substrates used for the epitaxial growth are known to strongly modify the electronic properties of

silicene, germanene, and stanene. In analogy with phosphorene and borophene previously described, sandwiching these 2D semiconductors between other 2D layers (i.e., *h*-BN) would induce protection from air exposure while simultaneously preserving their intrinsic properties which could be exploited in applications such as mid- and near-IR optoelectronics (Castellanos-Gomez 2016; Tao et al. 2015).

Recently, interest has turned to 2D mono-elemental structures of the VA group elements (arsenic, antimony, bismuth). Single-layered materials derived from arsenic, antimony, and bismuth are called arsenene (Zhang et al. 2015), antimonene (Ji et al. 2016), bismuthene (Reis et al. 2017), and even tellurene (Zhu et al. 2017) from the VIA group of elements. The transition of materials from metallic conductors to semiconductors upon reduction of the number of layers and consequent optical and electronic properties is an important aspect of these novel 2D systems, which deserves more investigation (Pumera & Sofer 2017). Though the study of these materials is still at the early stages, predictions and preliminary measurements of their intrinsic properties confirm that these novel 2D monolayers are complementary to conventional layered bulk-derived 2D materials, as summarized in a few recent reviews (Pumera & Sofer 2017; Zhang et al. 2017).

3.4.4 MXenes

A few years ago, the family of 2D materials has been significantly expanded by introducing 2D layers of transition-metal carbides, nitrides, and carbonitrides, known as MXenes (Anasori et al. 2015; Naguib et al. 2014). MXenes have been shown to be very promising building blocks of an impressive number of potential applications, including energy storage devices, such as Li-ion batteries and electrochemical capacitors (Ghidiu et al. 2014; Lukatskaya et al. 2013). MXene structures are generally produced by selectively etching layers of *sp* elements from their corresponding three-dimensional (3D) MAX phase. The MAX phases are layered 3D solids composed of 2D sheets of *MX* separated by *A* layers (Barsoum 2000), thus exhibiting a general formula $M_{n+1}AX_n$, where *M* represents an early transition metal (Sc, Ti, V, Cr, Zr, Nb, Mo, Hf, Ta), *A* represents an element from groups 13 to 16 (Al, Si, P, Ga, Ge, As, In, Sn), *X* represents either a carbon or a nitrogen atom, and *n* varies from 1 to 3. In contrast to graphite-like materials with strong intralayer covalent bonds and weak van der Waals interlayer interactions, the MAX phases are mostly composed of covalent, ionic, and metallic strong bonds. The chemical bonds between *A* and $M_{n+1}X_n$ are weaker than those between *M* and *X*, allowing for the extraction of *A* layers from the 3D crystals (Anasori et al. 2015; Naguib et al. 2014). Although the removal of *A* layers from the MAX phases cannot be achieved with the usual mechanical exfoliation method, but using strong acid treatment (hydrofluoric) and sonication, resulting in a 3D to 2D transformation. Today, more than 20 separate MXenes have been successfully synthesized using a similar procedure, and dozens more have been predicted (Anasori et al. 2015; Naguib et al. 2014).

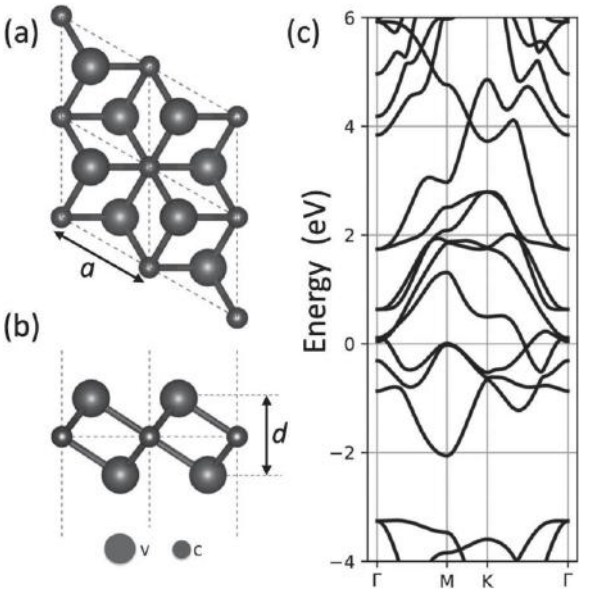

Figure 3.10 Top (a) and side (b) views of the crystal structure of an example of MXene monolayer: pristine V_2C. Vanadium atoms are in medium gray (large spheres) and carbon atoms are in dark gray (small spheres); *a* and *d* are the lattice constant and the layer thickness, respectively. (c) *Ab initio* electronic band structure of pristine V_2C along high-symmetry lines of the hexagonal Brillouin zone. The Fermi level is fixed as the reference of zero energy. (Adapted with permission from Champagne et al. (2018). Copyright (2018) by the American Physical Society)

As an example, the ground-state fully relaxed hexagonal structure of the pristine V_2C is presented in Fig. 3.10. The unit cell includes three atoms, two vanadium and one carbon, which resides in the $P\bar{3}m1$ space group (Fig. 3.10(a)). These atoms are therefore arranged in a triple-layer structure where the C layer is sandwiched between the two V layers, as illustrated in Fig. 3.10(b). The lattice constant *a* is equal to 2.89 Å, and the layer thickness *d*, defined as the V–V distance, equals 2.18 Å.

According to its electronic band structure, the V_2C monolayer exhibits a clear metallic behavior (see Fig. 3.10(c)). In V_2C-based systems, the C atom is involved in the bonding states through its outmost 2*s* and 2*p* orbitals, and V atoms are mainly involved through their 3*d* orbitals. In the vicinity of the Fermi level (from 2 eV and above) 3*d* states and are expected to give rise to electrical conductivity in the V_2C monolayer.

However, the pristine monolayer is an ideal situation since it is still presently highly challenging to exfoliate pristine MXene monosheets from the 3D MAX phase. Indeed, due to the use of etching agents, MXenes are always terminated with functional groups – such as −F, =O, and −OH – that are randomly distributed at the MXene surface. Consequently, the general formula of these chemically terminated MXene crystals is therefore $M_{n+1}X_nT_{n+1}$, where *T* represents the terminal groups (Champagne et al. 2018).

Depending on the concentration and the nature of these functional groups, both the electronic and the transport properties of MXene can be strongly affected as it is, for example, the case for the Ti_3C_2 MXene system which undergoes a metallic to indirect bandgap semiconductor transition (Hu et al. 2015). However, in the V_2C monolayer where surface functionalization with −F and −OH groups is energetically favorable (in contrast to oxygen termination), the metallic character of the V_2CT_2 structures is always preserved (Champagne et al. 2018). Finally, experimental measurements related to the electronic properties, including mobilities and effective masses of the charge carriers, should be performed in order to reach a better understanding of the electronic transport in both pristine and functionalized MXene systems.

3.5 van der Waals Heterostructures

Materials by design is one of the ultimate goal in condensed matter and materials science although very hard to reach in practice. However, the emergence of this novel family of 2D layers has recently allowed this unreachable dream to become reality. Indeed, 2D crystals can be easily stacked on top of each other, creating heterostructures where the different monolayers are held together by van der Waals (vdW) forces (see Fig. 3.11). Considering the large number and variety of 2D materials currently available (as illustrated in the previous sections), a huge set of vdW heterostructures can be constructed by combining and matching 2D monolayers exhibiting different properties, thus predetermining specific functionalities of the corresponding vdW assembly (Geim & Grigorieva 2013).

As already mentioned in the introduction, when different 2D crystals are stacked together, the synergetic effects are playing a key role. Charge redistribution as well as magnetic modification (by proximity effect) can occur between various monolayers of different nature in the stack. In addition, even if the vdW interactions between layers can be considered as long-range weak forces, the latter could induce significant structural changes in neighboring 2D crystals. For example, large in-plane contraction

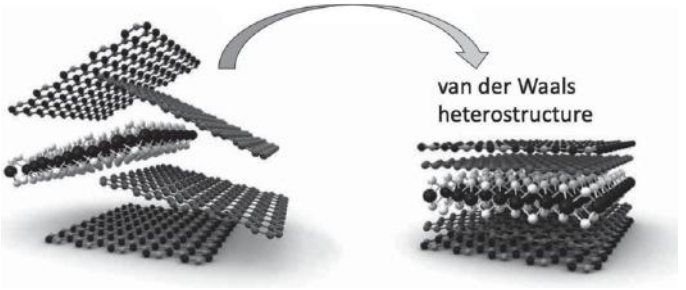

Figure 3.11 van der Waals heterostructures: owing to a large number of 2D crystals currently available, a huge set of vdW heterostructures exhibiting different functionalities can be created. Adapted from Novoselov et al. (2016). Reprinted with permission from AAAS.

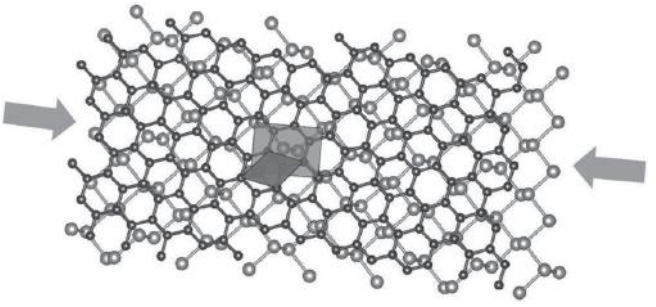

Figure 3.12 The stacking of two 2D materials on top of each other may induce strong intralayer deformations. Graphene and phosphorene are represented by dark and light gray spheres, respectively, with their corresponding incommensurable unit cells. The phosphorene monolayer is predicted to be strongly contracted by interlayer interactions when stacked with graphene. (Adapted with permission from Van Troeye et al. (2018). Copyright (2018) by the American Physical Society)

induced by interlayer interactions in graphene-phosphorene heterostructures have been theoretically predicted (see Fig. 3.12). Indeed, when graphene and phosphorene lattices are matched along the armchair direction (leading to a coherent interface that is found to be energetically favored), phosphorene has to stretch by an amount of ∼7% (Van Troeye et al. 2018). This strain is sufficient to trigger a direct to indirect bandgap transition in this system, highlighting the full potential of material by design in vdW-heterostructure.

These structural changes in vdW heterostructures can be tuned and controlled by adjusting the relative orientation between the individual 2D crystals (rotation and translation between layers). However, electron tunneling between layers varies strongly with the rotation angle between the crystal lattices, especially in graphene stacks. Recently, encapsulated graphene stack with boron nitride shaped in such a way that an atomic force microscope tip could push on it to vary the twist angle by as little as 0.2° has been proposed (Ribeiro-Palau et al. 2018). Such an ability to investigate arbitrary rotation angle in a single device has revealed features of the optical, mechanical, and electronic response in vdW heterostructures, establishing the capability to fabricate twistable electronic devices with tunable properties (Ribeiro-Palau et al. 2018).

Currently, most 2D heterostructures are composed by direct stacking of individual monolayer flakes of different materials. This assembly technique is called micro-mechanical stacking (see Fig. 3.11). Moreover, vdW heterostructures have also been synthesized using sequential CVD growth of monolayers or physical epitaxy. These novel controlled layered structures have already led to the observation of numerous exciting physical phenomena and the corresponding prototypes carried out with these vdW heterostructures have revealed new functionalities, presenting unprecedented possibilities of combining them for technological applications (Novoselov et al. 2016).

For example, capacitive coupling between two graphene layers through a thin layer of *h*-BN with a very large gap allows for very-high-quality electronic devices, where the charge carriers in the two graphene layers interact through Coulomb forces.

The spatially separated electron systems remain strongly coupled by electron–electron interactions, provided that the layer separation is comparable to a characteristic distance between charge carriers within layers. This remote coupling induces a phenomenon called Coulomb drag, in which an electric current passed through one of the layers causes frictional charge flow in the other layer (Gorbachev et al. 2012).

Bipolar field effect tunneling transistor based on graphene combined with semiconductor and insulating 2D crystals to create a tunnel junction has also been proposed (Britnell et al. 2012). The use of atomically thin *h*-BN as a tunneling barrier is particularly attractive due to its large bandgap (∼6 eV), low number of impurity states within the barrier, and high breakdown field. These graphene-based field-effect tunneling transistors exploit to advantage the low density of states in graphene and its one atomic layer thickness. These devices exhibit room temperature large switching ratios (∼50) and have potential for high-frequency operation and large-scale integration (Britnell et al. 2012). Higher on-off ratio for these field-effect tunneling transistors can be achieved if the changes in the Fermi energy in graphene are comparable with the gap in the tunneling barrier. Such a situation is achieved when *h*-BN is replaced by WS_2, leading to on-off ratio of $\sim 10^6$ (Georgiou et al. 2013).

As already briefly mentioned, an unprecedented degree of control of the electronic properties is available not only by means of the selection of materials in the stack but also when the crystallographic orientation of two graphene electrodes separated by a layer of hexagonal boron nitride are carefully aligned. In that case, the transistor device can achieve resonant tunneling with conservation of electron energy, momentum and, potentially, chirality (Mishchenko et al. 2014). Indeed, rotational misalignment of the two graphene crystals corresponds to a relative rotation of the two graphene Brillouin zones in the reciprocal space. If the misalignment is small enough ($<2^\circ$), then the momentum difference between the electronic states in the top and bottom graphene layers can be compensated electrostatically by applying bias and gate voltages, leading to the resonant tunneling and observation of the negative differential resistance (Mishchenko et al. 2014). Vertical integration of MoS_2–WSe_2–graphene and WSe_2–MoS_2–graphene heterostructures has also led to resonant tunneling in an atomically thin stack with spectrally narrow, room temperature negative differential resistance characteristics (Lin et al. 2015).

Regarding the interaction with light, optoelectronic devices based on graphene has been studied intensively (Bonaccorso et al. 2010). However, due to its low absorption coefficient, graphene-based photodetectors typically have very low responsivity. Consequently, other 2D materials such as TMDs (Wang et al. 2012) or few-layer phosphorene (Buscema et al. 2014) exhibiting large DOS (which guarantees large optical absorption) have been used as photodetectors (Koppens et al. 2014).

Combining 2D materials with different work functions can create vdW heterostructures for photovoltaic applications. Indeed, photoexcited electrons and holes are naturally separated in different TMD layers, giving rise to indirect excitons (Fang et al. 2014; Rivera et al. 2015). These excitons typically have long lifetimes, and their binding energy could be tuned by controlling the distance between the TMD layers. Moreover,

TMDs/graphene stacks are also interesting photoactive structures since van Hove singularities in the electronic density of states of TMD guarantees enhanced light-matter interactions, leading to enhanced photon absorption and electron-hole creation (which are collected in transparent graphene electrodes) (Britnell et al. 2013). Photovolatic devices based on these TMDs/graphene heterostructures are extremely efficient with photoresponsivity above 0.1 A/W (corresponding to an external quantum efficiency of above 30%).

Light-emitting diodes made by stacking up metallic graphene, insulating hexagonal boron nitride, and various semiconducting monolayers into complex but carefully designed vdW heterostructures introduce quantum-well engineering with one atomic plane precision (Withers et al. 2015). Emission can be tuned over a wide range of frequencies by appropriately choosing and combining 2D semiconductors (monolayers of transition metal dichalcogenides), thus providing the basis for flexible and semi-transparent electronics when the vdW heterostructure is prepared on elastic and transparent substrates (Withers et al. 2015).

Lastly, plasmons in graphene attract a lot of attention because it is possible to tune their frequency by changing the carrier concentration and, thus, the plasmonic frequency (Grigorenko et al. 2012). Plasmonic and phonon-polaritonic properties have also been investigated in other 2D materials (Dai et al. 2014). Propagating plasmons with unprecedented low plasmon damping combined with strong field confinement have been observed in high-quality graphene encapsulated between two *h*-BN films (Woessner et al. 2015). Encapsulation of graphene with *h*-BN eliminates the scattering of graphene plasmons with impurities. The main damping channels have been identified to be the intrinsic thermal phonons in the graphene and the dielectric losses in the *h*-BN, allowing for future development of graphene nanophotonic and nano-optoelectronic devices (Woessner et al. 2015). When sandwiching several graphene layers between *h*-BN spacers, plasmonic modes can hybridize in such multilayer systems, thus possibly entereing a regime where the plasmon polaritons in graphene and the phonon polaritons in *h*-BN coexist (Dai et al. 2015).

3.6 Conclusion

The family of 2D crystals is continuously growing, both in terms of variety and number of materials. Presently, only a few dozen 2D materials have been successfully synthesized or exfoliated. Progress in this area would be strongly accelerated by the availability of a broad portfolio of 2D candidate materials. Recently, theoretical search for novel 2D materials has been proposed, focusing on how easily the monolayers can be exfoliated from their parent compounds (Mounet et al. 2018). Starting from 108,423 unique, experimentally known 3D compounds, high-throughput calculations using van der Waals density functional theory allowed the identification of 1825 compounds that are either easily or potentially exfoliable. In particular, a subset of 1036 easily exfoliable cases provides novel structural prototypes (see Fig. 3.13) and simple ternary

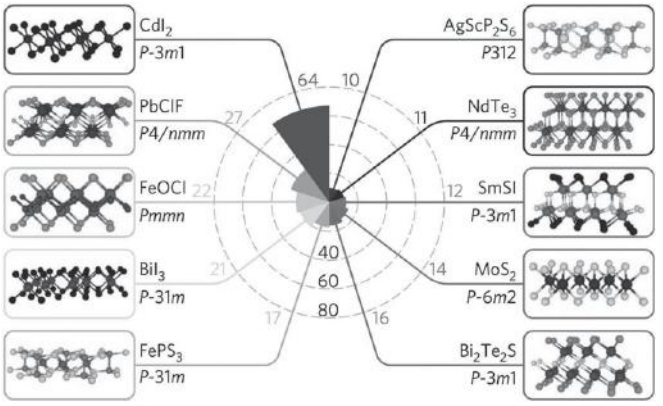

Figure 3.13 Most common 2D structural prototypes obtained from high-throughput *ab initio* calculations. Polar histogram showing the number of structures belonging to the 10 most common 2D structural prototypes in the set of 1,036 easily exfoliable 2D materials. A graphical representation of each prototype is shown, together with the structure-type formula and the space group of the 2D systems. (Reprinted by permission from Macmillan Publishers Ltd: *Nature Nanotechnology* (Mounet et al. 2018), copyright (2018))

compounds as well as a large portfolio of materials to search from for optimal properties (Mounet et al. 2018).

Since the physical properties of monolayers can often dramatically change from those of their parent 3D materials, these *ab initio* predicted 2D systems provide a new degree of freedom for applications while also unveiling novel physics, especially when these new 2D layers will be stacked in a desired fashion in a vdW heterostructure to engineer novel specific properties.

3.7 Further Reading

- As general suggested references on two-dimensional materials, and van der Waals heterostructures, we refer to Novoselov et al. (2016) and Avouris et al. (2017).

4 Quantum Transport: General Concepts

The previous sections have been devoted to the electronic structure of carbon-based materials and the new family of two-dimensional materials. The rest of the book is now focused on their transport properties. This part is meant as a nexus, providing a brief reminder on quantum transport with a focus on the tools that are needed later in the book. After a discussion of the most relevant length scales and the different transport regimes, three different formalisms are reviewed, namely Landauer theory, the Kubo formalism, and the semiclassical Boltzmann transport equation. More technical details concerning the use of Green's functions methods and the Lanczos method for computing the density of states and wave-propagation are discussed in Appendices C and D, respectively.

4.1 Introduction

4.1.1 Relevant Time and Length Scales

Electron transport through a device is a phenomenon that takes place in time and space and as such there are relevant time *and* length scales. Given a device with characteristic dimensions L_x, L_y, and L_z, if the system is metallic then one has the Fermi wavelength $\lambda_F = 2\pi/k_F$ associated with its Fermi wave-number k_F. The elastic mean free path ℓ_{el} can be defined as the distance that an electron travels before getting elastically backscattered (off impurities for example); $\ell_{\mathrm{el}} = v_F\tau_{\mathrm{el}}$, where τ_{el} is the mean time between those elastic scattering events which are usually produced by defects or imperfections in the crystal structure. In disordered systems, when the disorder strength is such that $\ell_{\mathrm{el}} \sim \lambda_F$, the wavefunctions become localized on a length scale ξ, the localization length.

Analogous to ℓ_{el}, one can define the inelastic mean free path $\ell_{\mathrm{in}} = v_F\tau_{\mathrm{in}}$ as the mean distance between inelastic scattering events such as those due to electron–phonon or weak electron–electron interactions. Generically, it is usual to speak of the electronic mean free path ℓ, without discerning the specific source, elastic or inelastic.[1] The phase coherence length ℓ_ϕ (and corresponding coherence time τ_ϕ) is defined as the length over

[1] In graphene the main sources of scattering include charged impurities, defects in the crystal structure and microscopic corrugations of the graphene sheet (also called ripples). Their relative importance is still debated.

Table 4.1 Typical magnitudes of the charge density (n), the mean free path ℓ, Fermi wavelength (λ_F), and the coherence length (L_ϕ) at 4 K in various materials.

	GaAs-AlGaAs	Metals	Graphene	SWNT	MWNT
n	4×10^{11} cm^{-2}	$10^{21}-10^{23}$ cm^{-3}	$10^{11}-10^{12}$ cm^{-2}	10^{11} cm^{-2}	,,
ℓ	$100-10^4$ nm	1–10 nm	50 nm–3 μm[a]	1 μm	10–40 nm
λ_F	40 nm	0.5 nm	$2\sqrt{\pi/n}$	0.74 nm	,,
L_ϕ	100 nm	0.5 μm	0.5 μm[b]	3 μm[c]	100 nm

[a] In suspended graphene, mean free paths of about 100 nm were found at 4 K for $n \sim 10^{11}$ cm^{-2} (and about 75 nm at 300 K) in Du et al. (2008), while Bolotin et al. (2008) estimate ℓ of up to 1.2 μm for $n \sim 2 \times 10^{11}$ cm^{-2}. On the other hand, reported values for devices made from graphene sandwiched in between hBN crystals go up to 3 μm (Mayorov et al. 2011).
[b] See Tikhonenko et al. (2009).
[c] Stojetz et al. (2005).

which the phase of the single-electron wavefunction is preserved (within an independent electron approximation), which limits the scale of quantum phase interferences. Typical values for graphene, carbon nanotubes, and other materials are given in Table 4.1.

4.1.2 Coherent versus Sequential Transport

Coherent or sequential? is probably one of the most crucial questions, since it dictates the general framework that better suits a particular system under investigation in a particular experimental condition (Foa Torres et al. 2003; Jonson & Grincwajg 1987; Luryi 1989; Weil & Vinter 1987). Note, however, that the answer most probably lies in between these two extreme situations (see also Section 4.5).

Let us imagine that we start with the sample (nanotube, graphene ribbon, etc.) decoupled from the electrodes. As the coupling between them is turned on, there is an increasing escape rate which determines the intrinsic width (Γ_α) of the levels (ε_α) corresponding to the isolated sample. The more isolated is the sample from the electrodes, the longer the lifetime τ_D of an electron in any of those levels and the smaller the intrinsic level width $\Gamma_\alpha = \hbar/\tau_D$. If the lifetime associated with the intrinsic level width is longer than the coherence time (τ_ϕ), then the electrons will spend enough time inside the sample to suffer phase breaking events leading to a decoherent regime.

In the decoherent limit, one may use a *sequential picture* for transport in which the electronic motion is divided, as in a theater play, into different parts:

1. *Tunneling in.* The electron is transmitted from the left electrode into the sample;
2. *Dwelling.* The electron dwells in the sample, eventually interacting with other electrons or with phonons/vibrational degrees of freedom;
3. *Tunneling out.* The electron tunnels into the right electrode or is reflected back to the left one.

A sometimes implicit assumption of such a picture is that transport is decoherent. Therefore, the description can be at a semiclassical level where only the occupation *probabilities* (and not the amplitudes) are taken into account into a set of rate equations. Typically, these rate equations take into account the different possible processes (tunneling in and out of the sample, electron–electron and inelastic interactions) through a Fermi golden rule for the associated transition rates. By solving these equations, one gets the occupation probabilities from which the current and other quantities of interest can be computed. The widely used Boltzmann equation belongs to this class of schemes, and is introduced later in Section 4.3.

Transport in the Coulomb blockade regime (see also Section 6.5.1) is usually described by such a sequential picture (Beenakker 1991). In this regime, the contacts to the electrodes are weak enough such that the charge inside the sample is well defined and quantified. One says that the transport is suppressed (or blocked) and is only possible at precise energies, which can be tuned by varying the gate voltage (conductance peaks). The energy scale governing such peaks is the charging energy (E_c): the energy necessary to compensate for the electron repulsion and add one more electron to the system.

When the coherence time is longer than the residence time in the sample, the tunneling processes through the contacts and dwell inside the sample cannot be treated in a separate fashion anymore. The picture is that of a coherent transport mechanism and the theater play becomes a weird quantum game. This is the realm where quantum interference effects and even more exotic phenomena involving correlated motion between electrons like the Kondo effect may take place.[2] The Landauer–Büttiker theory and the Kubo formalism, which are briefly introduced in Sections 4.2 and 4.4.4, provide an appropriate framework for coherent, noninteracting electrons.

A crucial magnitude controlling the transition between these regimes is the intrinsic energy level width Γ_α of the sample connected to the outside world. As one moves from the coherent to the sequential regime, Γ_α is reduced until it becomes the smallest energy scale in the problem (the sample being more and more disconnected from the electrodes). Simultaneously, the value of the charging energy increases from zero to a value where it dominates over the mean level spacing Δ and dictates a sequential and discretized transfer of charges from a source to a drain electrode.

A beautiful experiment showing this transition is reproduced in Fig. 4.1 (Babic and Schönenberger 2004). The coupling with the leads changes as the gate voltage V_g is varied, thereby producing a crossover from low transparency to high transparency contacts and allowing observation of the transition from coherent (lower V_g region in Fig. 4.1(a) and (b)) to sequential tunneling (high V_g region in the figures, where isolated resonances are observed). The conductance accordingly exhibits a wealth of phenomena, which includes, from higher to lower gate voltage: Coulomb blockade peaks, strong cotunneling, and Kondo effect, and destructive interference, which is

[2] The Kondo effect is one of the most studied many-body phenomena in condensed matter physics (for a review see Kouwenhoven and Glazman (2001)), and is also an active topic in graphene physics, both theoretically (Cazalilla et al. 2012; Cornaglia et al. 2009) and experimentally (Chen et al. 2011).

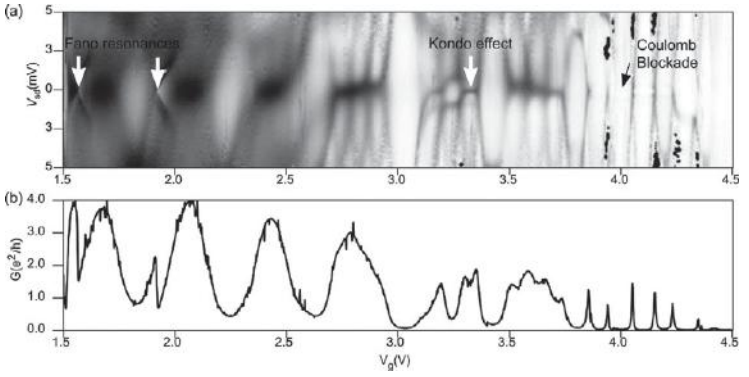

Figure 4.1 (a) Density plot of the differential conductance versus bias voltage V_{sd} and gate voltage V_g (high conductance in black and low conductance in white). (b) Linear response conductance versus gate voltage. The coupling to the leads strongly depends on the gate voltage, allowing for the observation of very different phenomena in the same experiment, namely, Coulomb blockade, Kondo effect, and Fano resonances. (Adapted from Babic and Schönenberger (2004). Copyright (2004) by the American Physical Society. Courtesy of Christian Schönenberger)

manifested as Fano resonances.[3] This experiment illustrates in a magnificent way that the occurrence and the nature of the quantum transport phenomena through a mesoscopic sample strongly depend on the conditions, the measurement setup, and the dominant energy scales of the system under study.

4.2 Landauer–Büttiker Theory

One of the most influential frameworks for the study of quantum transport is Landauer theory, pioneered originally by Rolf Landauer in early 1950s (Landauer 1957, 1970) and generalized later on by Büttiker et al. (1985) for multi-lead systems. The simplicity of Landauer's picture for transport boosted it as a driving force in the field of nanoscale transport. As will be shown later, several reasons make it particularly useful in the context of graphene-based devices, and therefore we dedicate the following pages to a brief presentation of its main points while trying to clarify the underlying assumptions and limitations.

Let us consider a sample or device that is connected through leads to reservoirs. A particular case with two leads is represented in Fig. 4.2. Within Landauer's approach, conductance through a device is seen as a scattering process where electrons injected from the reservoirs are incident onto the device and then scattered back into the

[3] Fano resonances, also known as anti-resonances in the context of electronic transport (Damato et al. 1989; Guinea & Vergés 1987), are a coherent effect of destructive interference pioneered by Fano (1935) in spectroscopy and observed since then in many contexts in different nanostructures (Miroshnichenko et al. 2010).

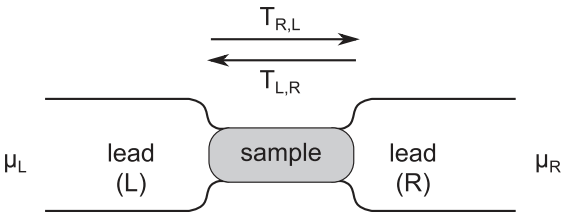

Figure 4.2 A setup where a small conductor is sandwiched between two leads (L and R). The leads are connected to reservoirs kept at equilibrium chemical potentials μ_L and μ_R which in turn determine their equilibrium occupation probabilities (Fermi functions) denoted by f_L and f_R.

reservoirs. Landauer's theory relates the conductance, measuring the ease with which the electrons flow, with the transmission probability through the device. The current through electrode $j(I_j)$ is given by

$$I_j = \frac{2e}{h} \int \sum_{i=1}^{N} \left[T_{j,i}(\varepsilon) f_i(\varepsilon) - T_{i,j}(\varepsilon) f_j(\varepsilon) \right] d\varepsilon, \tag{4.1}$$

where $T_{j,i}(\varepsilon)$ is the transmission probability of an electron of energy ε from lead i to lead j, and the integral is over all available energies. The factor 2 on the right-hand side of Eq. (4.1) comes from considering the electron spin, which here just duplicates the number of available channels. Therefore, the current is given by a balance between the contributions from the different leads weighted by their corresponding transmission probabilities.[4] These transmission probabilities can be conveniently expressed in terms of the Green's functions within the device region through the *trace formula*. The reader not familiar with this formalism is encouraged to follow Appendix C and complete the brief overview given here.

For a two-terminal setup in the low bias, zero temperature limit ($V \to 0$, $k_B T \to 0$), Eq. (4.1) can be simplified to

$$I = \frac{2e^2}{h} T_{\mathrm{RL}}(\varepsilon_F) V, \tag{4.2}$$

where T_{RL} is the total transmission probability from left to right, ε_F is the Fermi energy, and $I_L = I_R = I$ is the current through the device. The conductance is essentially given by the transmission probability in this limit.

It is important to note that there are no blocking factors multiplying the occupation probabilities in the leads (such as $f_i(1 - f_j)$) in the previous equation. Although for systems with time-reversal symmetry, the additional terms would just cancel out leaving the expression unchanged; the difference is a conceptual one. The blocking factors

[4] Note that one can also interpret Eq. (4.1) as the balance between two terms, each one being the product of the probability that a state of energy ε is occupied in lead $j(i)$ times the density of states of that channel times velocity of the corresponding state times the probability that it is transmitted T_{ij} to the other lead (T_{ji}). For one-dimensional channels the density of states is proportional to the inverse group velocity, canceling it out and leading to the referred formula.

would be an attempt to ensure that the final states are empty and therefore not blocked by the Pauli principle (which would somehow mean coming back to a sequential view of transport!). However, within Landauer's scattering viewpoint, the scattering states are occupied according to their asymptotic occupation probability given by the Fermi functions in the leads. These states are orthogonal and extend from the leads and throughout the whole device. Therefore, there is no need of an actual transition to pass from one side of the device to the other.[5]

To get more insight, both a heuristic (Section 4.2.1) and a more formal derivation (Section C.1) will be presented. But before that let us briefly discuss the current fluctuations. Besides the average current, its fluctuations from the average value are also of interest. They can be characterized by a current–current correlation function $\langle \Delta I(t) \Delta I(t') \rangle$, where $\Delta I(t) = I(t) - \langle I(t) \rangle$. Its statistical moments give the full counting statistics (Blanter & Büttiker 2000). Most often, one is interested in the low frequency current noise, which is given by the zeroth order moment (Blanter & Büttiker 2000). At zero temperature, when there are no fluctuations in the distribution of the incident electrons, the zero-frequency noise is given by

$$S_I = \frac{2e^3 |V|}{\pi \hbar} Tr \left(r^\dagger r t^\dagger t \right), \tag{4.3}$$

where $|V|$ is the bias voltage applied between the electrodes, and t and r are matrices containing the transmission and reflection amplitudes (evaluated at the Fermi energy) between the different channels. If we denote the scattering matrix by S, its element $S_{i,j}$ being the probability amplitude of going from channel j to channel i, then the transmission matrix t contains the off-diagonal elements of S while the reflection matrix r contains the diagonal elements of S. The matrix $t^\dagger t$ can be diagonalized, and its real eigenvalues give the transmission probabilities that we denote with T_q. On the basis of eigenchannels, the last equation can be written as (Blanter & Büttiker 2000)

$$S_I = \frac{2e^2}{\pi \hbar} \sum_{q=1}^{N} T_q (1 - T_q). \tag{4.4}$$

More generally, within Landauer's theory, the zero-frequency noise for a two-terminal conductor in thermal equilibrium at a temperature T is

$$S_I = \frac{2e^2}{\pi \hbar} \sum_{q=1}^{N} \int \Big(T_q \big[f_L (1 - f_L) + f_R (1 - f_R) \big] + T_q (1 - T_q) (f_L - f_R)^2 \Big) d\varepsilon, \tag{4.5}$$

which contains contributions from (i) the fluctuations of the incident electron beams (encoded in the Fermi functions) and (ii) the noise due to charge quantization. The zero-temperature Eq. (4.3) represents the pure shot noise contribution. An important remark emphasized by Blanter and Büttiker (2000) is that while the zero-temperature conductance can be expressed fully in terms of the transmission *probabilities* independently of

[5] See, for example, the discussion in chapter 2 of Datta (1995).

the choice of the basis, S_I cannot. *The scattering amplitudes (and not the probabilities) are then the crucial quantities ruling both the conductance and noise.*

4.2.1 Heuristic Derivation of Landauer's Formula

Let us consider a one-dimensional metallic system coupled to two 1D electronic leads which drive incoming and outgoing currents, as sketched in Fig. 4.3. The temperature of the system is set to zero, so only electrons at the Fermi level participate in the electronic current. This current originates from a potential difference between right and left leads with $e\Delta V \ll E_F$. Such potential difference is related to a density gradient $\delta n = n(E_F + e\Delta V) - n(E_F)$ ($n(E)$ being the electron density), which can be approximated, including spin degeneracy, by

$$\frac{\partial n}{\partial E}|_{E_F}.e\Delta V = 2e\Delta V/(\pi\hbar v_F). \tag{4.6}$$

On the other hand, this electron density difference δn can also be written in terms of the current densities in steady state as

$$\delta n = \frac{j + jR}{ev_F} - \frac{jT}{ev_F}, \tag{4.7}$$

introducing R and T, the reflection and transmission probabilities, respectively. From Eq. (4.7), one infers that $\Delta V = [j(1 + R - T)/(ev_F)] \times \pi\hbar v_F/(2e)$. The total current $I = Tj$, so that the resistance of the system reads finally

$$\mathcal{R} = \Delta V/I = \frac{h}{2e^2}\frac{R}{T}. \tag{4.8}$$

Based on this derivation, the quantum conductance becomes $G = 1/\mathcal{R} = 2e^2/h \times T/R$, which has an ill-defined value in the limit of perfect transmission ($T = 1$). Indeed, given current conservation, $R + T = 1$, a perfect transmission through the system means $T = 1$ and $R = 0$, or $G \to \infty$, which is clearly unphysical. The reason for such a singularity comes from the neglect of contact effects. This problem was pioneered

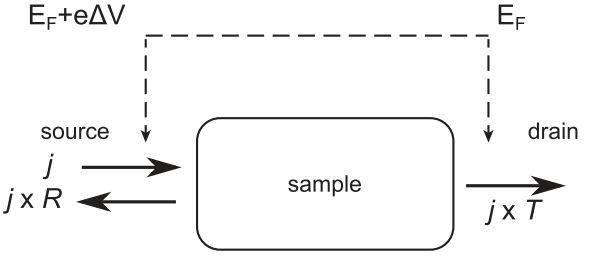

Figure 4.3 Scattering through a system with a single incoming and outgoing channel and an applied voltage difference ΔV. A current density j is injected from the source. The carriers are then scattered and a fraction R is reflected and a fraction T transmitted.

by Rolf Landauer (Imry & Landauer 1999; Landauer 1970) demonstrated that in the situation of ballistic transport across a given (low-dimensional) system, the resistance and dissipation will take place at the interface of the measured system and the metallic electrodes acting as charge reservoirs. This problem can be solved by rewriting the Landauer formula as

$$\mathcal{R} = \frac{h}{2e^2}\frac{1}{T} \tag{4.9}$$

$$= \frac{h}{2e^2} + \frac{h}{2e^2}\frac{1-T}{T}, \tag{4.10}$$

so that the quantum resistance is then seen to split into two parts for the single conducting channel case. The first term of Eq. (4.10) gives the contact resistance between the disorder-free one-dimensional metallic conductor and an electron reservoir with many more electron channels, whereas the second term of Eq. (4.10) actually provides information about the intrinsic resistance of the system, which can dominate the total resistance when the intrinsic transmission is very low. This second term is physically connected to the so-called four-point transport measurements, which allow access to such intrinsic resistance, by excluding contact effects.

4.3 Boltzmann Semiclassical Transport

The Boltzmann equation describes the transport properties of quantum particles (electrons, phonons) driven by a semiclassical dynamics. It determines how the particles of the system are accelerated in external fields, losing part of their accumulated energy through scattering-induced momentum relaxation. Scattering processes are determined by static (impurities, defects) as well as dynamical (phonons) disorders. The Boltzmann transport equation describes the dynamics of the distribution function $f_k(r,t)$, which gives the *probability* (and not the probability amplitude) of finding a particle in momentum-state $|\mathbf{k}\rangle$ in the neighborhood of $|\mathbf{r}\rangle$ and at time t. Its most general form states

$$\frac{\partial f_k(\mathbf{r},t)}{\partial t} + \mathbf{v}_k \cdot \nabla_{\mathbf{r}} f_k(\mathbf{r},t) + \mathbf{F} \cdot \nabla_{\mathbf{k}} f_k(\mathbf{r},t) = \left.\frac{\partial f_k(\mathbf{r},t)}{\partial t}\right|_{\text{coll}}, \tag{4.11}$$

with $\mathbf{F}$ describing external (Lorentz) forces acting on the particles, $\mathbf{v}$ denoting their velocity, and where $\frac{\partial f_k(\mathbf{r},t)}{\partial t}|_{\text{coll}}$ is the collision term which drives the system toward equilibrium, and depends on the sources of scattering and dissipation. The wave nature of electrons is accounted for in the collision term, as well as in the particles energetics (with $E(k)$ and $\mathbf{v}_k = \frac{1}{\hbar}\nabla_k E(k)$ given by the crystalline band structure of the clean system), but the particle dynamics is treated classically in the sense that quantum interferences between multiple scattering events are disregarded. The Boltzmann transport theory is therefore invalidated when localization phenomena enter into play and should instead be replaced by the Kubo approach (described in Section 4.4). In

the regime of high charge density and high temperatures, the Boltzmann transport theory applies reasonably well, however, even in low-dimensional materials such as graphene.

In Eq. (4.11), the collision term describes the abrupt changes of momentum due to scattering of the particles. To keep the calculation simple, we hereafter consider only elastic scattering (particle momentum is changed in the scattering process but energy is conserved), but electron–phonon coupling can be treated similarly (Hwang & Sarma 2008; Munoz 2012). The rate of change of the distribution function f_k due to scattering can be written as

$$\frac{\partial f_k(\mathbf{r},t)}{\partial t}|_{\text{coll}} = \sum_{k'} f_{k'}(1-f_k)p_{k',k} - \sum_{k'} f_k(1-f_{k'})p_{k,k'} \tag{4.12}$$

$$= \sum_{k'} (f_{k'} - f_k)p_{k,k'}. \tag{4.13}$$

The first term on the right-hand side of Eq. 4.12 accounts for scattering events from all other states $|\mathbf{k}'\rangle$ to $|\mathbf{k}\rangle$. The probability of one scattering event is proportional to the probability that the state $|\mathbf{k}'\rangle$ (resp. $|\mathbf{k}\rangle$) is occupied (resp. vacant), and to the transition probability $p_{k,k'}$. The second term on the right-hand side of Eq. (4.12) denotes the contribution of the scattering from $|\mathbf{k}\rangle$ to $|\mathbf{k}'\rangle$. As these processes decrease f_k, the second term gets a minus sign. To obtain Eq. (4.13), the detailed balance property $p_{k,k'} = p_{k',k}$ has been used. The transition probability from state $|\mathbf{k}\rangle$ to state $|\mathbf{k}'\rangle$ is given by Fermi's golden rule:

$$p_{k,k'} = \frac{2\pi}{\hbar}|\langle \mathbf{k}'|V|\mathbf{k}\rangle|^2 \delta(\varepsilon_{k'} - \varepsilon_k), \tag{4.14}$$

introducing the $\delta(\varepsilon_{k'} - \varepsilon_k)$ function ensuring energy conservation.

4.3.1 The Relaxation Time Approximation and the Boltzmann Conductivity

To solve Eq. (4.11), one needs further approximation. The most straightforward is the relaxation time approximation (RTA), which introduces a single timescale for the nonequilibrium distribution function $f_k(r,t)$ to relax to the Fermi–Dirac function $f_k^0 = 1/(\mathrm{e}^{\beta(\varepsilon_k - E_F)} + 1)$ ($\beta = 1/(k_B T)$ and E_F is the Fermi energy). One defines the deviation to its equilibrium state as $g_k = f_k - f_k^0$. The relaxation time approximation assumes that the system is driven back to its equilibrium position as

$$\left.\frac{\partial f}{\partial t}\right|_{\text{coll}} = -\frac{g_k}{\tau_k}, \tag{4.15}$$

with τ_k the relaxation time, which measures how fast the system relaxes to the equilibrium distribution after turning off the external field. The calculation of τ_k is related to

$$-\frac{g_k}{\tau_k} = \sum_{k'}(f_{k'} - f_k)p_{k,k'} \tag{4.16}$$

$$= \sum_{k'}(g_{k'} - g_k)p_{k,k'}, \tag{4.17}$$

assuming that the energy and the relaxation time do not depend on the direction of the k vector and considering only scattering with $k = k'$. Within the RTA, the Bloch–Boltzmann equation becomes

$$\frac{\partial f_k}{\partial t} = -\mathbf{v}_k \cdot \nabla_{\mathbf{r}} f_k - \frac{e\mathbf{E}}{\hbar} \cdot \nabla_{\mathbf{k}} f_k - \frac{g_k}{\tau_k}. \tag{4.18}$$

For a homogeneous electrical field and absence of temperature gradient, the steady-state solution can be written

$$\frac{e\mathbf{E}}{\hbar} \cdot \nabla_{\mathbf{k}} f_k + \frac{g_k}{\tau_k} = 0, \tag{4.19}$$

and using $\nabla_{\mathbf{k}} f_k = \hbar \mathbf{v}_k \partial f_k^0 / \partial \varepsilon_k + \partial g_k / \partial \mathbf{k}$, one finally obtains

$$f_k = f_k^0 - \left(\frac{\partial f_k^0}{\partial \varepsilon_k}\right) e\tau_k \mathbf{v}_k \cdot \mathbf{E}. \tag{4.20}$$

The relaxation time can be then calculated using Eq. (4.17) as

$$\frac{1}{\tau_k} = \sum_{k'}\left(1 - \frac{g_{k'}}{g_k}\right)p_{k,k'} \tag{4.21}$$

$$= \sum_{k'}\left(1 - \frac{\left(-\frac{\partial f_{k'}^0}{\partial \varepsilon_{k'}}\right) e\tau_{k'}\mathbf{v}_{k'} \cdot \mathbf{E}}{\left(-\frac{\partial f_k^0}{\partial \varepsilon_k}\right) e\tau_k \mathbf{v}_k \cdot \mathbf{E}}\right)p_{k,k'} \tag{4.22}$$

$$= \sum_{k'}\left(1 - \frac{\hat{\mathbf{k}}' \cdot \mathbf{E}}{\hat{\mathbf{k}} \cdot \mathbf{E}}\right)p_{k,k'}. \tag{4.23}$$

In the last step, the relation $\mathbf{v}_k = v_k \mathbf{k}/k = v_k \hat{\mathbf{k}}$ is used. Without loss of generality the vector $\mathbf{k}$ may be chosen to point in the x direction, so $\hat{\mathbf{k}} = \mathbf{e}_x$, and in two dimensions wavevectors are decomposed as $\hat{\mathbf{k}}' = \cos\theta_{k'}\mathbf{e}_x + \sin\theta_{k'}\mathbf{e}_y$, while $\mathbf{E} = E_x\mathbf{e}_x + E_y\mathbf{e}_y$. Therefore

$$\frac{1}{\tau_k} = \sum_{k'}\left(1 - \frac{E_x \cos\theta_{k'} + E_y \sin\theta_{k'}}{E_x}\right)p_{k,k'} \tag{4.24}$$

$$= \sum_{k'}(1 - \cos\theta_{k'})p_{k,k'}. \tag{4.25}$$

Note that the term proportional to $p_{k,k'} \sin\theta_{k'}$ cancels by summation, since $\sin\theta_{k'}$ is an odd function of $\theta_{k'}$ while $p_{k,k'}$ is symmetric with respect to $\theta_{k'}$. This result holds for isotropic scattering in k-space if all transition probabilities $p_{k,k'} = 0$ for $k \neq k'$. The inverse relaxation time is thus obtained by summing up the probabilities of all scattering events, weighted with the transport factor $(1 - \cos\theta_{k'})$, which favors large-angle scattering. This result makes sense physically as the large-angle scattering events more strongly alter the distribution function, hence controlling the behavior of the relaxation time. Calculation of the Boltzmann conductivity is derived from the current density $\mathcal{J}$, defined as (using Eq. (4.20))

$$\mathcal{J} = \frac{e}{\Omega} \sum_k v_k f_k \tag{4.26}$$

$$= -\frac{e^2}{\Omega} \sum_k \left(\frac{\partial f_k^0}{\partial \varepsilon_k} \right) \tau_k \mathbf{v}_k (\mathbf{v}_k \cdot \mathbf{E}). \tag{4.27}$$

This gives the conductivity in the RTA as

$$\sigma_{xx} = -\frac{e^2}{2\pi} \int k dk \left(\frac{\partial f_k^0}{\partial \varepsilon_k} \right) \tau_k v_k^2. \tag{4.28}$$

4.4 Kubo Formula for the Electronic Conductivity

The conductivity of a bulk material is defined at finite frequency ω as the tensorial ratio between the applied electric field and the resulting electronic current: $\mathbf{J}(\omega) = \boldsymbol{\sigma}(\omega)\mathbf{E}(\omega)$. We assume that the transport measurement direction is along the (Ox) axis so that only diagonal elements are taken into account: $\mathcal{J}_x(\omega) = \sigma(\omega)E_x(\omega)$. The Kubo approach is a technique to calculate linear response in materials (optical, electric, etc.). It is based on the *fluctuation–dissipation theorem* that establishes a correspondence between the *dissipative* out-of-equilibrium response (namely, the conductivity) and the *fluctuations* at equilibrium (the correlation function of the charge carrier velocities).

We provide here a comprehensive derivation of the Kubo formula for electronic conductivity (Lherbier 2008; Roche 1996; Triozon 2002), which is suitable for studying quantum transport phenomena in disordered graphene-based materials, based on numerical simulations. It is inspired by a derivation by Nevill Mott, which calculates the absorbed power driven by electronic transitions induced by the exchanges between the system and the electromagnetic field (P).

Let us assume an electronic system described by the Hamiltonian $\hat{\mathcal{H}}_0 = \frac{\hat{\mathbf{P}}^2}{2m} + \hat{\mathcal{V}}$, where $\hat{\mathcal{V}}$ gives the crystal potential which can also include the effect of crystal imperfections. Then assume that its electronic spectrum is given by $\varepsilon_k, |\Psi_k\rangle$. By applying an external (weak) electric field, the system will undergo internal fluctuations, which are usually well captured by electronic transition between states of the system at equilibrium. To compute σ, we start with the equation $P = \mathcal{J} \cdot \mathbf{E}$ with $\mathcal{J} = \sigma\mathbf{E}$.

The electric field $\mathbf{E}(t)$ is given by $E_0\cos(\omega t)\mathbf{u}_x$, but for computational convenience we use an oscillatory field throughout the derivation, while the limit to the static case is taken at the end ($\mathbf{E}(t) = E_0\mathbf{u}_x$) with $\omega \to 0$. The associated vector potential $\mathbf{A}(t)$ in the Coulomb gauge is

$$\mathbf{A}(t) = -\frac{E_0}{2i\omega}\left(\mathrm{e}^{\mathrm{i}\omega t} - \mathrm{e}^{-\mathrm{i}\omega t}\right)\mathbf{u}_x, \tag{4.29}$$

while the total power absorbed per unit time is

$$P_{\text{tot abs}} = \sum_{n,m} P_{\text{abs}}^{n\to m} - P_{\text{diss}}^{m\to n}. \tag{4.30}$$

The average power absorbed (P_{abs}) and dissipated (P_{diss}) per unit time can be estimated from the transition probabilities $\tilde{p}_{n\to m}$ from electronic states n to m (and inversely ($m \to n$)) and Fermi–Dirac distribution $f(E)$:

$$P_{\text{abs}}^{n\to m} = [\hbar\omega\, f(E_n)(1 - f(E_m))]\tilde{p}_{n\to m}, \tag{4.31}$$

$$P_{\text{diss}}^{m\to n} = [\hbar\omega\, f(E_m)(1 - f(E_n))]\tilde{p}_{m\to n}. \tag{4.32}$$

Such transition probabilities per unit time are derived from a first-order perturbation theory in the electric field as

$$\tilde{p}_{n\to m} = \frac{p_{n\to m}(t)}{t} = \frac{1}{\hbar^2 t}\left|\int_0^t dt'\, \mathrm{e}^{\mathrm{i}(E_m - En)t'/\hbar}\langle m|\delta\hat{\mathcal{H}}(t')|n\rangle\right|^2, \tag{4.33}$$

with $\delta\hat{\mathcal{H}}$ being the time-dependent perturbation of the total Hamiltonian. At first order, it directly relates to the velocity operator $\hat{\mathbf{V}}$ and vector potential $\mathbf{A}$ through

$$\delta\hat{\mathcal{H}}(t') = e\,\hat{\mathbf{V}}\cdot\mathbf{A}(t'), \tag{4.34}$$

$$\delta\hat{\mathcal{H}}(t') = e\hat{V}_x A_x(t') \quad \text{(for the 1D case)}. \tag{4.35}$$

Using (Eqs. 4.29–4.35) we obtain

$$P_{\text{tot abs}} = \frac{\pi\hbar e^2 E_0^2}{2\hbar\omega}\sum_{n,m}\left|\langle m|\hat{V}_x|n\rangle\right|^2\delta(E_m - E_n - \hbar\omega)\left[f(E_n) - f(E_m)\right], \tag{4.36}$$

and finally the total power absorbed per unit time and volume $P = \frac{P_{\text{abs}}}{\Omega}$ (Ω being the sample volume) is related to the conductivity by

$$P = \frac{P_{\text{tot abs}}}{\Omega} = \sigma\langle\mathbf{E}\cdot\mathbf{E}\rangle = \frac{\sigma E_0^2}{2}. \tag{4.37}$$

Using Eq. (4.37), where $\langle\cos^2(\omega t)\rangle$ has been replaced by its average value $1/2$, one gets the Kubo conductivity

$$\sigma(\omega) = \frac{\pi\hbar e^2}{\Omega}\sum_{n,m}\left|\langle m|\hat{V}_x|n\rangle\right|^2\delta(E_m - E_n - \hbar\omega)\frac{f(E_n) - f(E_m)}{\hbar\omega}. \tag{4.38}$$

If one uses the properties of $\delta(x)$ functions and rewrites the expression as a trace of operators, the general expression becomes

$$\sigma(\omega) = \frac{\pi\hbar e^2}{\Omega}\int_{-\infty}^{+\infty} dE\, \frac{f(E) - f(E+\hbar\omega)}{\hbar\omega}\mathrm{Tr}\left[\hat{V}_x^{\dagger}\delta\left(E-\hat{\mathcal{H}}\right)\hat{V}_x\delta\left(E+\hbar\omega-\hat{\mathcal{H}}\right)\right]. \tag{4.39}$$

It is also instructive to rewrite this formula introducing the autocorrelation function of velocity ($C(E,t)$), together with the mean square spreading of wavepackets defined as ($\Delta X^2(E,t)$). Using

$$\delta\left(E+\hbar\omega-\hat{\mathcal{H}}\right) = \frac{1}{2\pi\hbar}\int_{-\infty}^{+\infty} dt\, \mathrm{e}^{\mathrm{i}\left(E+\hbar\omega-\hat{\mathcal{H}}\right)t/\hbar} \tag{4.40}$$

inside the trace, which is further denoted by $\mathbb{A}_1$:

$$\mathbb{A}_1 = \mathrm{Tr}\left[\hat{V}_x^{\dagger}\delta\left(E-\hat{\mathcal{H}}\right)\hat{V}_x\delta\left(E+\hbar\omega-\hat{\mathcal{H}}\right)\right], \tag{4.41}$$

$$\mathbb{A}_1 = \frac{1}{2\pi\hbar}\int_{-\infty}^{+\infty} dt\, \mathrm{e}^{\mathrm{i}\omega t}\,\mathrm{Tr}\left[\hat{V}_x^{\dagger}\delta\left(E-\hat{\mathcal{H}}\right)\hat{V}_x\,\mathrm{e}^{\mathrm{i}\left(E-\hat{\mathcal{H}}\right)t/\hbar}\right], \tag{4.42}$$

$$\mathbb{A}_1 = \frac{1}{2\pi\hbar}\int_{-\infty}^{+\infty} dt\, \mathrm{e}^{\mathrm{i}\omega t}\,\mathrm{Tr}\left[\hat{V}_x^{\dagger}\delta\left(E-\hat{\mathcal{H}}\right)\,\mathrm{e}^{\mathrm{i}\hat{\mathcal{H}}t/\hbar}\,\hat{V}_x\,\mathrm{e}^{-\mathrm{i}\hat{\mathcal{H}}t/\hbar}\right]. \tag{4.43}$$

The velocity operator in its Heisenberg representation being

$$\hat{V}_x(t) = \left(\mathrm{e}^{\mathrm{i}\hat{\mathcal{H}}t/\hbar}\,\hat{V}_x\,\mathrm{e}^{-\mathrm{i}\hat{\mathcal{H}}t/\hbar}\right), \tag{4.44}$$

we get

$$\mathbb{A}_1 = \frac{1}{2\pi\hbar}\int_{-\infty}^{+\infty} dt\, \mathrm{e}^{\mathrm{i}\omega t}\,\mathrm{Tr}\left[\hat{V}_x^{\dagger}(0)\;\delta(E-\hat{\mathcal{H}})\,\hat{V}_x(t)\right]. \tag{4.45}$$

Then, one uses the general definition of quantum average for a given energy E from which any operator $\hat{Q}$ has

$$\langle\hat{Q}\rangle_E = \frac{\mathrm{Tr}\left[\delta(E-\hat{\mathcal{H}})\hat{Q}\right]}{\mathrm{Tr}\left[\delta(E-\hat{\mathcal{H}})\right]}. \tag{4.46}$$

Replacing $\hat{Q}$ by the product $\hat{V}_x(t)\hat{V}_x^{\dagger}(0)$,

$$\langle\hat{V}_x(t)\hat{V}_x^{\dagger}(0)\rangle_E = \frac{\mathrm{Tr}\left[\hat{V}_x^{\dagger}(0)\delta(E-\hat{\mathcal{H}})\hat{V}_x(t)\right]}{\mathrm{Tr}\left[\delta(E-\hat{\mathcal{H}})\right]}, \tag{4.47}$$

and using this result to rewrite $\mathbb{A}_1$,

$$\mathbb{A}_1 = \frac{1}{2\pi\hbar}\int_{-\infty}^{+\infty} dt\ \mathrm{e}^{\mathrm{i}\omega t}\ \mathrm{Tr}\left[\delta\big(E-\hat{\mathcal{H}}\big)\right]\ \big\langle \hat{V}_x(t)\hat{V}_x^{\dagger}(0)\big\rangle_E, \tag{4.48}$$

$$\mathbb{A}_1 = \frac{1}{2\pi\hbar}\mathrm{Tr}\left[\delta\big(E-\hat{\mathcal{H}}\big)\right]\int_{-\infty}^{+\infty} dt\ \mathrm{e}^{\mathrm{i}\omega t}\ \big\langle \hat{V}_x(t)\hat{V}_x^{\dagger}(0)\big\rangle_E, \tag{4.49}$$

$$\mathbb{A}_1 = \frac{1}{2\pi\hbar}\,\mathbb{A}_2\,\mathbb{A}_3, \tag{4.50}$$

$$\text{with}\quad \mathbb{A}_2 = \mathrm{Tr}\left[\delta\big(E-\hat{\mathcal{H}}\big)\right],\quad \text{and}\quad \mathbb{A}_3 = \int_{-\infty}^{+\infty} dt\ \mathrm{e}^{\mathrm{i}\omega t}\ \big\langle \hat{V}_x(t)\hat{V}_x^{\dagger}(0)\big\rangle_E. \tag{4.51}$$

Two interesting quantities emerge, with $\mathbb{A}_2$ the total density of states. The second quantity can be reformulated as ($\mathbb{A}_3$), using the definition of velocity autocorrelation function $C(E,t) = \langle \hat{V}_x(t)\hat{V}_x^{\dagger}(0)\rangle_E$, so that

$$\mathbb{A}_3 = \int_{-\infty}^{+\infty} dt\ \mathrm{e}^{\mathrm{i}\omega t}\ C(E,t), \tag{4.52}$$

$$\mathbb{A}_3 = \int_{-\infty}^{0} dt\ \mathrm{e}^{\mathrm{i}\omega t}\ C(E,t) + \int_{0}^{+\infty} dt\ \mathrm{e}^{\mathrm{i}\omega t}\ C(E,t), \tag{4.53}$$

$$\mathbb{A}_3 = \int_{0}^{+\infty} dt\ \mathrm{e}^{-\mathrm{i}\omega t}\ C(E,-t) + \int_{0}^{+\infty} dt\ \mathrm{e}^{\mathrm{i}\omega t}\ C(E,t), \tag{4.54}$$

and using $C(E,-t) = \langle \hat{V}_x(-t)\hat{V}_x^{\dagger}(0)\rangle_E = \langle \hat{V}_x(0)\hat{V}_x^{\dagger}(t)\rangle_E = C(E,t)^{\dagger}$, one gets

$$\mathbb{A}_3 = \int_{0}^{+\infty} dt\ \mathrm{e}^{-\mathrm{i}\omega t}\ C(E,t)^{\dagger} + \mathrm{e}^{\mathrm{i}\omega t}\ C(E,t), \tag{4.55}$$

$$\mathbb{A}_3 = \int_{0}^{+\infty} dt\ 2\Re\mathrm{e}\left(\mathrm{e}^{\mathrm{i}\omega t}\ C(E,t)\right). \tag{4.56}$$

One can easily show that the real part of the velocity autocorrelation function is proportional to the second derivative of the mean squared spread

$$\frac{\partial^2}{\partial t^2}\Delta X^2(E,t) = 2\Re\mathrm{e}\ C(E,t), \tag{4.57}$$

with $\Delta X^2(E,t)$ defined as

$$\Delta X^2(E,t) = \left\langle \left|\hat{X}(t)-\hat{X}(0)\right|^2\right\rangle_E. \tag{4.58}$$

One can consequently rewrite $\mathbb{A}_1$ as follows:

$$\mathbb{A}_1 = \frac{1}{2\pi\hbar}\,\mathbb{A}_2\int_{0}^{+\infty} dt\ 2\Re\mathrm{e}\left(\mathrm{e}^{\mathrm{i}\omega t}\ C(E,t)\right), \tag{4.59}$$

and $\mathbb{A}_1$ can be replaced in Eq. (4.39) to get another formulation of the Kubo conductivity (Lherbier 2008; Roche 1996; Triozon 2002):

$$\sigma(\omega) = \frac{e^2}{2}\int_{-\infty}^{+\infty} dE\, \frac{f(E) - f(E+\hbar\omega)}{\hbar\omega}\, \frac{\mathrm{Tr}\left[\delta(E-\hat{\mathcal{H}})\right]}{\Omega} \int_0^{+\infty} dt\; 2\Re\mathrm{e}\left(\mathrm{e}^{\mathrm{i}\omega t}\, C(E,t)\right). \tag{4.60}$$

This last Eq. (4.60) is the total density of states per volume unit $\rho(E) = \mathrm{Tr}\left[\delta(E-\hat{\mathcal{H}})\right]/\Omega$. This is a general form for σ, which can now be simplified taking two limits. First, let us go to the static electric field limit $\omega \mapsto 0$,

$$\sigma_{\mathrm{DC}} = -\frac{e^2}{2}\int_{-\infty}^{+\infty} dE\, \frac{\partial f(E)}{\partial E}\, \rho(E) \int_0^{+\infty} dt\; 2\Re\mathrm{e}\left(C(E,t)\right), \tag{4.61}$$

$$\sigma_{\mathrm{DC}} = -\frac{e^2}{2}\int_{-\infty}^{+\infty} dE\, \frac{\partial f(E)}{\partial E}\, \rho(E) \int_0^{+\infty} dt\, \frac{\partial^2}{\partial t^2}\Delta X^2(E,t), \tag{4.62}$$

$$\sigma_{\mathrm{DC}} = -\frac{e^2}{2}\int_{-\infty}^{+\infty} dE\, \frac{\partial f(E)}{\partial E}\, \rho(E) \lim_{t\mapsto\infty} \frac{\partial}{\partial t}\Delta X^2(E,t), \tag{4.63}$$

while the zero-temperature limit ($T \mapsto 0$) implies that $-\frac{\partial f(E)}{\partial E} \mapsto \delta(E-E_F)$, so that

$$\sigma_{\mathrm{DC}}(E_F) = \frac{e^2}{2}\int_{-\infty}^{+\infty} dE\, \delta(E-E_F)\, \rho(E) \lim_{t\mapsto\infty} \frac{\partial}{\partial t}\Delta X^2(E,t), \tag{4.64}$$

$$\sigma_{\mathrm{DC}}(E_F) = \frac{e^2}{2}\rho(E_F) \lim_{t\mapsto\infty} \frac{\partial}{\partial t}\Delta X^2(E_F,t). \tag{4.65}$$

This last expression means that $\frac{\partial}{\partial t}\Delta X^2(E_F,t)$ should converge in the limit $t \mapsto \infty$, to define a meaningful conductivity. The propagation of the wavepacket thus needs to establish a saturation regime before conductivity can be safely calculated. However, as shown in other chapters, the time-dependent scaling on the conductivity can be followed and allowed to follow localization phenomena as long as phase coherence is maintained. This formula, known as the Kubo conductivity (Kubo 1966), is the most general starting point to study quantum (or classical) transport in any type of disordered materials, provided that electron–electron interaction can be described as a perturbation with respect to the initial electronic structure, introducing additional transitions (inelastic scattering), but preserving the independent electron description of transport quantities.

4.4.1 Illustrations for Ballistic and Diffusive Regimes

The behavior of $\Delta X^2(t)$ and related diffusion coefficient $D_x(t)$ defined by

$$D_x(t) = \frac{\Delta X^2(t)}{t} \tag{4.66}$$

is easily determined in two important transport regimes. Below we outline some consequences of the transport regime on the scaling property of the quantum conductivity, as computed from the Kubo formula.

Ballistic Regime

First, in the absence of any structural imperfection, the electronic propagation remains ballistic with the mean square spread just defined by the initial velocity of the wavepacket $\Delta X^2(t) = v_x^2(0)t^2$, with $v_x(0)$ the velocity at $t = 0$. The diffusion coefficient is then linear in time, $D_x(t) = v_x^2(0)t$, while the Kubo conductivity is given by

$$\sigma_{\mathrm{DC}}(E)_{\mathrm{bal}} = \frac{e^2}{2}\rho(E)\lim_{t\mapsto\infty}\frac{\partial}{\partial t}\Delta X^2(E,t) = e^2\rho(E)\lim_{t\mapsto\infty} v_x^2(0,E)t, \tag{4.67}$$

so that $\sigma_{\mathrm{DC}}(E)_{\mathrm{bal}}$ diverges in the long time limit. This singularity is inherent to the fact that when deriving the linear response theory, a finite dissipation source, intrinsic to the sample, is introduced both physically and mathematically. The ballistic limit is therefore not well defined in this formalism, although as shown below, a complete equivalence exists with the Landauer–Büttiker formulation, and the quantization of the conductance can be obtained from the Kubo formula with some extra assumptions. The conductance of the materials can indeed be derived from the conductivity through $G = \sigma L^{d-2}$, with d the space dimension. For one-dimensional systems $G = \sigma/L$. Dividing Eq. (4.67) by the relevant length scale L, we can recover a quantized conductance expected in a ballistic regime (when reflectionless contacts are assumed). By replacing L by $2v_x t$ (since the length propagated during t is $2\sqrt{\Delta X^2(t)} = 2v_x t$), the conductance then becomes

$$G(E) = e^2\rho_{1\mathrm{D}}(E)\lim_{t\to\infty}\frac{v_x^2(E)t}{L} = e^2\rho_{1\mathrm{D}}(E)\lim_{t\to\infty}\frac{v_x^2(E)t}{2v_x(E)t}, \tag{4.68}$$

$$G(E) = \frac{e^2}{2}\rho_{1\mathrm{D}}(E)v_x(E) = \frac{2e^2}{h} = G_0, \tag{4.69}$$

using $\rho_{1\mathrm{D}}(E) = 2/\pi\hbar v_x(E)$ and with G_0 the conductance quantum (spin degeneracy included). So even in the most unfavorable transport regime, the quantization of the conductance can be recovered and identified to the situation of perfect transmission through reflectionless contacts (Landauer–Büttiker approach, Section 4.2)

Diffusive Regime

The velocity autocorrelation function in the time relaxation approximation is given by $\langle v_x(0)v_x(t)\rangle = v_x^2(0)\mathrm{e}^{-t/\tau}$ (introducing the transport time τ and restricting the discussion to elastic scattering events), which yields

$$\lim_{t\mapsto\infty}\Delta X^2(t) = \lim_{t\mapsto\infty} 2\tau v_x^2(0)\,[t-\tau] \longmapsto 2\tau v_x^2(0)t. \tag{4.70}$$

Similarly (using Eq. (4.66)), one gets $\lim_{t\mapsto\infty} D_x(t) \longmapsto 2\tau v_x^2(0)$. The Kubo formula for a diffusive regime then gives access to the semiclassical conductivity ($\sigma_{\rm sc}$):

$$\sigma_{\rm sc}(E) = \sigma_{\rm DC}(E)_{\rm diff} = \frac{e^2}{2}\rho(E) \lim_{t\mapsto\infty} \frac{\partial}{\partial t}\Delta X^2(E,t), \tag{4.71}$$

$$\sigma_{\rm sc}(E) = e^2\rho(E)\tau(E)v_x^2(0,E), \tag{4.72}$$

$$\sigma_{\rm sc}(E) = e^2\rho(E)v_x(0,E)\ell_e(E), \tag{4.73}$$

where the mean free path $\ell_e(E)$ is introduced. For the diffusive regime

$$\sigma_{\rm sc}(E) = \frac{e^2}{2}\rho(E) \lim_{t\mapsto\infty} D_x(E,t) = \frac{e^2}{2}\rho(E)D_x^{\rm max}(E), \tag{4.74}$$

where $D_x^{\rm max}$ corresponds to the maximum value ($D_x^{\rm max} = 2\tau v_x^2(0)$). In this regime, with the charge density defined as $n(E) = \int dE\rho(E)$, the mobility μ is given by

$$\mu(E) = \frac{\sigma_{\rm sc}(E)}{n(E)e}. \tag{4.75}$$

For free electrons $E(k) = (\hbar k)^2/2m$ and $v(k) = \hbar k/m$, with $\rho_{\rm 1D}(E) = \frac{2}{\pi\hbar}\left(\frac{m}{2E}\right)^{1/2}$ and $n_{\rm 1D}(E) = \frac{2}{\pi\hbar}(2mE)^{1/2}$, so that using Eqs. (4.72) and (4.75), the mobility finally is given by

$$\mu(E) = \frac{e^2\rho_{\rm 1D}(E)\tau(E)v^2(E)}{en_{\rm 1D}(E)} = \frac{e\tau(E)v^2(E)}{2E}, \tag{4.76}$$

$$\mu(E) = \frac{e\tau(E)\hbar^2k^2}{2\left(\frac{\hbar^2k^2}{2m}\right)m^2} = \frac{e\tau(E)}{m}, \tag{4.77}$$

which are familiar expressions for semiclassical transport (absence of quantum interferences). One notes that estimation of the mobility becomes problematic for graphene-based materials for plenty of reasons. First, for clean graphene-based materials (nanotubes, graphene ribbons, or two-dimensional graphene), the mean free path might become longer than the electrode spacing, so the use (or even the definition) of Eq. (4.75) becomes inappropriate since it neglects contact effects. Additionally, in the presence of intrinsic disorder (vacancies, adsorbed adatoms, etc.), strong scattering and a significant contribution of quantum interferences occur, which again invalidate the use of Eq. (4.75). Quantum interferences up to 100 K have been measured experimentally in disordered graphene materials (see for instance Moser et al. (2010)), so even if inelastic scattering restores in principle the validity of Eq. (4.75), the experimental estimations have to be scrutinized with care. One general assumption is that the quality of the sample can be appreciated by estimating the mobility at a charge density of (typically) 10^{11} cm^{-2} with varying temperature, and that the absolute value allows comparison of sample quality. In the numerical calculations (using the Kubo formula) that are discussed later, the estimations of mobility using Eq. (4.75) are made using the semiclassical conductivity computed at zero temperature.

4.4.2 Kubo versus Landauer

The Kubo approach is a quantum generalization of the semiclassical Bloch–Boltzmann approach for studying electron transport in materials, which includes all multiple scattering effects driven by disorder. The Kubo–Greenwood formalism (Kubo 1966) is well suited for exploring the intrinsic transport properties of a given disordered material of high dimensionality. It mainly applies to the study of weakly or strongly disordered systems, characterized by a diffusive regime and localization phenomena in the low-temperature limit. It gives all information on the intrinsic quantum conductivity which can be accessed experimentally by four-points transport measurements (meaning two electrodes for generating voltage drop and two others for measuring induced current). With this formalism, when the system is translational invariant, no scattering takes place, and the "intrinsic" mean free path is infinite. Differently, the Landauer–Büttiker transport formalism is directly linked with two-point transport measurements (meaning two identical electrodes for generating voltage drop and measuring induced current) and is proportional to the transmission probability for charges to be transfered through a given system connected to external electrodes. A connection between Kubo and Landauer can be made by rewriting the two-point resistance (computed with the Landauer–Büttiker method) as e.g., $R = R_0/T = R_0 + R_{\text{int}}$, making explicit the "intrinsic resistance" $R_{\text{int}} = R_0(1-T)/T$, which could be derived applying the Kubo–Greenwood approach.

Within this formalism, when the system is free of scattering or when the density of impurities is sufficiently low such that $\ell_e \gg L$ (L is the distance between source/drain electrodes) the transport regime is ballistic, with a transmission probability at energy E entirely proportional to the number of propagating modes, that is, $G(E) = G_0 N_\perp(E)$.

In the situation of a large amount of scatterers (such as chemical impurities), i.e., when $\ell_e \ll L$, the transport regime becomes diffusive and the conductance scales as $G(E) = G_0 N_\perp(E)\ell_e(E)/L$. An interpolation formula allows covering of the so-called quasiballistic regime with $T = N_\perp(E)/(1 + L/\ell_e)$. If the quantum transmission at the system/electrode interface is perfect (induces no scattering), then both Kubo and Landauer formalisms are totally equivalent, although some geometrical factors differentiate them if computed with the different formalisms (Akkermans & Montambaux 2007). The extracted Landauer mean free path ℓ_e^L and Kubo mean free path ℓ_e^K are expected to be proportional, $\ell_e^L = \kappa \ell_e^K (\kappa = 2$ for $d = 1, \kappa = \frac{\pi}{2}(d = 2)$, $\kappa = \frac{4}{3}(d = 3))$ (Akkermans & Montambaux 2007). In the case of a rectangular waveguide, the κ coefficient depends on the dimensionality of the system (Datta 1995).

For instance, to determine exactly the κ coefficient for a finite nanotube, one needs to solve the diffusion equation for the specified geometry and given boundary conditions (Datta 1995). $\kappa = 2$ at the charge neutrality point. This can also be shown using the Einstein relationship for conductivity, $\sigma_F = e^2 \rho_F D_F$, where $\rho_F = 4/\pi\hbar v_F$ is the total density of states at CNP, and $D_F = \ell_e v_F$ is the diffusivity coefficient at CNP. The total conductivity for the quasi-1D system is obtained by using Ohm's law, $G = G_0 N_\perp 2\ell_e/L$.

4.4.3 Validity Limit of Ohm's Law in the Quantum Regime

Ohm's law in the classical regime can be easily derived using the 1D formula for the conductance of a diffusive system, i.e., $G = \sigma_{sc} L^{d-2} = e^2 \rho(E) D/L$, with $\rho(E) = 2/h\nu_F$ and $D = \ell_e \nu_F$. Then $G = 2e^2/h\frac{\ell_e}{L}$ which uses the additivity rule of resistance, i.e., $\mathcal{R}(L_1 + L_2) = \mathcal{R}(L_1) + \mathcal{R}(L_2)$. In the quantum regime, if one uses the Landauer expression for the conductance/resistance, one demonstrates that the resistance $\mathcal{R}(L_1 + L_2) > \mathcal{R}(L_1) + \mathcal{R}(L_2)$ because of multiple scattering phenomena.

4.4.4 The Kubo Formalism in Real Space

An efficient real-space implementation of the Kubo formula was first developed by Roche and Mayou in 1997 for the study of quasiperiodic systems (quasicrystals) (Roche & Mayou 1997). It was then adapted by Roche and coworkers to allow exploration of mesoscopic (magneto)-transport in complex and disordered mesoscopic systems including carbon nanotubes, semiconducting nanowires, and graphene-based materials (Ishii et al. 2009; Latil et al. 2005; Lherbier et al. 2008; Roche 1999; Roche & Saito 2001; Roche et al. 2005). The typical disordered samples studied with such methodology already contain several tens of millions of orbitals, and with the use of high-performance computing resources, the simulation of samples with one billion atoms can be envisioned in the next decade. This numerical transport method therefore offers unprecedented exploration possibilities of complex quantum transport phenomena, not only in realistic models of disordered graphene-based materials, but also in any other types of materials of exciting scientific and technological interest (silicon nanowires (Persson et al. 2008), organic crystals (Ortmann & Roche 2011), topological insulators, etc.).

We present here the basic ingredients of the numerical implementation and provide in further sections extensive illustrations of its use in the study of disordered graphene-based materials (Lherbier 2008; Roche 1996; Triozon 2002). Appendix D provides an extensive technical derivation of such a real space (and order N) implementation using the Lanczos method, which is also reviewed in detail. We present here a summary of such a derivation since it will help us to explore most quantum transport regimes in complex forms of graphene-based materials. We start again with the general form of the Kubo conductivity:

$$\sigma(\omega) = \frac{2\pi e^2 \hbar}{\Omega} \int_{-\infty}^{+\infty} \frac{f(E) - f(E + \hbar\omega)}{\hbar\omega} \mathrm{Tr}\left[\hat{\mathrm{V}}_x \, \delta(E - \hat{\mathcal{H}}) \, \hat{\mathrm{V}}_x \, \delta(E - \hat{\mathcal{H}} + \hbar\omega)\right] dE, \tag{4.78}$$

where $\hat{\mathcal{H}}$ is the Hamiltonian operator, $\hat{\mathrm{V}}_x$ is the operator for the electronic velocity along the x axis, and $f(E)$ is the Fermi distribution function. The DC conductivity corresponds to the limit $\omega = 0$. Using the property

$$\lim_{\omega\to 0}\frac{f(E)-f(E+\hbar\omega)}{\hbar\omega}=-\frac{\partial f}{\partial E}=\delta(E-E_F) \tag{4.79}$$

and after a Fourier transform, the diagonal conductivity can be simplified to

$$\sigma_{\mathrm{DC}}=e^2\rho(E_F)\lim_{t\to\infty}\left[\frac{1}{t}\left\langle\Delta X^2(t)\right\rangle_E\right], \tag{4.80}$$

where $\rho(E_F)$ is the density of states per unit of volume and $\left\langle\Delta X^2(t)\right\rangle_E$ measures the electronic quadratic spread at energy E, defined as

$$\left\langle\Delta X^2(t)\right\rangle_E=\frac{\mathrm{Tr}\left[\delta(E-\hat{\mathcal{H}})\left(\hat{X}(t)-\hat{X}(0)\right)^2\right]}{\mathrm{Tr}\left[\delta(E-\hat{\mathcal{H}})\right]}, \tag{4.81}$$

where $\hat{X}(t)$ is the position operator along the x axis, written in the *Heisenberg representation* for the time t. We note that Eq. (4.80) is slightly different from Eq. (4.65), which is the most general starting point, but which is more computationally demanding. However, in most cases the simplification of using Eq. (4.80) is sufficient to extract the main physics. We refer the reader to Lherbier et al. (2012) for a numerical comparison of both formulas. We then modify Eq. (4.81), using the time-reversal symmetry and the properties of the trace. One can demonstrate that

$$\mathrm{Tr}\left[\delta(E-\hat{\mathcal{H}})\left(\hat{X}(t)-\hat{X}(0)\right)^2\right]=\mathrm{Tr}\left[A^\dagger(t)\,\delta(E-\hat{\mathcal{H}})\,A(t)\right], \tag{4.82}$$

$$A(t)=\left[\hat{\mathrm{X}},\hat{\mathrm{u}}(t)\right]=\hat{\mathrm{X}}\hat{\mathrm{u}}(t)-\hat{\mathrm{u}}(t)\hat{\mathrm{X}}, \tag{4.83}$$

where $\hat{\mathrm{X}}$ is the position operator in the Schrödinger representation and $\hat{\mathrm{u}}(t)=\exp(-\mathrm{i}\hat{\mathcal{H}}t/\hbar)$ is the usual evolution operator. Secondly, the trace in Eq. (4.81) is approximated by expectation values on random phase states. Random phase states are expanded on all the orbitals $|n\rangle$ of the basis set and defined thus:

$$|\mathrm{wp}\rangle=\frac{1}{\sqrt{N}}\sum_{n=1}^{N}\exp\left(2\mathrm{i}\pi\,\alpha(n)\right)\;|n\rangle, \tag{4.84}$$

where $\alpha(n)$ is a random number in the [0, 1] range. An average over few tens of random phases states is usually sufficient to calculate the expectation values,

$$\mathrm{Tr}[\ldots]\longrightarrow\langle\mathrm{wp}|\ldots|\mathrm{wp}\rangle, \tag{4.85}$$

and the spread (4.81) can finally be rewritten:

$$\left\langle\Delta X^2(t)\right\rangle_E=\frac{\langle\mathrm{wp}|\,A^\dagger(t)\,\delta(E-\hat{\mathcal{H}})\,A(t)\,|\mathrm{wp}\rangle}{\langle\mathrm{wp}|\,\delta(E-\hat{\mathcal{H}})\,|\mathrm{wp}\rangle}. \tag{4.86}$$

Equation (4.86) is now suitable for order $O(N)$ numerical techniques and calculation of the transport properties is possible. We leave additional technical details to Appendix D and turn now to a physical discussion of this approach. Actually, the quadratic spread

(Eq. 4.86) is a key quantity as it is directly related to the diffusion coefficient (or diffusivity) through

$$D_E(t) = \left\langle X^2(t) \right\rangle_E \cdot \frac{1}{t}, \tag{4.87}$$

whose time dependence fully determines the transport mechanism. It is worthwhile also to define the electronic spread

$$X_E(t) = \sqrt{\left\langle X^2(t) \right\rangle_E} = \sqrt{t D_E(t)}. \tag{4.88}$$

The three main transport mechanisms which can be generically followed through the time evolution of the wavepacket dynamics (illustrated in Fig. 4.4) are:

- *Ballistic regime*. Electrons travel through the systems without suffering any scattering, so that $D_E(t)$ and $X_E(t)$ remain linear functions in time, with slopes respectively equal to v_F^2 and v_F. Figure 4.4(a) shows a typical ballistic motion in clean 2D graphene at the Dirac point for metallic armchair nanotubes, whereas Fig. 4.5 shows the extracted energy-dependent velocity in clean two-dimensional graphene from the linear regime, which agrees perfectly with the analytical (exact) result. In particular, at the Dirac point, $v_F \sim 2.1\gamma_0$ Å$/\hbar$.
- *Diffusive regime*. Behavior in weakly disordered graphene is characterized by a saturation of $D_E(t \to \infty)$. The saturation value identifies the elastic relaxation (or transport) time τ (see Fig. 4.4(b)).
- *Localized regime*. Behavior in strongly disordered graphene is manifested by an increasing contribution of quantum interference, which reduces the diffusion coefficient, roughly following a $\sim 1/t$ decay. Spreading $X_E(t)$ reaches an asymptotic value that is related to the localization length $\xi(E)$ (see Fig. 4.4(c)).

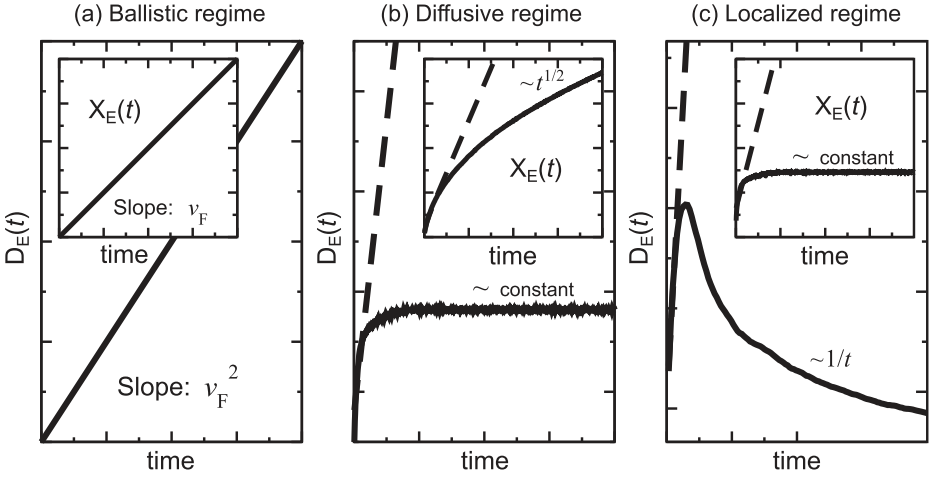

Figure 4.4 Typical behaviors of the diffusion and spread coefficients for the three characteristic regimes: (a) ballistic; (b) diffusive; and (c) localized. Courtesy of Dinh Van Tuan.

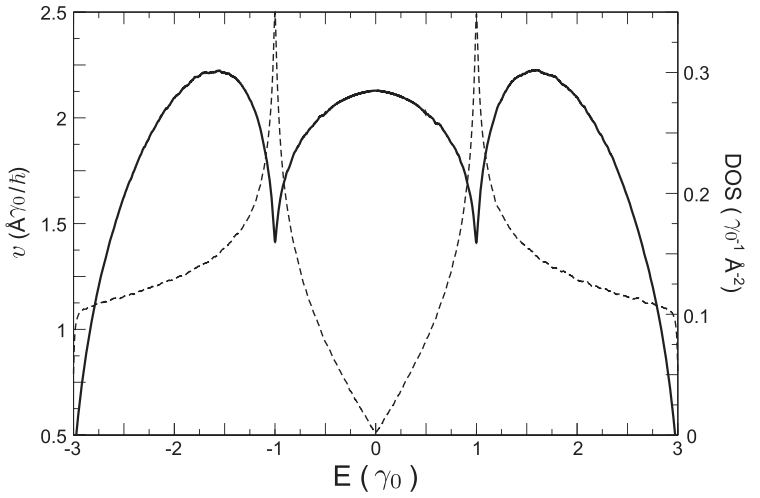

Figure 4.5 Velocity versus energy (solid line) and density of states (dashed line) for pristine graphene.

All the dynamics of the electronic system are actually conveyed by the $\hat{\mathcal{H}}$ operator. Since the Hamiltonian accounts for the presence of static disorder (e.g., randomly located defects), the time-dependent quantum dynamics of electronic wavepackets capture all multiple scattering phenomena including those accessible within the semi-classical transport regime (Bloch–Boltzmann), such as the elastic mean free path, or the localization length defining the Anderson insulator state. Inelastic scattering phenomena cannot be captured rigorously with such an approach, except in some indirect manner by coupling molecular dynamics with the time-dependent wavepacket approach.

4.4.5 Scaling Theory of Localization

The scaling theory of localization in disordered systems was developed in the early 1980s, initiated earlier by P. W. Anderson and further consolidated by Abrahams et al. (1979), who established comprehensive foundations of transport theory in disordered systems. Theoretical predictions have been confirmed by decades of experimental work. In one and two dimensions, any metallic system is predicted to be continuously driven to an (Anderson) insulating state as temperature decays to zero, and all states are localized at zero temperature. From a general perspective, the conductance of a system can be viewed as the sum ($\mathcal{P}_{P\to Q}$) over all probability amplitudes of propagating trajectories starting from one location P and going to another one Q in real space, or more explicitly

$$G = \frac{2e^2}{h}\mathcal{P}_{P\to Q}, \tag{4.89}$$

$$\mathcal{P}_{P\to Q} = \sum_i |\mathcal{A}_i|^2 + \sum_{i\neq j}\mathcal{A}_i\mathcal{A}_j e^{i(\alpha_i-\alpha_j)}, \tag{4.90}$$

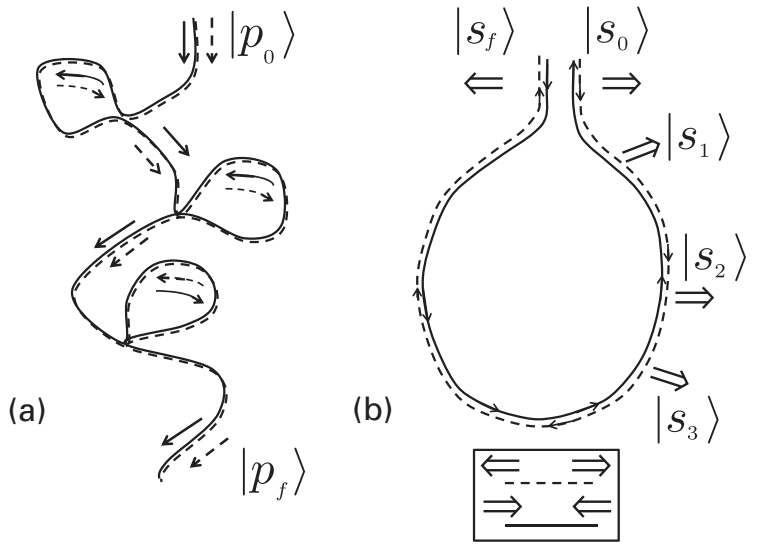

Figure 4.6 (a) Two clockwise and counterclockwise scattering trajectories which interfere constructively at various locations in real space where paths cross again. (b) Zoom-in of one particular loop where in addition to momentum shift upon scattering off impurities, adiabatic rotation of spin degree of freedom (conveyed by a weak spin–orbit scattering) is also pinpointed by arrows (two for up spin and down spin) on both trajectories.

defining $|\mathcal{A}_i|e^{i\alpha_i}$ as the probability amplitude of trajectory i. The conductance for a disordered system is obtained by averaging over an ensemble of random configurations, which suppresses almost all interfering terms, simplifying Eq. (4.90) to the sum of probabilities of individual trajectories, as expected from a classical calculation, $\langle G\rangle_{\text{dis.}} = \frac{2e^2}{h}\sum_i |\mathcal{A}_i|^2$.

This is, however, not completely correct since there exists a class of scattering trajectories which contain geometrical loops returning to an initial point in real space (illustrated in Fig. 4.6(a)). In the presence of time-reversal symmetry, the probability amplitude associated with the closed trajectory ($\mathcal{C}_+$) moving in clockwise along the loop turns out to interfere constructively with the one ($\mathcal{C}_-$) topologically identical, but moving counterclockwise (illustrated in Fig. 4.6(b)). Indeed, if we denote $\alpha_+ = \oint_{\mathcal{C}_+} \mathbf{p}\cdot d\mathbf{r}$, it is clear that $\alpha_- = \alpha_+$.

Accordingly, the quantum interferences driven by the contribution of all such families of trajectories are not canceled by disorder averaging and eventually enhance the probability of return to some origin, $\mathcal{P}_{O\to O} = 4|\mathcal{A}_O|^2$ (being twice the classical result in the absence of interferences ($|\mathcal{A}_O|^2 + |\mathcal{A}_O|^2$)). Such a contribution of quantum interferences which yields increased quantum resistance is also known as the Cooperon contribution (see Appendix C).

This weak localization phenomenon was first theoretically described in a seminal paper by Altshuler et al. (1985). An interesting point is that by applying an external

magnetic field, this interference effect is actually tunable by extra phase factors related to the vector potential. Indeed, since $\mathbf{p} \to \mathbf{p} + \frac{e}{c}\mathbf{A}$, the phase factors along clockwise and counterclockwise trajectories have a sign difference, $\alpha_\pm = \pm\frac{e}{\hbar}\oint \mathbf{A}\cdot d\mathbf{r}$. The total probability of return to some origin is then modified as (defining $\phi_0 = h/e$, the magnetic flux quantum)

$$|\mathcal{A}_0|^2 \left|1 + \mathrm{e}^{\mathrm{i}(\alpha_+ - \alpha_-)}\right|^2 = 2\,|\mathcal{A}_0|^2 \left(1 + \cos\frac{2\pi\varphi}{\phi_0/2}\right) \leq 4\,|\mathcal{A}_0|^2\,, \tag{4.91}$$

which means that the Cooperon contribution will always be reduced compared to its zero-field value, resulting in a resistance decrease upon switching on the field (negative magnetoresistance) (Bergman 1984). The quantum (Cooperon) correction $\delta\sigma(L)$ can be actually derived as a perturbative correction of the semiclassical result $\sigma(L) = \sigma_{\mathrm{sc}} + \delta\sigma(L)$ (see Appendix C), and rewritten in real space as

$$\delta\sigma(L) = -\frac{2e^2 D}{\pi\hbar\Omega}\int_0^\infty dt\mathcal{Z}(t)\left(\mathrm{e}^{-t/\tau_\varphi} - \mathrm{e}^{-t/\tau_{\mathrm{el}}}\right), \tag{4.92}$$

with $\mathcal{Z}(t) = \int d^d r P(\mathbf{r}, \mathbf{r}, t)$, the space integral of the total probability of returning to some origin, which obeys a diffusion law, of which a solution is $P(\mathbf{r}, \mathbf{r}, t) = 1/(4\pi Dt)^{d/2}$ (in D dimensions). In the integral, the factor $(\mathrm{e}^{-t/\tau_\varphi} - \mathrm{e}^{-t/\tau_{\mathrm{el}}})$ restricts the size of the loops, which contribute to interferences. Indeed, since trajectories develop in the diffusive regime ($t \geq \tau_{\mathrm{el}}$, τ_{el} is the elastic scattering time), and within the coherent regime ($t \leq \tau_\varphi$, with τ_φ the coherent time), all trajectories accomplished in a timescale shorter than τ_{el} and longer than τ_φ do not contribute to the total interference. In two dimensions, it is found that $\delta\sigma(L) = -(2e^2/\pi h)\ln(L/\ell_{\mathrm{el}})$ (Lee & Ramakrishnan 1985). The transition to the insulating state is continuous and reached when the quantum correction is of the same order as the semiclassical conductivity, that is, when $\Delta\sigma(L = \xi) \simeq \sigma_{\mathrm{sc}}$. This simple criterion allows us to establish a universal relationship (Thouless, 1973) between the two transport length scales of both (metallic and insulating) regimes, as $\xi = \ell_{\mathrm{el}}\exp(\pi\sigma_{\mathrm{sc}}/G_0)$ (Lee & Ramakrishnan 1985).

Spin/Pseudospin Effect on the Cooperon

It turns out that the presence of additional degrees of freedom such as the spin (or pseudospin in graphene) brings new features in the interference pattern. This was first theoretically established by Hikami et al. (1980) and then confirmed experimentally (Bergman 1984) on thin metallic film functionalized with deposited magnetic atoms. It is usually assumed that if $|s\rangle$ is the initial spin state, it can generally be rewritten as a superposition of the spin up $|\Uparrow\rangle$ and spin down $|\Downarrow\rangle$ states. In principle, there exist two main possibilities of how the spin orientation can be changed on the scattering path in the presence of spin–orbit coupling (defined by a Hamiltonian $\mathcal{H}_{\mathrm{so}}$). The first mechanism initially derived for metals, and known as the Elliot–Yafet mechanism, assumes that the presence of spin–orbit coupling results in a spin rotation each time the electron is scattered at the impurities. In contrast, the Dyakonov–Perel mechanism describes spin precession while the electron propagates between the scattering centers. The origin of

the spin precession has been generally described in terms of lack of inversion symmetry (i.e., in zinc blende crystals) or of an asymmetric potential shape of the quantum well forming a 2D electron gas (the Rashba effect).

Regardless of the underlying mechanism, if an electron propagates along a closed loop, its spin orientation is changed. The modification of the spin orientation can be expressed by a rotation matrix U. For propagation along the loop in a forward (f) direction, the final state $|s_f\rangle$ can be expressed by $|s_f\rangle = U|s\rangle$, where U is the corresponding rotation matrix. For propagation along the loop in a backward directions (b), the final spin state is given by $|s_b\rangle = U^{-1}|s\rangle$. Here, use is made of the fact that the rotation matrix of the counterclockwise propagation is simply the inverse of U. For interference between the clockwise and counterclockwise electron waves, not only the spatial component is relevant but also the interference of the spin component: $\langle s_b|s_f\rangle = \langle s|U^2|s\rangle$, making use of the fact that U is a unitary matrix. Weak localization, and thus constructive interference, is recovered if the spin orientation is conserved in the case that U is the unit matrix. However, if the spin is rotated during electron propagation along a loop, in general no constructive interference can be expected. Moreover, for each loop, a different interference will be expected. Interestingly, averaging over all possible trajectories even leads to a reversal of the weak localization effect. The generalization of the Cooperon factor in the presence of spin–orbit coupling has been demonstrated to be as illustrated in Fig. 4.6(b) (Chakravarty & Schmid 1986):

$$\delta\sigma = -\frac{2e^2D}{\pi\hbar\Omega}\int_0^\infty dt\mathcal{Z}(t)\langle\mathcal{Q}_{\rm so}(t)\rangle(\mathrm{e}^{-t/\tau_\varphi} - \mathrm{e}^{-t/\tau}). \tag{4.93}$$

The amplitude terms get extra phase factors related to the spin rotation, which accumulates along the scattering trajectory as $|s_{n+1}\rangle = \mathrm{e}^{-\mathrm{i}\Delta\theta S_z/\hbar}|s_n\rangle$, assuming that $\Delta\theta$ is some finite rotation angle while $|s_n\rangle$ denotes the spin state along the trajectory and $S_z = \frac{\hbar}{2}\sigma_z$. Then along the full trajectory the total spin-dependent accumulated phase factor can be described by introducing the time ordering operator $\mathcal{T}\mathcal{R}_t = \mathcal{T}\mathrm{e}^{-\frac{\mathrm{i}}{\hbar}\int_0^t\mathcal{H}_{\rm so}dt}$, with $\mathcal{H}_{\rm so} = \frac{\hbar}{4m^2c^2}\sigma\cdot(\nabla V(\mathbf{r})\times\mathbf{p})$, the spin–orbit component of the total Hamiltonian, $\boldsymbol{\sigma} = (\sigma_x, \sigma_y, \sigma_z)$ with Pauli matrices. The additional term entering into the Cooperon contribution is actually

$$\langle\mathcal{Q}_{\rm so}(t)\rangle = \sum_{\pm}\langle s_0|\mathcal{R}^\dagger_{-t}|s_f\rangle\langle s_f|\mathcal{R}_t|s_0\rangle. \tag{4.94}$$

In Fig. 4.6, clockwise and counterclockwise trajectories returning to some origin are shown together with some schematics of the adiabatic rotation of spin degree of freedom (assuming a weak spin–orbit coupling). Up and down spin are adiabatically rotated along the path yielding a $\pm\pi$ extra phase. The total Berry phase adds up to 2π, which yields sign reversal of the Cooperon contribution evidenced by the extra factor $\langle\mathcal{Q}_{\rm so}(t)\rangle = -1/2$ (see Chakravarty & Schmid 1986). In two dimensions and in the absence of magnetic field, the weak antilocalization correction to the conductivity can be generally recast as

$$\delta\sigma(L,\ell_e) = +\frac{2e^2}{\pi h}\ln\left(\frac{L}{\ell_{\rm el}}\right), \tag{4.95}$$

and the Kubo (quantum) conductivity can be rewritten as $\sigma = \sigma_{\rm BB} + |\frac{2e^2}{\pi h}\ln(\frac{L}{\ell_{\rm el}})|$, which means that the conductivity is increased, with respect to its semiclassical value, by the quantum interference contribution.

4.5 Quantum Transport beyond the Fully Coherent or Decoherent Limits

Beyond fully coherent or decoherent transport, the intermediate regime where decoherence partially suppresses quantum effects is also of high relevance. Such an intermediate regime is out of reach of the technical tools presented so far, and innovative theoretical approaches are crucially needed. A detailed presentation of new ideas and emerging methods to tackle such a problem is beyond the scope of this book, but a brief discussion and useful references are provided for interested readers.

The key question is how to model decoherent effects by keeping a simple one-body description. An early insight into this issue was given by Büttiker (1988a), who proposed that decoherent effects could be simulated by the action of an imaginary voltmeter attached to the sample; see the scheme in Fig. 4.7. The electrons that get absorbed by the voltmeter are reinjected so as to keep the zero-current condition on the imaginary electrode. Since no phase memory is retained between the incoming and reinjected electrons, phase coherence is steadily lost. This appealing picture has been used in many situations and has the advantage that it can be readily incorporated within Landauer's formalism.

For the simplest case of a single resonant level E_0 coupled to leads through escape rates Γ_L, Γ_R and a voltmeter through Γ_ϕ, a simple calculation shows that the effective transmission probability entering the Landauer conductance is

$$\widetilde{T}_{R,L}(\varepsilon) = \frac{\Gamma_R\,\Gamma_L}{(\varepsilon - E_0)^2 + (\Gamma_L + \Gamma_R + \Gamma_\phi)^2}\left\{1 + \frac{\Gamma_\phi}{\Gamma_L + \Gamma_R}\right\}. \tag{4.96}$$

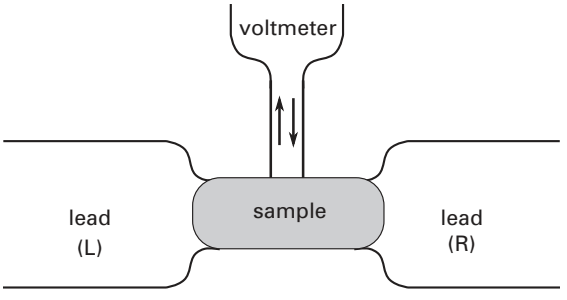

Figure 4.7 Scheme of Büttiker's imaginary voltage probe model for decoherence: decoherence can be modeled by the action of a voltmeter whose effect is to randomize the phase of the carriers. Each carrier entering the voltmeter is reinjected to keep the current balance but without a phase correlation, thereby randomizing the electronic phase.

Therefore, we can see that the conductance is the sum of a coherent term, where electrons do not suffer from any phase-breaking event, plus a decoherent term (second term in the curly brackets of the previous equation). Note that even the first term, which one would associate with the coherent component, is modified by the decoherent processes that change the escape rates in the denominator.

An important question at this point is whether this scheme can be implemented within a Hamiltonian model. D'Amato and Pastawski (1990) proposed a tight-binding model where the imaginary probes were included through complex self-energies with a self-consistent chemical potential adjusted in order to fulfill the voltmeter condition. Further generalizations were also presented in the study by Pastawski (1991). This technique has been further used in a variety of systems (Maassen et al. 2009; Nozaki et al. 2008) where the input values can be modeled so as to represent an effective decoherence rate from acoustic phonons or other sources.

4.6 Further Reading and Problems

- A general textbook on transport concepts in mesoscopic physics is provided by Datta (1995).
- For a very nice discussion on the role of symmetries in transport, see Büttiker (1988b).
- For a review on shot noise beyond the brief discussion given in Section 4.2, see Blanter and Büttiker (2000).
- On decoherence, the loss of interference, and the quantum-classical transition, we recommend Stern et al. (1990) and Zurek (2003).

Problems

4.1 *Landauer conductance of pristine carbon-based materials.*[6] In this computational exercise, you are encouraged to implement a calculation of the conductance for carbon nanotubes and graphene nanoribbons, using the Landauer formula introduced in Section 4.3.

(a) Consider a simple system where an infinite CNT or GNR (modeled through a tight-binding Hamiltonian) is divided into three regions: the left and right will take the role of leads and the central one will be the sample where you may change the site energies to emulate a bias voltage.
Hint: In the process, you may take advantage of the details provided in Appendix C for calculation of the self-energies due to the leads and the Green's functions of the central region. You may use the sample codes provided in our website as well as the datasets available for different systems.

(b) As a byproduct, you should also compute the local and total density of states for different systems and rationalize it.

[6] Problems 4.1 and 4.3 may also be solved after reading Chapter 5.

4.2 *Shot noise and exchange interference effects.* For a two terminal conductor, prove that the zero-frequency noise in the independent particle approximation is given by Eq. (4.3). Convince yourself that it cannot be written independently of the chosen basis in terms of transmission and reflection probabilities, as is the case with the conductance. This shows that the noise depends critically on the interference among the carriers from different channels and could therefore serve to probe it. It is also predictable for the shot noise to be particularly sensitive to interaction effects.

4.3 *Conductance through carbon-based materials using the Kubo formula.*

(a) Let us reconsider the previous exercise, but now using the Kubo formula introduced in Section 4.4.4. To do so, take advantage of the recursion methods introduced in Appendix D. You may use the sample codes provided in our website.

(b) For almost the same cost, you can compute the local and total density of states.

** Additional exercises and solutions are available at our website.

5 Klein Tunneling and Ballistic Transport in Graphene and Related Materials

In this chapter, we start with a presentation of the so-called Klein tunneling mechanism, which is one of the most striking properties of graphene. Later, we give an overview of ballistic transport both in graphene and related materials (carbon nanotubes and graphene nanoribbons). After presenting a simple real-space mode-decomposition scheme, which can be exploited to obtain analytical results or to boost numerical calculations, we discuss Fabry–Pérot interference, contact effects, and the minimum conductivity in the two-dimensional (2D) limit.

5.1 The Klein Tunneling Mechanism

The Klein tunneling mechanism was first reported in the context of quantum electrodynamics. In 1929, physicist Oskar Klein (1929) found a surprising result when solving the propagation of Dirac electrons through a single potential barrier. In nonrelativistic quantum mechanics, incident electrons tunnel a short distance through the barrier as evanescent waves, with exponential damping with the barrier depth. In sharp contrast, if the potential barrier is of the order of the electron mass, $eV \sim mc^2$, electrons propagate as antiparticles whose inverted energy–momentum dispersion relation allows them to move freely through the barrier. This unimpeded penetration of relativistic particles through high and wide potential barriers has been one of the most counterintuitive consequences of quantum electrodynamics, but despite its interest for particle, nuclear, and astrophysics, a direct test of the *Klein tunnel effect* using relativistic particles still remains out of reach for high-energy physics experiments.[1]

In 1998, Ando, Nakanishi, and Saito deduced a full suppression of backscattering in metallic carbon nanotubes for long-range disorder, as a consequence of Berry's phase and electron–hole symmetry (Ando et al. 1998). In 2006, Katsnelson, Novoselov, and Geim demonstrated that massless Dirac fermions in graphene offer a unique test of Klein's *gedanken* experiment (Klein 1929). This remarkable prediction was then

[1] We emphasize that despite its name, the Klein tunnel effect does not involve tunneling as usually meant in quantum mechanics because it does not rely on evanescent waves. It is the roles of pseudospin conservation and electron–hole symmetry that are crucial in this case.

confirmed by a series of finely tuned experiments (Stander et al. 2009; Young & Kim 2009, 2011). A collimating effect on ballistically transmitted carriers was revealed through analysis of the conductance oscillations (and phase shift in the conductance fringes at low magnetic fields) in a graphene-based p–n junction, providing compelling evidence of the perfect transmission of carriers normally incident on the junctions (Cheianov & Fal'ko 2006; Shytov et al. 2008). In the following, we provide a complete derivation of the analytical calculation for both a single layer and bilayers.

5.1.1 Klein Tunneling through Monolayer Graphene with a Single (Impurity) Potential Barrier

Let us consider a system such as the one represented in Fig. 5.1: two normal regions with a potential barrier in between. To obtain the transmission probability, we follow a simple scheme and solve for the wavefunctions in each of the regions and then match them.

The 2D Wavefunction of an Electron in Graphene

As discussed in Section 2.2.2, the graphene electronic structure at low energy can be obtained from the two-component effective equation $\mathcal{H}\Psi = E\Psi$, where

$$\mathcal{H} = \hbar v_F \begin{pmatrix} 0 & \hat{k}_x - \mathrm{i}\hat{k}_y \\ \hat{k}_x + \mathrm{i}\hat{k}_y & 0 \end{pmatrix} = \hbar v_F (\sigma_x \hat{k}_x + \sigma_y \hat{k}_y), \tag{5.1}$$

where σ_x, σ_y are Pauli spin matrices and $\hat{\mathbf{k}} = (\hat{k}_x, \hat{k}_y) = -\mathrm{i}\nabla$ is a wavevector operator. In the previous equation, we have dropped the subindex K_+ in the Hamiltonian; the

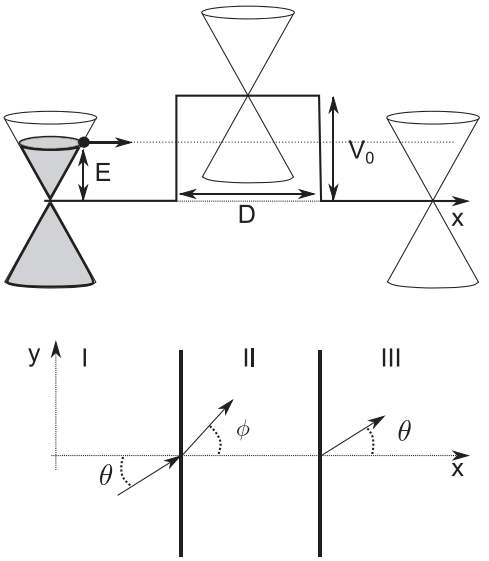

Figure 5.1 Scattering of Dirac electron by a square potential.

calculations for the other valley proceed in an analogous way. The 2D spinor wavefunction is written as

$$\Psi_{s\mathbf{k}}(\mathbf{r}) = \begin{pmatrix} \Psi_1 \\ \Psi_2 \end{pmatrix} \exp(\mathrm{i}\mathbf{k}\mathbf{r}), \tag{5.2}$$

Substituting Eq. (5.2) into 5.1 yields

$$\hbar v_F \begin{pmatrix} 0 & k_x - \mathrm{i}k_y \\ k_x + \mathrm{i}k_y & 0 \end{pmatrix} \begin{pmatrix} \Psi_1 \\ \Psi_2 \end{pmatrix} = E \begin{pmatrix} \Psi_1 \\ \Psi_2 \end{pmatrix}. \tag{5.3}$$

To solve this equation, we use the band dispersion

$$E_{s\mathbf{k}} = s\hbar v_F |k|, \tag{5.4}$$

where $s = +1$ and -1 denote the conduction band and valence bands, respectively. By substituting into Eq. (5.3), we obtain

$$\Psi_2 = \frac{k_x + \mathrm{i}k_y}{s|k|} \Psi_1 = s\mathrm{e}^{\mathrm{i}\phi} \Psi_1, \tag{5.5}$$

with

$$k_x = |k| \cos\phi, \qquad k_y = |k| \sin\phi, \tag{5.6}$$

so the corresponding momentum space pseudospinor eigenfunction becomes

$$\Psi_{s,\mathbf{k}} = \begin{pmatrix} \Psi_1 \\ \Psi_2 \end{pmatrix} = \begin{pmatrix} 1 \\ s\mathrm{e}^{\mathrm{i}\phi} \end{pmatrix} \Psi_1, \tag{5.7}$$

and the wavefunction is

$$\Psi(x,y) = \begin{pmatrix} \Psi_1(x,y) \\ \Psi_2(x,y) \end{pmatrix} = \begin{pmatrix} 1 \\ s\mathrm{e}^{\mathrm{i}\phi} \end{pmatrix} \Psi_1 \mathrm{e}^{\mathrm{i}k_x x + \mathrm{i}k_y y}. \tag{5.8}$$

Using the normalization condition of the wavefunction, we finally get $\Psi_1 = \frac{1}{\sqrt{2}L}$, where L^2 is the area of system; this is

$$\Psi(x,y) = \frac{1}{\sqrt{2}L} \begin{pmatrix} 1 \\ s\mathrm{e}^{\mathrm{i}\phi} \end{pmatrix} \mathrm{e}^{\mathrm{i}k_x x + \mathrm{i}k_y y}. \tag{5.9}$$

Now that we have the wavefunctions for the different regions, let us proceed by appropriately matching them.

Wavefunction Matching

Let us calculate the wavefunction in different regions of the Klein tunneling model and then evaluate the transmission probability. We consider a potential barrier that has a rectangular shape with width D and is infinite along the y axis,

$$V(x) = \begin{cases} V_0 & \text{in region II,} \\ 0 & \text{in regions I, III.} \end{cases} \tag{5.10}$$

Wavefunctions in Different Regions

We assume that the incident electron wave propagates at an angle ϕ in region I and then diffracts into region II with angle θ with respect to the x axis. As we showed above, the wavefunction in region I is given by Eq. (5.9). Because the potential does not change along the y axis, the y component of momentum is conservative,

$$k_y^I = k_y^{II} = k_y^{III} = k_y. \tag{5.11}$$

Furthermore, the potentials in regions I and III are the same so $k^I = k^{III}$, so that the electron wave in region III also propagates at an angle θ with respect to the x axis and

$$k_x^I = k_x^{III} = k_x. \tag{5.12}$$

Similar to Eq. (5.3), the Schrödinger equation in region II becomes

$$\begin{pmatrix} V_0 & \hbar v_F (k_x^{II} - \mathrm{i}k_y) \\ \hbar v_F (k_x^{II} + \mathrm{i}k_y) & V_0 \end{pmatrix} \begin{pmatrix} \Psi_1^{II} \\ \Psi_2^{II} \end{pmatrix} = E \begin{pmatrix} \Psi_1^{II} \\ \Psi_2^{II} \end{pmatrix}. \tag{5.13}$$

From this, we deduce

$$k_x^{II} = \sqrt{(E - V_0)^2 / (\hbar v_F)^2 - k_y^2}, \tag{5.14}$$

$$\tan\theta = \frac{k_y}{\sqrt{(E - V_0)^2 / (\hbar v_F)^2 - k_y^2}}. \tag{5.15}$$

The wavefunction in the different regions can be written in terms of incident and reflected waves:

$$\Psi^I(x,y) = \frac{1}{\sqrt{2}L} \left\{ \begin{pmatrix} 1 \\ s\mathrm{e}^{\mathrm{i}\phi} \end{pmatrix} \mathrm{e}^{\mathrm{i}(k_x x + k_y y)} + r \begin{pmatrix} 1 \\ s\mathrm{e}^{\mathrm{i}(\pi - \phi)} \end{pmatrix} \mathrm{e}^{\mathrm{i}(-k_x x + k_y y)} \right\}, \tag{5.16}$$

$$\Psi^{II}(x,y) = \frac{1}{\sqrt{2}L} \left\{ a \begin{pmatrix} 1 \\ s'\mathrm{e}^{\mathrm{i}\theta} \end{pmatrix} \mathrm{e}^{\mathrm{i}(k_x^{II} x + k_y y)} + b \begin{pmatrix} 1 \\ s'\mathrm{e}^{\mathrm{i}(\pi - \theta)} \end{pmatrix} \mathrm{e}^{\mathrm{i}(-k_x^{II} x + k_y y)} \right\}, \tag{5.17}$$

$$\Psi^{III}(x,y) = \frac{t}{\sqrt{2}L} \begin{pmatrix} 1 \\ s\mathrm{e}^{\mathrm{i}\phi} \end{pmatrix} \mathrm{e}^{\mathrm{i}(k_x x + k_y y)}, \tag{5.18}$$

where $s = \mathrm{sgn}(E)$ and $s' = \mathrm{sgn}(E - V_0)$. This provides the whole set of wavefunctions for the different regions of the scattering problem.

The Transmission Probability and Klein Tunneling

The coefficients r, a, b, t are obtained by requiring continuity of the wavefunction,

$$\Psi^{I}(0,y) = \Psi^{II}(0,y), \tag{5.19}$$

$$\Psi^{II}(D,y) = \Psi^{III}(D,y). \tag{5.20}$$

Substituting the wavefunctions by their generic forms, we get for the first equation

$$\begin{cases} 1 + r = a + b, \\ s(\mathrm{e}^{\mathrm{i}\phi} + r\mathrm{e}^{\mathrm{i}(\pi-\phi)}) = s'(a\mathrm{e}^{\mathrm{i}\theta} + b\mathrm{e}^{\mathrm{i}(\pi-\theta)}). \end{cases} \tag{5.21}$$

Similarly, for the second, we obtain

$$\begin{cases} a\mathrm{e}^{\mathrm{i}q_xD} + b\mathrm{e}^{-\mathrm{i}q_xD} = t\mathrm{e}^{\mathrm{i}k_xD}, \\ s'(a\mathrm{e}^{\mathrm{i}(\theta+q_xD)} + b\mathrm{e}^{\mathrm{i}(\pi-\theta-q_xD)}) = ts\mathrm{e}^{\mathrm{i}(\phi+k_xD)}, \end{cases} \tag{5.22}$$

where $q_x = k_x^{II}$. From Eq. (5.21), we have

$$b = -\frac{s\mathrm{e}^{\mathrm{i}\phi} - s'\mathrm{e}^{\mathrm{i}\theta}}{s\mathrm{e}^{\mathrm{i}\phi} + s'\mathrm{e}^{-\mathrm{i}\theta}} a\mathrm{e}^{2\mathrm{i}q_xD}. \tag{5.23}$$

Substituting Eq. (5.23) into the first expression in Eq. (5.21), we obtain

$$a = \frac{s\mathrm{e}^{\mathrm{i}\phi} + s'\mathrm{e}^{-\mathrm{i}\theta}}{-2\mathrm{i}s\mathrm{e}^{\mathrm{i}\phi}\sin(q_xD) + 2s'\cos(\theta + q_xD)}(1+r)\mathrm{e}^{-\mathrm{i}q_xD}. \tag{5.24}$$

Using Eq. (5.23) and Eq. (5.24), we obtain

$$b = -\frac{s\mathrm{e}^{\mathrm{i}\phi} - s'\mathrm{e}^{\mathrm{i}\theta}}{-2\mathrm{i}s\mathrm{e}^{\mathrm{i}\phi}\sin(q_xD) + 2s'\cos(\theta + q_xD)}(1+r)\mathrm{e}^{\mathrm{i}q_xD}. \tag{5.25}$$

Substituting Eq. (5.24) and Eq. (5.25) into the second expression of Eq. (5.21), we finally find that

$$s(\mathrm{e}^{\mathrm{i}\phi} - r\mathrm{e}^{-\mathrm{i}\phi}) = \frac{(ss'\mathrm{e}^{\mathrm{i}(\phi+\theta)} + 1)\mathrm{e}^{-\mathrm{i}q_xD} + (ss'\mathrm{e}^{\mathrm{i}(\phi-\theta)} - 1)\mathrm{e}^{\mathrm{i}q_xD}}{-2\mathrm{i}s\mathrm{e}^{\mathrm{i}\phi}\sin(q_xD) + 2s'\cos(\theta + q_xD)}(1+r), \tag{5.26a}$$

$$\Leftrightarrow \qquad s(\mathrm{e}^{\mathrm{i}\phi} - r\mathrm{e}^{-\mathrm{i}\phi}) = \frac{2ss'\mathrm{e}^{\mathrm{i}\phi}\cos(\theta - q_xD) - 2\mathrm{i}\sin q_xD}{-2\mathrm{i}s\mathrm{e}^{\mathrm{i}\phi}\sin(q_xD) + 2s'\cos(\theta + q_xD)}(1+r), \tag{5.26b}$$

$$\Leftrightarrow \qquad r = \frac{\mathrm{i}\mathrm{e}^{\mathrm{i}\phi}\sin(q_xD)(\sin\phi - ss'\sin\theta)}{\sin(q_xD) - ss'\left[\sin\phi\sin\theta\sin(q_xD) - \mathrm{i}\cos\phi\cos\theta\cos(q_xD)\right]}. \tag{5.26c}$$

The transmission can then be obtained straightforwardly from $T(\phi) = tt^* = 1 - rr^* = 1 - R$:

$$T(\phi) = \frac{\cos^2\theta\cos^2\phi}{\cos^2(q_xD)\cos^2\theta\cos^2\phi + \sin^2(q_xD)(1 - ss'\sin\theta\sin\phi)^2}. \tag{5.27}$$

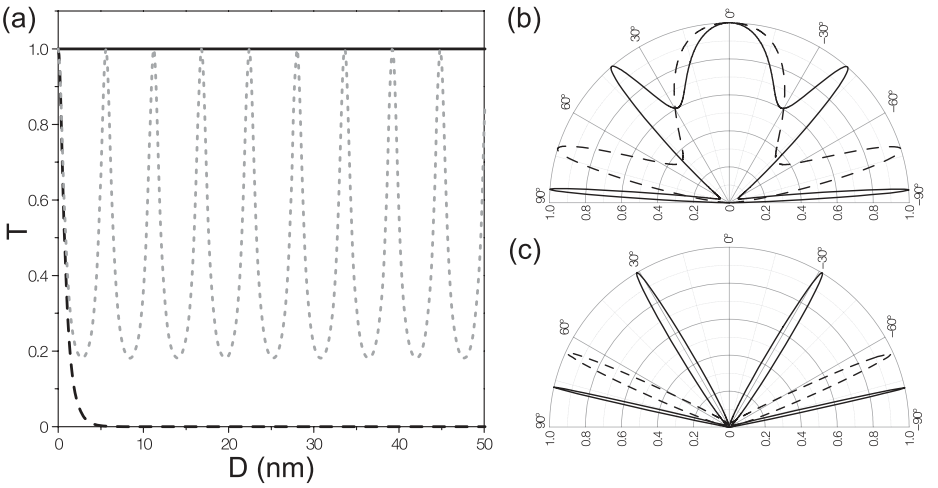

Figure 5.2 (a) Transmission probability $T(E)$ for normally incident electrons in single-layer and bilayer graphene (black solid and black dashed lines, respectively), and in a non-chiral zero-gap semiconductor (gray dotted line) as a function of width D of the tunnel barrier. In this plot the barrier for monolayer graphene is 450 meV and about 240 meV for the other two materials. $T(E)$ through a 100 nm-wide barrier as a function of the incident angle is shown for single-layer (b) and bilayer (c) graphene. In each of these plots, two curves are shown; they correspond to a Fermi energy of $\sim$ 80 (solid line) and 17 meV (dashed line), and $\lambda \sim 50$ nm. The barrier heights V_0 are 200 and 50 meV for the solid lines in (b) and (c), respectively, and 285 and 100 meV for the dashed lines in (b) and (c), respectively. (Adapted by permission from Macmillan Publishers Ltd: *Nature*, Katsnelson et al. 2006, copyright (2006))

In the limit $|V_0| \gg |E|$, the value of $\theta \to 0$ can be replaced in Eq. (5.27), which becomes

$$T(\phi) = \frac{\cos^2\phi}{\cos^2(q_x D)\cos^2\phi + \sin^2(q_x D)} = \frac{\cos^2\phi}{1 - \cos^2(q_x D)\sin^2\phi}. \tag{5.28}$$

Equation (5.28) means that under resonance conditions $q_x D = \pi N, N = 0, \pm 1, \ldots$, the barrier becomes totally transparent ($T = 1$). Additionally, the barrier always remains perfectly transparent for angles close to normal incidence, $\varphi = 0$ (see Fig. 5.2), which stands as a feature unique to massless Dirac fermions and is directly related to the Klein paradox in QED. It is important to note that this perfect transmission for normal incidence is not a resonance effect. Indeed, this perfect tunneling can be rationalized in terms of the conservation of pseudospin. In the absence of pseudospin-flip processes, an electron moving to the right can be scattered only to a right-moving electron state or left-moving hole state (see also the discussion in Section 2.2.2). The matching between directions of pseudospin for quasiparticles inside and outside the barrier results in perfect tunneling. In the strictly one-dimensional (1D) case, such perfect transmission of Dirac fermions has also been discussed in the context of electron transport in carbon nanotubes (see Section 6.1).

5.1.2 Klein Tunneling through Bilayer Graphene with a Single (Impurity) Potential Barrier

The 2D Wavefunction of an Electron in Bilayer Graphene

The Hamiltonian of an electron in bilayer graphene has the form

$$H = -\frac{\hbar^2}{2m}\begin{pmatrix} 0 & (\hat{k}_x - \mathrm{i}\hat{k}_y)^2 \\ (\hat{k}_x + \mathrm{i}\hat{k}_y)^2 & 0 \end{pmatrix}. \tag{5.29}$$

Similar to the 2D spinor wavefunction of single-layer graphene, the wavefunction of bilayer graphene in the ith region satisfies

$$-\frac{\hbar^2}{2m}\begin{pmatrix} 0 & (\hat{k}_x - \mathrm{i}\hat{k}_y)^2 \\ (\hat{k}_x + \mathrm{i}\hat{k}_y)^2 & 0 \end{pmatrix}\Psi^i_{s\mathbf{k}}(\mathbf{r}) = (E - V_i)\Psi^i_{s\mathbf{k}}(\mathbf{r}), \tag{5.30}$$

where the wavefunction has the following form (the electrons are free in the y direction and the momentum in the y direction is unchanged):

$$\begin{aligned}\Psi^i_{s\mathbf{k}}(\mathbf{r}) = \Bigg(& a_i \begin{pmatrix} \Psi^1_1 \\ \Psi^1_2 \end{pmatrix}_i \mathrm{e}^{\mathrm{i}k_{ix}x} + b_i \begin{pmatrix} \Psi^2_1 \\ \Psi^2_2 \end{pmatrix}_i \mathrm{e}^{-\mathrm{i}k_{ix}x} \\ & + c_i \begin{pmatrix} \Psi^3_1 \\ \Psi^3_2 \end{pmatrix}_i \mathrm{e}^{\kappa_{ix}x} + d_i \begin{pmatrix} \Psi^4_1 \\ \Psi^4_2 \end{pmatrix}_i \mathrm{e}^{-\kappa_{ix}x} \Bigg) \mathrm{e}^{\mathrm{i}k_y y}. \end{aligned} \tag{5.31}$$

Substituting such an expression for $\Psi^i_{s\mathbf{k}}(\mathbf{r})$ into Eq. (5.30), and following the same steps as for the monolayer case, we find that

$$\begin{pmatrix} \Psi^1_1 \\ \Psi^1_2 \end{pmatrix}_i = \begin{pmatrix} 1 \\ s_i \mathrm{e}^{2i\phi_i} \end{pmatrix} \Psi^1_{1i}, \tag{5.32a}$$

$$\begin{pmatrix} \Psi^2_1 \\ \Psi^2_2 \end{pmatrix}_i = \begin{pmatrix} 1 \\ s_i \mathrm{e}^{-2i\phi_i} \end{pmatrix} \Psi^2_{1i}, \tag{5.32b}$$

$$\begin{pmatrix} \Psi^3_1 \\ \Psi^3_2 \end{pmatrix}_i = \begin{pmatrix} 1 \\ -s_i h_i \end{pmatrix} \Psi^3_{1i}, \tag{5.32c}$$

$$\begin{pmatrix} \Psi^4_1 \\ \Psi^4_2 \end{pmatrix}_i = \begin{pmatrix} 1 \\ -s_i / h_i \end{pmatrix} \Psi^4_{1i}, \tag{5.32d}$$

where

$$\begin{aligned} & s_i = \mathrm{sgn}(V_i - E), \qquad \hbar k_{ix} = \sqrt{2m|E - V_i|}\cos\phi_i, \\ & \hbar k_y = \sqrt{2m|E - V_i|}\sin\phi_i = const, \\ & \kappa_{ix} = \sqrt{k_{ix}^2 + 2k_y^2}, \qquad h_i = \left(\sqrt{1 + \sin^2\phi_i} - \sin\phi_i\right)^2. \end{aligned}$$

The way to obtain the first two pseudospinors is the same as for single-layer graphene, whereas the two others can be derived as follows:

$$-\frac{\hbar^2}{2m}\begin{pmatrix}0 & (\hat{k}_x-\mathrm{i}\hat{k}_y)^2\\ (\hat{k}_x+\mathrm{i}\hat{k}_y)^2 & 0\end{pmatrix}\begin{pmatrix}\Psi_1^3\\ \Psi_2^3\end{pmatrix}_i \mathrm{e}^{\kappa_{ix}x+\mathrm{i}k_y y}=(E-V_i)\begin{pmatrix}\Psi_1^3\\ \Psi_2^3\end{pmatrix}_i \mathrm{e}^{\kappa_{ix}x+\mathrm{i}k_y y}, \tag{5.33a}$$

$$-\frac{\hbar^2}{2m}\begin{pmatrix}0 & (\hat{k}_x-\mathrm{i}\hat{k}_y)^2\\ (\hat{k}_x+\mathrm{i}\hat{k}_y)^2 & 0\end{pmatrix}\begin{pmatrix}\Psi_1^4\\ \Psi_2^4\end{pmatrix}_i \mathrm{e}^{-\kappa_{ix}x+\mathrm{i}k_y y}=(E-V_i)\begin{pmatrix}\Psi_1^4\\ \Psi_2^4\end{pmatrix}_i \mathrm{e}^{-\kappa_{ix}x+\mathrm{i}k_y y}. \tag{5.33b}$$

From this, we obtain

$$\begin{pmatrix}0 & (\kappa_{ix}+k_y)^2\\ (\kappa_{ix}-k_y)^2 & 0\end{pmatrix}\begin{pmatrix}\Psi_1^3\\ \Psi_2^3\end{pmatrix}_i=\frac{2m(E-V_i)}{\hbar^2}\begin{pmatrix}\Psi_1^3\\ \Psi_2^3\end{pmatrix}_i, \tag{5.34a}$$

$$\begin{pmatrix}0 & (\kappa_{ix}-k_y)^2\\ (\kappa_{ix}+k_y)^2 & 0\end{pmatrix}\begin{pmatrix}\Psi_1^4\\ \Psi_2^4\end{pmatrix}_i=\frac{2m(E-V_i)}{\hbar^2}\begin{pmatrix}\Psi_1^4\\ \Psi_2^4\end{pmatrix}_i, \tag{5.34b}$$

so we have the relations

$$\kappa_{ix}^2=k_y^2+\frac{2m|E-V_i|}{\hbar^2}=k_y^2+k_i^2=k_{ix}^2+2k_y^2, \tag{5.35a}$$

$$\Psi_{2i}^3=-s_i\frac{(\kappa_{ix}-k_y)^2}{k_i^2}\Psi_{1i}^3=-s_i h_i\Psi_{1i}^3, \tag{5.35b}$$

$$\Psi_{2i}^4=-s_i\frac{k_i^2}{(\kappa_{ix}-k_y)^2}\Psi_{1i}^4=-\frac{s_i}{h_i}\Psi_{1i}^4. \tag{5.35c}$$

Therefore, the wavefunction in the ith region is

$$\Psi_{s\mathbf{k}}^i(\mathbf{r})=\begin{pmatrix}\psi_1^i(x,y)\\ \psi_2^i(x,y)\end{pmatrix}, \tag{5.36}$$

where

$$\psi_1^i=\left(a_i\mathrm{e}^{\mathrm{i}k_{ix}x}+b_i\mathrm{e}^{-\mathrm{i}k_{ix}x}+c_i\mathrm{e}^{\kappa_{ix}x}+d_i\mathrm{e}^{-\kappa_{ix}x}\right)\mathrm{e}^{ik_y y},$$

$$\psi_2^i=s_i\left(a_i\mathrm{e}^{\mathrm{i}(k_{ix}x+2\phi_i)}+b_i\mathrm{e}^{-\mathrm{i}(k_{ix}x+2\phi_i)}-c_i h_i\mathrm{e}^{\kappa_{ix}x}-\frac{d_i}{h_i}\mathrm{e}^{-\kappa_{ix}x}\right)\mathrm{e}^{ik_y y}.$$

This gives the general form of the wavefunctions for the bilayer case.

Transmission Probability and Chiral Tunneling in Bilayer Graphene

Equation (5.36) gives the form of wavefunctions in the different regions. To avoid divergence of the wavefunction as $x\to-\infty$ ($x\to+\infty$), $d_1=0$ ($c_3=0$) in region I (III). There is no reflected wave in region III so $b_3=0$. Using the continuity

conditions for both components of the wavefunction and their derivatives, for the case of an electron beam that is incident normally ($\phi = 0$) and low barrier $V_0 < E$:

$$\begin{aligned}
a_1 + b_1 + c_1 &= a_2 + b_2 + c_2 + d_2,\\
a_1 + b_1 - c_1 &= a_2 + b_2 - c_2 - d_2,\\
k_1(\mathrm{i}a_1 - \mathrm{i}b_1 + c_1) &= k_2(\mathrm{i}a_2 - \mathrm{i}b_2 + c_2 - d_2),\\
k_1(\mathrm{i}a_1 - \mathrm{i}b_1 - c_1) &= k_2(\mathrm{i}a_2 - \mathrm{i}b_2 - c_2 + d_2),\\
a_2\mathrm{e}^{\mathrm{i}k_2D} + b_2\mathrm{e}^{-\mathrm{i}k_2D} + c_2\mathrm{e}^{k_2D} + d_2\mathrm{e}^{-k_2D} &= a_3\mathrm{e}^{\mathrm{i}k_1D} + d_3\mathrm{e}^{-k_1D},\\
a_2\mathrm{e}^{\mathrm{i}k_2D} + b_2\mathrm{e}^{-\mathrm{i}k_2D} - c_2\mathrm{e}^{k_2D} - d_2\mathrm{e}^{-k_2D} &= a_3\mathrm{e}^{\mathrm{i}k_1D} - d_3\mathrm{e}^{-k_1D},\\
k_2(\mathrm{i}a_2\mathrm{e}^{\mathrm{i}k_2D} - \mathrm{i}b_2\mathrm{e}^{-\mathrm{i}k_2D} + c_2\mathrm{e}^{k_2D} - d_2\mathrm{e}^{-k_2D}) &= k_1(\mathrm{i}a_3\mathrm{e}^{\mathrm{i}k_1D} - d_3\mathrm{e}^{-k_1D}),\\
k_2(\mathrm{i}a_2\mathrm{e}^{\mathrm{i}k_2D} - \mathrm{i}b_2\mathrm{e}^{-\mathrm{i}k_2D} - c_2\mathrm{e}^{k_2D} + d_2\mathrm{e}^{-k_2D}) &= k_1(\mathrm{i}a_3\mathrm{e}^{\mathrm{i}k_1D} + d_3\mathrm{e}^{-k_1D}),
\end{aligned} \tag{5.37}$$

where $k_1 = k_{1x} = \kappa_{1x} = \frac{\sqrt{2mE}}{\hbar}$ and $k_2 = k_{2x} = \kappa_{2x} = \frac{\sqrt{2m|E-V_0|}}{\hbar}$. From these equations, we have $\psi_1 = -\psi_2$ both inside and outside the barrier. For the case of an electron beam that is incident normally ($\phi = 0$) and high barrier $V_0 > E$, we have equations similar to Eq. (5.37), but with $s_2 = -s_1 = -s_3 = -1$ from which we obtain the transmission coefficient t:

$$t = \frac{a_3}{a_1} = \frac{4\mathrm{i}k_1k_2}{(k_2 + \mathrm{i}k_1)^2\mathrm{e}^{-k_2D} - (k_2 - \mathrm{i}k_1)^2\mathrm{e}^{k_2D}}. \tag{5.38}$$

The transmission probability T is given by

$$T = |t|^2 = \frac{4k_1^2k_2^2}{(k_1^2 + k_2^2)^2\sinh^2(k_2D) + 4k_1^2k_2^2}. \tag{5.39}$$

Therefore, T in this case decays exponentially with the height and width of the barrier. This is in striking contrast with monolayer graphene where transmission is unity. For bilayer graphene, pseudospin conservation does not forbid backscattering. The results for both cases are shown in Fig. 5.2, where they are also compared with those for a non-chiral zero-gap semiconductor.

5.2 Ballistic Transport in Carbon Nanotubes and Graphene

One of the main problems hindering molecular electronics has been the poor quality of the contacts between the molecular sample and the metallic electrodes. This leads to low conductance values and usually takes us out of the coherent regime analyzed in this section (see Section 4.1.2). The outstanding quality of the contacts achieved for carbon nanotubes and graphene devices changed this picture radically allowing, for example, for the observation of ballistic transport and Fabry–Pérot interference

(Herrmann et al. 2007; Kim et al. 2007; Liang et al. 2001; Wu et al. 2007; Wu et al. 2012), which is addressed in the following pages.

5.2.1 Ballistic Motion and Conductance Quantization

The intrinsic electronic transport along the nanotube axis is perfectly ballistic if the measured conductance is quantized (and L-independent), only varying with the number of available conducting channels at the considered energy ($N_\perp(E)$). In that regime, $G(E) = 2e^2/h \times N_\perp(E)$ (including spin degeneracy). The quantized conductance profile for a given nanotube can actually be directly deduced from the band structure features, by counting the number of channels at a given energy. A metallic armchair nanotube presents only two quantum channels at the charge neutrality point (CNP), resulting in $G(E_F) = 2G_0$. At higher energies, the conductance increases as more channels become available for transport. Figure 5.3 shows the electronic bands and conductance of a clean (5, 5) metallic tube.

This situation has been experimentally measured for very clean metallic nanotubes with ohmic contacts between the SWNT and metallic (palladium) voltage probes (Javey et al., 2003, 2004). Figure 5.4 (left panel) shows the $I_{DS}(V_{DS})$ for metallic single-walled carbon nanotubes (SWNTs) (Pd Ohmic contacts) with lengths ranging from 700 nm down to 55 nm. The low-bias regime is clearly linear, and makes it possible to extract a corresponding conductance $G = dI/dV$, which turns out to be very close to the maximum quantized value $4e^2/h$ and (as expected) shows almost no temperature dependence (Fig. 5.4 (right panel)). Using semiclassical (Bloch–Boltzmann) transport simulations, mean free path acoustic phonon scattering is estimated to be in the order of 300 nm, whereas for optical phonon scattering, the inelastic length is estimated to be

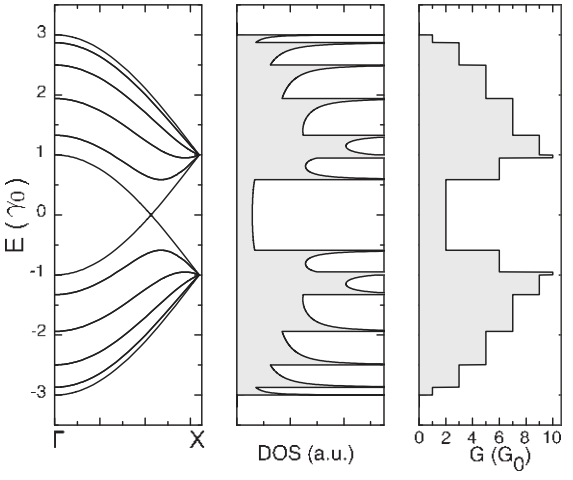

Figure 5.3 Band structure (left), density of states (middle), and conductance (right) for a (5, 5) armchair nanotube.

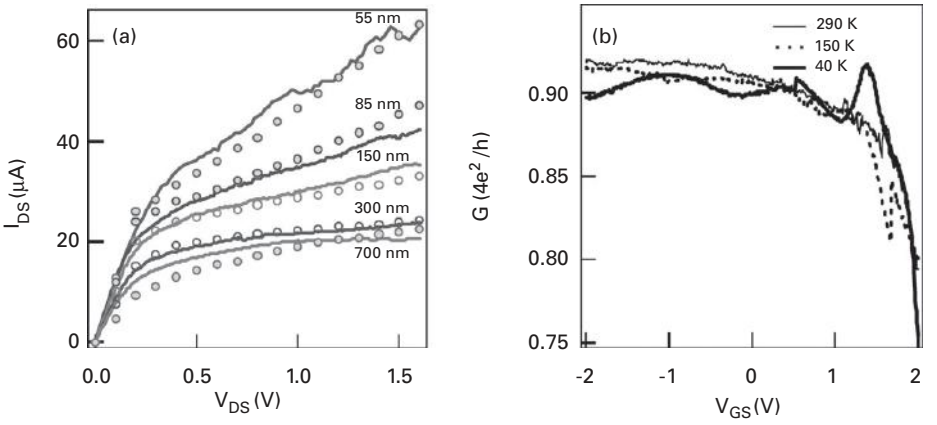

Figure 5.4 (a) Electrical properties of ohmically contacted metallic SWNTs of various lengths (diameters $d \in [2, 2.5]$ nm, oxide thickness is 10 nm). Solid lines are experimental $I_{DS} - V_{DS}$ curves, while symbols are Monte Carlo simulations. (b) Conductance versus gate voltage recorded (under a low bias of $V_{DS} \simeq 1$ mV) at 290, 150, and 40 K. (Adapted from Javey et al. 2004. Copyright (2004) by the American Physical Society. By courtesy of Hongjie Dai)

about 15 nm (see Section 6.1.1 for more details). Transport through very short (10 nm) nanotubes is free of significant acoustic and optical phonon scattering and thus ballistic and quasiballistic at the low- and high-bias voltage limits, respectively. High currents of up to 70 μA can flow ballistically through a short nanotube section in between Pd contacts (Javey et al. 2003, 2004).

These values are, however, the uppermost theoretical limits that can be experimentally accessible. In practical situations, lower values are found since quantum transmission is limited by interface symmetry mismatch, inducing Bragg-type backscattering. Additionally, topological and chemical disorders, as well as intershell coupling for multiwalled nanotubes, introduce intrinsic scattering along the tube, which also lowers the total transmission probability. Both effects will have an impact on the transmission through the different conducting channels or modes in the leads. If $T_n(E) \leq 1$ is the transmission probability through one of those channels at energy E, the conductance is given by $G(E) = G_0 \sum_{n=1,N_\perp} T_n(E)$ (Datta 1995).

To make the last statements more concrete, in the following subsection, we introduce a useful way of decomposing the system (be it a carbon nanotube or a graphene nanoribbon) into independent channels or modes, thereby giving a picture of what these conduction channels are.

5.2.2 Mode Decomposition in Real Space

Solving the Hamiltonian by *brute force* to obtain the transport/electronic properties of pristine carbon nanotubes or graphene (armchair edge) nanoribbons, even by using a decimation procedure, is computationally demanding and much physical insight might be lost. In the following, a simple procedure to break the Hamiltonian into independent

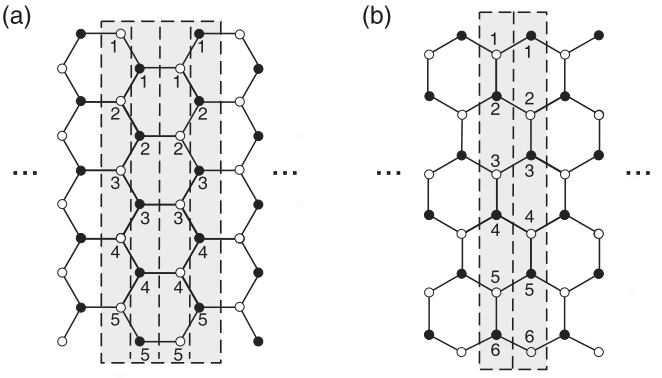

Figure 5.5 Representation of the atomic positions for different terminations of graphene nanoribbons: (a) armchair and (b) zigzag. The dashed boxes separate different layers of carbon atoms. Note that zigzag and armchair carbon nanotubes can be obtained, respectively, from (a) and (b) by imposing periodic boundary conditions along the vertical direction. In the case of armchair nanotubes, one has to additionally arrange for the number of atoms in each layer to be an even number.

building blocks is described. The trick is simple but tremendously powerful: a suitable unitary transformation performs the desired decomposition, which serves as a starting point for either more efficient computational codes or insightful analytical calculations. The following paragraphs follow previous works carried out for nanotubes (Mingo et al. 2001) as well as graphene ribbons (Rocha et al. 2010; Zhao & Guo 2009).

Figure 5.5 shows arrangements of carbon atoms for nanoribbons of armchair and zigzag edges. By adding a periodic boundary condition along the vertical direction, this represents as well the arrangement for the case of carbon nanotubes where curvature effects are neglected. In general, the Hamiltonian can be written in a block-matrix form where each block corresponds to the orbitals inside each layer (as depicted in Fig. 5.5) for a particular diameter/width of the nanotube/nanoribbon. The idea is to find a basis where all these block matrices have a diagonal form. As we see below, depending on the boundary conditions, this is sometimes possible thereby rendering a decomposition of the 2D lattice into several independent 1D lattices.

The nearest-neighbor π orbitals Hamiltonian is given by

$$\mathcal{H} = \begin{pmatrix} \cdots & & & & & & \\ & \mathcal{H}_{l_1} & \mathcal{V}_1 & & & & \\ & \mathcal{V}_1^\dagger & \mathcal{H}_{l_2} & \mathcal{V}_2 & & & \\ & & \mathcal{V}_2^\dagger & \mathcal{H}_{l_3} & \mathcal{V}_1^\dagger & & \\ & & & \mathcal{V}_1 & \mathcal{H}_{l_4} & \mathcal{V}_2^\dagger & \\ & & & & \mathcal{V}_2 & \mathcal{H}_{l_5} & \cdots \end{pmatrix}, \tag{5.40}$$

where $\mathcal{H}_{l_i} = E_i \mathbb{I}_{m\times m}$ is the block matrix corresponding to the orbitals in the ith layer and $\mathcal{V}_1$ and $\mathcal{V}_2$ are the hopping matrices connecting layers of different type. The precise

form of these matrices depends on the particular system at hand. In the following, we consider zigzag and armchair nanotubes and armchair graphene nanoribbons.

Zigzag carbon nanotubes. Let us consider an $(n, 0)$ carbon nanotube. In this case, $m = n$ and

$$\mathcal{V}_1 = \gamma_0 \begin{pmatrix} 1 & 0 & \cdots & 1 \\ 1 & 1 & & \\ 0 & 1 & 1 & \cdots \\ \cdots & & \cdots & \ddots \end{pmatrix}, \tag{5.41}$$

and $\mathcal{V}_2 = \gamma_0 \mathbb{I}_{n\times n}$. $\mathcal{V}_1$ can be easily diagonalized, i.e., there is an $(n \times n)$ matrix C such that $C^\dagger \mathcal{V}_1 C$ has a diagonal form. The eigenvectors of the matrix $\mathcal{V}_1$ are plane waves around the nanotube circumferential direction:

$$|\varphi_q\rangle = \frac{1}{\sqrt{n}} \sum_{j=1}^{n} \exp(\mathrm{i}k_q j)\, |j\rangle\,, \tag{5.42}$$

where $q = 1, \ldots, n$ is the mode index, and $|j\rangle$ represents the π orbital localized at the jth atom in a given layer. Since $\mathcal{V}_2$ and $\mathcal{H}_{l_i}$ are proportional to the identity, they commute with $\mathcal{V}_1$ and the transformation defined by the previous equation (let us call it $\mathcal{C}$) diagonalizes all the matrices simultaneously. Using a change of basis transformation of the form

$$\mathcal{U} = \begin{pmatrix} \cdots & & & \cdots \\ & \mathcal{C} & 0 & 0 \\ & 0 & \mathcal{C} & 0 \\ & 0 & 0 & \mathcal{C} \\ \cdots & & & \cdots \end{pmatrix}, \tag{5.43}$$

the transformed Hamiltonian is represented by n uncoupled chains with alternating hoppings γ_0 and $\gamma_q = 2\gamma_0 \exp(-\mathrm{i}\pi q/n)\cos(q\pi/n)$ $(q = 1, \ldots, n)$ with q the mode index. Each of these modes is represented in Fig. 5.6.

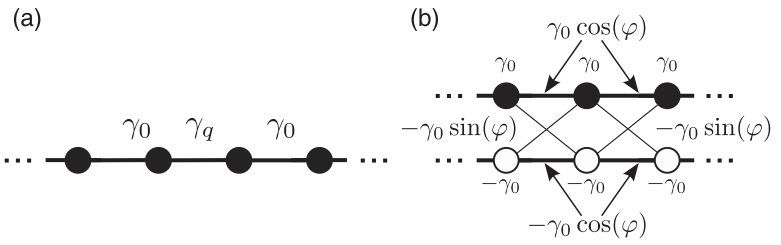

Figure 5.6 Representation of the modes/eigenchannels resulting after the mode decomposition described in the text for: (a) zigzag carbon nanotubes and armchair graphene nanoribbons; and (b) armchair carbon nanotubes.

Given that dimers with alternating hoppings like the ones above always have a gap unless the hoppings have equal absolute value, one can see that whenever n is a multiple of 3, $|\gamma| = |\gamma_q|$ is satisfied for $q = n/3, 2n/3$, and the system is metallic. The modes with $q = n/3, 2n/3$ are in this case the only ones which contribute to the density of states and the conductance in the vicinity of the charge neutrality point. Readers are encouraged to undertake Problem 5.3 at the end of this chapter.

Armchair graphene nanoribbons. In this case, $m = n$ and $\mathcal{V}_2 = \gamma_0 \mathbb{I}_{n\times n}$, hence

$$\mathcal{V}_1 = \gamma_0 \begin{pmatrix} 1 & 0 & \cdots & 0 \\ 1 & 1 & & \\ 0 & 1 & 1 & \cdots \\ & & \cdots & \ddots \end{pmatrix}. \tag{5.44}$$

Note that $\mathcal{V}_1$ differs from what is given in Eq. (5.41) only in the matrix element in the upper right corner (which gives the periodic boundary condition for carbon nanotubes). However, in contrast to the case of zigzag tubes, the matrix $\mathcal{V}_1$, Eq. (5.44), cannot be diagonalized. Therefore, a different strategy is required and a new basis set for armchair ribbons has to be obtained by imposing a "particle-in-a-box" assumption as described below.

Inspired by the geometrical arrangement of the A and B sublattices, an alternative block-diagonal change of basis transformation can be adopted:

$$\mathcal{U} = \begin{pmatrix} \ddots & & & & & & \\ & \mathcal{C}_1 & & & & & \\ & & \mathcal{C}_2 & & & & \\ & & & \mathcal{C}_2 & & & \\ & & & & \mathcal{C}_1 & & \\ & & & & & \ddots & \end{pmatrix}, \tag{5.45}$$

where the arrangement of the matrices $\mathcal{C}_1$ and $\mathcal{C}_2$ is periodically repeated with a four-layer periodicity (the same as the lattice). The matrix elements of $\mathcal{C}_1$ and $\mathcal{C}_2$ are chosen to satisfy hard boundary conditions:

$$[\mathcal{C}_1]_{i,q} = \frac{2}{\sqrt{2n+1}} \sin\left(\frac{2iq\pi}{2n+1}\right), \tag{5.46}$$

$$[\mathcal{C}_2]_{i,q} = \frac{2}{\sqrt{2n+1}} \sin\left(\frac{(2i-1)q\pi}{2n+1}\right). \tag{5.47}$$

Interestingly, the blocks of the transformed Hamiltonian $\mathcal{H}' = \mathcal{U}^\dagger \mathcal{H} \mathcal{U}$ are all diagonal. Indeed, the blocks proportional to the identity matrix remain invariant ($\mathcal{H}'_{l_i} = \mathcal{H}_{l_i}$, $\mathcal{V}'_2 = \mathcal{V}_2$), while $[\mathcal{V}'_1]_{i,q} = [\mathcal{C}_1^\dagger \mathcal{V}_1 \mathcal{C}_2]_{i,q} = 2\gamma_0 \delta_{i,q} \cos(q\pi/(2n+1))$. Therefore, the graphene armchair nanoribbon can also be represented as n-independent one-dimensional

chains with alternating hoppings γ_0 and $\gamma_q = 2\gamma_0 \cos(q\pi/(2n+1))$, $q = 1, \ldots, n$. A simple analysis of the electronic structure of each of these modes/eigenchannels shows that, for metallic armchair nanoribbons, there is a single mode with a nonvanishing density of states close to the charge neutrality point (see also Problem 5.3).

Armchair carbon nanotubes. Let us consider (m, m) armchair SWNTs. The carbon atoms are arranged into layers as shown in Fig. 5.5(b), which in this case corresponds to a $(3, 3)$ SWNT once periodic boundary conditions are taken along the vertical direction. In this case, $n = 2m$, $\mathcal{V}_1 = \mathcal{V}_2^\dagger = \gamma_0 \mathbb{I}_{n\times n}$ and the only nontrivial matrices are the $\mathcal{H}_{l_i}$. By applying a change of basis transformation such as the one proposed in Problem 5.3, it is possible to obtain a set of decoupled circumferential modes (Mingo et al. 2001). The Hamiltonian for each of these modes is represented in Fig. 5.6 and corresponds to ladders rather than 1D chains, $\varphi_q = \pi q/m$ with $q = 0, 1, \ldots, m-1$. The circumferential mode contributing to the density of states at the charge neutrality point corresponds to $\varphi = 0$, leading to two decoupled 1D chains.

5.2.3 Fabry–Pérot Conductance Oscillations

Let us consider a device made up of a high-quality sample, which is connected to electrodes through *almost* perfect contacts. *Almost* is the crucial word here. It implies a departure from certainty – when the contacts are perfect, transmission is perfect, and therefore there is no uncertainty! – thereby giving room for interference. Indeed, the interference between the "paths" corresponding to different numbers of reflections at the interfaces may lead to a phenomenon similar to the Fabry–Pérot interference found in optics. But this time, one has an *electrical* Fabry–Pérot interferometer working on the basis of *quantum* interference.

Several experiments have reported a successful realization of Fabry–Pérot interference both in carbon nanotube devices (Herrmann et al. 2007; Kim et al. 2007; Liang et al. 2001; Wu et al. 2007) and in graphene devices (Wu et al. 2012, Oksanen et al. 2014). The evidence relies on the observation of oscillations in the conductance as the gate voltage is changed. In the following, we comment on these results and outline a way to rationalize them through a minimal model. Though, throughout this book we have mostly been confronted with Hamiltonian models, this time scattering matrices are our starting point.

The experimental setup used, for example, in Liang et al. (2001) consists of a metallic carbon nanotube coupled to left and right electrodes and a gate (see scheme in Fig. 5.7(a)). The presence of Fabry–Pérot interference in this electrical measurement setup was verified by using the gate (V_g) and bias (V) voltages as control parameters in low-temperature experiments (Liang et al. 2001) as shown in Fig. 5.7(c). At first sight, this plot may seem reminiscent of the conductance pattern usually found in the Coulomb blockade regime. We emphasize, however, that this is not the case as can be appreciated by looking at the scale bar on the right. Indeed, the conductance minima (dark regions) do not show any blockade since the conductance remains close to $3e^2/h$. The maxima are not very far from the quantum limit of $4e^2/h$ for a metallic nanotube

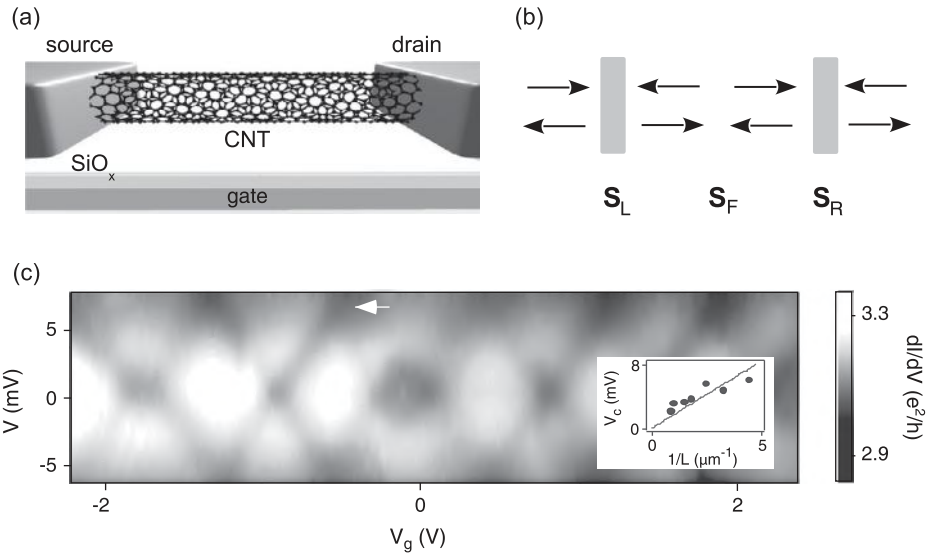

Figure 5.7 (a) A typical experimental setup used to observe Fabry–Pérot oscillations in the conductance of SWNTs. (b) The reflections and transmissions at the interfaces of the device which are modeled through the scattering matrices S_L (left lead), S_R (right lead) and S_F (for free propagation inside the sample). (c) Experimental results from Liang et al. (2001) showing the conductance as a function of the bias (V) and gate (V_g) voltages for a 220 nm long SWNT at 4 K. (Reprinted by permission from Macmillan Publishers Ltd: *Nature*; (Liang et al. 2001), copyright 2001)

in the first conductance plateau. Furthermore, since the level spacing is approximately constant close to the charge neutrality point, the regularity of the pattern gives access to a typical energy, which in this case turns out to be the level spacing, whereas in the Coulomb blockade regime (see Section 6.5.1), the charging energy sets the dominant energy scale. The dependence of the spacing between the maxima on the inverse length of the device is plotted in the inset to Fig. 5.7(c) and shows the expected linear law.

Scattering matrix modeling. It is instructive to rationalize this experiment by resorting to the Landauer formalism in a minimal model as outlined below (details are left for Problem 5.5). To this end, we need to compute the transmission probability. Instead of using Green's functions for a model Hamiltonian, here we follow Liang et al. (2001) and propose a simple model for the scattering matrices corresponding to each of the processes involved in the interference: (i) partial reflections at the contacts and (ii) free propagation through the sample. The composition of these scattering matrices makes calculation of the scattering matrix of the overall system possible.

The scattering matrix relates the incoming and outgoing probability amplitudes at a given scatterer. In this case, we have two active channels in the system; therefore S_α ($\alpha = L, R, F$) has dimension 4×4. $[S_L]_{ij}$ are the transmission and reflection amplitudes between the different channels $i, j = 1, 2, 3, 4$, where $i, j = 1, 2$ ($i, j = 3, 4$) correspond to the channels on the left (right).

Scattering matrices for free propagation through the sample. If one assumes that the two propagating channels do not mix, the ballistic propagation inside the nanotube can be captured by

$$S_F = \begin{pmatrix} 0 & 0 & e^{i\phi_1} & 0 \\ 0 & 0 & 0 & e^{i\phi_2} \\ e^{i\phi_1} & 0 & 0 & 0 \\ 0 & e^{i\phi_2} & 0 & 0 \end{pmatrix}, \tag{5.48}$$

where ϕ_1 and ϕ_2 represent the phases accumulated during the propagation inside the sample in each of the two propagating channels.

Scattering matrices for the contacts. Let S_L and S_R be the scattering matrices for the left and right contacts, respectively. The partial reflections at the contacts can be modeled in S_L and S_R by adding a suitable set of parameters. Here, we show the alternative proposed by Liang et al. (2001), which consists in writing them as an exponential, thereby ensuring unitarity:

$$S_{L(R)} = \exp\left(i \begin{pmatrix} r_2 & r_1 \exp(\pm i\delta_1) & 0 & 0 \\ r_1 \exp(\pm i\delta_1) & r_2 \exp(\pm i\delta_2) & 0 & 0 \\ 0 & 0 & r_2 & r_1 \exp(\mp i\delta_1) \\ 0 & 0 & r_1 \exp(\mp i\delta_1) & r_2 \exp(\mp i\delta_2) \end{pmatrix} \right). \tag{5.49}$$

Furthermore, r_1 and r_2 can be assumed to be energy independent, leaving all the dependence on the bias and gate voltages in the phase shifts appearing in S_F. Using the above matrices, the total scattering matrix S_T can be obtained by composing them. In Problem 5.5, you are invited to continue with this calculation in detail. Once this is done, knowledge of S_T then allows for calculation of the Landauer conductance as a function of the bias and gate voltages. The Fabry–Pérot conductance maps simulated using this scattering matrix modeling compare very well with the experimental one as shown in Fig. 5.8 from Liang et al. (2001). Comparison with the experiment at hand may allow the extraction of useful information: Do the metal contacts introduce important intermode coupling? Are there other effects not considered here that may play a role? In the results shown in Fig. 5.8, the parameters used to adjust the experimental behavior did require an intermode coupling (i.e., a nonvanishing r_1).

Indeed, many issues which are beyond simple description above have been addressed over the past years, including the appearance of additional low-frequency modulation of the interference pattern (Jiang et al. 2003) and interaction effects (Kim et al. 2007).

We note that other very sensitive experiments have also probed the zero-frequency noise in the Fabry–Pérot regime (Herrmann et al. 2007; Kim et al. 2007; Wu et al. 2007) for SWNTs. Experiments suggest, in some cases, a good quantitative agreement with a coherent noninteracting picture (Herrmann et al. 2007), while other results show moderate deviations (Wu et al. 2007) which are attributed to either electron–electron interactions (Herrmann et al. 2007; Wu et al. 2007) or decoherence (Herrmann et al. 2007).

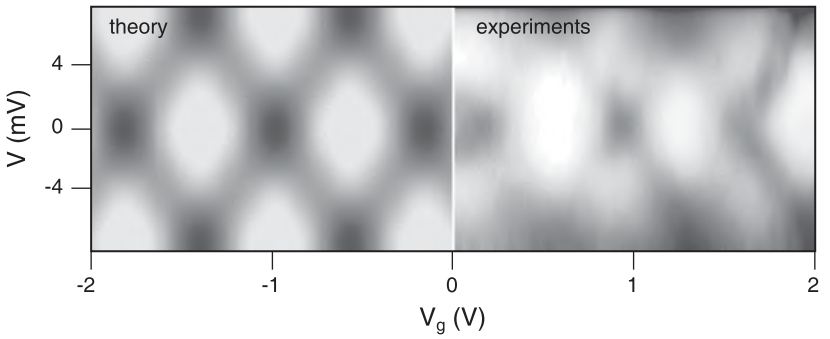

Figure 5.8 Calculated (left) and measured (right) conductance patterns as a function of V and V_g for a 220 nm SWNT device. Dark corresponds to 2.9 e^2/h and white to 3.2 e^2/h. (Reprinted by permission from Macmillan Publishers Ltd: *Nature* (Liang et al. 2001), copyright 2001)

Results compatible with a Tomonaga–Luttinger liquid were also found for weak backscattering at the contacts (Kim et al. 2007). We mention that the presence of enhanced Coulomb interaction in low dimensionality was predicted to give rise to the formation of a Luttinger liquid (Luttinger 1963), a phenomenon which was then applied to the case of metallic carbon nanotubes (Egger 1999; Egger & Gogolin 1997). The theoretical fingerprints for Luttinger liquid in nanotubes include peculiar power-law behavior of the temperature-dependent conductance, with an exponent depending on the contact geometry, or spin–charge separation. Transport evidence of such many-body states has been reported experimentally, but in very specific conditions, including a high-quality metallic single-walled nanotube connected to external reservoirs with at least one poor (tunneling) contact (Bockrath et al. 1999; Gao et al. 2004). A more detailed presentation of the background and experiments is given in Charlier et al. (2007).

We close this subsection by noting that, more recently, Fabry–Pérot oscillations have also been reported in sub-100 nm length graphene devices (Wu et al. 2012) and also in outstanding experiments on suspended graphene devices (Grushina & Morpurgo 2013; Rickhaus et al. 2013).

5.2.4 Contact Effects: SWNT-Based Heterojunctions and the Role of Contacts between Metals and Carbon-Based Devices

Up to now, we have been mostly focused on intrinsic effects in carbon-based devices. However, it may be crucial to capture the contact effects, i.e., the contact resistance between the measured material (nanotubes, graphene) and the conducting electrodes. The electrodes are generally formed by other materials like palladium or gold, though there is also great interest in *all-carbon* devices (Anantram & Léonard 2006).

SWNT-Based Heterojunctions

The electronic structure of an intramolecular nanotube-based heterojunction was first investigated by Chico et al. (1996), who considered the case of the junction of two

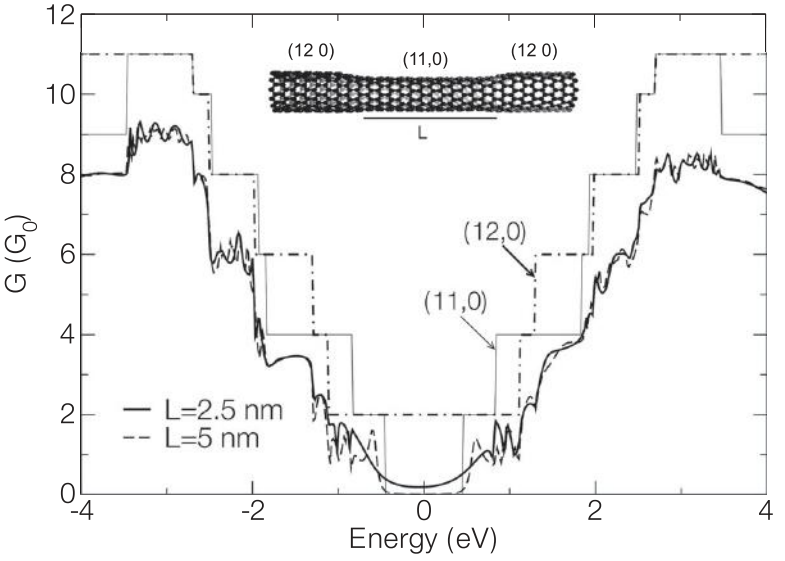

Figure 5.9 Conductance profile for a single semiconducting nanotube $(11, 0)$ and a metallic nanotube $(12, 0)$, together with the conductance of the double junction $(12, 0)$–$(11, 0)$–$(12, 0)$ (a ball-and-stick structure is shown in the inset).

nanotubes of different diameter connected through pentagon–heptagon pairs. A different configuration (illustrated in the inset of Fig. 5.9) is that of a double heterojunction, where the leads are formed by $(12, 0)$ nanotubes while the central region contains an $(11, 0)$ semiconducting one. These junctions have been experimentally observed and measured by STM (Ouyang et al. 2001a) (for a review see (Odom et al. 2002)). The conductance between the STM tip and the device in different regions gives information on the local density of states. The different position of the peaks associated with the van Hove singularities allows characterization of the device. In this case, a good agreement has been found with the predictions of a simple π orbitals model.

What about the transport properties of such devices? Following a calculation within the Landauer–Büttiker formalism (Triozon et al. 2005), one obtains the conductance shown in Fig. 5.9 as a function of the Fermi energy in the low-temperature limit. Here, a simple *tight-binding* model for the π orbitals with a single hopping parameter for all carbon–carbon bonds is used. The solid and the dashed black lines are the conductance for an internal tube of 2.5 and 5.0 nm, respectively. The results for the $(11, 0)$ and $(12, 0)$ SWNTs are also shown for reference. The overall decrease of the conductance is evident, with the conductance being limited by the smallest number of modes, min $(N_{(12,0)}, N_{(11,0)})$, at the given energy. The small conductance for the shorter junction is due to tunneling through the gap and is already suppressed for 5.0 nm. The results for a longer system of 100 nm (not shown here) do not change much, with faster oscillations near the gap being the main difference.

Contacts between a Metal and a Metallic Carbon-Based Material

The contact resistance of metallic interfaces mainly depends on the local atomic bonding and orbital rehybridization at the contact, and remains finite even for vanishing bias potential. As an illustration, let us consider the case of a metal-metallic CNT-metal junction. The scattering rate between the metal and the nanotube (which is also related to the self-energy of the contact Σ) can be estimated using a simple Fermi golden rule. Assuming that $|k_m\rangle = \sum_l e^{ik_m \cdot l}|\varphi_m^l\rangle$ (resp. $|k_F\rangle = \sum_l e^{ik_F \cdot l}|\varphi_{\rm NT}^l\rangle$) are the propagating states with k_m (k_F) the wavevector in the metal (resp. nanotube), we take $|\varphi_{\rm NT}^l\rangle$ the localized atomic basis orbitals (p_z-like) in cell (ℓ) that will have a finite overlap with $|\varphi_m^{l'}\rangle$ only for a few unit cells, defining the contact area (($l - l'$) small).

The scattering rate between metal and nanotube is related to $\langle k_m|\mathcal{H}_{\rm contact}|k_F\rangle$. This matrix element depends on the chemical nature of the interface bonding (covalent, ionic, etc.) and on the overlap $\langle\varphi_{\rm NT}^l|\varphi_m^{l'}\rangle$, which changes depending on the interface geometry (end or side/bulk contacts, length of the contact as illustrated in Fig. 5.10), together with the momentum of the atomic orbitals contributing to $|k_m\rangle$. The optimization of the coupling is achieved when the wavevector conservation is maximally satisfied, i.e., $\sim \delta(k_m - k_F)$. For metallic armchair tubes, a larger coupling rate is obtained for $k_m \simeq 2\pi/3\sqrt{3}a_{cc}$, while a smaller metallic wavevector induces a smaller coupling rate. The tunneling rate from the metal to the nanotube can be effectively written as

$$1/\tau \sim \frac{2\pi}{\hbar}|\langle k_m|\mathcal{H}_{\rm contact}|k_F\rangle|^2 \rho_{\rm NT}(E_F)\rho_m(E_F), \tag{5.50}$$

with $\rho_{\rm NT}(E_F)$ ($\rho_m(E_F)$) the density of states of the nanotube (metal) at the Fermi level. Intriguingly, several experiments on metallic tubes have reported $G \simeq G_0$ at low bias, instead of the two theoretically predicted channels, assuming the π–π^* degeneracy at the charge neutrality point. This could be explained either by one channel becoming completely reflective or by a specific mismatch between the symmetries of the incoming and outgoing states.

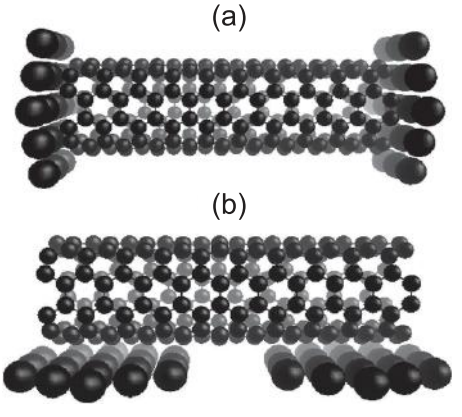

Figure 5.10 Contact types between a nanotube and electrode first layers: (a) end contacts; and (b) side or bulk contacts. Courtesy of Juan-José Palacios (2003)

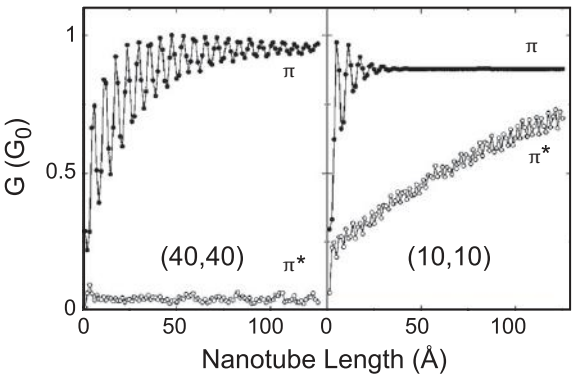

Figure 5.11 Contribution of π and π^* channels at CNP to the total nanotube conductance for armchair (10, 10) and (40, 40) tubes, and modeling the metal contact by a jellium. Adapted from Mingo & Han (2001). (Reprinted with permission from Mingo & Han (2001). Copyright (2001) by the American Physical Society)

This issue was raised by Mingo and Han (Mingo & Han 2001) who investigated such an imbalance in coupling strength between the π–metal (jellium) contact and the π^*–metal contact, by using quantum simulation with a Landauer–Büttiker approach. Figure 5.11 shows the contribution of the two channels to the conductance at the charge neutrality point as a function of nanotube length (for two different nanotube diameters). The transmission probability of the π^*–metal is clearly seen to almost vanish for a sufficiently large diameter, supporting the scenario of interface symmetry mismatch.

Metal/Semiconducting Nanotube/Metal Junctions

The different case of interfaces between metals and semiconducting nanotubes (M-SCSWNT-M junctions) deserves particular consideration, given their central role in the operation of nanotube-based field-effect transistors (see Section 5.2.4). Here, the formation of interface dipoles and Schottky barriers at the interface can produce very large contact resistance and a tunneling transport regime at low bias and low temperatures. The charge redistribution at the metal/semiconductor interface can be described by the band bending and existence of metal-induced gap states. Those features strongly depend on the relative positions of the Fermi level and band edges of the metal and nanotube in contact, as discussed further below (Heinze et al. 2002).

Several other papers have also emphasized the importance of the hybridization between carbon and metal orbitals at the contact (for instance Nemec et al. 2006), while other work has discussed the role of the Schottky barrier (Anantram & Léonard 2006). The variations of the contact geometry (end, side, or melted), nanotube length, and metal type, can certainly explain why the experimental data are markedly scattered. Much effort is being devoted to controlling these contacts, as reported for example in (Xia et al. 2011) where a transport efficiency of about 75% is achieved for palladium–graphene junctions. Moreover, while charge transfers, interface states, and the Schottky barrier

physics are within the scope of *ab initio* simulations, computational limitations make it still impossible to compute any transport properties on micrometers long tubes (and in the presence of gate and bias voltages) at any degree of accuracy. Finally, for higher bias voltage between conducting probes, due to the potential drop profile along the tube, the modifications of bands along the tube axis produce additional backscattering (Anantram 2000). This Bragg reflection is a fundamental point that could explain the experimental observation of limited turn-on current with increasing bias voltage (Poncharal et al. 2002).

Schottky Barriers and SWNT-Based Field-Effect Transistors

Léonard and Tersoff pioneered theoretical studies on Schottky barriers in SWNT–metal contact interfaces, unraveling the fact that their peculiar nanoscale dimension and unconventional electrostatics (with poor screening effects) should result in a totally inefficient Fermi-level pinning mechanism, a fact suggesting fine-tunability of the Schottky-barrier height, eventually disappearing with the formation of a purely ohmic contact (Léonard & Tersoff, 1999, 2000a, 2000b, 2002). Nanoscale interfaces were thus envisioned as providing an unprecedented means to eliminate the inconvenient Schottky barrier hindering hole and electron injection. After tremendous efforts to precisely characterize the SB physics in carbon nanotube-based field-effect transistors (SWNT-FETs) (Martel et al. 2001), Javey et al. (2003) finally reported compelling experimental evidences of Schottky barrier suppression in SWNT-FET by using contacts between palladium and semiconducting nanotube with sufficiently large tube diameter (Javey et al. 2003, Kim et al. 2005), a result which brought hope for the advent of all-carbon nanotube-device nanoelectronics (Tersoff 2003).

Nevertheless, there is still a fundamental need for in-depth understanding of nanoscale interfaces, since a large dispersion of experimental measurements is usually obtained (Anantram & Léonard 2006; Franklin & Chen 2010; Leonard & Talin 2011; Svensson & Campbell 2011). One problem lies in the experimental techniques commonly used to study contacts to bulk materials, which cannot be exploited at nanoscale, and poor statistics over devices shows a large discrepancy in the reported Schottky barrier heights as well as several contradictory conclusions (Martel et al. 2001). From this perspective, accurate simulation of nanotube-transistor current–voltage characteristics are needed for capturing the precise role of SWNT diameter and interface atomic structure of the metal/nanotube junction, as well as the contribution of chemical doping, since all those aspects eventually drive device control and performances. As argued by (Tersoff 2003), the atomic-scale reasons for the disappearance of the SB-barrier for certain devices remain to be fully clarified. Many questions remain unsolved, such as: Why should palladium give a smaller Schottky barrier than platinum, gold, or titanium? The answer to this question should be sought in the chemical sticking properties of the metal to carbon structures, or in some combination of metal-/carbon-dependent interfacial charging properties and long-range electrostatics. To date, however, those questions are very challenging computationally, and would require self-consistent calculations fully based on first-principles methods to unveil the process of Schottky barrier formation for

different types of nanoscale metal–nanotube interfaces. Besides, since ohmic contacts have been achieved for nanotubes with diameter above 2 nm (but with limited ON/OFF performances) (Kim et al. 2005), this theoretical knowledge would also be highly desirable for further monitoring and elimination of the SB in narrower tubes, whose electrical properties would be more favorable for practical devices.

5.3 Ballistic Motion through a Graphene Constriction: The 2D Limit and the Minimum Conductivity

The conductivity of a ballistic clean graphene has been discussed in the situation of a specific transport setup consisting of two heavily doped leads bridging a central (undoped) graphene region pinned at the Dirac point (charge neutrality point) and with geometry characterized by W and L, which are respectively the width and the length of the sandwiched graphene sample.

When considering a clean graphene sample in the ballistic regime where the electron mean free path $\ell_{el} \gg L$, the transport problem shares some similarities with Klein tunneling phenomena, where due to the chiral nature of the electrons, the transmission is always finite at specific angles through a p–n–p or n–n–n junction. One considers a graphene ribbon of length L and width W in the limit of short and wide armchair ribbons ($L < W$) with hardwall or smooth confining potential at the edges. The system is kept at energies around the CNP, and it is connected to two leads at high potential with a large number N of active conductive channels. Through solution of the noninteracting Dirac equation with such geometry, the conductivity is given by the number of evanescent modes, as $\sigma = (L/W)(4e^2/h)\sum_{n=1} T_n$, with $T_n = |1/\cosh(q_n L)|^2$, the transmission probability with q_n being the transverse wavevector, which can be rewritten as

$$\sigma = \frac{4e^2}{h}\frac{L}{W}\sum_{n=0}^{\infty}\frac{1}{\cosh 2[\pi(n+1/2)L/W]} \longrightarrow \frac{4e^2}{\pi h} \quad (W \gg L). \tag{5.51}$$

Equation (5.51) can be derived using a twisted boundary condition $\Psi(y = 0) = \sigma_x\Psi(y = 0)$ and $\Psi(y = W) = -\sigma_x\Psi(y = W)$, where σ_x is a component of the Pauli matrix (Tworzydło et al. 2006). This particular boundary condition mimics the massless Dirac fermions inside the graphene sample but infinitely massive Dirac fermions in the leads. Now, the above formula in the wide sample ($W \gg L$) limit converges to a universal value $\frac{4e^2}{\pi h}$, which is known as the *quantum limited conductivity* of graphene in the clean limit (as illustrated in Fig. 5.12). This theoretical result has been tested numerically by calculations based on a *tight-binding* model (Cresti et al. 2007). This peculiar transmission property has been also confirmed experimentally (Miao et al. 2007).

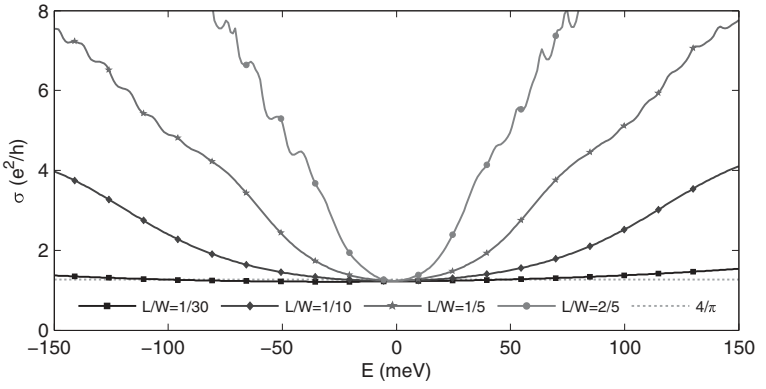

Figure 5.12 Conductivity versus energy for an armchair nanoribbon with lateral width $W = 150$ nm (and varying length in between highly doped source/drain contacts, $L = 5$, 15, 30, and 60 nm). The minimum conductivity $\frac{4e^2}{\pi h}$ is also drawn with a horizontal dashed line. Courtesy of A. Cresti.

5.4 Further Reading and Problems

- Regarding Klein tunneling, we recommend the presentation in (Katsnelson 2012). For a recent review on this subject, including the connection to phenomena in quantum optics, such as the Snell–Descartes law of refraction, total internal reflection, Fabry–Perot resonances, and total internal reflection, we recommend (Allain & Fuchs 2011).

Problems

5.1 *Potential step for Dirac fermions.* Consider Dirac fermions incident on a potential step of height V_0.

(a) Formulate three general conservations laws. (*Hint*: Remember that the Hamiltonian is time independent and that it is translational invariant in one direction (y). What can you say about the current density along the direction perpendicular to the step?)

(b) Derive the transmission probability.

5.2 *Pseudospin conservation and the absence of backscattering.* Consider massless Dirac electrons entering a region where the potential is proportional to the identity matrix. Prove that for normal incidence they cannot be backscattered.

5.3 *Mode decomposition.*

(a) Following the lines of Section 5.2.2, deduce the mode decomposition for armchair SWNTs.

(b) Consider the mode-decomposition for armchair SWNTs and GNRs as well as zigzag SWNTs given in Section 5.2.2. Determine the Hamiltonian for each of the

independent modes that have (when possible) a nonvanishing DOS at the charge neutrality point. What can you say about the degeneracy close to this point?

(c) Compose the total density of states and the conductance by superposing the results for each of the independent modes for a $(5, 0)$ SWNT and for an armchair 8-aGNR.

5.4 *The zigzag challenge.* Starting from a simple *tight-binding* Hamiltonian and following the spirit of Section 5.2.2, you are challenged to obtain a suitable mode-decomposition for the case of zigzag GNRs. Can you do it? Pay attention to the choice of unit cell.

5.5 *Fabry–Pérot conductance maps.* Following Section 5.2.3, we ask you to reconsider the setup of Fig. 5.7(a) and derive an expression for the Fabry–Pérot conductance map in Fig. 5.7(c). To this end, we propose the following.

(a) Establish a simple model for the scattering matrices at the contacts and for the free propagation inside the sample. You may choose a model as the one proposed in the text or choose your own parameterization.

(b) Compose the partial scattering matrices in (a) to obtain the total scattering matrix for the device.

(c) Use these results to obtain the linear response conductance (Landauer) as a function of the gate and bias voltages.

(d) *Questions for further thought:* What would happen if the leads introduce intermode coupling? How would these results change if instead of a carbon nanotube one considers a graphene nanoribbon? What would be the effect of defects on the conductance patterns? (Suggested reading: Jiang et al. 2003; Liang et al. 2001.)

5.6 *Current noise for noninteracting electrons in the Fabry–Pérot regime.* Using the results of the previous exercise, determine the zero-frequency noise for the setup of Fig. 5.7(a). (Suggested reading: Herrmann et al. 2007; Kim et al. 2007; Wu et al. 2007.)

5.7 *Fabry–Pérot conductance maps revisited.* Let us reconsider the problem of the Fabry–Pérot conductance maps. This time, you are encouraged to start from a simple *tight-binding* model for an infinite SWNT, which is divided into three regions; the central one of length L is going to be our resonant cavity and the rest the left and right leads. To simulate the weaker contact with the leads, you may set a weakened carbon–carbon hopping between the leads and the central region, preserving the rotational symmetry of the system. Then by exploiting the mode decomposition of Section 5.2.2, try to obtain the conductance maps within the Landauer–Büttiker formalism. Discuss the limitations of the model.

** Additional exercises and solutions available at our website.

6 Quantum Transport in Disordered Graphene-Based Materials

This chapter gives an overview of the main quantum transport properties in disordered graphene-based materials with a focus on the analysis of main transport length scales and conduction regimes that develop when short-range or long-range defects are incorporated inside the honeycomb lattice. First, consider the generic models of disorder are considered, such as the Anderson disorder or a density of impurities modeled by long-range Gaussian potential. Numerical implementations of the Kubo method presented earlier, and technically described in Appendix D, are used and validated by direct comparison with analytical results for both low-dimensional (nanotubes, nanoribbons) and two-dimensional graphene, especially in the semiclassical transport regime.

Next, weak and strong localization phenomena are investigated, and the typical mean free path and localization for a given density of defects are estimated. The effects of more specific impurities, such as monovacancies, structural disorder, or grain boundaries – unique to graphene-based materials – are also investigated in-depth, with simplified (but realistic enough) *tight-binding* models. Finally, some fundamental issues concerning Coulomb blockade physics are presented.

6.1 Elastic Mean Free Path

The elastic mean free path (ℓ_{el}) is a key quantity in mesoscopic transport which dictates the crossover between ballistic and diffusive regimes. The behavior of ℓ_{el} in nanotubes and graphene nanoribbons exhibits unique scaling features, and can vary by orders of magnitude under a small Fermi level shift, owing to the close proximity of linearly dispersive bands and parabolic-like energy subbands. This allows spectacular tuning (using electrostatic gates or chemical doping) of transport regimes from ballistic to localization for the same sample.

It is first instructive to analyze the case of short-range disorder, which allows illustration of common properties of transport length scales in all considered graphene-based low-dimensional materials. The Anderson potential for disorder is the most generic model for investigating localization phenomena in low dimension, being very convenient for both analytical derivations and numerical simulations. It was introduced by Anderson in the late 1950s (Anderson 1958). The Anderson disorder is a white noise (uncorrelated) disorder, which is generally introduced through modulations of the onsite

energies of a π orbital *tight-binding* Hamiltonian ($\varepsilon_\pi = \varepsilon_\pi + \delta\varepsilon_\pi$). The disorder strength is tuned by choosing randomly $\delta\varepsilon_\pi \in [-W/2, W/2]$ (with, for instance, a uniform probability distribution with $\mathcal{P} = 1/W$). For weak enough disorders, $\ell_{\rm el}$ can then be derived analytically for both metallic carbon nanotubes and graphene nanoribbons Cresti et al. We provide the essential results below. Let us begin with the case of 2D graphene, which offers the possibility of a straightforward analytical derivation, introducing the total density of states, approximated as

$$\rho(E) = \frac{2|E|}{\pi(\hbar v_F)^2}. \tag{6.1}$$

By writing $\ell_{\rm el} = v_F\tau$ and using the Fermi golden rule (perturbation theory) to compute the elastic scattering time, τ ($\tau^{-1} = (2\pi/\hbar)\rho(E_F)W^2/12$), one finally obtains

$$\ell_{\rm el} \propto 1/|E|, \tag{6.2}$$

which diverges when $|E| \to 0$. This crude estimation pinpoints a difficulty in calculating transport length scales when the Fermi level lies close to the Dirac point. A numerical calculation within the Kubo approach allows evaluation of $\ell_{\rm el}$ at a quantitative level in 2D disordered graphene with Anderson scattering potential (numerical simulations are presented in Section 6.2.4).

In quasi-1D systems such as SWNTs and GNRs, scattering angles are restricted either to forward-scattering events at zero angle, which leads to momentum relaxation but does not affect the elastic transport length scale, or to backscattering events at an angle of π, which thus monitor the behavior of $\ell_{\rm el}$. Using the Anderson disorder model, White and Todorov first derived an analytical formula for the low-energy elastic mean free path ($\ell_{\rm el}$) (Roche et al. 2000; White & Todorov 1998) using a two-bands model. A simple derivation is provided below, mainly following the path set out in White and Mintmire (1998). For armchair metallic nanotubes, the scattering rate obtained in perturbation theory gives

$$\frac{1}{2\tau(E_F)} = \frac{2\pi}{\hbar}\left|\langle\Psi_{n1}(k_F)|\,\hat{U}\,|\Psi_{n2}(-k_F)\rangle\right|^2 \rho(E_F) \times N_c N_{\rm Ring}, \tag{6.3}$$

with N_c and $N_{\rm Ring}$ being the respective number of pair atoms along the circumference and the total number of rings taken in the unit cell (used for diagonalization), whereas the eigenstates at the Dirac point are given by

$$\begin{aligned}
|\Psi_{n1,n2}(k_F)\rangle &= \frac{1}{\sqrt{N_{\rm Ring}}} \sum_{m=1,N_{\rm Ring}} \mathrm{e}^{imk_F}|\alpha_{n1,n2}(m)\rangle, \quad \text{with} \\
|\alpha_{n1}(m)\rangle &= \frac{1}{\sqrt{2N_c}} \sum_{n=1}^{N_c} \mathrm{e}^{\frac{2i\pi n}{N_c}} \Big(|p_z^A(mn)\rangle + |p_z^B(mn)\rangle \Big), \\
|\alpha_{n2}(m)\rangle &= \frac{1}{\sqrt{2N_c}} \sum_{n=1}^{N_c} \mathrm{e}^{\frac{2i\pi n}{N_c}} \Big(|p_z^A(mn)\rangle - |p_z^B(mn)\rangle \Big).
\end{aligned} \tag{6.4}$$

We consider here the simple case of an uncorrelated Anderson disorder defined by

$$\begin{aligned}
\langle p_z^A(mn) \mid \hat{U} \mid p_z^A(m'n') \rangle &= \varepsilon_A(m,n)\delta_{mm'}\delta_{nn'}, \\
\langle p_z^B(mn) \mid \hat{U} \mid p_z^B(m'n') \rangle &= \varepsilon_B(m,n)\delta_{mm'}\delta_{nn'}, \\
\langle p_z^A(mn) \mid \hat{U} \mid p_z^A(m'n') \rangle &= 0,
\end{aligned} \tag{6.5}$$

with $\varepsilon_B(m,n)$ and $\varepsilon_A(m,n)$ denoting the onsite energies of electron at atoms A and B in position (m,n), values which are taken at random within an interval $[-W/2, W/2]$ and with probability $\mathcal{P} = 1/W$. Replacing Eq. (6.4) in Eq. (6.3), and using Eq. (6.5), a simple calculation gives

$$\frac{1}{\tau(E_F)} = \frac{\pi\rho(E_F)}{\hbar}\left(\frac{1}{\sqrt{N_c N_{\text{Ring}}}}\sum_{N_c N_{\text{Ring}}}\varepsilon_A^2 + \frac{1}{\sqrt{N_c N_{\text{Ring}}}}\sum_{N_c N_{\text{Ring}}}\varepsilon_B^2\right), \tag{6.6}$$

and finally

$$\ell_{\text{el}} = 18\sqrt{3}a_{\text{cc}}(\gamma_0/W)^2 N. \tag{6.7}$$

Such an expression shows that for fixed disorder strength, ℓ_{el} upscales linearly with the nanotube diameter, an unusual property suggesting a ballistic regime in the limit of very large diameter (or equivalently two-dimensional graphene). In Section 6.1.1, experimental data evidencing micrometers long mean free paths up to room temperature confirm such exceptional conduction capability of metallic carbon nanotubes.

As typical parameters, we consider an armchair (5, 5) nanotube, with disorder $W = 0.2\gamma_0$, and after applying Eq. (6.7), $\ell_{\text{el}} \sim 550$ nm, a value much longer than the circumference, thus indicating a ballistic motion for long distances. Figure 6.1 shows ℓ_{el} in armchair metallic nanotubes with increasing diameters (from (5, 5) to (30, 30)), using the Kubo approach implemented within the order N method (see Section 4.4.4). The results fully validate the predicted scaling law with tube diameter in the vicinity of the Dirac point (with, for instance, $\ell_{\text{el}}(15,15)/\ell_{\text{el}}(5,5) = 3$).

An additional remarkable feature lies in the strong energy dependence of ℓ_{el}, particularly close to onsets of new subbands (or van Hove singularities). Besides, for higher energy subbands, the $1/W^2$ remains, but ℓ_{el} are found to be much smaller, without a linear scaling property with diameter. Such a large tunability of transport length scales upon small energy level shift was the origin of intense debate concerning the inherent transport mechanisms in single- and multiwalled carbon nanotubes in the late 1990s. The ballistic or diffusive nature of transport is shown here to be highly dependent on the energy-dependent transport mechanism, beyond the nature and strength of superimposed disorder. We note that multiwalled carbon nanotubes were shown to be particularly interesting, owing to intrinsic incommensurability between neighboring shells, allowing for the emergence of a diffusive regime, and quantum interference phenomena in the limit of ultraclean systems (Roche & Saito 2001; Roche et al. 2001). Concerning

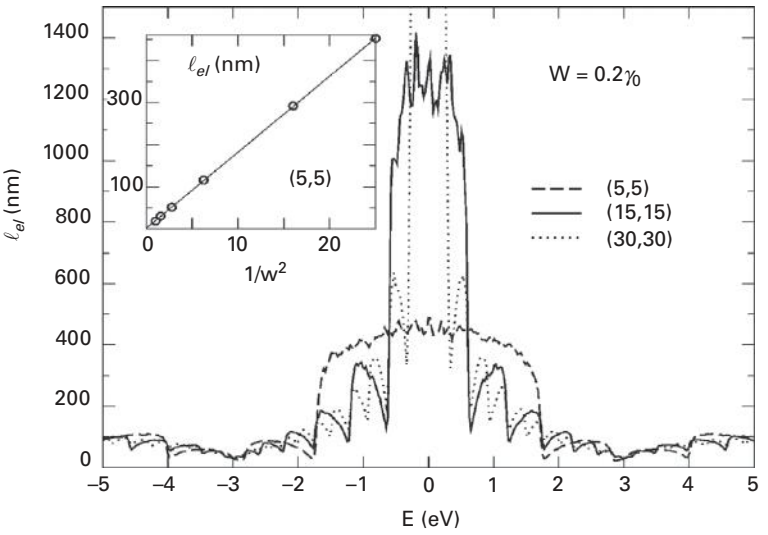

Figure 6.1 Energy-dependent mean-free path as a function of diameter. Inset: ℓ_{el} versus W showing the $1/W^2$ scaling Fermi. (Reprinted with permission from Triozon et al. (2004). Copyright (2004) by the American Physical Society)

graphene nanoribbons, ℓ_{el} can also be derived in a similar fashion in metallic armchair graphene nanoribbons as (Areshkin et al. 2007)

$$\ell_{\mathrm{el}} = 12(\gamma_0/W)^2(N+1)a_{\mathrm{CC}}, \tag{6.8}$$

which also scales linearly with the ribbon width and follows $\ell_{\mathrm{el}} \sim 1/W^2$.

In conclusion, low-dimensional (metallic) graphene-related systems exhibit mean free paths that may diverge with increasing diameter or ribbon width for a fixed disorder strength W. Notwithstanding, only armchair nanotubes truly behave as 1D massless Dirac fermions close to the charge neutrality point since gaps form for all types of GNRs when edge boundary conditions are properly taken into account (chemical passivation of unsaturated dangling bonds, edge reconstruction, etc.). In that sense, armchair metallic nanotubes present the unique case of one-dimensional ballistic conductors up to room temperature.

6.1.1 Temperature Dependence of the Mean Free Path

The results presented in the section above have established the zero-temperature limit for ℓ_{el}. Although the coupling between electrons and acoustic vibrational degrees of freedom is weak at low temperatures, the temperature dependence of the mean free path can only be derived when properly taking into account inelastic scattering mediated by electron–phonon coupling. Besides, the temperature dependence of a nanotube resistance can also be driven by the electrical bias-induced excitation of phonon modes whose characteristics will depend on applied bias voltage, regardless of the temperature of the surrounding experimental setup.

In the low-temperature (and low-bias) regime, only acoustic modes play some role, which can be accounted for using perturbation theory (Fermi golden rule) and the Boltzmann transport equation (Lazzeri & Mauri 2006). Alternatively, the effect of low-energy vibrational disorder (introducing time-dependent lattice distortions) can also be explored through the Kubo approach, using a time-dependent renormalization of the off-diagonal coupling matrix elements of the Hamiltonian (Ishii et al. 2010). As a result, an inelastic (temperature-dependent) mean free path can be calculated: we named ℓ such a mean free path, which differs from $\ell_{\rm el}$, which gives the zero-temperature limit.

Technically, the time-dependent atomic displacements obtained by molecular dynamics can be transfered to renormalization of π–π off-diagonal coupling elements $\gamma_{ij}(t)$, which thus encode the electron–phonon interaction in both harmonic and anharmonic regimes, as discussed in Gheorghe et al. (2005). A possible starting point is the empirical form $\gamma_{ij}(t) = \gamma_{ij}^0 |\mathbf{R}_i^0 - \mathbf{R}_j^0|^2 / |\mathbf{R}_i(t) - \mathbf{R}_j(t)|^2$ (Harrison 1989), with $\gamma_{ij}^0 = 2.5\,\text{eV}$, where $\mathbf{R}_i(t)$ represents the atomic position at time t and $\mathbf{R}_i^0$ is at equilibrium. The phonon-vibration effects are accounted for by the molecular dynamics (MD) simulation using the Brenner–Tersoff potential for C–C bonds (Brenner 1990). For fixed temperature T, the velocities of carbon atoms are normalized at each time step by the conditions of $\sum_{i=1}^{N_c} M_c \dot{\mathbf{R}}_i^2/2 = 3N_c k_B T/2$, where M_c and N_c are mass and number of carbon atoms, and k_B is the Boltzmann constant (Ishii et al. 2009).

Figure 6.2 shows the computed resistances of (5, 5) SWNTs at $T = 0$ K and $T = 60$ K as a function of SWNT length L and for $W = 0.2$ (Anderson disorder). It is interesting

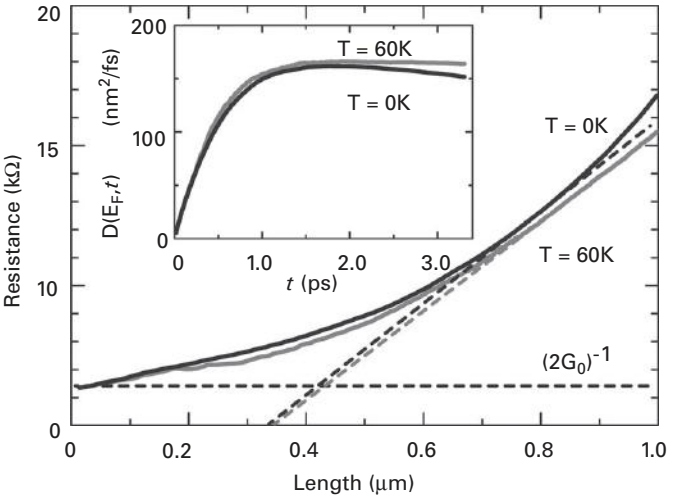

Figure 6.2 Length dependence of the total resistance for a (5, 5) SWNT at 0 K (black line) and 60 K (gray line) with Anderson disorder potential $W = 0.2$. $(2G_0)^{-1}$ is also shown (horizontal dashed line), with $G_0 = 2e^2/h$. The other dashed line pinpoints the crossover from the ballistic to the diffusive regime. Inset: Time dependence of the diffusion coefficient for the same parameters. (Figure adapted from Ishii et al. (2010). Copyright (2010) by the American Physical Society)

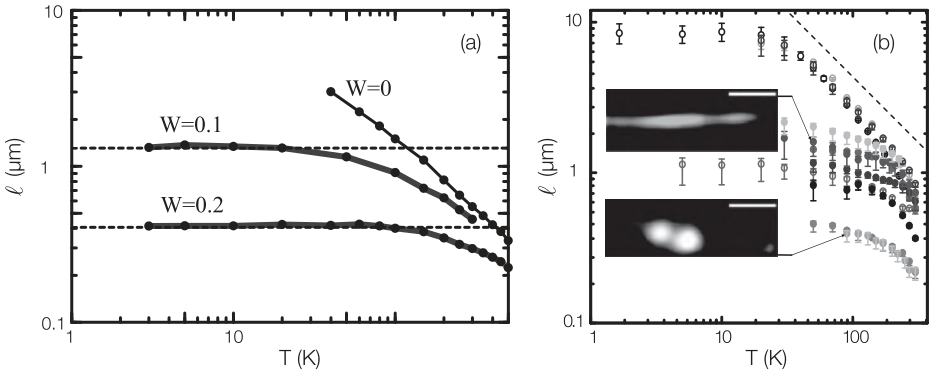

Figure 6.3 (a) Temperature dependence of the mean free paths for a (5, 5) SWNT with both dynamical disorder and several strengths of the static disorder potential W. (Reproduced with permission from Ishii et al. (2010). Copyright (2010) by the American Physical Society.) (b) Mean free path for several nanotubes (metallic and semiconducting). Most metallic SWNTs (open circles) saturate at higher values than that of semiconductors (closed circles), T^{-1} (dashed line). Insets: Scanning gate microscopy images taken on two different devices. Less current intensity is indicated by brighter color (gray). Defects are highlighted by the bright region (suppressed current). Scale bar is 500 nm. (Reproduced with permission from Purewal et al. (2007). Copyright (2007) by the American Physical Society. Courtesy of Philip Kim)

to observe that the decay of the diffusion coefficient at zero temperature (inset) due to localization effects is fully suppressed at $T = 60$ K (as expected when introducing decoherence effects). Importantly, the length-dependent resistance pinpoints the crossover from a ballistic-like (length-independent) to a diffusive behavior in which the increase of resistance scales linearly with tube length. The crossing point of the two asymptotic lines for ballistic and diffusive regimes enables estimation of the mean free path, $\ell \sim 0.4$ μm at $T = 60$ K (for $W = 0.2$) (Ishii et al. 2010).

In Fig. 6.3(a), the logarithm plot of temperature-dependent $\ell(T)$ is shown for $W = 0, 0.1$, and 0.2 with increasing temperature. The low-temperature behavior of $\ell(T)$ is clearly fixed by the static disorder strength ($T < 50$ K), whereas electron–phonon scattering events dominate in the high-temperature regime, whatever the static disorder strength. The scaling behavior $\ell(T) \sim T^{-1}$ obtained numerically is in perfect agreement with Fermi's golden rule (Suzuura & Ando 2002) and with experimental data (Purewal et al. 2007) shown in Fig. 6.3(b).

6.1.2 Inelastic Mean Free Path in the High-Bias Regime

At very high temperature or in the high-bias voltage regime (that is, for $V_{\text{bias}} \geq 0.2$ V), the contribution of inelastic phenomena eventually yields strong current saturation. This was first reported by Yao and coworkers in metallic tubes (Yao et al. 2000). In this experiment, a low-bias linear current–voltage characteristic is first observed, followed by a current saturation for $V_{\text{bias}} \sim 1$ V, regardless of the temperature of the sample. The overall $I(V)$ response function is actually well-described by a phenomenological law,

$$I = \frac{V}{R_0 + V/I_0}, \tag{6.9}$$

with R_0 and I_0 two constants giving, respectively a voltage-independent intrinsic resistance and a current saturation value in the order of 20−130 μA (regardless of the tube diameter). The interpretation assumes that the saturation comes from the strong inelastic backscattering of electrons coupled to optic (or zone boundary) vibrational modes. In this scenario, the inelastic mean free path is the propagating length needed for electrons to accumulate an additional energy of $\sim\hbar\Omega_{\rm ph}$, the relevant optical phonon mode that will instantaneously produce electron backscattering. Assuming a linear potential drop between voltage probes separated by L, i.e., $V(l) = V_{\rm bias}(1 - l/L)$, where l is the distance from the source, then the energy gain reads $e\int_0^{\ell_{\rm ie}} \partial V/\partial l dl = \hbar\Omega_{\rm ph}$ from which one finds $\ell_{\rm ie} = (\hbar\Omega_{\rm ph}L)/eV_{\rm bias}$. Besides, assuming that the length-dependent resistance can be split into two contributions, by virtue of the Mathiessen rule, one can write

$$R(L) = \frac{h}{4e^2}\frac{L}{\ell_{\rm el}} + \frac{h}{4e^2}\frac{L}{\ell_{\rm ie}} = R_0 + \frac{h}{4e^2}\frac{eV_{\rm bias}}{\hbar\Omega_{\rm ph}} = R_0 + \frac{V_{\rm bias}}{I_0}$$

with $R_0 = h/4e^2 L_{\rm tube}/\ell_{\rm el}$ the intrinsic resistance and $\ell_{\rm el}$ the elastic mean free path, whereas $I_0 = (4e/h)\hbar\Omega_{\rm ph}$, which is indeed in the range 20 − 30 μA depending on the chosen phonon energy. Note that if $\ell_{\rm el}$ is an intrinsic measure of the elastic disorder strength (defect density, etc.) which is a bias- and temperature-independent quantity, $\ell_{\rm ie}$ is voltage dependent in this model, but at a fixed voltage it should remain inversely proportional to the nanotube length. Intriguingly however, by using a semiclassical Boltzmann approach, a fitting of the experimental data is achieved taking a fixed $\ell_{\rm ie}$ (for a fixed tube length), independent of the voltage bias (Yao et al. 2000).

The observation of a length-dependent scaling of the resistance has been reported in several experimental works (Javey et al. 2004; Park et al. 2004). Lower resistance was measured for shorter tubes, and current saturation was shown to be reduced when decreasing $L_{\rm tube}$ from 700 to 50 nm at which no saturation was observed for voltage bias up to 1.5 V. Again, the analysis within the Fermi golden rule and Boltzmann approach allows extrapolation of some typical values for the inelastic scattering lengths that can be as short as 10 nm (Javey et al. 2004).

However, the discrepancy or strong fluctuations between theoretical estimates obtained by fitting procedures and the computed $\ell_{\rm ie}$ (with perturbative theory), even when using *ab initio* calculations (Lazzeri & Mauri 2006; Lazzeri et al. 2006), raises some fundamental questions about the applicability of Fermi's golden rule, the Mathiessen rule and semiclassical transport theory to tackle inelastic quantum transport in metallic carbon nanotubes, or within the context of carbon nanotubes-based field-effect transistors (Appenzeller et al. 2004). The most probable scenario is that a scheme beyond the widely used Boltzmann equation is needed in situations like this, which lie between the fully decoherent and fully coherent regimes.

Furthermore, nonperturbative effects of electron–phonon interaction, which are beyond the validity of the Boltzmann approach, may also emerge. Indeed, although the Peierls distortion mechanism is ineffective in metallic SWNTs to produce a

semiconducting state even at very low temperatures (Mintmire et al. 1992; Saito et al. 1992b) (except possibly for very short radius SWNTs (Connétable et al. 2005)), modifications in the phonon band structure due to a related mechanism, the Kohn anomaly (Kohn 1959a), are observable at moderate temperatures in both SWNTs (Farhat et al. 2007) and graphene (Pisana et al. 2007). A related Peierls-like mechanism was proposed at high bias, leading to nonequilibrium gaps at half the optical phonon energy above/below the charge neutrality point ($\pm\hbar\Omega/2$), which in turn would be observable as a small plateau in the current–voltage characteristics. The theoretical method adopted to tackle such phenomena employs the generalized Landauer–Büttiker formula expanded in a higher dimensional space (the electron–phonon Fock space) (Anda et al. 1994; Bonča & Trugman 1995). This approach can cope with the strong coupling of electrons to certain symmetry-selected phonon modes, a regime out of reach of perturbative methods and semiclassical transport concepts. We refer to Foa Torres and Roche (2006) and Foa Torres et al. (2008) for more details.

6.1.3 Quantum Interference Effects and Localization Phenomena in Disordered Graphene-Based Materials

A knowledge of the mean free path $\ell_{\rm el}$ in disordered graphene-related systems is a first essential step since it allows identification of the frontier between the ballistic and the diffusive propagation of wavepackets. The localization length ξ is the other physical length scale that defines the transition toward the insulating regime in which the conductance further decays exponentially with the system length as $G \sim G_0 \exp(-L/\xi)$ (Section 4.4.5).

Weak localization phenomena have been clearly observed in multiwalled carbon nanotubes with diameter ranging from ~ 3 to 20 nm (Bachtold et al. 1999; Stojetz et al. 2005) as well as in graphene nanoribbons with widths in the order of $\sim 200 - 500$ nm (Tikhonenko et al. 2008). Weak antilocalization (WAL) has also been observed in graphene-based materials and relate to the pseudospin-related Berry's phase interferences, and induced sign reversal of the quantum correction (Section 4.4.5). Also, the transition from weak antilocalization to weak localization has also been reported for reduced ribbon width (Tikhonenko et al. 2008). As the width of the graphene ribbons is reduced from ~ 20 nm down to ~ 5 nm, weak antilocalization is eventually suppressed, owing to an increasing contribution of edge defects and enhanced contribution of other disorder sources (topological, vacancies, adsorbed impurities, etc.).

It is instructive to analyze the variation of quantum transport features with varying dimensionality or defect-induced broken symmetries. Weak localization effects are generally revealed experimentally by tuning the strength of quantum corrections through the application of an external magnetic field (as explained in Section 4.4.5). However, for low-dimensional systems such as carbon nanotubes or graphene ribbons (with typical diameters or widths $\leq$10 nm), large magnetic fields also severely affect the electronic band structures, making the analysis of resulting magnetofingerprints much

more difficult. Some illustrative examples have been presented in multiwalled carbon nanotubes (Bachtold et al. 1999; Stojetz et al. 2005), and in graphene nanoribbons (Poumirol et al. 2010; Ribeiro et al. 2011).

We provide here the most representative quantum localization effects in graphene nanoribbons. As seen in Chapter 2, zigzag-type GNRs display quite peculiar electronic properties, with low-energy wavefunctions sharply localized along the ribbon edges. Using the Landauer–Büttiker approach, the scaling properties of the quantum conductance of these systems can be numerically investigated. The typical energy dependence of conductance profiles for both zGNR and aGNR of width ∼20 nm are shown in Fig. 6.4(a) and (b), for the clean, weak disorder ($W = 0.5$) and strong disorder ($W = 2$) limits. For weak disorder ($W = 0.5$, Fig. 6.4(a)), transport in aGNR seems much less altered than the behavior displayed by zGNR. This contrasts with

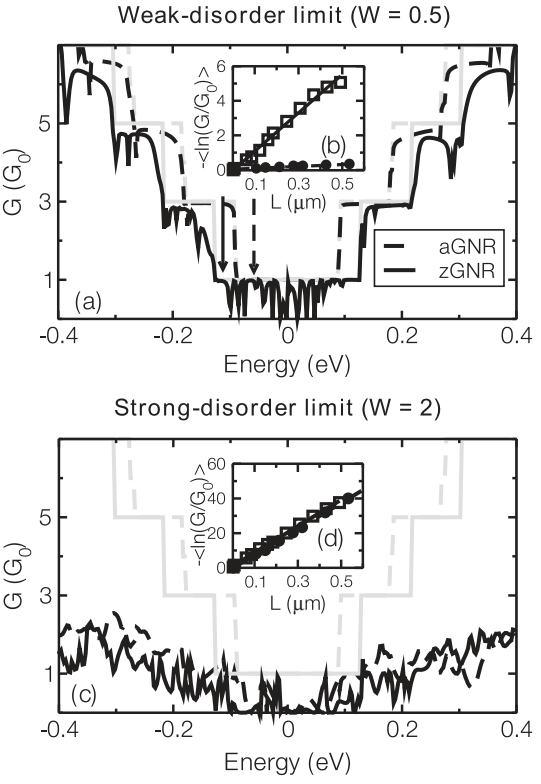

Figure 6.4 (a) Conductance for a single disorder configuration of a zigzag (solid black line) and an armchair (dashed black line) GNR with width ∼20 nm ($W = 0.5$). Gray lines correspond to ideal zigzag (solid line) and armchair (dashed lines) ribbons. (b) Configuration averaged (over ∼400 samples) normalized conductance as a function of GNR length for both zigzag and armchair GNRs. The solid (dashed) arrow shows the energy at which the calculations for the zGNR (aGNR) have been performed. (c) and (d) Same information as for (a) and (b) but for a larger disorder strength ($W = 2$). (Adapted from Lherbier, Biel et al. (2008) by courtesy of Blanca Biel)

the case of stronger disorder ($W = 0.5$), where the conductance of both aGNR and zGNR are strongly reduced at low energies, with similar fluctuations indicating strong localization (Fig. 6.4(c)). Figure 6.4(b) and (d) show the exponential damping of averaged conductances (over ~ 400 different disorder configurations), i.e., $\langle \ln G/G_0 \rangle \sim L/\xi$. By fitting these numerical results, ξ values in zigzag ribbons are found to be smaller than armchair ribbons by up to two orders of magnitude at high enough energies. In contrast, for larger disorder strength, such as $W = 2$ (Fig. 6.4(c)), the localization lengths for both types of ribbons become almost indistinguishable, showing that edge symmetry then loses its integrity.

An important result of mesoscopic physics (presented in Section 4.4.5) is the existence of a fundamental relationship between $\ell_{\rm el}$ and ξ (referred to as the Thouless relation (Thouless 1977)). In a strictly 1D system, it can be analytically demonstrated that $\xi = 2\ell_{\rm el}$, whereas for quasi-1D systems (with $N_\perp(E)$ conducting channels), the relation is generalized as

$$\xi(E) = [\beta(N_\perp(E) - 1)/2 + 1]\ell_{\rm el}(E), \tag{6.10}$$

with β a factor dependent on the time-reversal symmetry (Beenakker 1997). Avriller et al. (2007) have extensively confirmed the applicability of such a foundational relation between transport length scales in chemically doped metallic carbon nanotubes, using the Landauer–Büttiker conductance method.

6.1.4 Edge Disorder and Transport Gaps in Graphene Nanoribbons

Low-temperature conductance measurements in the Coulomb blockade regime display large fluctuations (Stampfer et al. 2009) (see also Section 6.5.2) with an enhanced depletion of the conductance at low energy, referred to as a transport (or mobility) gap. The origin of such a transport gap has been debated theoretically, especially regarding the role of edge-disorder-induced localization effects (Akhmerov & Beenakker 2008; Areshkin et al. 2007; Cresti & Roche 2009; Evaldsson et al. 2008; Mucciolo et al. 2009; Wimmer et al. 2008). As shown below, the topological complexity of edge imperfections observed experimentally needs to be accounted for when analyzing the transport properties in edge-disorder GNRs.

In what follows, we discuss the transport properties in edge-disordered GNRs using Green's function technique (Cresti et al. 2007). As an illustration, we focus on the impact of various edge-disorder configurations by scrutinizing the conductance properties of several 16-zGNRs (with length $L = 500$ nm), with randomly removed carbon edge atoms with equal probability 7.5%, and varying complexity of the edge defects topology (see Fig. 6.5). The disorder profile is defined by the probability P, controlling the number of defects on each edge to $P \times L/a$, where $a = 2.46$ Å is the lattice parameter (within a precision of 2%). The edge-disorder profile is developed from a pristine zGNR and by removing edge carbon atoms randomly (as depicted in Fig. 6.5). The probability of removing atoms is chosen such that the total number of defects remains proportional

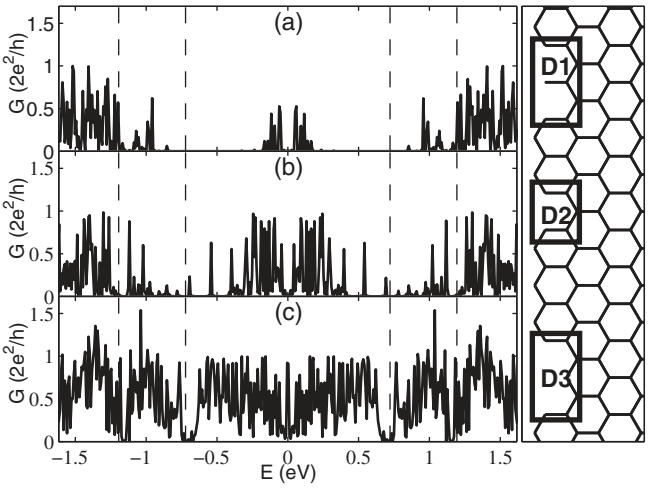

Figure 6.5 Left: Conductance of a disordered 16-zGNR (with length $L = 500$ nm) with 7.5% of randomly removed edge carbon atoms. Case (a) includes dangling atom defects (D1) and single (D2), and double (D3) missing hexagon defects, whereas D1 is prohibited in case (b) and D1 and D2 are disallowed for case (c). Right: A disordered ribbon edge with D1, D2, and D3 defects shown in boxes. (Reproduced with permission from Cresti and Roche (2009). Copyright (2009) by the American Physical Society)

to P. Transport properties for different defect types and comparable disorder strength can therefore be contrasted. Figure 6.5(a) denotes the richest edge defects profile which contains Klein defects (single dangling edge atoms, defect D1), together with missing hexagon defects, either one (defect D2), or two (defect D3).

Depending on the topology of edge defects, large transport fluctuations are obtained. Figure 6.5(a) shows the 16-zGNR conductance profile with the highest disorder complexity (largest variety of edge defects). The strong suppression of transmission in the first plateau (region marked by two vertical lines close to $E = 0$), suggests an Anderson insulating regime with a localization length $\xi \lesssim L$. The conductance of a disordered ribbon in which Klein defects (D1) are discarded is shown in Fig. 6.5(b). In that case, the conductance remains large in the first plateau, but appears more suppressed at higher energies. Finally, by removing the possibility of both Klein defects and single missing hexagons (D1 and D2), a completely different transport regime forms (for the same length of the graphene ribbon). Figure 6.5(c) shows that the conductance is very close to $G_0 = 2e^2/h$, which gives the ballistic limit of the clean system (Wakabayashi et al. 1999). The conductance can thus range from a localized to a quasiballistic regime depending on the local defect complexity and ribbon length. The structural property of local edge defects has therefore a genuine impact on resulting transport properties of GNRs.

The average conductance $G = \overline{T} \times (2e^2/h)$, where $\overline{T}$ is the averaged transmission coefficient over 1000 different configurations, is shown in Fig. 6.6, for 16-zGNR with single missing hexagons distributed with a probability $P = 7.5\%$. The quantized

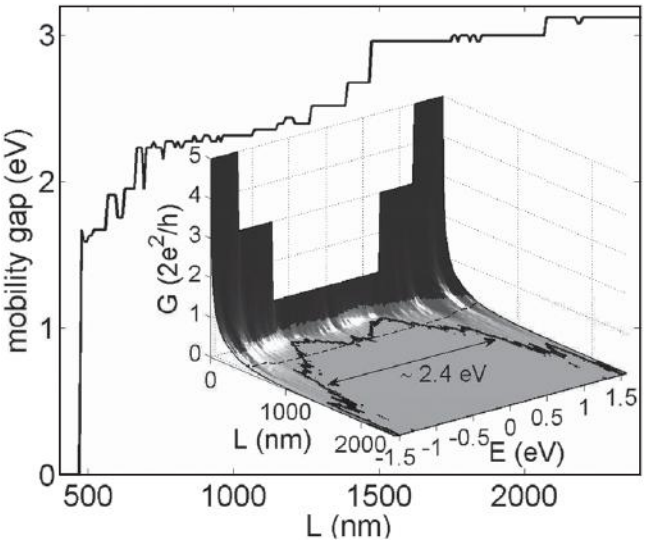

Figure 6.6 Transport gap evolution with L. Inset: Average conductance (1000 different configurations) of disordered 16-zGNR (defects are single missing hexagons with density $P = 7.5\%$). The bold line marks the (L, E) region for which $G < 0.01 \times 2e^2/h$. The L dependence of the transport gap width starts from $L \geq 470$ nm (dashed line). A particular value is shown (double arrow line) at $L = 1250$ nm. (Reproduced with permission from Cresti and Roche (2009). Copyright (2009) by the American Physical Society. Courtesy of Alessandro Cresti)

conductance of pristine GNRs sets the limit at $L = 0$. With increasing L, the transport regime evolves from a diffusive to an insulating state evidenced by the exponential decay of the conductance (Fig. 6.6). The crossover between diffusive and localization regimes is identified by comparing $\Delta(T)/\overline{T}$ and $\Delta(\ln T)/\overline{\ln T}$ (Δ stands for the standard deviation). The *transport (or mobility) gap* of the GNR is defined by an energy region for which $G < 0.01 \times 2e^2/h$. Here, such a transport gap is obtained when $L \geq 470$ nm (dotted line), but then further enlarges with the ribbon length, owing to the accumulation of quantum interferences. The existence of highly chemically reactive and disordered edges enhances the transport gap fluctuations, yielding a clear caveat against using nanoribbons in nanoelectronic devices, which would require perfectly controlled current–voltage characteristics, with very small sample-to-sample fluctuations.

6.2 Transport Properties in Disordered Two-Dimensional Graphene

6.2.1 Two-Dimensional Disordered Graphene: Experimental and Theoretical Overview

The nature of disorder in graphene and its impact on transport properties deserve a detailed investigation. First, because there exist many possible sources of disorder which are introduced during the material fabrication (graphite exfoliation, epitaxial, or

CVD growth) as well as during the device fabrication, which includes transfer to other substrate, contact deposition, electrical current cleaning, and so forth. These methods produce either local or more long-range lattice imperfections – defects, impurities, ripples, and long-range strain deformations – which impact graphene's electronic and transport properties in different ways, also depending on the charge densities and magnitude of screening phenomena. The possibility of observing unique transport features such as Klein tunneling, electron collimation, or weak antilocalization phenomena is unique in condensed matter, but strongly sensitive to the nature of crystalline imperfections, and the atomic range of the corresponding disorder potential.

Defects in exfoliated graphene transfered to a silicon dioxide substrate generally range from local structural imperfections or glued adatoms to long-range Coulomb scattering potentials produced by charged impurities (trapped in the oxide) or ripples quenched by substrate roughness after graphene deposition. In the high-density limit, a nearly linear carrier-density-dependent conductivity $\sigma(n) \sim n$ has been observed experimentally (Yan & Fuhrer 2011) (and convincingly interpreted with semiclassical physics, Section 4.3). Close to the Dirac point, when graphene is deposited onto SiO_2, the formation of so-called electron–hole puddles (which are spatially fluctuating charge densities) produces percolation transport which precludes transition to the formation of the expected insulating state.

For sufficiently clean graphene, the Dirac point conductivity usually remains finite even down to cryogenic temperatures, but its value is not universal and varies from sample to sample (depending on sample quality and precise preparation process). Significantly low electron–phonon scattering has been experimentally reported (Chen et al. 2008), implying that static disorder (especially close to the Dirac point) dominates low-temperature resistivity. Figure 6.7 (right inset) shows typical behavior for a pristine graphene sample in a large density range, which can be well-fitted with $\sigma(n) = (1/(ne\mu_L) + \rho_S)^{-1}$ with $\mu_L \sim 26,000$ cm^2/Vs, and $\rho_S = 53\ \Omega$, while the density is extracted from gate voltage V_g using $n = C_g(V_g - V_g{}^{\min})/e$ ($V_g{}^{\min}$ being the value at which conductivity is minimum, while typical gate capacitance $C_g = 11$ nF/cm^2) (taken from Chen et al. (2008)).

A popular quantity to characterize graphene's structural quality is the charge mobility, which at zero temperature is given by $\mu(E) = \sigma_{\rm sc}(E)/en(E)$, where $\sigma_{\rm sc} = e^2\rho(E)v(E)\ell_{\rm el}$ is the semiclassical conductivity deduced from the Einstein formula, with $\rho(E)$ the DOS, $n(E)$ the charge density at energy E, $\ell_{\rm el}$ the elastic mean free path, and e the elementary charge (assuming zero temperature). Close to the charge neutrality (or Dirac) point, the measured experimental conductivities are mostly found to range within $\sim 2 - 5e^2/h$, although the charge mobility can vary by almost one order of magnitude (Jiang et al. 2007; Oezyilmaz et al. 2007; Zhang et al. 2006). This effect has been attributed to the change of charge density due to the doping from the substrate and/or contacts.

On the theoretical side, the calculation of the Kubo conductivity for 2D graphene with short-range disorder, and within the self-consistent Born approximation (SCBA), yields $\sigma_{xx}^{\min} = 4e^2/\pi h$ (h is the Planck constant) for the two Dirac nodes (Shon & Ando 1998)

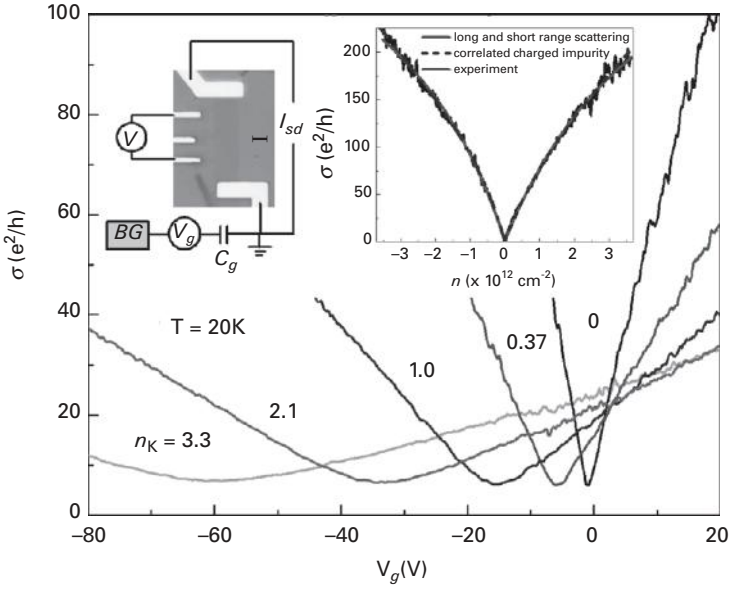

Figure 6.7 Conductivity versus gate voltage (at K) for pristine (undoped) graphene (right inset), and chemically doped graphene (main plot). Different curves are for potassium coverage density ranges within $[0.37, 3.3] \times 10^{12}$ cm^{-2}. Top-left inset is an optical microscope image of the monolayer graphene device, with a schematic of the measurement circuit. Courtesy of M. Fuhrer. (Reproduced with permission from Yan and Fuhrer (2011). Copyright (2011) by the American Physical Society)

(see Section 6.2.4), which is typically $1/\pi$ smaller than most of the experimental data. Numerical calculations using the Kubo formula confirm such a prediction (Lherbier, Biel et al. 2008; Lherbier et al. 2011, Nomura & MacDonald 2006). By contrast, by assuming that elastic scattering is dominated by a screened Coulomb potential (ionized impurities), Nomura & MacDonald 2006 have numerically reproduced the low-energy dependence of the electronic conductivity using a full quantum approach of the Kubo formula and performing a finite-size scaling analysis. They found that $\sigma_{xx}^{\min} \sim e^2/h$ close to the Dirac point, in better agreement with most experiments. Other calculations have analyzed the effect of screened Coulomb potential on semiclassical Bloch–Boltzmann conductivity, taking into account the role of background zero potential fluctuations (electron–hole puddles) (Das Sarma et al. 2011). These space-dependent charged inhomogeneities provide percolation paths for the propagating charges down to the zero-density limit, which prohibit the exploration of transport at the Dirac point and yield a nonuniversal minimum conductivity which is sample dependent.

Unique transport features develop in graphene with low disorder. The Klein tunneling (KT) mechanism (see Section 5.1) is the first intrinsic and spectacular manifestation of massless Dirac fermion physics where backward reflection is partially or totally suppressed (depending on the incident angle of the incoming wavepacket and the height and width of the barrier) when charge crosses a local tunneling barrier. This result

contrasts with usual behavior in Schrödinger physics in which the propagation of an electronic wavepacket is exponentially damped when crossing a barrier of increasing width. Klein tunneling stands as an efficient mechanism to suppress localization effects, provided that the impurity potential is sufficiently long-range to prohibit intervalley scattering between the two inequivalent Dirac cones. The KT mechanism is inherent to the symmetric electron–hole electronic band structure and the pseudospin degree of freedom associated with the AB sublattice degeneracy. In metallic carbon nanotubes (Ando et al. 1998), a similar mechanism leads to a total suppression of backscattering, enforcing a ballistic motion of charges up to micrometers and up to room temperature.

Pseudospin shares similar symmetries with the spin degree of freedom, and as such, the corresponding wavefunctions acquire extra phase factor which, when accumulated along a closed trajectory, produces an interference pattern dominated by a Berry's phase. The observation of the WAL in graphene (Tikhonenko et al. 2008, 2009) is such a manifestation of pseudospin effects on phase interferences. In 2006, McCann and colleagues provided a solid theoretical derivation of the Cooperons quantum correction in the presence of pseudospin-related Berry's phase factors (McCann et al. 2006). The nature of disorder and contribution of intravalley versus intervalley scattering events is actually crucial for clarifying the predominance of weak localization (WL) versus WAL phenomena, as discussed later (see Section 6.2.6 for details). The possibility of strong (Anderson) localization is also inherent to the nature of disorder, and is expected to follow the weak localization regime, as dictated by the scaling theory of localization (Lee & Ramakrishnan 1985).

Finally, intentional doping of graphene is a versatile way to tune electronic properties. The first experimental attempt was made using a controlled flux of atomic potassium, introducing physisorbed atoms to the graphene substrate, and resulting in a Fermi level shift and conductivity decrease. Figure 6.7 illustrates such a chemical doping effect driven by the physisorption of potassium atoms, which produce scattering centers and weak electron transfer to the graphene substrate. When the potassium coverage density ranges are varied within $[0.37, 3.3] \times 10^{12}$ cm^{-2}, a continuous degradation of the conductivity is observed together with an energy downshift of the minimum conductivity (measured at the Dirac point) driven by charge-transfer effects (Chen et al. 2008; Yan & Fuhrer 2011). In parallel, theoretical calculations suggested that boron and nitrogen impurities in substitution of carbon atoms would bring more spectacular impact in conduction, such as electron–hole transport asymmetry (Lherbier, Biel et al. 2008) or mobility gaps in doped graphene nanoribbons (Biel, Triozon, Niquet et al. 2009).

In the next sections, we present the various possible sources of disorder in two-dimensional graphene and their specific impact on transport properties. We start from the more academic (but generic) short-range potential such as the Anderson disorder or long-range potential profile (Coulomb potential), and continue with more structurally and chemically invasive defects such as adsorbed oxygen and hydrogen atoms (see Section 10.4). The latter allow stronger tunability of disorder strength, functionalities (such as intrinsic magnetism), and transport regimes in graphene materials. General analytical results are derived either using the semiclassical Boltzmann transport

equation or its quantum generalization (Kubo–Greenwood method). The main transport characteristics in various forms of disordered graphene-related systems are ascertained, and the limitations of the semiclassical transport description are given and illustrated. We also discuss how weak antilocalization phenomena develop and what governs the crossover from weak to strong localization, using a comprehensive disorder model. This is followed by an analysis of the impact of structural defects such as monovacancies and divacancies, as well as grain boundaries in polycrystalline graphene, which fix an intrinsic limit for charge mobilities in CVD-grown graphene. Finally, quantum transport in strongly damaged graphene is discussed, with a focus on defects such as monatomic oxygen- and hydrogen-adsorbed defects, which are the focus of many recent experiments.

6.2.2 Metallic versus Insulating State and Minimum Conductivity

The effect of disorder in metallic materials has been a greatly debated issue. A key question has been to understand how a metallic system will change to an insulating state with the increase in disorder in the material. Sir Nevill Mott proposed that the metallic state persists as long as the mean free path remains larger than the Fermi wavelength (Mott 1990). Beyond that scale, the system was proposed to undergo a discontinuous transition to the insulating regime, with vanishing conductivity at zero temperature. Assuming the conductivity as $\sigma = \frac{e^2}{h} k_F \ell_{\mathrm{el}}$, this argument leads to a minimum conductivity given by $\sigma_{\min} = \frac{e^2}{h} k_F \lambda_F \sim \frac{e^2}{h}$ (known as the Ioffe–Regel criterion), before it abruptly vanishes at the metal–insulator transition.

It is worth noting that the effect of disorder in graphene is a rather delicate issue since the applicability of usual perturbative treatments (Fermi golden rule) and validity of a semiclassical approach (Bloch–Boltzmann) become questionable close to the Dirac point in many regards. First the assumption of weak disorder requires $\lambda_F \ll \ell_{\mathrm{el}}$, which becomes problematic close to the Dirac point since $\lambda_F \sim 2\sqrt{\pi/n} \to \infty$ as $n \to 0$ (when approaching the Dirac point). In the presence of disorder, the density of states is, however, increased compared to the clean case and charge density is then not strictly going down to zero. As discussed and illustrated in this section, different types of disorders produce a varying nature of electronic states close to the Dirac point, with inequivalent degree of localization depending on the underlying broken symmetries.

Weak Coulomb scatterers (charges trapped in the oxide) generate real space or charge inhomogeneities which, in the vicinity of the Dirac point, yield the formation of electron–hole puddles on the scale of about 30 nm. The absence of valley mixing then induces maximum effects of the Berry's phase, Klein tunneling, and antilocalization phenomena. The observed minimum conductivity in graphene, and absence of a localization regime, has been related to percolation transport conveyed by Klein-tunneling mechanisms (Chenaiov et al. 2007; Katsnelson 2012). In contrast, sharp defects such as vacancies or other types of structural defect with strongly broken local symmetries promote the predominance of intervalley scattering events and drive the electronic system to the Anderson insulating state.

6.2.3 Boltzmann Transport in Two-Dimensional Graphene

Using the expression derived in Section 4.3, the starting point for computing the relaxation time in graphene within the Fermi golden rule is given by

$$\frac{1}{\tau} = \frac{2\pi}{\hbar}\sum_{q}(1-\cos\theta_{k+q})|\langle k+q|\hat{U}|k\rangle|^2\delta(\varepsilon_{k+q}-\varepsilon_k), \tag{6.11}$$

introducing a scattering potential $\hat{U}$ which has an arbitrary form for the moment. Note that the relaxation time is also named *transport time*, and differs from the elastic scattering time, which is the lifetime of a plane wave state. (It is given by the same Eq. (6.11), excluding the $1-\cos\theta_{k+q}$ term.) The ratio between both timescales allows for some discussion about the nature of underlying disorder (Monteverde et al. 2010).

Figure 6.8 shows the different angles introduced for transformation of the integral factors. The following equations are straightforward to demonstrate: $q = 2k\sin\theta_{k+q}/2$ (the momentum transfer), $\theta_q = \pi/2 + \theta_{k+q}/2$, and $\cos\theta_q = -q/2k$. The $\sum_q$ sum is converted into an integral via $\sum_q = S/(2\pi)^2\int d^2q$, so that

$$\frac{1}{\tau} = \frac{2\pi}{\hbar}\frac{S}{(2\pi)^2}\int_0^{\infty} qdq\int_{-\pi}^{+\pi} d\theta_q(1-\cos\theta_{k+q})|\langle k+q|\hat{U}|k\rangle|^2\delta(\varepsilon_{k+q}-\varepsilon_k). \tag{6.12}$$

The term $|\langle k+q|\hat{U}|k\rangle|^2$ can be replaced by $n_i|V(q)|^2(1+\cos\theta_{k+q})/2$, where n_i is the impurity density, $V(q)$ the Fourier transform of the scattering potential, and the cosine term in parenthesis derives from the chirality factor that arises from the projection of the spinor wavefunctions between the incoming and outgoing states (for the case of no valley mixing). Indeed, recalling that the general form of the eigenstates reads as

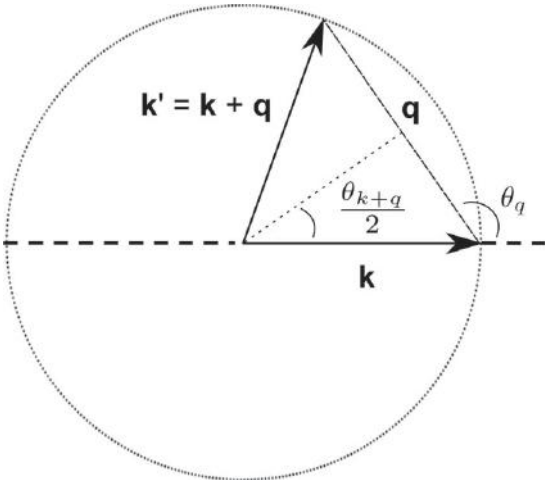

Figure 6.8 The wavevectors used in derivation of the relaxation scattering time. q denotes the total momentum transfer involved in the scattering event.

$$\Psi = \frac{1}{\sqrt{2}} \begin{pmatrix} 1 \\ e^{i\theta_k} \end{pmatrix} e^{i\mathbf{k}\cdot\mathbf{r}}, \tag{6.13}$$

$$\text{where } e^{i\theta_k} = \frac{k_x + ik_y}{|k|}, \tag{6.14}$$

the overlap between two wavevectors is

$$\int \Psi^{\dagger}(\mathbf{k})\Psi(\mathbf{k}+\mathbf{q})d\mathbf{r} = \frac{1}{2}(1,1)\cdot \begin{pmatrix} 1 \\ e^{i\theta_{k+q}} \end{pmatrix} = \frac{1}{2}(1 + e^{i\theta_{k+q}}), \tag{6.15}$$

which yields $|\int \Psi^{\dagger}(\mathbf{k})\Psi(\mathbf{k}+\mathbf{q})d\mathbf{r}|^2 = \frac{1}{2}(1+\cos\theta_{k+q})$. Equation (6.12) is finally rewritten by changing variables in the integrand using properties of the δ function. Straightforward calculations show that $\delta(\varepsilon_k - \varepsilon_{k+q}) = \frac{1}{\hbar v_F q}\delta(\cos\theta_q + \frac{q}{2k})$, and $1/\tau$ reads

$$\begin{aligned} \frac{1}{\tau} &= \frac{n_i}{2\pi\hbar^2 v_F}\int_0^{2k} |V(q)|^2 dq \int_{-1}^{+1} \frac{d\cos\theta_q}{\sqrt{1-\cos^2(\theta_q)}}(1-\cos^2\theta_{k+q})\delta\left(\cos\theta_q + \frac{q}{2k}\right) \\ &= \frac{n_i\rho(E_F)}{4\hbar}\int_0^{\pi} |V(q)|^2(1-\cos^2\theta_{k+q})d\theta_{k+q}. \end{aligned} \tag{6.16}$$

The first expression of Eq. (6.16) is clearly limited to variations of q from 0 to $2k$, while the contribution of the integrand of Eq. (6.16) cancels at $\theta = \pi$ as a consequence of pseudospin interferences. Depending on the form of $V(q)$, different Boltzmann conductivity behaviors are obtained, including long-range Coulomb ($V(q = 2k_f \sin(\theta/2)) \sim q^{-1}$), Gaussian white noise ($V(q) \sim q_0$), and Gaussian correlated disorder ($V(q) \sim e^{-q^2}$) mimicking a screened potential, as well as resonant scatterers that cause a maximal phase shift of $\pi/2$ between incoming and outgoing wavefunctions (Stauber et al. 2007). The expression of the Boltzmann conductivity (at zero temperature) can be derived from the Einstein (or Drude) formula $\sigma = 4e^2\rho(E)D(E)$, where $\rho(E) = 2|E|/(\pi \times (\hbar v_F)^2)$ gives the DOS close to the Dirac point, and $D(E) = v_F^2\tau/2$ the diffusion coefficient in the diffusive regime (remember $|E| = \hbar v_F\sqrt{n}$, introducing the charge density n). Then the semiclassical conductivity $\sigma_{sc}(E)$ reads

$$\sigma_{sc}(E) = \frac{4e^2}{h} \times \frac{|E|\tau}{2\hbar} = \frac{4e^2}{h}\frac{k\ell_{el}(E)}{2}, \tag{6.17}$$

with the transport time τ given by Eq. (6.16). The final expression of the Boltzmann conductivity depends on the nature of the scattering potential. Short-range scatters are defined by fluctuations of the potential profile on the scale of the carbon–carbon spacing (vacancies, adatoms, etc.) and introduce marked valley mixing (coupling between k vectors distant in the Brillouin zone, located at different valley–intervalley scattering). The Anderson model is one example of such disorder, which for sufficiently large potential strength breaks all symmetries of graphene. In contrast, long-range scatters are defined by potential profiles which change smoothly at the atomic scale, restricting scattering events to short momentum transfer in reciprocal space. This limits the

possibility of scattering events to intravalley transitions, which has profound consequences on all transport properties.

Long-Range Disorder

Coulomb scattering in graphene stems from long-range variations in the electrostatic potential caused by the presence of trapped charged impurities in the underlying substrate. This disordered Coulombian potential is further screened by the conduction electrons propagating through graphene, so its local strength becomes density-dependent (greater screening is expected at higher electron density). The long-range character of the induced electrostatic interaction could be included in the model of bare Coulomb-type scattering centers such as

$$U_i = \frac{1}{4\pi\epsilon_r\epsilon_0}\sum_{j=0}^{N_{\text{imp}}}\frac{e^2}{|r_i - r_j|}, \tag{6.18}$$

where ϵ_0 and ϵ_r stand, respectively, for the vacuum and relative permittivities and N_{imp} represents the number of scattering centers or impurities. However, the application of the bare Coulomb potential can only be justified for low values of the electron density when the screening effects limiting the range of the potential are negligible (Rycerz et al. 2007). To go beyond this, the simplest screened potential would be given by the Thomas–Fermi approximation,

$$U_i = U_{\text{TF}}\sum_{j=0}^{N_{\text{imp}}}\frac{\mathrm{e}^{-\xi_{\text{TF}}|r_i - r_j|}}{|r_i - r_j|}, \tag{6.19}$$

where the parameters U_{TF} and ξ_{TF} describe the strength and the range of the scattering centers for the Thomas–Fermi potential. The inclusion of screening makes it possible to achieve both the limits of Coulomb scattering (for low n) and short-range scattering (for high n). However, the singularity at $r_i = r_j$ in the Thomas–Fermi potential, Eq. (6.19), causes numerical instabilities. Using a self-consistent calculation of the impurity scattering in the random phase approximation (RPA), the scattering rate is found to be proportional to $\sqrt{n}/n_i$ (assuming a random distribution of charged impurities with density n_i), which leads to a Boltzmann conductivity at high density ($n \gg n_i$) (Adam et al. 2007),

$$\sigma_{\text{sc}} = \frac{e^2 v_F \tau}{\hbar}\sqrt{\frac{n}{\pi}} = \frac{Ce^2}{h}\frac{n}{n_i}, \tag{6.20}$$

with C a dimensionless parameter related to the scattering strength, and $C \simeq 20$ within the random-phase approximation (taking the dielectric screening from the SiO_2 substrate). Chen et al. (2008) experimentally explored the effect of charged impurities on the carrier conductivity by doping graphene with a controlled potassium flux in ultra-high vacuum (UHV). The gate voltage of minimum conductivity was found to become more negative with increase in doping (with reduced mobility), resulting from the electron doping induced by K atoms, which shifts the Fermi level up in energy with

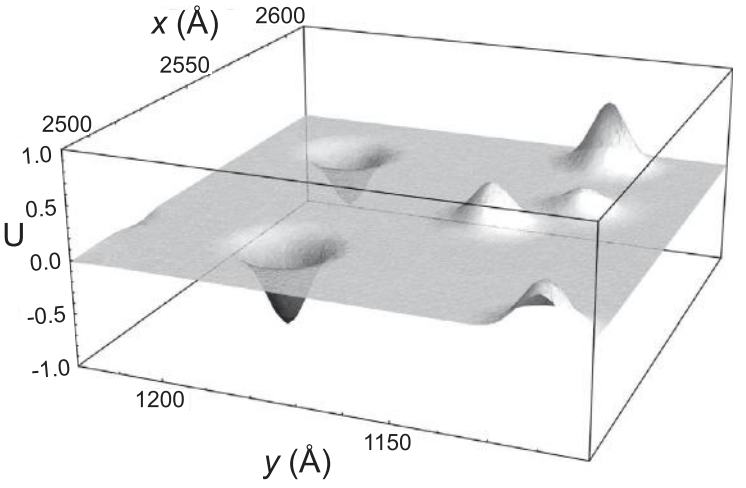

Figure 6.9 The long-range disorder potential $U(x, y)$. Courtesy of Frank Ortmann (Ortmann et al. 2011)

respect to the Dirac point. The value of $\sigma(V_g)$ was also found to become more linear with the increase in doping concentration n_i, in agreement with Eq. (6.20) (as seen in Fig. 6.7 main plot).

It is further convenient to use a model for screened potential based on a Gaussian function, to allow a more comprehensive analytical derivation of the semiclassical conductivity (Nomura & MacDonald 2007; Zhang et al. 2009). A realization of the disorder potential is introduced by randomly choosing N_{imp} lattice sites $\mathbf{r}_1, \mathbf{r}_2, \mathbf{r}_3, \ldots, \mathbf{r}_{N_{\text{imp}}}$ out of the total number N carbon sites in the disordered sample, and by randomly choosing the potential amplitude U_n at the nth site in the interval $[-W/2, W/2]$ (W given in γ_0 units). We then smooth the potential over a range ξ by convolution with a Gaussian function (see Fig. 6.9 for illustration):

$$U_{\text{imp}}(\mathbf{r}) = \sum_{n=1}^{N_{\text{imp}}} U_n e^{\frac{-|\mathbf{r}-\mathbf{r}_n|^2}{2\xi^2}}. \tag{6.21}$$

Assuming random configurations of different graphene samples with same size, ξ, W, and $n_{\text{imp}} = N_{\text{imp}}/N$, provides a statistical ensemble for a given disorder strength. We fix the impurity effective range $\xi = 3a_{\text{cc}} = 0.426$ nm as a typical value for a long-range potential, but vary W to describe different screening situations. Such a potential mimics the effect of screened charges trapped in the substrate. The disorder strength is quantified by the dimensionless correlator (Nomura & MacDonald 2007; Rycerz et al. 2007; Zhang et al. 2009),

$$K_0 = \frac{(L/N_{\text{imp}})^2}{(\hbar v_F)^2} \sum_{i=1}^{N_{\text{imp}}} \sum_{j=1}^{N_{\text{imp}}} \langle U_{\text{imp}}(r_i) U_{\text{imp}}(r_j) \rangle \tag{6.22}$$

of the random impurity potential (with vanishing average $\langle U_{\rm imp}\rangle = 0$ over disorder configurations). The impurity potential correlation function equals

$$\langle U_{\rm imp}(\mathbf{r})U_{\rm imp}(\mathbf{r}')\rangle = \frac{K_0(\hbar v_F)^2}{2\pi\xi^2}\mathrm{e}^{-\frac{|r-r'|^2}{2\xi^2}}. \tag{6.23}$$

Using $|V(q)|^2 = K_0(\hbar v_F)^2\mathrm{e}^{-q^2\xi^2/4}$, the scattering time (Eq. 6.16) can be derived, and after straightforward calculations, the Boltzmann conductivity is given by

$$\sigma_{\rm sc}(E) = \frac{4e^2}{h}\frac{\pi n\xi^2\mathrm{e}^{\pi n\xi^2}}{K_0 I_1(\pi n\xi^2)} \tag{6.24}$$

$$= \frac{2\sqrt{\pi}e^2}{K_0 h}\left[(2\pi n\xi^2)^{3/2} + O(n\xi^2)^{1/2}\right], \tag{6.25}$$

with the carrier density $n = k_F^2/\pi$ and I_1 the modified Bessel function ($I_1(x) = 1/\pi\int_0^\pi \mathrm{e}^{x\cos\theta}\cos\theta d\theta + 1/\pi\int_0^\infty \mathrm{e}^{(-x\cosh t - t)}dt$). $K_0 = 40.5 n_{\rm imp}(W/2\gamma_0)^2(\xi/\sqrt{3}a)^4$ where $n_{\rm imp} = N_{\rm imp}/N$ denotes the relative concentration (Klos & Zozoulenko 2010; Rycerz et al. 2007).

The leading term for high density can also be obtained considering the classical diffusion of a particle undergoing small-angle deflections from the random potential U. Defining $z = \pi n\xi^2$, $\sigma_{\rm sc}$ then exhibits two different limits. For $|z| \ll 1 \rightarrow \sigma_{\rm sc} \sim$ constant while $|z| \gg 1 \rightarrow \sigma_{\rm sc} \sim n^{3/2}$. The situation $|z| \ll 1$ arises when the Fermi wavelength is larger than the effective screening length $\lambda \gg \xi$, which describes a strong quantum scattering, while the opposite condition $|z| \gg 1$ drives to a classical scattering $\lambda \ll \xi$.

Short-Range Disorder: Anderson Disorder

A simple approximation for describing a short-range potential can be defined as $U(\mathbf{r}) = \sum_j U_j\delta(r - r_j)$, where U_j are onsite energies which are taken as random within a certain energy scale and following a given distribution (uniform, Gaussian, correlated distribution, etc.). By directly applying the Fermi golden rule, one obtains at the simplest approximation level

$$\frac{1}{\tau} = \frac{2\pi}{\hbar} \times \frac{\langle n_{\rm imp}U_i^2\rangle}{2}\frac{|E|}{2\pi(\hbar v_F)^2}, \tag{6.26}$$

and defining a dimensionless parameter $W = \frac{\langle n_{\rm imp}U_i^2\rangle}{4\pi(\hbar v_F)^2}$, we get $\tau = \frac{2\pi}{\hbar}|E|W$ and

$$\sigma_{\rm BB} = \frac{2e^2}{\pi h} \times \frac{1}{W}, \tag{6.27}$$

which means that the Bloch–Boltzmann conductivity is a constant, independent of the energy close to the Dirac point (illustrated in Fig. 6.13 inset). The Anderson disorder roughly mimics neutral impurities such as structural defects, dislocation lines, or adatoms, although the local geometry and chemical reactivity of defects and impurities actually demand more sophisticated *ab initio* calculations if aiming at quantitative predictions. An interesting aspect of this model is, however, that numerical simulations can

be contrasted with analytical results derived in the SCBA (Ostrovsky et al. 2006; Shon & Ando 1998). First, the density of states is obtained as

$$\rho(E) = -\frac{1}{\pi L^2}\sum_{\alpha}\Im m\langle G_{\alpha,\alpha}(E+\mathrm{i}\eta)\rangle = 4\Gamma(E)/(\pi n_i u^2), \tag{6.28}$$

with $\Gamma(E) = \Im m\Sigma(E+\mathrm{i}\eta)$ derived from the self-energy, which satisfies the recurrent equation (which is solved numerically)

$$\Sigma(E+\mathrm{i}\eta) = \frac{n_i u^2}{2\pi}(E-\Sigma(E+\mathrm{i}\eta))\int_0^{k_c}\frac{kdk}{(E-\Sigma(E+\mathrm{i}\eta))^2-(\gamma k)^2}, \tag{6.29}$$

with n_i the defect density and u^2 the average squared disorder strength. A mapping of this model to the Anderson disorder is possible by adjusting parameters to obtain the same average values and variances, i.e., $n_i(1-n_i)|u| = W/\sqrt{12}$ and $k_c = \gamma_0/\epsilon_0$, the cutoff where $\epsilon_c = 50\epsilon_0$ in the simulations. ϵ_0 is an arbitrary energy scale assumed to have the same order of magnitude as relevant energies such as E, Δ, and Γ in the SCBA, $\Delta(E) = \Re e\Sigma(E+\mathrm{i}\eta)$ (Shon & Ando 1998). Figure 6.10 shows the density of states (DOS), computed with a Lanczos-type method (Section 4.1), which is reported as a function of W. The disorder-free DOS (dashed line) shows typical behavior with a linear increase at low energy and the presence of two sharp van Hove singularities at $E = \pm\gamma_0$. As W increases, two different features are observed. At high energies, van Hove singularities are smoothed, whereas close to the charge neutrality point, Anderson

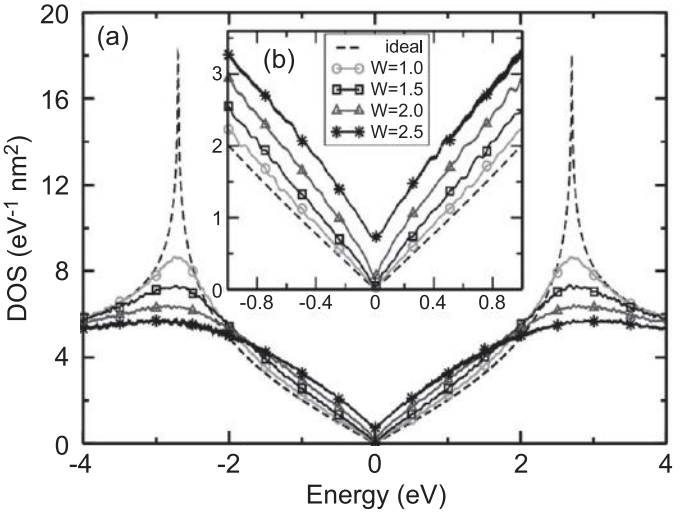

Figure 6.10 (a) DOS of an ideal (dashed lines) and disordered graphene sheets for several values of $W \in \{1; 1.5; 2; 2.5\}$. (b) Zoom- in of the energy area around the charge neutrality point. (Reproduced with permission from Lherbier, Biel et al. (2008). Copyright (2008) by the American Physical Society)

disorder enhances the DOS in full agreement with analytical results (Shon & Ando 1998). (See Fig. 6.10(b) for a close-up.)

Short-Range Disorder: Strong Scattering of Local Impurities

Finally, note that other different types of short-range defects such as vacancies and cracks in graphene flakes have also been predicted to produce midgap states in graphene (Stauber et al. 2007). By considering that an incident particle is a massless Dirac particle, we can use 2D scattering theory to access the transport time as well as the conductivity. We consider impurities (distributed randomly in the graphene network with a density n_i) defined by a strong local scattering potential such as $U(r) = V_0 > 0$ if $r < R$, and zero otherwise (deep circular potential well), where V_0 is the potential strength while R is the potential range. We next consider an incident low-energy massless Dirac particle with wavevector k such that $kR \ll 1$ (see Fig. 6.11), so that the scattering amplitude has the form (Katsnelson 2012)

$$f(\theta) = \frac{e^{2i\delta(k)} - 1}{i\sqrt{2\pi k}}(1 + e^{-i\theta}) = \frac{-\sqrt{\pi/2k}}{\frac{J_0(\tilde{k}R)}{kRJ_1(\tilde{k}R)} + \ln\left(\frac{2}{kR\gamma_E}\right) + i\pi/2}(1 + e^{-i\theta}),$$

where $\delta(k)$ is the s wave scattering phase shift, $\gamma_E = 1.781$, and J_n are Bessel functions. The wavevector $\tilde{k}$ is defined as $\tilde{k} = |\hbar v_F k - V_0|/\hbar v_F$, $v_F = 10^6$ ms^{-1} in a graphene monolayer. The weak potential limit is given by weak $V_0 \ll \hbar v_F k$ and $\tilde{k} \sim k$, whereas the strong potential limit assumes $V_0 \gg \hbar v_F k$ and $\tilde{k} \sim V_0/\hbar v_F$. Here, we focus on the strong disorder limit so that $\tilde{k}R \sim V_0 R/\hbar v_F$ which is k-independent. The differential cross section $dA/d\theta$ and transport times are given by

$$\frac{dA}{d\theta} = |f(\theta)|^2 = \frac{8\sin^2\delta(k)}{\pi k}\frac{1 + \cos\theta}{2},$$
$$\frac{1}{\tau} = n_i v_F \int (1 - \cos\theta)|f(\theta)|^2 d\theta,$$

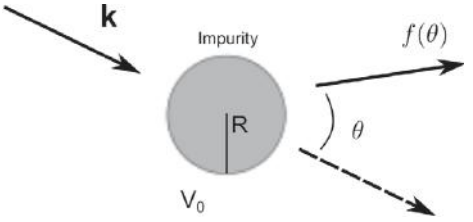

Figure 6.11 A scattering event of incident electron with momentum k, on short-range impurity potential, with scattering amplitude $f(\theta)$ in a direction defined by scattering angle θ.

and the transport cross section and total cross section are

$$A_{\rm tr} = \int d\theta(1-\cos\theta)|f(\theta)|^2 = \frac{4\sin^2\delta}{k}.$$

The transport time τ can be determined from $A_{\rm tr}$ using the relation $1/\tau = n_i v_F A_{\rm tr} = 4n_i v_F \sin^2\delta(k)/k$, while the conductivity derives from

$$\sigma = \frac{2e^2}{\pi h} v_F k_F \tau(k_F).$$

To derive the k_F dependence of τ and σ, we consider different limits determined by the three terms in the denominator of $f(\theta)$ in the equation for scattering amplitude above. When $J_0(\tilde{k}R) \sim 0$, the logarithmic term predominates. This is possible since $\tilde{k}R \sim V_0 R/\hbar v_F$ can be larger than one even if $kR \ll 1$ (resonant case). In this situation, the phase shift of the scattered wavefunction becomes

$$\delta(k) \sim -\frac{\pi}{2\ln(kR)} \to 0,$$

which leads to a transport cross section and transport time

$$A_{\rm tr} \sim \frac{4\delta^2}{k} \sim \frac{\pi^2}{k\ln^2(kR)},$$

$$\tau \sim \frac{k\ln^2(kR)}{n_i v_F \pi^2} \sim k\ln^2(kR). \tag{6.30}$$

This finally gives a conductivity which becomes roughly linear in the charge density as

$$\sigma = \frac{2e^2}{\pi h}\frac{n}{n_i}\ln^2(\sqrt{\pi n}R), \tag{6.31}$$

where n_i is the short-range defect density. This equation mimics the one for charged impurities, Eq. (6.20), with a slightly logarithmic dependence of the conductivity on the charge carrier density. One observes the mathematical singularity of Eq. (6.31), which suggests a diverging resistivity $1/\sigma \to \infty$ in the vicinity of the Dirac point, outlining a limit of such derivation. These disorder models are, however, quite complicated to compare with experimental data. This is partly due to the simplification made in the modeling and the various sources of disorder usually present in a real situation. It is, however, very useful to draw basic conclusions with respect to the strength and range of the disorder, which nevertheless encode a certain universality.

6.2.4 Kubo Transport: Graphene with Anderson Disorder

The effect of short-range scattering potential (Anderson disorder potential) with the disorder strength (W) is now analyzed using the Kubo conductivity. The mean free path $\ell_{\rm el}(E)$ is deduced from the saturation of the diffusion coefficients (using the numerical

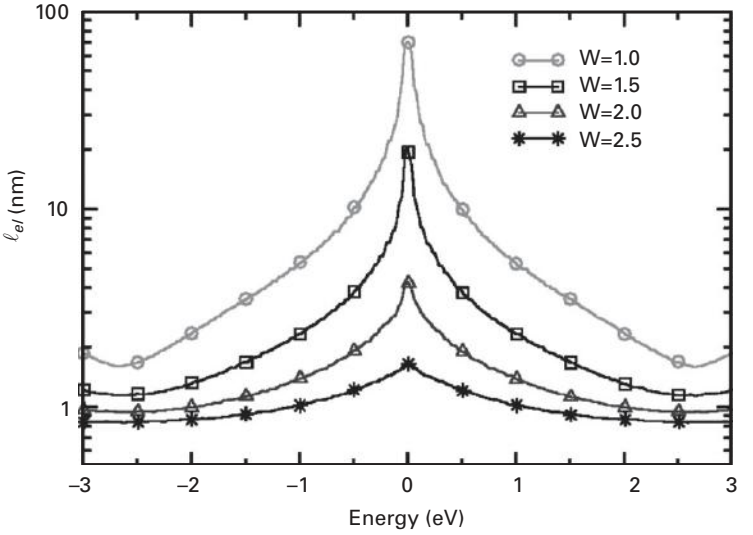

Figure 6.12 Mean free path versus energy ($\ell_{\rm el}$) for various strengths of the Anderson disorder potential.

method presented in Sections 4.4.4 and 4.2). Figure 6.23(a) gives several $D(t, E = 0)$ time evolution behaviors at the Dirac point. After the starting quasiballistic spreading of the wavepackets, a saturation regime develops and is followed by a decay of $D(t, E = 0)$ when quantum interferences are strong enough (see Section 6.2.7). The behavior of $\ell_{\rm el}(E)$ is shown in Fig. 6.12.

The semiclassical conductivity has actually been derived by Shon and Ando (1998) using a perturbation theory and the SCBA. The semiclassical part of the conductivity, $\sigma_{xx} \sim {\rm Tr}\langle v_x \Im m G(E + {\rm i}\eta) v_x \Im m G(E + {\rm i}\eta)\rangle_{\rm conf.}$, can then be simplified by $\langle G(E)G(E')\rangle \sim \langle G(E)\rangle\langle G(E')\rangle$ (all interference effects driven by Cooperon contributions are neglected), and is then deduced to be (Shon & Ando 1998)

$$\sigma_{\rm sc}(E) = \frac{1}{2}\frac{e^2}{\pi^2\hbar}\left[\left(\frac{E-\Delta(E)}{\Gamma(E)} + \frac{\Gamma(E)}{E-\Delta(E)}\right)\arctan\left(\frac{E-\Delta(E)}{\Gamma(E)}\right)+1\right]. \qquad (6.32)$$

A peculiar energy dependence of $\sigma_{\rm sc}(E)$ is obtained, together with a universal minimum value at the Dirac point, where $\sigma_{\rm sc} = 4e^2/\pi h$ (Fig. 6.13, main plot). Using the Kubo method, $\sigma_{\rm sc}$ is evaluated for various W (Fig. 6.13), and found to agree very well with the SCBA results. In particular, for $W = 2$, the dimensionless parameter $A = (4\pi\gamma_0)/(n_i u^2)$ is fixed at $A = 21$ to get a convincing fit for energies up to $2\epsilon_0$ with $\epsilon_0 = 0.3$ eV. The SCBA result fails, however, to describe the transport coefficient in the presence of strong disorder, since the neglect of quantum interferences jeopardizes the observation of localization (see Section 4.4.5).

The mobility (μ) versus charge energy is given in Fig. 6.14 for several strengths of the Anderson disorder. Similar energy dependencies are obtained for $\mu(E)$ and $\ell_{\rm el}(E)$.

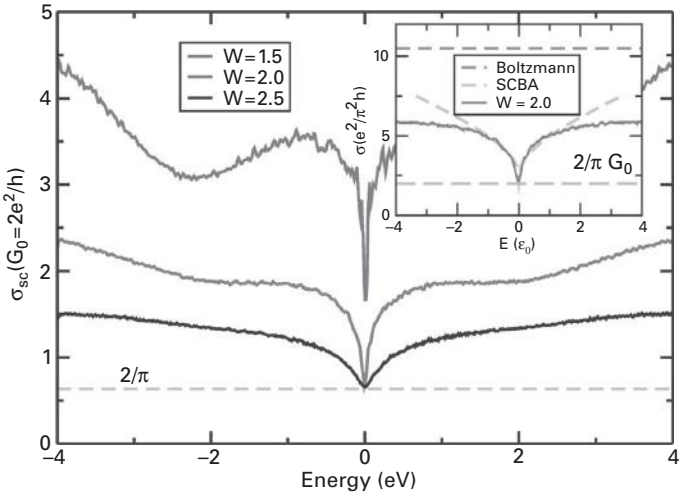

Figure 6.13 Main plot: semiclassical conductivity for Anderson disorder strengths of $W = 1.5, 2.0$, and 2.5. The dashed line denotes the minimum value of $\sigma_{\rm sc} = 4e^2/\pi h$. Inset: Boltzmann result (horizontal dashed line) and self-consistent Born approximation (dashed line) using Eq. (6.32) with fitting factor $A = 21$ for $W = 2$. (Reprinted from Roche et al. (2012). Copyright (2012), with permission from Elsevier)

At low energies, a simple Fermi golden rule captures the downscaling of μ with W, although it diverges precisely at the Dirac point. In most semiclassical simulations, the Dirac point charge density becomes vanishingly small, which introduces a nonphysical singularity in the mobility. By numerically integrating the disordered DOS, it is, however, possible to compute a finite charge density at the Dirac point, offering a more meaningful discussion of the Dirac point transport physics (see Section 10.3.1 for a particularly striking example and discussion). Experimental transport measurements of graphene samples deposited onto silicon oxide are also reported in Fig. 6.14 (right), from Tan et al. (2007). Different experimental samples with varying quality exhibit a charge density dependence of μ, which is seen to vary with absolute value of μ. The Anderson disorder leads to a theoretical $\mu(n)$, which seems to best reproduce samples with higher mobilities. However, a quantitative analysis is out of reach of a simplified disorder model, and would have to account for many other sources of scattering.

6.2.5 Kubo Transport: Graphene with Gaussian Impurities

In this section, we explore the effect of long-range (Gaussian) disorder potential (mathematically defined in Section 6.2.3) on transport features. We first investigate how quantum transmission develops through a finite size system containing a single scatter, following the interesting work of (Zhang et al. 2009). By diagonalizing the Hamiltonian of a small supercell with N carbon sites (and a single impurity), the band structure $E_k, \psi_k = \sum_{i=1}^{N} a_{ki}|i\rangle$ is obtained as well as the participation ratio $\mathcal{P}_k$ defined by

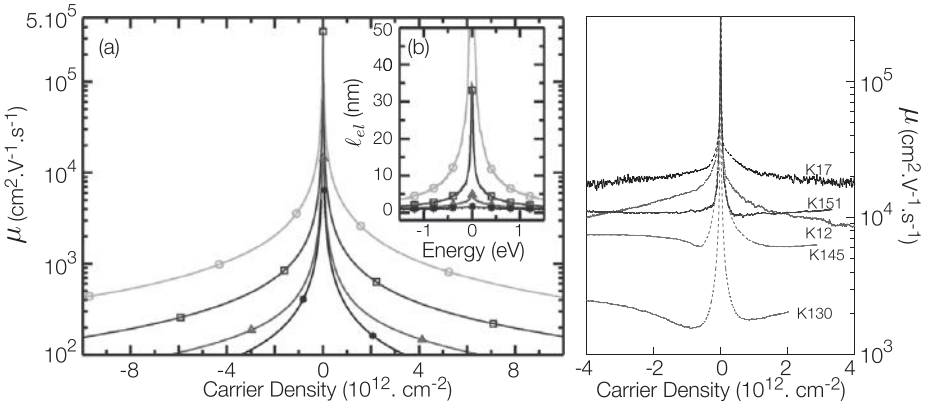

Figure 6.14 Left: Charge mobility with carrier density (a) and mean free path (b) for $W = 1, 1.5, 2, 2.5$ (from top to bottom). (Reproduced with permission from Lherbier, Biel et al. (2008). Copyright (2008) by the American Physical Society.) Right: Experimental mobility. (Reproduced with permission from Tan et al. (2007), courtesy of Philip Kim. Copyright (2007) by the American Physical Society)

$\mathcal{P}_k = \frac{\left(\sum_{i=1}^{N} a_{ki}^2\right)^2}{N\left(\sum_{i=1}^{N} a_{ki}^4\right)}$. The quantity $\mathcal{P}_k$ is a measure of the localization of electronic states. Localized states are defined by $\mathcal{P}_k \sim 1/N$, whereas extended states require that $\mathcal{P}_k$ remains constant with system size (as shown in Fig. 6.15).

The results obtained with varying the potential height V ($V > 0$) are shown in Fig. 6.15(a–d). For $V \leq 0.2\gamma_0$, states remain Dirac-like inside and outside the barrier (for incoming-left and outgoing-right electrons), as depicted in Fig. 6.15(e) and (f). The formation of bound states is obtained by further increasing V, as revealed by the small values of $\mathcal{P}$ in the negative energy region near the Dirac point (Fig. 6.15(c)). For positive injected energy (arrow with solid line in Fig. 6.15(g)), the electron is not far from K both inside and outside the barrier, which preserves the Klein tunneling mechanism. In contrast, for negative energy (arrow with dashed line in Fig. 6.15(g)), the presence of a non-Dirac barrier (marked by the arrow/barrier) affects electron tunneling, and induces a localization of the state around the impurity (bound states). When V is increased up to $V \sim \gamma_0$ (Fig. 6.15(h)), the Klein tunneling is totally suppressed owing to the radical change of the electronic structure.

The relative contribution of intervalley versus intravalley scattering has been computed for both the single scatter limit and for an average result of a disordered system (Zhang et al. 2009). The valley-resolved scattering amplitude $\mathcal{A}$ is calculated following Ando (1991). The sum of all the scattering amplitudes can be related to the sum over all propagating channels at E_F, which is written as $N_c = \mathcal{A}_{\text{intra}} + \mathcal{A}_{\text{inter}} = \mathcal{A}$ (Fig. 6.16). This interesting analysis allows differentiation of the transport regime depending on the relative strength of intervalley versus intravalley scattering. As seen in Fig. 6.16, the intravalley contribution predominates as long as the onsite impurity potential remains smaller than γ_0. In such a case, Klein tunneling or weak antilocalization phenomena

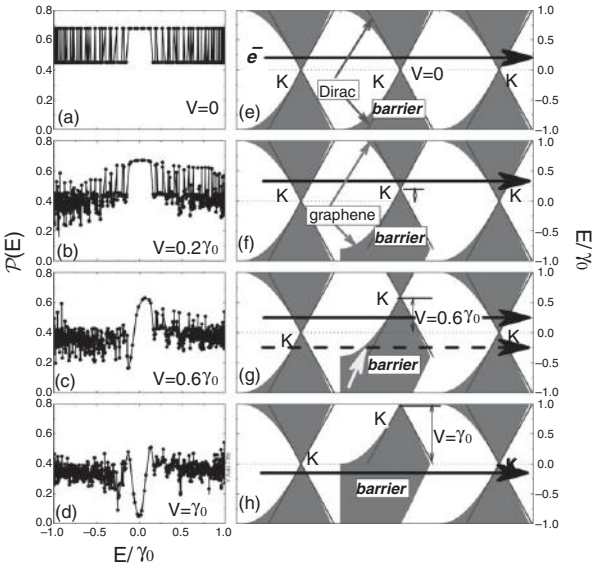

Figure 6.15 (a–d) Participation ratio for graphene with $N = 70 \times 40$, with a single impurity at the center with different potential barrier height $V \geq 0$, and fixed $\xi = 1.73a$. (e–h) Scattering process corresponding to the left counterparts. (Adapted with permission from Zhang et al. (2009). Copyright (2007) by the American Physical Society. Image courtesy of Wu-Ming Liu)

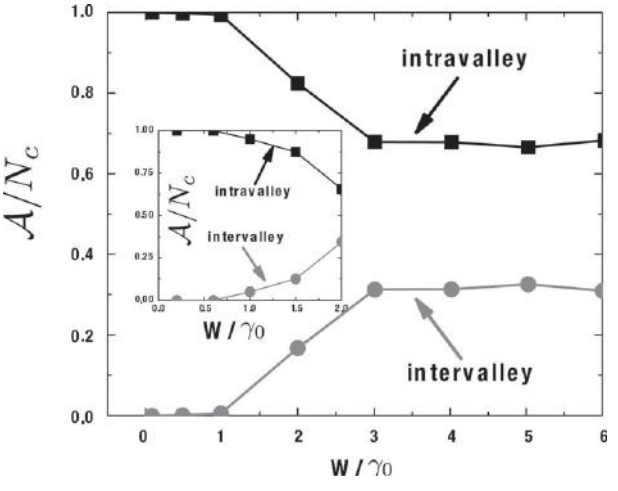

Figure 6.16 Normalized scattering amplitudes of intravalley and intervalley versus W. Each point is an average of over 100 samples on a square graphene sheet with 112×64 sites. Inset: Same results for the single-impurity case at the Dirac point. (Adapted with permission from Zhang et al. (2009). Copyright (2007) by the American Physical Society. Image courtesy of Wu-Ming Liu)

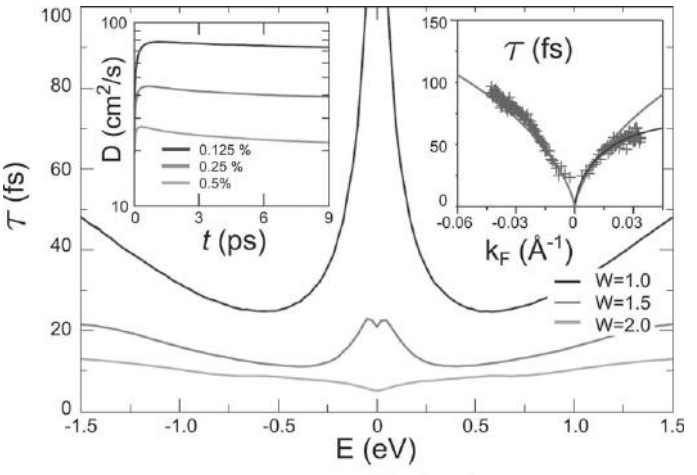

Figure 6.17 Main plot: Transport time τ for several values of the onsite disorder strength W. Left inset: Diffusion coefficient at Dirac point for chosen impurity densities and $W = 2$. Right inset: k_F dependence of the measured transport time for four different graphene samples. (Adapted with permission from Monteverde et al. (2010). Copyright (2010) by the American Physical Society)

mainly dominate the total conductivity. In the absence of intervalley scattering, one notes that Bardarson et al. (2007) have also numerically studied the one-parameter scaling behavior. Their results show that the Dirac point conductivity scales logarithmically with sample size, but does not reach a scale-invariant limit ($\beta(\sigma) = d\ln\sigma/d\ln L > 0$), confirming that Dirac fermions evade Anderson localization and remain delocalized as long as valleys are not mixed by scattering. In conclusion, the true impact of long-range disorder is markedly dependent on the W value.

We can further deepen the analysis of the quantum transport properties using numerical analysis of the quantum Kubo transport. Fig. 6.17 (inset) shows the evolution of the wavepacket dynamics (through time-dependent diffusion coefficients) at the Dirac point ($E = 0$) for $W = 2$ and increasing impurity density ($n_i = 0.125\%, 0.25\%, 0.5\%$). The diffusion coefficients reach a saturation regime, typically after 1 ps, indicating a diffusive regime. At much longer timescales, a time-dependent decay of the diffusion coefficient is observed (regardless of the energy and impurity density), indicating the onset of weak localization phenomena. The maximum value of $D(t) = D_{\max}$ provides the elastic mean free path $\ell_{\rm el} = D_{\max}/2v_F$ and the total transport time $\tau = \ell_{\rm el}/v_F$, where $v_F = 8.7 \times 10^5\ {\rm m\,s^{-1}}$ is the Fermi velocity.

Figure 6.17 (main plot) gives the transport time (deduced from the numerical diffusion coefficient (inset)) for three values of $W = 1.0, 1.5$, and 2.0 in γ_0 units. The behavior of $\tau(E)$ in the vicinity of the Dirac point is found to strongly vary depending on the disorder strength considered. For $W = 2.0$, $\tau(E = 0) \approx 5$ fs, and increases almost linearly at higher energies. By contrast, for $W = 1.5$ and $W = 1.0$, τ exhibits an upturn close to the Dirac point followed by a saturation value of $\tau(E = 0)$ (about four times

larger for $W = 1.5$) due to a finite density of states. For the weakest disorder ($W = 1$), $\tau(E) \sim 1/E$ for low energies and $\tau(E) \sim E$ at higher energies.

An experimental estimation of the transport time $\tau(k_F)$ is also shown in Fig. 6.17 (right inset) for four different exfoliated graphene samples with mobilities ranging from 3000 to 5000 cm^{-1} (Monteverde et al. 2010). The wavevector (or energy) dependence is similar to the simulated transport time for $W = 2.0$, which decays as the charge density is reduced. The experimental data are further reasonably fitted using

$$\tau(k_F) = \frac{k_F \ln^2(k_F R)}{\pi^2 n_i v_F}, \tag{6.33}$$

taking $n_i \sim 10^{12}$ cm^{-2} and R in the order of the lattice spacing. This form is consistent with resonant scattering due to short-range disorder as introduced in Section 6.2.3, and yields a typical semiclassical behavior of the conductivity given by Eq. (6.31). An opposite energy-dependent behavior of $\tau(k_F)$ is observed experimentally for bilayer graphene, indicating a possible interpretation in terms of larger screening strength (Monteverde et al. 2010).

The behavior of the elastic scattering time can be analyzed using the Fermi golden rule. Together with the energy dependence of the density of states roughly proportional to E, we found an energy-dependent contribution for τ by Fourier transforming the long-range potential. For weak disorder, the low-energy relaxation time is approximated by $\tau \propto 1/(E(1 - cE^2)) \approx 1/E + cE$, so that a low-energy peak and a linear slope at higher energies separated by a minimum τ at finite E are expected. In the simulations, such an expected weak disorder limit is obtained for $W = 1.0$ (Fig. 6.17), while for larger disorder, the above estimation has to be revised. For $W = 1.5$, the DOS at the Dirac point is finite and the leading term for $\tau(E)$ at low-energy $1/E$, stemming from the DOS, is strongly reduced. As a result, the minimum for $\tau(E)$ still exists but is relocated to smaller energies ($E \approx 400$ meV). For stronger disorder ($W = 2.0$), the DOS at the Dirac point is large enough that the minimum at finite E disappears.

The Kubo conductivity for the case of Gaussian impurities with density $n_i = 4\%$ and $\xi = 16a$ in the density interval $|z| \leq 35$ (Radchenko et al. 2012) is shown in Fig. 6.18 (main plot). Therefore, for $|z| \gg 1$, σ shows a linear density dependence $\sigma \sim n$, whereas the semiclassical Boltzmann approach (see Eq. (6.25)) predicts a superlinear dependence $\sigma \sim n^{3/2}$ and a vanishing conductivity at the Dirac point. This outlines one limitation of the semiclassical approach in the regime of low densities, where the effects of multiple scattering impact on DOS and semiclassical transport length scales (mean free path) are neglected. A similar discrepancy is obtained for the case $|z| \leq 1$ for which neither the density dependence of σ nor the absolute values is correctly obtained using the Boltzmann equation (Eq. (6.25)) (Radchenko et al. 2012). Another disagreement is also reported in Radchenko et al. (2012) for the case of short-range Gaussian impurities. Figure 6.18 (inset) shows the Kubo conductivity (at $E = 0.2\gamma_0$) for the case of $n_i = 2\%$ of Gaussian impurities with onsite impurity potential of $\sim 37\gamma_0$. No logarithmic correction (as predicted by Eq. (6.31)) is obtained with the full

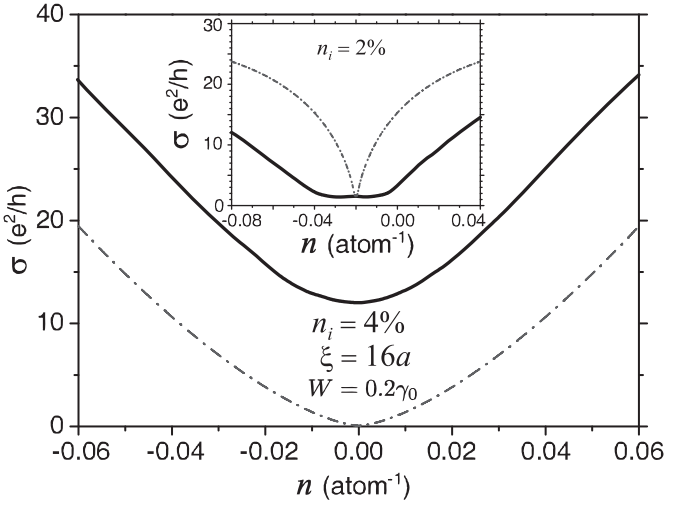

Figure 6.18 Main frame: Conductivity versus electron density n (the number of electrons per C atom) for random Gaussian impurities $n_i = 4\%$ ($\xi = 16a$) using the Kubo formula (bold line) or the Boltzmann result according to Eq. (6.25) (dashed line). Inset: Conductivity versus electron density n for random impurities with density $n_i = 2\%$ for the Kubo conductivity (bold line) and for the Boltzmann conductivity using Eq. (6.31) (dashed line). Curves are shifted to the charge neutrality point at $n \sim 0.02$ (Adapted with permission from Radchenko et al. (2012). Copyright (2012) by the American Physical Society. By courtesy of T. M. Radchenko)

Kubo calculation, which instead evidences a plateau of the semiclassical conductivity, similar to the case of homogeneous Anderson disorder (Section 6.2.4).

6.2.6 Weak Localization Phenonema in Disordered Graphene

Broken Symmetries and Weak Antilocalization: Cooperon Contribution

Through classification of disorder symmetry classes, a generalized diagrammatic theory of quantum interferences in graphene has been derived (Falko et al. 2007; Kechedzhi et al. 2007; McCann et al. 2006). It describes the contributions of various particle–particle correlation functions (associated with a given class of scattering diagrams), or Cooperons, to the total quantum correction of the semiclassical conductivity whose strength is monitored by several phenomenological parameters (intravalley versus intervalley elastic scattering times). The magnetoconductance $\Delta\sigma(B)$ obtained by this theory is then used for fitting experimental curves. The full derivation of such a theory is a highly technical and tedious exercise which goes beyond the scope of this book. We just summarize the main features concerning the various contributions of Cooperons, which either decrease (weak localization – WL) or increase (weak antilocalization – WAL) the quantum conductivity with respect to its semiclassical value. For such purposes, we recall the effective Hamiltonian describing massless Dirac fermions but including

the trigonal warping deformation. Near the corners $K_\pm$ of the hexagonal Brillouin zone, the effective description of the Hamiltonian can be rewritten as (Falko et al. 2007)

$$\hat{\mathcal{H}} = v_F \Pi_z (\sigma_x p_x + \sigma_y p_y) + \mu \Pi_0 [\sigma_y (p_x p_y + p_y p_x) - \sigma_x (p_x^2 - p_y^2)] + \hat{U}_{\rm dis}, \qquad (6.34)$$

where the first term determines the massless Dirac fermions, while the second term accounts for the trigonal warping correction (with a threefold symmetry) to the Dirac cone. $\hat{\mathcal{H}}$ takes into account in-plane nearest neighbor A/B hopping with the first (second) term representing the first- (second-) order term in an expansion with respect to momentum $\mathbf{p}$ measured from K_+ and K_-. Here $\sigma_0 \equiv \mathbb{I}, \sigma_{x,y,z}$ gives the AB lattice space Pauli matrices, whereas the inter-/intravalley matrices are denoted by $\Pi_0 \equiv \mathbb{I}, \Pi_{x,y,z}$. The latter term in Eq. (6.34) entails the disorder potential. Such an effective Hamiltonian operates in the space of four-component wavefunctions $[\Psi_{K_+}(A), \Psi_{K_+}(B), \Psi_{K_-}(B), \Psi_{K_-}(A)]$ describing the electronic amplitudes on A and B sites and in the valleys $K_\pm$ (see Section 2.2.2). Electrons in the conduction and valence bands differ by the isospin projection onto the momentum direction, so that $\sigma \cdot \mathbf{p}/|\sigma \cdot \mathbf{p}| = 1$ in the conduction band, and $\sigma \cdot \mathbf{p}/|\sigma \cdot \mathbf{p}| = -1$ in the valence band for the K_+ valley. By contrast, in the K_- valley, the electron chirality is mirror-reflected, so that $\sigma \cdot \mathbf{p}/|\sigma \cdot \mathbf{p}| = -1$ for the conduction band and $\sigma \cdot \mathbf{p}/|\sigma \cdot \mathbf{p}| = +1$ for the valence band. For an electron in the conduction band, the plane wave states can be written generically as

$$|\Psi_{K_\pm,\mathbf{p}}(\mathbf{r})\rangle = \frac{e^{i\mathbf{p}\cdot\mathbf{r}/\hbar}}{\sqrt{2}} \left(e^{i\theta_p/2} \, |\downarrow\rangle_{K_\pm,\mathbf{p}} \pm e^{-i\theta_p/2} \, |\uparrow\rangle_{K_\pm,\mathbf{p}} \right), \qquad (6.35)$$

$$|\Psi_{K_\pm,-\mathbf{p}}(\mathbf{r})\rangle = \frac{e^{-i\mathbf{p}\cdot\mathbf{r}/\hbar}}{\sqrt{2}} \left(e^{i\theta_p/2} \, |\downarrow\rangle_{K_\pm,-\mathbf{p}} \mp e^{-i\theta_p/2} \, |\uparrow\rangle_{K_\pm,-\mathbf{p}} \right), \qquad (6.36)$$

with, for instance, $|\uparrow\rangle_{K_+,\mathbf{p}} = [1,0,0,0]$, $|\downarrow\rangle_{K_+,\mathbf{p}} = [0,1,0,0]$ and $|\uparrow\rangle_{K_-,\mathbf{p}} = [0,0,1,0]$, $|\uparrow\rangle_{K_-,\mathbf{p}} = [0,0,0,1]$, and with the factors $e^{\pm i\theta_p/2}$ encoding the Berry's phase effects (Section 2.2.2). One defines pseudospin up $|\uparrow\rangle$ (resp. pseudospin down $|\downarrow\rangle$) for restriction of the wavefunction to the A (resp. B) sublattice. The trigonal deformation of the Dirac cone exhibits a $\mathbf{p} \to -\mathbf{p}$ asymmetry of the electron dispersion inside each valley, as illustrated in Fig. 6.19(a): $E(K_\pm, \mathbf{p}) \neq E(K_\pm, -\mathbf{p})$. Owing to time-reversal symmetry, trigonal warping shows, however, some symmetry between two valleys as $E(K_\pm, \mathbf{p}) = E(K_\mp, -\mathbf{p})$.

The final Cooperon correction to the semiclassical conductivity results from the full (disorder averaged) phase interference of electronic trajectories, which are topologically identical with time-reversal symmetry (as sketched in Figs. 4.6(a) and 6.19(b)). Such quantum correction is formally described in terms of the Cooperon contributions (introduced in Section C.3), which are (for spin-1/2 particles) classified as singlets and triplets in terms of isospin (AB lattice space) and pseudospin (inter-/intravalley) indices (given through Eqs. (6.35) and (6.36)). With regard to the isospin (sublattice) composition of Cooperons, only singlet modes are mathematically found to be relevant (bringing a pole in the corresponding two-particle correlation function for the total backscattering

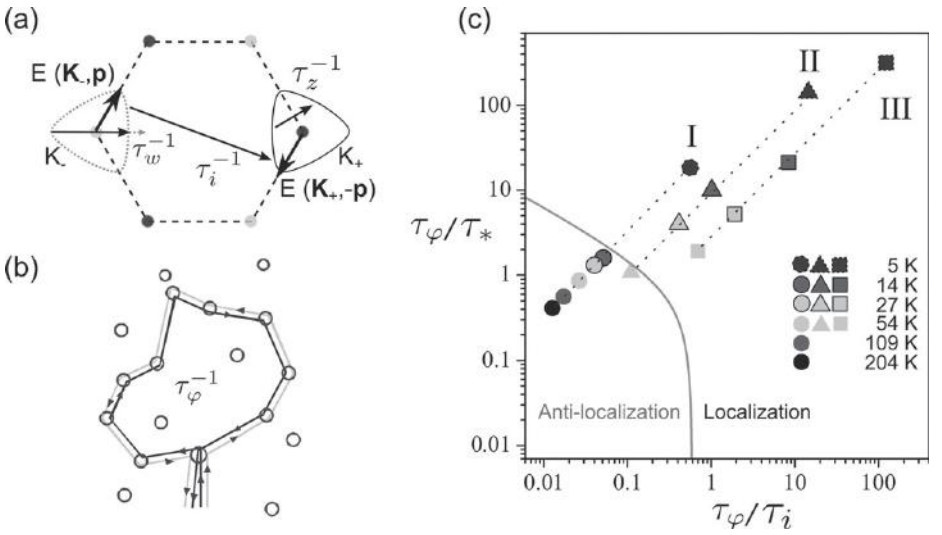

Figure 6.19 (a) Shape of the Fermi surface at finite Fermi energy, illustrating the processes responsible for trigonal warping (τ_w^{-1}), chirality-breaking (τ_z^{-1}), and intervalley scattering (τ_i^{-1}); with $\tau_*^{-1} = \tau_w^{-1} + \tau_z^{-1}$ (Horsell et al. 2008). (b) Real-space diagram of the closed trajectories responsible for quantum interferences correction, which are limited in size by the dephasing rate τ_φ^{-1}. (c) The scattering times related to quantum interferences in graphene. The solid curve separates the regions of electron localization and antilocalization. ((b) and (c) are adapted with permission from Tikhonenko et al. (2009). Copyright (2009) by the American Physical Society)

amplitude $\mathbf{p}' = -\mathbf{p}$). This can be seen in the correlator describing two plane waves $\sim\Psi_{\mathbf{K}_+,\mathbf{p}}\Psi_{\mathbf{K}_-,-\mathbf{p}}$, with $\Psi_{K_+,\mathbf{p}}$ and $\Psi_{K_-,-\mathbf{p}}$, propagating in opposite directions along a ballistic segment of the closed trajectory (as in Fig. 4.6(a)), which displays the generic form (Falko et al. 2007) $|\uparrow\rangle_{\mathbf{K}_+,\mathbf{p}}|\downarrow\rangle_{\mathbf{K}_-,-\mathbf{p}} - |\downarrow\rangle_{\mathbf{K}_+,\mathbf{p}}|\uparrow\rangle_{\mathbf{K}_-,-\mathbf{p}} - e^{-i\varphi}|\uparrow\rangle_{\mathbf{K}_+,\mathbf{p}}|\uparrow\rangle_{\mathbf{K}_-,-\mathbf{p}} + e^{i\varphi}|\downarrow\rangle_{\mathbf{K}_+,\mathbf{p}}|\downarrow\rangle_{\mathbf{K}_-,-\mathbf{p}}$ containing only sublattice-singlet terms (the first two terms) because triplet terms (the last two terms) disappear after averaging over the momentum direction ($\langle e^{i\varphi}\rangle = 0$).

Diagrammatic calculations show that the total Cooperon can then be mainly divided into *intravalley Cooperons* (interfering trajectories confined to a single valley) and *intervalley Cooperons* (interfering trajectories containing valley mixed trajectories) (McCann et al. 2006). Each Cooperon contribution is confined by two cutoff timescales (see Sections 4.4.5 and C.3 for details), namely the elastic (temperature-independent) relaxation times related to a given class of elastic scattering events ($\tau_{zz}, \tau_{\perp z}, \tau_{\perp\perp}, \ldots$) and the coherence time τ_φ, which dictates the maximum length of interfering trajectories. Denoting $\{x, y\} \equiv \perp$, the total scattering time can actually be split (assuming total x/y symmetry) in a generic form as

$$\frac{1}{\tau} = \frac{1}{\tau_0} + \frac{1}{\tau_{zz}} + \frac{2}{\tau_{\perp z}} + \frac{2}{\tau_{z\perp}} + \frac{4}{\tau_{\perp\perp}}, \tag{6.37}$$

where disorder effects are included in all three directions of space x, y, z. For instance, in the specific case of Gaussian white noise potential defined by

$$\langle u_{sl}(\mathbf{r})u'_{s'l}(\mathbf{r}')\rangle = u_{sl}\delta_{s,s'}\delta_{l,l'}\delta(\mathbf{r}-\mathbf{r}'),$$

the several elastic scattering times (which are all longer than the momentum relaxation time τ_0) will then be defined as $\hbar\tau_{sl}^{-1} = \pi\rho(E_F)u_{sl}^2$. A nonreconstructed vacancy would contribute to all terms except $u_{\perp z}$ and $u_{z\perp}$, while bond disorder would contribute to all terms except u_{zz}. A more realistic disorder potential will make the analytical calculation of timescales out of reach and numerical simulations are required to go beyond phenomenology, although no direct calculation of those elastic length scales is technically possible (in contrast to $\tau_0 = \tau$, the momentum relaxation time), except through the fitting of the numerical magnetoconductance curves (as discussed in Section 6.2.6). The full diagrammatic calculation of the Cooperon correction to the conductivity reduces to (Falko et al. 2007; Kechedzhi et al. 2007; McCann et al. 2006)

$$\delta\sigma = \frac{2e^2D}{\pi h}\int\frac{d^2q}{(2\pi)^2}(\mathcal{C}_0^x + \mathcal{C}_0^y + \mathcal{C}_0^z - \mathcal{C}_0^0), \tag{6.38}$$

where the two first Cooperon terms ($\mathcal{C}_0^x + \mathcal{C}_0^y$) give the intravalley contributions (including trigonal warping), whereas the two others ($\mathcal{C}_0^z - \mathcal{C}_0^0$) provide the intervalley parts. The last term in Eq. (6.38), $\mathcal{C}_0^0$, is the main Cooperon contribution, which dictates the sign of the quantum correction $\delta\sigma$, when coherence time is sufficiently long ($\tau_\varphi > \tau_i$). The intervalley component $\mathcal{C}_0^z$ is determined by the intervalley scattering rate (cutoff) $\tau_i^{-1} = 4\tau_{\perp\perp}^{-1} + 2\tau_{z\perp}^{-1}$, while the two intravalley components $\mathcal{C}_0^x$ and $\mathcal{C}_0^y$ are determined by cumulative inter-/intravalley scattering rates (also including the trigonal warping effect), with $\tau_*^{-1} = \tau_w^{-1} + 2\tau_z^{-1} + \tau_i^{-1}$ and with $\tau_z^{-1} = 2\tau_{\perp z}^{-1} + \tau_{zz}^{-1}$.

Let us consider the effect of the trigonal warping deformation of the Dirac cone on interference phenomena, following Falko et al. (2007). In the quantum interference picture, two phases θ_+ and θ_- are accumulated along the time-reversal symmetric paths, and the cumulated π Berry's phase fixes the phase difference of a given trajectory $\delta = \theta_+ - \theta_- = \pi N$ (where N is the winding number of a trajectory), and determines the strength of the WAL correction. Notwithstanding, the asymmetry of the electron dispersion brought about by the trigonal warping (Fig. 6.19(a)) deviates δ from πN. Indeed, since any closed trajectory is a combination of ballistic intervals characterized by momenta $\pm p_j$ (for the two directions) and duration t_j, each segment's contribution to the total phase difference is given by $\delta_j = [E(\mathbf{p}_j) - E(-\mathbf{p}_j)]t_j$ (taking the energy versus momentum relation of the second term of the Hamiltonian Eq. (6.34)). Since δ_j are random and uncorrelated, the mean square of the total phase difference simplifies to $\sim\langle(t_j\delta_j)^2\rangle_\varphi t/2\tau_0$. A relaxation rate related to trigonal warping is further deduced from $\mathrm{e}^{-\frac{1}{2}\langle\delta^2\rangle_\varphi} = \mathrm{e}^{-t/\tau_w}$, which yields $\tau_w^{-1} = 2\tau_0(\mu E_F^2/\hbar v_F^2)^2$, where τ_0 is the momentum relaxation time, $v_F = \sqrt{3}a\gamma_0/2\hbar = 10^6\ \mathrm{m\,s^{-1}}$, and $\mu = 3\gamma_0 a^2/8\hbar^2$ ($\gamma_0 = 3$ eV, $a = 0.26$ nm). For the typical parameters in measured samples (Tikhonenko et al. 2009), $\tau_w^{-1} = 0.001\ \mathrm{ps}^{-1}$ for the Dirac region ($E_F \simeq 30$ meV, $\tau_0 \sim 0.1$ ps) and

$\tau_w^{-1} = 0.3\ \text{ps}^{-1}$ for the highest measured concentration ($E_F \simeq 130$ meV, $\tau_0 \sim 0.05$ ps). Trigonal warping of the Fermi surface is found to have a very weak effect compared to estimated intravalley scattering timescales (Falko et al. 2007). One notes that trigonal warping effects should play an important role whenever τ_w becomes the smallest timescale, suppressing the two intravalley Cooperons together with their corresponding WAL fingerprints.

It is worth noting that the two intervalley Cooperons are not affected by trigonal warping due to time-reversal symmetry of the system, which requires $E(\mathbf{K}_\pm, \mathbf{p}) = E(\mathbf{K}_\mp, -\mathbf{p})$ (Fig. 6.19(a)). These two Cooperons cancel each other in the case of weak intervalley scattering, thus giving $\delta\sigma \sim 0$. However, intervalley scattering, with a rate τ_i^{-1} larger than the decoherence τ_φ^{-1} breaks the exact cancellation of the two intervalley Cooperons and partially restores weak localization. Following McCann et al. (2006), Kechedzhi et al. (2007), and Falko et al. (2007), the global effect of Cooperons on the transport observable is finally recast (using Eq. (6.38)) as

$$\Delta\sigma(B) = e^2/\pi h \left\{ \mathcal{F}\left(\frac{\tau_B^{-1}}{\tau_\varphi^{-1}}\right) - \mathcal{F}\left(\frac{\tau_B^{-1}}{\tau_\varphi^{-1} + 2\tau_i^{-1}}\right) - 2\mathcal{F}\left(\frac{\tau_B^{-1}}{\tau_\varphi^{-1} + \tau_i^{-1} + \tau_*^{-1}}\right) \right\}, \tag{6.39}$$

with τ_i, τ_ω, τ_s, and $\tau_B = \hbar/2eDB$ being the scattering times, while τ_φ denotes the coherence time. The above formula shows that depending on the relative strength of intravalley versus intervalley scattering, negative (weak localization) or positive magnetoresistance (weak antilocalization) will be obtained. The function $\mathcal{F}(x)$ can be approximated by $\mathcal{F}(x) \simeq x^2/24$ for $x \ll 1$, which has different consequences depending on the quantum coherence time.

In the high-temperatures regime, τ_φ becomes small enough such that τ_i^{-1} and τ_*^{-1} (which are temperature independent) can be neglected next to τ_φ^{-1} and one easily reduces Eq. (6.39) to

$$\Delta\sigma(B) \simeq -\frac{2e^2}{\pi h}\mathcal{F}\left(\frac{\tau_B^{-1}}{\tau_\varphi^{-1}}\right) < 0. \tag{6.40}$$

So when the magnetic field increases, $\Delta\sigma(B)$ decreases, and a weak antilocalization effect develops, instead of the usual weak localization correction. *In the low-temperatures regime*, τ_φ becomes eventually very long, so that the second and third terms of Eq. (6.39) become negligible compared to the first one, so that

$$\Delta\sigma(B) \simeq \frac{e^2}{\pi h}\mathcal{F}\left(\frac{\tau_B^{-1}}{\tau_\varphi^{-1}}\right) < 0. \tag{6.41}$$

We observe again the opposite phenomenon to that described at low temperatures, that is, weak localization is found to prevail. Finally, *in the intermediate temperatures regime*, when τ_φ^{-1} is in the order of the intervalley and intravalley scattering rates τ_i^{-1} and τ_*^{-1}, the final correction depends on the ratio τ_i/τ_*. When intravalley scattering

dominates, then $\tau_* \ll \tau_i$, and weak antilocalization drives the magnetoconductance profile, whereas weak localization takes place if $\tau_i \ll \tau_*$.

This theory has been verified by a series of fine-tuned experimental measurements confirming the existence of weak antilocalization effects, whose origin thus stems from the pseudospin-driven Berry phase interference term (Horsell et al. 2008; Tikhonenko et al. 2008, 2009). In particular, Tikhonenko and coworkers have experimentally confirmed such a complex phase diagram (see Fig. 6.19, right frame).

It is worth mentioning that the Cooperon theory, presented as derived in the perturbative regime, remains at some point phenomenological, owing to the introduced elastic timescales beyond the momentum relaxation time (τ_0), which cannot be derived analytically for a general model of (realistic) disorder. Additionally, if τ_0 is directly connected to the diffusion coefficient in the diffusive regime, the other timescales are not directly accessible from zero-field transport coefficients, and their effect is only revealed through the positive or negative contribution of the total Cooperon to the semiclassical conductivity. Therefore, estimations of these temperature-independent timescales demand particular care and further scrutiny. Actually, numerical simulations give a further access to the connection (and crossovers) between these localization phenomena and the underlying nature of microscopic disorder. In the following, a single additional scattering time is found to be enough to measure the ratio between intravalley versus intervalley scattering, which dictates the dominating localization phenomenon (weak localization or weak antilocalization).

Crossover between Weak Localization and Weak Antilocalization: Numerical Analysis

Let us investigate localization effects under a magnetic field for disordered graphene with Gaussian impurities. We introduce a magnetic field through the Peierls phase (Ortmann et al. 2011), with a flux per hexagon given by $\phi = \oint \mathbf{A}\cdot d\mathbf{l} = h/e \sum_{\text{hexagon}} \varphi_{\alpha\beta}$. A gauge is implemented where $\sum_{\text{hexagon}} \varphi_{\alpha\beta}$ can take integer multiples of $1/(N_x N_y)$ with N_x and $N_y = N_x + 1$ defining the sample size (Ortmann et al. 2011).

The application of an external magnetic field is seen to induce some significant changes in the time dependence of the diffusion coefficients (Fig. 6.20). First for $W = 2$ (referred to as a strong disorder case), the time dependence of $D(t, B)$ exhibits a clear suppression of quantum interferences (Fig. 6.20(a)) with increasing magnetic strength, as expected in the weak localization regime. On reducing W to $W = 1.5$, this trend starts to deviate at $B = 0.137$ T since, after initial suppression of quantum interferences, the diffusion coefficient decreases with increasing magnetic field, although it remains constant at long times (Fig. 6.20(b)). Such a fingerprint of WAL indicates a stronger contribution of intravalley processes (sketched in Fig. 6.20, bottom pictures). This tendency becomes even more pronounced for $W = 1$ (Fig. 6.20(c)), but care in interpretation has to be taken once all intervalley scattering events have been suppressed (as suggested by Zhang et al. (2009), and shown in Fig. 6.15), since activation of the Klein tunneling mechanism might then totally dominate scattering phenomena,

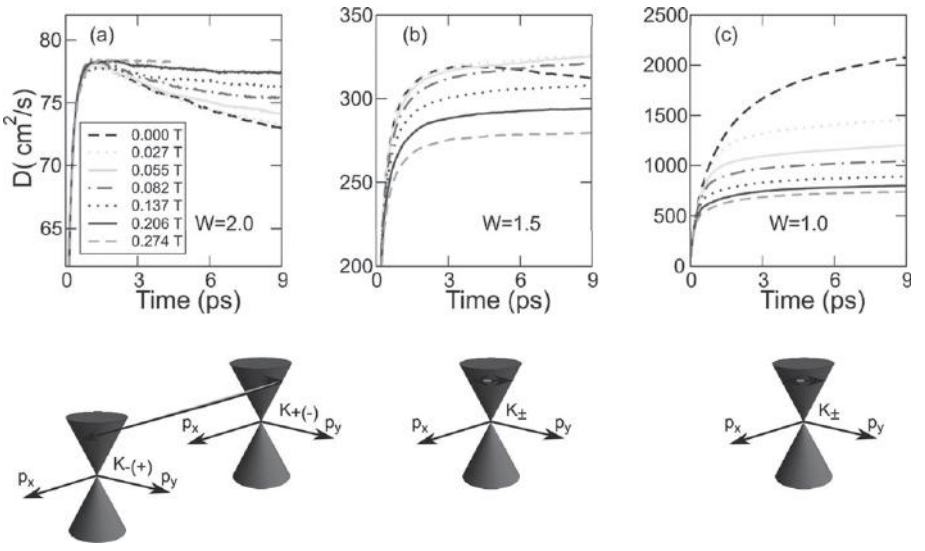

Figure 6.20 Magnetic field–dependent Dirac point diffusion coefficient for several values of W ($W = 2$ (a), $W = 1.5$ (b), and $W = 1$ (c)), with fixed $n_i = 0.125\%$ and correlation length $\xi = 0.426$ nm. Adapted from Ortmann et al. (2011)

jeopardizing the establishment of the diffusive regime, and WAL. This is further discussed below by analyzing the magnetoconductance patterns.

Several (theoretical) magnetoconductance $\Delta\sigma(B) = \sigma(B) - \sigma(B = 0)$ profiles are shown in the left panels of Figs. 6.21 and 6.22 for two different disorder strengths. For $W = 2$ (Fig. 6.21), the sign of $\Delta\sigma(B)$ (positive magnetoconductance) manifests a weak-localization behavior, regardless of the Fermi energy. Figure 6.21 (right) shows the experimental data obtained by Tikhonenko and coworkers, which exhibit similar trends (Tikhonenko et al. 2008, 2009). All experimental curves measured at low temperature ($T = 5$ K) also exhibit positive magnetoconductance whatever the induced charge densities (Fig. 6.21, right panel), which thus agrees with Eq. (6.41).

For smaller disorder ($W = 1.5$), the sign of $\Delta\sigma(B)$ is seen to change at sufficiently high-magnetic field, suggesting a crossover from weak localization to weak antilocalization (Fig. 6.22, left panel). The estimation of the elastic mean free path ($\ell_{\rm el} \sim 9-20$ nm) remains much smaller than the simulated sample size, warranting the occurrence of the diffusive regime and quantum interferences. Figure 6.22 (right) shows the experimental data at higher temperature, $T = 27$ K, for the same charge densities as in Fig. 6.21 (Tikhonenko et al. 2008, 2009). Here, the onset of weak antilocalization at a higher temperature agrees with Eq. (6.40) derived earlier.

It is instructive to observe that in Zhang et al. (2009) (and Fig. 6.15) the strength of valley, mixing is steadily enhanced when increasing disorder from $W = 1$ to $W = 2$ (while keeping $\xi = 0.426$ nm). The strong contribution of intervalley scattering for

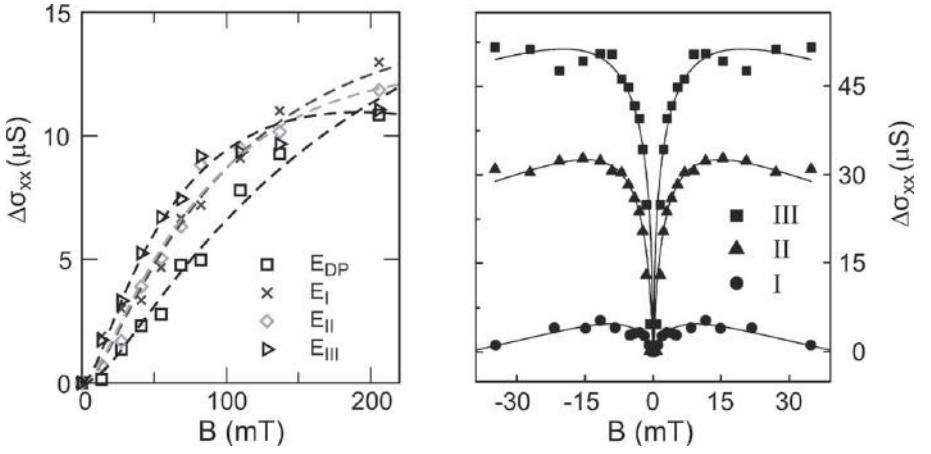

Figure 6.21 Left panel: $\Delta\sigma(B)(n_i = 0.125\%, \xi = 0.426$ nm) for four different Fermi level positions ($E_{\mathrm{DP}} = 0$, $E_{\mathrm{I}} = 0.049$ eV, $E_{\mathrm{II}} = 0.097$ eV, and $E_{\mathrm{III}} = 0.146$ eV). Averages over 32 different configurations are performed. Dashed lines are fits from analytical curves. Right panel: Experimental data extracted from Tikhonenko et al. (2009) obtained at $T = 5$ K. Here I, II, and III refer to charge densities at about 2×10^{11} cm^{-2}, 10^{12} cm^{-2}, and 2.3×10^{12} cm^{-2}, respectively. (Right panel reproduced with permission from Tikhonenko et al. (2009). Copyright (2009) by the American Physical Society. Figure reprinted from Roche et al. (2012). Copyright (2012), with permission from Elsevier)

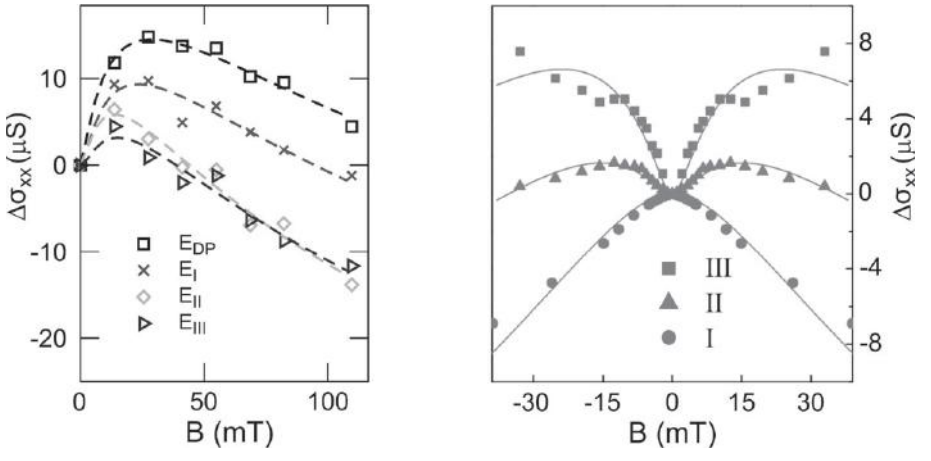

Figure 6.22 Left panel: $\Delta\sigma(B)$ for four different Fermi level positions ($E_{\mathrm{DP}} = 0$, $E_{\mathrm{I}} = 0.049$ eV, $E_{\mathrm{II}} = 0.097$ eV, and $E_{\mathrm{III}} = 0.146$ eV) after Ortmann et al. (2011). Sixty-four configurations have been averaged. Dashed lines are fits to analytical curves. Right panel: Experimental magneto-conductance curves measured at $T = 27$ K extracted from Tikhonenko et al. (2009). (Right panel reproduced with permission from Tikhonenko et al. (2009). Copyright (2009) by the American Physical Society. Figure reprinted from Roche et al. (2012). Copyright (2012), with permission from Elsevier)

the case $W = 2$ supports the computed positive magnetoconductance. Besides, by decreasing the disorder strength (from $W = 2$ to $W = 1.5$), WAL emerges in conjunction with the reduction of intervalley processes. We can also contrast numerical simulations with a phenomenological law that solely includes an extra single elastic scattering time τ_* (dictating the relative strength of valley mixing). Then for $W \geq 1$ both intravalley and intervalley processes jointly contribute, whereas intervalley scattering is suppressed when $W < 1$. The relevant expression for $\Delta\sigma(B)$ can be rewritten as

$$\Delta\sigma(B) = e^2/\pi h \left\{ \mathcal{F}(\tau_B^{-1}/\tau_\varphi^{-1}) - 3\mathcal{F}(\tau_B^{-1}/(\tau_\varphi^{-1} + 2\tau_*^{-1})) \right\}, \tag{6.42}$$

where $\mathcal{F}(z) = \ln z + \psi(1/2 + z^{-1})$, $\psi(x)$ is the digamma function and $\tau_B^{-1} = 4eDB/\hbar$ (McCann et al. 2006). Least-squares fits (dashed lines) are superimposed on the simulated $\Delta\sigma(B)$ (symbols), taking $\tau_\varphi = 9$ ps (the maximum computed time). For $W = 2$ and $W = 1.5$, τ_* ranges within $[1.1 - 2.3]$ ps and $[1.5 - 6.3]$ ps, respectively (increasing values with increasing energy), thus confirming the weak localization regime for lowest B, which is fully consistent with McCann et al. (2006) ($\tau_i < \tau_\varphi$).

It is thus demonstrated that pseudospin effects are tunable by adjusting a single disorder parameter W, which denotes the depth of an impurity-driven local Coulomb potential. When $W \geq 1$ (unit of γ_0), local energetics between nearest neighbors A and B sites fluctuate enough to increase intervalley scattering, which progressively predominates over the intravalley contribution (Zhang et al. 2009). The comparison with experimental data, however, deserves an additional comment. Indeed, in the simulation, the crossover from weak localization to weak antilocalization occurs as the Fermi level is moved from high energies to lower energies. The experimental data obtained at finite temperatures (Fig. 6.22) show an opposite trend. First, one should mention that the disorder model used here is kept constant with changing charge density. A self-consistent screening calculation of the scattering potential should be more suitable, but screening is expected to be less efficient for lower densities (screening will essentially decrease the value of W). Thus the crossover from WL to WAL is not expected to change by using energy-dependent (and differently screened) scattering potential. Second, the simulations are performed at zero temperature and should therefore be ultimately compared with the lowest temperature measurements. In Fig. 6.21, one sees the absence of WAL, which agrees with the simulation, considering a sufficiently deep onsite impurity potential.

6.2.7 Strong Localization in Disordered Graphene

The simulation using the Kubo formula and Anderson disorder (Section 6.2.4) shows that the semiclassical conductivity remains high and always larger than or equal to the SCBA limit value $\sigma_{sc} = 4e^2/\pi h$. This value is first observed at the Dirac point. However, the conductivity would not be sensitive to localization effects except in the presence of some decoherence mechanisms such as electron–electron scattering or electron–phonon coupling (Lee & Ramakrishnan 1985). Here at zero temperature,

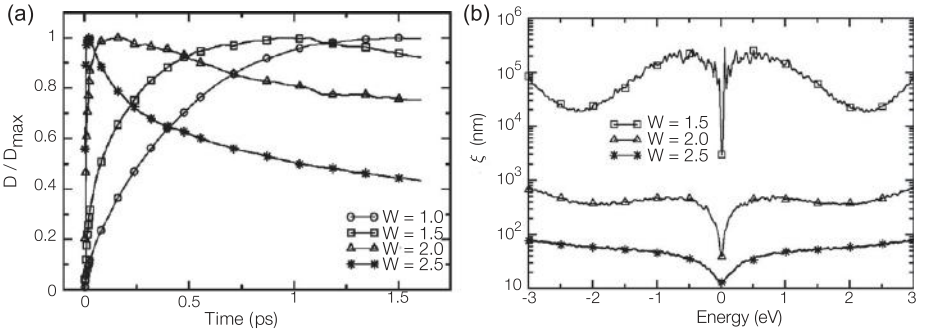

Figure 6.23 (a) Diffusion coefficient $D(E,t)$ as a function of time for various disorder strengths and Fermi energies. $D(E,t)$ has been normalized with respect to its maximum value $D_{\max}(E)$ to allow an easier comparison between the different curves. (b) $\xi(E)$ for three disorder strengths. (Reproduced with permission from Lherbier, Biel et al. (2008). Copyright (2008) by the American Physical Society)

the time dependence of the diffusion coefficient clearly evidences the contribution of localization effects that develop beyond the diffusive regime. Figure 6.23(a) shows $D(E,t)$ at the Dirac point for different Anderson disorder strengths W. A saturation of $D(E,t)$ pinpoints the diffusive regime, while its further decay at longer times (which is enhanced for increasing W) indicates a larger contribution of the quantum interferences correction.

The 2D localization length ξ can be estimated using the fact that the transition to the insulating state occurs when the quantum correction, which scales as $\Delta\sigma(L) = (G_0/\pi)\ln(L/\ell_{\rm el})$ (L is the length scale associated with the propagation time), is of the order of the semiclassical conductivity $\sigma_{\rm sc}$. Given that localization occurs when $\Delta\sigma(L=\xi) \simeq \sigma_{\rm sc}$, we thus obtain

$$\xi = \ell_{\rm el}\exp(\pi\sigma_{\rm sc}/G_0). \tag{6.43}$$

Some numerical results for the Anderson disorder, using Eq. (6.43), are shown in Fig. 6.23(b) for several disorder strengths (average over several tens of configurations has been performed). It is clear that the general shape of $\xi(E)$ is mainly dominated by the behavior of $\sigma_{\rm sc}(E)$ (see Fig. 6.13), which is expected because of the exponential dependence of $\xi(E)$ on $\sigma_{\rm sc}(E)$. As a result, although $\ell_{\rm el}$ diverges when approaching the Dirac point (Fig. 6.12), $\xi(E)$ shows an opposite trend, with a minimum value at lowest energies. It is also worth observing that even for disorder strengths as large as $W \sim 6$ eV, $\xi(E=0) \geq 10$ nm, while it quickly increases with energy, reaching several microns. For more realistic values of W in the order of 1 eV, $\xi(E) \sim 10$ μm. Localization of electronic states in graphene with Anderson disorder is therefore very inefficient, although shorter localization lengths are found at the Dirac point. This feature is actually quite general for all types of short-range disorders (see Section 10.3.1 for complementary analysis on oxygen-damaged graphene).

6.3 Graphene with Monovacancies

This section focuses on the effect of monovacancies (or missing carbon atoms) on quantum transport in graphene. Figure 6.24 shows a scanning tunnel microscope (STM) picture of a single monovacancy on graphite previously irradiated with Ar^+ ions (Ugeda et al. 2010). Although various types of vacancies have been observed in disordered graphene, monovacancies are particularly interesting since they do not break electron–hole (chiral) symmetry. However, by breaking A/B sublattice symmetry, vacancies offer the possibility (similar to adsorbed hydrogen atoms) to generate the formation of local magnetic moments and long-range magnetic ordering (antiferromagnetic, ferromagnetic or paramagnetic states), although the issue remains theoretically debated, owing to the complexity to cope with a self-consistent calculation of the interaction between localized magnetic moments (including Coulomb screening effects) and therefore the stable formation of short, medium, or long-range magnetic ordering.

Monovacancies particularly affect the electronic structure of graphene at the Dirac point, introducing zero-energy modes (ZEM) whose impact on the Dirac point transport physics could be fundamental for explaining experiments in ultraclean graphene (Ponomarenko et al. 2011). Also, transport properties have been predicted to be very sensitive to the way the sublattice symmetry is broken (Ostrovsky et al., 2006). For equally distributed vacancies among the two sublattices, a saturation (or even increase) of the conductivity at (from) $\sigma_0 = 4e^2/\pi h$ with increasing density of vacancies has been reported in the tunneling regime of a very short graphene channel (Ostrovsky et al. 2010), whereas another calculation (using the Kubo formula) has claimed the emergence of a quantum critical point due to the ZEM and with $\sigma_0 = 4e^2/\pi h$ as a quantum conductivity in the bulk limit. Finally some calculations have found a saturation or even increase of the conductivity with density of defects (Ferreira & Mucciolo 2015; Yuan et al. 2010; Zhu et al. 2012), in full contradiction with the scaling theory of Anderson localization.

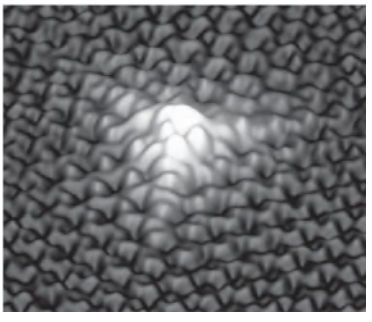

Figure 6.24 STM picture of a single vacancy in graphite. (Reproduced with permission from Ugeda et al. (2010). Copyright (2010) by the American Physical Society. Courtesy of J. M. Gomez-Rodriguez and I. Brihuega)

We explore here transport in graphene with vacancies using the Kubo method (and some results derived from the Landauer-Büttiker formula), which makes it possible to provide a more comprehensive explanation of effects of monovacancies on quantum transport properties in disordered graphene.

A vacancy in the honeycomb lattice leaves three dangling covalent bonds, which might eventually reassemble into one double bond and one dangling bond, but here we restrict the study to nonreconstructed vacancies. The vacancies are then theoretically modeled by suppressing hopping terms between the orbital at a vacancy site and its nearest neighbors. Another possibility of describing the vacancy at a given site is to add a very large onsite potential (e.g., in the order of $U_v = -6\gamma_0 = +17.4$ eV for the simulation presented later). The TB Hamiltonian is given by

$$\mathcal{H} = -\sum_{<i,j>} \left(\gamma_0 |i\rangle\langle j| + h.c.\right) - \sum_{<i_v,j>} \left(\gamma_0 |i_v\rangle\langle j| + h.c.\right) + \sum_{i_v} U_v |i_v\rangle\langle i_v|, \tag{6.44}$$

where i_v indexes the ith vacancy site and the brackets in the summation indices indicate that the corresponding sum is over nearest neighbors. An important issue is the distribution statistics of the vacancies among the two A and B sublattices. Indeed, using the rank-nullity theorem, an imbalance of vacancies between the two sublattices A and B has been shown to create ZEM, that is, the formation of impurity states at the Dirac point (Pereira et al. 2008). This demonstration requires taking only first-neighbor interactions into account, and goes as follows. Consider a system with m vacancies on lattice B and $(m+1)$ vacancies on lattice A. Both lattices have the same number of sites: $N_A = N_B = N_{\text{sites}}/2$. Using the AB representation of the Hamiltonian, Eq. (6.44), and reordering the real-space basis of subspaces A and B so that sites corresponding to vacancies come last, we get for the interaction matrix $\mathcal{H}_{BA}$ operating from subspace B onto subspace A:

$$\mathcal{H}_{BA} = \begin{pmatrix} \tilde{\mathcal{H}}_{\mathcal{BA}} & \mathcal{O}_{m,N_A-m} \\ \mathcal{O}_{N_B-m} & \mathcal{O}_m \end{pmatrix}, \tag{6.45}$$

where $\mathcal{O}_{n,p}$ is the null matrix of dimension $n \times p$. Since there are $m+1$ vacancies on sublattice A, the $N_A - (m+1)$th basis vector in subspace A represents a vacancy. It verifies: $\mathcal{H}_{BA}|N_A - (m+1)\rangle = 0$. Consequently, the last line of matrix $\tilde{\mathcal{H}}_{\mathcal{BA}}$ is null and this operator has at least one eigenvector associated with the eigenvalue 0. From this vector we can obtain a vector in B space by completing with zeros. We call this new vector φ. Also, we have

$$\mathcal{H}_{BB} = \begin{pmatrix} \epsilon_B \times \mathbb{I}_{N_B-m} & \mathcal{O}_{N_B-m,m} \\ \mathcal{O}_{m,N_B-m} & (\epsilon_B + U_v) \times \mathbb{I}_m \end{pmatrix}, \tag{6.46}$$

where $\mathbb{I}_n$ is the identity matrix of size n, and ϵ_B the onsite energy on the B sublattice in the clean case. By construction, φ verifies: $\mathcal{H}_{BB}(\varphi) = \epsilon_B \varphi$. Finally, applying the total Hamiltonian (6.44) to vector $(0, \varphi)$ yields

$$\mathcal{H}\begin{pmatrix}0\\ \varphi\end{pmatrix} = \begin{pmatrix}0\\ \mathcal{H}_{BA}(\varphi) + \mathcal{H}_{BB}(\varphi)\end{pmatrix} = \epsilon_B \begin{pmatrix}0\\ \varphi\end{pmatrix}. \tag{6.47}$$

Therefore, the additional vacancy on one sublattice creates an electronic state at the onsite energy and located on the other sublattice. Since for graphene $\epsilon_B = \epsilon_A = 0$, these modes will be created at the Dirac point. This creation of modes at zero energy mainly affects the spectrum near the Dirac point. The formation of an energy gap Δ_g has been derived in Pereira et al. (2008), and for a vacancy concentration n, it is predicted that

$$\Delta_g \backsimeq \frac{\hbar v_F}{d}, \tag{6.48}$$

with $d = n^{-1/2}$ the average distance between vacancies. Note that when vacancies are equally distributed over the two sublattices, ZEM should not appear if $U_v \neq 0$. Also, even if the distribution is numerically enforced to be random over both sublattices, some ZEM appear due to statistical error, as might be the case in the numerical study (Zhu et al. 2012), in which unexplained ZEM have been reported. In the following, we enforce a strict distribution of vacancies among both sublattices, with a focus on the two cases of main interest, namely the situation for which vacancies are equally distributed among different A and B sublattices, and the situation for which all vacancies belong to the same sublattice, say the A sublattice (AA).

6.3.1 Electronic Structure of Graphene with Monovacancies

Electronic structure calculations are performed using the Lanczos recursion method on a sample of 10^6 atoms with periodic boundary conditions (Section D.1). This sample size allows for a randomization of the distribution of vacancies. The chosen parameters for the Lanczos calculations are $N = 1500$ recursion steps with energy resolution of $\eta = 0.005|\gamma_0| = 0.015$ eV. We investigate several concentrations of vacancies n up to 1% for the two cases where the vacancies are either equally distributed among the two sublattices (AB) or restricted to a single sublattice (AA).

The numerical results for the DOS in the AB case are plotted in Fig. 6.25 for vacancy densities varying from 0.1% to 1%. We restrict the analysis to the energy region around the Dirac point where most of the modifications occur. Note that we also observe a softening of the van Hove singularities at higher energies (not shown here), but hole–particle (chiral) symmetry is conserved.

The vacancies induce an increase of the spectral density around the Dirac point, with a flattening with increasing density of vacancies. Although the DOS seems to increase close to the Dirac point, as in Pereira et al. (2008), the chosen numerical resolution to capture the zero-energy physics must be very high. DOS in the AA case are plotted in Fig. 6.26, for the same concentrations. Here again, the system remains particle–hole symmetric. As expected, the breaking of A–B symmetry (see Fig. 6.26, insets) generates a peak at zero energy, although it has been softened numerically.

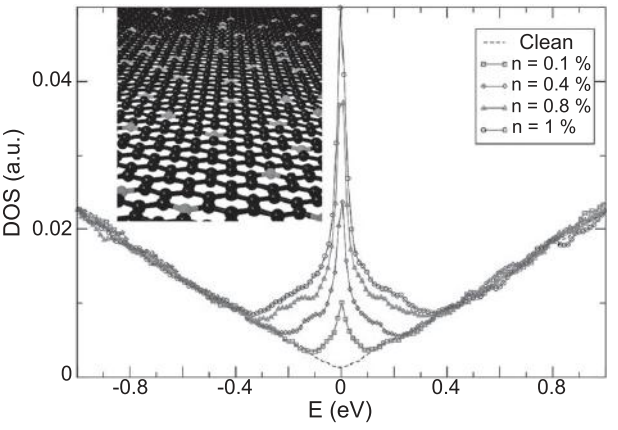

Figure 6.25 DOS for vacancy concentrations $n = 0.1\%, 0.4\%, 0.8\%, 1\%$ distributed equally over the two sublattices, and for the clean case. Inset: Ball-and-stick views of graphene with AB vacancy distribution. Vacant sites and bonds are colored in gray.

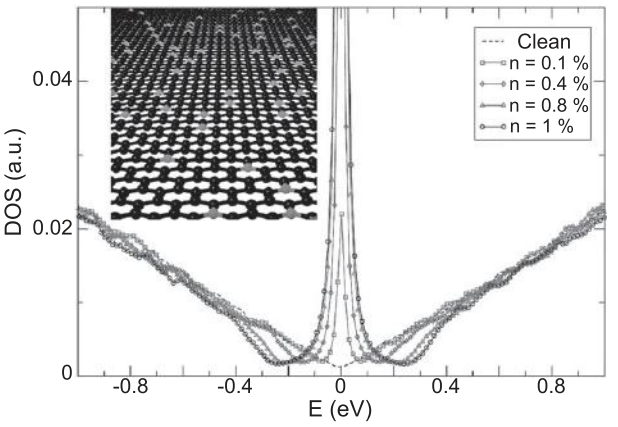

Figure 6.26 DOS for same concentrations of vacancies as in Fig. 5.28 distributed on one sublattice only. Inset: Ball-and-stick views of graphene with AA vacancy distribution. Vacant sites and bonds are colored in gray.

The peak height increases with vacancy concentration and induces a decay of the DOS on each side of the Dirac point, which is actually related to the formation of gaps. For more clarity, we define an energy ϵ up to which the DOS can be considered as negligible and plot, in Fig. 6.27, Δ_g against $n^{1/2}$, which is found to scale linearly, agreeing with Eq. (6.48). In both AB and AA cases, vacancies preserve hole–particle symmetry and affect the electronic structure around the Fermi energy, although in a different manner. In the first case, the DOS increases and tends to flatten, while for the AA distribution, there is a depletion of the DOS around the Fermi energy with a finite concentration of ZEM in the middle.

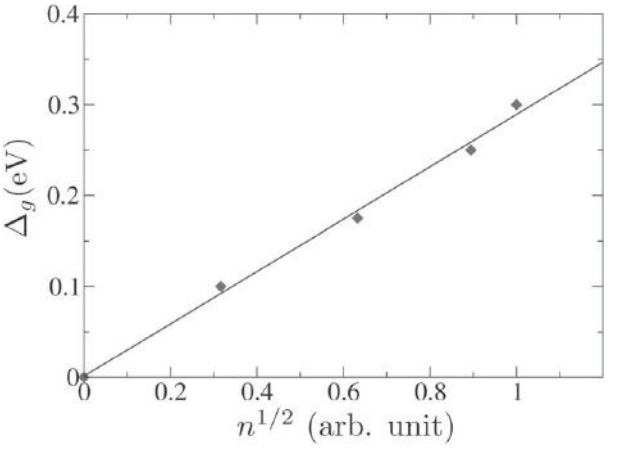

Figure 6.27 Width of the gap Δ_g estimated from Fig. 6.26 as a function of $\sim n_i^{1/2}$, with n_i the density of vacancies. The continuous line is a linear fit of the simulation.

6.3.2 Transport Features of Graphene with Monovacancies

For a low density of vacancies distributed roughly equally on both sublattices in a random manner, one expects that the defect-induced short-range scattering will lead to diffusive and subsequently localization effects. These transport regimes have been studied and confirmed by several authors (Cresti, Ortmann et al. 2013; Fan et al. 2014; Trambly de Laissardière & Mayou 2013). The Anderson localization was found numerically in Fan et al. (2014), evidenced by an exponential increase of the resistivity versus sample size (or temperature downscaling) for all energies of the Dirac spectrum. Similar conclusions were obtained in other works, although the Dirac point transport physics was debated for a while and Cresti, Ortmann et al. (2013) extracted from their numerics $\sigma \sim 1/L^{\beta}$ with $\beta \sim 2$, a result that could be consistent with the peculiar localization properties of ZEM. The authors favored the power-law regime to be consistent with the power law localization of the wavefunctions, but as discussed at the end of the section, by improving the numerical convergence of the calculations, the robustness of the Anderson localization regime is established.

Below, we show the Kubo conductivity obtained in the semiclassical and the quantum regimes, which are followed by analyzing the dynamics and scaling properties of the propagating electronic wavepackets (Section D.1). The random phase states (RPS) evolve during a little more than 15 ps, and the total system is a rectangular sheet of 212×122 Å^2, chosen large enough to limit finite-size effects (Cresti et al. 2013). For each concentration and distribution of vacancies, the maximum of the diffusion coefficient $D^{\max}(E)$ is first estimated, together with the mean free path $\ell_{\rm el}(E)$ and the Fermi velocity $v(E)$. From these values, one deduces $\sigma_{\rm sc}$ the semiclassical conductivity in the diffusive regime. We also follow the time-evolution of the Kubo conductivity to quantify the contribution of quantum interferences, using the approximation

$$\sigma = \frac{e^2}{2}\rho(E)\frac{D(E,t)}{t}. \tag{6.49}$$

Numerical results for the fully balanced AB configuration are summarized in Fig. 6.28. The semiclassical conductivity is plotted as a function of energy (main plot, full line) with a density of vacancies of 0.8%. Away from the Dirac point, σ_{sc} increases with energy, while it exhibits a plateau above the value $\sigma_{sc} = 4e^2/\pi h$ (black, dotted line). This result confirms earlier theoretical predictions (Ostrovsky et al. 2010; Zhu et al. 2012). The scale-dependent conductivity for the same concentration of vacancies is also shown after a time $t = 15$ ps (dashed and dotted line), and is seen to decay below σ_0, pinpointing the onset of localization phenomena, which are stronger for larger vacancy concentration (as illustrated by the dashed curve which corresponds to the conductivity at timescale $t = 15$ ps for a concentration $n = 1\%$). To confirm the presence of localization effects, the evolution of diffusion coefficients $D(E,t)$ at $n = 0.8\%$ is shown for several energies in the region of the plateau. Values of $D(E,t)$ are seen to reach a saturation regime after a few femtoseconds, and then start to decline sublinearly, as expected in a weak localization regime (see Fig. 6.28, left inset).

Figure 6.28 (right inset) further displays $\ell_{el}(E)$ for various concentrations: 0.1%, 0.2% and 0.4% (from top to bottom). At the Fermi energy, the mean free path is below 10 nm for a concentration of 0.1%, while for 0.4%, $\ell_{el}(E)$ is just a few interatomic distances, suggesting short localization lengths. Only at sufficiently higher energies do we observe that ℓ_{el} roughly scales as $1/n$. An important feature revealed by these

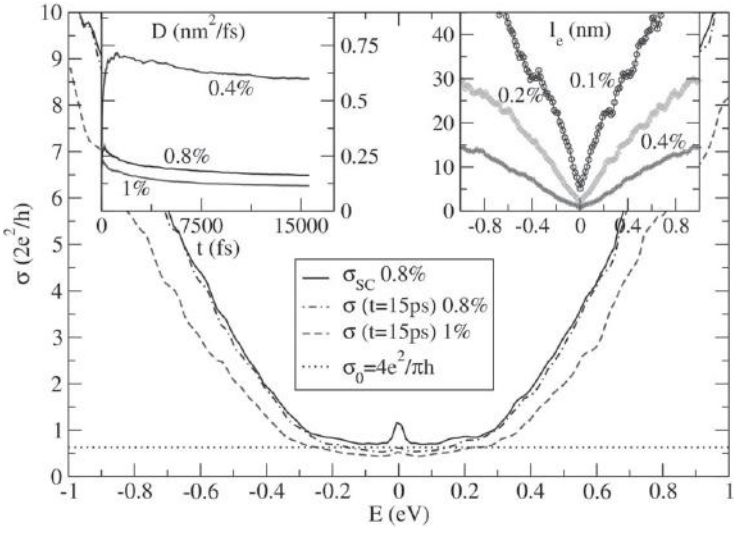

Figure 6.28 Main plot: Semiclassical (full line) and Kubo conductivity (dashed line, dash, and points) versus energy for different concentrations of vacancies, equally distributed among sublattices. Left inset: Evolution of diffusion coefficients calculated at $E = 0.15$ eV, for different concentrations of vacancies. Right inset: Elastic mean free path against energy for different vacancy concentrations.

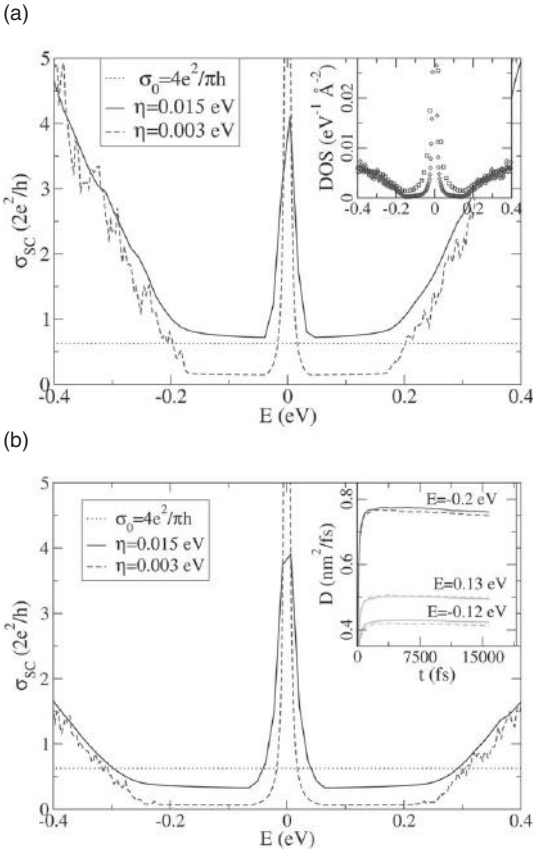

Figure 6.29 (a) Main plot: $\sigma_{sc}(E)$ for $n = 0.4\%$ of vacancies on one sublattice, for two different energy resolutions $\eta = 0.003$ (dashed line), 0.015 eV (full line). Inset: Corresponding DOS (squares: $\eta = 0.015$ eV, diamonds: $\eta = 0.003$ eV). (b) Main plot: $\sigma_{sc}(E)$ for $n = 0.8\%$ of vacancies on one sublattice, for two different energy resolutions $\eta = 0.003$ eV (dashed line), 0.015 eV (full line). Inset: Evolution of diffusion coefficients at chosen energies.

simulations is that the energy scale on which transport is affected by vacancies matches the one found previously when studying the electronic structure (see Fig. 6.25). All these results concerning the AB configuration are consistent with previous studies on weakly hydrogenated graphene (Leconte et al. 2011; Soriano et al. 2011). It is also interesting to note that the Dirac point conductivity scaling follows a power law, which could be a fingerprint of ZEM (Cresti, Ortmann et al. 2013), although more extensive simulations have concluded to an Anderson localization regime (Fan et al. 2014).

Figure 6.29(a) (main plot) presents the semiclassical conductivity in the AA case for $n = 0.4\%$, for two different energy resolutions: $\eta = 0.005\gamma_0 \backsimeq 0.015$ eV (dashed line) and $\eta = 0.001\gamma_0 \backsimeq 0.003$ eV (full line). Both curves exhibit a behavior similar to that found in the AB case (see Fig. 6.28), except for a peak lying in the middle of the plateau, at the Fermi energy. The first curve, for $\eta = 0.015$ eV, saturates above σ_0, as

was observed by Leconte et al. (2011). However, with increasing degree of resolution in energy (for the same density of vacancies), the conductivity drops dramatically and goes below the classical limit; only the midgap peak is increased. The inset reveals the underlying phenomenon: here are plotted corresponding DOS for the two energy resolutions (the better the resolution, the higher the DOS obtained). Figure 6.29(b) (main plot) exhibits a similar evolution of the $\sigma_{sc}(E)$ when increasing the density of vacancies to $n = 0.8\%$. For both energy resolutions, σ_{sc} decays under σ_0 around the Dirac point, with a marked peak exactly at the Fermi energy. For $\eta = 0.003$ eV and $n = 0.8\%$, the DOS in the region close to the Dirac point ($E < 0.25$ eV) strongly resembles a gap within numerical resolution. This evolution toward a gap when decreasing the resolution confirms the results presented in Pereira et al. (2008), which suggest that in the zero temperature limit ($\eta \to 0$) the system is an Anderson insulator at the Dirac point.

It is worth noticing that one could draw incorrect conclusions by a too superficial consideration of the behavior of the diffusion coefficients $D(t)$ for states with energies lying inside the gap. The analysis is made by looking at numerics in Fig. 6.29(b) (inset), for two energy resolutions $\eta = 0.015$ eV (full lines) and $\eta = 0.003$ eV (dashed lines). From the simulations and selected energies, one sees that $D(t)$ quickly reach a saturation regime but then surprisingly remain constant at long elapsed times, suggesting a diffusive regime in which quantum effects would be suppressed. This result would be really unexpected since by looking only at $D(t)$, one could conclude that localization effects are suppressed when enforcing the vacancy distribution on one of the two sublattices. Nevertheless, the observed formation of a gap in the density of states clearly suggests that $D(t)$ should be driven to zero in the limit $\eta \to 0$, and this is actually confirmed by increasing the energy resolution from $\eta = 0.015$ to 0.003 eV. The $D(t)$ are clearly seen to decay when $\eta \to 0$ (localized states), whereas the spectral weight of these states being negligible on average, so they should bring an irrelevant contribution to the temperature-dependence in conductivity experiments.

A more rigorous study has been performed in Fan et al. Figure 6.30 shows, for graphene with 1% vacancies, the main scaling behavior of the Kubo conductivity σ at the Dirac point and at an energy of 0.1 eV above. The exponential decay is unquestionable, and from the fits to the conductivity, the localization lengths ξ for two selected energies are extracted and shown as symbols in Fig. 6.30 (inset) with values of $\xi(E = 0) \simeq 8.5$ nm and $\xi(E = 0.1) \simeq 14.2$ nm. These numerical data obtained from the Kubo conductivity perfectly agree with the calculations using the Landauer-Büttiker formula and one-parameter scaling theory (Kramer & MacKinnon 1993; MacKinnon & Kramer 1981) (solid line). An estimation of $\xi(E)$ using the Thouless relationship $\xi(E) = \lambda(E) \exp\left[\frac{\pi \sigma_{sc}(E)}{G_0}\right]$ (dashed line) is also shown.

One notes that the Thouless relationship result well agrees at $E = 0.1$ eV with other results, but gives an overestimated value for ξ at the Dirac point since the numerical value of the zero-energy semiclassical conductivity is not numerically well defined in this limit (see the DOS in Fig. 6.25). In any case, Fig. 6.30 shows clearly that the Dirac point conductivity decays exponentially with increasing length and the estimated localization length agrees perfectly with that predicted from the one-parameter

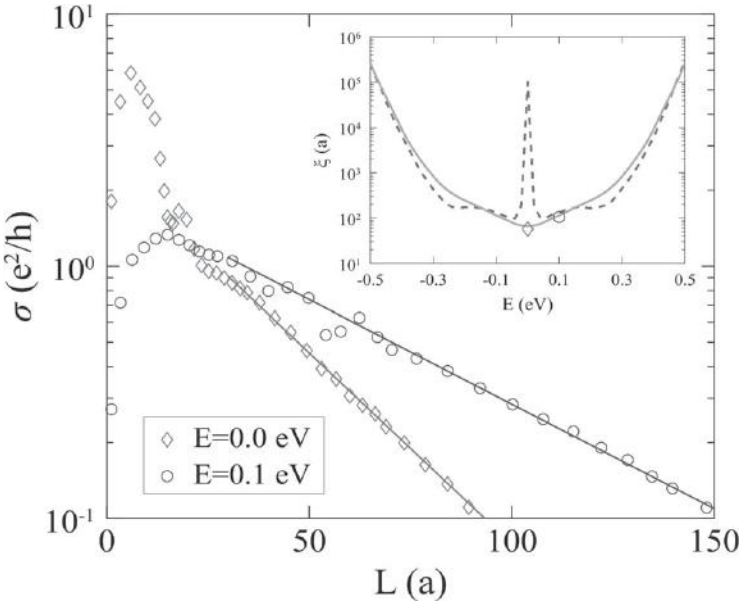

Figure 6.30 Conductivity σ as a function of length L in graphene with 1% vacancy defects. The inset shows the localization length as a function of the Fermi energy calculated from a direct numerical fit and using the scaling theory of localization ($a = 0.142$ nm). (The inset is reproduced with permission from Fan et al. (2014). Copyright (2014) by the American Physical Society. Courtesy of Zheyong Fan)

scaling theory (Kramer & MacKinnon 1993; MacKinnon & Kramer 1981). This validates the formation of an Anderson localization regime at the Dirac point in presence of vacancies.

Other numerical results have been analyzed in terms of the formation of a critical state at the Dirac point (Ferreira & Mucciolo 2015; Ostrovsky et al. 2010). Ostrovsky and coworkers found a saturation of the Landauer-Büttiker conductivity at a value of $4e^2/\pi h$ when increasing the vacancy density, a behavior suggesting the suppression of localization phenomena and a resulting length invariant quantum conductivity (Ostrovsky et al. 2010). Importantly, these results do not apply to the bulk limit but to a situation where boundary conditions (very short channel length against ribbon width) induce direct tunneling between evanescent states at contact, whose density scales with the number of vacancies. By contrast, Ferreira and Mucciolo obtained a Kubo conductivity of $4e^2/\pi h$ at the Dirac point (Ferreira & Mucciolo 2015), which they assigned to a quantum critical point. Such peculiar value for the bulk quantum conductivity of zero spectral measure seems to have a questionable physical meaning, whereas quantum transport simulations reported in Cresti, Ortmann et al. (2013); Trambly de Laissardière and Mayou (2013) and Fan et al. (2014) advocate for a dominant Anderson regime for all the energy spectrum and suggest some delicate numerical convergence issue, as extensively discussed in Fan et al. (2019).

6.4 Polycrystalline Graphene

6.4.1 Motivation and Structural Models

Chemical vapor deposition (CVD) enables the growth of very large films of relatively good quality graphene. However, these films are polycrystalline and incorporate a large number of interconnected domains (of different sizes) through grain boundaries, which are formed roughly as lines of structural defects and differ randomly in crystalline orientations one from another. The formation of extended topological defects is observed at the interface between grains: the grain boundaries (GBs).

Figure 6.31 (in UHV and low temperature) shows a scanning tunneling microscope picture of a grain boundary in graphene, where the different orientations of the two adjacent grains are clearly visible on the corresponding Moiré pattern. These interface regions contain a large amount of structural defects, especially odd-numbered carbon rings, that will act as strong scattering centers, limiting charge mobilities. Moreover, a grain boundary breaks the translational symmetry of the system so that wavefunctions from the two coalescent grains interfere in a destructive manner along the GB, which generate interface states. A theoretical model (Ferreira et al. 2011) proposes charge accumulation along grain boundaries, creating an electrostatic potential that would cause GBs to act as extended electron scatterers.

We note that certain highly symmetric line defects (as shown in Fig. 2.34) can actually give rise to an interesting valley-filtering effect (Gunlycke & White 2011). For instance, in the case depicted in Fig. 6.32(a), the incoming low-energy electron states are given by Eq. (2.27) that we repeat here:

$$|\Psi_{\xi,s}\rangle = \frac{1}{\sqrt{2}} \begin{pmatrix} 1 \\ s\mathrm{e}^{+\mathrm{i}\xi\theta_k} \end{pmatrix}, \tag{6.50}$$

where ξ is the valley index ($\xi = \pm 1$ gives the wavefunction in the $K_\pm$ valley) and $s = \pm 1$ is the band index (electron or hole band). The angle $\theta_k = \arctan(k_y/k_x)$ defines the angle of the wavevector measured from the center of the corresponding valley.

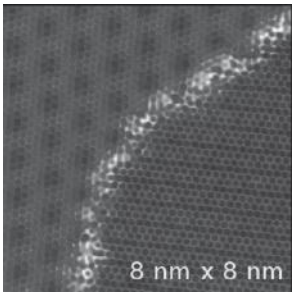

Figure 6.31 Scanning tunneling microscope picture of a grain boundary. Two different Moiré patterns for individual grains are clearly visible. Courtesy of José-Maria M. Gomez-Rodriguez

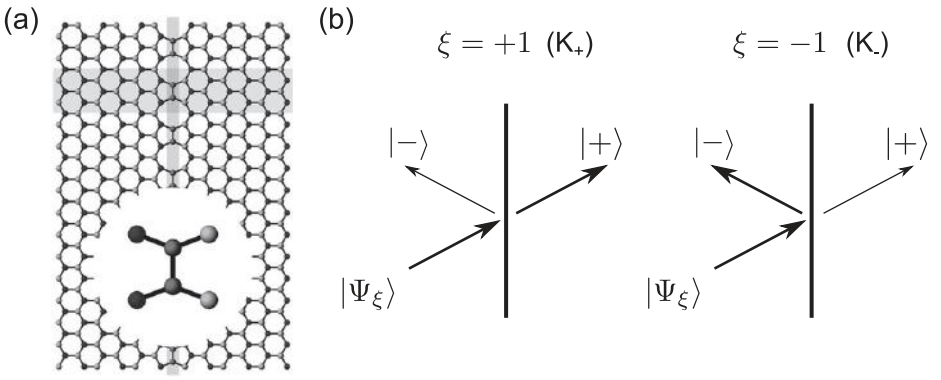

Figure 6.32 (a) A line defect in graphene. (b) Valley states scattering off the line defect. The sublattice symmetric $|+\rangle$ and antisymmetric $|-\rangle$ components of the incident state $|\Psi_\xi\rangle$ are transmitted and reflected, respectively. At the two valleys, K_+ and K_-, an incident quasiparticle state is defined by the valley index ($\xi = \pm 1$) and wavevector k, where the latter points in the direction k given by the angle of incidence θ_k. The scattering is shown to be valley-dependent (Gunlycke & White 2011). ((a) is reproduced with permission from Gunlycke and White (2011). Copyright (2011) by the American Physical Society)

The first (second) component of the vector on the right-hand side of the previous equation gives the probability amplitude in the A (B) sublattice.

Following Gunlycke and White (2011), let us consider waves incident from the left and write $\mathbf{k} = k(\cos\theta_k, \sin\theta_k)$ with $k = |\mathbf{k}|$. Then, using these relations one can write the right-moving solutions as:

$$|\Psi_\xi\rangle = \frac{1}{\sqrt{2}} \begin{pmatrix} 1 \\ \mathrm{i}e^{-\mathrm{i}\xi\theta_k} \end{pmatrix}. \tag{6.51}$$

In the limit $k \to 0$, the reflection operator and the graphene translation operator perpendicular to the line defect commute. This allows construction of symmetry-adapted states $|\pm\rangle$ that are eigenstates of both operators (do not confuse the $\pm$ with the values of ξ). The reflection operator maps A onto B sites and vice versa, and therefore it can be represented by the operator σ_x acting on the two sublattices. From the eigenstates of σ_x, we get

$$|\pm\rangle = \frac{1}{\sqrt{2}} = \begin{pmatrix} 1 \\ \pm 1 \end{pmatrix}. \tag{6.52}$$

The graphene states expressed in the symmetry-adapted basis become

$$|\Psi_\xi\rangle = \frac{1 + \mathrm{i}e^{-\mathrm{i}\xi\theta_k}}{2}|+\rangle + \frac{1 - \mathrm{i}e^{-\mathrm{i}\xi\theta_k}}{2}|-\rangle. \tag{6.53}$$

Gunlycke and White (2011) found that there exist two symmetric states at the Fermi level without a node on the line defect, carrying quasiparticles across the line defect

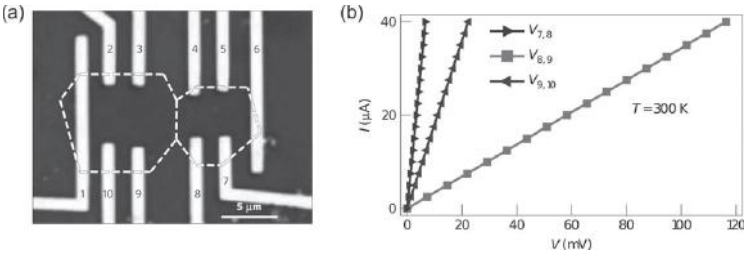

Figure 6.33 (a) An experimental device with multiple electrodes forming contact over two coalesced grains (dashed lines). (b) Current versus bias voltage, measured within each grain and across the grain boundary. The legend shows the corresponding electrode pairs for each curve. (Adapted with permission from Macmillan Publishers Ltd: *Nature Materials*, Yu et al. (2011), copyright (2011))

without scattering. The calculation of the transmission probability across the line defect is

$$T_\xi = |\langle + | \Psi_\xi \rangle|^2 = \frac{1}{2}(1 \pm \sin\theta_k), \tag{6.54}$$

which immediately means that the line defect is semitransparent and its transparency depends on the valley ($T_{K_+} + T_{K_-} = 1$). At a high angle of incidence, there can be almost full transmission or reflection, depending on the valley index ($K_\pm$).

Recent work based on full tight-binding description of such line defects showed that the valley filtering effect can be reversed by applying a gate voltage (Ingaramo & Foa Torres 2016). This occurs because of a *valley-dependent Fano resonance splitting* (Ingaramo & Foa Torres 2016).

The impact on transport of a single boundary has also been measured experimentally (Ma et al. 2017; Yu et al. 2011). Figure 6.33(a) and (b) shows respectively the experimental setup and current–voltage curves measured within two adjacent CVD-grown grains (curves for $V_{7,8}$ and $V_{9,10}$) and at the boundary (curve for $V_{8,9}$). All curves exhibit a linear behavior from which the conductance can be derived (e.g., $G_{8,9} = \frac{dI}{dV}|_{V_{8,9}}$). From this measurement, it is clear that the current is reduced (together with corresponding conductance) when electrons have to cross a grain boundary. A complementary study by Tsen et al. (2012) combining electron transmission microscopy with electrical measurements has also revealed links between electrical and geometrical properties of GBs. However, these studies have generally been carried out on few samples and for a better examination of the potential of CVD-graphene for applications (such as transparent electrodes), a fundamental connection between the morphologies of polycrystalline graphene and their transport features is highly desirable.

Although CVD grown films can be produced at large scales, their corresponding electrical performances remain a bit disappointing when compared with those of exfoliated graphene. A better understanding of the impact of GBs at the macroscopic scale is thus highly desirable to guide experimentalists and engineers for further optimization of the growth processes. A comprehensive description of the correlation between mobility,

sheet resistance, and average grain size is key, as well as the scaling properties of electronic and thermal transport in addition to mechanical properties (when increasing average grain size for instance). Excellent reviews can be found in Cummings, Duong et al. (2014); and Isacsson et al. (2017).

At present, based on atomic-resolution images (An et al. 2011; Huang et al. 2011; Kim et al. 2011; Kurasch et al. 2012) and theoretical models (Yazyev & Louie 2010a), it is a relatively well-established fact that different grains in polycrystalline graphene preferably stitch together predominantly via pentagon–heptagon pairs. Additionally, diffraction-filtered imaging has provided some mapping of the location, orientation, and shape of hundreds of grains and boundaries, revealing an unexpectedly small and intricate patchwork of grains interconnected by tilt boundaries (Kim et al. 2011). However, a typical grain boundary is covered by adsorbates, which indicates that the local configuration of atoms in these areas can differ from the ideal pentagon–heptagon chains.

In what follows, we will discuss some electronic and transport properties of polycrystalline graphene models introduced by Jani Kotakoski (Kotakoski & Meyer 2012). The polycrystalline graphene structures are created by initially fixing only the number of grains and the size of the sample and then randomly growing each of the grains with similar random orientation. The dynamical growth of the structure stops when all the grains have reached neighboring grains in all directions. The equilibrium structures are then created using molecular dynamics simulations (Kotakoski & Meyer 2012). This procedure leads the formation of corrugated structures with realistic misorientation angle distribution and ring statistics (see Fig. 6.34). Such structures have been additionally flattened while ensuring that the local atomic density at any point in the structure remained reasonable. We mention that multiscale modeling of polycrystalline

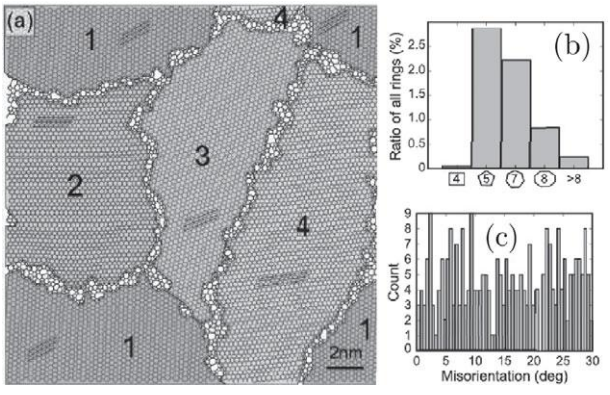

Figure 6.34 Model structures for polycrystalline graphene. (a) Top view of a periodic 20 nm × 20 nm graphene sheet with four grains, as marked by the numbered shaded areas. The lines indicate orientations of the graphene lattice within each grain. (b) Distribution of misorientation angles for the bicrystalline sample structures used in this study. (c) Relative probabilities for nonhexagonal carbon rings in the same structures. (Reproduced with permission from Kotakoski and Meyer (2012). Copyright (2007) by the American Physical Society)

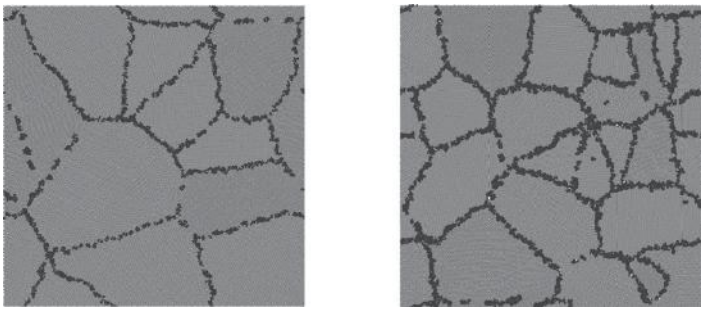

Figure 6.35 Left and right panels are ball-and-stick models for samples S1 and S2, respectively, with grain boundaries outlined in dark tint. Courtesy of Jani Kotakoski.

graphene has been also performed by Hirvonen and coworkers using phase field crystal models. Such models predict realistic formation energies and defect structures of grain boundaries, and are thus ideally suited to deal with ultralarge system sizes required by the polycrystalline nature of graphene (Hirvonen et al. 2016).

For the rest of the discussion, we focus on the electronic and transport properties of two different samples (from here designated S1 and S2; see Fig. 6.35) in which the average grain sizes are 18 nm and 13 nm, respectively.

6.4.2 Electronic Properties of Polycrystalline Graphene

The electronic and transport properties of these flat disordered lattices can be well investigated using a simple π–π^* orthogonal *tight-binding* (TB) model, described by a single p_z orbital per carbon site, with nearest neighbors hopping γ_0, and zero onsite energies. The study was carried out on about 600×600 Å^2 sheets including $N_{\text{sites}} = 138,292$ carbon atoms for sample S1 and $N_{\text{sites}} = 137,985$ carbon atoms for sample S2 (shown in Fig. 6.35). Periodic boundary conditions were applied to the structures to minimize finite size effects. A criterion to search the first nearest neighbors was set empirically to $1.15 \times a_{\text{CC}}$. The local fluctuations of bond length are small enough to reasonably keep a constant value of γ_0 for the transfer integral. The density of states is then computed using the Lanczos recursion method with $N = 1000$ recursion steps and an energy resolution $\eta = 0.01\gamma_0 \simeq 0.03$ eV (Van Tuan et al. 2013).

The DOS of S1 and S2 show little difference from that of pristine graphene (Fig. 6.36 main plot). This suggests that grain boundaries correspond to weak disorder preserving electron–hole symmetry. Only the presence of some enhanced density of zero energy modes and a slight smoothing of van Hove singularities at $E = \pm\gamma_0$ reveal the presence of the disorder. Figure 6.36 (inset) shows that S2 (which is more fragmented than S1) has a larger DOS especially close to the charge neutrality point, reflecting a higher density of midgap states (Stauber et al. 2007).

We next identify grain boundaries by searching for atoms for which the bond length of at least one nearest neighbor differs from the pristine carbon spacing ($a_{\text{CC}} = 1.42$ Å) by

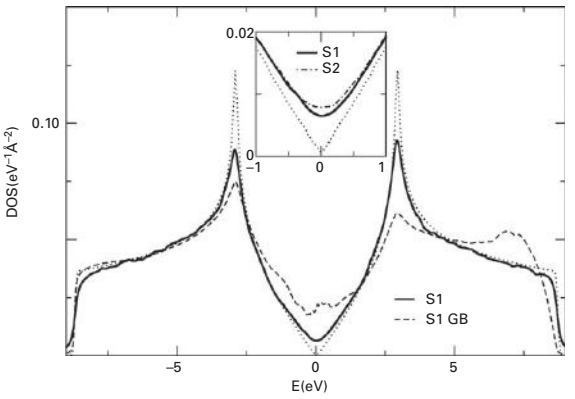

Figure 6.36 Main plot: DOS for pristine graphene (dotted line), polycrystalline graphene S1 (bold line), and the DOS average over grain boundary sites only of S1 (dashed line). Inset: Zoom in the DOS of S1 and S2 (dot-dashed) together with pristine graphene (dashed lines).

0.03 Å or more. Figure 6.36 (main plot) shows the average of local DOS (LDOS) over all boundary sites of S1 (applying the recursion method to a random phase state strictly located on boundary sites). The averaged density shows a very marked contribution of midgap states (Stauber et al. 2007), together with a strong suppression of van Hove singularities at $\pm\gamma_0 = \pm 2.9$ eV. The electron–hole symmetry is also considerably broken owing to the presence of many odd-membered rings along the GB.

6.4.3 Mean Free Path, Conductivity and Charge Mobility

Figure 6.37 (inset) shows the time dependence of $D(t)$ at the Dirac point for both samples S1 and S2. From the maximum values, $\ell_{\rm el}(E)$ (and $\sigma_{\rm sc}$) are deduced (Fig. 6.37, main plot). Despite some genuine electron–hole asymmetry for energies higher than 3 eV (far from the experimentally relevant energy window), $\ell_{\rm el}$ are found to be weakly changing over an energy window around the charge neutrality point, with $\ell_{\rm el}(E, {\rm S1}) \in [6, 10]$ nm for S1 and $\ell_{\rm el}(E, {\rm S2}) \in [4, 7]$ nm for S2. In Fig. 6.37, we also show a rescaled energy-dependent value given by $\sqrt{2} \times \ell_{\rm el}(E, {\rm S2})$, which is surprisingly close to the behavior of $\ell_{\rm el}(E, {\rm S1})$ for S1. It turns out that the corresponding grain size perfectly matches with such a rescaling factor; that is, the grain size for S2 is about $\sqrt{2}$ times smaller than the typical grain size of S1.

From the results above and more extensive simulations, a remarkably simple scaling law of the mean free path with the average grain size ($d_{\rm gz}$) has been identified, namely $\ell_{\rm el} \sim d_{\rm gz}$, a scaling that is also reflected on the charge mobility and sheet resistance of the polcyrstalline sample (Van Tuan et al. 2013). We observe in Fig. 6.38 (inset) the energy dependence of $\sigma_{\rm sc}(E)$, which manifests as energy-dependent variation similar to the mean free path (as well as some linear dependence with charge density in the low-energy limit). An interesting feature is that $\sigma_{\rm sc}(E)$ remains much larger than the minimum value $4e^2/\pi h$ (horizontal dashed line), which fixes the theoretical limit

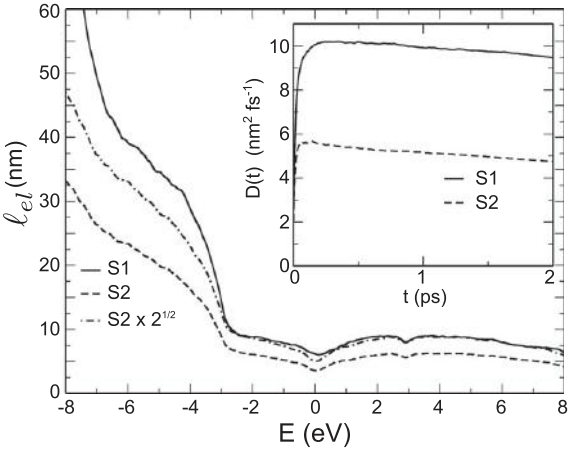

Figure 6.37 Main plot: Mean free path for S1 ($\ell_{\rm el}(E, S1)$, solid curve) and S2($\ell_{\rm el}(E, S2)$, dashed curve), together with a rescaled value $\sqrt{2} \times \ell_{\rm el}(E, S2)$ (dot-dashed curve). Inset: Time evolution of D at the Dirac point for sampler $S1$ and $S2$.

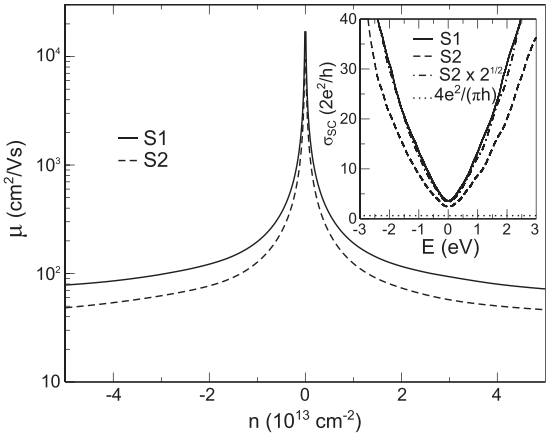

Figure 6.38 Charge mobility $\mu(E)$ for both samples (main plot) along with the semiclassical conductivity $\sigma_{\rm sc}(E)$ (inset). Horizontal dashed line in the inset gives $4e^2/\pi h$. (Adapted with permission from Van Tuan et al. (2013). Copyright (2013) American Chemical Society)

in the diffusive regime, as derived within the SCBA and valid for any type of disorder. This indicates that polycrystalline graphene remains a good conductor.

The charge mobility, $\mu(E) = \sigma_{\rm sc}(E)/en(E)$, with $n(E)$ being the carrier density, is found to vary within 100 cm^2 V^{-1} s^{-1} to $\sim 2 \times 10^4$ cm^2 V^{-1} s^{-1} for $n = 10^{12} - 10^{13}$ cm^{-2}, in very satisfactory agreement with the typically reported values for polycrystalline graphene in recent literature (Tsen et al. 2012). We stress that the computed values of $\mu(E)$ are valid down to the charge neutrality point (that is to the smallest charge density $n(E)$), since we account for the disorder-induced finite DOS, which yields nonzero charge density (and thus no singularity as $1/n(E)$).

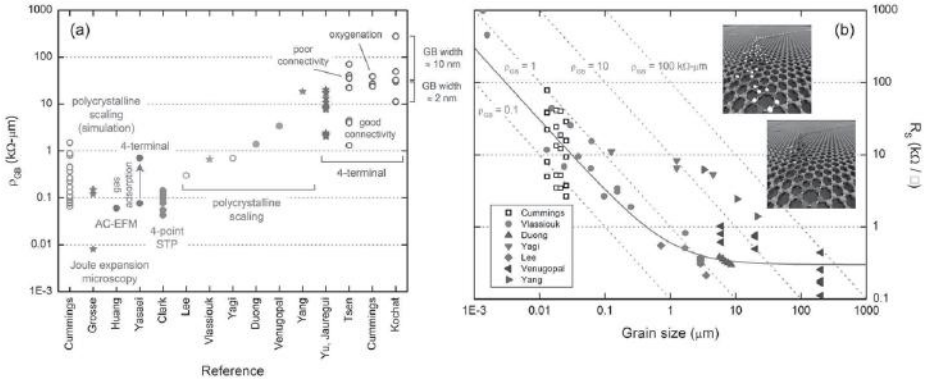

Figure 6.39 (a) Grain boundary resistivity values (ρ_{GB}) extracted from the literature. Open circles are measurements at the charge neutrality point, closed circles are measurements far from the charge neutrality point, and stars are for measurements for unknown Fermi level location. (b) Experimental sheet resistances as a function of grain size from various published works. The solid gray line outlines the scaling law of Eq. (6.55), with $R_s^G = 300\ \Omega/\square$ and $\rho_{GB} = 0.3\ k\Omega\ \mu m$. In both panels, the spread of simulation results stems from varying chemical functionalization degree of grain boundaries (see insets). Figures reproduced from Isacsson et al. (2017); see this reference for more details and all references of mentioned experimental data.

The semiclassical conductivity σ_{sc} of polycrystalline graphene scales linearly with the average grain size (Van Tuan et al. 2013). An interesting point is that the impact of GBs can be recast through the scaling relation (Cummings, Duong et al. 2014)

$$R_s = R_s^G + \rho_{GB}/l_G, \tag{6.55}$$

where $R_s \equiv 1/\sigma_{sc}$ is the sheet resistance of the polycrystalline graphene, R_s^G is the sheet resistance within the graphene grains, l_G is the average graphene grain size, and ρ_{GB} is the GB resistivity. By calculating R_s for polycrystalline samples with a variety of grain sizes and fitting to Eq. (6.55), Cummings et al. extracted an intrinsic GB resistivity of $\rho_{GB} = 0.07\ k\Omega\ \mu m$ (Cummings, Duong et al. 2014). This value is on the low end of those obtained experimentally. However, as shown in Fig. 6.39(a), the value of ρ_{GB} depends significantly on the measurement technique, doping level, material quality, and degree of chemical functionalization (Isacsson et al. 2017).

Actually, the spread of simulation results indicates that ρ_{GB} is modulated by more than one order of magnitude upon varying the density of chemical adsorbates on GBs. Figure 6.39(b) displays the impact of GBs on the experimental electrical properties of polycrystalline graphene through values of sheet resistance versus grain size. Simulation results are shown as open squares, with the spread of values resulting from different degrees of chemical functionalization of the GBs. Overall, the measurements follow the scaling trend described by Eq. (6.55), and the crossover between GB-dominated and grain-dominated transport occurs for grain sizes in the range of 1–10 μm.

An important information for experimental research is that the charge mobility for a (clean) polycrystalline graphene sample with an average grain size of 1 μm (and at a charge density of $n = 3 \times 10^{11}\,\mathrm{cm}^{-2}$) should be in the order of $\mu \sim 300.000\,\mathrm{cm}^2\,\mathrm{V}^{-1}\,\mathrm{s}^{-1}$, whereas to achieve a sheet resistance of 10 Ω/□ (technology target for transparent conductors) would require clean samples with 100 μm average grain size. This is typically one to two orders of magnitude larger compared to estimates from today's experimental data. Such a difference is likely due to the chemical contamination of the grain boundaries (Cummings, Duong et al. 2014; Isacsson et al. 2017). A joint experimental and theoretical study of hydrogenated and oxidized CVD graphene samples has shown that oxygen defects (such as epoxy) accumulate at grain boundaries and eventually provoke strain-induced cracks in the sample and subsequent strong decay of the charge mobility of related devices (Seifert et al. 2015). This does not occur in presence of hydrogen defects, which distribute more homogenously across the samples.

Finally, we note that for the high-quality polycrystalline models studied here numerically, one sees very weak time-dependent decay of $D(t)$ after the saturation value, which indicates a negligible correction due to quantum interferences and localization effect, as confirmed by transport measurements (Yu et al. 2011). The values obtained for ℓ_{el} and $\sigma_{\mathrm{sc}}(E)$ allow an estimation of the localization length $\xi(E)$ of electronic states. Using the scaling analysis $\xi(E) = \ell_{\mathrm{el}}(E)\exp(\pi h\sigma_{\mathrm{sc}}(E)/2e^2)$ (Lee & Ramakrishnan 1985), one obtains localization lengths in the order of $\xi \simeq 10$ μm over a large energy window around the charge neutrality point. This contrasts with values in the order of $\xi \simeq 10$ nm usually obtained with typically 1% of structural defects or covalently bonded adatoms (Lherbier et al. 2012).

To conclude, one observes that the use of CVD graphene in electronic applications rely highly on the production of large area high-quality graphene, and thus dictates an engineering challenge consisting in growing large single-crystalline graphene free from grain boundaries. The technical problem is that fabricating large single-crystalline graphene implies low growth rate and high energy consumption, primarily caused by the required high growth temperature and long growth time. This could eventually restrict highly efficient large scale graphene production for industrial purposes, but as shown in this chapter, the electronic transport properties of clean and polycrystalline graphene are actually very good provided they remain clean from extra chemical contamination so that further improvement is within reach by controlling surface contamination and avoiding the incorporation of defects and cracks upon transfer from metallic to insulating substrates. Accordingly, as fostered by ZongFan Liu from the Beijing Graphene Institute in China, novel growth processes should be developed to overcome such limitations (Sun et al. 2018).

6.5 Graphene Quantum Dots

Electron–electron interactions in graphene systems are generally expected to expected to have an important role, especially: (i) close to the Dirac point, where the low carrier

concentration strongly reduces the screening effects of the Coulomb interactions; (ii) in flat bands, where the quenching of the kinetic energy may lead to enhanced interactions; and (iii) when confinement is strong as in graphene quantum dots. Other effects such as spin–orbit coupling may also play an important role and this is addressed in Section 8.2.

Quantum dots (Alhassid 2000; Kastner 1992; Kouwenhoven et al. 1997) are obtained by confining the electrons in a sample in all three spatial dimensions, much as in an atom but in a length scale orders of magnitude larger. Furthermore, the possibility of contacting them using electrodes allows us to reveal their electronic properties via transport measurements, reaching a much higher magnetic flux than would be possible in atoms. Notwithstanding, it must be noted that as a result of the larger size, the quantization energies of these artificial atoms (of about 1 meV) are smaller than for atoms, and therefore low temperatures are required to resolve them.

Quantum dots made of nanometer-thick graphite layers were demonstrated in early work (Bunch et al. 2005), and a few years later, graphene quantum dots were achieved (Geim & Novoselov 2007; Ponomarenko, Schedin & Katsnelson, 2008; Stampfer et al. 2008), attracting much attention (Stampfer, Guttinger & Molitor, 2012). But why graphene instead of GaAs or other materials? In the following, a brief overview of graphene quantum dots tries to shed light on this and other questions. But first let us review some basics on the Coulomb blockade.

6.5.1 Generalities on Coulomb Blockade

The phenomenon known as Coulomb blockade (Kastner 1992; Kouwenhoven et al. 1997) takes place when the quantum dot is weakly coupled to the leads as represented in Fig. 6.40(a). The conductance then falls below e^2/h and the charge inside the island gets quantized. The relevant energy scales are the level spacing $\delta\varepsilon$ between the single particle levels of the dot, the intrinsic level widths $\Gamma_{L(R)}$ of a given energy level due to the left and right electrodes, the charging energy E_c, and the thermal energy k_BT.

The first experiments on the Coulomb blockade were done in metallic grains (Giaever & Zeller 1968) where the mean level spacing $\Delta = \langle\delta\varepsilon\rangle$ is much smaller than k_BT. In this situation, we have $\Delta \ll k_BT \ll E_c$ and the grain energy spectrum can be considered as a continuum. The electrostatic energy of $\mathcal{N}$ electrons in the quantum dot is given by (Kastner 1992)

$$U(\mathcal{N}) = (\mathcal{N}e)^2/(2C) - \mathcal{N}e\eta V_g, \tag{6.56}$$

where C is the effective capacitance of the quantum dot and ηV_g is the energy shift of the states in the quantum dot due to the gate voltage V_g. By rewriting the previous equation as $U(\mathcal{N}) = (Q - Q_0)^2/(2C) + \textit{constant}$ with $Q = \mathcal{N}e$ and $Q_0 = C\eta V_g$, one sees that $U(\mathcal{N})$ is a parabola with minimum at $Q = Q_0$. Now suppose that V_g is chosen such that a given value of $\mathcal{N}$ minimizes U, then the energy needed to add or take an electron out of the quantum dot is $e^2/(2C)$ and there is an energy gap of $E_c = e^2/C$ for excitations. For low enough temperatures ($k_BT < e^2/(2C)$), this leads to a blockade in the electron and hole flow to the quantum dot.

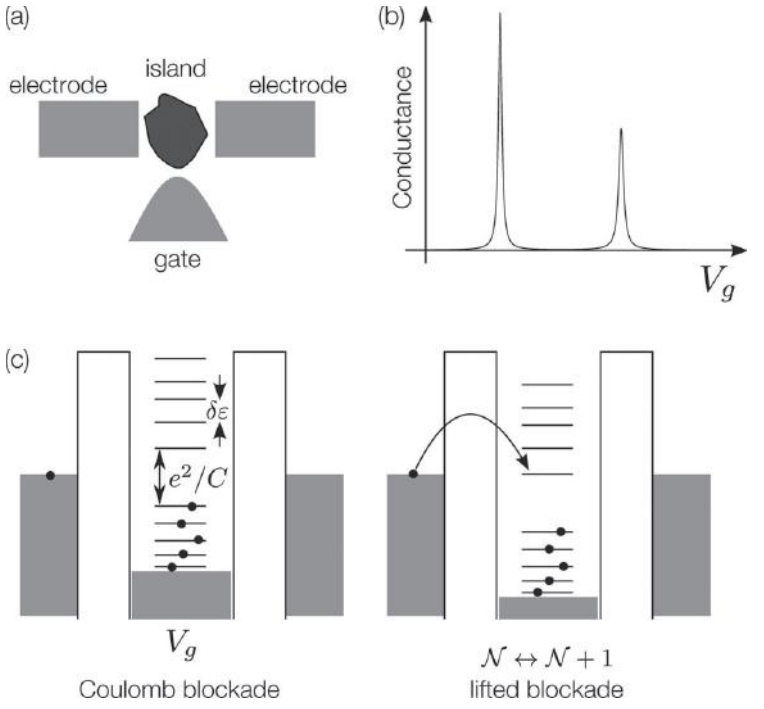

Figure 6.40 (a) A quantum dot weakly coupled to electrodes and in the presence of a gate voltage. (b) Two consecutive conductance peaks vs. gate voltage showing a blockade region in between. (c) Representation of the energy levels for two situations: when blocking is active (left) and at a conductance peak (right).

However, when $Q_0 = (\mathcal{N}+1/2)e$, one has $U(\mathcal{N}) = U(\mathcal{N}+1)$, i.e., the configurations with $\mathcal{N}$ and $\mathcal{N}+1$ electrons are degenerate, and the tunneling of charge to and out of the dot is allowed, leading to a conductance peak. This is observed as a series of conductance peaks separated by regions of vanishing conductance as the gate voltage is changed.

When the quantum dots are small enough such that the level spacing is larger than k_BT, one is in the regime of *quantum* Coulomb blockade: $k_BT < \Delta \ll E_c$. A term due to the filling of the discrete levels E_j must be added to $U(\mathcal{N})$:

$$U(\mathcal{N}) = Q^2/(2C) + \sum_{j=1}^{\mathcal{N}} \left(E_j - e\eta V_g\right). \tag{6.57}$$

The separation between the $\mathcal{N}$th and the $\mathcal{N}+1$th conductance peaks can be obtained from

$$\left(e\eta V_g\right)_{\mathcal{N}+1} - \left(e\eta V_g\right)_{\mathcal{N}} = e^2/C + (E_{\mathcal{N}+1} - E_{\mathcal{N}}) = E_c + \delta\varepsilon. \tag{6.58}$$

Therefore, the separation between the conductance peaks is controlled by the charging energy plus a smaller term due to the spacing of the dot levels. A scheme summarizing this is presented in Fig. 6.40(b) and (c).

Besides providing information on the quantum dot level spacing, the fluctuations in the intensity of the conductance peaks in the quantum Coulomb blockade regime offer complementary information on the wavefunctions in the quantum dot. Indeed, using the standard (sequential) theory (Beenakker 1991), one obtains for the conductance peak $G_{\max}$ in resonance with the jth dot level

$$G_{\max} = \frac{2e^2}{h} \frac{\pi}{2k_B T} \frac{\Gamma_{j,\mathrm{L}} \Gamma_{j,\mathrm{R}}}{(\Gamma_{j,\mathrm{L}} + \Gamma_{j,\mathrm{R}})}. \tag{6.59}$$

This expression is obtained for a single nondegenerate level E_j by assuming that the intrinsic level widths are the smallest energy scale in the problem ($\Gamma_j = \Gamma_{j,L} + \Gamma_{j,R} \ll \delta\varepsilon, k_B T$) and a *constant interaction model* (Alhassid 2000) (E_c independent of the number of electrons in the dot). Since Γ_j can be related to the overlap between the electrodes and the dot wavefunctions, the conductance peaks provide information on the latter (Jalabert et al. 1992).

Studies of a large number of Coulomb blockade conductance peaks and the associated level spacings reveal reproducible universal statistical features, i.e., features that are independent of the particular device; see Alhassid (2000) and references therein. They can be explained by thinking of these islands as nano-/meso-scale electron billiards which are classically chaotic. This fact leads to a peculiar level spacing statistics exhibiting repulsion among neighboring levels described by the Wigner–Dyson distribution (Alhassid 2000). The theoretical level spacing statistics can be derived within random matrix theory and follows one of the Gaussian random ensembles: Gaussian orthogonal ensemble (GOE) or Gaussian unitary ensemble (GUE) depending on whether or not the time-reversal symmetry is broken (Alhassid 2000). Conductance peaks also obey specific statistics which can be derived by similar methods (Alhassid 2000; Jalabert et al. 1992).

Experimentally, achieving good statistics for the level spacings and the conductance peaks is a difficult task since as the gate voltage is changed, the charging energy and the tunneling into the leads may be modified as well. For the case of the conductance peaks, many independent realizations can be obtained by applying a variable magnetic field, thereby improving the statistics (Chang et al. 1996; Patel et al. 1998).

6.5.2 Confining Charges in Graphene Devices

In quantum dots formed of semiconducting materials like GaAs, gating carefully chosen regions is enough to confine the charges. However, this is ineffective for graphene devices due to Klein tunneling (see Section 5.1). The absence of a true bandgap in bulk graphene makes controlling the electron flow a challenging task. Notwithstanding, tunable confinement has been demonstrated by etching graphene into nanoribbons,

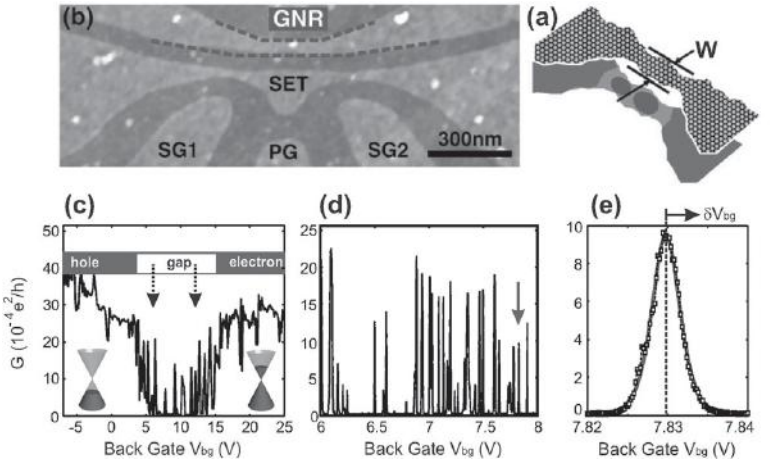

Figure 6.41 (a) An etched graphene nanoribbon (GNR) of width W and the underlying charge puddles. (b) Scanning force microscopy image showing an etched graphene nanoribbon together with a single electron transistor (SET) used to detect single charging events in the ribbon. SG1, PG, and SG2 are lateral gates used for operation of the SET. (c) Low bias conductance of the nanoribbon versus back gate showing a gap between the regimes of hole and electron transport. (d) and (e) are zooms of (c); (e) shows a detail of a single sharp resonance within the gap. (Reproduced with permission from Stampfer et al. (2009). Copyright (2009) by the American Physical Society. Courtesy of C. Stampfer)

which serve as the contacts between a larger graphene sample and the electrodes (Geim & Novoselov 2007; Ponomarenko et al. 2008; Stampfer et al. 2008) or in graphene nanoribbon *pn* junctions (Liu, Oostinga et al. 2009).

One must be aware, however, that a disorder potential in the nanoribbons may induce electron–hole puddles producing charged islands along the ribbon direction (Liu, Oostinga et al. 2009; Stampfer et al. 2009; Todd et al. 2009). This introduces new energy scales such as the charging energy of the quantum dots that are formed, thereby making it a more difficult problem than one would have naively expected. Figure 6.41 (reproduced from Stampfer et al. 2009) illustrates this issue.

Tunability of a graphene quantum dot can be achieved by using a back gate as well as side gates, which allow pinching off the constrictions independently. An example of a tunable Coulomb blockade device is shown in Fig. 6.42(a) and (b). A trace of the source-drain current as a function of the gate voltage for this device is shown in Fig. 6.42(c). The conductance oscillations were shown to be regular over more than ten conductance peaks with a period of 18.2 mV, as shown in Figure 6.42(d). Fig. 6.42(e) shows a density plot of the differential conductance as a function of the bias and plunger gate voltages.

From the width of the Coulomb diamonds along the vertical direction, one can infer a charging energy $E_c \sim 3.5$ meV. An independent estimation of E_c can be obtained by modeling the island as a disk with diameter d and calculating its self-capacitance (Güttinger et al. 2012; Kouwenhoven et al. 1997) $C_{\text{disk}} = 4\epsilon_0\epsilon d$, where ϵ can be

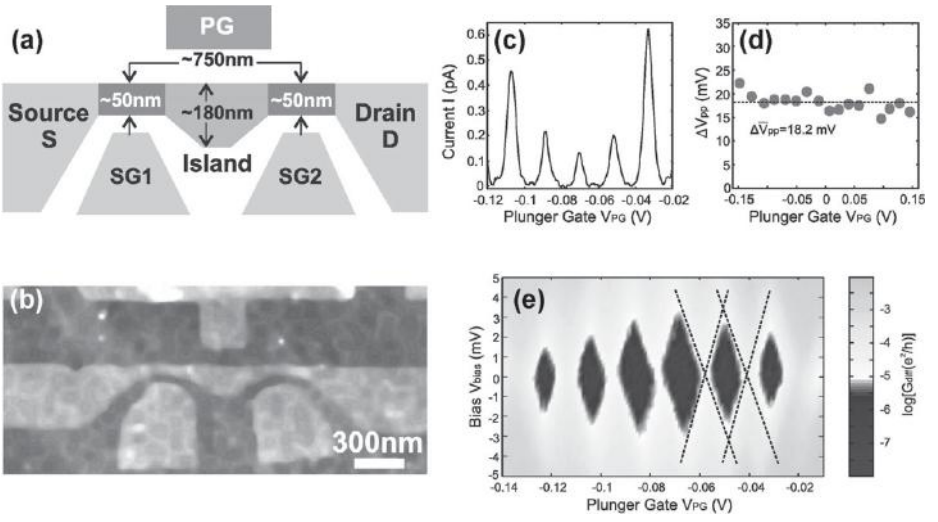

Figure 6.42 (a) and (b) An all-graphene quantum-dot device. (c) The oscillation in the source-drain current as a function of the plunger gate PG as indicated in (a). The peak spacing for 18 consecutive current peaks is plotted in (d). The differential conductance as a function of the bias and plunger gate voltages is shown as a density plot in (e). (Reprinted with permission from Stampfer et al. (2008). Copyright (2008), American Institute of Physics. Courtesy of C. Stampfer)

estimated as the average of the dielectric constant of the oxide underneath and the vacuum ϵ, $\epsilon = (\epsilon_{ox} + 1)/2 \simeq 2.5$. Since this simple model underestimates the capacitance of the island, which is increased by the capacitive coupling of the island to the gates and the leads, the resulting charging energy $E_c^{\text{disk}} = e^2/C_{\text{disk}}$ can be used as an upper bound for the charging energy of the island E_c ($E_c \sim 2.5 \times E_c^{\text{disk}}$) (Güttinger et al. 2012).

From Fig. 6.42(d), one can see that there are no important fluctuations in the separation between Coulomb peaks, from which we can conclude that the island spacing is much smaller than E_c. This is confirmed by Fig. 6.42(e), which shows no additional lines due to excited states or cotunneling events.

Smaller dots ($d < 100$ nm) may reveal important information about the level statistics of the graphene island (Ponomarenko et al. 2008). But is there any difference between graphene quantum dots and those made of conventional semiconductors? This is an interesting and debated question (Huang, Lai & Grebogi 2010; Libisch, Stampfer & Burgdörfer 2009; Ponomarenko et al. 2008). Whereas in the absence of a magnetic field for a chaotic dot made of a usual semiconductor material one would expect level statistics given by the GOE, the level spacing of a chaotic Dirac or neutrino billiard was predicted to follow the GUE (Berry & Mondragon 1987) (a time-reversal symmetry breaking due to chirality). Although experimental evidence in this direction has been presented (Ponomarenko et al. 2008), time-reversal symmetry at zero magnetic field is restored when both valleys are taken into account (see, for example, Beenakker (2008), and other authors have shown numerical evidence for GOE statistics in both

clean chaotic billiards (Libisch et al. 2009) and disordered dots with defects (Huang et al. 2010).

So far, we have seen that tunable confinement is possible in single-layer graphene devices by connecting the graphene island with the electrodes through graphene constrictions. There are two factors that complicate the controllability of these confining constrictions: (a) the formation of electron–hole puddles as mentioned before and (b) edge roughness. Electron–hole puddles may be lessened by suspending the device, thereby isolating it from the substrate. An alternative would be to use a substrate such as hexagonal boron nitride (Dean et al. 2010) where disorder effects are reduced. Edge roughness, on the other hand, changes the ribbon properties as predicted (Evaldsson et al., 2008; Mucciolo et al., 2009; Querlioz et al., 2008), increasing the differences between different geometries (as observed in Han et al. (2007), and Chen et al. (2007)), introducing localization and inducing energy gaps. Improving the edge sharpness can be achieved, for example, by optical annealing (Begliarbekov et al. 2011) or by bottom-up fabrication of GNRs (Cai et al. 2010).

A different strategy was presented in Allen et al. (2012), where quantum confinement has been demonstrated in suspended bilayer graphene with external electric fields used to open a bandgap. Given that a suspended 2D sample is used, the experiments are clean from edge-disorder and substrates effects.

Other interesting phenomena not mentioned before include controlling the spin degree of freedom in graphene quantum dots and exploring elastic and inelastic cotunneling phenomena. Interested readers may find more in specialized reviews (Güttinger et al. 2012).

6.6 Further Reading and Problems

- For a general presentation on disorder effects in carbon nanotubes, see Roche et al. (2006).
- Readers interested in transport through edge states and the influence of disorder (not covered here) may follow the presentation in Wimmer (2009). A clever way to do interferometry with these states is discussed in Usaj (2009).
- For a very recent and detailed review on graphene quantum dots, we recommend Güttinger et al. (2012).

Problems

6.1 *Conductance through a SWNT with a single vacancy.* As another example of application of Landauer's theory to carbon-based devices, let us consider the case of transport through a metallic carbon nanotube with a single vacancy. The simplest forms of introducing the vacancy within a π-orbital model are (i) disconnecting one of the orbitals or (ii) introducing a very large onsite energy at one lattice point. Both models give equivalent results for the Landauer conductance.

(a) Calculate the conductance in the presence of this defect.

(b) You are encouraged to rationalize the conductance decrease due to the vacancy using the mode-decomposition introduced in Section 5.2.2. (For a complementary approach that uses an effective Hamiltonian instead of the *tight-binding* model used here, we refer to Matsumura and Ando (2001).)

6.2 *Conductance in the presence of a single Stone–Wales defect.* Consider a nanotube with a single Stone–Wales defect.

(a) By using a simple *tight-binding* model, where only the topology of the hoppings is changed, compute the density of states and the conductance.

(b) Repeat your calculation for a graphene nanoribbon. Do the results depend on the position of the defect?

6.3 *Transmission through a line defect and valley filtering.* Consider the line defect in Fig. 6.32(a).

(a) Consider electrons that are incident on the line defect from the left. Express the solutions for the wavefunctions on each valley (in bulk graphene) for these left-moving electrons.

(b) Following Gunlycke and White (2011), note that in the $k \to 0$ limit, the reflection operator and the graphene translation operator perpendicular to the line defect commute. Then obtain symmetry-adapted states $|\pm\rangle$ that are eigenstates of both operators.

(c) Compute the transmission probabilities for states on each valley and show that this line defect acts a valley filter.

6.4 *Elastic mean free path of carbon nanotubes and graphene nanoribbons.*

(a) Follow up our discussion in Section 6.1 based on White and Mintmire (1998) and derive Eq. (6.7) ($\ell_{\rm el} = 18\sqrt{3}a_{\rm cc}(\gamma_0/W)^2N$) for the elastic mean free path in carbon nanotubes. Discuss the dependence of $\ell_{\rm el}$ on the tube diameter.

(b) Discuss the dependence of $\ell_{\rm el}$ on the width for the case of a graphene nanoribbon. (*Hint*: For this last question you may follow Areshkin et al. (2007).)

6.5 *Level spacings of GaAs and graphene quantum dots compared.*

(a) Compare the typical level spacing for a quantum dot made of GaAs and one made of graphene with the same diameter d. In which one are confinement effects going to be more important?

(b) Look for experimental data in the literature to confirm your assertion and point out the main differences between the conductance oscillations in small and large diameter dots.

** Additional exercises and solutions available at our website.

7 Quantum Hall Effects in Graphene

The concept of *Berry phase* has become a cornerstone in condensed matter physics, with remarkable observable consequences such as the quantum Hall effect in graphene. We start this chapter by introducing the Berry phase in the context of the solid-state theory, which includes the definition of this geometric phase intricated to its mathematical cement known as Berry Curvature. Next, we briefly ellaborate on some of its consequences on the semiclassical transport theory by introducing the notion of anomalous velocity, which induces the valley Hall effect phenomenon. We then continue by overviewing some of the salient effects of quantum phases driven by internal degrees of freedom and external magnetic fields on the electronic and transport properties of graphene-based materials, including the peculiarities observed in the quantum Hall effect regime and driven by the additional pseudospin-related Berry's phase. This chapter will also explain how to incorporate the effects of gauge fields as phase factors of tight-binding parameters, followed by various illustrations of the field-dependent electronic properties of carbon nanotubes and single-layer graphene, showing their simple (although spectacular) consequences on transport properties, all aspects predicted theoretically and confirmed experimentally. Finally, we introduce Haldane's model of a Chern insulator, providing the first framework for achieving a quantum Hall effect without Landau levels, thereby preparing our way for the quantum spin-Hall effect to be discussed in Chapter 8.

7.1 Berry Phase

The Berry phase (or Pancharatnam–Berry phase) was introduced in 1984 by Michael Berry (Berry 1984) emphasizing how geometric phases of time-evolving wavefunctions provide a powerful and unifying concept in several branches of classical and quantum physics. Since then, this concept has acquired a paramount importance in condensed matter and many advances have been achieved on relating the theory of such phases and their observable consequences (Resta 2000; Xiao et al. 2010). Here, we briefly introduce the concept and then comment on its importance for describing the electronic and transport properties in graphene-based materials and two-dimensional materials described by honeycomb lattices.

Let us consider a Hamiltonian $\mathcal{H}(\vec{\lambda})$ that depends on a collection of parameters $\vec{\lambda} = (\lambda_1, \lambda_2, \ldots, \lambda_n)$, which, in turn, may depend on time. The adiabatic theorem tells that if $\vec{\lambda}$ changes slowly in time, then a particle initially in a eigenstate $|\psi_{j,\vec{\lambda}}\rangle$ (with eigenenergy $\varepsilon_{j,\vec{\lambda}}$) will remain in that state (apart from corrections that vanish in the limit of slow enough variation). What comes as a surprise is what happens with the phase of such a state. The state at time t differs from the initial one in a phase. The factors multiplying the initial state include two contributions:

(i) The first term reads $\exp[(-i/\hbar)\int_0^t dt' \varepsilon_{j,\vec{\lambda}}(t')]$, and describes the (expected) phase acquired because of the dynamics, also called the *dynamical phase*;
(ii) The second factor, $\exp(i\gamma(t))$, gives the *geometric phase*, which may even persist after a cyclic change of parameters. The geometric phase after such cyclic variation is called the Berry phase and can be understood as a correction capturing the effect of the states that are projected out in the adiabatic approximation.[1]

The geometric phase can be recast in a convenient form by noting that the phase difference between the jth eigenstate corresponding to slightly different values of $\vec{\lambda}$ is

$$e^{-id\gamma_j} = \frac{\langle \psi_{j,\vec{\lambda}} | \psi_{j,\vec{\lambda}+d\vec{\lambda}} \rangle}{|\ \langle \psi_{j,\vec{\lambda}} | \psi_{j,\vec{\lambda}+d\vec{\lambda}} \rangle\ |}. \tag{7.1}$$

Using this equation, one can write the change in the phase $d\gamma_j$ as

$$d\gamma_j = i \langle \psi_{j,\vec{\lambda}} | \hat{\nabla}_\lambda \psi_{j,\vec{\lambda}} \rangle \cdot d\vec{\lambda} = \mathcal{A}_j \cdot d\vec{\lambda}, \tag{7.2}$$

where we have defined $\mathcal{A}_{j,\vec{\lambda}} \equiv i \langle \psi_{j,\vec{\lambda}} | \hat{\nabla}_\lambda \psi_{j,\vec{\lambda}} \rangle$, which is called the Berry connection (and sometimes also Berry vector potential) as it defines the phase connecting eigenvectors, which correspond to Hamiltonians nearby in parameter space.

Although the Berry connection is not gauge invariant, the *Berry phase* defined on a closed directed curve $\mathcal{C}$,

$$\gamma_j = \oint \mathcal{A}_{j,\vec{\lambda}} \cdot d\vec{\lambda}, \tag{7.3}$$

becomes gauge invariant as it only depends on the initial and ending points of the geometrical contour in the Brillouin zone. Another key mathematical quantity is the so-called Berry curvature Ω_j, which is given by the curl of the Berry connection:

$$\Omega_j(\vec{\lambda}) \equiv \nabla_\lambda \times \mathcal{A}_{j,\vec{\lambda}}. \tag{7.4}$$

Thus, the flux of the Berry curvature through the surface whose frontier is the contour $\mathcal{C}$ gives the Berry phase. The Berry curvature is therefore a very useful quantity, which through the Berry phase pilots the time-dependent evolution of propagating wavefunctions.

[1] One must recall that one of the assumptions is that the levels are nondegenerate so that at each instant, the eigenstates of the Hamiltonian (corresponding to the instantaneous values of the parameters) remain in a one-to-one relation with each other. In this process, the states other than the one under consideration are essentially being projected out. Their effect is manifested in the Berry phase.

A fundamental question is how can we connect this parameter variation with the physics of a crystal? The answer to this question was pioneered by Joshua Zak, who provided a formulation of the Berry phase for the energy bands in solids (Zak 1989). The role of the parameter space is taken naturally by the space of wave-vectors $\mathbf{k}$, labeling the Bloch-type solutions in a crystal $|\Psi_{\mathbf{k}}\rangle = e^{i\mathbf{k}\cdot\mathbf{r}}|\psi_{\mathbf{k}}\rangle$, and the role of the eigenstates is played by the periodic part of the Bloch-type solutions $|\psi_{\mathbf{k}}\rangle$ satisfying $\langle\mathbf{r}|\psi_{\mathbf{k}}\rangle = \langle\mathbf{r}+\mathbf{R}|\psi_{\mathbf{k}}\rangle$, with $\mathbf{R}$ a Bravais lattice vector. The $|\psi_{\mathbf{k}}\rangle$ are the eigenstates of $\mathcal{H}(\mathbf{k})$, which takes the role played by the Hamiltonian in our previous discussion.

This way, the concept of Berry phase is conveniently ported to the case of the states in a crystal, and we can now use all the previous expressions by making the appropriate replacements. The variation of $\mathbf{k}$ in parameter space can be thought of as a variation induced dynamically on a wavepacket upon the action of, for example, a magnetic field. The interesting point is that when $\mathbf{k}$ moves in the wave-vector space, the Bloch states will in general acquire a Berry phase. The Berry phase is an intrinsic property of the band structure features. Being fully defined by the eigenstates (and not the eigenergies), it provides information, which is complementary to that of the energy spectrum, and therefore an additional label for the crystal energy bands.

For single-particle physics, the so-called Chern number is determined by the integration of the Berry curvature over the whole Brillouin zone, and when it takes an integer value (or half-integer for many-body wavefunctions), it acquires the nature of a *topological invariant* of the wavefunction correlations (expressed through the Kubo Hall conductivity). Its groundbreaking role in explaining the unprecedented quantization (and robustness to disorder) of the Hall plateaus has been pioneered by Mahito Kohmoto (1985). Here, we will mention a few useful properties of the Berry curvature and related concepts for later use in the rest of this chapter (Xiao et al. 2010):

(i) The first property is a statement of a conservation law for the Berry curvature:

$$\sum_j \Omega_j(\mathbf{k}) = 0. \tag{7.5}$$

Thus, the sum of the Berry curvature over all available bands is zero at each point in parameter space.

(ii) If the crystal has inversion symmetry (IS), then

$$\Omega_j(\mathbf{k}) = \Omega_j(-\mathbf{k}). \tag{7.6}$$

(iii) If the crystal has time-reversal symmetry (TRS), then

$$\Omega_j(\mathbf{k}) = -\Omega_j(-\mathbf{k}). \tag{7.7}$$

Because of this property, in the presence of TRS, the integral of the Berry curvature over the full Brillouin zone vanishes. Thus, a TRS breaking ingredient such as a magnetic field is typically needed to get nontrivial Chern number. This will be the subject of later sections in this chapter.

As a result of (ii) and (iii), in the presence of both inversion and time-reversal symmetry, either $\Omega_j(\mathbf{k}) \equiv 0$ for all $\mathbf{k}$, or it is not defined. As we will see, the latter point is crucial for the case of graphene, where in spite of having both symmetries, the Berry phase differs from zero.

The existence of a nontrivial Berry phase has been demonstrated to have many profound consequences in quantum physics (Kohmoto 1985; Thouless 1998; Xiao et al. 2010), and in graphene and carbon nanotubes, it conveys phenomena such as absence of backscattering, Klein tunneling, weak antilocalization, the zero-energy Landau level, and an anomalous quantum Hall effect, as presented throughout this book.

7.2 Graphene's Berry Phase and Its Observation in ARPES Experiments

One particularly relevant manifestation of the Berry phase in graphene stems from the pseudospin quantum degree of freedom associated with the sublattice degeneracy of the honeycomb lattice. The experimental observation of such Berry phase has been made possible thanks to photoemission spectroscopy studies performed by the group of Alessandra Lanzara (Hwang et al. 2011).

First, let us observe that under 2π rotation, the eigenstates of the Dirac excitations in graphene get a π phase factor (the π-Berry phase). Indeed, using the rotation operator $\mathcal{R}(\theta) = \mathrm{e}^{-\mathrm{i}\boldsymbol{\theta}\cdot\mathbf{S}/\hbar}$, with $\mathbf{S} = \hbar/2\hat{\sigma}_z$ for spin-1/2 particles, it is readily shown that $\mathcal{R}(\theta = 2\pi)|\Psi_{\mathrm{K}_\pm}(s = \pm 1)\rangle = \mathrm{e}^{\mathrm{i}\pi\hat{\sigma}_z}|\Psi_{\xi,s}\rangle = -|\Psi_{\xi,s}\rangle$ (using $\mathrm{e}^{-\mathrm{i}\theta(\hat{n}\cdot\hat{\sigma})/\hbar} = \cos\theta + \mathrm{i}(\hat{n}\cdot\hat{\sigma})\sin\theta$). By computing the Berry connection using Eq. (7.4), we obtain

$$\mathbf{A} = -i\langle\psi_k|\hat{\nabla}_k|\psi_k\rangle = \frac{-i}{2}(1, \mathrm{e}^{-\mathrm{i}\theta})\cdot\begin{pmatrix} 0 \\ i\nabla_k\theta\mathrm{e}^{\mathrm{i}\theta}\end{pmatrix} = \frac{\mathbf{e}_\theta}{2|\mathbf{k}|}, \tag{7.8}$$

($\mathbf{e}_\theta$ is a unit vector perpendicular to $\mathbf{p}$) while

$$\gamma_c = \oint \mathbf{A}\cdot d\mathbf{k} = \int_0^{2\pi} d\mathbf{k}\cdot\frac{\mathbf{e}_\theta}{2|\mathbf{k}|} = \pi. \tag{7.9}$$

The observation of a Dirac cone and the existence of pseudospin-related quantum phases has been confirmed through angle-resolved polarization-dependent photoemission spectroscopy (ARPES) (Hwang et al. 2011; Liu et al. 2011). Figure 7.1 shows the experimental photoelectron intensity maps at the Fermi level E_F versus the two-dimensional wave-vector $\mathbf{k}$ for single-layer graphene for the two polarization geometries. The main feature in the intensity maps of both geometries is an almost circular Fermi surface centered at the K point. Additionally, the angular intensity distribution is seen to be polarization-dependent in the sense that the minimum intensity position is in the first Brillouin zone for X-polarization, while the maximum intensity position is in the first Brillouin zone for Y-polarization geometry, suggesting a π rotation of the maximum intensity in the $k_x - k_y$ plane around the K point upon rotating the light polarization by $\pi/2$, from X to Y. This result can be demonstrated by computing

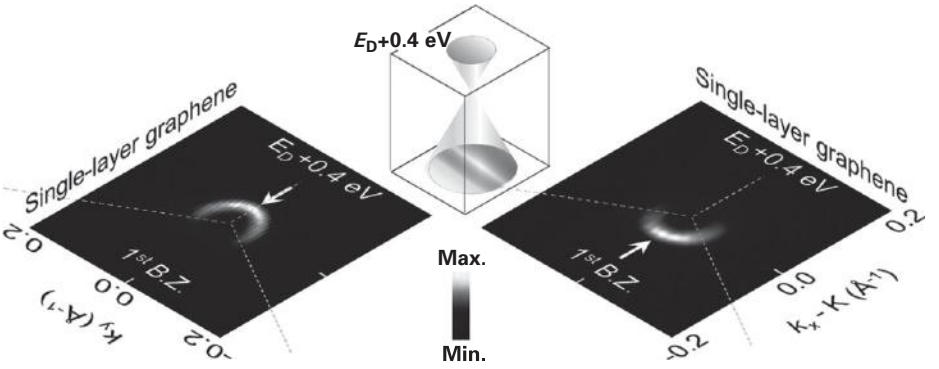

Figure 7.1 Measured intensity maps of single-layer graphene at energy $E = E_F$ with X- and Y-polarized light, respectively. Intensity maxima are denoted by white arrows and the electronic band structure of single-layer graphene is shown in the sketch. E_F is 0.4 eV above the Dirac point energy. (Reproduced with permission from Hwang et al. (2011). Copyright (2011) by the American Physical Society. By courtesy of Choonkyu Hwang)

the wave-vector-dependent photoelectron intensity $I_k = |\langle \mathbf{k}+\mathbf{Q}|\mathcal{H}_{\rm elm}(\mathbf{k},\mathbf{Q})|\Psi_{sk}\rangle|^2$, introducing the field-induced transition matrix element between graphene eigenstates and $|f_{\mathbf{k}+\mathbf{Q}}\rangle = 1/\sqrt{2}(1,1)$, the plane-wave final state projected onto the p_z orbitals of graphene. (Note that all states are expressed using the basis set of Bloch sums of localized p_z orbitals at sublattices A and B.) The interaction Hamiltonian coupling to electromagnetic waves of wave-vector $\mathbf{Q}$ is obtained by using the velocity operator and the external vector potential as $-\frac{e}{c}\hat{\mathbf{A}}\cdot\hat{\mathbf{v}}$ ($A(\mathbf{r},t) = \mathbf{A}_{\mathbf{Q}}e^{i(\mathbf{Q}\cdot\mathbf{r}-\omega t)}$), which can be approximated close to the Dirac point by $\mathcal{H}_{\rm elm}(\mathbf{q}+\mathbf{K}) \sim \frac{ev_F}{\hbar c}(A_x^0\sigma_x + A_y^0\sigma_y)$. Finally, one obtains for both polarizations $I_k^{X-\rm pol} \sim \sin(\theta_q/2)$, whereas $I_k^{Y-\rm pol} \sim \cos(\theta_q/2)$ from which it is clear that the photoemission intensity map is rotated by π when the light polarization is rotated by $\pi/2$ (Hwang et al. 2011).

7.3 Anomalous Velocity and Valley Hall Effect

The dynamics of Bloch electrons in the presence of electromagnetic field occupies a central role since the early days of solid-state theory. Applying a weak electric field produces a change of the electronic wave-vector, i.e., a motion in momentum space. A crucial quantity is the electron velocity, which is typically written as (Ashcroft & Mermin 1976a):

$$v_n(\mathbf{k}) = \frac{1}{\hbar}\frac{\partial \varepsilon_n(\mathbf{k})}{\partial \mathbf{k}}, \tag{7.10}$$

where $\varepsilon_n(\mathbf{k})$ corresponds to the eigenenergy of the state with wavevector $\mathbf{k}$ in band n. This expression gives the velocity of the Bloch electrons, which is field-independent

(which is very convenient given that the electric field breaks the translational invariance, thereby jeopardizing the application of Bloch's theorem).

However, the description of the semiclassical dynamics needs to be modified when a nonvanishing Berry curvature is present. Specifically, it can be shown that an anomalous term involving the Berry curvature *and* the electric field **E** appears:

$$v_n(\mathbf{k}) = \frac{1}{\hbar}\frac{\partial \varepsilon_n(\mathbf{k})}{\partial \mathbf{k}} - \frac{e}{\hbar}\mathbf{E} \times \Omega_n(\mathbf{k}), \tag{7.11}$$

which needs to be supplemented with the equation of motion:

$$\dot{\mathbf{k}} = -\frac{e}{\hbar}\mathbf{E}. \tag{7.12}$$

The second term on the right-hand side of Eq. (7.11) is known as the *anomalous velocity* and although it had already been obtained in the 1950s (Karplus & Luttinger 1954; Kohn & Luttinger 1957) its connection with the Berry curvature came decades later. (For a review, we refer to Xiao et al. (2010).) Being perpendicular to the electric field, the anomalous velocity is expected to lead to a Hall effect, namely the generation of a voltage difference transverse to the electric current.

By using the symmetry properties of the Berry curvature (Section 7.1), we can get a better grasp of when this anomalous term can play a role. One of the most interesting outcomes is the possibility of having a Hall effect which, unlike the conventional one, does not arise from an applied magnetic field. Indeed, one could have a Hall effect arising solely from inversion symmetry breaking.

Let us consider the case of graphene with broken inversion symmetry. This can arise, for example, as a substrate effect; when graphene is placed on hexagonal boron nitride, the onsite potential becomes different on each sublattice (Zhou et al. 2007). This leads to a gap opening and also to a Berry curvature which is nonzero and with opposite signs on each valley. Thus, when an electric field is applied, electrons in different valleys will move in opposite directions perpendicular to the electric field, thereby giving a *valley Hall* current in the bulk (Xiao et al. 2007, 2010).

Exploiting the valley degree of freedom critically requires generating and detecting valley polarized currents. There are several proposals for generating valley polarized currents, including using a constriction in a suitable geometry (Rycerz et al. 2007), using line defects (Gunlycke & White 2011; Ingaramo & Foa Torres 2016) (as discussed in Section 6.4.1), or strain (Fujita et al. 2010; Stegmann & Szpak 2016, 2018). The valley Hall effect, on the other hand, offers an alternative path for detecting a valley polarized current. Recent experiments reported the observation of such effect in transport (Gorbachev et al. 2014), though it is currently debated (Marmolejo-Tejada et al. 2018).

A similar scheme can be applied to bilayer graphene where the breaking inversion symmetry can be induced and tuned by applying an electric field perpendicular to the graphene bilayer (Shimazaki et al. 2015). Finally, onset of quantized valley Hall effect from nonlocal transport measurements in very high-quality hBN-encapsulated graphene (ballistic) devices suggests the formation of valley-polarized edge states in a gapped structure (Komatsu et al. 2018), whereas the exciting possibility of simultaneously

generating in graphene a bulk valley-polarized dissipative transport and a quantum valley Hall effect by combining strain-induced gauge fields (for a recent review on this topic we refer to Naumis et al. (2017)) and real magnetic fields has been proposed theoretically (Settnes et al. 2018).

7.4 The Peierls Substitution

To study the effects of a magnetic field $\boldsymbol{B}$ in graphene, we need to revise how to introduce it in the Hamiltonian. In a *tight-binding* or lattice Hamiltonian (which contrasts with the nearly free electron limit), this is typically done by using the so-called Peierls substitution (after Rudolf Peierls (Peierls 1933)), whereby the hoppings connecting i and j, γ_{ij}, are transformed as[2] (Kohn 1959b):

$$\gamma_{ij}(\boldsymbol{B}) = \exp\left(\mathrm{i}\frac{q}{\hbar}\int_{\boldsymbol{r}_i}^{\boldsymbol{r}_j}\boldsymbol{A}\cdot d\boldsymbol{\ell}\right) \times \gamma_{ij}(\boldsymbol{B}=\boldsymbol{0}). \tag{7.13}$$

The hoppings at zero field are multiplied by a phase factor (known as the Peierls' phase) equal to the charge q (which is equal to $-e$) divided by $\hbar$ times the line integral of the vector potential $\boldsymbol{A}$ ($\boldsymbol{B} = \mathbf{rot}\boldsymbol{A}$) on a straight path connecting $\boldsymbol{r}_i$ and $\boldsymbol{r}_j$. This is very convenient as it is not necessary to recompute the material parameters when changing the magnetic field but rather the change in the phase, which is much easier to calculate.

In the continuum limit, this is equivalent to the substitution:

$$(\hbar/i)\nabla \rightarrow (\hbar/i)\nabla - q\boldsymbol{A}, \tag{7.14}$$

also known as minimal coupling.[3] The crucial point is that the gauge invariance of the Schrödinger equation has to be preserved. This means that following a gauge transformation ($\boldsymbol{A} \rightarrow \boldsymbol{A} + \nabla\chi$), we need to transform the operators (or the states) accordingly.

The Peierls substitution provides a direct way to assess the effects of a magnetic field based on a tight-binding model and is the basis of many calculations. The underlying approximations are, however, quite subtle and have been the subject of considerable debate (Alexandrov & Capellmann 1991; Kohn 1959b; Luttinger 1951). Usually, it is derived assuming slowly varying potentials on the lattice scale (Luttinger 1951) (requiring, for example, that the basis of localized orbitals remains unaffected by the magnetic field). Other subtle issues arise especially when interactions beyond nearest neighbors are present, and one might question, for example, the choice of a straight path in the line integral. For a detailed discussion on these issues, we refer to Boykin et al. (2001).

As a particle loops around a lattice's unit cell, it acquires a phase ϕ, which is equal to the sum of the individual phases along the path, see Fig. 7.2. This phase can be regarded

[2] For a brief account on this, we refer to *The Feynman Lectures on Physics*, volume III, section 21–2, available at www.feynmanlectures.caltech.edu/.

[3] Note that we use here the international system of units (SI). In the CGS system, the substitution reads $(\hbar/i)\nabla \rightarrow (\hbar/i)\nabla - (q/c)\boldsymbol{A}$, where c is the speed of light.

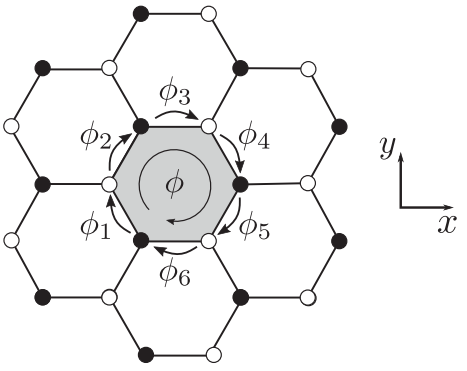

Figure 7.2 Scheme depicting the phases ϕ_j picked up by the nearest-neighbor hoppings along a plaquette of the graphene lattice when a magnetic field is present. The total phase along the closed loop is ϕ is the sum of the individual phases dictated by the Peierls substitution.

as a manifestation of the celebrated Aharanov–Bohm phase (Aharonov & Bohm 1959), the (geometric) phase accumulated by a charged particle when moving in a magnetic field:

$$\phi_{AB} = \frac{q}{\hbar} \oint_{\mathcal{C}} \boldsymbol{A} \cdot d\boldsymbol{\ell}, \tag{7.15}$$

which is also written as -2π times Φ_B, the magnetic flux through the area enclosed by the contour $\mathcal{C}$ divided by the magnetic flux quantum $\Phi_0 \equiv h/e$. Note that the natural periodicity here is given by h/e, whereas in other cases such as superconductors, it is given by the superconducting magnetic flux quantum, $h/(2e)$, where the factor 2 stems from the charge of the Cooper pairs.

It is usual to specify the magnitude of the magnetic field in terms of the *flux per plaquette*. The flux per plaquette is the magnetic flux through a unit cell (plaquette) of the lattice. The flux per plaquette in units of the magnetic flux quantum is thus very convenient for specifying the magnitude of the magnetic field in a numerical implementation.

One must notice that the original translational invariance of the lattice is generally lost because of the presence of the magnetic field, and a new (magnetic) length scale emerges. As we will see later on, this is not the case with Haldane's model, where similar physics is obtained as an intrinsic property of the lattice.

7.5 Aharonov–Bohm Gap Opening and Orbital Degeneracy Splitting in Carbon Nanotubes

In 1993, Ajiki and Ando (1993, 1996) theoretically predicted that an axial magnetic field should tune the nanotube band structure between a metal and a semiconductor,

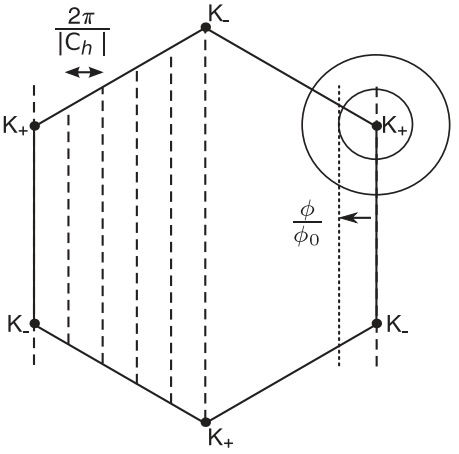

Figure 7.3 Brillouin zone of a graphene sheet together with allowed states for an armchair tube (dashed lines) at zero magnetic flux. Allowed electronic states near the **k**-points under an axial magnetic field are given as dotted lines, while circles give the equipotentials close to the Dirac point.

owing to the modulation of the electronic wavefunctions through the Aharonov–Bohm phase (Aharonov & Bohm 1959). For too strongly disordered nanotubes (Bachtold et al. 1999; Roche & Saito 2001), such a phenomenon is actually masked by the $\Phi_0/2$ Altshuler–Aronov–Spivak magnetoresistance oscillations (Altshuler et al. 1981), so it requires clean nanotubes and a ballistic regime to be observed. After a series of initial magnetotransport experiments (Stojetz et al. 2005; Strunk et al. 2006), the fascinating possibility of turning a metallic nanotube to a semiconducting one and vice versa has finally been nicely confirmed in a careful experiment (Fedorov et al. 2007).

Besides, the application of a perpendicular magnetic field was also predicted to generate Landau levels (LLs) with peculiar features (Roche et al. 2000; Saito et al. 1994). The confirmation of such an interesting structure of LL in nanotubes has been revealed in clean nanotubes (ballistic regime) through the B-dependent modulation of a Fabry–Perot cavity (Raquet et al. 2008). The peculiarities of LL in graphene nanoribbons have also recently been revealed in experiments (Poumirol et al. 2010; Ribeiro et al. 2011). For two-dimensional graphene, strong perpendicular magnetic fields produce the quantum Hall effect, which is addressed in Section 7.7. Below, we provide the essential theory for understanding magnetic-field dependences of electronic structure and transport in these systems.

When the B-field is applied parallel to the tube axis, a spectacular field-dependent bandgap is generated as well as symmetry breaking of the orbital degeneracy. To deepen this effect, let us consider the two-dimensional Cartesian coordinates $\tilde{\mathbf{r}} = (\tilde{x}, \tilde{y})$ in the basis defined by $(\mathbf{C}_h, \mathbf{T})$. The vector potential is thus rewritten as $\mathbf{A} = (\phi/|\mathbf{C}_h|, 0)$, while the phase factor between two π orbitals located at $\tilde{\mathbf{r}}_i = (\tilde{x}_i, \tilde{y}_i)$ and $\tilde{\mathbf{r}}_j = (\tilde{x}_j, \tilde{y}_j)$ becomes $\varphi_i - \varphi_j = i\phi(\tilde{x}_i - \tilde{x}_j)/|\mathbf{C}_h|$. As a consequence, the periodic boundary conditions on the quantum phase are changed following

$$\Psi_k(\mathbf{r} + |\mathbf{C}_h|) = \mathrm{e}^{\mathrm{i}\mathbf{k}\cdot\mathbf{C}_h}\mathrm{e}^{\mathrm{i}\frac{2\pi}{\phi_0}\int_{\mathbf{r}}^{\mathbf{r}+\mathbf{C}_h}\mathbf{A}(\mathbf{r}')\cdot d\mathbf{r}'}\Psi_k(\mathbf{r}), \tag{7.16}$$

and the additional magnetic phase factor thus reduces to $2\pi\phi/\phi_0$, so that the change in the quantum momentum becomes

$$\kappa_\perp \to \kappa_\perp(\phi) = \frac{2\pi}{|\mathbf{C}_h|}\left(q \pm \frac{\alpha}{3} + \frac{\phi}{\phi_0}\right), \tag{7.17}$$

with $\alpha = 0$ for metallic tubes, whereas $\alpha = \pm 1$ for semiconducting tubes. In Fig. 7.3, the modification of available electronic states is illustrated in reciprocal space. Using (7.17), the field-dependent gap oscillation for an initially metallic tube is

$$\Delta E_B = E^+_{q=0}(k_\parallel, \phi/\phi_0) - E^-_{q=0}(k_\parallel, \phi/\phi_0) = 3\Delta E_0\phi/\phi_0, \tag{7.18}$$

if $\phi \le \phi_0/2$ while $\Delta E_0 = 2\pi a_{\mathrm{cc}}\gamma_0/|\mathbf{C}_h|$ denotes the gap at zero flux. If $\phi_0/2 \le \phi \le \phi_0$, then $\Delta E_B = 3\Delta E_0\,|1 - \phi/\phi_0|$, so that the bandgap exhibits an oscillation between 0 and $2\pi a\gamma_0/|\mathbf{C}_h|$ with period ϕ_0 (Ajiki & Ando 1993, 1996). For example, $\Delta E_B \approx 75$ meV at 50 T for a $(22, 22)$ tube (diameter ≈ 3 nm), while $\Delta E_B \approx 40$ meV at 60 T for a $(10, 10)$ tube (diameter $= 1.4$ nm). To obtain a magnetic field equivalent to $\phi = \phi_0$ in nanotubes with diameters of 1, 10, 20, and 40 nm, magnetic fields of 5325, 53, 13, and 3 T, respectively, are needed.

Besides the ϕ_0-periodic bandgap oscillation, the Aharonov–Bohm effect influences the whole subband structure through the field-dependent energy splitting of the van Hove singularities (Roche et al. 2000). Indeed, in the absence of a magnetic field, each energy level is fourfold degenerate (including spin and orbital degeneracy). The orbital degeneracy is attributed to the symmetry between clockwise (+) and counterclockwise (−) electronic motions around the tube. In the presence of the axial magnetic field, electrons in degenerate (+) and (−) eigenstates acquire opposite orbital magnetic moment $\pm\mu_{\mathrm{orb}}$, which thus yields an upshift of the energy of (+) and a downshift of the energy of (−), lifting the orbital degeneracy (van Hove singularity splitting) (Roche et al. 2000).

This mechanism is illustrated in the DOS plots for a $(5, 5)$ tube in Fig. 7.4 in which the tube is metallic at zero magnetic field. The calculation has been performed using a simple *tight-binding* model in the π orbital approximation, while the nearest-neighbor hopping integrals are renormalized in the presence of the magnetic field using Eq. (7.13). As predicted, by applying a finite magnetic flux ϕ threading the tube, the bandgap opens and increases linearly with ϕ, to reach a maximum value at half flux quantum ($\phi_0/2$). Further, the bandgap is linearly reduced until it finally closes again when the field reaches a flux quantum (not shown here). For all armchair (n, n) metallic tubes, the magnitude of the field-dependent splitting of the qth van Hove singularity (vHs) can actually be derived analytically as

$$\Delta E_B(q, \phi/\phi_0) = 2\gamma_0\left[\sin\frac{\pi}{q}\left(\cos\frac{\pi\phi}{q\phi_0} - 1\right) - \cos\frac{\pi}{q}\sin\frac{\pi\phi}{q\phi_0}\right]. \tag{7.19}$$

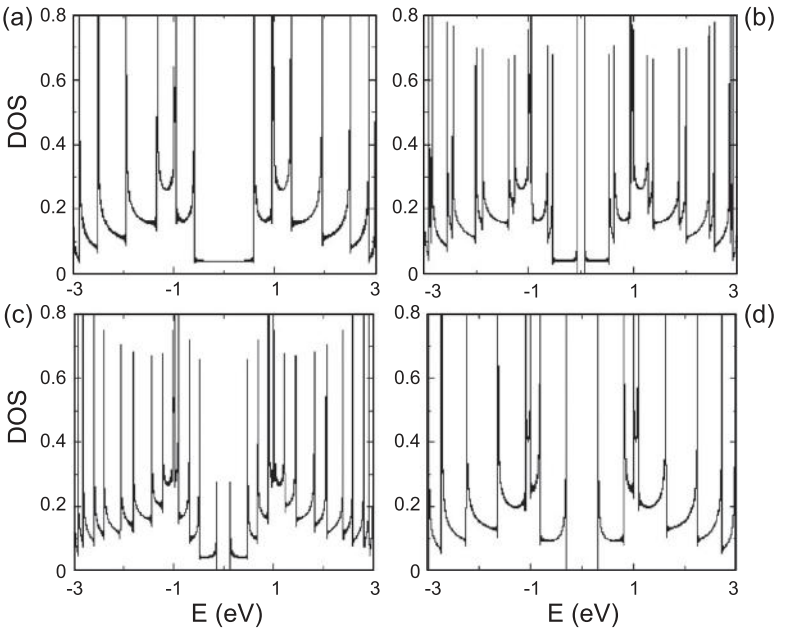

Figure 7.4 Density of states of a $(5, 5)$ nanotube under increasing magnetic flux values: (a) $\phi/\phi_0 = 0$; (b) $\phi/\phi_0 = 0.1$; (c) $\phi/\phi_0 = 0.2$; and (d) $\phi/\phi_0 = 0.5$.

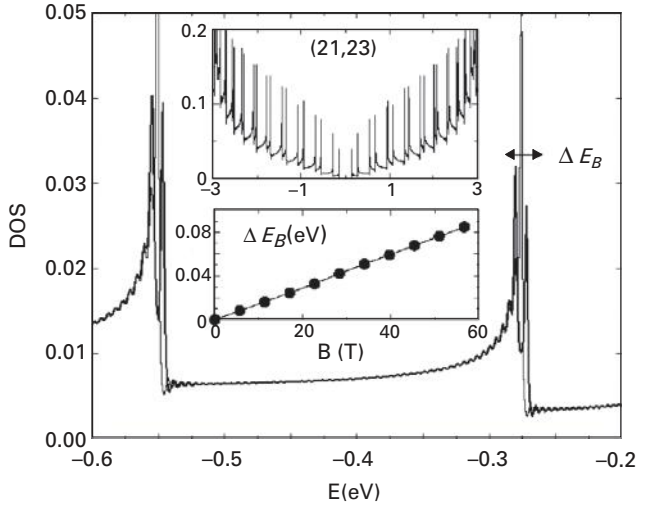

Figure 7.5 Density of states of a $(21, 23)$ tube at zero and finite flux. Top inset: expanded plot of the DOS. Bottom inset: evolution of the vHs splitting ΔE_B as a function of magnetic field. (Reproduced with permission from Charlier et al. (2007). Copyright (2007) by the American Physical Society)

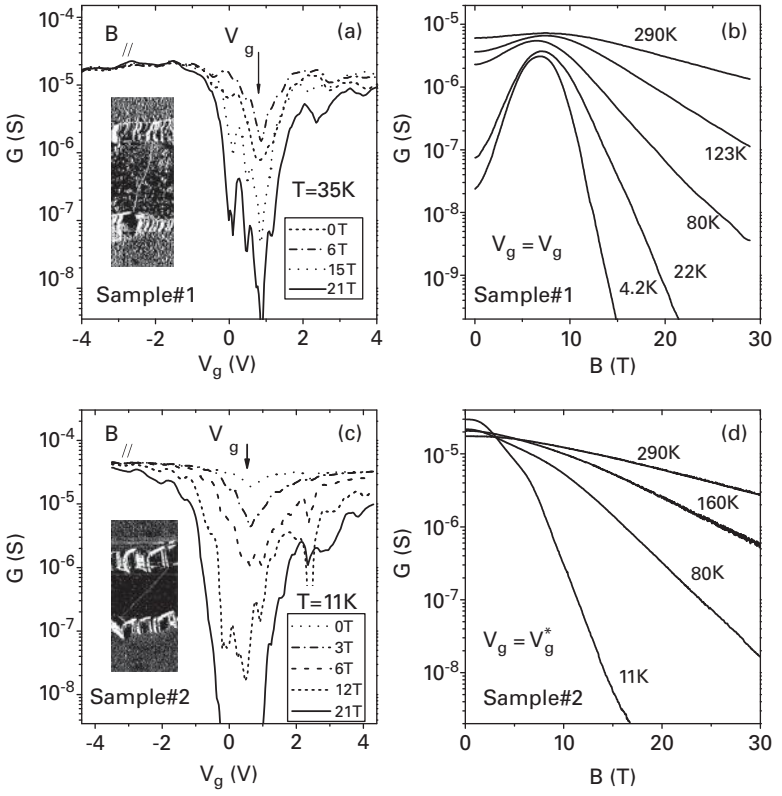

Figure 7.6 (a, c) Transfer characteristics $G(V_g)$ of (CNT-FETs) at axial magnetic fields from 0 to 21 T. At $V_g = V_g^*$, a strong suppression of conductivity is observed at high magnetic fields. The insets show the AFM images of CNTFETs. (b, d) Magnetoconductance curves $G(B)$ measured at $V_g = V_g^*$ at different temperatures. (Figure courtesy of G. Fedorov)

Semiconducting tubes [i.e., (n, m) tubes with $n - m = 3\ell \pm 1$ (ℓ being an integer)] are affected in a similar way, but the gap expression is slightly different. One finds $\Delta E_B = \Delta E_0 \, |1 - 3\phi/\phi_0|$, if $0 \leq \phi \leq \phi_0/2$ and $\Delta E_B = \Delta E_0 \, |2 - 3\phi/\phi_0|$ when $\phi_0/2 \leq \phi \leq \phi_0$. Hence, the initial zero-field energy gap (ΔE_0) continuously decays with ϕ, reaching zero at $\phi = \phi_0/3$. The gap further opens as ϕ increases from $\phi_0/3$, reaching a local maximum ($\Delta E_0/2$) at $\phi = \phi_0/2$, before closing again at $\phi = 2\phi_0/3$, and finally recovering its original value ΔE_0 at $\phi = \phi_0$. Figure 7.5 shows the DOS of a 3 nm diameter semiconducting single-walled tube with and without magnetic flux (main panel) near a van Hove singularity as well as the evolution of the vHs splitting with the field (bottom inset).

The van Hove singularity splitting has been observed by spectroscopic experiments (Zaric et al. 2004), while magnetoresistance oscillations were first studied in disordered and large-diameter multiwall carbon nanotubes (Bachtold et al. 1999), first revealing Altshuler–Aronov–Spivak $\phi_0/2$-periodic magnetoresistance oscillations driven by the

quantum interferences (Altshuler et al. 1981). Several years afterwards, the joint contribution of field-modulated bandstructure features was confirmed (Stojetz et al. 2005; Strunk et al. 2006). Three-terminal devices with conduction channels formed by quasi-metallic carbon nanotubes were shown to operate as nanotube-based field-effect transistors under strong magnetic fields (Fedorov et al. 2007).

Figure 7.6 shows the transfer characteristics of two samples measured at different magnetic fields (Fedorov et al. 2007). At zero field, the $G(V_g)$ curve exhibits ambipolar behavior, indicating the presence of a small 10 meV gap in the electronic spectrum, typical of non-armchair metallic nanotubes. A magnetic field in the axial direction strongly affects the transfer characteristics (Fig. 7.6(a) and (c)). The effect of an axial magnetic field is most pronounced at the gate voltage V_g^* corresponding to the minimum value of conductance. The exact value of V_g^* changes with temperature, but not with magnetic field for $B > 10\,\mathrm{T}$. When the magnetic field is changed between 6 and 15 T, the conductance $G(V_g^*)$ (sample 1, Fig. 7.6(a)) drops by about three orders of magnitude at 35 K. A similarly strong effect is observed in another sample (Fig. 7.6(c)). The off-state conductance of the devices is actually found to exponentially decrease with the magnetic flux intensity, confirming the gap opening driven by the Aharonov–Bohm effect (Fedorov et al. 2007). Remarkably, intrinsic properties of a quasi-metallic CNT, such as the helical symmetry, as well as the characteristics of the Schottky barriers formed at the metal–nanotube contacts, can also be obtained by using temperature-dependent magnetoresistance measurements (see Fedorov et al. 2007, for details).

7.6 Landau Levels in Graphene

The massless Dirac fermion nature of electronic excitations in monolayer graphene is beautifully manifested in the high magnetic field regime: graphene's energy spectrum splits up into non-equidistant Landau levels (LL) (Goerbig 2011; McClure 1956), as represented in the scheme in Fig. 7.7. This contrasts with the Landau level spectrum for non-Dirac electrons which has equidistant levels, thereby serving as a smoking gun of graphene's Diracness (Novoselov, Geim et al. 2005; Zhang et al. 2005).

To describe the spectrum in the presence of an external perpendicular magnetic field B, one can resort to the Peierls substitution, which is applicable as long as the characteristic magnetic length $l_B = \sqrt{\hbar/eB}$ remains much larger than the lattice spacing. This is actually the case for experimentally accessible magnetic fields since $a/l_B \simeq 0.005 \times \sqrt{B\,[\mathrm{T}]}$. Alternatively, one can use equivalent minimal coupling when working in the continuum in the long wavelength approximation. In the following, we will use the latter option to derive analytical expressions.

We denote the gauge-invariant kinetic momentum with $\Pi \equiv -i\hbar\nabla + e\mathbf{A}(\mathbf{r})$, where $\mathbf{A}(\mathbf{r})$ is the vector potential that generates the magnetic field $B\mathbf{e}_z = \nabla \times \mathbf{A}(\mathbf{r})$ perpendicular to the graphene plane. Using the commutation relation $[r_\mu, p_\nu] = i\hbar\delta_{\mu,\nu}$ between

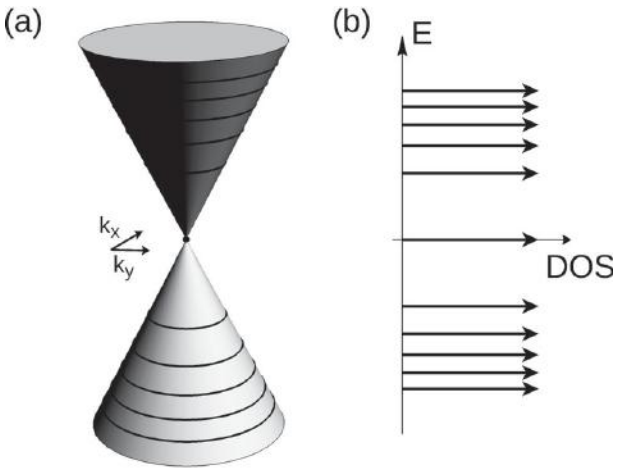

Figure 7.7 (a) Shows a Dirac cone with the unevenly spaced Landau levels superimposed. The density of states (DOS) containing delta functions at the Landau levels is shown in (b).

the components r_μ of the position operator and $p_\mu = -i\hbar\partial/\partial x_\mu$ of the canonical momentum operator ($r_\mu = x, y$ for the 2D plane), one obtains the noncommutativity between the components of the kinetic momentum

$$[\Pi_x, \Pi_y] = -\mathrm{i}\frac{\hbar^2}{l_B^2}, \tag{7.20}$$

such that these components may be viewed as conjugate. Let us introduce the convenient ladder operators

$$\hat{a} = \frac{l_B}{\sqrt{2}\hbar}\left(\Pi_x - \mathrm{i}\Pi_y\right) \text{ and } \hat{a}^\dagger = \frac{l_B}{\sqrt{2}\hbar}\left(\Pi_x + \mathrm{i}\Pi_y\right), \tag{7.21}$$

which satisfy the usual commutation relation $[\hat{a}, \hat{a}^\dagger] = 1$, as in the case of the harmonic oscillator. In terms of these ladder operators, the linearized Hamiltonian, which in the absence of magnetic field is given by $H_{\mathbf{q}}^{\mathrm{eff},\xi} = \xi\hbar v_F(q_x\sigma_x + \xi q_y\sigma_y)$ (see Section 2.2), for a finite magnetic field becomes (Goerbig 2011)

$$H_B^\xi = \xi\sqrt{2}\frac{\hbar v_F}{l_B}\begin{pmatrix} 0 & \hat{a} \\ \hat{a}^\dagger & 0 \end{pmatrix}, \tag{7.22}$$

where (when contrasted to the zero-field Hamiltonian) the A and B components have interchanged in the spinors describing electrons around the K_- point ($\xi = -$).

The solution of the equation $H_B^\xi\psi_n = E_{\lambda n}\psi_n$, in terms of the two-spinors,

$$\psi_n = \begin{pmatrix} u_n \\ v_n \end{pmatrix}, \tag{7.23}$$

provides the Landau level spectrum of electronic excitations in graphene

$$\hat{a}^\dagger \hat{a}\, v_n = \left(\frac{E_{\lambda n}}{\sqrt{2}\hbar v_F / l_B}\right)^2 v_n, \tag{7.24}$$

which indicates that $v_n \propto |n\rangle$ is an eigenstate of the number operator $\hat{a}^\dagger \hat{a}$, $\hat{a}^\dagger \hat{a}|n\rangle = n|n\rangle$, with energies

$$E_{\lambda n} = \lambda \frac{\hbar v_F}{l_B}\sqrt{2n}, \tag{7.25}$$

where $\lambda = \pm$ denotes the levels with positive and negative energy, respectively (Goerbig 2011). Furthermore, substitution of this result in the eigenvalue equation yields $u_n \propto \lambda \hat{a}|n\rangle$.

Note that the term *relativistic* is used to distinguish the $\lambda\sqrt{Bn}$ dispersion of the levels from the conventional (nonrelativistic) Landau levels, which disperse linearly in Bn. This has been verified by different experiments as, for example, STM measurements (Andrei et al. 2012). Interestingly, this type of experiments can also unveil the localization properties of the Landau levels.

A remarkable difference with respect to nonrelativistic Landau levels in metals (with parabolic bands) is the presence of a zero-energy Landau level with $n = 0$. This level needs to be treated separately, and indeed the solution of the eigenvalue equation yields an eigenvector

$$\psi_{\xi, n=0} = \begin{pmatrix} 0 \\ |n = 0\rangle \end{pmatrix}, \tag{7.26}$$

with a single nonvanishing component. As a consequence, zero-energy states at the K_+ point are restricted to the B sublattice, whereas those at the K_- have a nonvanishing weight only on the A sublattice. For Landau levels with $n \neq 0$, the eigenstates

$$\psi^{\xi}_{\lambda, n\neq 0} = \frac{1}{\sqrt{2}} \begin{pmatrix} |n-1\rangle \\ \xi\lambda|n\rangle \end{pmatrix} \tag{7.27}$$

are spinors in which both sublattices are equally populated, but the components correspond to different nonrelativistic Landau states. More information about the extension to the situation of the strongly interacting case can be found in Goerbig (2011).

In 2013, by measuring high field magnetotransport properties of graphene on top of a boron nitride substrate, the long-sought-after *Hofstadter's butterfly*[4] (Hofstadter 1976) was finally unveiled (Dean et al. 2013; Ponomarenko et al. 2013). This was made possible thanks to the Moiré pattern created by the interaction between graphene and boron nitride and related long superlattices periodicities (on the order of tens of nanometers). Besides providing the first direct evidence of the fractal spectrum predicted by Hofstadter, this demonstrated the enormous potential of layered structures.

[4] Hofstadter's butterfly is a fractal pattern in the energy spectrum of a 2D system in a magnetic field. It arises due to the interplay between the lattice periodicity and the one imposed by the magnetic field and leads to a butterfly-like shape when one looks to the spectrum (energy versus magnetic flux).

Finally, we would like to comment that in another recent study Tarnopolsky et al. (2019) point out that the flatness of the bands at magic angles (Suárez Morell et al. 2010), which became a focus of attention after the discovery of superconductivity in twisted bilayer graphene (Cao, Fatemi, Fang et al. 2018; Cao, Fatemi, Demir et al. 2018), has analytical connections to quantum Hall wave function (Tarnopolsky et al. 2019).

7.7 Quantum Hall Effect in Graphene

First discovered by Klaus von Klitzing in 1980 (von Klitzing et al. 1980), the quantum Hall effect is a quantum-mechanical version of the effect discovered by Edwin Hall 100 years earlier in 1879. In the (classical) Hall effect, a current through a sample with a perpendicular magnetic field leads to a voltage perpendicular to both of them. This Hall voltage results from the preferential deflection of carriers produced by the Lorentz force. The quantum mechanical version found by Klaus von Klitzing offers a rich and thrilling path to one of the most interesting chapters of contemporary physics. Indeed, it led to a whole family of Hall effects, while ultimately offering an entrance to the physics of topological insulators.

The effect in which the Hall conductivity σ_{xy} becomes quantized,

$$\sigma_{xy} = 2Ne^2/h,$$

and the longitudinal conductivity becomes vanishingly small, $\sigma_{xx} \sim 0$, was first observed in two-dimensional electron systems produced in semiconductor heterostructures under extreme conditions of low temperatures and strong magnetic fields (von Klitzing et al. 1980).

The prefactor N in σ_{xy} is the filling factor, and in the original experiments (von Klitzing et al. 1980) turned out to be an integer ($N = 1, 2, 3, \ldots$) with a precision that in more recent experiments reaches up to nearly one part in a billion. This came as a great surprise as the values of the conductance plateaus were universal, independent of the details of the material, sample geometry, etc. It is a noteworthy example of a fundamental and useful discovery: it was a manifestation of a macroscopic quantum effect. Its use in metrology started to be discussed already a day after the discovery (von Klitzing 2005).

The integer quantum Hall effect (IQHE) (von Klitzing et al. 1980) is explained in terms of single-particle orbitals of an electron in a magnetic field and is intimately connected to the quantization of the spectrum into Landau levels. In constrast, it can also happen that N is a fractional number, $N = 1/3, 2/5, 3/7, 2/3, 3/5, \ldots$; in this case, the fractional quantum Hall effect (FQHE) fundamentally relies on strong electron–electron interactions, and the existence of so-called charge–flux composites known as composite fermions (Laughlin 1983; Tsui et al. 1982). As we will see, given the sublattice and valley degeneracies in graphene, one may also interpret the result in terms of half integers and call it fractional, but the physics is that of the conventional IQHE and can be explained without interactions.

For everyone participating in or witnessing this adventure, the role of our hero, graphene, in the history of the Quantum Hall effect and the birth of topological insulators has been fascinating, first as a model (the playground for Haldane's model (Haldane 1988)) and then as a real material, allowing for the realization of the effect at room temperature (Novoselov et al. 2007) and now appearing as the material of choice in metrology (Janssen et al. 2013; Ribeiro-Palau et al. 2015), and again as a first candidate for a topological insulator (Kane & Mele 2005b), then forgotten and now resurfacing thanks to new studies searching for proximity induced enhancement of spin-orbit coupling. (More on this in Chapter 8.)

7.7.1 Experimental Observation of Hall Quantization in Graphene

Owing to the peculiar nature of the Landau levels spectrum with energy spacing given by $E_n = \mathrm{sgn}(n)\sqrt{2\hbar v_F{}^2 eB|n|}$, the well-known integer quantum Hall effect (IQHE) (von Klitzing et al. 1980) observed in conventional two-dimensional electron systems transforms to a relativistic half-integer (anomalous) QHE in graphene whose quantized Hall conductivity becomes (Goerbig 2011; Novoselov, Jiang et al. 2005; Zhang et al. 2005):

$$\sigma_{xy} = 4e^2/h \times (N + 1/2). \tag{7.28}$$

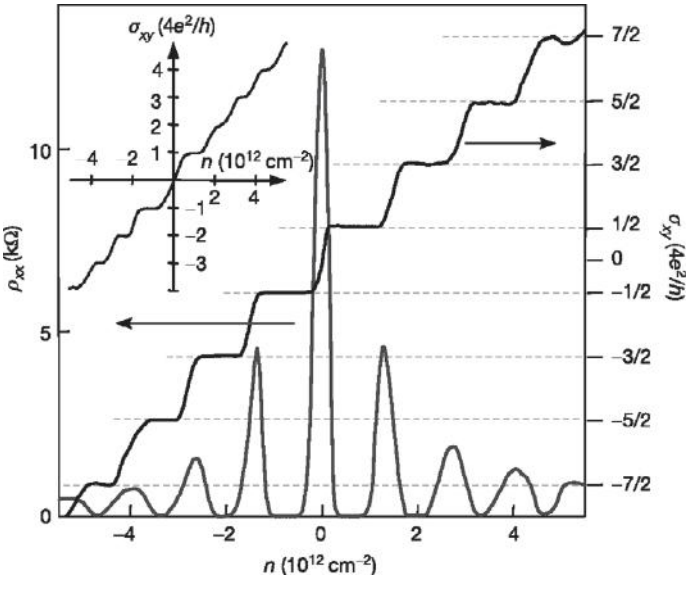

Figure 7.8 Longitudinal resistivity (ρ_{xx}) and Hall conductivity (σ_{xy}) as a function of charge density in monolayer graphene at 14 T and 4 K. The inset shows the case of bilayer graphene. (Reprinted by permission from Macmillan Publishers Ltd: *Nature* (Novoselov, Jiang et al. 2005), copyright (2005). Courtesy of Andre Geim)

Such an anomalous QHE was simultaneously reported by the groups of Manchester University (Novoselov, Jiang et al. 2005) and Columbia University (Zhang et al. 2005). Figure 7.8 shows both the charge density dependence of the longitudinal resistivity (ρ_{xx}) and Hall conductivity (σ_{xy}) at 14 T and 4 K as reported in (Novoselov, Jiang et al. 2005). We note that the quantum Hall effect in graphene has been named *half-integer* to distinguish it from the integer and the fractional quantum Hall effects. The shift in the first quantum Hall plateau can be related directly, through a semiclassical argument, to the Berry phase of π mentioned earlier in this chapter.

Interestingly, quantized plateaus of the Hall conductivity have also been reported at room temperature and with magnetic fields as low as 20 T in Novoselov et al. (2007). Although much efforts were devoted to reach higher temperatures using semiconductor heterostructures, current efforts have failed to achieve a quantum Hall regime with temperatures over 30 K. In this sense, graphene offers a playground for such macroscopic quantum effect at room temperature, while also allowing for better prospects for metrological applications (Janssen et al. 2013; Ribeiro-Palau et al. 2015).

The reason behind this extraordinary observation of the quantum Hall effect at room temperature is twofold: On the one hand, the larger difference between the $n = 0$ and the $n = \pm 1$ Landau levels (scaling more conveniently with the magnetic field as compared to usual semiconductors), and on the other hand, the large mobilities that remain almost unchanged in the temperature range between 4 K and room temperature (Novoselov et al. 2007).

7.7.2 Remarks for the Numerical Investigation of the Hall Response

As we have seen, the Hall response can be probed through multiterminal measurements. The contacts are typically arranged in a cross or H-type configuration. Current is passed from source to drain while the contacts in the perpendicular direction are used as voltmeters. In the coherent regime, this can be simulated quite naturally within the Landauer-Büttiker picture explained in Section 4.2. However, as compared with the two-terminal setups, one finds additional difficulties associated with the geometry. In a Green's functions–based calculation, the self-energies due to the leads will introduce effective high-order couplings between the sites at the interface between the sample (arbritrarily chosen central region of the device) and the lead. This, in turn, requires modifying the simple recursive Green's functions methods explained in Appendix C. An alternative to sort this problem is the so-called knitting algorithm (Kazymyrenko & Waintal 2008).

More recently, higher level libraries such as KWANT (Groth et al. 2014) have taken the modeling and simulation of this type of multiterminal devices to a more comfortable level. Indeed, the KWANT library (Groth et al. 2014) allows for a much easier calculation of the transport properties, which is perfectly tailored for such complex geometries. One needs to define the desired lattice, its interaction parameters, and the shape of the device area; the code takes care of solving the harder part of the problem. Even in such

a case, however, there is one issue that needs to be solved beforehand: the selection of a proper gauge for the vector potential.

The magnetic field is introduced through the Peierls' substitution explained earlier in this chapter. Choosing, for example, a Landau gauge for a magnetic field of magnitude B along z:

$$\mathbf{A}_L = -By\hat{x}, \tag{7.29}$$

gives the following Peierls phase between sites i and j:

$$\phi_{ij}^L = -B(x_i - x_j)\frac{y_i + y_j}{2}. \tag{7.30}$$

This vector potential depends on the absolute y coordinate, and hence it preserves the lead translational invariance along x but it does not for leads that are tilted with respect to this direction. The gauge thus needs to be chosen so as to preserve translational invariance in all the leads, while smoothly interpolating between them in the sample region. A prescription that fulfills this requirement is the following (Baranger & Stone 1989; Shevtsov et al. 2012):

$$\phi_{ij} = \phi_{ij}^L + \Phi_i - \Phi_j, \tag{7.31}$$

where Φ_i is given by

$$\Phi_i = -B(1 - \cos(2\theta))\frac{x_i y_i}{2} + B\sin(2\theta)\frac{x_i^2 - y_i^2}{4} \tag{7.32}$$

for all sites i belonging to a lead (forming an angle θ with the x axis) and zero otherwise (i.e., the sites in the sample).

Therefore, in the presence of a magnetic field, we add a Peierls phase to each matrix element $\gamma_{i,j}$, which is the sum of ϕ_{ij}^L (the one corresponding to the usual Landau gauge) and the difference of the potentials associated to the initial and final sites. With this prescription, we preserve the translational invariance in all leads.

7.7.3 The Mystery of the Zero-Energy Landau Level Splitting

One striking fingerprint of the graphene Landau level spectrum is the formation of a fourfold degenerate zero-energy Landau level (twofold valley and spin degeneracies) where electrons and holes coexist. The anomalous QHE is actually tightly interwoven with the π Berry's phase and pseudospin degree of freedom, which requires decoupled K_+ and K_- valleys (Ostrovsky et al. 2008). In the presence of disorder-induced sublattice symmetry breaking and strong valley mixing, QHE is predicted not to differ for any other two-dimensional system (Aleiner & Efetov 2006; Altland 2006; Ostrovsky et al. 2008).

Several experiments performed in high-mobility samples have confirmed the presence of additional quantized Hall plateaus at $\sigma_{xy} = 0$, associated with splitting of the zero-energy LL. The level splitting may have different origins, such as spin and/or

sublattice degeneracies, which could be driven by a Zeeman interaction or a disorder-induced symmetry-breaking effect (Li et al. 2009), or electron–electron interactions (Jiang et al. 2007; Nomura & MacDonald 2006; Zhang et al. 2006), although the issue remains complicated and probably material quality dependent. The nature of the $\sigma_{xy} = 0$ quantized plateau has also been envisioned as a possible manifestation of an unconventional dissipative QHE, which would assume a finite σ_{xx} value at the Dirac point (in between split Landau levels) (Abanin et al. 2006, 2007; Checkelsky et al. 2008; Jia et al. 2008; Zhang et al. 2010). Such dissipative QHE (with finite conductivity $\sigma_{xx} \sim 1 - 2e^2/h$) is predicted to be conveyed by the formation of counterpropagating (gapless) edge states carrying opposite spin. Finite σ_{xx} ($\simeq e^2/(\pi h)$) at the Dirac point has also been obtained numerically in some disordered graphene models (introducing bond disorder in a *tight-binding* model), and tentatively related to the formation of extended states centered at zero energy, but without evidence of a fully quantized σ_{xy} (Jia et al. 2008).

The anomalous dissipative nature of the QHE remains, however, in puzzling contradiction with many other experiments reporting divergent Dirac point resistivity (Checkelsky et al. 2008) and a conventional nondissipative QHE regime. The measurement of a temperature-dependent activated behavior of $\sigma_{xx}(T)$ further supports the nondissipative nature of the plateau $\sigma_{xy} = 0$ in the presence of spin-splitting gap opening (Giesbers et al. 2009; Kurganova et al. 2011; Zhao et al. 2012). Thus much effort is still required on both theoretical and experimental sides to develop a comprehensive picture of QHE in disordered graphene. One can also expect that the physics of QHE in disordered graphene is much richer, with possible unconventional and defect-specific fingerprints of the magnetotransport features and localization/delocalization mechanisms. The possibility to structurally and chemically vary the quality and properties of graphene by chemical substitutions, functionalization, or the formation of hybrid materals (for instance, graphene/boron nitride samples) offers interesting challenges for further exploration of QHE. We finally outline the prediction of highly unconventional zero-energy Hall conductance plateau in the absence of an energy bandgap and Landau-level degeneracy breaking, driven by the formation of impurity-induced critical states (Leconte et al. 2016), which could possibly explain puzzling experimental data in strongly disordered graphene samples (Nam et al. 2013).

7.7.4 Universal Longitudinal Conductivity at the Dirac Point

We briefly analyze here the behavior of the dissipative conductivity (σ_{xx}) of the zero-energy Landau level in the presence of Anderson disorder, and also with or without additional A/B sublattice symmetry-breaking potentials. This illustrates some basic and general features of disorder-induced localization effects on QHE, and the modifications induced by energy-level splitting. The Kubo longitudinal σ_{xx} and Hall conductivities are computed in the presence of disorder and external magnetic fields with varying

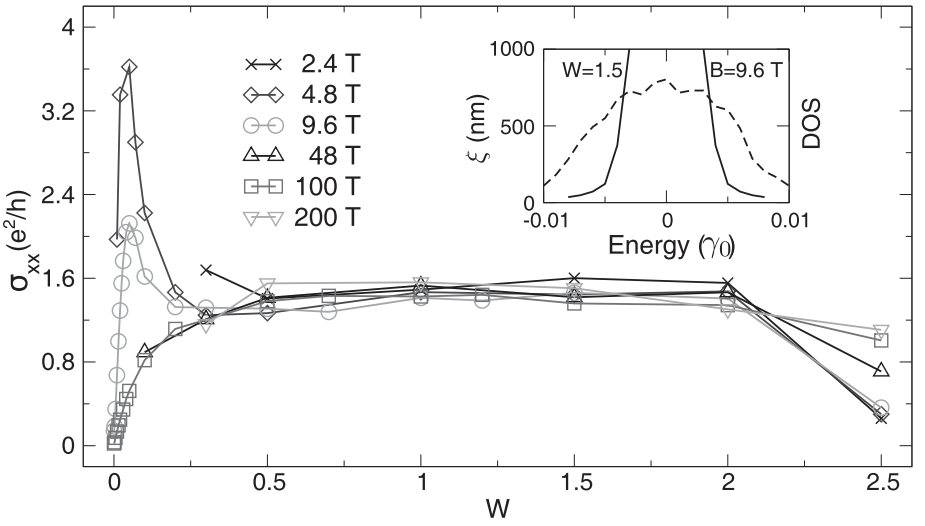

Figure 7.9 Main plot: Dirac point Kubo conductivity with varying Anderson disorder potential W. Localization length $\xi(E)$ (inset) at the center of the zero-energy Landau level (solid line) and density of states (dashed line and arbitrary units) for $W = 1.5$ and $B = 9.6$ T. (Reproduced with permission from Ortmann and Roche (2013). Copyright (2013) by the American Physical Society)

strengths (within the experimentally accessible range of parameters, from a few tesla to several tens of tesla). $\sigma_{xy}(E)$ is computed using a recently developed order-N approach derived by Frank Ortmann (Ortmann & Roche 2013). The longitudinal conductivity has already been discussed, whereas the novel algorithm for the Hall conductivity $\sigma_{xy}(E)$ is essentially implemented from

$$\sigma_{xy}(E) = -\frac{2}{V}\int_0^\infty dt e^{-\eta t/\hbar}\int_{-\infty}^{\infty} dE' f(E'-E) \times \mathrm{Re}\left[\langle\varphi_{\mathrm{RP}}|\delta(E'-\hat{H})\hat{j}_y\frac{1}{E'-\hat{H}+i\eta}\hat{j}_x(t)|\varphi_{\mathrm{RP}}\rangle\right], \tag{7.33}$$

with $\hat{j}_x = \frac{ie_0}{\hbar}[\hat{H}, \hat{X}]$, the current operator ($\hat{X}$ the position operator), while $\eta \to 0$ is a small parameter required for achieving numerical convergence.

Figure 7.9 shows the conductivity $\sigma_{xx}(E, B, W)$ of the zero-energy LL for a graphene with Anderson disorder and a perpendicular magnetic field. A clear absence (or suppression) of localization is seen for disorder up to $W = 2$. The values of $\sigma_{xx}(E = 0, B, W \leq 2)$ are shown in Fig. 7.9 (maximum computational time of the wavepacket spreading is 12 ps). At high enough energies, localization effects come into play in relation to the formation of mobility edges, as manifested by a finite localization length (ξ) at the tails of the zero-energy LL (see $W = 1.5$ in Fig. 7.9). When the disorder strength exceeds $W = 2.5$, all states including the zero-energy LL eventually localize, prohibiting the QHE state (Ortmann & Roche 2013; Sheng et al. 2006).

Actually, as seen in Fig. 7.9, three different transport regimes for σ_{xx} are identified depending on the disorder strength and applied magnetic field (Ortmann & Roche 2013). In the absence of disorder, all states are localized by the magnetic field ($\sigma_{xx} \to 0$), whereas small disorder induces delocalization, as seen in the enhancement of σ_{xx} with W. For disorder such that $W \simeq 0.1$, σ_{xx} increases roughly linearly with W, regardless of the magnetic field (tuned from 4.8 T to 100 T). The value of $d\sigma_{xx}/dW$ depends on the magnetic field, and is seen to be larger for lower B. This actually agrees with the scaling of the magnetic length $l_B \propto B^{-1/2}$, which reduces disorder-induced delocalization effects as B is increased (and magnetic length is shortened).

Strikingly, for a large range of disorder values $W \in [0.3, 2]$ and for magnetic strengths varying between 2.4 and 200 T, the dissipative conductivity σ_{xx} saturates to a constant value $\simeq 1.4e^2/h$. Finally, in the limit of strong disorder ($W > 2.5$), all states become localized and the system is driven to the insulating state (for moderate B). Differently from the low-W limit, the conductivity is higher for stronger fields, indicating reversed roles of disorder and B field compared to the zero-disorder limit, i.e., disorder localizes states while the magnetic field tends to suppress localization effects.

By introducing a sublattice symmetry-breaking disorder, pseudospin-split states are found to convey different critical bulk conductivities $\sigma_{xx} \simeq e^2/h$, regardless of the splitting and superimposed Anderson disorder strengths, dictating the width of the $\sigma_{xy} = 0$ plateau (Ortmann & Roche 2013). The pseudospin-splitting is included through a heuristic model, which shifts all onsite energies of A (and B) lattice sites by a constant quantity V_A (and V_B). When all A and B sites are differentiated in energy according to $V_\mathrm{A} = -V_\mathrm{B}$, a gap of $V_\mathrm{A} - V_\mathrm{B} = 2V_\mathrm{A}$ is naturally formed. The superposition of both potentials mimics some weak imbalance in the adsorption site in the sense of a slightly preferred sublattice (Anderson disorder is such that $|V_\mathrm{A}| \ll W$). In between pseudospin-split critical states, σ_{xx} eventually vanishes owing to intervalley-induced localization effects. Interestingly, it is found that by keeping the product pV_A constant, the same splitting strengths and split-gap (p the density of impurities breaking the sublattice symmetry) are obtained.

The analysis of $\sigma_{xx}(L)$ for various energies makes it possible to discriminate localized states from critical states, which remain delocalized as seen by a length-independent σ_{xx}. A typical result (σ_{xx}, σ_{xy}) is shown in Figure 7.10 (maximum propagation time of wavepackets is $t = 6$ ps while disorder is set to $W = 0.2$). The maximum value of the doubly peaked σ_{xx} is found to be field-independent. Two peaks of σ_{xx} are actually related to disorder-induced pseudospin-splitting. Remarkably, the peak maxima σ_{xx} are not half of the maximum obtained in the unsplit case but reduced by a factor of $\simeq 0.7$. Fig. 7.10 finally shows that $\sigma_{xx}(E = 0) \to 0$ while the double-peak height of $\simeq e^2/h$ is robust for different magnetic fields and disorder strength pV_A (Ortmann & Roche 2013). The Hall conductivity ($W = 0$) σ_{xy} for $pV_\mathrm{A} = 0$ (gray) and $pV_\mathrm{A} = 0.005$, $p = 2.5\%$ (black) and corresponding DOS (dashed lines) at 45 T and $W = 0.002$ are shown in Fig. 7.10 (right inset).

To date, available experimental data do not provide any universality concerning the critical values of σ_{xx}, which often show electron–hole asymmetry and variability

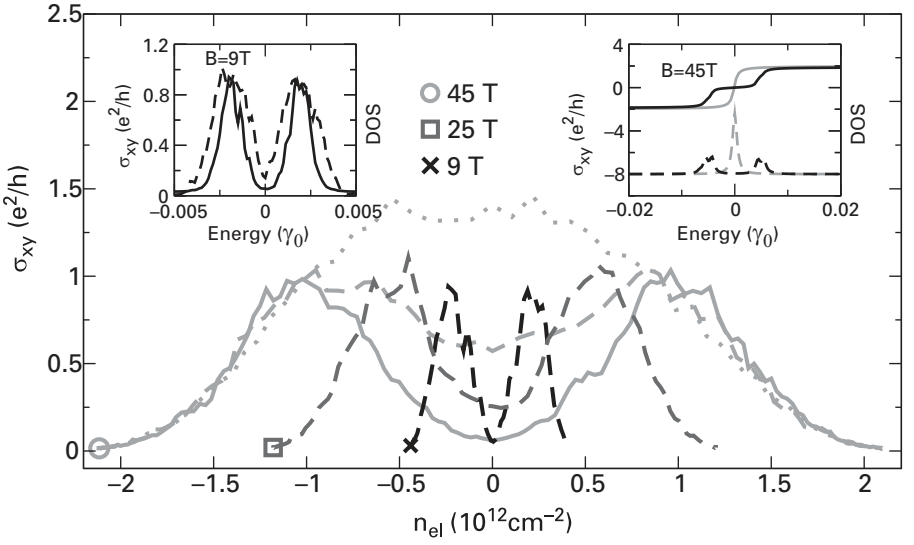

Figure 7.10 Longitudinal and Hall conductivities with and without sublattice impurity potential. Main plot: $\sigma_{xx}(t = 6$ ps) for $W = 0.2$ using $pV_A = 0.0005$ (dotted line), $pV_A = 0.001$ (dashed lines), and $pV_A = 0.002$ (solid line). Magnetic fields as indicated. Left inset: $\sigma_{xx}(t = 6$ ps) (solid line), DOS (dashed line) for $W = 0.2$, $pV_A = 0.004$. Right inset: Hall conductivity ($W = 0$) σ_{xy} for $pV_A = 0$ and $pV_A = 0.005$, $p = 2.5\%$, together with the corresponding DOS (dashed lines) at 45 T and $W = 0.002$. (Reproduced with permission from Ortmann and Roche (2013). Copyright (2013) by the American Physical Society)

(Giesbers et al. 2009; Kurganova et al. 2011; Zhao et al. 2012). It is expected that the study of QHE in chemically modified graphene (for instance, upon atomic deposition, hydrogen or oxygen adsorption, doping, strain, etc.) will reveal a plethora of additional interesting features of transport coefficients, allowing for an in-depth scrutiny of the connection between microscopic localization phenomena and the resulting phase diagram (σ_{xx}, σ_{xy} versus magnetic field and temperature) of the QHE.

7.8 The Haldane Model

In this section, we introduce a model of great importance in the theory of topological states of matter, which is strongly connected with the physics of the quantum Hall effect described before. Formulated in 1988 by Duncan Haldane (Haldane 1988), the playground for this model is graphene (which at that time was only a theoretical one).

Inspired by the quantum Hall effect discovered earlier by Klaus von Klitzing (von Klitzing et al. 1980), Haldane was set to find a realization of the same effect but without Landau levels. In the presence of a magnetic field, the typical length scale becomes the magnetic length, and therefore it is not a property of the lattice. In order to have a nonvanishing Chern number, one needs more prominently a gap as the summation of the

Berry curvatures over all bands needs to be zero. For a single-band system, this would immediately lead to a vanishing Chern number.

Since in graphene, the Dirac point is protected by inversion and time-reversal symmetry, we need to break any of those. (Changing the lattice period through a Kekul pattern would also work, but we are not considering that here.) Breaking inversion symmetry alone by introducing, for example, a staggering (also called Semenoff mass (Semenoff 1984)) opens a gap but the Chern number vanishes. This results from the symmetry properties of the Berry curvature noted earlier, in a system with preserved TRS, $\Omega_j(\mathbf{k}) = -\Omega_j(-\mathbf{k})$, and thus the integral of the Berry curvature over the full Brillouin zone vanishes.

Haldane then introduced a new type of mass term, which like a magnetic field breaks time-reversal symmetry. This term was introduced as next-nearest-neighbor hoppings with a phase akin to that in the Peierls substitution but chosen so that there is no net flux per plaquette. The full Hamiltonian reads:

$$\mathcal{H} = \Delta \sum_j \xi_j c_j^\dagger c_j + \gamma_0 \sum_{\langle i,j \rangle} c_i^\dagger c_j + \gamma_2 \sum_{\langle\langle i,j \rangle\rangle} \mathrm{e}^{-i\epsilon_{ij}\phi} c_i^\dagger c_j, \tag{7.34}$$

where the double brackets in the last summation indicate sum over second-nearest neighbors and $\xi_j = +1$ when $j \in A$ and $\xi_j = -1$ when $j \in B$. Thus, the sign of the phase acquired depends on whether the path from j to i is clockwise or anticlockwise.

Haldane's model is sketched in Fig. 7.11. Two terms are incorporated over the usual ones in the simple tight-binding model for graphene: *(i) Complex second-nearest-neighbors hoppings breaking time-reversal symmetry.* The second-nearest-neighbor hoppings are given by $\gamma_2 \exp(-\mathrm{i}\epsilon_{ij}\phi)$, $\epsilon_{ij} = \mathrm{sign}(\mathbf{d_1} \times \mathbf{d_2})_z$, $\mathbf{d_1}$ and $\mathbf{d_2}$ are unit vectors along the direction of the two bonds connecting the next-nearest neighbor sites and ϕ is a chosen flux (like in the Peierls substitution introduced earlier). The sign of such phases is indicated in the figure. *(ii) A mass term which breaks inversion symmetry.* This term is simply a staggered on-site energy, which is taken to be equal to $+\Delta$ for the A-sites and $-\Delta$ for the B-sites.

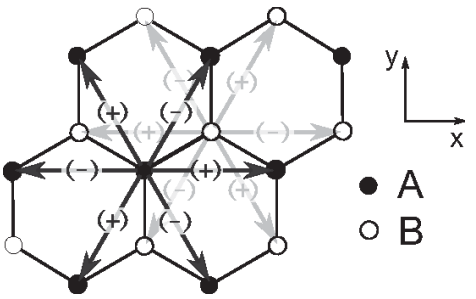

Figure 7.11 Scheme showing the connectivity between the lattice sites in the Haldane model. Complex second-nearest neighbors-hopping are added to graphene's lattice; the sign of the corresponding phases is indicated in the figure. Furthermore, lattice sites A and B have onsite energies $+\Delta$ and $-\Delta$, respectively.

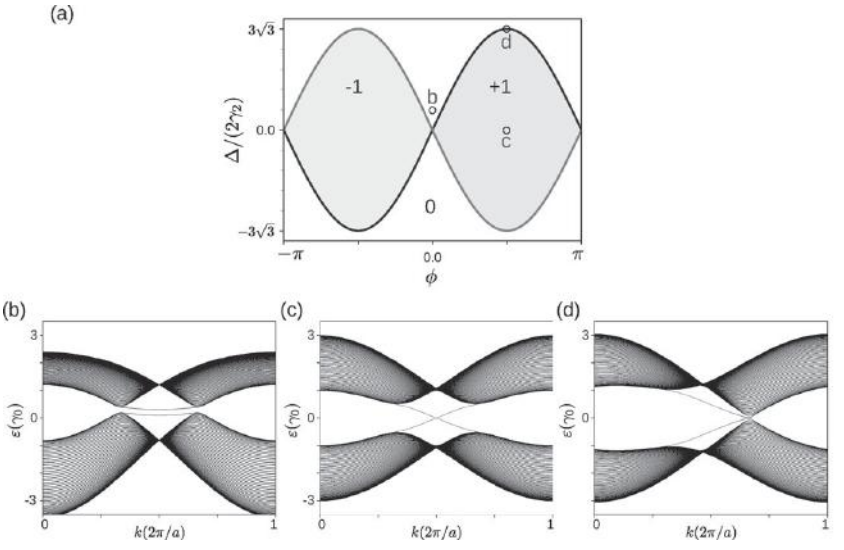

Figure 7.12 (a) Phase diagram for the Haldane model introduced in the text. The regions are marked with the values of the corresponding Chern numbers, $+1$, -1, and 0. The energy dispersions for the points marked with b, c, and d are shown below. The states bridging the bulk gap turn out to be localized close to the edges. In (b–d), $\gamma_2 = 0.1\gamma_0$.

The interplay between the two mass terms (the Semenoff and the Haldane masses) leads to a phase diagram as shown in Fig. 7.12. The Chern numbers are indicated in the different areas, separated by full lines at the points where the Chern number becomes ill defined. (The system is metallic.)

To understand why the two masses have competing effects, one observation is due: The Semenoff mass, being local, has no k-dependence and the mass term is the same for both inequivalent Dirac cones, thereby leading to a gapped spectrum as shown in Fig. 7.12(b). In contrast, the Haldane term has opposite signs for each cone. This leads to a band-inversion for the case of the Haldane mass which is ultimately responsible for the edge states bridging the gap (as shown in Fig. 7.12(c)). The case in Fig. 7.12(d) is a special one as the states bridging the closed and open cones are dispersive. These states are not topological though since short-range scatterers may lead to transitions between them and the continuum of states available at the same energy.

A breakthrough was presented in 2005 when Kane & Mele (2005a and 2005b) realized that the physics of this model could be connected to spin–orbit interaction, a work that paved the way for the era of topological insulators. Essentially, graphene with intrinsic spin–orbit coupling (see Chapter 8) can be written as two copies of the Haldane model with opposite phase (equal to pi/2), one for spin up and the other for spin down.

Interestingly, Haldane's model has been realized in ultracold matter experiments as an effective Hamiltonian (Jotzu et al. 2014). Notwithstanding, to date this model has not proven a suitable physical model for describing any real two-dimensional material. Very

recently, a modified Haldane model was proposed (Colomés & Franz 2018), a model exhibiting dispersive antichiral edge states, which are modes propagating in the same direction at both parallel ribbon edges and compensated by bulk counterpropagating modes. Such edge states, resilient to disorder, have been proposed as analogs to the Fermi arcs in 3D Dirac and Weyl semimetals and could be useful for low-power electronics or spintronics. Additionally, the optical properties of the modified Haldane model displays a rich phase diagram showing tunable pseudospin polarization, valley polarization, and circular dichroism, with the unprecedented possible simultaneous realization of both perfect valley polarization and circular dichroism enabling the co-integration of photonics and valleytronics in a single material or device (Vila et al. 2019). Variants of this model in bilayer configurations have been proposed to achieve one-way tranport of charge, valley and spin (Berdakin et al. 2018; Dal Lago et al. 2017; Foa Torres et al. 2016).

7.9 Further Reading and Problems

- For a review of Berry phase effects in condensed matter theory, see Xiao et al. (2010).
- An account of the experimental manifestations in graphene can be found in Young et al. (2014).

Problems

7.1 *Three golden rules for Berry curvature.* Demonstrate the rules mentioned in the text, Eqs. (7.5), (7.6), and (7.7). Interpret each of them and mention at least one consequence associated with each.

7.2 *Landau levels in graphene.* Consider the low-energy approximation for electrons in graphene. Consider a magnetic field perpendicular to the graphene plane.

(a) By using the Peierls substitution $\hat{\mathbf{p}} \rightarrow \hat{\mathbf{p}} + e\mathbf{A}$ (where $\mathbf{A}$ is the vector potential determining the magnetic field $\mathbf{B}$, $\mathbf{B} = \nabla \times \mathbf{A}$), solve for the spectra and obtain the Landau levels. What is the degeneracy of each Landau level?

(b) Compare your response to (a) with that for the case of a normal metal.

(c) The Landau level with $n = 0$ is a special one. Comment on this Landau level and the character of the corresponding wavefunction.

7.3 *Haldane's model.* Haldane's model is sketched in Fig. 7.11. Two terms are added in addition to the usual ones in the simple tight-binding model for graphene: *(i) Complex second-nearest neighbors hoppings breaking time-reversal symmetry.* The second-nearest neighbors hoppings are given by $\gamma_2 \exp(-\mathrm{i}\epsilon_{ij}\phi)$, $\epsilon_{ij} = \mathrm{sign}(\mathbf{d_1} \times \mathbf{d_2})_z$, $\mathbf{d_1}$ and $\mathbf{d_2}$ are unit vectors along the direction of the two bonds connecting the next-nearest neighbor sites and ϕ is a chosen flux (as in the Peierls substitution introduced in this chapter). The sign of such phases is indicated in the figure. *(ii) A mass term which breaks inversion symmetry.* This term is simply a staggered

on-site energy, which is taken to be equal to $+\Delta$ for the A-sites and $-\Delta$ for the B-sites.

The full tight-binding Hamiltonian reads:

$$\mathcal{H} = \Delta \sum_j \xi_j c_j^\dagger c_j + \gamma_0 \sum_{\langle i,j \rangle} c_i^\dagger c_j + \gamma_2 \sum_{\langle\langle i,j \rangle\rangle} e^{-\mathrm{i}\epsilon_{ij}\phi} c_i^\dagger c_j,$$

where the double brackets in the last summation indicate sum over second-nearest neighbors and $\xi_j = +1$ when $j \in A$ and $\xi_j = -1$ when $j \in B$.

(a) Compute the electronic structure for an infinite sheet for different values of ϕ and Δ and compare with those for graphene and graphene with a mass term (Δ terms in the above Hamiltonian).

(b) Repeat point (a) for the case of a ribbon. Show that graphene with a mass term differs from Haldane's model *at the edges*.

(c) Plot the probability associated to the wave-functions in (b) at different energies. Discuss your results. Argue why the Haldane model does not give an ordinary band insulator.

8 Spin-Related Phenomena

8.1 Introduction

Charge and spin are fundamental properties of electrons, which are intensively harnessed in modern technologies of information processing, computing, and data storage. The binary or analogue information are implemented through the control of charge currents in active devices (field-effect transistors [FET]) and logic circuits, whereas the spin is currently mainly used for tuning magnetoresistance signals and embedding data storage and data retrieval in core memories and hard disk drives (Chappert et al. 2007). As highlighted in the International Technology Roadmap for Semiconductors (ITRS, *www.itrs2.net/*), electronic architectures, which would entirely rely on spin physics, could revolutionize the world of information processing and memory storage with the possibility to develop ultralow-power, fast, and strongly miniaturized technologies covering a wide landscape in Internet of Things.

The field of spintronics was sparked with a scientific breakthrough in the 1980s, when the giant magnetoresistance (GMR) effect, first predicted theoretically by Albert Fert from CNRS-THALES in France, and later confirmed experimentally, thanks to the improvement in fabrication of multilayers composed of alternating ferromagnetic with ultrathin (nanometer scale) nonmagnetic conductive layers. After the initial report in 1985 of spin-polarized electron injection from a ferromagnetic metal to a normal metal by Johnson and Silsbee (1985), the foundational step made by Albert Fert (Baibich et al. 1988) and Peter Grünberg (Binasch et al. 1988), both awarded the 2007 Nobel Prize in Physics, was to report GMR in thin-film structures elaborated by an alternating sequence of ferromagnetic and nonmagnetic layers.

GMR is a significant change in the electrical resistance of the multilayer structure which is controlled by the magnetization of adjacent ferromagnetic layers (which can either be in a parallel or an antiparallel alignment). The overall resistance is relatively low for parallel alignment and relatively high for antiparallel alignment. The magnetization direction of such magnetic layers is then controlled by external magnetic fields and the dependence of electron scattering on the spin orientation. Such quantum effect was further refined in the tunneling magnetoresistance (TMR), a similar magnetoresistive effect occurring in magnetic tunnel junction (MTJ), which consists of two ferromagnets separated by a thin insulator (spin device called spin valve). GMR and TMR have been

used to develop a plethora of applications including magnetic field sensors (used to read data in hard disk drives), microelectromechanical systems (MEMS), biosensors, or medical devices. But GMR multilayer structures also constitute the building blocks of all magnetoresistive random access memories (MRAM), which store huge amount of information bits (Fert 2008). Even more recently, the discoveries of the spin transfer torque effect (STT) and the spin–orbit torque (SOT), which permit the control of the magnetization with an electrical current (Garello et al. 2018; Locatelli et al. 2014; Ralph & Stiles 2008), have triggered a second revolution in spintronics. Since magnetoresistive effects allow the readout of increasingly small magnetic bits, STT and SOT now provide enabling mechanisms to manipulate – precisely, rapidly, and at low energy cost – the magnetic states, which are central information medium for spintronic devices and technologies. Already STT-MRAM technologies are emerging in the data storage market, whereas recent reports at IMEC show promising perspective for large-scale implementation of SOT-MRAM technologies (Garello et al. 2018).

Since the beginning, graphene (and related two-dimensional materials) has attracted attention of the spintronics community. Indeed, the unique electronic band structure of massless Dirac fermions combined with ultralow intrinsic spin–orbit coupling (SOC) was anticipated to clearly favor long distance and fast transmission of spin information (Han et al. 2014; Roche & Valenzuela 2014; Seneor et al. 2012). The pioneering work in the group of Bart van Wees has echoed such high expectations (Tombros et al. 2007), and has been followed by a decade of intense research (Dlubak et al. 2012; Guimaraes et al. 2012; Roche et al. 2015) to eventually obtain spin diffusion lengths exceeding tens of micrometers at room temperature (and spin lifetime above 10 ns) and in scalable graphene materials (Drogeler et al. 2016). Yet the obtained spin diffusion lengths differ by several orders of magnitude compared to early theoretical works predicting spin lifetime values up to the microsecond or even the millisecond scale (Ertler et al. 2009; Huertas-Hernando et al. 2006), that is three to six orders of magnitude larger.

Besides, graphene also offers a fantastic platform for designing efficient *spin manipulation protocols*, and hence for the generation of a full spectrum of spintronic nanodevices for beyond CMOS while being compatible with more-than-Moore CMOS and nonvolatile low-energy MRAM memories (Dery et al. 2012). Of particular interest is the prediction that the coating of magnetic materials with graphene enables stronger control on the perpendicular magnetocrystalline anisotropy, which would strongly reduce the current density needed to switch elementary magnetic memory building block (for instance, in the STT-MRAM or SOT-MRAM) (Roche et al. 2015). Additionally, the interfacing of graphene with other strong SOC materials (such as TMDs), magnetic insulators – such as Europium Sulfide (EuS), Europium oxide (EuO), or high Curie temperature Yittrium Iron Garnet (YIG) – as well as topological insulators or two-dimensional magnetic materials offer remarkable possibilities to manipulate spin transport via the effective magnetic fields induced by proximity (Hallal et al. 2017; Huang et al. 2018; Khokhriakov et al. 2018; Leutenantsmeyer et al. 2017; Song et al. 2018; Yang et al. 2013). In that respect, the recently discovered spin-FET

(Dankert & Dash 2017; Yan et al. 2016) and the *giant spin transport anisotropy* (Benitez et al. 2018; Cummings et al. 2017; Ghiasi et al. 2017; Leutenantsmeyer et al. 2018; Omar & van Wees 2017; Song et al. 2018; Xu et al. 2018) point toward a new dimension for the design of innovative spin-driven active devices. Finally, graphene also provides solutions for the integration of several circuit elements on the same platform. For instance, nonvolatile graphene FETs with ferroelectric gates have been demonstrated to operate as three-terminal resistive memories, while graphene-based memristors are interesting since they may act both as memory and logic elements (Jeong et al. 2010). From all these perspectives, graphene, being compatible with more-than-Moore CMOS and nonvolatile low-energy memory technologies, brings revolutionary opportunities for achieving efficient spin manipulation and for the creation of a full spectrum of spintronic nanodevices, including ultra low-energy devices and circuits comprising (re-)writable microchips, transistors, logic gates, and more.

In the following, Section 8.2 first presents the essential aspects of spin–orbit coupling (SOC) properties in graphene, including the derivation of the SOC from the Dirac equation, as well as the implementation of such interaction in tight-binding or continuous models. The DFT results are also reviewed with a focus on the strengths of the various possible SOC terms emerging from intrinsic or extrinsic factors. Section 8.3 describes how the spin lifetime is usually measured in experiments and presents the variability of estimates, found to be strongly material-dependent (including quality of graphene and interfacing with the substrate). Section 8.4 analyzes the two main conventional spin relaxation mechanisms (namely Elliot–Yafet and Dyakonov–Perel) with a theoretical description of how such mechanisms need to be revised for graphene electronic states, in particular in the limit of clean graphene devices where spin transport becomes dictated by the entanglement between the spin and the pseudospin degrees of freedom (Van Tuan et al. 2014). Finally, Section 8.5 covers other transport phenomena sensitive to weak proximity effect between graphene and strong SOC materials, such as weak antilocalization, spin Hall effect (SHE), spin transport anisotropy, or spin torque physics.

8.2 Spin–Orbit Coupling in Graphene

Understanding the origin and nature of SOC in graphene is fundamental to further study of the main spin transport properties. In a nutshell, SOC is a relativistic effect (which can be derived from the Dirac equation) between electrons and a local electric field either due to internal or external electric fields, and which has the general form $\mathcal{H}_{\rm so} = \frac{\mu_B}{2mc^2}\vec{E}\cdot(\vec{\sigma}\times\vec{p})$. Indeed, fast moving electrons sense an effective magnetic field in their rest frame, which by virtue of the Zeeman effect affects their spin degree of freedom through a generic term written as $\mathcal{H}_{\rm so} = \frac{g\mu_B}{2}\vec{B}_R\cdot\vec{\sigma}$. The corresponding effective magnetic field $\vec{B}_R \sim \vec{E}\cdot(\vec{p}\times\hat{z})$ (usually named a Rashba field) is parallel to the graphene plane, and induces a precession of the electron spin with a frequency (Larmor frequency) given by $\Omega = \frac{\mu_B|\vec{B}_R|}{\hbar}$.

8.2.1 Derivation from the Dirac Equation

A more complete derivation, from the relativistic Dirac Hamiltonian, is both instructive and necessary to further elaborate realistic tight-binding parameters in complex interface geometries. It starts with the definition of the Hamiltonian as (Dirac 1928, 1930):

$$H = \begin{pmatrix} 0 & c\mathbf{p}\cdot\boldsymbol{\sigma} \\ c\mathbf{p}\cdot\boldsymbol{\sigma} & 0 \end{pmatrix} + \begin{pmatrix} mc^2 & 0 \\ 0 & -mc^2 \end{pmatrix} + V \tag{8.1}$$

The solution of the Dirac equation $H|\psi\rangle = E|\psi\rangle$ is a two-component wave function (spinor) $|\psi\rangle = (\psi_A, \psi_B)^T$ which satisfies

$$\psi_B = \frac{c\mathbf{p}\cdot\boldsymbol{\sigma}}{E - V + mc^2}\psi_A \tag{8.2}$$

$$\mathbf{p}\cdot\boldsymbol{\sigma}\frac{c^2}{E - V + mc^2}\mathbf{p}\cdot\boldsymbol{\sigma}\,\psi_A = (E - V - mc^2)\psi_A \tag{8.3}$$

In the nonrelativistic limit, ψ_B becomes negligible compared to ψ_A, since from $E = mc^2 + \epsilon$ and $V \ll mc^2$, Eq. (8.2) is rewritten as

$$\psi_B = \frac{\mathbf{p}\cdot\boldsymbol{\sigma}}{2mc}\psi_A \ll \psi_A \tag{8.4}$$

and at the lowest order in (v/c), Eq. (8.3) reduces to the Schrödinger equation.[1]

$$\left(\frac{p^2}{2m} + V\right)\psi_A = \epsilon\psi_A \tag{8.5}$$

Here ψ_A is solution of the Schrödinger wave function ψ. At higher orders of (v/c), the normalization condition of the wave function implies

$$\int \left(\psi_A^+\psi_A + \psi_B^+\psi_B\right) = 1 \tag{8.6}$$

and by using Eq. (8.4), one finds

$$\int \psi_A^+\left(1 + \frac{p^2}{4m^2c^2}\right)\psi_A = 1 \tag{8.7}$$

A normalized wave function is obtained when $\psi = \left(1 + \frac{p^2}{8m^2c^2}\right)\psi_A$. Substituting it into the Dirac equation, and using for $\frac{c^2}{E-V+mc^2}$ the expansion $\frac{1}{2m}\left(1 - \frac{\epsilon - V}{2mc^2} + \cdots\right)$, one derives after some rearrangement, the Pauli equation

$$\left(\frac{p^2}{2m} + V - \frac{p^4}{8m^3c^2} - \frac{\hbar}{4m^2c^2}\boldsymbol{\sigma}\cdot\mathbf{p}\times\nabla V + \frac{\hbar^2}{8m^2c^2}\nabla^2 V\right)\psi = \epsilon\psi \tag{8.8}$$

where the first and second terms are usual parts of the nonrelativistic Hamiltonian, while the third term denotes the relativistic correction to the kinetic energy, the fourth term is the SOC term, and the final part is a potential-induced energy shift. The SOC term can

[1] Using $(\boldsymbol{\sigma}\cdot\boldsymbol{A})(\boldsymbol{\sigma}\cdot\boldsymbol{B}) = \mathbf{A}\cdot\mathbf{B} + i\boldsymbol{\sigma}\cdot(\mathbf{A}\times\mathbf{B})$

actually be derived in a more intuitive manner, assuming that an electron is moving with a velocity $\mathbf{v}$ under the action of an electric field $-e\mathbf{E} = -\nabla V$. Such an electric field is generated by an external potential V, stemming either from the presence of adatoms or due to the interaction and symmetry breaking induced by an underlying substrate. The electron is equivalently submitted in its rest frame to an effective magnetic field $\mathbf{B} = -\mathbf{v} \times \mathbf{E}/c$, leading to an interaction energy as

$$V_{\mu_s} = -\boldsymbol{\mu}_s \mathbf{B} = -\frac{g_s \mu_B}{2ec} \boldsymbol{\sigma} \cdot \mathbf{v} \times \nabla V = -\frac{g_s \hbar}{4m^2 c^2} \boldsymbol{\sigma} . \mathbf{p} \times \nabla V = -\frac{\hbar}{2m^2 c^2} \boldsymbol{\sigma} \cdot \mathbf{p} \times \nabla V \tag{8.9}$$

This result turns out to double the SOC term appearing in the Pauli equation, a difference explained by Thomas (1926). Fundamentally, the electron moves in a rotating frame of reference, which leads to its spin precession under the action of

$$\mathbf{B} = -\frac{\mathbf{v} \times \mathbf{E}}{2c} \tag{8.10}$$

which yields the full SOC term

$$V_{\mathrm{SOC}} = -\frac{\hbar}{4m^2 c^2} \boldsymbol{\sigma} \cdot \mathbf{p} \times \nabla V \tag{8.11}$$

We now rewrite the SOC term as a force $\mathbf{F}$

$$H_{\mathrm{SOC}} = \alpha \, (\mathbf{F} \times \mathbf{p}) \cdot \mathbf{s} = -\alpha \, (\mathbf{s} \times \mathbf{p}) \cdot \mathbf{F} \tag{8.12}$$

where α is an unknown parameter. We use $\mathbf{s}$ instead of $\boldsymbol{\sigma}$ to denote the spin degree of freedom to avoid confusion with the pseudospin in graphene. The inversion symmetry generates an in-plane electric field (force) at the origin of the intrinsic SOC. In the presence of a structure's mirror symmetry with respect to any nearest-neighbor bond (see Fig. 8.1(a)), the intrinsic SOC vanishes, while the next-nearest-neighbor intrinsic SOC has a nonzero value. Accordingly

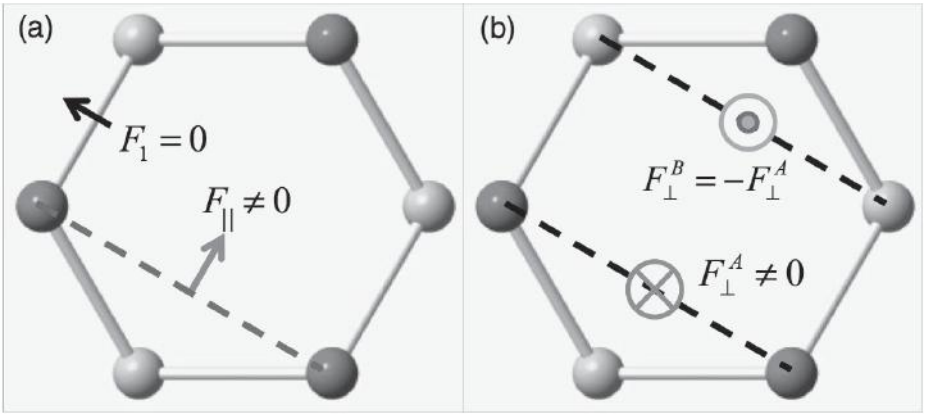

Figure 8.1 SOC in graphene: (a) Intrinsic SOC forces. (b) Rashba SOC force. (Reproduced from van Tuan (2016). Courtesy of Dinh Van Tuan)

$$H_I = i\gamma_2 \left(\mathbf{F}_{//} \times \mathbf{d}_{ij}\right) \cdot \mathbf{s} = \frac{2i}{\sqrt{3}} V_I \mathbf{s} \cdot (\hat{\mathbf{d}}_{kj} \times \hat{\mathbf{d}}_{ik}) \tag{8.13}$$

where γ_2 and V_I are material-dependent parameters, $\hat{\mathbf{d}}_{ij}$ is the unit vector from atom j to its next-nearest-neighbors i, and k is the nearest neighbor of i and j. Besides, the graphene band structure is also altered by the presence of an out-of-plane electric field (see Fig. 8.1(b)), originating from a gate voltage or charged impurities in the substrate or adatoms. This external electric field breaks the spatial inversion symmetry and introduces a nearest-neighbor (extrinsic) SOC. This Rashba SOC (which induces spin flip transitions between nearest neighbors) displays a generic form

$$H_R = i\gamma_1 \left(\mathbf{s} \times \hat{\mathbf{d}}_{ij}\right) \cdot F_\perp \mathbf{e}_z = iV_R \hat{\mathbf{z}} \cdot (\mathbf{s} \times \hat{\mathbf{d}}_{ij}) \tag{8.14}$$

where j is the nearest neighbor of i and γ_1 and V_R are material and interface-dependent parameters. The full SOC-tight-binding (TB) Hamiltonian finally reads

$$\mathcal{H} = -\gamma_0 \sum_{\langle ij \rangle} c_i^+ c_j + \frac{2i}{\sqrt{3}} V_I \sum_{\langle\langle ij \rangle\rangle} c_i^+ \mathbf{s} \cdot (\hat{\mathbf{d}}_{kj} \times \hat{\mathbf{d}}_{ik}) c_j + iV_R \sum_{\langle ij \rangle} c_i^+ \hat{\mathbf{z}} \cdot (\mathbf{s} \times \hat{\mathbf{d}}_{ij}) c_j \tag{8.15}$$

Close to the Dirac point, a low-energy Hamitonian approximation $h(\mathbf{k})$ can be easily derived on the basis $\{|A\rangle, |B\rangle\} \otimes \{|\uparrow\rangle, |\downarrow\rangle\}$, with

$$h(\mathbf{k}) = h_0(\mathbf{k}) + h_R(\mathbf{k}) + h_I(\mathbf{k}) \tag{8.16}$$

and where

$$\begin{aligned} h_0(\mathbf{k}) &= \hbar v_F \left(\eta \sigma_x k_x + \sigma_y k_y\right) \otimes 1_s \\ h_R(\mathbf{k}) &= \lambda_R \left(\eta [\sigma_x \otimes s_y] - [\sigma_y \otimes s_x]\right) \\ h_I(\mathbf{k}) &= \lambda_I \eta \left[\sigma_z \otimes s_z\right] \end{aligned} \tag{8.17}$$

with Fermi velocity $v_F = \frac{3}{2}\gamma_0$, Rashba SOC $\lambda_R = \frac{3}{2}V_R$, and intrinsic SOC $\lambda_I = 3\sqrt{3}V_I$ (Qiao et al. 2012), all SOC terms being momentum-independent. The spin directly couples with the pseudospin instead of momentum as in conventional metals or semiconductors, while the usual SOC term ($\mathbf{k} \times \mathbf{s}$) is small and usually neglected. By diagonalizing the Hamiltonian given in Eq. (8.16), the low-energy electronic bands are derived (Gmitra et al. 2009; Rashba 2009):

$$\epsilon_{\mu\nu}(\mathbf{k}) = \mu\lambda_R + \nu\sqrt{(\hbar v_F k)^2 + (\lambda_R - \lambda_I)^2} \tag{8.18}$$

where μ and $\nu = \pm 1$ are band indexes. In the absence of Rashba SOC, the electronic system is gapped with $\Delta = 2\lambda_I$ (see Fig. 8.2(c) left panel). In the presence of a Rashba SOC, the competition between Rashba and intrinsic SOC determines the existence or not of a finite Δ value. The gap remains finite if $\Delta = 2(\lambda_I - \lambda_R)$ for $0 < \lambda_R < \lambda_I$ (Fig. 8.2(c)), whereas it closes when $\lambda_R > \lambda_I$, and the electronic structure then becomes

a zero-gap semiconductor with quadratically dispersing bands (Fig. 8.2(c) right panel). The analytical form of the eigenfunctions is written as

$$\psi_{\mu\nu}(\mathbf{k}) = \left(\chi_-|\eta e^{-i\eta\varphi}\left[\frac{\epsilon_{\mu\nu}-\lambda_I}{\nu\hbar v_F k}\right]^{\eta}, 1\rangle + \mu\chi_+|-i\eta e^{-i(1+\eta)\varphi}, ie^{-i\varphi}\left[\frac{\lambda_I-\epsilon_{\mu\nu}}{\nu\hbar v_F k}\right]^{\eta}\rangle\right)/C_{\mu\nu}$$

with $\tan\varphi = k_y/k_x$ and the normalization constant $C_{\mu\nu} = \sqrt{2}\left(1+\left[\frac{\lambda_I-\epsilon_{\mu\nu}}{\hbar v_F k}\right]^{2\eta}\right)^2$. The expectation value of the spin polarization of electronic states is further derived as (Gmitra et al. 2009; Rashba 2009),

$$\mathbf{s}_{\mu\nu}(\mathbf{k}) = \frac{\hbar v_F(\mathbf{k}\times\hat{\mathbf{z}})}{\sqrt{(\hbar v_F k)^2+(\lambda_I-\mu\lambda_R)^2}} = \frac{\hbar v_F k}{\sqrt{(\hbar v_F k)^2+(\lambda_I-\mu\lambda_R)^2}}\mathbf{n}(\mathbf{k}) \tag{8.19}$$

where $\mathbf{n}(\mathbf{k}) = (\sin\varphi, -\cos\varphi, 0)$ is the unit vector along the spin direction called spin vector. As seen from Eq. (8.19), the remarkable characteristic of the spin polarization is that it remains in plane and perpendicular to the electron momentum $\mathbf{k}$, while its magnitude vanishes when $k \to 0$. As a result, near the Dirac point, the spin and the pseudospin are strongly coupled, a fact which generates strong entanglement between the spin and pseudopsin dynamics and gives rise to an hitherto unknown source for spin relaxation, especially dominating in the ultra clean graphene limit (see Section 8.4.3 and Cummings & Roche 2016; Van Tuan et al. 2014, 2016).

Importantly, one notes that at high energies $\hbar v_F k \gg \lambda_R + \lambda_I$ and the pseudospin becomes fully controlled by the momentum dynamics via $h_0(\mathbf{k})$ and thus aligns in the same direction (in plane). The spin dynamics is then dictated by its coupling with pseudospin via $h_R(\mathbf{k})$, which leads to the saturation (to 1) of the spin polarization for a certain momentum in Eq. (8.19). By successive unitary rotations of $h(\mathbf{k})$ first into the eigenbasis of $h_0(\mathbf{k})$ and then into the spin basis with respect to the direction $\mathbf{n}(\mathbf{k})$, an effective Bychkov-Rashba-type 2×2 Hamiltonian is obtained for both holes and electrons (Ertler et al. 2009),

$$\tilde{h}(\mathbf{k}) = \nu(\hbar v_F k - \lambda_I) - \nu\lambda_R\mathbf{n}(\mathbf{k})\cdot\mathbf{s} \tag{8.20}$$

The second term in Eq. (8.20) resembles the Bychkov-Rashba Hamiltonian in semiconductor heterostructures $H_{\mathbf{k}} = \hbar\boldsymbol{\Omega}(\mathbf{k})\cdot\mathbf{s}/2$, evidencing that the SOC also acts on the electrons spin as an in-plane magnetic field, of constant amplitude but perpendicular to $\mathbf{k}$. In this effective magnetic field, the spin precesses with a frequency and a period of (Ertler et al. 2009)

$$\Omega = \frac{2\lambda_R}{\hbar}, \qquad T_\Omega = \frac{\pi\hbar}{\lambda_R} \tag{8.21}$$

All these results have been confirmed quantitatively by numerical simulations using real-space order-N method implemented for spin dynamics (Cummings & Roche 2016; Van Tuan et al. 2014, 2016) (see Section 8.7).

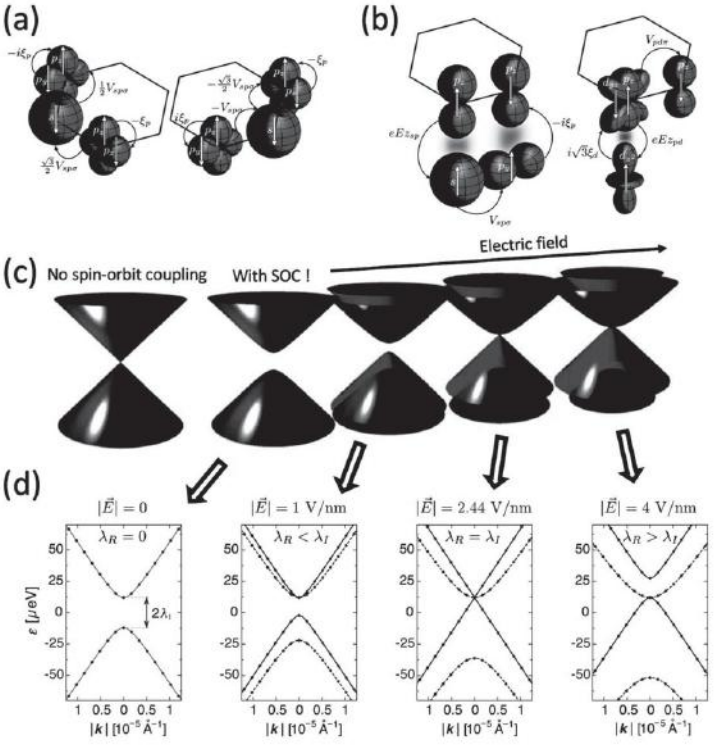

Figure 8.2 (a) Two of the possible *nnn* hopping paths through the *s*, *p* orbitals, arrows, with a corresponding spin, shown by arrows on the orbitals. The opposite sign for the clockwise (left) and the anticlockwise (right) effective hopping is determined by the signs of the two SOCs of the *p* orbitals. (b) A representative leading hopping path, arrows, which is responsible for the Rashba SOC effect, by coupling states of different spins, illustrated by arrows on the orbitals. The effective hopping is between nearest neighbors. Left: dominant *p* orbital contribution. Right: negligible *d* orbital contribution. For clarity, the orbitals of the same atoms are separated vertically, according to their contribution either to the σ-bands (bottom) or to the π-bands (top). (c) Band structures of graphene with spin–orbit coupling in an external transverse (varying) electric field. Touching Dirac cones exist only when spin–orbit coupling is neglected (first from left). When SOC is switched on, the orbital degeneracy at the Dirac point is lifted and the spin–orbit gap appears (second from left). In an external electric field perpendicular to graphene, due to a gate or a substrate, the Rashba effect lifts the remaining spin degeneracy of the bands (third, fourth, and fifth from left). If the intrinsic and Rashba couplings are equal, at a certain value of the electric field, two bands form touching Dirac cones again (fourth from left). If the Rashba coupling dominates (fifth from left), the spin–orbit gap closes. (d) *Ab initio* band structures of graphene are represented by circles and fitted with an analytical model. The spin branch $\mu = 1$ is shown in solid and $\mu = -1$ in dashed, corresponding to the different Dirac cones in (a). The calculated Fermi velocity is $v_F = 0.833 \times 10^6$ m/s (Fermi level is at zero). ((a) and (b) are reproduced with permission from Konschuh et al. (2010). Copyright (2010) by the American Physical Society. (c) is reproduced by permission from Macmillan Publishers Ltd: *Nature Nanotechnology* (Han et al. 2014), copyright (2014). (d) is reproduced with permission from Gmitra et al. (2009). Copyright (2009) by the American Physical Society. Images courtesy of J. Fabian and M. Gmitra)

8.2.2 Theoretical Estimation of the SOC Terms Magnitude

SOC in graphene is clearly expected to be weak owing to the low atomic number of carbon ($Z = 6$, while spin–orbit interaction scales as Z^4). Moreover, the natural occurrence of zero nuclear spin isotope C^{12} is close to 99% and makes hyperfine interaction a vanishingly small decoherence mechanism. The precise magnitude of SOC is actually a highly complicated question, but concurrently a critical information to determine the spin lifetime and the dominant spin relaxation mechanism. A theoretical estimate for intrinsic SOC $\lambda_I \sim 100\,\mu\,\text{eV}$ has been first proposed by Kane and Mele (2005a). This value was reduced by Min et al. (2006) to $0.5\,\mu\,\text{eV}$ by using microscopic TB model and second-order perturbation theory, a result later supported by Huertas-Hernando et al. (2006) with a TB model and by Yao et al. (2007) using first-principles calculations. Another DFT calculation of Boettger and Trickey (2007), using a Gaussian-type orbital fitting function methodology finally provided $25\,\mu\,\text{eV}$. The studies published in Huertas-Hernando et al. (2006); Yao et al. (2007); Min et al. (2006) gave similarly small values for λ_I, but these calculations only involved the SOC induced by the coupling between p_z (forming the π bands) and s orbitals (forming the σ band). However, as pointed out in Konschuh et al. (2010), the coupling of the p_z orbitals to the d orbitals (see Fig. 8.2(a) and (b)) dictates the spin–orbit effects near the $K(K')$-points. Indeed, owing to a finite overlap between the neighboring p_z and d_{xz}, d_{yz} orbitals, the intrinsic splitting λ_I is linearly proportional to the spin–orbit splitting of the d states, ξ_d (orbitals higher than d have a smaller overlap and contribute less). However, due to the absence of the direct overlap between the p_z and σ-band orbitals, the spin–orbit splitting induced by the $\sigma - \pi$ mixing depends only quadratically on the spin–orbit splitting of the p_z orbital, ξ_p, yielding a negligible contribution (Huertas-Hernando et al. 2006; Min et al. 2006; Yao et al. 2007) (Fig. 8.2(a)).

$$\lambda_I \simeq \frac{2(\varepsilon_p - \varepsilon_s)}{9V_{sp\sigma}^2}\xi_p^2 + \frac{9V_{pd\pi}^2}{2(\varepsilon_d - \varepsilon_p)^2}\xi_d \tag{8.22}$$

where $\varepsilon_{s,p,d}$ are the energies of s, p, d orbitals, respectively and $V_{sp\sigma}$ and $V_{pd\pi}$ are hopping parameters of the p orbital to the s and d orbital, respectively. This TB calculation leads to an intrinsic SOC of $\lambda_I = 12\mu\,\text{eV}$ (Konschuh et al. 2010), agreeing with DFT simulations (Gmitra et al. 2009). Such results also suggest that the Rashba term (absent for zero electric field) is tunable with an external electric field E (which is perpendicular to graphene plane)

$$\lambda_R \simeq \frac{2eEz_{sp}}{3V_{sp\sigma}}\xi_p + \sqrt{3}\frac{eEz_{sp}}{(\varepsilon_d - \varepsilon_p)}\frac{3V_{pd\pi}}{(\varepsilon_d - \varepsilon_p)}\xi_d \tag{8.23}$$

where z_{sp} and z_{pd} are the expectation values $\langle s|\hat{z}|p_z\rangle$ and $\langle p_z|\hat{z}|d_{z^2}\rangle$, respectively, of the operator $\hat{z}$ (Fig. 8.2(b)). All these calculations predicted that the Rashba SOC is directly proportional to the electric field E, but the estimated values vary by about one order of magnitude from $5\,\mu\,\text{eV}$ in Gmitra et al. (2009) to 40–$50\,\mu\,\text{eV}$ in

Huertas-Hernando et al. (2006) and Ast and Gierz (2012) and to 67 μeV in Min et al. (2006), for a typical electric field of $E = 1\,\mathrm{V/nm}$.

8.3 Spin Transport Measurements and Spin Lifetime

The estimation of the spin lifetime (as well as the spin diffusion coefficient) is generally achieved through spin valve and Hanle spin precession measurements (Fig. 8.3). In these nonlocal transport experiments, injected (in-plane polarized) spins diffuse far away from the main charge current flow, precess under the action of an external (and perpendicular) magnetic field and slowly (or fastly) loose their polarization depending on the nature and strength of disorder and extrinsic SOC sources. The measured nonlocal magnetoresistance signals are generally analyzed by solving a one-dimensional spin-Bloch diffusion equation, which assumes a diffusive (random walk) propagation of spin, and relate the resistance to microscopic parameters through

$$R_{\mathrm{nl}} \sim \int_0^{+\infty} \frac{1}{\sqrt{4\pi Dt}} e^{-\frac{L^2}{4D_S t}} \cos(\omega_L t) e^{-\frac{t}{\tau_S}} \tag{8.24}$$

with $D_S = v_F \tau_s^2$ (τ_s the spin lifetime) the spin diffusion coefficient, ω the Larmor frequency, and L the distance in between electrodes. The first measurement of electron spin relaxation was performed by Tombros et al. (2007) using mechanical exfoliated

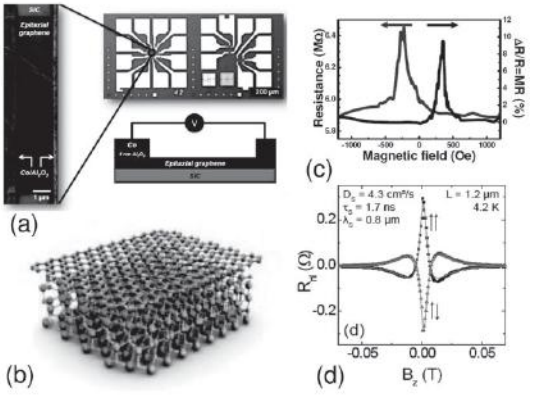

Figure 8.3 (a-left) Plan-view scanning electron microscope image of a two-terminal local spin valve. The width of the epitaxial graphene channel on SiC is 10 μm, and the distance between the two Al_2O_3/CO electrodes is $L = 2$ μm. (a-right) Optical image of the entire structure, including contact pads. (b) Ball-and-stick mode of monolayer graphene on top of SiC. (c) Large local ΔR spin signals measured at 4 K. (d) Oscillating and decaying device resistances as a function of the applied magnetic field (Hanle measurement).((a) and (b) are adapted by permission of Macmillan Publishers Ltd: *Nature Physics* (Dlubak et al. 2012), copyright (2012). (c) is adapted from Seneor et al. (2012) with permission)

single-layer graphene (SLG) on SiO_2 substrate (with mobility of the devices about 2000 $cm^2\,V^{-1}\,s^{-1}$). The authors extracted a spin lifetime of a few hundreds of ps and spin diffusion length of several micrometers (at room temperature), similar to the values obtained for conventional metals or semiconductors. Similar values have been reported by subsequent measurements in similar graphene devices (Han and Kawakami 2011; Han et al. 2010), and interestingly the spin transport properties were generally found to be relatively insensitive to the temperature and weakly dependent on the direction of spin injection and charge density. Since the spin relaxation mechanism was believed to originate from extrinsic sources of SOC (substrate, adatoms), spin measurements for varying quality of graphene samples, and nature of substrates were then performed by many experimental groups.

The measurement of spin diffusion length on large scale, epitaxially grown graphene on SiC(0001) was first reported in 2012 by Maassen et al. (2012). A spin lifetime (τ_s) value of a few nanoseconds, one order of magnitude larger than in exfoliated graphene on SiO_2, was initially deduced. However, the spin diffusion coefficient $D_s \approx 4\,cm^2/s$ was found to be 80 times smaller than expected (compared to the charge diffusion coefficient), yielding 70% lower value for spin diffusion length λ_s. The longer τ_s but much smaller D_s was tentatively explained by the influence of localized states arising from the buffer layer at the interface between the graphene and the SiC surface, and coupled to the spin transport channel (Maassen et al. 2013). Measurements also manifested a weakly temperature-dependent τ_s with a decay of D_s by more than 40% and τ_s by about 20% at room temperature. Assuming that the removal of the underneath substrate would reduce extrinsic SOC, spin measurements on suspended graphene were further undertaken (Guimaraes et al. 2012). However, despite a much higher mobility ($\mu \approx 10^5\,cm^2\,V^{-1}\,s^{-1}$), the increase in the spin diffusion coefficient ($D_s = 0.1\,m^2/s$) was only one order of magnitude when compared to SiO_2 supported graphene. This indicated that despite longer mean free path, in the order of a micrometer, and reduced impurity scattering, the spin lifetime upper limit could not exceed a few hundreds of picoseconds with spin diffusion length of a few micrometers. The next significant advance was made by the group of Fert, reporting room temperature spin diffusion length of hundreds of micrometers (Dlubak et al. 2012; Seneor et al. 2012) (see Fig. 8.3), a result contrasting prior estimates although the way to extract the spin transport length scales in both types of experiments differed substantially, giving rise to conflicting interpretations (Roche & Valenzuela 2014). Finally, other groups used CVD method to grow graphene on copper (Cu) substrate and studied the effect of corrugation on spin lifetime (Avsar et al. 2011; Drogeler et al. 2016). They observed similar spin transport lengths as in exfoliated graphene and showed that ripples in graphene flakes have minor effects on spin dynamics. The record spin lifetime achieved to date with polycrystalline CVD graphene is about *10 ns at room temperature* (Drogeler et al. 2016), a result which seems to set an upper limit for spin transport in scalable graphene, of relevance for practical applications.

Importantly, one has to observe that the usual way to estimate the spin lifetime (and spin diffusion length) using Eq. (8.24) cannot tackle the situation of ballistic

(or quasiballistic) charge motion, and needs further generalization when the quality of samples is such that the mean free paths reache several hundreds of nanometers and exceed the electrode spacing (Du et al. 2008). Additionally, for more disordered graphene, the contribution of quantum interferences and localization phenomena (which in certain materials persist up to 100 K) are neglected and could affect any estimation. Finally, τ_s can be also estimated independently from two-terminal spin valves measurements (using a phenomenological approach), but turns out to yield estimations, which differ by orders of magnitudes compared to Hanle measurements (both types of measurement setups are illustrated in Fig. 8.3 and adapted from Dlubak et al. (2012) and Seneor et al. (2012)).

In conclusion, despite earlier theoretical predictions of spin lifetimes in the range of microseconds or even milliseconds (Ertler et al. 2009), after a decade of improved experimental measurements in much cleaner graphene samples, the upper limit for the spin lifetime saturates at about 10 ns, which is three to six orders of magnitude lower than the original theoretical values. Proposals to explain the unexpectedly short spin relaxation lengths include spin decoherence due to interactions with the underlying substrate, the presence of random distribution of magnetic impurities and the adsorption of molecules, the generation of ripples or corrugations, the presence of strain, topological lattice disorder, graphene edges, etc. (see Han and Kawakami (2011)). However, the presence of a dielectric oxide, low impedance contacts, or enhanced spin-flip processes do not seem to affect the spin relaxation times. To further advance in the understanding of spin transport, an in-depth description of possible spin relaxation mechanisms is detailed in the forthcoming section.

8.4 Spin Dynamics and Relaxation Mechanisms

The sources for spin relaxation have been a puzzle for long and fiercely debated in the literature. Inspired by the knowledge about spin transport in metals and semiconductors (Fabian et al. 2007), two mechanisms were proposed in graphene, namely the *Elliot-Yafet* (EY) (Elliot 1954; Ochoa et al. 2012) and the *Dyakonov-Perel* (DP) (D'yakonov & Perel 1971a, 1971b; Huertas-Hernando et al. 2009) mechanisms.

The EY mechanism has been derived for spin relaxation in metals, and related the spin dynamics with the electron scattering off impurities or phonon events. Each scattering event changes the electron momentum, with a finite spin-flip probability, which is derived by a perturbation theory (assuming weak spin–orbit scattering). As a result, an SOC-dependent scattering potential produces admixtures of spin and electron momentum in the wave functions, so that scattering changes electron momentum and simultaneously induces spin-flip event. This gives rise to weak antilocalization phenomena in the low-temperature regime, and more interestingly, a typical scaling behavior of the spin lifetime with momentum relaxation as $\tau_s^{\mathrm{EY}} \sim c_0 \tau_p$ (c_0 a scaling parameter generally in the order of few tens thousands). However, the DP mechanism usually occurs in materials lacking inversion symmetry (such as small bandgap

semiconductors). In such situations, the SOC generates an effective momentum-dependent magnetic field about which electron spin precesses during its propagation and in between scattering events. The longer the time an electron travels, the larger angle the electron spin precesses and as a consequence, the larger the spin dephasing between electrons, since at each scattering event, the direction and frequency of the precession changes randomly. As a result, the spin lifetime is inversely proportional to elastic scattering time $\tau_s^{\mathrm{DP}} \sim \tau_p^{-1}$.

On the experimental side, systematic studies of spin dynamics in SLG and bilayer graphene (BLG) spin valves with tunneling contact were performed in Han and Kawakami (2011). In SLG, the spin lifetime was found to vary linearly with momentum scattering time τ_p, suggesting the predominance of an EY-mechanism for spin relaxation, in contrast to the case of BLG, for which the scaling between τ_s and τ_p was found to follow the DP scaling. One notes that surprisingly, Pi and coworkers also reported that τ_s increases with decreasing τ_p in the surface chemical doping experiment with Au atoms on graphene (Pi et al. 2010), indicating that the DP mechanism is important there. This experiment led to the conclusion that charged impurity scattering is not the dominant mechanism for spin relaxation, despite its importance for momentum scattering. Even more puzzling, Zomer et al. (2012) performed spin transport measurements on graphene deposited on boron nitride with mobilities up to $4 \cdot 10^4\ \mathrm{cm}^2\ \mathrm{V}^{-1}\ \mathrm{s}^{-1}$ and showed that neither EY nor DP mechanisms alone allow for a fully consistent description of spin relaxation, but maybe a combination of both. A tentative crossover has been proposed to be related to the charge density, while different mechanisms for spin relaxation are assumed to coexist, but without any clue concerning their respective microscopic origin. Furthermore, electron spin is expected to relax faster in BLG than in SLG because the SOC in BLG is one order of magnitude larger than the one in SLG due to the mixing of π and σ bands by interlayer hopping (Guinea 2010), but the experimental results showed an opposite behavior (Han and Kawakami 2011; et al. 2011), increasing the confusion. Spin lifetime in BLG is a few nanoseconds and was interpreted as dictated by DP (Han and Kawakami 2011; et al. 2011). Most recent results have concluded on a DP mechanism for graphene on silicon oxide, presenting lowest mobilities, whereas graphene on boron nitride exhibits a more complex behavior (Drogeler et al. 2014, 2016; Guimarães et al. 2014), which has been analyzed in terms of spin dephasing regime as discussed in Section 8.4.3. In Avsar et al. (2011), the spin properties in CVD-grown monolayer (bilayer) graphene samples were found to be dominated by the EY-type (DP-type) relaxation mechanism. Simultaneously, the corresponding transport time scales were found to be $\ell_e = v_F \times \tau_p \sim 20$–$30$ nm, with $\tau_s \sim 175$–230 ps for monolayer, and $\ell_e = v_F \times \tau_p \sim 30$–$50$ nm, $\tau_s \sim 260$–340 ps for bilayers. Therefore, despite similar mean free paths (a few tens of nanometers) and spin lifetimes, the scaling behavior of ℓ_e vs. τ_s was opposite and not understood.

A theoretical derivation has been proposed for disordered monolayer graphene, by taking into account the Dirac cone physics. The authors found scaling as $\tau_s \sim \epsilon_F^2 \tau_p / \lambda_R^2$, that is, of EY type (Ochoa et al. 2012) (see Section 8.4.2 below). However, such a result

assumes the absence of intervalley scattering and the estimated spin lifetimes are much too long compared to experimental data.

In conclusion, to determine the upper limit for spin lifetime and the corresponding dominant mechanisms for spin relaxation, a lot of effort has been put in by both experimentalists and theoreticians, but without reaching any consensus. The discrepancy between the theoretical and experimental estimates remains puzzling. Besides, the theoretical derivations of both EY and DP mechanisms for graphene generally assume a strong coupling of momentum with pseudospin, a property which breaks down near the Dirac point (see Section 8.4.3). All these results clearly point out a lack of theoretical understanding of spin dynamics and spin relaxation mechanisms in graphene, demanding for a deeper theoretical inspection with quantum simulation of spin transport, to explore the regimes out of reach of perturbative treatments and traditional semiclassical transport phenomenology. We hereafter provide a deeper insight into the spin dynamics of electrons in graphene in the presence of disorder and SOC, showing what is similar to other materials and what is unique to massless Dirac fermions with internal degrees of freedom.

8.4.1 Dyakonov–Perel Mechanism

From a general perspective, the presence of an in-plane magnetic field $\mathbf{B}_{\parallel}(\mathbf{k}) \sim \boldsymbol{\Omega}(\mathbf{k})$, related to a Rashba SOC, triggers the precession of the electron spin in between scattering events. Random scattering thus induces motional narrowing of this spin precession, and will drive the spin relaxation phenomenon (see Fig. 8.4(a–d)). The spin relaxation rates for the α-th spin component following the DP mechanism can be actually written as (Ertler et al. 2009)

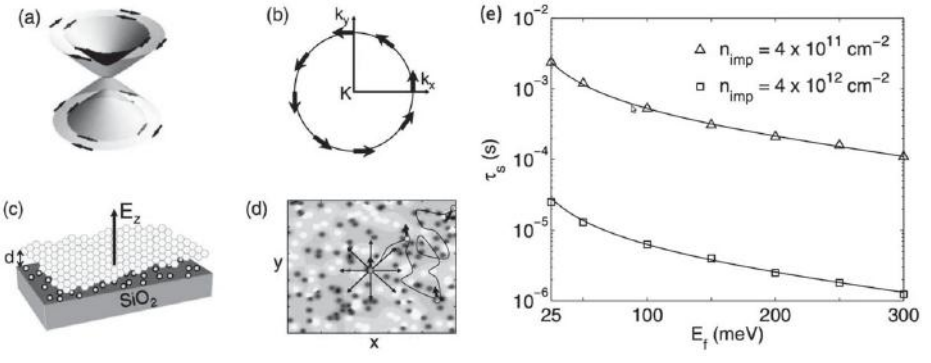

Figure 8.4 DP spin relaxation in graphene: (a) Dirac coin when SOC is included. (b) $\mathbf{B}_{\parallel}(\mathbf{k})$ along the Fermi circle. (c) Charged impurities in substrate induce electric field in graphene. (d) Illustration of the spin relaxation in a spatially random potential due to the charged carriers. (e) Calculated spin relaxation time τ_s as a function of the Fermi energy E_F. (Reproduced with permission from Ertler et al. (2009). Copyright (2009) by the American Physical Society)

$$\frac{1}{\tau_{s,\alpha}^{\mathrm{DP}}} = \tau^* \left(\langle \mathbf{\Omega}^2(\mathbf{k}) \rangle - \langle \mathbf{\Omega}_\alpha^2(\mathbf{k}) \rangle \right) \tag{8.25}$$

where τ^* is the correlation time of the random spin–orbit field. In graphene, this value coincides with momentum relaxation time $\tau^* = \tau_p$ (Ertler et al. 2009; Fabian et al. 2007) and the symbol $\langle \cdots \rangle$ expresses an average over the Fermi surface. Because $\langle \mathbf{\Omega}^2(\mathbf{k}) \rangle = (2\lambda_R/\hbar)^2$, $\langle \mathbf{\Omega}_z^2(\mathbf{k}) \rangle = 0$, and $\langle \mathbf{\Omega}_{x,y}^2(\mathbf{k}) \rangle = \frac{1}{2}(2\lambda_R/\hbar)^2$, the DP relation for spin relaxation in graphene is (following (Ertler et al. 2009; Huertas-Hernando et al. 2009))

$$\tau_{s,z}^{\mathrm{DP}} = \frac{\hbar^2}{4\lambda_R^2 \tau_p} \qquad \text{and} \qquad \tau_{s,\{x,y\}}^{\mathrm{DP}} = 2\tau_{s,z}^{\mathrm{DP}} = \frac{\hbar^2}{2\lambda_R^2 \tau_p} \tag{8.26}$$

Since the spin lifetime is inversely proportional to the momentum relaxation time, *the DP spin relaxation length is independent of mean free path* (Huertas-Hernando et al. 2009).

$$\lambda_s = \sqrt{D\tau_s} = \sqrt{\frac{1}{2} v_F^2 \tau_p \tau_s} = \frac{\hbar v_F}{2\sqrt{2}\lambda_R} \tag{8.27}$$

Figure 8.5 provides an illustrative overview of the dynamics of spin polarization of electrons moving through graphene away from the Dirac point and in the strong disorder regime. The dependence of the polarization dynamics on disorder strength is dictated by the transport time τ_p. An effective spin–orbit coupling λ_R (as induced by adatoms for instance) leads to spin precession when the injected electrons are polarized out of the plane or along the direction of momentum. The spin precession time is obviously given by $T_\Omega = \pi\hbar/\lambda_R$. Panel (a) shows the case when $\tau_p \ll T_\Omega$, a regime which is typically seen in various experiments and dirtier samples. Different snapshots at different times (T_1, T_2, T_3) show that the ensemble-averaged spin polarization (S_z in panel (d)) decays weakly since elastic scattering interferes with the spin precession. A scattering event experienced by one propagating state randomizes its momentum, and hence the orientation of the effective field about which the spin precesses. Being no longer coherent with the other states, such randomization drives spin relaxation in the ensemble. The spin relaxation time depends on how strongly the precession of the scattered state deviates from the rest of the ensemble. If the scattering time is short ($\tau_p \ll T_\Omega$), the difference in the precession remains small. The time-dependent profiles clearly yield a scaling law, which follows $S_z \sim \cos(2\pi t/T_\Omega)e^{-t/\tau_s}$, where T_Ω is the spin precession time.

By increasing the scattering time ($\tau_p \simeq T_\Omega$), faster spin decoherence is obtained (panel (b)), as confirmed by comparing the corresponding averaged polarization (panels (d) and (e)). This illustrates the DP mechanism for which the spin lifetime scales inversely with the transport time ($\tau_s \sim 1/\tau_p$). Panel (c) shows the clean limit (with small residual disorder such that $\tau_p \gg T_\Omega$), where only a few scattering events occur during the time sequence, and spin precesses over long timescale. The average polarization (panel (f)) then clearly exhibits such spin precession characterized by oscillations with period T_Ω. On top of this, the spin signal decays continuously owing to

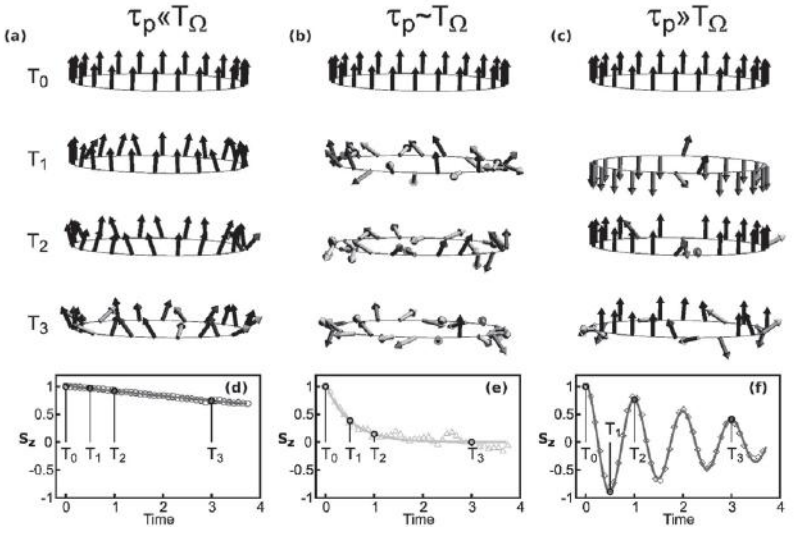

Figure 8.5 Time evolution of spin expectation value for various τ_p. (a) shows the case of ultrashort τ_p, whereas the change of the spin dynamics for intermediate (resp. long values) are reported in (b) and (e) (respectively (c) and (f)). (a)–(c) illustrate how spin vectors evolve for increasing time as indicated in (d)–(f), respectively. (d)–(f) display the time dependence of the polarization averaged over the Fermi circle. Courtesy of Frank Ortmann (adapted from Avouris et al. (2017))

scattering and dephasing effects. The decay is weaker for lower scattering, suggesting that τ_s should be maximized for long τ_p, usually observed at energies closest to the Dirac point. However, based on further quantum simulations, we find the opposite behavior, i.e., τ_s is minimized at $E = 0$ and that a simplified description of spin motion fails to capture the more subtle phenomenon governing the Dirac point spin physics (Section 8.4.3).

Similar to the spin dynamics picture developed above, the phenomenology proposed in Ertler et al. (2009) assumes some homogeneous Rashba SOC together with an underlying disorder potential (with tunable density of impurities), which should roughly capture the effect of the interaction between graphene and an oxide substrate, including the trapped charged impurities distributed at random (electron–hole puddles). However, the analytical estimates and Monte Carlo simulations (Ertler et al. 2009) with DP mechanism show that the corresponding spin relaxation times are between micro- to milliseconds (see Fig. 8.4(e)), that is several orders of magnitude larger than the experimental results.

Actually, such values for the spin lifetime are deduced from Monte Carlo simulations, which assume that along any given classical trajectory ($[\mathbf{r}(t), \mathbf{k}(t)]$), the spin dynamics is described by Bloch spin equation $\frac{d\mathbf{S}}{dt} = \Omega_R[\mathbf{r}(t)](\mathbf{n}[\mathbf{k}(t)] \wedge \mathbf{S})$ assuming some energy-independent spin precession frequency (Fabian et al. 2007). Finally, τ_s is numerically obtained by averaging over random trajectories with different initial momenta, assuming that $t \gg \tau_{\mathrm{tr}}$. The result from a fit of numerics to $S_\alpha(t) \sim e^{-t/\tau_\alpha}$ gives $\tau_\alpha \simeq \mu\mathrm{s} - \mathrm{ms}$

for typical density of Coulomb impurities (Ertler et al. 2009). Another prediction of this work, in full contradiction to all experimental data, is that the spin lifetime is maximum at the Dirac point (see Fig. 8.4(e)). As shown by Cummings and Roche (2016), the assumption of a constant Ω_R for all energies is incorrect and fails to capture multiple interferences and dephasing, which ultimately drive the spin dynamics and relaxation (Section 8.4.3).

8.4.2 Elliot–Yafet Mechanism for Graphene

Here, we present the main steps of the derivation proposed by Ochoa et al. (2012) concerning the calculation of the spin relaxation time for Dirac fermions under certain approximations (weak SOC and single valley restriction). Their derivation assumes a SOC effect dominated by a Rashba SOC, but the result surprisingly suggests an EY mechanism. As mentioned in Section 8.2.2, the intrinsic SOC obtained by TB model and DFT calculations is in the order of a few μeV (Huertas-Hernando et al. 2006; Konschuh et al. 2010; Min et al. 2006; Yao et al. 2007), which can become smaller than the Rashba SOC. In the case of slowly varied Rashba SOC induced by electric field or ripples, the Hamiltonian can be written in the form

$$\mathcal{H} = -i\hbar v_F \boldsymbol{\sigma} \cdot \nabla + \lambda_R(\boldsymbol{\sigma} \times \boldsymbol{s}) \tag{8.28}$$

Because of the Rashba SOC, Bloch states with well-defined spin polarization are no longer eigenstates of the Hamiltonian. The Bloch eigenstates are then written as (Ochoa et al. 2012)

$$\Psi_{\boldsymbol{k},\pm} = \left[\begin{pmatrix} 1 \\ \frac{\epsilon_{\boldsymbol{k}\pm}}{\hbar v_F k} e^{i\theta_{\boldsymbol{k}}} \end{pmatrix} \otimes |\uparrow\rangle \pm i \begin{pmatrix} \frac{\epsilon_{\boldsymbol{k}\pm}}{\hbar v_F k} e^{i\theta_{\boldsymbol{k}}} \\ e^{2i\theta_{\boldsymbol{k}}} \end{pmatrix} \otimes |\downarrow\rangle \right] \mathrm{e}^{i\boldsymbol{k}\boldsymbol{r}}. \tag{8.29}$$

where $\theta_{\boldsymbol{k}} = \arctan(k_y/k_x)$ and the energy $\epsilon_{\boldsymbol{k}\pm} = \pm\lambda_R + \sqrt{(\hbar v_F k)^2 + \lambda_R^2}$ is obtained from Eq. (8.18) with $\lambda_I = 0$. When $\lambda_R = 0$, the eigenstates in Eq. (8.29) have their spin pointing along (helicity $+$) or opposite to (helicity $-$) the transport direction. This contrasts with the case $\lambda_R \neq 0$ but in the case of $\lambda_R/\epsilon_F \ll 1$, each of these eigenstates with chiral states $\pm$ can be identified using perturbation theory (Ochoa et al. 2012).

Within the Born approximation, the local scattering potential $U(\mathbf{r})$ becomes diagonal in the sublattice and spin degrees of freedom, and the scattering amplitudes $f^0_{\pm}(\theta)$ for chiral channels $\pm$ for an incoming electron with positive chirality (in the case of $\lambda_R = 0$) are given by (Ochoa et al. 2012):

$$\begin{aligned} f^0_{+}(\theta) &= -(\hbar v_F)^{-1} \sqrt{\frac{k}{8\pi}} U_{\mathbf{q}} e^{-i\theta}(1 + \cos\theta) \\ f^0_{-}(\theta) &= -(\hbar v_F)^{-1} \sqrt{\frac{k}{8\pi}} U_{\mathbf{q}} i e^{-i\theta} \sin\theta \end{aligned} \tag{8.30}$$

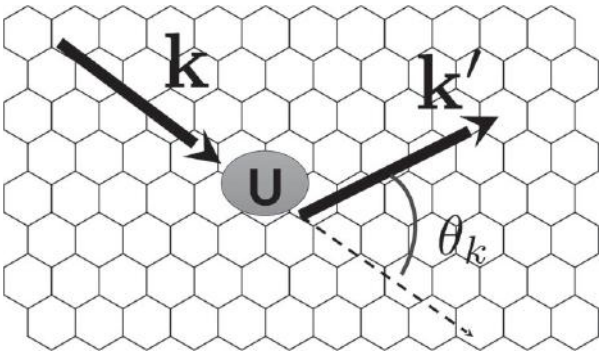

Figure 8.6 Illustration of the scattering potential $U(\mathbf{r})$ in the chiral channels.

where $U_{\mathbf{q}}$ is the Fourier transformation of the scattering potential evaluated for $\mathbf{q} = \mathbf{k}' - \mathbf{k}$ and for an angle θ (see Fig. 8.6) between $\mathbf{k}'$ and $\mathbf{k}$. When the Rashba SOC is included, one finds

$$f_{+}^{\lambda_R}(\theta) = -(\hbar v_F)^{-2}\sqrt{\frac{1}{8\pi k_+}}\,(\epsilon + (\epsilon - 2\lambda_R)\cos\theta)\,U_{\mathbf{q}_+}e^{-i\theta}$$

$$f_{-}^{\lambda_R}(\theta) = -(\hbar v_F)^{-2}\sqrt{\frac{1}{8\pi k_-}}\,(\epsilon + 2\lambda_R)\,U_{\mathbf{q}_-}ie^{-i\theta}\sin\theta \tag{8.31}$$

where $k_\pm = (\hbar v_F)^{-1}\sqrt{\epsilon^2 \mp 2\epsilon\lambda_R}$ and $\mathbf{q}_\pm = \mathbf{k}'_\pm - \mathbf{k}$. The probability for a spin-flip process induced by scattering in both chiral channels and driven to the presence of the SOC is determined through

$$S(\theta) = \frac{\sum_{\pm 1}|f_{\pm}^{0}(\theta)||f_{\pm}^{\lambda_R}(\theta) - f_{\pm}^{0}(\theta)|}{\sum_{\pm 1}|f_{\pm}^{0}(\theta)|^2} \tag{8.32}$$

denoting the amount of spin relaxed in the direction defined by θ. The total amount of spin relaxation during a scattering event stems from the average of $S(\theta)$ integrated over the whole Fermi surface:

$$S = \langle S(\theta)\rangle = \frac{1}{2\pi}\int d\theta S(\theta, \epsilon = \epsilon_F) \tag{8.33}$$

Additionally, one easily shows that $f_{\pm}^{\lambda_R}(\theta) - f_{\pm}^{0}(\theta) \sim \lambda_R/\epsilon_F$ when expanding Eq. (8.31) in powers of λ_R/ϵ_F. This implies that $S(\theta) \sim \lambda_R/\epsilon_F$, which is independent of $U(\mathbf{r})$. This result first derived for weak disorder (Huertas-Hernando et al. 2009) was later generalized (beyond perturbation theory) for the cases of scattering by boundary, strong scatterers, and clusters of impurities (Ochoa et al. 2012). Assuming such a form of $S(\theta)$, the EY relation for graphene can be derived. Indeed, the spin rotation at each collision is $S \sim \lambda_R/\epsilon_F$ so that the total change of spin orientation after N_{col} collisions scales as $\sqrt{N_{\text{col}}}\epsilon_F/\lambda_R$. Dephasing occurs when $\sqrt{N_{\text{col}}}\epsilon_F/\lambda_R \sim 1$ and hence after a time

$\tau_s^{\mathrm{EY}} = N_{\mathrm{col}}\tau_p$. This leads to the EY scaling $\tau_s^{\mathrm{EY}} \approx \frac{\epsilon_F^2}{\lambda_R^2}\tau_p$, observing that the spin lifetime τ_s is here not only proportional to τ_p but also depends on the carrier density (and thus the Fermi energy ϵ_F). In this regime, the spin diffusion length is proportional to the elastic mean free path ℓ_e according to $\lambda_s = \sqrt{D\tau_s} = \sqrt{\frac{1}{2}v_F^2\tau_p\tau_s} \sim \ell_e\frac{\epsilon_F}{\sqrt{2}\lambda_R}$. This derivation has a true pedagogical virtue but its applicability to realistic models of disordered graphene is limited as well as for the understanding of spin dynamics in graphene in the clean limit.

8.4.3 Spin–Pseudopsin Entanglement and Spin Relaxation

Pseudospin-related effects (and the associated Berry phase) are known to drive most of the unique transport signatures of graphene (Klein tunneling, weak antilocalization, anomalous quantum Hall effect), but the role of such extra degree of freedom on spin relaxation has been discovered only recently. Pseudospin and spin dynamics are usually perceived as decoupled from one another, with pseudospin dynamics much faster when compared to spin rotation. However, this picture collapses in the vicinity of the Dirac point, a region that is out of reach for semi-classical and perturbative approaches, but is particularly relevant for experiments. In the presence of SOC, spin couples to orbital motion, and therefore to pseudospin (Rashba 2009) so that spin and pseudospin dynamics cannot be treated independently. Here, we present the main ideas underpinning a new relaxation mechanism and driven by a spin–pseudospin entanglement effect. To capture the unusual behavior of the spin lifetime at low energies, it is first instructive to investigate the Kane-Mele-Rashba (KMR) Hamiltonian in the vicinity of both valleys K and K'. From Eqs. 8.16 and (8.17), it is obvious that at low energy (when $|\vec{k}| \to 0$), the term which couples pseudospin and momentum ($h_0(\vec{k})$) vanishes, in contrast to the Rashba term ($h_R(\vec{k})$), which connects spin and pseudospin. Hence close to the Dirac point, the term $h_R(\vec{k})$ dictates the spin and pseudospin precession motion and leads to a spin–pseudospin locking feature. On the contrary, for high energies ($|\vec{k}| > 0$), the term $h_0(\vec{k})$ exceeds the Rashba term and disrupts the locking effect. Figure 8.7 gives the computed band structure of the Kane-Mele-Rashba Hamiltonian (Eq. (8.17)) assuming 8% impurity coverage (Van Tuan et al. 2014). The Rashba term generates a counter-propagating spin texture in the k_x, k_y plane that tends to vanish close to the Dirac point as (Rashba 2009):

$$\vec{S}_{\nu\mu}(\vec{k}) = \frac{\mu\hbar v_F(\vec{k}\times\vec{z})}{\sqrt{\lambda_R^2 + \hbar^2 v_F^2 k^2}} \tag{8.34}$$

We further calculate the modulus of the spin polarization vector $|\vec{S}| = |(\langle s_x\rangle, \langle s_y\rangle, \langle s_z\rangle)|$ from the eigenstates of the full Hamiltonian in Eq. (8.16) with both intrinsic and Rashba SOC

$$\Psi_{\vec{k},\pm} = \left[\begin{pmatrix} c_{A,\uparrow} \\ c_{B,\uparrow} \end{pmatrix} \otimes |\uparrow\rangle \pm i \begin{pmatrix} c_{A,\downarrow} \\ c_{B,\downarrow} \end{pmatrix} \otimes |\downarrow\rangle\right] e^{i\vec{k}\vec{r}}. \tag{8.35}$$

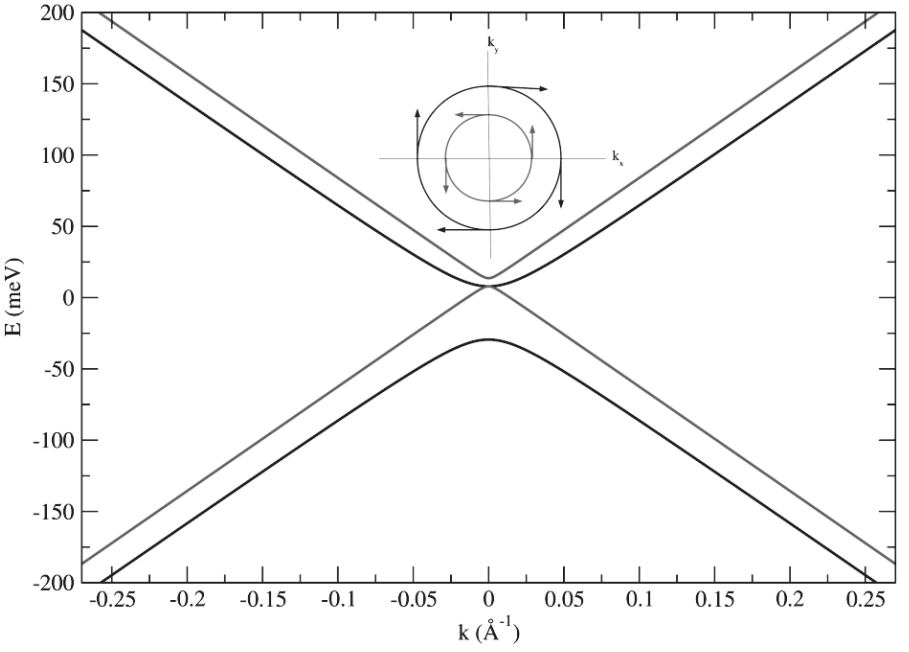

Figure 8.7 Band structure calculated using the Kane-Mele-Rashba model for 8% adatom concentration generating an overall Rashba SOC. The inset shows the typical Rashba-like spin texture for the conduction bands. (Reprinted by permission from Macmillan Publishers Ltd: *Nature Physics*, Van Tuan et al. 2014, copyright (2014))

In the presence of the Rashba SOC term, the Bloch states with well-defined spin polarization are no longer eigenstates of the complete Hamiltonian (Ochoa et al. 2012). The clear signature of spin–pseudospin entanglement is actually evidenced at low energies ($\vec{k} \to 0$) since the electronic states write

$$\Psi^{\mathrm{I}}_{\vec{k},\pm} = \begin{pmatrix} 0 \\ 1 \end{pmatrix} \otimes |\uparrow\rangle \pm \begin{pmatrix} i \\ 0 \end{pmatrix} \otimes |\downarrow\rangle \tag{8.36}$$

$$\Psi^{\mathrm{II}}_{\vec{k},\pm} = \begin{pmatrix} 1 \\ 0 \end{pmatrix} \otimes |\uparrow\rangle \pm \begin{pmatrix} 0 \\ i \end{pmatrix} \otimes |\downarrow\rangle. \tag{8.37}$$

In both cases, a change in sublattice (pseudospin) index entails a change in spin index. This means that at low energy, spin and pseudospin are completely locked and $|\vec{S}| \approx 0$. The situation is different for high energies ($|\vec{k}| > 0$); when pseudospin–momentum coupling comes into play, all coefficients become equally weighted ($|c_{\sigma,s}| \approx 0.5$), and spin and pseudospin are unlocked leading to $|\vec{S}| \approx 1$.

It is also instructive to explore the spin propagation in graphene using more general quantum dynamics methods, and taking into account the specificities of the graphene band structure in the presence of SOC and disorder (energy broadening and

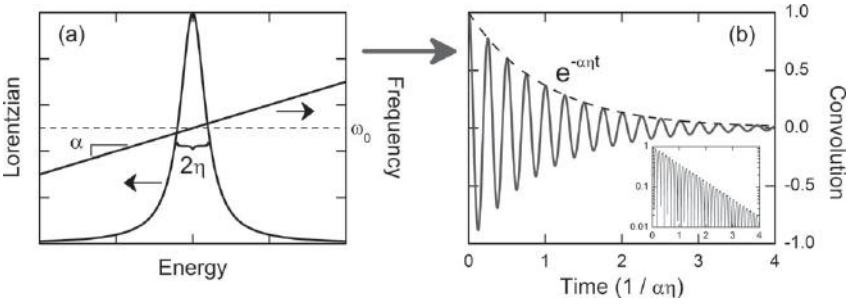

Figure 8.8 (a) Convolution of the spin precession frequency (right axis) with a Lorentzian energy broadening (left axis). The η parameter gives the HWHM of the Lorentzian, while α denotes the variation of the spin precession frequency. (b) Exponentially decaying cosine, with frequency ω_0 and decay time $1/\alpha\eta$. By courtesy of A.W. Cummings, reproduced from Avouris et al. (2017)

electron–hole puddles). Pioneering studies have been realized using an exact calculation of spin dynamics through time-dependent evolution methods (see Section 8.4.3 for technical details) (Cummings & Roche 2016; Van Tuan 2016; Van Tuan et al. 2014, 2016). The advantage of such approaches is to capture the effect of both disorder of any kind and strong SOC regimes, beyond the reach of perturbation theory.

Concerning the nature of disorder in (clean) exfoliated graphene samples, it is known that the strength and size of electron–hole puddles can vary significantly for different substrates – such as SiO_2 or hexagonal boron nitride (h-BN) – and in the situation of clean supported graphene, it is generally assumed that a weak Rashba SOC field is always present because of mirror symmetry breaking and surrounding electric fields. When the disorder is strong enough to yield $\tau_p \ll T_\Omega$ (case of electron–hole puddles for graphene/SiO_2), then the numerical simulations (Van Tuan et al. 2016) confirm the scaling for the spin lifetime as $\tau_s \sim 1/n_i$, where n_i is the puddle density and the ratio $\tau_s^\perp/\tau_s^\parallel = 1/2$, in full agreement with the conditions required for the DP regime (Zhang & Wu 2012) (see also Fig. 8.9).

However, for cleaner graphene samples and flat substrates (e.g., electron–hole puddles for h-BN), the regime $\tau_p \gg T_\Omega$ can be eventually reached; a regime where DP regime ceases to apply, as well as the conventional EY regime. In such a quasiballistic transport regime in graphene, τ_p is no longer a relevant timescale for understanding spin relaxation. It has actually been found that in this limit, the spin relaxation is dictated by the presence of energy broadening and, more importantly a *nonuniform precession frequency*, a fundamental ingredient which has been neglected in prior studies (Ertler et al. 2009). The presence of SOC generates the effective magnetic field B_{eff} which monitors the spin rotation. When the magnitude of B_{eff} (or its direction) depends on the electron energy (or momentum) distribution (defined by temperature or effective disorder-induced broadening), then the total spin signal derives from interference and dephasing between different precession frequencies. As a matter of illustration, let us focus on the case illustrated in Fig. 8.8, where the spin precession frequency varies

linearly with $\omega(E) = \omega_0 + \alpha E$, while the energy occupation for electrons is given by a Lorentzian distribution $L(E) = \eta/[\pi(E^2 + \eta^2)]$ (η as the half-width at half-maximum (HWHM)). From simple considerations, the total spin signal $s(t)$ is obtained from (Cummings & Roche 2016)

$$L(E)\cos(\omega(E)t) = \int_{-\infty}^{+\infty} (\eta/\pi)/(E^2 + \eta^2)\cos((\alpha E + \omega_0)t)dE = e^{-\alpha\eta t}\cos(\omega_0 t) \tag{8.38}$$

Equation (8.38) indicates that the combination of energy broadening and nonuniform spin precession leads to a dephasing of the spin signal, which is eventually lost at a rate proportional to both the broadening η and the precession variation. This decay (not necessarily exponential) occurs even in the ballistic regime provided the existence of a frequency mixing in energy or momentum. Indeed, when the Lorentzian distribution is replaced with a Gaussian distribution, Eq. (8.38) gives $e^{-(\alpha\sigma t)^2/2}$, with σ the standard deviation, whereas a Fermi distribution produces $\Xi t/\sinh(\Xi t)$ ($\Xi = \alpha\pi kT$ and kT is the thermal energy) (Cummings & Roche 2016).

In conclusion, if the DP mechanism dominates for dirty graphene with low mobility, in the limit of clean (and even ballistic) limit, a new spin dephasing mechanism, driven by strong coupling between spin and pseudospin, gives rise to an intricate mixing of precession frequencies which dictate the energy variation of the spin lifetime, as well as its upper value (Cummings & Roche 2016; Van Tuan et al. 2014, 2016). Actually, the approximation of an energy-independent spin precession frequency made in Ertler et al. (2009) was demonstrated to be the origin of the astonishing discrepancy of such earlier calculations compared with experimental data (Cummings & Roche 2016).

For the full picture, Fig. 8.9 shows the $\tau_s(1/\tau_p)$ for both numerical and experimental data taken from Drogeler et al. (2014). In the main frame, the simulation for the SiO_2 substrate, the scaling matches well with the DP relation, $\tau_s = (T_\Omega/2\pi)^2/\tau_p$, where $T_\Omega = 2\pi\hbar/(3V_R)$, whereas for the *h*-BN substrate, the opposite scaling trend is seen, with τ_s proportional to τ_p, reminiscent of the EY mechanism. The crossover is related to the ratio τ_p/T_Ω. For SiO_2, one clearly obtains a regime where $\tau_p \ll T_\Omega$ meaning that momentum scattering frequently interrupts the spin dynamics, inducing motional narrowing of the precession as described in the DP relaxation mechanism. However, for the *h*-BN substrate, numerical simulations show that $\tau_p \geq T_\Omega$, allowing for spin precession between scattering events. In this case, the momentum scattering acts as an effective broadening of states, leading to increased dephasing and relaxation. This behavior can be qualitatively reproduced by tuning the broadening parameter in the case of clean graphene (dashed line). Similar trends have been obtained in experiments that compare spin relaxation on SiO_2 and *h*-BN substrates (Drogeler et al. 2014). As shown in the inset of Fig. 8.9, these measurements indicate an inverse relationship between τ_s and the sample mobility for SiO_2 substrates in agreement with DP (Zhang & Wu 2012). Meanwhile, spin lifetimes of SLG on *h*-BN substrates appear to show a positive correlation between τ_s and the mobility, therefore supported with the new theoretical picture.

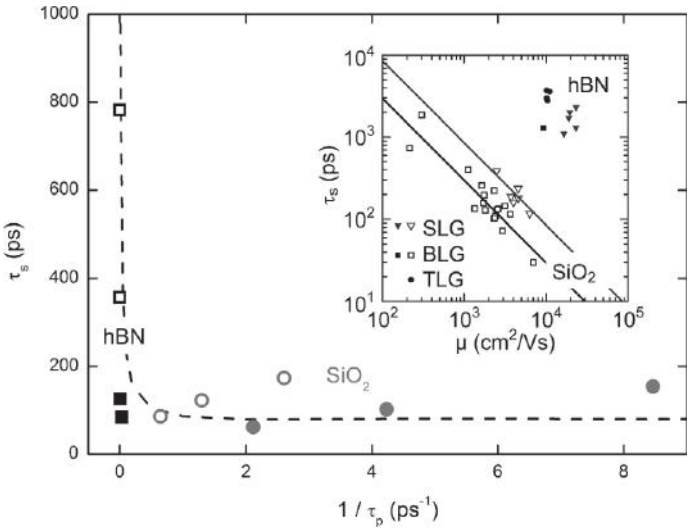

Figure 8.9 Spin lifetime vs. $1/\tau_p$ for graphene in the presence of SOC and e-h puddles. Squares (circles) are for graphene on *h*-BN (SiO_2) substrate. Closed (open) symbols are for spin relaxation at the Dirac point (at $E = -200$ meV). The dashed line shows the spin lifetime assuming only energy broadening (top axis). Inset: Experimental results for spin lifetime vs. electron mobility on *h*-BN and SiO_2 substrates. (The main panel is reprinted from Van Tuan et al. (2016). The inset is reprinted with permission from Drogeler et al. (2014)). Copyright (2014) American Chemical Society)

8.5 Manipulating Spin by Proximity Effects

In order to advance toward more versatile use of graphene in spintronic devices, the creation and manipulation of polarized (or pure) spin currents is a fundamental step. Remarkable progress has been made in that direction by harnessing weak proximity effects interfacing graphene with magnetic insulators and strong SOC materials such as transition metal dichalcogenides (TMDs) and topological insulators (Garcia et al. 2018; Hallal et al. 2017; Huang et al. 2018; Khokhriakov et al. 2018; Leutenantsmeyer et al. 2017; Song et al. 2018; Yang et al. 2013). Electronic structures of TMDs are strongly determined by SOC effects, and they also present the advantage of very good interface matching with graphene, which facilitates the imprint of spin-dependent features of graphene while maintaining its superior charge transport properties.

In lateral devices, proximity effects can be probed through Hanle spin precession measurements but also through the weak antilocalization analysis. Further, the resulting transfer of spin features to graphene has raised expectations to use such van der Waals heterostructures for improved spin Hall effect (SHE) (Avsar et al. 2014) as well as spin torque phenomenon (Rodriguez-Vega et al. 2017). Finally, the recently discovered family of 2D magnetic materials, such as layered magnetic insulator CrI_3 (Klein et al. 2018) opens fascinating perspectives for ultraminiaturized vertical magnetic tunnel junctions,

as well as other other possible proximity effects in lateral devices. In the following, we briefly review the main aspects of the underlying physics and ongoing issues.

8.5.1 Manipulating Spin Using 2D Magnetic Substrates

Magnetic anisotropy is an important requirement for realizing two-dimensional magnetism. Indeed, magnetic order is theoretically prohibited in the 2D isotropic Heisenberg model at finite temperatures by the Mermin–Wagner theorem (Mermin & Wagner 1966). Consequently, magnetic anisotropy removes this restriction, enabling for instance, the occurrence of 2D Ising ferromagnetism.

The magnetic properties of a layered crystal can dramatically change when it is cleaved to the few-layer limit (Huang et al. 2018). One example is chromium triiodide (CrI_3), a van der Waals magnetic insulator that displays out-of-plane ferromagnetic behavior in the monolayer (2D Ising ferromagnet). Surprisingly, it adopts an alternating ferromagnetic alignment in few-layer crystals, giving a layered antiferromagnetic ground state in the bilayer (Huang et al. 2018). Through electrostatic doping, the magnetic ground state of these materials can be controlled electrically (Huang et al. 2018), thus allowing for the manipulation of these ultrathin magnets with potential applications in spintronics. Moreover, the magnetic state in van der Waals magnetic tunnel junctions fabricated from few-layer CrI_3 crystals can be probed (Klein et al. 2018). This arises from the sensitive dependence of quantum electron tunneling on the barriers magnetic state. These new results on 2D ferromagnets allow for the exploration of new magnetoelectric phenomena and van der Waals spintronics based on 2D materials.

8.5.2 Magnetic Proximity Effects in Vertical Spin Devices

Magnetic tunnel junction (MTJ) is one of the building blocks of spintronics applications (Chappert et al. 2007). The key element of an MTJ is its tunnel barrier, most commonly made of MgO or Al_2O_3. Achieving precise control of the barrier thickness down to only a few atoms while avoiding thickness nonuniformity, pinholes, or point defects remains a major challenge for these metal oxides. This has led to considerable interest in integrating materials that remain stable as atomically thin monolayers, such as the layered 2D materials into MTJs (Piquemal-Banci et al. 2016).

Vertical spin devices combining magnetic materials and two-dimensional layers are intensively investigated given that improved TMR performances could directly impact memory storage technologies (see Fig. 8.10). Recently, strong influence of proximity effect (e.g., hybridization) on 2D materials at the interface with ferromagnets have been reported (Piquemal-Banci et al. 2018). Indeed, an insulating *h*-BN layer at a ferromagnetic interface (such as Co, Fe, ...) could become metallic due to the strong hybdridization. This normally unpolarized *h*-BN layer becomes spin polarized acting as a spin filter with strong spin polarization $>50\%$ TMR (see Fig. 8.10). Finally, this effect

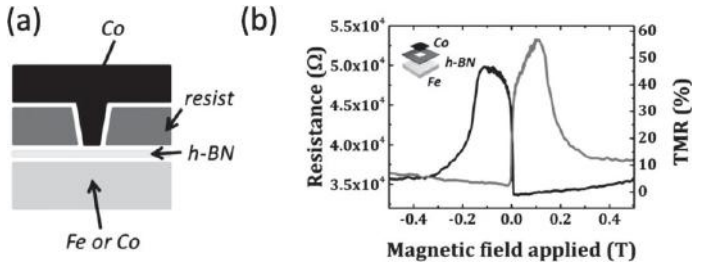

Figure 8.10 2D-magnetic tunnel junctions based on hexagonal boron nitride. (a) Sketch of the 2D section of the magnetic tunnel junctions. (b) Tunnel magnetoresistance signal measured on a Co/*h*-BN/Fe magnetic tunnel junction at 2 mV. (Adapted with permission from Piquemal-Banci et al. (2018). Copyright (2018) American Chemical Society)

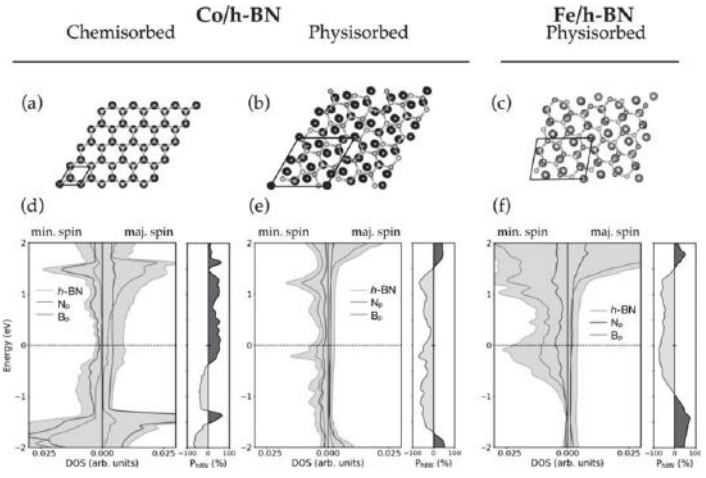

Figure 8.11 Representation of bilayer *h*-BN on Co hcp (0001) within the (a) commensurate and (b) incommensurate configurations. (c) Representation of monolayer *h*-BN on Fe fcc (110). Spin-resolved projected density of states onto the boron and nitrogen atoms (d–f), corresponding to the three atomic configurations depicted in the upper panel. Gray curves correspond to the projection of the density of states on the *h*-BN layers. Darker curves identify the contributions associated with the *p*-orbitals of nitrogen and boron. For each stacking configuration, the spin polarization of *h*-BN is depicted on the right of each panel, illustrating both the excess of majority and minority spins. (Adapted with permission from Piquemal-Banci et al. (2018). Copyright (2018) American Chemical Society)

was shown to be voltage dependent since an inversion of the TMR sign was observed as a function of voltage in a 2D-based magnetic tunnel junction. Through analysis of spin polarizations of *h*-BN/Co and *h*-BN/Fe interfaces extracted from experimental spin signals in light of spin filtering, the presence of two hybrid chemisorbed/physisorbed *h*-BN interfaces was suggested. *Ab initio* calculations confirmed that this modification of the *h*-BN/metal coupling (chemisorption versus physisorption) induces an inversion of the spin-polarization of the *h*-BN layer (see Fig. 8.11). These results illustrate the

strong potential of *h*-BN for MTJs and are expected to ignite further investigations of other 2D materials (graphene, TMDs, . . .) for large signal spin devices.

8.5.3 Weak Antilocalization in Graphene/TMD Heterostructures

Several measurements of Weak Antilocalization (WAL) in a graphene/TMD heterostructure were made with TMD as WS_2, WSe_2, and MoS_2 substrates (Völkl et al. 2017; Wakamura et al. 2018; Wang Ki, et al. 2015; Yang et al. 2016, 2017), but the estimation of spin transport length scales from those studies, using a conventional WAL theory frame has led to contradictory interpretations, although typical spin transport times were estimated to be a few picoseconds. In Yang et al. (2016, 2017), the relaxation time was found to scale inversely with the momentum scattering time, and could be tuned by ∼10% in either direction with a vertical electrical field. This was analyzed in terms of the DP mechanism of spin relaxation induced by Rashba SOC. (A Rashba strength of $\lambda_R \approx 0.4$ meV was estimated.) Independent measurements of graphene/WSe_2 also interpreted their spin relaxation process as a DP mechanism and evaluated a Rashba SOC of $\lambda_R \approx 0.7$–1 meV (Völkl et al. 2017).

Meanwhile, a comprehensive set of WAL measurements demonstrated the importance of eliminating classical effects from the magnetoconductance (Wang et al. 2016). At high temperatures, the dephasing time τ_ϕ becomes very short, washing out interference effects, and any dependence of the conductivity on the magnetic field can be considered to arise from classical effects. In these measurements, subtracting the high-temperature magnetoconductivity curves from the low-temperature curves resulted in a sharp WAL peak and little to no upturn of $\Delta\sigma$ at higher fields; see Fig. 8.12(a) and (b) where a flat profile of $\Delta\sigma$ is indicative of very fast spin relaxation. Indeed, fits to WAL theory yield upper bounds of $\tau_{so} \leq 0.1$–0.4 ps. As shown in Fig. 8.12(c), this behavior is found over many devices, including different TMDCs (MoS_2, WS_2, and WSe_2) and a wide range of mobilities (3000–110, 000 $cm^2/V{\cdot}s$). By analyzing Shubnikov-de Haas oscillations in bilayer graphene/WSe_2 devices, the Rashba SOC strength was estimated to be $\lambda_R \approx 10$–15 meV, which is one order of magnitude larger than what was found in other measurements or in *ab initio* simulations (Gmitra et al. 2016; Wang et al. 2016; Yang et al. 2016).

If these measurements demonstrate strong proximity-induced SOC in graphene, the interpretation disregards the contribution of valley-Zeeman SOC, which however has been predicted theoretically (Cummings et al. 2017), and confirmed by Hanle measurements (Benitez et al. 2018; Ghiasi et al. 2017), to be responsible for fast relaxation of the in-plane spins (and yielding a giant spin lifetime anisotropy). As shown very recently, a careful analysis of WAL measurements can reveal this behavior (Zihlmann et al. 2018). According to the theory of McCann and Fal'ko, two spin relaxation times have to be introduced with the first one τ_{sym} determined by both intrinsic and valley-Zeeman SOC, while the second τ_{asy} is dominated by Rashba SOC (McCann & Fal'ko 2012). As discussed in Yang et al. (2016, 2017); Völkl et al. (2017), and

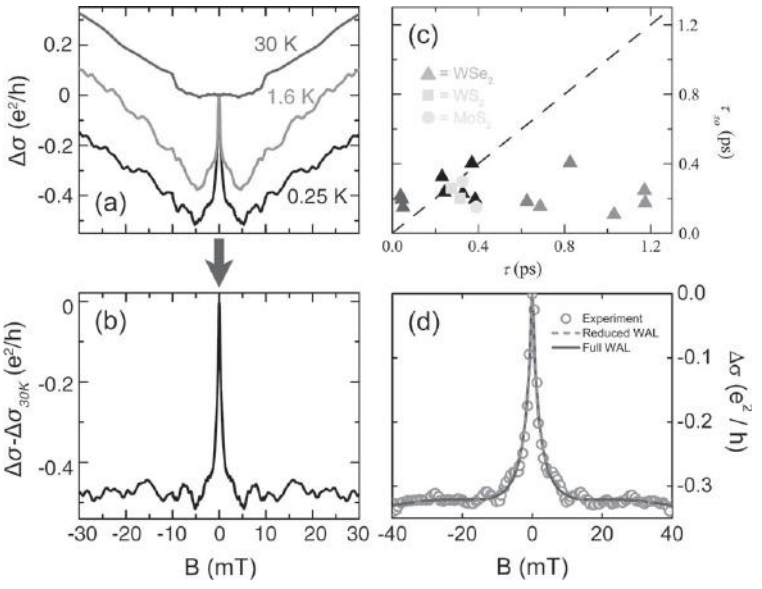

Figure 8.12 (a) Temperature-dependent evolution of the magnetoconductance in a graphene/WS_2 heterostructure. Subtracting the high-temperature classical signal gives the normalized magnetoconductivity shown in (b). Panel (c) shows a summary of WAL measurements made using this background subtraction, yielding a uniform spin–orbit time across a wide range of devices and TMDCs. Panels (a)–(c) are reproduced from Wang, Ki et al. (2016). (d) Fits to magnetoconductance (from Wakamura et al. (2018)) are made using the WAL formulas (see Garcia et al. (2018) for deeper analysis). (Reproduced from Garcia et al. (2018), with permission from The Royal Society of Chemistry)

Zihlmann et al. (2018), the contribution of intrinsic SOC is negligible, so that τ_{sym} is entirely dictated by the valley-Zeeman SOC. Following an analysis made in Garcia et al. (2018), it is found that $\tau_{\text{asy}} = 2\tau_s^{\perp}$ and $\tau_{\text{so}} = \tau_s^{\parallel}$, which allows the determination of both λ_R and λ_{VZ}. Additionally, the spin lifetime anisotropy can be estimated as $\zeta = \tau_{\text{asy}}/2\tau_{\text{sym}}$. In recent measurements of graphene/WSe_2 devices (Zihlmann et al. 2018), such an analysis gets $\lambda_R \approx 0.35$ meV, $\lambda_{\text{VZ}} \approx 0.2$–2 meV, and $\zeta \approx 20$. These results agree well with DFT simulations (Gmitra et al. 2016; Wang Ki, et al. 2015; Yang et al. 2016), spin relaxation theory (Cummings et al. 2017), and Hanle measurements of spin lifetime anisotropy (Benitez et al. 2018; Ghiasi et al. 2017), and thus highlight the importance of considering the valley-Zeeman SOC when studying quantum transport in these systems.

8.5.4 Spin Transport Anisotropy

The ratio between spin lifetimes for out-of-plane and in-plane polarizations $\tau_{s,\perp}/\tau_{s,\parallel}$ is a fingerprint of the spin–orbit coupling effects occurring in a given system. For two-dimensional metallic materials with strong (in-plane) Rashba SOC, such ratio is strictly

equal to 1/2, a result derived analytically (Fabian et al. 2007; Zhang & Wu 2012). Curiously, most experiments studying the case of graphene/SiO_2 or graphene/*h*-BN have not found any anisotropy (i.e., $\tau_{s,\perp} = \tau_{s,\parallel}$) (Guimarães et al. 2014; Haydock et al. n.d.; Raes et al. 2017). Such experimental data contrast with spin dynamics simulations (Van Tuan et al. 2016) and suggest either the presence of magnetic impurities (Kochan et al. 2014; Soriano et al. 2015) or the randomization of the Rashba SOC field (in both magnitude and direction), which could both lead to the vanishing of the Rashba-induced spin anisotropy. Although this remains to be fully clarified, the interfacing of graphene with much stronger SOC materials such as TMD has allowed for demonstration of the efficiency of proximity effects to imprint new spin properties to graphene electronic states.

The nature of spin relaxation in graphene/TMD systems has been explored theoretically by Cummings et al. (2017), through the study of the spin dynamics in a randomly fluctuating magnetic field (following the method published in Fabian et al. (2007)). The low-energy Hamiltonian of the graphene/TMD is written as $H = H_0 + H_\Delta + H_I + H_R + H_{\text{PIA}}$ (Gmitra et al. 2016)

$$\begin{aligned} H_0 &= \hbar v_F(\kappa\sigma_x k_x + \sigma_y k_y), \\ H_\Delta &= \Delta\sigma_z, \\ H_I^{A/B} &= \frac{1}{2}\left[\lambda_I^A(\sigma_z + \sigma_0) + \lambda_I^B(\sigma_z - \sigma_0)\right]\kappa s_z, \\ H_{\text{PIA}}^{A/B} &= \frac{a}{2}\left[\lambda_{\text{PIA}}^A(\sigma_z + \sigma_0) + \lambda_{\text{PIA}}^B(\sigma_z - \sigma_0)\right](k_x s_y - k_y s_x), \\ H_R &= \lambda_R(\kappa\sigma_x s_y - \sigma_y s_x). \end{aligned} \tag{8.39}$$

where v_F is the Fermi velocity, $\kappa = 1(-1)$ for the K (K′) valley, σ_i (s_i) are the sublattice (spin) Pauli matrices, k_i are the wave vector components relative to K or K′, and $a = 0.246$ nm is the graphene lattice constant. H_0 describes the Dirac cone, and H_Δ is a TMD-dependent staggered sublattice potential. $H_I^{A/B}$ and $H_{\text{PIA}}^{A/B}$ are the intrinsic and the pseudospin inversion asymmetry (PIA) SOC, respectively, the latter of which is permitted by broken $z/-z$ symmetry in graphene (Kochan et al. 2017). Due to the broken sublattice symmetry, these terms can have different strengths and signs on the A and B sublattices ($\lambda_I^{A/B}$ and $\lambda_{\text{PIA}}^{A/B}$). Finally, H_R is the Rashba SOC induced by a perpendicular electric field. In the following, TB parameters are taken from Table I of Gmitra et al. (2016).

Equation (8.39) is practical for performing TB calculations, but it is also convenient to combine the sublattice-dependent terms as $H = H_0 + H_\Delta + H_I + H_{\text{VZ}} + H_R + H_{\text{PIA}} + H_{\Delta_{\text{PIA}}}$ with (Cummings et al. 2017)

$$\begin{aligned} H_I &= \lambda_I\kappa\sigma_z s_z, \\ H_{\text{VZ}} &= \lambda_{\text{VZ}}\kappa s_z, \\ H_{\text{PIA}} &= a\lambda_{\text{PIA}}\sigma_z(k_x s_y - k_y s_x), \\ H_{\Delta_{\text{PIA}}} &= a\Delta_{\text{PIA}}(k_x s_y - k_y s_x), \end{aligned} \tag{8.40}$$

where $\lambda_I = (\lambda_I^A + \lambda_I^B)/2$, $\lambda_{\mathrm{VZ}} = (\lambda_I^A - \lambda_I^B)/2$, $\lambda_{\mathrm{PIA}} = (\lambda_{\mathrm{PIA}}^A + \lambda_{\mathrm{PIA}}^B)/2$, and $\Delta_{\mathrm{PIA}} = (\lambda_{\mathrm{PIA}}^A - \lambda_{\mathrm{PIA}}^B)/2$. In this form, H_I is the usual intrinsic SOC in graphene, which opens a topological gap $2\lambda_I$ at the Dirac point. H_{VZ} is a valley Zeeman term, which polarizes the bands out of the graphene plane with opposite orientation in the K and K′ valleys. H_{PIA} renormalizes the Fermi velocity, while $H_{\Delta_{\mathrm{PIA}}}$ leads to a k-linear splitting of the bands, similar to the case of a 2D electron gas with Rashba SOC (Bychov & Rashba 1984). Except for the PIA terms, this Hamiltonian is identical to the one considered in previous works (Wang Ki, et al. 2015, 2016; Yang et al. 2016). The spin dynamics is then investigated from the total effective SOC field by rewriting Eq. (8.40) in the basis of the eigenstates of H_0 and projecting onto the conduction and valence bands. At high energy, the Hamiltonian reduces to (Cummings et al. 2017)

$$\begin{aligned} H &= H_0 + \frac{1}{2}\hbar\vec{\omega}(t)\cdot\vec{s}, \\ \hbar\omega_x &= -2(ak\Delta_{PIA} \pm \lambda_R)\sin\theta, \\ \hbar\omega_y &= 2(ak\Delta_{PIA} \pm \lambda_R)\cos\theta, \\ \hbar\omega_z &= 2\kappa\lambda_{\mathrm{VZ}}, \end{aligned} \tag{8.41}$$

where k is the wave vector magnitude, θ is the direction of k with respect to k_x, and $\vec{\omega}$ is the spin precession frequency of the effective SOC field. The in-plane components of $\vec{\omega}$ give a Rashba-like spin texture, where $+(-)$ is for the conduction (valence) band. Strong PIA SOC leads to electron–hole asymmetry. The out-of-plane component of $\vec{\omega}$ is determined by λ_{VZ} and changes sign between valleys. The overall texture of the effective SOC field is pictured in Fig. 8.13. Due to momentum scattering, each component of $\vec{\omega}$ fluctuates in time, and the correlation of the fluctuating field can be described by (Fabian et al. 2007)

$$\overline{\omega_\alpha(t)\omega_\beta(t')} = \delta_{\alpha\beta}\overline{\omega_\alpha^2}\mathrm{e}^{-|t-t'|/\tau_{c,\alpha}}, \tag{8.42}$$

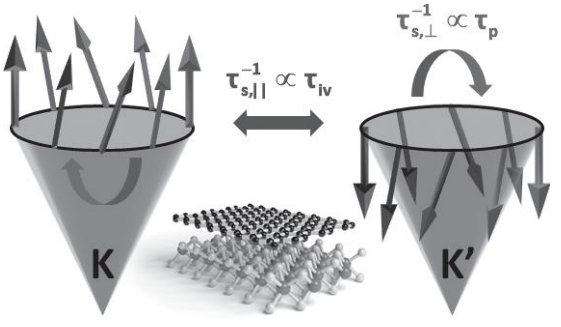

Figure 8.13 Illustration of spin physics in graphene/TMD heterostructures. The tall arrows depict the effective SOC field within the Dirac cones at K and K′ valleys. Intervalley scattering dominates the in-plane spin dynamics, while overall momentum scattering controls the out-of-plane behavior. Courtesy of A.W. Cummings

where the correlation time of fluctuation $\tau_{c,\alpha}$ depends on the components of $\vec{\omega}$. The in-plane components $\omega_{x/y}$ depend only on θ, so that $\tau_{c,x} = \tau_{c,y} = \tau_p$ (momentum scattering time). However, the out-of-plane component ω_z depends on the valley index with $\tau_{c,z} = \tau_{iv}$ (intervalley scattering time). Assuming that $\tau_{c,\alpha}\omega_\alpha \ll 1$, applying Eqs. (8.41) and (8.42) to the equation of motion for the density matrix (Fabian et al. 2007),

$$\frac{\mathrm{d}\overline{\rho_I(t)}}{\mathrm{d}t} = \left(\frac{1}{i\hbar}\right)^2 \int_0^{t\gg\tau_c} [\overline{V_I(t), [V_I(t'), \overline{\rho_I(t)}]}]\,\mathrm{d}t', \tag{8.43}$$

with $V_I(t) = \frac{1}{2}\hbar\vec{\omega}(t)\cdot\vec{s}_I(t)$ and $\vec{s}_I(t) = \mathrm{e}^{iH_0t/\hbar}\vec{s}\mathrm{e}^{-iH_0t/\hbar}$, one obtains

$$\begin{aligned}
\tau_{s,x}^{-1} &= \overline{\omega_z^2}\tau_{iv} + \overline{\omega_y^2}\tau_p,\\
\tau_{s,y}^{-1} &= \overline{\omega_z^2}\tau_{iv} + \overline{\omega_x^2}\tau_p,\\
\tau_{s,z}^{-1} &= (\overline{\omega_x^2} + \overline{\omega_y^2})\tau_p.
\end{aligned} \tag{8.44}$$

In Eq. (8.44), the out-of-plane spin relaxation follows $\tau_{s,\perp}^{-1} \equiv \tau_{s,z}^{-1} = 2[(ak\Delta_{\mathrm{PIA}} \pm \lambda_R)/\hbar]^2\tau_p$ (DP regime), with an increased SOC by the PIA term. However, the in-plane relaxation includes contributions from both the intervalley and the overall momentum scattering. Since $\tau_{\mathrm{iv}} > \tau_p$ and DFT calculations have found that $\lambda_{\mathrm{VZ}} > \lambda_R$ for the tungsten-based TMDs (Gmitra et al. 2016; Wang Ki, et al. 2015; Yang et al. 2016), the in-plane relaxation rate becomes $\tau_{s,\parallel}^{-1} \equiv \tau_{s,x}^{-1} = \tau_{s,y}^{-1} \approx (2\lambda_{\mathrm{VZ}}/\hbar)^2\tau_{\mathrm{iv}}$. Ignoring the PIA term, the spin lifetime anisotropy then becomes $\tau_{s,\perp}/\tau_{s,\parallel} \approx (\lambda_{\mathrm{VZ}}/\lambda_R)^2(\tau_{\mathrm{iv}}/\tau_p)$. Using DFT values of $\lambda_{\mathrm{VZ}} = 1.2$ meV and $\lambda_R = 0.56$ meV for graphene on WSe_2 (Gmitra et al. 2016), and assuming relatively strong intervalley scattering ($\tau_{\mathrm{iv}} \sim 5\tau_p$), a spin lifetime anisotropy of ~20 is obtained. The nature of the spin relaxation, with $\tau_{s,\parallel}$ determined by τ_{iv} and $\tau_{s,\perp}$ by τ_p, is shown schematically in Fig. 8.13.

Equation (8.44) is valid for strong intervalley scattering ($\tau_{\mathrm{iv}}\omega_z \ll 1$), so that the corresponding fast fluctuation of ω_z provokes a motional narrowing of the in-plane spin precession and an inverse dependence of $\tau_{s,\parallel}$ on τ_{iv}. In contrast, in the regime $\tau_{\mathrm{iv}} \to \infty$, a constant out-of-plane SOC field monitors the time-dependence of the in-plane components of the precessing electron spin, and one gets

$$\begin{aligned}
\tau_{s,x}^{-1} &= \overline{\omega_y^2}\tau_p^*,\\
\tau_{s,y}^{-1} &= \overline{\omega_x^2}\tau_p^*,\\
\tau_{s,z}^{-1} &= (\overline{\omega_x^2} + \overline{\omega_y^2})\tau_p^*,
\end{aligned} \tag{8.45}$$

where $\tau_p^* = \tau_p/(\omega_z^2\tau_p^2 + 1)$. In the absence of intervalley scattering $\tau_{s,\perp}/\tau_{s,\parallel} = 1/2$, as in Rashba systems (Fabian et al. 2007). To check the above picture numerically the graphene/TMD system is modeled by the TB form of Eq. (8.39), together with a disorder term $H_{\mathrm{dis}} = \sum_{i,s} V_{\mathrm{dis}}(\vec{r}_i)\, c_{\mathrm{is}}^\dagger c_{\mathrm{is}}$, where $c_{\mathrm{is}}^\dagger(c_{\mathrm{is}})$ is the creation (annihilation) operator at site i with spin s, and $V_{\mathrm{dis}}(\vec{r}_i)$ is the potential at site i. The disorder is described by

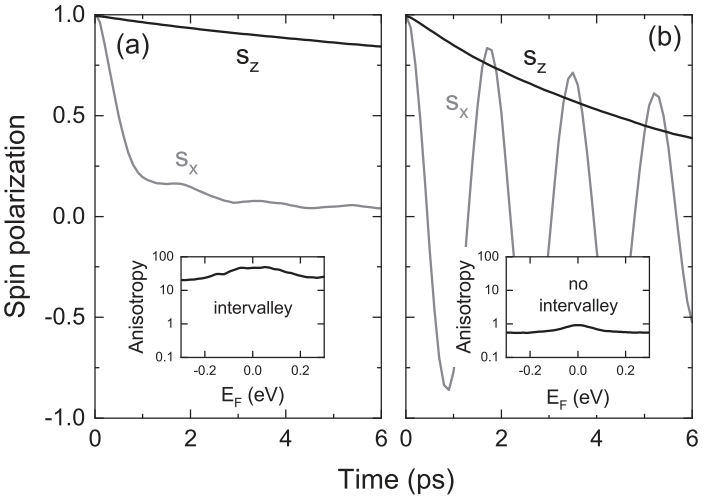

Figure 8.14 Spin dynamics in the graphene/WSe_2 system for (a) strong and (b) negligible intervalley scattering. The insets show the corresponding anisotropies of spin lifetimes. (Reproduced with permission from Cummings et al. (2017). Copyright (2017) by the American Physical Society. Courtesy of A.W. Cummings)

Gaussian-shaped electron–hole puddles with $V_{\rm dis}(\vec{r}_i) = \sum_{j=1}^{N} \epsilon_j \exp(-|\vec{r}_i - \vec{r}_j|^2/2\xi^2)$, with the strength ϵ_j of each scatterer randomly chosen within $[-\epsilon, \epsilon]$, and with a uniform width $\xi = \sqrt{3}a$ (Adam et al. 2011). In the dilute limit, τ_p and $\tau_{\rm iv}$ are inversely proportional to the number of scatterers N, while ϵ controls their relative magnitude (larger ϵ giving stronger intervalley scattering) (Ortmann et al. 2011; Zhang et al. 2009). Charge and spin transport are investigated using the real-space wave packet propagation method (Cummings, Cresti et al. 2014; Van Tuan et al. 2016). The momentum relaxation time $\tau_p(E)$ is deduced from the time evolution of the diffusion coefficient $D(E, t)$, while the spin lifetime is evaluated from the time-dependence of the expectation value of the wave packet spin $\vec{s}(E, t)$, fitting the numerics either to $\exp(-t/\tau_{s,\alpha})$ or to $\exp(-t/\tau_{s,\alpha})\cos(\omega_z t)$. The density of charge scatterers is characterized as a percentage of the number of carbon atoms, $n = N/N_C \times 100\%$.

Figure 8.14(a) and (b) show $\vec{s}$ for disorder profiles corresponding to intervalley scattering in the strong limit (defined by the parameters $n = 0.1\%$ and $\epsilon = 2.8\,\text{eV}$) and the weak limit (defined as $n = 1\%$ and $\epsilon = 0.5\,\text{eV}$). The τ_p obtained for these disorder parameters have values similar to the experimental estimates (Wang Ki, et al. 2015, 2016; Yang et al. 2016). For strong intervalley scattering, the in-plane component of $\vec{s}$ decays much more quickly than the out-of-plane component, and spin precession is suppressed (Fig. 8.14(a) inset). In contrast, in the case with negligible intervalley scattering the in-plane spin component precesses about the effective spin–orbit field with frequency $\omega_z = 2\lambda_{\rm VZ}/\hbar$, and relaxes more slowly than the out-of-plane component (Fig. 8.14(b) inset). This behavior is consistent with Eqs. (8.44) and (8.45). A giant anisotropy is reported in the inset of Fig. 8.14(a), with $\tau_{s,\perp} = 20$–200 ps

and $\tau_{s,\parallel} \approx 1$ ps. Actually, the values of τ_s estimated from Eq. (8.44) well agree with the numerical simulations and the spin dynamics model. Note that the fit of $\tau_{s,\parallel}$ assumes a typical intervalley scattering time of $\tau_{iv} = 5\tau_p$ (Zhang et al. 2009). Additionally, by increasing the disorder density to $n = 1\%$, τ_s is rescaled by a factor of 10, confirming the inverse relationship between τ_s and $\tau_{p,\mathrm{iv}}$ (not shown here; see Cummings et al. (2017)). The numerical spin lifetimes in the absence of intervalley scattering, i.e., when $\tau_{s,\parallel} \gg \tau_{s,\perp}$ yield, as expected, an anisotropy of 1/2 (inset of Fig. 8.14(b)).

To conclude, the combined presence of the imprinted Rashba and valley-Zeeman SOC lead to a peculiar spin texture of graphene electronic states, which in situation of strong intervalley scattering largely enhance spin randomization, but only of the in-plane spin component. In the DP regime, the relaxation rates of the out-of-plane and in-plane spins can be actually written generally as

$$\begin{aligned}\left(\tau_s^{\perp}\right)^{-1} &= \left(2\frac{ak\Delta_{\mathrm{PIA}} \pm \lambda_R}{\hbar}\right)^2 \tau_p, \\ \left(\tau_s^{\parallel}\right)^{-1} &= \left(\frac{2\lambda_{\mathrm{VZ}}}{\hbar}\right)^2 \tau_{\mathrm{iv}} + \frac{1}{2}\left(\tau_s^{\perp}\right)^{-1}.\end{aligned} \tag{8.46}$$

The out-of-plane spin thus follows a typical Rashba-induced relaxation process, with an electron–hole asymmetric behavior that originates from the PIA SOC. Meanwhile, because $\tau_{\mathrm{iv}} > \tau_p$ by definition and typically $\lambda_{\mathrm{VZ}} > \lambda_R$, the in-plane relaxation rate is dominated by the valley-Zeeman SOC, and converges to the typical Rashba behavior only when intervalley scattering or valley-Zeeman SOC are absent. Experimentally, the effect of PIA has not been observed, which could be an indication that in real systems this effect is somehow suppressed. For that reason, it can be neglected in the final expression for the spin lifetime anisotropy considering only Rashba and valley-Zeeman SOC (Garcia et al. 2018)

$$\zeta \equiv \frac{\tau_s^{\perp}}{\tau_s^{\parallel}} \approx \left(\frac{\lambda_{\mathrm{VZ}}}{\lambda_R}\right)^2 \left(\frac{\tau_{\mathrm{iv}}}{\tau_p}\right) + \frac{1}{2}. \tag{8.47}$$

Those results have been confirmed by a microscopic theory of spin dynamics in weakly disordered graphene with uniform proximity-induced SOC in which a time-dependent perturbative treatment is employed to derive the spin Bloch equations (Offidani & Ferreira 2018), and also verified experimentally (Benitez et al. 2018; Ghiasi et al. 2017), therefore standing as a smoking gun of large SOC proximity effects induced in graphene by strong SOC materials. Finally, the theoretical possibility to tune, by gate voltage, such spin current anisotropy has been predicted in graphene/topological insulators heterostructures (Song et al. 2018), and then realized in bilayer and monolayer graphene/TMDs structures (Xu et al. 2018; Leutenantsmeyer et al. 2018).

8.6 Spin Hall Effect

8.6.1 Introductory Picture and Basics

Let us first present an instructive spin phenomenon, which takes place when an electron beam crosses a spatial region where *an inhomogeneous magnetic field* is applied. This effect (Zeeman effect) was historically measured by Stern-Gerlach, and through this they confirmed the existence of the electron spin intitially proposed by W. Pauli (Gerlach & Stern 1922). This phenomenon, which leads to a magnetic field–driven spin separation of propagating electrons (driven by an electric field), can be derived easily assuming that incoming electronic wave packets will encounter a spatial region determined by an inhomogeneous magnetic field; for instance $B_z = B_0 + \beta \cdot z$. Then the wave packet spin component (with generic form $|\Psi_0\rangle = a|\Uparrow_z\rangle + b|\Downarrow_z\rangle$) will become sensitive to the magnetic field once crossing the corresponding region. This interaction between spin and magnetic field is described by a new Hamiltonian term as $\mathcal{H} = -\mu_0 \vec{S} \cdot \vec{B}$ or $\mathcal{H} = -\mu_0 B_z \sigma_z$. This leads to

$$\mathcal{H} = \begin{bmatrix} -\mu_0(B_0 + \beta \cdot z) & 0 \\ 0 & +\mu_0(B_0 + \beta \cdot z) \end{bmatrix} = \begin{bmatrix} C(z) & 0 \\ 0 & -C(z)) \end{bmatrix}$$

which can be easily diagonalized with solutions $\mathcal{H}|\Uparrow_z\rangle = C(z)|\Uparrow_z\rangle$ and $\mathcal{H}|\Downarrow_z\rangle = -C(z)|\Downarrow_z\rangle$, and thus the time evolution of the wave packet can be written as $|\Psi(t)\rangle = e^{-i\mathcal{H}t/\hbar}|\Psi_0\rangle$ or $|\Psi(t)\rangle = ae^{-iC(z)t/\hbar}|\Uparrow_z\rangle + be^{+iC(z)t/\hbar}|\Downarrow_z\rangle$. Accordingly, the probability to measure up-spin becomes larger, for $z > 0$ which is modulated by $e^{+i\mu_0 B_0 t/\hbar} e^{+i\mu_0 \beta z t/\hbar}|\Uparrow_z\rangle$, while the probability to measure down-spin becomes larger for $z < 0$ which is modulated by $e^{-i\mu_0 B_0 t/\hbar} e^{-i\mu_0 \beta z t/\hbar}|\Downarrow_z\rangle$, defining $k_z^{\Uparrow} = +\mu_o \beta t/\hbar$ and $k_z^{\Downarrow} = -\mu_o \beta t/\hbar$. This shows that the magnetic field separates the incoming electrons according to their spin polarization, and if a screen is placed on the trajectory of the electron beam, the observed splitting on the screen is a direct proof of the existence and peculiarity of the spin degree of freedom.

The spin Hall effect (SHE) has a similar origin, but here the effective (inhomogeneous) magnetic field stems from SOC effects. When electrons propagate under the action of an electric field in a strong SOC material (either due to internal symmetry or SOC-dependent impurities), then a spin-dependent Lorentz force leads to the appearance of spin accumulation on the lateral surfaces (i.e., signs of the spin directions being opposite on the opposing boundaries) (Dyakonov & Perel 1971c; D'yakonov & Perel' 1971d; Hirsch 1999; Sinova et al. 2015; Zhang 2000). More precisely, SHE can be generated by two main microscopic mechanisms, the first one being an extrinsic mechanism driven by a spin-dependent Mott scattering, where carriers with opposite spin diffuse in opposite directions when colliding with material imperfections or impurities, whereas the second driving force is intrinsic to the internal SOC symmetries of materials lacking inversion symmetry (generally small bandgap semiconductors). The intrinsic SHE is often presented in analogy with the Magnus effect for which a spinning ball in air deviates from its straight path in a direction depending on the sense of rotation. In

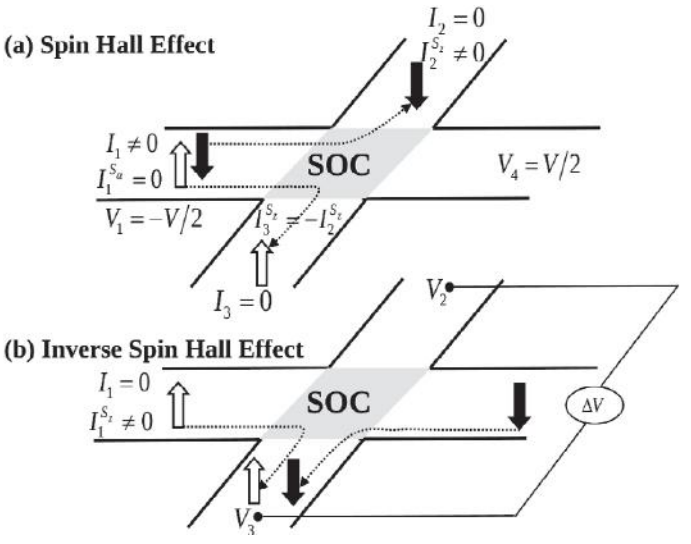

Figure 8.15 Illustration of the direct and inverse SHE, assuming example of 2D system like graphene within the *xy*-plane: (a) in the direct SHE, conventional unpolarized charge current I_1 generates transverse pure spin current $I_2^{S_z}$ or spin accumulation (when transverse leads are removed) of opposite sign at opposite lateral edges; (b) in the inverse SHE, pure spin current $I_1^{S_z}$ generates transverse charge current I_2 or voltage V_2V_3 in an open circuit. (Reproduced from Cresti et al. (2016), with kind permission of Società Italiana di Fisica. Courtesy of B. Nikolić)

SHE the analog of the air is an effective internal electric field, and the relative motion between the magnetic moment (associated to the spin) and the electric field generates a spin-dependent distortion of the electron trajectories. A clear interest and advantage of SHE is that one can then manipulate spin by electrical means without the use of ferromagnetic materials or real magnetic fields.

The first experimental confirmation of SHE was obtained by optical techniques probing spin accumulation in semiconductors (Kato et al. 2004; Wunderlich et al. 2005), but soon after, evidence for room temperature SHE was directly obtained by electrical detection, using small (of size ~ 1 μm), metallic (Hoffmann 2013; Valenzuela & Tinkham 2006), and semiconductor (Ehlert et al. 2014) samples. Another important reciprocal effect is the inverse SHE, occurring when an injected pure spin current generates transverse charge current or transverse voltage in an open circuit. The inverse SHE has become a "standard detector" of pure spin currents (Sinova et al. 2015). The two SHE effects are equivalent to each other due to Onsager reciprocity relations (Hankiewicz et al. 2005) and are pictured in Fig. 8.15 (using four-terminal device geometry).

To compare efficiency of SHE-driven conversion of charge into spin in different materials, one often uses the figure of merit known as the spin Hall angle θ_{sH} (SHA) defined by the ratio of driving charge current and resulting spin current. Assuming that an injected charge current (defined by $I_1 = I_1^{\uparrow} + I_1^{\downarrow} \neq 0$ and $I_1^{S_\alpha} = I_1^{\uparrow} - I_1^{\downarrow} = 0$) generates

a pure spin current (defined as $I_2^{S_z} = I_2^{\uparrow} - I_2^{\downarrow} \neq 0$ and $I_2 = I_2^{\uparrow} + I_2^{\downarrow} = 0$) then the SHA is given by

$$\theta_{\mathrm{sH}} = \frac{I_2^{S_z}}{I_1}. \tag{8.48}$$

This quantity is dimensionless when using the same units for spin and charge currents, which are defined in terms of the spin-resolved charge currents $I^{\uparrow}$, $I^{\downarrow}$ carrying spins pointing along the $\alpha = \{x, y, z\}$-axis. Note that separated spins are orthogonal to spin flux, as illustrated in Fig. 8.15 for two-dimensional samples. The definition in Eq. (8.48) is suitable for calculations based on the Landauer-Büttiker (LB) formula while for calculations based on the Kubo formula for bulk conductivities the SHA is written as (Cresti et al. 2016)

$$\theta_{\mathrm{sH}} = \frac{\sigma_{xy}^{z}}{\sigma_{xx}}, \tag{8.49}$$

where σ_{xy}^{z} is the SH conductivity and σ_{xx} is the longitudinal charge conductivity. From the expression above, it is clear that the evaluation of SH from a bulk formula supposes that the system is in a diffusive regime so that Kubo conductivities have finite values, and one has to remark that one cannot make SHA arbitrarily large by reducing σ_{xx} with more and more disorder and defects since what drives the formation of the spin current should also be connected to the source of dissipation, so the applicability range of Eq. (8.49) is limited.

In the experimental literature, the highest reported values for θ_{sH} are typically in the order of $\sim 10^{-4}$ for semiconductors and increase up to ~ 0.01 for metals like Pt and ~ 0.1 for metals like β-Ta and β-W (Sinova et al. 2015). The use of graphene and other two-dimensional materials to increase θ_{sH} has been the subject of intense discussion and controversies. Below we summarize the main results.

8.6.2 Enhanced SHE in Graphene?

In 2013, combining direct and inverse SHE, Balakrishnan et al. (2013, 2014) performed all electrical nonlocal measurements in chemically modified graphene devices. From the analysis of their data, they extracted a very large value $\theta_{\mathrm{sH}} \simeq 0.2$–$0.9$ suggesting a giant SHE. This experiment has attracted a lot of attention but has also raised serious concerns. Indeed these experiments have utilized heavy adatoms like Cu, Au, Ag (Balakrishnan et al. 2014) or even light adatoms like hydrogen (Balakrishnan et al. 2013) and fluorine (Avsar et al. 2015) in order to locally enhance SOC in the graphene region surrounding the adatom. This method of enhancing SOC in graphene seems difficult to control and the observation of very similar results for quite different adsorbants is puzzling.

The report of SHE for hydrogenated graphene was actually severely questioned by other groups (Kaverzin & van Wees 2015; Wang, Cai et al. 2015), and recently nonlocal measurements in the H-bar geometry also evidenced a large nonlocal resistance, but

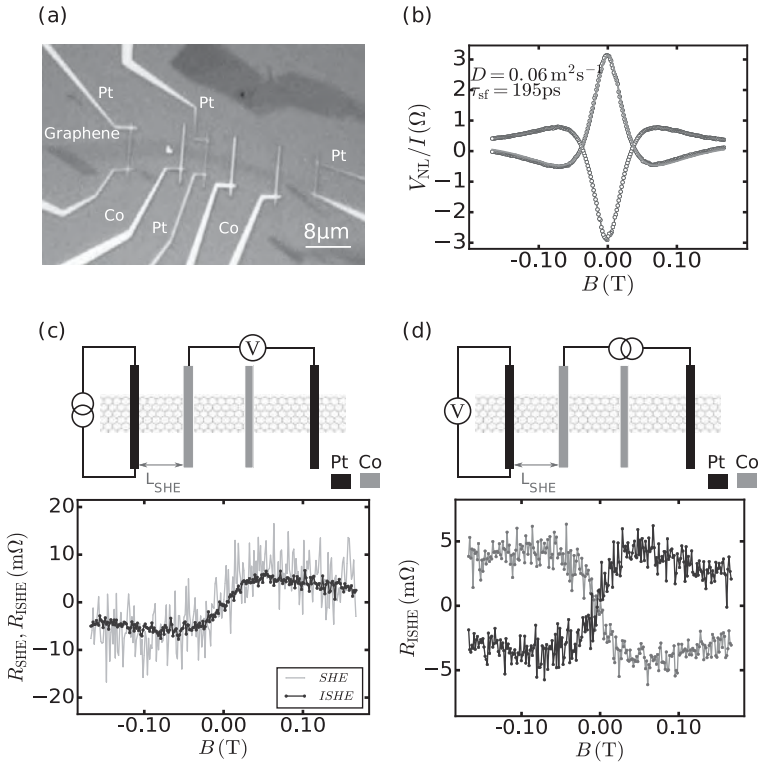

Figure 8.16 (a) Optical image of a typical graphene/Pt spin device. The two Co wires (150 and 200 nm wide) and two Pt wires (150 nm wide) located at the right side constitute the reference device for standard Hanle measurements. The Pt wires in the middle and in the extreme right are used to perform the spin Hall measurements. (b) Standard Hanle measurement obtained for the parallel and antiparallel magnetic state of the reference device at room temperature. The continuous line shows the best fitting of the data from which the spin-dependent parameters of graphene are extracted. ((c), (d)) Probe configurations and corresponding experimental results obtained at room temperature for the SHE (light gray curve in (c)) and ISHE at $V_g = 0$ in a device for which the channel length is 4 μm. The ISHE measurements in (d) show the dependence of the signal on the orientation of the magnetization *M*, of the injector, light gray for upwards magnetization and dark gray for downwards magnetization. In all the measurements, the magnetic field *B* is applied out of the sample plane. For clarity, small background signals have been extracted from the experimental results in (c) (8.5 mΩ) and (d) (13.5 mΩ). (Figure adapted from Torres et al. (2017), by courtesy of W. Savero Torres)

not sensitive to an applied in-plane magnetic field (Völkl et al. 2018). Additionally, the measured inverse SHE by electrical spin injection failed to confirm large spin Hall angle suggested by the SHE interpretation of the nonlocal measurements (Balakrishnan et al. 2013). Finally, a more rigorous theoretical derivation also supports a much smaller SHA, and therefore all results definitely indicate that the large nonlocal resistance obtained in hydrogenated graphene samples is not caused by a spin-related origin (Balakrishnan et al. 2013; Völkl et al. 2018).

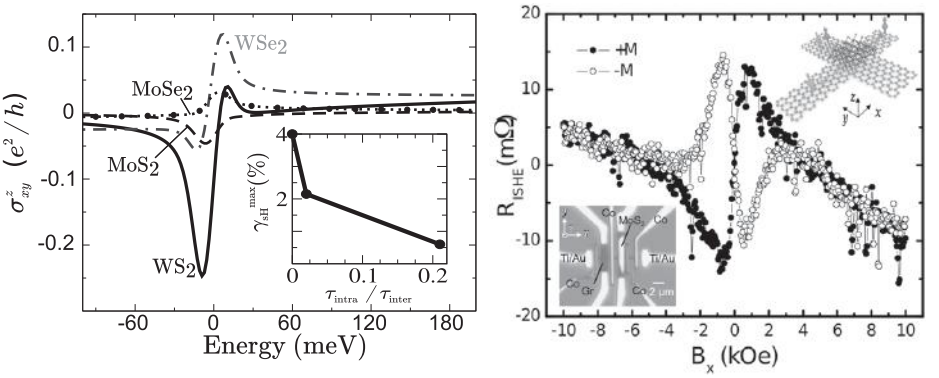

Figure 8.17 Left panel: Spin Hall conductivity for various graphene/TMD heterostructures. Inset: scaling of the θ_{sH} with intervalley scattering strength for WS_2 (Garcia et al. 2017, 2018. Courtesy of J.H. Garcia.) Right panel (main frame): Nonlocal spin-to-charge conversion curves obtained by applying a charge current between Co electrode 3 and the right Ti/Au electrode and measuring the voltage across the graphene/MoS_2 stripe. The magnetic field is applied along the in-plane hard-axis direction (B_x) for initial positive (black) and negative (white symbols) magnetization directions of the Co electrodes. (Inset top right): Sketch of proximity-induced SHE in graphene. A charge current applied along the graphene/MoS_2 stripe (y-axis) results in a spin current with out-of-plane (along z) spin polarization in the graphene channel along x. Bottom left inset: Optical microscope image of one device. It contains graphene shaped into two Hall bars connected each other. The ends of the graphene stripes are connected to Ti/Au contacts. The MoS_2 flake lies on one of the graphene Hall bars. Four Co/TiOx electrodes are placed on top of graphene. (Adapted with permission from Safeer et al. (2019). Copyright (2019) American Chemical Society. Courtesy of F. Casanova)

In monolayer graphene/Pt devices, Savero Torres et al. reported a two-order of magnitude enhancement of the spin Hall signal when compared to their fully metallic counterparts. The enhancement stems from an unusually large effective SHA of up to 0.15 in combination with efficient spin injection and the large spin resistance of graphene (see Fig. 8.16). The later leads to the observation of 100% spin absorption in Pt observed when graphene is in monolayer form. The analytical model proposed in this work shows that the effective spin relaxation time in graphene can be accurately determined using the (inverse) SHE as a means of detection (Torres et al. 2017). Additionally, the possibility for obtaining SHE induced by proximity effect in graphene/TMD has been also studied experimentally (Avsar et al. 2014) and theoretically in Garcia et al. (2017, 2018). By using real-space methodology to compute σ^z_{xy} and σ_{xx}, θ_{sH} as large as $1\% - 10\%$ was predicted for graphene/WS_2 heterostructures, and for a Fermi level nearby the Dirac point (see Fig. 8.17, left panel).

A more convincing experimental evidence of SHE in graphene/TMD has finally been reported (Safeer et al. 2019), indicating that there are many rooms at the interface between graphene and strong SOC two-dimensional materials to tailor the spin transport physics and the generation of large (pure) spin currents. Figure 8.17 (right panel) shows antisymmetric Hanle curves, which reverse by switching the initial magnetization

direction. This confirms that, at the graphene/MoS_2 region, the out-of-plane spins are converted into a charge current, which in open circuit condition gives rise to a nonlocal resistance (Safeer et al. 2019). We note that an unambiguous demonstration of tunable room-temperature spin galvanic and spin Hall effects in graphene/WS2 has been reported (Antonio Benítez et al.).

8.7 Spin Transport Formalism and Computational Methodologies

Hereafter we present the developed computational methodologies to follow the time evolution of the spin polarization using real-space approach (van Tuan 2016). To include spin in the wavefunction we use the two-component spinor to represent the spin wavefunction

$$|\Psi\rangle = \begin{pmatrix} \Psi_\uparrow \\ \Psi_\downarrow \end{pmatrix} \tag{8.50}$$

And the random-phase state used to obtain maximum computational efficiency

$$|\Psi_{\mathrm{RP}}\rangle = \frac{1}{\sqrt{N}} \sum_{i=1}^{N} \begin{pmatrix} \cos\left(\frac{\theta_i}{2}\right) \\ e^{i\Phi_i} \sin\left(\frac{\theta_i}{2}\right) \end{pmatrix} e^{2i\pi\alpha_i} |i\rangle, \tag{8.51}$$

where (Φ_i, θ_i) is the spin orientation of electron of orbital $|i\rangle$ in spin spherical coordinate system

The spin dynamics of the system are then directly related to the time-dependence of spin polarization $\boldsymbol{S}(t)$, which can be given by the expectation value of the spin Pauli operator.

$$\boldsymbol{S}(t) = \langle \boldsymbol{\sigma}(t) \rangle = \langle \psi(0) | \boldsymbol{\sigma}(t) | \psi(0) \rangle \tag{8.52}$$

where $\boldsymbol{\sigma}(t) = e^{\frac{i\hat{H}t}{\hbar}} \boldsymbol{\sigma} e^{\frac{-i\hat{H}t}{\hbar}}$ is the spin operator in Heisenberg representation. However, this expectation gives the spin polarization for the whole spectrum, which is not meaningful. Finding the expectation value at a specific energy is more important. In order to do so,

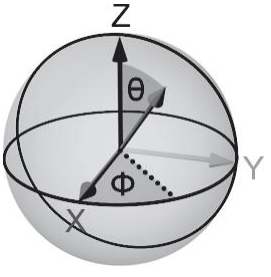

Figure 8.18 Spherical coordinate system (Bloch sphere) for describing the spin polarization in real space.

we use the formula for quantum average of any operator at a given energy

$$\boldsymbol{S}(E,t) = \frac{\mathrm{Tr}\left[\delta(E-\hat{H})\boldsymbol{\sigma}(t)\right]}{\mathrm{Tr}\left[\delta(E-\hat{H})\right]} = \frac{\mathrm{Tr}\left[\delta(E-\hat{H})\boldsymbol{\sigma}(t)+\boldsymbol{\sigma}(t)\delta(E-\hat{H})\right]}{2\mathrm{Tr}\left[\delta(E-\hat{H})\right]} \tag{8.53}$$

Approximating the trace by expectation values on random-phase states $|\psi(0)\rangle = |\varphi_{\mathrm{RP}}\rangle$ is the strategy to get a faster calculation.

$$\boldsymbol{S}(E,t) = \frac{\langle\psi(0)|\delta(E-\hat{H})\boldsymbol{\sigma}(t)+\boldsymbol{\sigma}(t)\delta(E-\hat{H})|\psi(0)\rangle}{2\langle\psi(0)|\delta(E-\hat{H})|\psi(0)\rangle} \tag{8.54}$$

$$= \frac{\langle\psi(t)|\delta(E-\hat{H})\boldsymbol{\sigma}+\boldsymbol{\sigma}\delta(E-\hat{H})|\psi(t)\rangle}{2\langle\psi(0)|\delta(E-\hat{H})|\psi(0)\rangle} \tag{8.55}$$

where the time evolution of the wave packets $|\psi(t)\rangle = e^{\frac{-i\hat{H}t}{\hbar}}|\psi(0)\rangle$ is obtained by solving the time-dependent Schrödinger equation. This is the equation we use for the calculation of spin polarization.

Let's denote the quantity in the numerator of Eq. (8.55) as

$$\mathbf{P}(E,t) = \langle\psi(t)|\boldsymbol{\sigma}\delta(E-\hat{H})|\psi(t)\rangle \tag{8.56}$$

Equation (8.55) becomes

$$\boldsymbol{S}(E,t) = \frac{\Re\mathrm{e}\,(\mathbf{P}(E,t))}{\langle\psi(0)|\delta(E-\hat{H})|\psi(0)\rangle} \tag{8.57}$$

The denominator is directly proportional to the density of states $\rho(E)$ and can be computed by the real-space method while the numerator can be calculated by including the energy resolution η

$$\begin{aligned}
\mathbf{P}(E,t) &= \left\langle\psi(t)|\boldsymbol{\sigma}\delta(E-\hat{H})|\psi(t)\right\rangle \\
&= \left\langle\psi(t)|\boldsymbol{\sigma}\frac{1}{2\pi}\left[\frac{1}{\eta-i(E-\hat{H})}+\frac{1}{\eta+i(E-\hat{H})}\right]|\psi(t)\right\rangle \\
&= \frac{1}{2\pi}\sum_j \langle\psi(t)|\boldsymbol{\sigma}|\phi_j\rangle\left\langle\phi_j|\left[\frac{1}{\eta-i(E-\hat{H})}+\frac{1}{\eta+i(E-\hat{H})}\right]|\psi(t)\right\rangle \\
&= \frac{i}{2\pi}\sum_j \boldsymbol{\mu}_j\left\langle\phi_j|\left[\frac{1}{E+i\eta-\hat{H}}-\frac{1}{E-i\eta-\hat{H}}\right]|\psi(t)\right\rangle \\
\mathbf{P}(E,t) &= \frac{i}{2\pi}\sum_j \boldsymbol{\mu}_j\left[\left\langle\phi_j|\frac{1}{z-\hat{H}}|\psi(t)\right\rangle-\left\langle\phi_j|\frac{1}{z^*-\hat{H}}|\psi(t)\right\rangle\right]
\end{aligned}$$

where $\boldsymbol{\mu}_j = \langle\psi(t)|\boldsymbol{\sigma}|\phi_j\rangle$ with any complete basic set $\{|\phi_j\rangle\}$ and $z = E+i\eta$.

By building an orthonormal basis with the Lanczos method (see Appendix B), beginning with $|\phi_1\rangle = |\psi(t)\rangle$, we have

$$\mathbf{P}(E,t) = \frac{i}{2\pi}\sum_{j=1}\boldsymbol{\mu}_j\left[\left(\frac{1}{z-H}\right)_{j,1} - \left(\frac{1}{z^*-H}\right)_{j,1}\right] \tag{8.58}$$

where H is the tridiagonal matrix of $\hat{H}$ in the Lanczos basis

$$H = \left(H_{ij}\right) = \begin{pmatrix} a_1 & b_1 & 0 & \cdots \\ b_1 & a_2 & b_2 & \\ 0 & b_2 & a_3 & \cdots \\ \vdots & & \vdots & \ddots \end{pmatrix} \tag{8.59}$$

Now to get a solution, we need to compute the first column of the inverted matrices $z - H$ and $z^* - H$, which we call κ and $\overline{\kappa}$, respectively

$$(z-H)K = 1 \quad \Rightarrow \quad \sum_n (z-H)_{mn}\kappa_n = \delta_{m1} \tag{8.60}$$

writing Eq. (8.60) explicitly

$$\begin{aligned} (z-H_{11})\kappa_1 - H_{12}\kappa_2 &= 1 \\ -H_{21}\kappa_1 + (z-H_{22})\kappa_2 - H_{23}\kappa_3 &= 0 \\ &\vdots \\ -H_{n,n-1}\kappa_{n-1} + (z-H_{nn})\kappa_n - H_{n,n+1}\kappa_{n+1} &= 0 \end{aligned}$$

From κ_1 we can get the others

$$\begin{aligned} \kappa_2 &= \frac{(z-H_{11})\kappa_1 - 1}{H_{12}} \\ \kappa_3 &= \frac{(z-H_{22})\kappa_2 - H_{21}\kappa_1}{H_{23}} \\ &\vdots \\ \kappa_n &= \frac{(z-H_{n-1,n-1})\kappa_{n-1} - H_{n-1,n-2}\kappa_{n-2}}{H_{n-1,n}} \end{aligned}$$

We can do the same for $\overline{\kappa}$ just by replacing z by z^*. Using the fact that $\overline{\kappa}_1 = \kappa_1^*$, we can show that $\overline{\kappa}_j = \kappa_j^*$. Finally, we get the formula for Eq. (8.58)

$$\begin{aligned} \mathbf{P}(E,t) &= \frac{i}{2\pi}\sum_{j=1}\boldsymbol{\mu}_j\left[\kappa_j - \overline{\kappa}_j\right] \\ \mathbf{P}(E,t) &= -\frac{1}{\pi}\sum_{j=1}\boldsymbol{\mu}_j \Im\mathrm{m}\left(\kappa_j\right) \end{aligned} \tag{8.61}$$

Substituting this formula into Eq. (8.57) leads to the final expression for spin polarization

$$\boldsymbol{S}(E,t) = -\frac{1}{\pi\,\Omega\rho(E)}\sum_{j=1}\Re\mathrm{e}\left(\boldsymbol{\mu}_j\right)\Im\mathrm{m}\left(\kappa_j\right). \tag{8.62}$$

8.8 Further Reading

- On graphene spintronics, see Han et al. (2014) and Roche et al. (2015).
- On spin Hall effects and nonlocal measurements, see Sinova et al. (2015) and Valenzuela (2009).

9 Quantum Transport beyond DC

In this chapter, we give a taste of quantum transport beyond direct current (DC) conditions, when time-dependent potentials are applied to a device. Our main focus is on Floquet theory, one of the most useful approaches for driven systems. Section 9.4 is devoted to an overview of some of the most recent advances on driven transport in graphene-related materials, while Section 9.5 presents an illustrative application to laser-illuminated graphene.

9.1 Introduction: Why AC Fields?

Though less explored, quantum transport beyond the DC conditions considered in previous sections also offers fascinating opportunities. Alternating current (AC) fields such as alternating gate voltages, alternating bias voltages, or illumination with a laser can be used to achieve *control* of the electrical response (current and noise), thereby providing a novel road for *applications*. Furthermore, there are many *novel phenomena* unique to the presence of AC fields such as quantum charge pumping (Altshuler & Glazman 1999; Büttiker and Moskalets 2006; Switkes et al. 1999; Thouless 1983), i.e., the generation of a DC current even in the absence of a bias voltage due to quantum interference,[1] coherent destruction of tunneling (Grossmann et al. 1991), or laser-induced topological insulators (Kitagawa et al. 2011; Lindner et al. 2011).

The activity in this area has grown rapidly in the arena of nanoscale systems (Kohler et al. 2005; Platero & Aguado 2004). Notwithstanding, it was not until the last few years that advances in the applications to graphene-related systems started to flourish. (See the overview in Section 9.4.)

Let us consider the two paradigmatic situations schematized in Fig. 9.1, namely a graphene device with two time-dependent gate voltages applied to different parts of the sample (a) or subjected to laser illumination (b). In both situations, the electronic excitations can be modeled through a time-dependent Hamiltonian of the general form:

$$\hat{\mathcal{H}}(t) = \hat{\mathcal{H}}_0 + \hat{\mathcal{H}}_1(t). \tag{9.1}$$

[1] For a closed system, the generation of a circulating current is called "quantum stirring" (Sela & Cohen 2008).

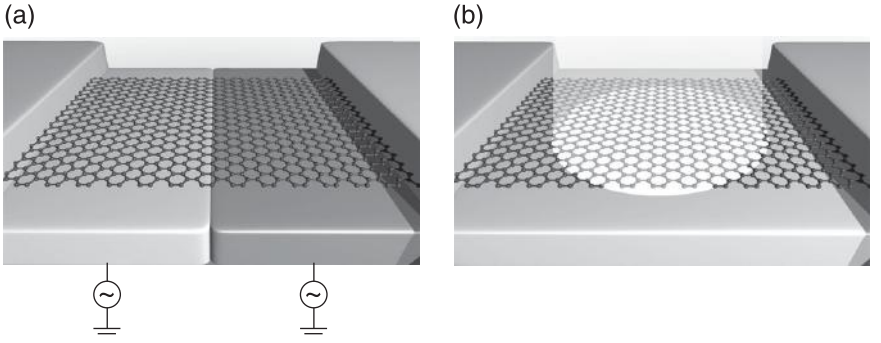

Figure 9.1 Two paradigmatic situations of transport beyond the DC limit: a graphene sample contacted between two electrodes in the presence of (a) two AC gates in the sample region (represented by shaded areas) and (b) laser illumination applied perpendicularly to the graphene plane.

In the first case, a simple model of the alternating gates would be to add a harmonic modulation of the site energies in a *tight-binding* Hamiltonian (Foa Torres and Cuniberti 2009; Orellana & Pacheco 2007), whereas in the second case laser illumination can be included through a time-dependent vector potential (Calvo et al. 2011; Oka & Aoki 2009; Syzranov et al. 2008).

This time dependence renders the usual separation of space and time variables inapplicable, thereby making the calculation of the transport response more cumbersome. For the particular case of time-periodic Hamiltonians, one can exploit the time periodicity to achieve elegant and simple solutions, as shown in Section 9.3. Furthermore, if the time variation is sufficiently slow one may use the appealing adiabatic theory mentioned in Section 9.2.

9.2 Adiabatic Approximation

To obtain meaningful approximations, two relevant timescales need to be weighted: the electronic traversal time through the sample τ_D and the period of the time-periodic potential T. If τ_D is much shorter than T, the Hamiltonian is effectively static during the electrons' trip through the device. The corrections due to the slow time dependence of the potential can be calculated through the "adiabatic" theory (Brouwer 1998; Büttiker et al. 1994; Entin-Wohlman et al. 2002; Kashcheyevs et al. 2004).

Within this framework, the current which flows in response to a cyclic variation of a set X_j of device-control parameters is expressed in terms of the scattering matrix $S(X_j)$ of the system (Brouwer 1998; Büttiker et al. 1994). Since the scattering matrix $S(X_j)$ is calculated for a stationary situation where the potentials are *frozen* at time t, the response of the system is assumed to depend on time only through the parametric time-dependence $X_j(t)$. In general, the current will contain a component due to the bias voltage

as well as a component which survives even for vanishing bias voltage (Brouwer 1998). This last component is called the *pumped current*, while the first one is a generalization of the Landauer current (Entin-Wohlman et al. 2002).

This approximation works reasonably well for alternating gates where the achievable frequencies determine an energy scale $\hbar\Omega$, which is much smaller than all the other energy scales in the problem (100 GHz correspond to a photon energy of 0.41 meV, which in turn matches $k_B T$ for a temperature of 4.75 K). Some illustrations of its use in graphene-related materials can be found in Prada et al. (2009) and Zhu and Chen (2009) and references therein. In situations where the leading-order (adiabatic) correction vanishes, going beyond the adiabatic approximation becomes crucial (Foa Torres et al. 2011; San-Jose et al. 2011; Zhou & Wu 2012).

9.3 Floquet Theory

Floquet theory (Kohler et al. 2005; Sambe 1973; Shirley 1965) is based on the application of a theorem due to Gaston Floquet to obtain the solutions of the Schrödinger equation with a time-periodic potential.

Formulated long before Bloch's theorem, Floquet's theorem (Floquet 1883) can be thought of as its analog for *time*-periodic (instead of space-periodic) Hamiltonians. Given a Hamiltonian with a time period T, there is a complete set of solutions of the form

$$\psi_\alpha(r,t) = \exp(-\mathrm{i}\varepsilon_\alpha t/\hbar)\phi_\alpha(r,t), \tag{9.2}$$

where ε_α are the quasienergies and $\phi_\alpha(r,t+T) = \phi_\alpha(r,t)$ are the Floquet states. It can be shown that Floquet states corresponding to quasienergies differing in an integer multiple of $\hbar\Omega$ are physically equivalent, i.e., linearly dependent, and therefore only states within $-\hbar\Omega/2 \leq \varepsilon_\alpha < \hbar\Omega/2$ need to be considered. This is the analog of the first Brillouin zone when using Bloch's theorem. Furthermore, one notices that the states given by Eq. (9.2) separate the slow dynamics (contained in the exponential factor) from the fast dynamics (given by Floquet states $\phi_\alpha(r,t)$).

Replacing the solutions given by Eq. (9.2) into the time-dependent Schrödinger equation (TDSE) gives

$$\left[\hat{\mathcal{H}}(r,t) - \mathrm{i}\hbar\frac{\partial}{\partial t}\right]\phi_\alpha(r,t) = \varepsilon_\alpha\phi_\alpha(r,t). \tag{9.3}$$

This equation has the same form as the usual time-independent Schrödinger equation but with two main differences:

(1) Equation (9.3) is an eigenvalue problem in Floquet space $\mathcal{R}\otimes\mathcal{T}$, where $\mathcal{R}$ is the usual Hilbert space and $\mathcal{T}$ is the space of periodic functions with period $T = 2\pi/\Omega$. The Fourier space $\mathcal{T}$ is spanned by the set of orthonormal vectors $\langle t\,|n\rangle \equiv \exp(\mathrm{i}n\Omega t)$, where n is an integer. If $|\mathrm{i}\rangle$ is a basis for $\mathcal{R}$, a suitable basis for

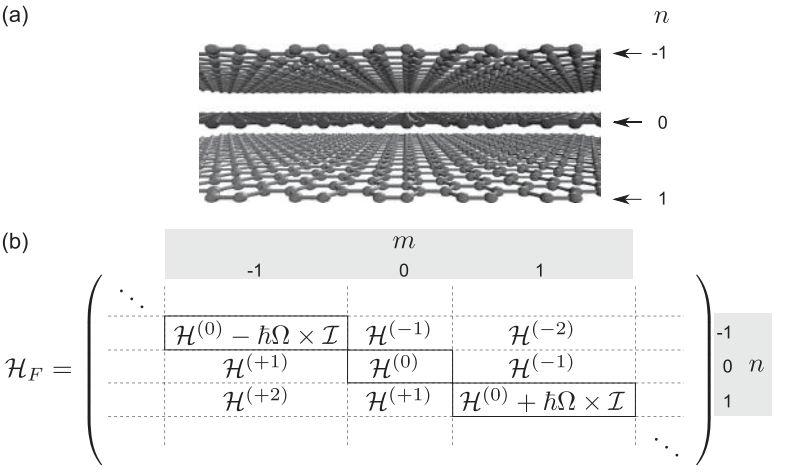

Figure 9.2 (a) By using Floquet theory, the TDSE is mapped to an equivalent time-independent problem in a higher dimensional space. This scheme shows a monochromatically driven graphene sample along with the replicas corresponding to up to ± 1 photon excitations. Though formally the number of replicas is infinite, in practice, the $(\mathcal{T})$ space is truncated until convergence of the desired response function is achieved. (b) Floquet Hamiltonian in matrix form with blocks defined according to the number of "photon" excitations n, m. $\mathcal{H}^{(n)} = \frac{1}{T}\int_0^T dt \mathcal{H} \mathrm{e}^{-\mathrm{i}n\Omega t}$ is the nth Fourier component of the Hamiltonian.

Floquet space (Sambe 1973) is $\{|i, n\rangle \equiv |i\rangle \otimes |n\rangle\}$. The index n can be assimilated to the number of "photon" excitations (or modulation quanta) in the system as noted by Shirley (1965).

(2) The role of the Hamiltonian is played by the Floquet Hamiltonian

$$\hat{\mathcal{H}}_F = \hat{\mathcal{H}} - i\hbar\frac{\partial}{\partial t}, \tag{9.4}$$

whose matrix elements in Floquet space are given by

$$\langle i, m| \hat{\mathcal{H}}_F |j, n\rangle = \frac{1}{T}\int_0^T dt \langle i| \hat{\mathcal{H}} |j\rangle \mathrm{e}^{-\mathrm{i}(n-m)\Omega t} + n\hbar\Omega\delta_{n,m}. \tag{9.5}$$

Therefore, the time-dependent problem has been mapped to a time-independent one in a higher dimensional space (as represented in Fig. 9.2(a)). The diagonal elements of the Hamiltonian take into account the number of "photons" in the system while the matrix elements connecting the different states are determined by the Fourier components of the time-dependent potential. The Floquet Hamiltonian can be cast in the block-matrix form shown schematically in Fig. 9.2(b).

9.3.1 Average Current and Density of States

To obtain the current through the device one may assume: (i) noninteracting electrons, (ii) a harmonic time-dependent field limited to a finite region of the sample, and (iii) a

sample connected to semi-infinite electrodes where thermalization takes place. Under these assumptions, a coherent calculation gives an appealing expression for the time-averaged current (Kohler et al. 2005):

$$\bar{I} = \frac{1}{T}\int_0^T dt\, I(t) = \frac{2e}{h}\sum_n \int \left[T^{(n)}_{R,L}(\varepsilon) f_L(\varepsilon) - T^{(n)}_{L,R}(\varepsilon) f_R(\varepsilon) \right] d\varepsilon, \tag{9.6}$$

where $T^{(n)}_{R,L}(\varepsilon)$ is the probability for an electron on the left (L) with energy ε to be transmitted to the right (R) reservoir while exchanging n photons. These probabilities are weighted by the usual Fermi–Dirac distribution functions $f_{R(L)}$ for each electrode.

To compute the transmission probabilities between the different inelastic channels, as needed to obtain the total current, Eq. (9.6), we may relate them to the Floquet–Green function (see also Foa Torres 2005; Martinez 2003), the Green's functions for the Floquet Hamiltonian, $G_F = (\varepsilon \mathcal{I} - \mathcal{H}_F)^{-1}$, in a way similar to the usual scattering theory (Kohler et al. 2005; Stefanucci et al. 2008):

$$T^{(n)}_{R,L}(\varepsilon) = \mathrm{Tr}\left[\Gamma_{R,n}(\varepsilon) G_{(R,n),(L,0)}(\varepsilon) \Gamma_{L,0}(\varepsilon) G^{\dagger}_{(R,n),(L,0)}(\varepsilon) \right], \tag{9.7}$$

where $G_{(R,n),(L,0)}(\varepsilon)$ is the block matrix for the Floquet–Green function connecting the left and right electrodes with the exchange of n photons. Note that the subindex F was omitted to simplify the notation. The escape rates to the electrodes now take into the account the different possible elastic and inelastic channels through the additional subindex n:

$$\Gamma_{\alpha,n}(\varepsilon) = \mathrm{i}\left[\Sigma_\alpha(\varepsilon + n\hbar\Omega) - \Sigma^{\dagger}_\alpha(\varepsilon + n\hbar\Omega) \right], \tag{9.8}$$

where $\Sigma_\alpha(\varepsilon)$ is the usual retarded self-energy correction due to electrode $\alpha = L, R$.[2] In a multiterminal configuration as typical for measuring the Hall response, special care needs to be taken as the presence of pumping currents might affect the calculation, see Foa Torres et al. (2014).

For an expression of the noise as characterized by the zeroth moment of the current–current correlation function, we refer to Kohler et al. (2005). For noninteracting systems, this formalism gives results equivalent to those of the nonequilibrium Green's function (Keldysh) formalism (Arrachea & Moskalets 2006).

In the presence of an AC field, one may compute the DC component of the spectral function. This time-averaged density of states is given by (Oka & Aoki 2009; Zhou & Wu 2011)

$$\mathrm{DOS}(\varepsilon) = -\frac{1}{\pi}\lim_{\eta\to 0^+} \mathrm{Im}\left[\sum_i \langle i, 0 |\, G_F(\varepsilon + i\eta)\, | i, 0 \rangle \right], \tag{9.9}$$

which is the trace of the Floquet–Green function restricted to the block corresponding to zero photons.

[2] A derivation of Eq. (9.7) in this multichannel case can be found in the appendix of Stefanucci et al. (2008).

It is important to note that a truncation of Floquet space is needed to compute these probabilities. Indeed, one considers only the Floquet states $|j, n\rangle$ within some range for n, i.e., $|n| \leq N_{\max}$. This range can be successively expanded until the answer converges, giving thus a variational (*non-perturbative*) method. The case of an AC bias may seem difficult to handle within this scheme, since it introduces a modulation not restricted to the sample. However, one can use a suitable gauge transformation to map an AC bias voltage into a time-dependent field acting on the borders of the sample region (Kohler et al. 2005).

9.3.2 Homogeneous Driving and the Tien–Gordon Model

If the time-dependent field is applied homogeneously to the sample, i.e.,

$$\hat{\mathcal{H}}_{\text{sample}}(r) = \hat{\mathcal{H}}^0_{\text{sample}}(r, t) + eV_{\text{ac}} \cos(\Omega t)\hat{\mathcal{I}}, \tag{9.10}$$

a separation of the space and time variables in the time-dependent Schrödinger equation is still possible (Platero & Aguado 2004):

$$\psi(r, t) = \psi^0(r, t) \exp(-\mathrm{i}e(V_{\text{ac}}/\hbar\Omega) \sin(\Omega t)), \tag{9.11}$$

where $\psi^0(r, t)$ are the solutions in the absence of the time-dependent potential. By expanding the complex exponential in Fourier series,

$$\mathrm{e}^{-\mathrm{i}(eV_{\text{ac}}/\hbar\Omega)\sin(\Omega t)} = \sum_n J_n \left(\frac{eV_{\text{ac}}}{\hbar\Omega}\right) \mathrm{e}^{\mathrm{i}n\Omega t}, \tag{9.12}$$

one already has the solutions in the Floquet form (Kohler et al. 2005). After some algebra one gets

$$\bar{I} = \frac{2e}{h} \sum_n \left| J_n \left(\frac{eV_{\text{ac}}}{\hbar\Omega}\right)\right|^2 \int T(\varepsilon)(f_L(\varepsilon) - f_R(\varepsilon))d\varepsilon. \tag{9.13}$$

Here $T = T_{R,L} = T_{L,R}$ is the transmission in the absence of driving force. This has the same form as the solution proposed by Tien and Gordon (1963) to describe photon-assisted processes. Note that if inversion symmetry is broken, $(x \to -x)$ $T_{R,L} \neq T_{L,R}$, and therefore there could be a pumped charge even with only one time-dependent parameter.[3] This is called *single-parameter* pumping (or monoparametric pumping) and requires going beyond the adiabatic approximation (which gives a vanishing response in such a case).[4]

[3] As a side note, we point out a recent work reexamining the photocurrents induced when illuminating noncentrosymmetric materials (in the absence of any bias voltage) from the viewpoint of quantum pumping (Bajpai et al. 2019).

[4] See, for example, Moskalets and Büttiker (2002), Foa Torres (2005), Kaestner et al. (2008).

9.3.3 Time-Evolution Operator

In the general case of a time-dependent Hamiltonian, the time-evolution operator $\hat{\mathcal{U}}(t, t_0)$ (defined such that $\hat{\mathcal{U}}(t, 0)\psi(t_0 = 0) = \psi(t)$) can be written as

$$\hat{\mathcal{U}}(t, 0) = \mathsf{T} \exp\left(-\frac{\mathrm{i}}{\hbar}\int_0^t dt\, \hat{\mathcal{H}}(t)\right), \tag{9.14}$$

where T is the time-ordering operator. When the Hamiltonian is time-periodic, $\hat{\mathcal{H}}(t + nT) = \hat{\mathcal{H}}(t)$ (n an integer), the time-evolution operator shares the same time periodicity. Therefore, knowing the time-evolution operator at one driving period allows building a map into the evolved states $\psi(t = nT)$ at *any* integer multiple of T, however large is n. Indeed,

$$\hat{\mathcal{U}}(nT, 0) = \mathsf{T}\prod_0^n \exp\left(-\frac{\mathrm{i}}{\hbar}\int_0^T dt\, \hat{\mathcal{H}}(t)\right) \tag{9.15}$$

$$= \prod_0^n \mathsf{T} \exp\left(-\frac{\mathrm{i}}{\hbar}\int_0^T dt\, \hat{\mathcal{H}}(t)\right) \tag{9.16}$$

$$= \left[\hat{\mathcal{U}}(T, 0)\right]^n, \tag{9.17}$$

where in the second line one uses the fact that since the Hamiltonian is T-periodic, the terms in the product are equal and therefore commute, allowing the time-ordering operator to be brought inside the product.

Furthermore, it can be shown that $\hat{\mathcal{U}}(T, 0)$ is related in a striking way to the Floquet Hamiltonian:

$$\hat{\mathcal{U}}(T, 0) = \exp\left(-\frac{\mathrm{i}}{\hbar}\hat{\mathcal{H}}_F T\right), \tag{9.18}$$

i.e., a Floquet state with quasienergy ε_α acquires a phase $\exp(-\mathrm{i}\epsilon_\alpha T/\hbar)$ after one period T. Hence, if one wants to compute the stroboscopic evolution of a system with a T-periodic Hamiltonian at times $t = nT$, it can be done just as for time-independent Hamiltonians, but the role of the stationary eigenfunction is now played by the Floquet states and instead of the Hamiltonian one needs to use the Floquet Hamiltonian.

9.4 Overview of AC Transport in Carbon-Based Devices

Interest in AC transport in carbon-based devices has been inspired by diverse sources: from developing new methods able to cope with more atoms or give the full time-dependent response (in contrast with time-averaged values) (Perfetto et al. 2010; Stefanucci et al. 2008), to proposing different setups that exploit the peculiarities of these materials for enhancing quantum pumping both in the adiabatic (Alos-Palop & Blaauboer 2011; Grichuk & Manykin 2010; Prada et al. 2009; Zhu & Chen 2009) and

nonadiabatic regimes (Foa Torres et al. 2011; San-Jose et al. 2011; Zhou & Wu 2012),[5] to finding new ways of generating backscattering in spite of Klein tunneling effects in graphene (Savelev et al. 2012)[6] or even the generation and control of laser-induced topological states in a monolayer (Gu et al. 2011; Kitagawa et al. 2011; Perez-Piskunow et al. 2014; Usaj et al. 2014) and bilayer graphene (Suárez Morell & Foa Torres 2012). Although most of the work in these issues has been theoretical, there are already several experiments available. Quantum pumping, for example, has been studied in carbon nanotubes (Leek et al. 2005) and more recently also in graphene (Conolly et al. 2013) where it promises to close the metrological triangle by allowing us to redefine the ampere. A related ratchet effect probing inversion symmetry breaking due to substrate or adatoms has also been probed recently (Drexler et al. 2013). The role of defects in AC transport through graphene-based materials is an important issue that requires further progress. In the context of adiabatic quantum pumping, the role of topological defects was examined in Ingaramo and Foa Torres (2013).

A strong momentum to this area is also expected to come from the experimental community working on laser-induced effects and nanophotonics. We refer to Bonaccorso et al. (2010) and Glazov and Ganichev (2013).

Floquet theory, in particular, has been applied to a variety of carbon-based devices including Fabry–Pérot interferometers with AC gating (Foa Torres and Cuniberti 2009; Rocha et al. 2010) and nonadiabatic quantum pumps (Foa Torres et al. 2011; San-Jose et al. 2011; Zhou & Wu 2012). Another example is developed in more detail in Section 9.5, where the captivating possibility of opening a bandgap in graphene through illumination with a laser field (Calvo et al. 2011; Oka & Aoki 2009; Syzranov et al. 2008) is discussed.

Further theoretical studies propose new ways of achieving states akin to those of a topological insulator through laser illumination, a *Floquet topological insulator* (Cayssol et al. 2013, Kitagawa et al. 2011; Lindner et al. 2011; Perez-Piskunow et al. 2014). A topological insulator (Hasan & Kane 2010) exhibits a bulk bandgap as for a usual insulator, but has surface or edge states which are gapless and protected by time-reversal symmetry. These states turn out to be insensitive to smooth changes in the potential or disorder. To date, the materials exhibiting topological properties are scarce and the ability to control their transport features is very challenging and limited (Hasan & Kane 2010). Being able to change the topological properties in the *same* material by using a laser field could open fascinating doors for novel ways of controlling electronic states of matter (Lindner et al. 2011), particularly in graphene devices (both monolayer (Kitagawa et al. 2011; Perez-Piskunow et al. 2014) and bilayer graphene (Suárez Morell & Foa Torres 2012)). The description of the topological properties of a system with a time-dependent Hamiltonian, however, remains a challenging technical task (Rudner et al. 2013). One of the proposals (Kitagawa et al. 2011) is building

[5] The issue of quantum pumping in graphene nanomechanical resonators is also discussed in Low et al. (2012).

[6] Savelev et al. (2012) offer a solution for the problem of an *arbitrary* spacetime-dependent scalar potential.

an effective time-independent Hamiltonian, chosen so that its dynamics mimics one of the time-dependent system at $t = n \times T$ (T being the period of the field). Using this stroboscopic picture, the topological properties result from applying the usual classification for time-independent systems to the effective Hamiltonian. Many more questions, however, remain open: Is it possible to produce laser-induced protected states in graphene in an experimentally relevant regime? What is the nature of those states and how robust are their conduction properties?

Perez-Piskunow et al. (2014) advance in this direction by presenting the first analytical solution and a proposal for unveiling "laser-induced chiral edge states" in graphene. The interplay between spin–orbit interaction and a laser in bulk graphene was explored in Scholz et al. (2013).

9.5 AC Transport and Laser-Induced Effects on the Electronic Properties of Graphene

Among the many promising areas sparked by graphene research, graphene photonics (and optoelectronics) is one of the brightest.[7] Since the very beginning, light has been one of the best tools for noninvasive characterization of carbon-based materials (Jorio et al. 2011). But light can also be used for achieving useful functions that take advantage of the extraordinary properties of these materials: from improved energy harvesting[8] and novel plasmonic applications[9] to graphene photodetectors (Konstantatos et al. 2012).

Recently, the captivating possibility of controlling the electronic properties of graphene through simple illumination with a laser field (Kibis 2010; Oka & Aoki 2009; Syzranov et al. 2008) has been examined through atomistic calculations (Calvo et al. 2011, 2012), calculations of the optical response (Busl et al. 2012; Zhou & Wu 2011), among other interesting issues (Abergel & Chakraborty 2009; San-Jose et al. 2012; Savelev & Alexandrov 2011). The basic idea is that laser illumination may couple states on each side of the Dirac point, inducing a bandgap at energies $\pm\hbar\Omega/2$, if the field intensity and frequency Ω are appropriately tuned.

Here we analyze this in more detail following recent studies (Calvo et al. 2011, 2012; Oka & Aoki 2009). We start by considering an electromagnetic field modeled in a semiclassical approximation: a monochromatic plane wave of frequency Ω traveling along the z axis, perpendicular to the plane defined by the graphene sheet (see Fig. 9.3(a)).

By using a Weyl's gauge, the electromagnetic field is represented through a vector potential $\mathbf{A}(t) = (A_x \cos(\Omega t)\ \mathbf{x} + A_y \cos(\Omega t + \phi)\ \mathbf{y})$ (the electric field being directly related to the time derivative of $\mathbf{A}$), where A_x, A_y, and the phase ϕ can be set to go from linear to circular polarization. The interaction with the laser field is modeled through the

[7] See, for example, Bonaccorso et al. (2010), Xia et al. (2009), Karch et al. (2011).
[8] See, for example, Gabor et al. (2011) and the more recent results in Tielrooij et al. (2013).
[9] Graphene plasmonics is a blooming field; see, for example, Koppens et al. (2011); Chen et al. (2012).

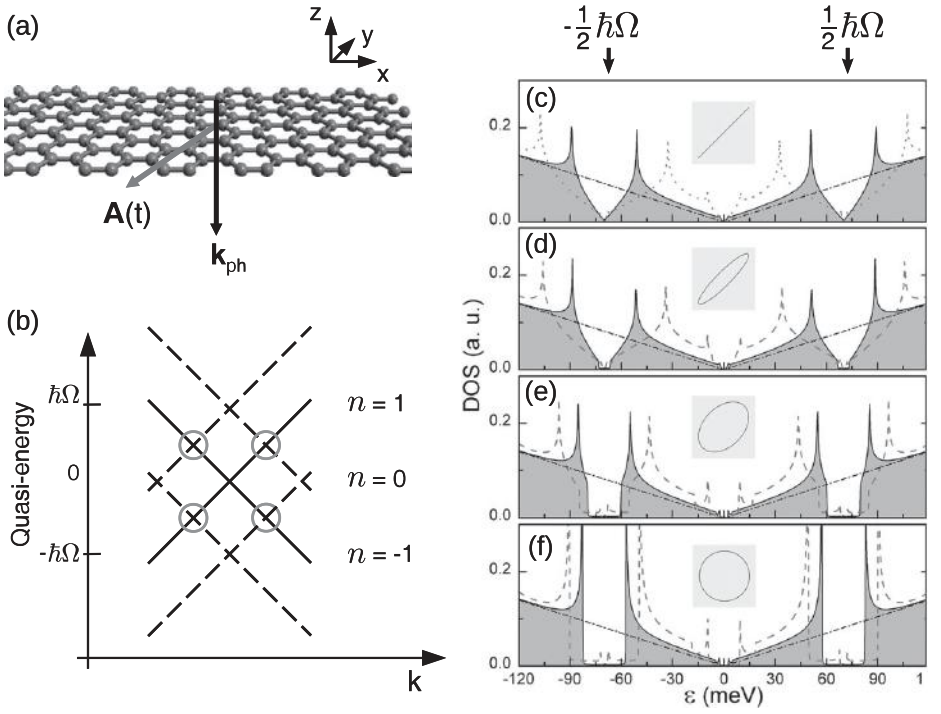

Figure 9.3 (a) A graphene sample illuminated by a laser field perpendicular to the graphene plane. (b) The quasi-energy spectra along a particular k direction. The crossing points including the first two Floquet replicas are marked with circles. (c–f) Average density of states for (c) linear, (d) $\varphi = 0.125\pi$, (e) $\varphi = 0.375\pi$, and (f) circular polarizations taking $\hbar\Omega = 140$ meV. The black solid line is for $I = 32$ (mW/μm^2), while the gray dashed line corresponds to $I = 130$ (mW/μm^2). The case in the absence of irradiation is shown with a dash-dotted gray line for comparison. (Adapted with permission from Calvo et al. (2011). Copyright 2011, American Institute of Physics.)

Hamiltonian

$$\mathcal{H}(t) = v_F \hat{\sigma} \cdot [\mathbf{p} - e\mathbf{A}(t)]\,, \tag{9.19}$$

where $v_F \simeq 10^6$ m/s denotes the Fermi velocity as usual and $\hat{\sigma} = (\hat{\sigma}_x, \hat{\sigma}_y)$, the Pauli matrices describing the pseudospin degree of freedom.

As made clear below, a correct description of our problem crucially requires a solution valid beyond the adiabatic approximation. Here we can exploit the Floquet theory introduced in Section 9.3, which is an appropriate approach for such electron–photon scattering processes. Once the Hamiltonian is defined, one can proceed by computing the matrix elements of the Floquet Hamiltonian leading to the replica picture discussed in Section 9.3. This is the basis for the calculation of the transport properties and the time-averaged DOS. We skip the details here, which are left for Problem 9.4 (more can be found in Calvo et al. 2013), and discuss some results.

Figure 9.3(c–f) shows how the time-averaged density of states (DOS) for bulk graphene changes as the polarization goes from linear to circular. For linear polarization, one observes a strong depletion for energies close to $\pm\hbar\Omega/2$. These depletions evolve into gaps, called *dynamical gaps* (Oka & Aoki 2009; Syzranov et al. 2008), for circular polarization. Furthermore, close to the Dirac, point a mini-gap opens for circular and elliptic polarizations. A closer scrutiny of these figures shows that the gaps mentioned are areas with a small negligible DOS in the bulk limit and for the parameter range explored here.

To rationalize this behavior, one can take advantage of the Floquet picture explained before. A scheme with the quasienergy spectra close to the Dirac point including $n = 0, \pm 1$ photons is shown in Fig. 9.3(b). The dispersion relation for the states $\left\{|\mathbf{k}, n\rangle_{\pm}\right\}$ for $n = 0$ is represented with a solid line, while those for $n = \pm 1$ are shown with dashed lines. The effects of the AC field are expected to be stronger at the crossing points marked with circles, leading to the opening of energy gaps at those points provided that the Hamiltonian has a nonvanishing matrix element. From geometrical considerations, one can see that the crossing of the states differing in one photon lies exactly at $\pm\hbar\Omega/2$. These degeneracies are increased by the AC field, leading to the gaps observed in Fig. 9.3(c–f). Analytical expressions for the dependencies of these gaps on the field parameters can be obtained in a direct way (Calvo et al. 2011). While the dynamical gaps depend linearly on the amplitude of the vector potential, this dependence is quadratic at the mini-gap around zero (which is produced by a virtual photon emission and reabsorption process).

But, are there any consequences on the conductance? To answer this question, one can compute the DC component of the conductance within a *tight-binding* model and following a transport calculation, such as the one introduced in Section 9.3. The results are shown in Fig. 9.4 for the case of linearly polarized light along the x direction. In this case, the calculation for an armchair ribbon can be done in an efficient way by using the mode decomposition introduced in Section 5.2.2. One can observe that the conductance also shows an important depletion around the dynamical gaps.

Here, we have chosen the laser wavelength within the mid-infrared region, i.e., $\lambda \simeq 9\,\mu\text{m}$. A careful analysis (Calvo et al. 2011) shows that in this frequency region, the effects should be maximized while keeping reasonable power levels. Furthermore, gating graphene to reach dynamical gaps located at $\sim$70 meV is also within experimental reach. Further work along these lines hints that lateral confinement in laser-illuminated graphene nanoribbons may have an important role, especially in small ribbons of a few nanometers wide (Calvo et al. 2012). Bilayer graphene also shows similar features, though trigonal warping effects may introduce important changes in the low-energy spectra (Suárez Morell & Foa Torres 2012).

The emergence of this peculiar structure of gaps in the Dirac spectrum of an illuminated sample has been experimentally observed in careful ARPES experiments (Wang et al. 2013). These experiments were carried out by illuminating the three-dimensional topological insulator Bi_2Se_3 with a mid-infrared laser. Its surface states form a Dirac cone. Thus, the theory outlined before applies and the experiment

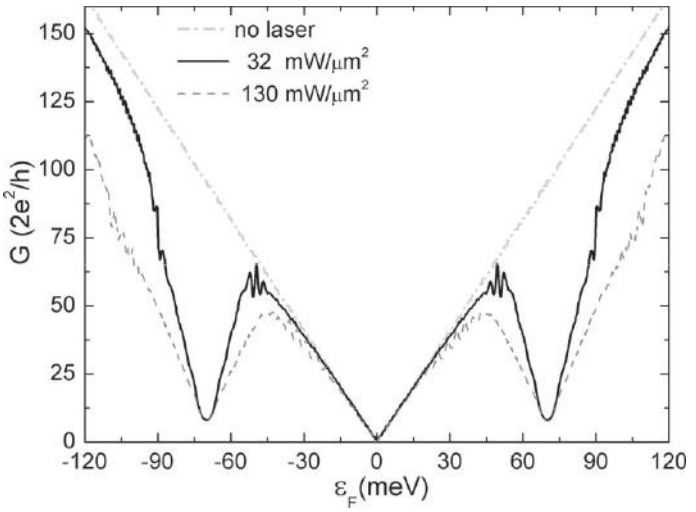

Figure 9.4 DC component of the conductance calculated for a graphene stripe of 1 μm times 1 μm in the presence of a linearly polarized laser as a function of the Fermi energy. The solid line is for a laser power of 32 mW/μm^2 while the dashed line corresponds to 130 mW/μm^2. (Reprinted with permission from Calvo et al. (2011). Copyright 2011, American Institute of Physics.)

(Wang et al. 2013) indeed shows the formation of laser-induced bandgaps under circularly polarized light.

A natural question at this point is whether these laser-induced gaps are topological (and thus bear edge states bridging the gap) or not. A study on the emergence of chiral edge states bridging the dynamical gaps is presented in Perez-Piskunow et al. (2014) and Usaj et al. (2014). Figure 9.5 shows how edge states develop at the dynamical gap in an illuminated graphene ribbon once the width is large enough. These states are smoking guns of the underlying topological nature of the states. A detailed map of the associated invariants for different laser frequencies and intensities is presented in Perez-Piskunow et al. (2015). More recent results also showed the possibility of realizing an isolator, a device where transmission occurs only in one direction and not in the opposite (this is, a nonreciprocal effect leading to one-way transport), in laser-illuminated bilayer graphene (Dal Lago et al. 2017).

Another fingerprint revealing the nature of these peculiar states is their Hall response (Dehghani et al. 2015). There has been a considerable amount of debate around this issue, even in the coherent regime. While some authors predicted a quantized response as in the integer quantum Hall effect (Kitagawa et al. 2011), others argued on the presence of an anomalous suppression of the transport response (Kundu et al. 2014). Full numerical simulations of a laser-illuminated graphene sample showed that not all the laser-induced edge states may contribute to the Hall conductance (Foa Torres et al. 2014), at least in the weak electron–photon coupling regime. Recent experiments consistent with this have been reported recently (McIver et al. 2018).

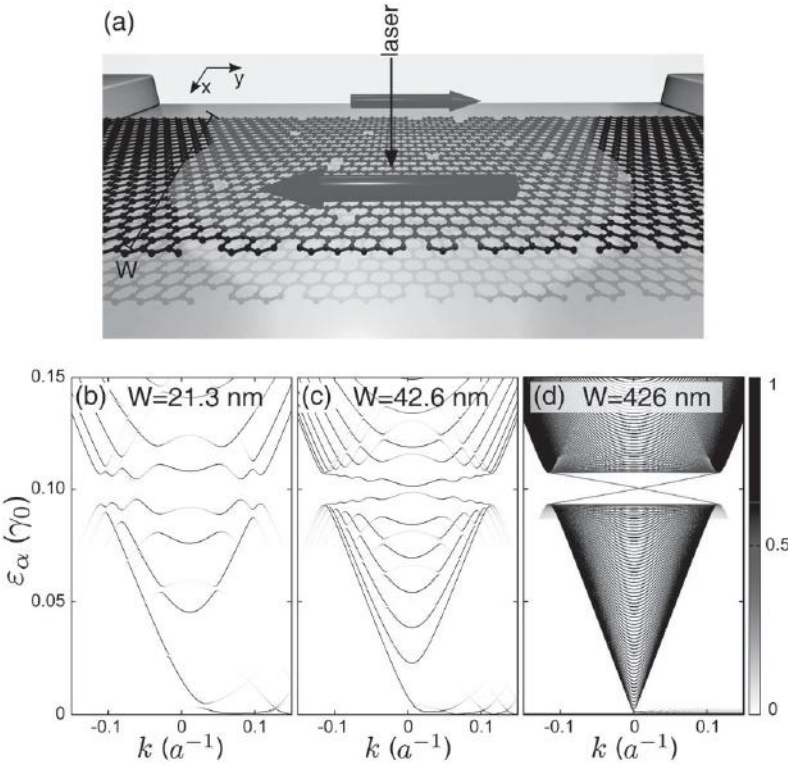

Figure 9.5 Panel (a) shows a scheme of a typical two-terminal setup where a laser of frequency Ω shines on a section of an eventually disordered graphene ribbon. The circular polarization is shown to induce chiral edge states akin those in the integer quantum Hall regime. Panels (b)–(d) show the evolution of the quasienergy dispersion as the system width W is increased ((b) $W = 21.3\,\text{nm}$, (c) $W = 42.6\,\text{nm}$, and (d) $W = 426\,\text{nm}$). In these numerical results, $\hbar\Omega = 0.2\gamma_0$ and $N_{\max} = 2$. The color scale indicates the weight contributing to the average density of states. (Reprinted with permission from Perez-Piskunow et al. (2014). Copyright 2014, American Physical Society.)

We close this section by pointing out that this physics may have an impact on other areas such as condensates (Crespi et al. 2013) and photonic crystals, where experiments are already available (Rechtsman et al. 2013). We expect that future experimental work in this area may help to unveil this interesting physics.

9.6 Further Reading and Problems

- For a review on AC transport in nanostructures, see Kohler et al. (2005).
- Readers interested in Floquet theory may also enjoy the foundational papers (Sambe 1973; Shirley 1965).
- For a very nice introduction to quantum pumping, we suggest Büttiker and Moskalets (2006) and references therein.

Problems

9.1 *Quantum pumping: generating a current at zero DC-bias.* In this exercise, we try to shed light on the mechanism behind quantum charge pumping. To this end, we follow Büttiker and Moskalets (2006) and consider a one-dimensional system consisting of two regions with alternating potentials, $V_1 = V_0 \cos(\Omega t)$ and $V_2 = V_0 \cos(\Omega t + \phi)$, separated by a distance D.

(a) Analyze the transmitted amplitudes (specially the inelastic ones) and show that the phase difference ϕ may induce a directional asymmetry in the transmission probability, so that $T_{\leftarrow} \neq T_{\rightarrow}$. ($V_0$ can be considered to be small to simplify the analysis. Then only channels with plus or minus one photon need be included.)

(b) Interpret the asymmetry found before in terms of an interference effect in Floquet space.

(c) Obtain the dependence of $T_{\leftarrow} - T_{\rightarrow}$ on the phase difference ϕ.

9.2 *Fast or slow?* Search the literature for the typical and the largest frequencies that can be achieved using conventional electronics (e.g. ac gate or ac voltage). Compute the photon energy and obtain the associated temperature. Contrast your results with those corresponding to optical frequencies and ellaborate a conclusion.

9.3 *AC gated Fabry–Pérot interferometers and the quantum wagon-wheel effect.* Reconsider the simple model for a Fabry–Pérot resonator made of an infinite CNT of Problem 5.7. This time, we follow Foa Torres and Cuniberti (2009) and Rocha et al. (2010), and add a homogeneous alternating potential to the central part of the system, which is modeled by adding an onsite term $eV_{\mathrm{AC}} \cos(\Omega t)$. V_{AC} and Ω are the oscillation amplitude and frequency, respectively.

(a) Compute the changes in the conductance (dI/dV_{bias}) as a function of a bias voltage V_{bias} (which can modeled through a symmetric shift of the leads' onsite energies by $\pm V_{\mathrm{bias}}$) and a stationary gate voltage V_{gate} applied to the central part of the system. Check the contour plots of the conductance as a function of these two variables for different values of the driving frequencies. Show that the conductance recovers the pattern found for the stationary case ($V_{\mathrm{AC}} = 0$) when $\hbar\Omega$ is commensurate with the mean level spacing in the central region Δ (*wagon-wheel effect*). Compare this with the results obtained for other values of the frequency.

(b) Compute the zero-frequency noise (see Kohler et al. (2005) for explicit formulas) as a function of the driving parameters V_{AC} and $\hbar\Omega$. Show that this time the stationary values are recovered when $\hbar\Omega$ is commensurate with *twice* the mean level spacing (named *quantum* wagon-wheel effect because it relies on the phase shift of the carriers (Foa Torres & Cuniberti 2009)). Interpret your results.

9.4 *Laser-illuminated graphene.* Consider the case of laser-illuminated graphene as presented in Section 9.5.

(a) Starting from the Hamiltonian given by Eq. 9.19, write its Fourier components and give an expression for the matrix elements of the Floquet Hamiltonian following Eq. (9.5).

(b) Obtain analytical expressions for the gaps within a small-intensity approximation.
(c) Design the steps needed for the evaluation of the average DOS (Eq. (9.9)).
(d) Design a numerical code for numerical evaluation of the DOS. You may help yourself by using the codes already available through our website.

** Additional exercises and solutions available at our website.

10 *Ab Initio* and Multiscale Quantum Transport in Graphene-Based Materials

This chapter illustrates the several possible computational approaches that can be used toward a more realistic modeling of disorder effects on electronic and transport properties of carbon-based nanostructures. Multiscale approaches are first presented, combining *ab initio* calculations on small supercells with *tight-binding* models developed from either a fitting of *ab initio* band structures or a matching between conductance profiles with a single defect/impurity. Chemical doping with boron and nitrogen of carbon nanotubes and graphene nanoribbons (GNRs) is discussed in detail, as well as adsorbed oxygen and hydrogen impurities for two-dimensional graphene, both being of current fundamental interest. Finally, fully *ab initio* transport calculations (within the Landauer–Büttiker conductance framework) are discussed for nanotubes and graphene nanoribbons, allowing for even more realism, albeit with limited system sizes, in description of complex forms of edge disorder, cluster functionalization, or nanotube interconnection.

10.1 Introduction

In the following sections, disordered and chemically doped carbon nanotubes and graphene nanoribbons are explored. The main scientific goal consists in illustrating how defects and impurities introduce resonant quasi-localized states at the origin of electron–hole transport asymmetry fingerprints, with the possibility of engineering *transport (or mobility) gaps*. Several multiscale approaches are described to develop various *tight-binding* models from first-principles calculations. A first technical strategy (illustrated on boron-doped nanotubes, Section 10.2.2) consists in designing a *tight-binding* model by fitting the *ab initio* band structures. Such an approach is used to describe doped metallic nanotubes, but actually ceases to be accurate for graphene nanoribbons, owing to complex screening effects introduced by edges.

A second approach consists in adjusting the *tight-binding* parameters by searching for a good match with first-principles transport calculations for a short nanotube or ribbon with a single dopant. This is illustrated in Sections 10.2.3 and 10.5.11 for nitrogen-doped nanotubes and boron (and nitrogen)-doped graphene nanoribbons. Using the reparameterized *tight-binding* models, mesoscopic transport can then be investigated in micrometer-long and disordered semiconducting nanotubes and graphene ribbons with

random distribution of chemical impurities. By studying the statistics of transmission coefficients, transport length scales such as the mean free paths (ℓ_{el}) and localization lengths (ξ) are predicted, together with crossovers between transport regimes. The scaling between ℓ_{el} and ξ is demonstrated to be in full agreement with the generalized form of the Thouless relationship, thus offering the first quantitative test for fundamental theories of mesoscopic physics (Section 10.2.3).

Finally, full *ab initio* transport calculations in both disordered graphene ribbons and defective carbon nanotubes are presented in Section 10.5, for various types of defects such as edge defects or grafted molecules and randomly distributed clusters. Although these calculations are much more computationally demanding, they prove to be essential in a situation of enhanced chemical complexity at the nanoscale, while they offer more possibilities for quantitative comparison with experimental data.

10.2 Chemically Doped Nanotubes

10.2.1 Tight-Binding Hamiltonian of the Pristine Carbon Nanotube

The electronic properties of an armchair (n, n) carbon nanotube (CNT) are first described using a *tight-binding* Hamiltonian with a single p_z orbital per site and only nearest-neighbors hopping integrals. Within this approach, the Hamiltonian only depends on the network connectivity. Such an assumption is valid and accurate enough for describing the energy bands near the charge neutrality point. Note that the numerical studies are restricted to weak disorder, meaning that the elastic mean free path $\ell_e \gg \lambda_F$ ($\lambda_F = \frac{3}{2}\sqrt{3}a_{\mathrm{cc}} \approx 3.7$ Å).

10.2.2 Boron-Doped Metallic Carbon Nanotubes

In order to investigate the transport properties of boron-doped (metallic) carbon nanotubes, the first step consists in a calculation of the electronic structure of armchair (10, 10) nanotubes containing 2500 cells using periodic boundary conditions (10^5 atoms) and the zone-folding approximation (ZFA) (Latil et al. 2004). A conventional *tight-binding* Hamiltonian can be defined as follows:

$$\hat{\mathcal{H}} = \sum_{\alpha=1}^{N} \varepsilon_\alpha |\alpha\rangle\langle\alpha| + \sum_{\langle\alpha,\beta\rangle} \left[\gamma_{\alpha\beta}|\alpha\rangle\langle\beta| + h.c.\right], \tag{10.1}$$

where the first sum is achieved over all the $p_\perp$ orbitals, while the second is limited to first neighbors of the α site. In Eq. 10.1, the matrix elements ε_α denote the onsite energies, while $\gamma_{\alpha\beta}$ are the hopping integrals.

The ZFA technique applied to boron-doped carbon nanotubes consists in deriving the local electronic properties in the vicinity of an atomic substitution. Unfortunately, the *tight-binding* methods are usually not suitable to account for charge transfer between

different atomic species. However, by adding a corrective electrostatic potential to the onsite energies, the effects of electric fields, charge transfer, or electric dipole moments can be taken into account. The corresponding corrections (added as extra terms to the onsite energies) are usually calculated self-consistently (solving a Schrödinger–Poisson equation). The onsite energies ε_α in Eq. 10.1 are labeled ε_C, ε_B for carbon and boron atoms, respectively. The γ_{CC} and γ_{BC} describe the inequivalent hopping integrals. Practically, these parameters are obtained by fitting the ZFA band structure to the *ab initio* calculations (Latil et al. 2004).

In order to capture the electronic fingerprints of carbon orbitals in the vicinity of the B impurity, the electronic structure of a supercell containing 31 carbon atoms and a single B atom is first examined using a DFT approach within the LDA approximation. The electronic density for the last (half) occupied band is found to be distributed only on the $p_\perp$ orbitals for atoms located close to the impurity, up to the third-nearest neighbors of the B impurity. This localization of the highest occupied molecular state-lowest unoccupied molecular state (HOMO-LUMO) band allows us to restrict the correction to carbon atoms only up to this level of accuracy. Additionally, such a result suggests that the hopping integrals between sites are not affected by the charge transfer. Moreover, the boron atom is supposed to be "carbon-like," i.e., $\gamma_{\mathrm{CC}} = \gamma_{\mathrm{BC}} = \gamma$. Consequently, only six parameters need to be adjusted: the single hopping integral γ, the carbon and boron onsite energies ε_C and ε_B, and the renormalized carbon onsite energies ε_3, ε_2, and ε_1 (respectively, third-, second-, and first-nearest neighbors of the boron impurity).

These parameterizations are performed using a least square energy minimization scheme between DFT-LDA and ZFA band structures. At first, the *ab initio* electronic band structure of an isolated graphene sheet is used to fit the hopping terms. As a low boron density is considered, the chemical potentials (Fermi energies) of the two subsystems are equal, resulting in $\varepsilon_C = E_{F,\,\mathrm{supercell}} = E_{F,\mathrm{CNT}}$. The band structure obtained with the optimal parameters can thus be favorably compared to the DFT-LDA band structure (not shown here) (Latil et al. 2004). The best fit for the hopping integral gives $\gamma = 2.72\,\mathrm{eV}$, while onsite energies are $\varepsilon_B = +2.77\,\mathrm{eV}$, $\varepsilon_1 = -0.16\,\mathrm{eV}$, $\varepsilon_2 = +0.21\,\mathrm{eV}$, $\varepsilon_3 = +0.39\,\mathrm{eV}$, and $\varepsilon_C = -1.56\,\mathrm{eV}$. Finally, the spectrum is shifted to fix the charge neutrality point (E_F) to 0 eV.

As illustrated in Fig. 10.1(a), the DOS of a 0.1% B-doped (10, 10) CNT exhibits the typical acceptor peak (E_1), as confirmed by *ab initio* calculations (Choi et al. 2000). Depending on the energy, three different transport regimes are obtained, as illustrated in Fig. 10.1(b). At energy E_2 above the Fermi level (far from the impurity resonance level), the diffusion coefficient scales almost linearly with time, indicating a quasiballistic motion and a weak sensitivity to the presence of boron impurities.

By contrast, at the Fermi energy, the saturation of $D(E_F, t) \to D_0 \sim \ell_e v_F$ denotes a diffusive regime. The extracted ℓ_e is found to decay linearly with dopant concentration, following Fermi's golden rule (Fig. 10.2, left). However, the mean free path is also predicted to increase linearly with the nanotube diameter (Fig. 10.2, right). This upscaling with diameter for a fixed disorder is a unique character of metallic nanotubes, as derived in Section 6.1. Interestingly, the typical values obtained numerically for ℓ_e turn

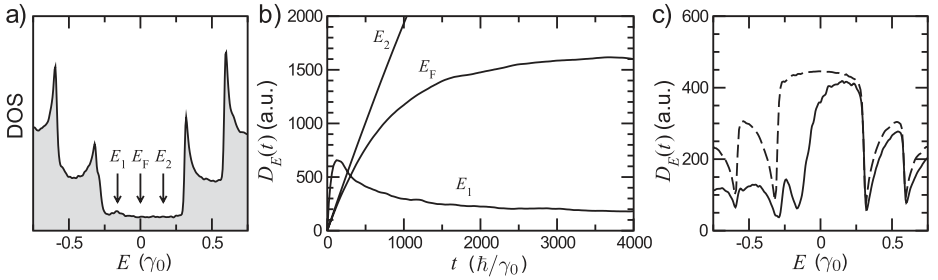

Figure 10.1 (a) Density of states of a 0.1% B-doped (10, 10) CNT. (b) $D_E(t)$ for three different energies (indicated by arrows in (a)). $D_E(t)$ for energy E_1 is 10 times magnified. (c) $D_E(t)$ at an elapsed time $t = 200\hbar/\gamma_0$, for the same B-doped CNT (solid line) and a pristine CNT (dashed line). Courtesy of S. Latil

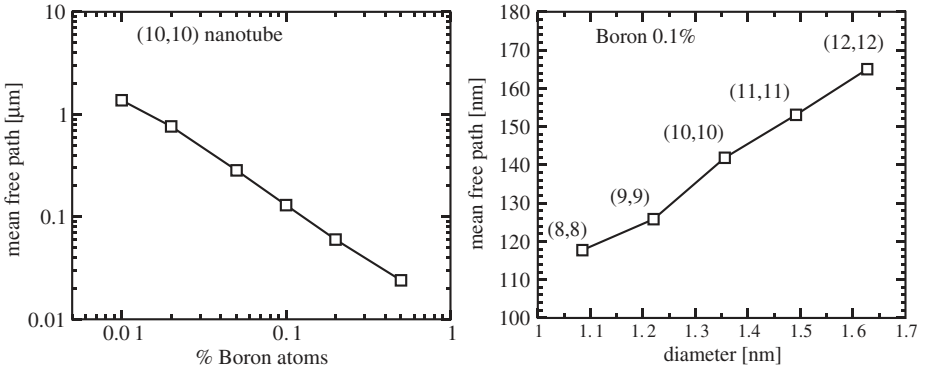

Figure 10.2 Mean free path ℓ_e estimated at the Fermi energy for B-doped (n, n) nanotubes. Left: Evolution of ℓ_e for a (10, 10) nanotube with varying boron densities. Right: Evolution of ℓ_e vs. tube diameter for a fixed concentration of B atoms (0.1%).

out to agree reasonably well with experimental data (Liu et al. 2001) ($\ell_e \sim$ 175–275 nm for boron-doped nanotubes with diameters in the range 17–27 nm, and 1.0% of boron impurities).

Finally, at the resonant energy of the quasi-bounded states (E_1), the diffusivity exhibits a $\sim 1/t$ behavior, typical signature of a localization phenomenon. In Sections 10.2.3 and 10.5.11, a more extensive analysis of quantum interferences and localization phenomena is achieved, including extraction of the localization lengths, directly from the scaling analysis of transmission coefficients (for 1D systems) or using the predicted logarithmic law to describe weak localization quantum corrections (for two-dimensional disordered graphene).

It is worth mentioning that the chemical disorder induces strong electron–hole conduction asymmetry (see Fig. 10.1(c)). This is further observed in the length dependence of conductance. Indeed, by increasing the (effective) channel length of the device denoted L_{device} from $\sim$10 nm to $\sim$1 μm (Fig. 10.3), the contribution of quantum

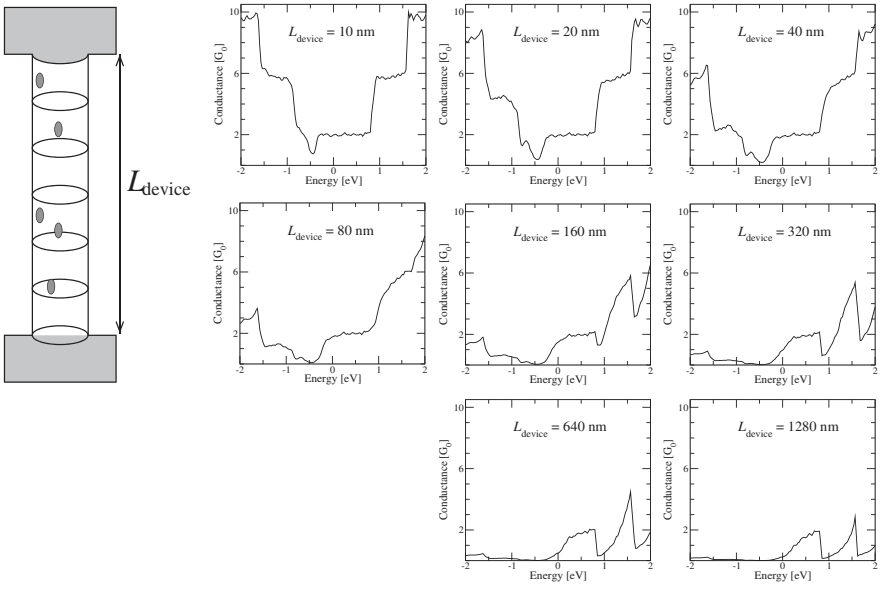

Figure 10.3 Quantum conductance for a device (with varying channel length) made of a single (10, 10) nanotube containing 0.1% of boron impurities. Courtesy of Sylvain Latil

interferences comes into play and further amplifies the electron–hole conductance asymmetry. For instance, the hole conductance has been totally suppressed, whereas electron conductance remains close to its maximum value ($2G_0$) for a nanotube length of about 1.2 μm. Such a phenomenon of resonant scattering will actually be suggested to open interesting perspectives for the design of unipolar graphene-based field-effect transistors with improved ON/OFF current ratio (see Section 10.5.11).

10.2.3 Nitrogen-Doped Metallic Carbon Nanotubes

The Single Nitrogen Impurity Case

An alternative approach to capture the effect of chemical impurities and resonant scattering is presented below. Using first-principles calculations, the energy-dependent conductance profile is first computed for a finite length armchair (n, n) CNT, where a single carbon atom (labeled δ) has been substituted by a nitrogen impurity. Next, the evolution of scattering potential around an impurity is computed self-consistently using an *ab initio* code (SIESTA (Soler et al. 2002)). Effective onsite and hopping matrix elements are then directly extracted from the *ab initio* simulations (thus including structural optimization of the system), and a simplified *tight-binding* Hamiltonian with a single orbital per site is developed using the following form:

$$\hat{\mathcal{H}}_\delta = \sum_\alpha V_{\delta,\alpha} \left|\alpha\right\rangle \left\langle\alpha\right| - \sum_{<\alpha,\beta>} \left(\gamma_{\alpha\beta} \left|\alpha\right\rangle \left\langle\beta\right| + h.c.\right). \tag{10.2}$$

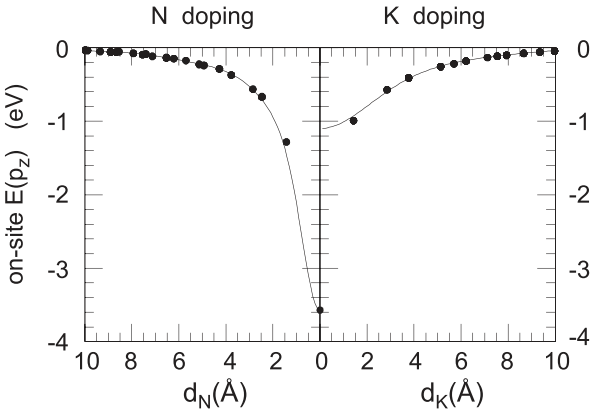

Figure 10.4 Onsite p_z orbital energies in doped graphene sheet upon (left) N doping and (right) K doping. Filled circles correspond to the two p_z orbitals in the *ab initio* calculation (solid line gives the Gaussian fit). The abscissa indicates the distance (in Angstroms) from a carbon atom to the N impurity (in the substitution case), and to the hexagon center on which the K impurity projects (in the physisorption case). (Reproduced with permission from Adessi et al. (2006). Copyright (2006) by the American Physical Society. Courtesy of Christophe Adessi)

The main effect of a single-nitrogen impurity can be captured by a proper renormalization of onsite energetics through $V_{\delta,\alpha}$, conserving the hopping integrals $\gamma_{\alpha\beta} \approx \gamma_0 = 2.9\,\text{eV}$. The evolution of the *ab initio* onsite energies for π orbitals as a function of the distance to the impurity can be fitted by a Gaussian-like function over a range of 10 Å (Adessi et al. 2006), as depicted in Fig. 10.4. In the present simulation, nitrogen atoms in substitution are compared to physisorbed potassium atoms. The potential well created by a N impurity in substitution is clearly much deeper than the one associated with the partially screened K^+ ion (Fig. 10.4). In particular, the ability of adsorbed K ions to trap electrons is significantly reduced as compared to N impurities. We note that even though screening of Coulomb potential is known to be much weaker in low dimension, the K-induced potential does not seem to be much longer in range than the one generated by the nitrogen impurity. However, some arbitrariness still remains in the choice of the *ab initio* atomic-like basis (spatial extent, completeness, etc.), which could significantly alter the impurity potential with fluctuations as large as $\sim$1 eV. One reasonable approximation consists in adjusting the onsite π potential impurity around the obtained *ab initio* value and optimizing the agreement between *tight-binding* and *ab initio* conductance profiles (see below).

Such an impurity potential breaks the reflection symmetry plane of the nanotube, generating two resonant quasibound states in the conductance profile, shown in Fig. 10.5. The first resonance (located at low energy in the π^* band) is of even parity (s-wave) and broad in energy. In contrast, the second sharper resonance (located at higher energy) has odd parity (p-wave). Both resonances suppress one conduction channel of given parity. The energy position of the s-wave resonance can be finally adjusted with respect to the

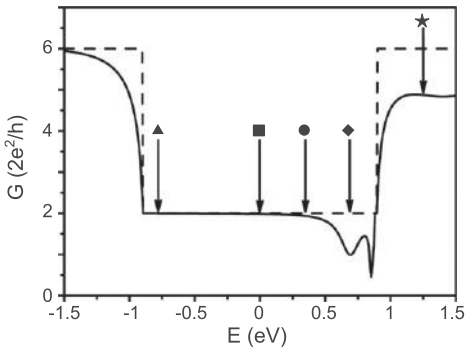

Figure 10.5 Conductance curve versus energy for both the pristine (dashed line) and doped with a single nitrogen impurity (solid line) (10, 10) armchair nanotube. (Adapted with permission from Avriller et al. (2006). Copyright (2006) by the American Physical Society)

first van Hove singularity (less than a tenth of an eV) by tuning the onsite nitrogen potential, therefore improving the agreement with the *ab initio* calculation (Choi et al. 2000).

Doping with a Random Distribution of Nitrogen Atoms

Using such an effective impurity potential $V_{\delta\alpha}$, it is now possible to explore the mesoscopic transport properties of chemically doped nanotubes with nitrogen impurities (for a fixed doping density n_{dop}). The total Hamiltonian of the disordered nanotube is written as

$$\hat{\mathcal{H}}(\Omega) = \sum_{\delta\in\Omega}\sum_{\alpha} V_{\delta,\alpha}\,|\alpha\rangle\,\langle\alpha| - \gamma_0 \sum_{<\alpha,\beta>} \big(|\alpha\rangle\,\langle\beta| + |\beta\rangle\,\langle\alpha|\big), \tag{10.3}$$

where Ω denotes an ensemble of impurity distributions, satisfying the chosen doping level. All disorder configurations have the same probability ($P(\Omega)$) of occurring and the resulting conductance average is computed from $\overline{G} = \sum_{\Omega} P(\Omega)G(\Omega)$. The mean distance between impurities $\ell_{\text{imp}} = a/2nn_{\text{dop}}$ becomes a new length scale of the problem. For a (10, 10) CNT, $\ell_{\text{imp}} = 0.12/n_{\text{dop}}$ Å, and for a doping rate $n_{\text{dop}} = 0.1\%$, the mean distance between impurities is $\ell_{\text{imp}} \approx 12$ nm. Consequently, the nanotube lengths must satisfy $L \geq l_{\text{imp}}$.

The normalized conductance $T(\Omega) = G(\Omega)/G_0$ depends on the distribution Ω of impurities, hence becoming a random variable, statistically defined by its mean value $\bar{T} = \frac{1}{\text{card}(\{\Omega\})}\sum_{\Omega} T(\Omega)$, and its root-mean-squared (RMS) fluctuation $\Delta T = \sqrt{\overline{T^2} - \bar{T}^2}$. Analysis of the dependence of the conductance probability distribution $P(T; E, L)$ on energy E and length L gives access to all transport length scales (ℓ_{el} and ξ). For instance, the elastic mean free path is extracted from the curve $\bar{T}(L)$, using the interpolation given by Eq. 10.4. The values obtained for ℓ_{el} (Fig. 10.6) are in very good agreement with estimations based on the Kubo method (Avriller et al. 2007).

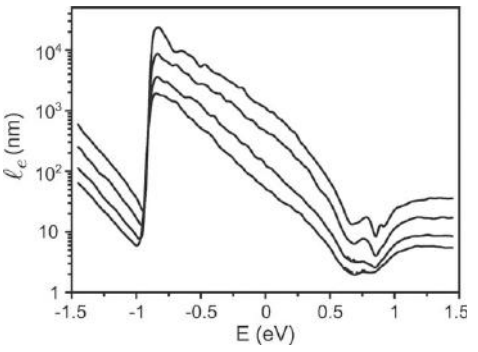

Figure 10.6 Electronic mean free paths in a (10, 10) nanotube doped with nitrogen impurities with $n_{\text{dop}} = 0.05\%, 0.1\%, 0.2\%, 0.3\%$ (from top to bottom) estimated using the Kubo method presented in Section 4.4.4. (Adapted with permission from Avriller et al. (2006). Copyright (2006) by the American Physical Society)

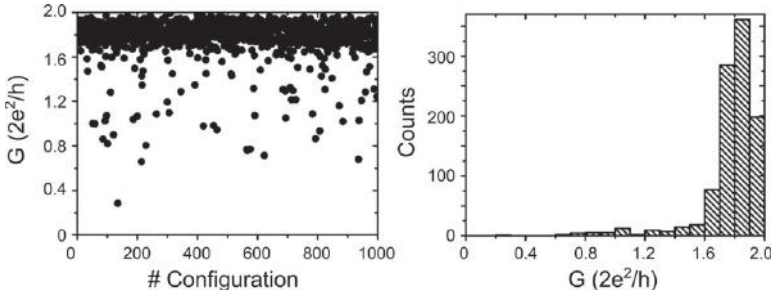

Figure 10.7 Left: Conductance values (at $E = 0.35$ eV) as a function of the disorder configuration ($L = 20\,\text{nm} \leq \ell_{\text{el}}$). Right: Corresponding conductance histogram. (Reproduced with permission from Avriller et al. (2007). Copyright (2007) World Scientific)

The whole range of transport regimes is discussed below for the (10, 10) nanotube with 0.1% nitrogen impurities (Avriller 2008).

Conductance Statistics

Conductance Profiles in the Quasi Ballistic Regime

All results on conductance statistics are presented for a selected energy ($E = 0.35$ eV, indicated by an arrow and filled circle in Fig. 10.5). The dispersion of conductance values (by varying disorder configuration) for $L = 20\,\text{nm} < \ell_{\text{el}} \sim 122$ nm is given in Fig. 10.7. $P(T)$ is found to be very narrow with a maximum close to its ballistic value ($T \approx 2$). The first two moments of the transmission distribution exhibit well-defined values $\bar{T} = 1.8$ and $\Delta T = 0.2$, pinpointing a crossover from a ballistic to a diffusive regime.

The length scaling of the conductance obtained can be captured by adding a resistance quantum per channel to the diffusive contribution, i.e., $R \approx R_0/N_\perp + R_0/N_\perp(L/\ell_{\text{el}})$, giving

$$\bar{T} = N_\perp \frac{1}{1 + \frac{L}{\ell_{\text{el}}}}, \tag{10.4}$$

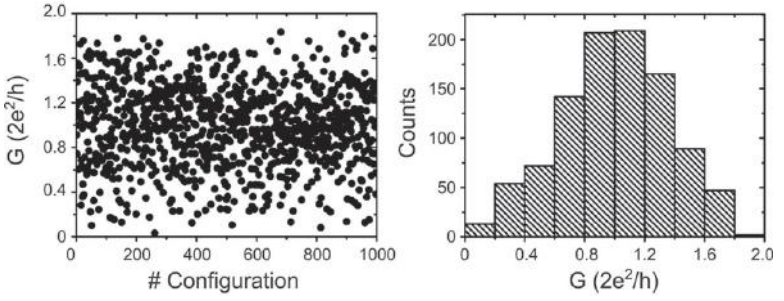

Figure 10.8 Left: Conductance values (at $E = 0.35$ eV) as a function of the disorder configuration ($L = 122\,\text{nm} \sim \ell_{\text{el}}$). Right: Corresponding conductance histogram. (Reproduced with permission from Avriller et al. (2007). Copyright (2007) World Scientific)

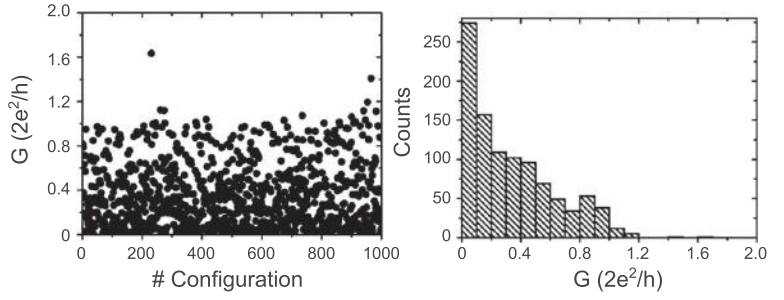

Figure 10.9 Left: Conductance values (at $E = 0.35$ eV) as a function of the disorder configuration ($L = 400\,\text{nm} > \xi$). Right: Corresponding conductance histogram. (Reproduced with permission from Avriller et al. (2007). Copyright (2007) World Scientific)

which yields to the expected asymptotic limits $\bar{T} \approx N_\perp$ for $L \ll \ell_{\text{el}}$ and $\bar{T} \approx N_\perp \ell_{\text{el}}/L$ for $L \gg \ell_{\text{el}}$, but remains approximative at the transition ($L \sim \ell_{\text{el}}$). The transition regime occurs when the tube length is similar to the mean free path. Figure 10.8 depicts the dispersion of T in the ballistic regime, that is for $L \sim \ell_{\text{el}} = 122$ nm. Here, the distribution $P(T)$ becomes Gaussian-like and fully symmetric, with first moments given by $\bar{T} = 1.0$ and $\Delta T = 0.3$.

Conductance Profiles in the Localized Regime

The localized regime is reached when the nanotube length L becomes longer than the localization length ξ, with $\exp\{\overline{\ln T}\}$ decreasing as $\overline{\ln T} = -L/\xi$ (Gómez-Navarro et al. 2005; Hjort & Stafström 2001; Kostyrko et al. 1999). For example, the corresponding dispersion values for T in such a regime ($L = 400\,\text{nm} > \xi = 170\,\text{nm}$) are reported in Fig. 10.9. The formation of the localized regime is evidenced by a strongly asymmetric distribution $P(T)$, a peak near zero transmission and a long tail toward higher values of T.

The first moments $\bar{T} \simeq \Delta T = 0.3$ do not reflect the shape of $P(T)$. In order to characterize such a regime, the most suitable statistical indicator is actually given by $\overline{\ln T}$ (Abrahams et al. 1979; Anderson et al. 1980). Figure 10.10 shows the dispersion

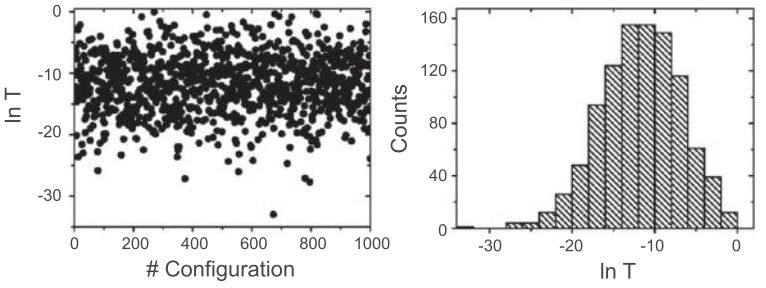

Figure 10.10 Left: Conductance dispersion as a function of the sample number for the case $L = 400\,\text{nm} > \xi$. Right: Corresponding conductance histogram. (Reproduced with permission from Avriller et al. (2007). Copyright (2007) World Scientific)

of $\ln T$ for $L = 2000\,\text{nm} \gg \xi = 170\,\text{nm}$. The distribution $P(\ln T)$ becomes more symmetric with first moments $\overline{\ln T} = -11.7$ and $\Delta \ln T = 4.8$.

Transport Regimes and Crossovers

Through scrutiny of the length dependences of $\Delta T/\bar{T}$ and $|\Delta \ln T/\overline{\ln T}|$ at $E = 0.35\,\text{eV}$, the crossover between transport regimes can be identified (Avriller et al. 2007). Indeed, $\Delta T/\bar{T}$ is found to increase as a function of L, whereas $|\Delta \ln T/\overline{\ln T}|$ peaks near $L = \ell_{\text{el}}$ and further decays with increasing length. The crossing point of the two curves occurs at $L = L_c \approx 385\,\text{nm}$ (in our case) where the relative fluctuations of $\bar{T}$ and $\overline{\ln T}$ become similar. The regime remains thus quasiballistic as long as $\Delta T/\bar{T} < 1$, whereas the localization regime forms when $\Delta T/\bar{T} > 1$ and $|\Delta \ln T/\overline{\ln T}| < 1$. At $L = L_c$, the resistance of the nanotube is of the order of the resistance quantum, which thus confirms the onset of the localization regime, following an argument given by Thouless in 1977 (Thouless 1977). Indeed, Thouless proposed viewing the normalized conductance as the ratio between two characteristic energy scales, namely $G/G_0 \approx E_{\text{th}}/\Delta$ where $E_{\text{th}} = \hbar D/L^2$ and Δ, the mean level spacing. Localization takes place when $E_{\text{th}} \approx \Delta$, that is when the conductance becomes smaller than the quantum of conductance (Thouless 1977).

Localization Length (ξ) *and Thouless Relationship*

The localization length at $E = 0.35\,\text{eV}$ is extracted from the curve $\overline{\ln T}(L)$. Taking into account points for which $L > L_c$, the curve is fitted with the scaling law $\overline{\ln T} = -L/\xi$. Random matrix theory (RMT) allows some connection between both transport length scales by studying statistical properties of eigenvalues of the $\hat{t}_{\text{LR}}\hat{t}_{\text{LR}}^{\dagger}$ matrix. In disordered wires, the statistics of the joint distribution of transmission coefficients $P(T_1, \ldots, T_{N_\perp}; L)$ have been studied in-depth (Mello et al. 1988). In the asymptotic metallic (localized) regime (when $\ell_{\text{el}} \ll L \ll \xi$ ($\xi \ll L$)), the joint probability distribution can actually be written analytically. The ratio ξ/ℓ_{el} is found to be driven by the symmetry class of the Hamiltonian and not the microscopic nature of the underlying disorder model.

The general relation between mean free path and localization lengths was derived by Beenakker for multimode wires, $\xi/\ell_{\text{el}} = \frac{1}{2}\{\beta(N_\perp - 1) + 2\}$ (Beenakker 1997). The

β coefficient depends on the symmetry class of the Hamiltonian under time-reversal transformation. When the system is invariant under time reversal (belonging to the orthogonal class), $\beta = 1$, whereas when time-reversal symmetry is broken (the system then belonging to the unitary class), $\beta = 2$. The first case is obtained in a metallic system without spin–orbit coupling or magnetic field, whereas the second arises in the presence of a magnetic field. This relationship is a generalization of the Thouless relationship for 1D-disordered systems where $\xi = 2\ell_{\mathrm{el}}$ (Thouless 1973) and for disordered wires in the limit of a high number of channels $\xi \approx N_{\perp}\ell_{\mathrm{el}}$.

In the case of (10, 10) nanotubes doped randomly with nitrogen impurities, the weak disorder approximation and geometric restriction of the wire are satisfied. It is, however, difficult to establish the extent to which the *tight-binding* model presented for doped nanotubes matches with the scattering matrix hypothesis, that is, if the universal mean values of RMT are equivalent to our model mean values. The difficulty comes from the fact that the CNT's Hamiltonian is the sum of a given initial periodic Hamiltonian combined with a random potential profile driven by the chemical impurities, whereas RMT is based on an entropy ansatz, regardless of the underlying energetics of the problem. Accordingly, the energy-dependent behavior of transport scaling properties is not within the reach of the RMT. Only in specific regions of the spectrum can the fluctuating part dominate and drive to universal behavior.

For (10, 10) nanotubes doped with 0.1% of nitrogen atoms, the scaling properties of the averaged conductance $\bar{T}$ are strongly energy-dependent. Figure 10.11 illustrates the weak energy dependence of conductance $G(L)$, for L varying from 10 to 3000 nm. At $E = -0.78\,\mathrm{eV}$, the conduction remains quasiballistic ($\bar{T} \approx 2$), whereas at the quasibound state resonance energy $E = 0.69\,\mathrm{eV}$, strong localization develops. Such a possibility of tailoring the conduction regime (and conductance value) from a ballistic motion to an Anderson insulator is unique to graphene-related systems and proves to be extremely useful for device applications in Section 10.5.11

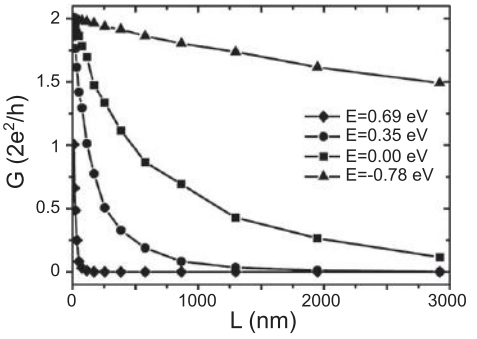

Figure 10.11 Length dependence of the Landauer conductance for a disordered (10, 10) nitrogen-doped nanotube at several energies and fixed doping $n_{\mathrm{dop}} = 0.1\%$. Averages are performed over 200 configurations of disorder. (Reproduced with permission from Avriller et al. (2007). Copyright (2007) World Scientific)

10.3 Two-Dimensional Disordered Graphene with Adatoms Defects

10.3.1 Monatomic Oxygen Defects

In this section, we focus on the impact on quantum transport of monatomic oxygen atoms adsorbed on graphene. Atomic oxygen has been observed experimentally by means of scanning tunneling measurements (Hossain et al. 2012) as illustrated in Fig. 10.12. A weak ozone treatment (O_3) of the graphene sample actually generates such epoxy defects, as discussed experimentally by Moser et al. (2010). The influence of physisorbed O_2 molecules on the electronic properties of graphene turns out to be negligible in contrast to these epoxy groups.

An important observation is that oxygen atoms find their equilibrium position by bridging two first-neighbor carbon atoms so that locally, the A/B sublattice symmetry is not fully broken (consistent with the absence of local magnetism). The bridge between the oxygen and its carbon neighbors slightly displaces locations of both carbon atoms but does not form a covalent bond. The resulting epoxy defects are found to be stable at room temperature.

In order to analyze transport properties of oxygen-functionalized graphene, *ab initio* calculations are mandatory to develop a suitable *tight-binding* Hamiltonian. Indeed, a standard π electron orthogonal tight-binding (TB) model based on first-nearest-neighbor interactions of the p_x and the p_z orbitals of oxygen with carbon can be easily derived from DFT simulations (Leconte et al. 2011). The combined contribution of the s and p_z orbitals of carbon binding with oxygen is reduced to a single orbital. Practically, an *ab initio* band structure calculation is performed on a supercell containing a single epoxy defect. The bands near the Fermi energy are then fitted using TB parameters, as detailed in Leconte et al. (2010, 2011).

The effect of epoxy defects on transport allows us to discuss a longstanding debated issue related to the validity of the semiclassical Boltzmann approach in disordered graphene. Consequently, the corresponding assumptions and the current debate are summarized first.

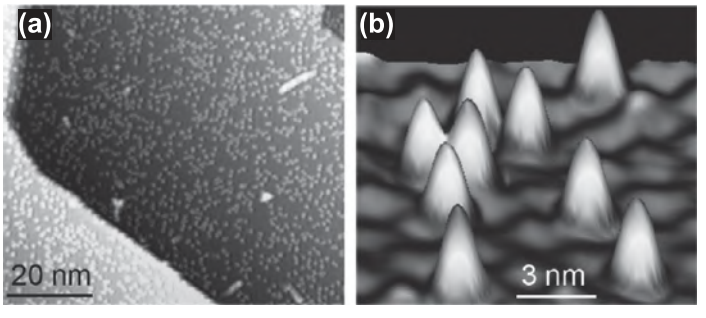

Figure 10.12 (a) STM image of epitaxial graphene after exposure to monatomic oxygen. (b) High-resolution STM picture of several chemisorbed oxygen atoms on graphene. (Adapted by permission from Macmillan Publishers Ltd: *Nature Chem*. Hossain et al. (2012), copyright (2012). Courtesy of Mark Hersam)

Does Boltzmann Conductivity Capture Dirac Point Physics?

At low energy, the presence of electron–hole puddles generates transport percolation precluding Anderson localization (Das Sarma et al. 2011). In first transport experiments, the origin of the absence of Anderson localization and the reported minimum conductivity were attributed to these puddles. (See Section 6.2.1 for a complete overview.)

In a puzzling experiment on clean graphene sandwiched between two boron-nitride layers, the suppression of electron–hole puddles was observed to result in a large increase of the Dirac point resistivity, suggesting a transition to the Anderson localization regime (Ponomarenko et al. 2011). However, the role of quantum interferences has been fiercely questioned, with an alternative scenario being argued based on Boltzmann transport (that is, absence of localization phenomena) and ascribing the divergence of the resistivity to a vanishingly small density of states (Das Sarma et al. 2011).

The use of the Boltzmann approach relies on approximating the conductivity as

$$\sigma^*_{\text{Drude}}(E) = (4e^2/h) \times k\ell_{\text{el}}(E)/2, \tag{10.5}$$

using $\rho(E) = 2|E|/(\pi \times (\hbar v_F)^2)$. From Eq. 10.5, the conventional downscaling with defect densities can be deduced as $\sigma^*_{\text{Drude}}(V_g) \simeq 1/n_i$. But the conductivity decay is stronger close to the Dirac point, suggesting a different interpretation of the data (Ponomarenko et al. 2011), as argued in Das Sarma et al. (2012). However, this interpretation has still to be studied with care since within the self-consistent Born approximation, the semiclassical conductivity should reach a limit value given by $4e^2/\pi h$. Figure 10.13 illustrates this minimal conductivity: σ^*_{Drude} (left) and the exact result σ_{Kubo} (right). The approximation performed in Eq. 10.5 actually drives the semiclassical conductivity to zero, especially in the vicinity of the Dirac point, in contradiction with the exact result, which remains larger or equal to $\frac{4e^2}{\pi h}$. Both, the Kubo conductivity and experimental data

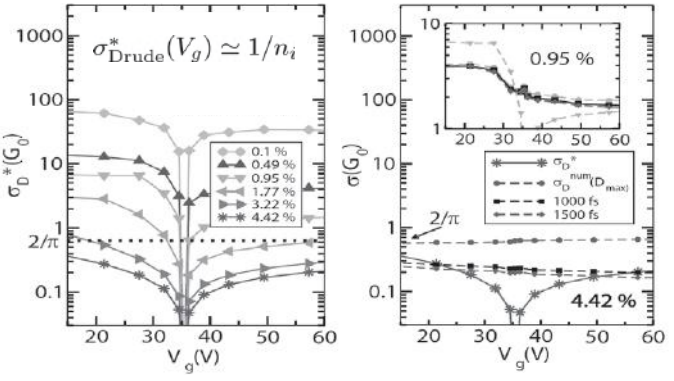

Figure 10.13 Left: Boltzmann conductivity versus gate voltage (or energy) for graphene with several densities of epoxide defects. Right: Kubo conductivity and semiclassical conductivity for two defect densities 0.95% (inset) and 4.42% (main plot). Two other curves depicting conductivity in the localization regimes at longer times are also drawn. Adapted from Leconte et al. (2010)

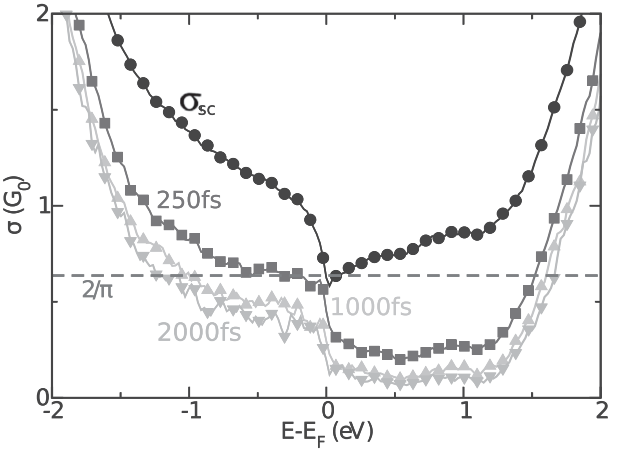

Figure 10.14 Kubo conductivity (at different times of wavepacket evolution) in a graphene sample containing 4.42% of impurities randomly distributed in the plane. The minimum value of $\sigma_{sc} = 4e^2/\pi h$ is indicated by the horizontal dashed line. (Reprinted from Roche et al. (2012). Copyright (2012), with permission from Elsevier)

(Moser et al. 2010) confirm that, especially close to the Dirac point, localization effects are significant up to about 100 K, driving the system to an Anderson insulating regime.

Localization Effects in Oxygen-Damaged Graphene

Figure 10.14 presents the semiclassical conductivity (σ_{sc}) together with the quantum Kubo conductivity computed at different timescales (beyond the diffusive regime) for 4.42% epoxy defects randomly distributed in graphene. These calculations are achieved by computing $D_x(E,t)$ and by evaluating $\sigma(E,t) = \frac{1}{4}e^2\rho(E)D(E,t)$. Oxygen defects produce quasibound states at some resonant energies, thus breaking the symmetry between electron and holes transport. Such asymmetry has already been seen in the local density of states but further develops in the energy profiles of $\ell_e(E)$, $\sigma_{sc}(E)$, and localization contributions (Leconte et al. 2011). For long enough timescales, $\sigma(E,t) \ll 4e^2/h\pi$, indicating the strong contribution of quantum interferences and localization effects.

The time evolution of the Kubo conductivity clearly shows quantum interference effects, which can easily be understood from the scaling theory of localization. In a two-dimensional disordered system (such as the one pictured in Fig. 10.15 (left)), two different scaling behaviors are predicted depending on the strength of quantum interferences, namely the weak localization regime defined by (Leconte et al. 2011; Lherbier et al. 2012),

$$\sigma(L) - \sigma\big|_{D^{\max}} = -\frac{e^2}{\hbar\pi^2}\ln\left(\frac{L}{\sqrt{2}\ell_{el}}\right), \tag{10.6}$$

and the strong localization regime driven by $\sigma(L) \sim \exp\left(-\frac{L(t)}{\xi}\right)$, where ξ is the localization length, while $L(t) = 2\sqrt{2\Delta X^2(t)}$ is the average length scale probed

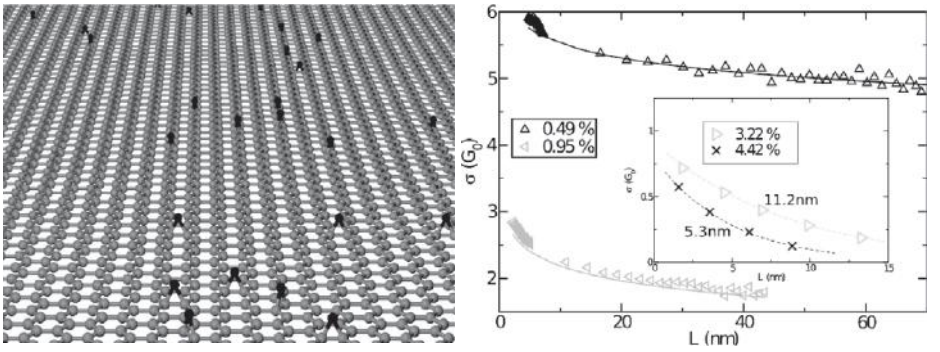

Figure 10.15 Left: Ball-and-stick model of epoxy defects adsorbed on graphene. Right: Weak localization corrections to $\sigma_{\rm sc}$ for different impurity densities at energy 0.8 eV for weak defect (main) and strong defect density (inset). Adapted from Roche et al. (2012)

by the wavepacket. The transition from the weak to the strong regime occurs at $k_F \ell_{\rm el} \sim 1$. For a defect density of 4.42%, $\ell_{\rm el} \leq 3$ Å satisfies this criterion for all energies between 0.5 and 1 eV. The value of ξ can thus be estimated, either using $\xi(E) = \ell_{\rm el} \exp(\pi \sigma_{\rm sc}/G_0)$ (Lee & Ramakrishnan 1985), or directly extracted from the exponential scaling decay of conductance with length.

Figure 10.15 (right) illustrates that in the weak disorder limit (up to $\sim 1\%$ of defects) both the numerical $\sigma(L)$ (symbols) and the analytical $\sigma_{D^{\rm max}} - e^2/\hbar\pi^2 \ln\left(\frac{L}{\sqrt{2}\ell_{\rm el}}\right)$ (solid lines) are in reasonable agreement. The fitting loses its quality for larger defect density owing to the transition to strong localization. Assuming an exponential decay of the conductivity, ξ values are estimated to be of the order of 11.2 and 5.3 nm for defect densities of 3.22% and 4.42%, respectively (at $E - E_F = 0.8$ eV), making quantitative comparison with experimental data possible (Moser et al. 2010). With use of the Landauer–Büttiker method, the effect of epoxy defects on quantum transport in graphene nanoribbons has been found to generate mobility gaps and larger electron–hole transport asymmetry (Cresti et al. 2011).

10.3.2 Atomic Hydrogen Defects

Adsorption of hydrogen atoms on graphene introduces sp^3 defects, thus breaking the AB symmetry and turning the material into a large bandgap insulator (*graphane*) in the large density limit.[1] In the present section, we study the low hydrogen density limit and contrast the transport results depending on the underlying A/B sublattice symmetry breaking. This issue is of genuine concern since the Lieb theorem predicts that any imbalance between A and B sites generates ferromagnetic ordering in the groundstate, with total magnetic moment related to $S = 1/2|n_A - n_B|$ with $n_{A,B}$ the

[1] *Graphane* was theoretically described in Sluiter and Kawazoe (2003) and Sofo et al. (2007), and experimental evidence was presented in Elias et al. (2009).

functionalized sites of type A (or B) (Lieb 1989). Such a magnetism is taken into account through a self-consistent (spin-dependent) Hubbard Hamiltonian in which the Coulomb interaction is accounted for by means of the Hubbard model in its mean-field approximation (Soriano et al. 2011) and defined as follows:

$$\mathcal{H} = \gamma_0 \sum_{<i,j>,\sigma} \left(c^{\dagger}_{i,\sigma} c_{j,\sigma} + h.c. \right) + U \sum_i \left(n_{i,\uparrow} \langle n_{i,\downarrow} \rangle + n_{i,\downarrow} \langle n_{i,\uparrow} \rangle \right), \tag{10.7}$$

where $c^{\dagger}_{i,\sigma}$ ($c_{j,\sigma}$) is the creation (annihilation) operator in the lattice site i (j) with spin σ, U is the onsite Coulomb repulsion, and $n_{i,\downarrow}$, $n_{i,\uparrow}$ are the self-consistent occupation numbers for spin-down and spin-up electrons, respectively. The ratio U/t is adequate to reproduce the spin density obtained from first-principles calculations. To compute $\langle \hat{n}_{i\uparrow} \rangle = \int dE f(E_F - E) \rho_{i\uparrow}(E)$, a self-consistent procedure is used: $\langle \hat{n}_{i\sigma} \rangle_0 \Rightarrow \mathcal{H} \Rightarrow \rho_{i\sigma} \Rightarrow \langle \hat{n}_{i\sigma} \rangle$. Once the convergence is achieved, two different sets of spin-dependent onsite energies $\varepsilon_{i\uparrow} = U \langle \hat{n}_{i\uparrow} \rangle (1 - \langle \hat{n}_{i\downarrow} \rangle)$ and $\varepsilon_{i\downarrow} = U \langle \hat{n}_{i\downarrow} \rangle (1 - \langle \hat{n}_{i\uparrow} \rangle)$ are obtained, allowing estimation of the magnetization $\mathcal{M}_i = \langle \hat{n}_{i\uparrow} \rangle - \langle \hat{n}_{i\downarrow} \rangle / 2$. Assuming weak spin–orbit coupling, two different spin-dependent Kubo conductivities can be predicted:

$$\sigma_{\uparrow,\downarrow}(E,t) = (e^2/2) \mathrm{Tr}[\delta_{\uparrow,\downarrow}(E - \hat{H})] D_{\uparrow,\downarrow}(E,t), \tag{10.8}$$

with $\mathrm{Tr}[\delta_{\uparrow,\downarrow}(E - \hat{H})/S]$ and $D_{\uparrow,\downarrow}(E,t)$, respectively, the spin-dependent density of states per surface unit at Fermi energy E and the diffusion coefficients.

Figure 10.16 (inset) shows $D_{\uparrow}(E,t)$ at three selected energies for $n_x = 0.8\%$, assuming the hydrogen defects are randomly distributed in the graphene matrix but equally

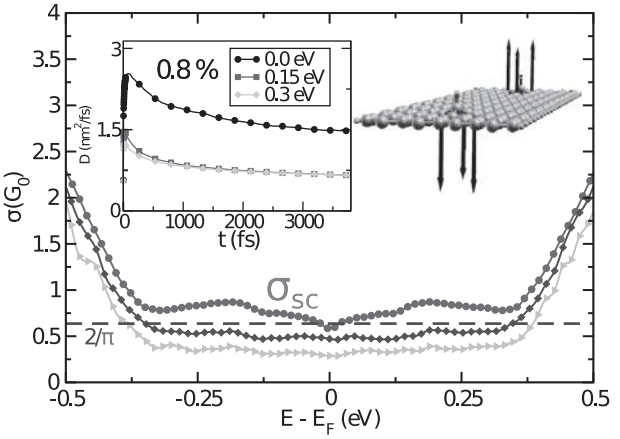

Figure 10.16 Main plot: Kubo conductivities for the nonmagnetic state with $n_x = 0.8\%$ hydrogen impurities: semiclassical value $4e^2/h\pi$ (horizontal dashed line), quantum conductivity at 250 fs (rhombus symbols), and 2000 fs (triangle symbols). Inset: Diffusion coefficients (spin-up channel) for selected energies. Antiferromagnetic spin polarization (opposite arrows) on H defects is also pictured in the ball-and-stick model. (Reprinted from Roche et al. (2012). Copyright (2012), with permission from Elsevier)

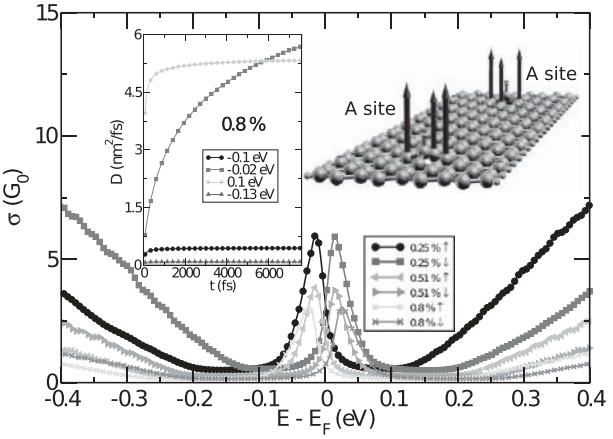

Figure 10.17 Spin-dependent Kubo conductivities (at elapsed time $t = 7600$ fs) for different hydrogen defect densities, enforcing a local ferromagnetic ordering (AA). Diffusion coefficients (spin-up channel) for selected energies (inset). Ball-and-stick model illustrates two hydrogen defects with ferromagnetic spin polarization (arrows). (Reprinted from Roche et al. (2012). Copyright (2012), with permission from Elsevier)

on each A/B sublattice. The diffusion coefficients reach a saturation regime after a few hundreds of femtoseconds, and then exhibit a logarithmic decay (fingerprint of weak localization). The corresponding semiclassical and Kubo conductivities evaluated at long times are illustrated in Fig. 10.16 (main plot). The Drude conductivity $\sigma_{\rm sc}$ is seen to remain larger than $4e^2/\pi h$, whereas quantum interferences yield $\sigma_{\uparrow,\downarrow}(E,t) \leq \sigma_{\rm sc}$, as reported for two elapsed times $t = 250$ fs and $t = 2000$ fs (Fig. 10.16 (main plot)).

If hydrogen defects are solely occupying one of the two sublattices, an unconventional transport regime develops. Figure 10.17 (inset) gives the corresponding diffusion coefficients, which are found to saturate at sufficiently long times, but without further decay, in contrast with Fig. 10.16. The corresponding saturation of the Kubo conductivity to its semiclassical value indicates a puzzling absence of localization effects (Fig. 10.17, main plot), which presently lacks theoretical explanation. Indeed, although such a choice of defect functionalization preserves one sublattice free from sp^3 contamination, the related suppression of quantum interferences remains difficult to capture using analytical arguments. One prediction is, however, that the existence of local ferromagnetic ordering could be reflected in an anomalously robust metallic state, a phenomenon which could be further discussed in relation to the concept of a "supermetallic state" introduced by Ostrovsky, Gornyi, and Mirlin for monovacancies (Cresti et al., 2013; Ostrovsky et al. 2006). Recent experiments on hydrogenated graphene have shown some modulations of pure spin currents, tentatively related to the interaction between propagating spins and hydrogen-induced local magnetic moments (McCreary et al. 2012).

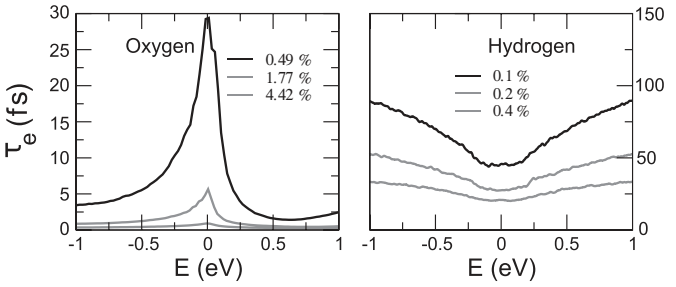

Figure 10.18 Scattering time τ for various densities of adsorbed monatomic oxygen (left) or hydrogen defects (right). (Reprinted from Roche et al. (2012). Copyright (2012), with permission from Elsevier)

10.3.3 Scattering Times

An interesting observation lies in the relation between the energy dependence of the transport times and the nature of underlying disorder and symmetry-breaking mechanisms. This is actually of great interest for determining the relation between local symmetry-breaking effects and resulting transport features at the mesoscopic scale. To illustrate this point, τ computed with the Kubo approach is shown for oxygen adatom (left) and hydrogen adatom (right) densities in Fig. 10.18. The behavior of τ for epoxide defects actually looks very similar to that of the long-range Coulomb impurities with onsite potential depth ($W = 1.5$, Fig. 6.17, main plot), whereas hydrogen defects look closer to the short-range disorder case (Fig. 6.17 for $W = 2$).

The fingerprint of $\tau(E)$ for hydrogen defects looks very similar to the Anderson disorder with $W = 2$. As mentioned above, adsorbed hydrogen atoms locally break the sp^2 symmetry and A/B degeneracy, in contrast to epoxide defects. Interestingly, the absolute values of scattering times are only weakly sensitive to the defect density, and $\tau(E = 0) \sim 25$–30 fs for $n_i \simeq 0.4\%$, but their energy dependence reflects local symmetry-breaking mechanisms. These features are fingerprints for specific defects, thus allowing possible discussion about potential sources of disorder in experiments (Monteverde et al. 2010).

10.4 Structural Point Defects Embedded in Graphene

As already described in detail in Section 2.6, structural defects (such as vacancies) in graphene can be intentionally introduced by ion or electron-beam irradiation. Using Ar^+ irradiation of carbon nanotubes for instance, an Anderson localization was induced and experimentally observed using scanning tunneling microscope (STM) techniques (Gómez-Navarro et al. 2005). Usually, it is believed that single vacancies (also called monovacancies) freely migrate and recombine to easily form divacancy defects (Lee, Wang et al. 2005). The conductivity of irradiated two-dimensional

graphene has however been found to saturate at the Dirac point above e^2/h even down to cryogenic temperatures, remaining a puzzling unexplained feature (Chen et al. 2009). Recent STM analysis of irradiated graphene has also revealed the signature of resonant states produced by divacancies (Ugeda et al. 2010). In the present section, we discuss how a strong (Anderson) localized regime can be tuned by varying the density of such types of structural defects (Banhart et al. 2011; Cockayne et al. 2011; Kotakoski et al. 2011), which can be intentionally introduced in the graphene substrate.

Here, we focus on the three structural imperfections (already observed experimentally) described in Section 2.6, namely the Stone–Wales (SW) defect and two types of divacancies (missing two carbon atoms). In contrast to monovacancies, those defects are all nonmagnetic. SW defects are commonly observed in sp^2 carbon-based materials (Lee & Stone 1985), and can be seen as generated by a 90° rotation of a carbon–carbon bond. This topological transformation produces two heptagons connected with two pentagons (Fig. 10.19(a)). The first divacancy reconstruction yields two pentagons and one octagon (named 585, Fig. 10.19(b)), while the second relates to the formation of three pentagons and three heptagons (named 555-777, Fig. 10.19(c)). *Ab initio* calculations (Lherbier et al. 2012) suggest that the formation energy of the 555-777 divacancy is smaller than that of the 585 divacancy by about 0.9 eV in graphene, which differs from nanotubes where curvature stabilizes the former reconstruction (Lee, Wang et al. 2005).

As described in Section 2.6, *tight-binding* models for pristine graphene and for defects are derived by extracting the suitable TB parameters directly from the SIESTA Hamiltonian used to calculate the *ab initio* band structures (Lherbier et al. 2012). The effects of these topological defects on the electronic properties of graphene have also been investigated in Chapter 2. TB densities of states of randomly distributed structural defects in the honeycomb lattice, as depicted in Fig. 2.32, confirm that the defect signatures, inducing energy resonances, are preserved in the DOS of random disordered system.

In order to model even more realistic systems, the case of a mixture of defects is now explored by considering graphene planes containing 50%–50% of SW/585, SW/555-777, and finally 585/555-777. The corresponding DOS estimated for a defect concentration of 1% in total (half of one type and half of the other type) are represented in Fig. 10.19(d–f)). These DOS containing a mixture of two types of defects are compared also with the DOS of graphene planes containing a single type of defect separately (defect concentration: 0.5%). The features observed in the DOS of the mixed systems are roughly the sum of the individual features of each defect type. The particular case of SW/585 is interesting in the sense that the resonance peaks of these two defects are almost symmetric with respect to the Dirac point (Fig. 10.19(d)), tending to overlap and leading to an increase of the DOS at the Dirac point. In this special situation, there is no more a clear minimum of DOS associated with the Dirac point. With the addition of other types of defects, a large increase of the DOS at the Dirac point can be foreseen (Fig. 10.19). This is actually what is observed in Haeckelite planes (Terrones et al. 2000) and in highly defective or amorphous graphene membranes (Holmström et al. 2011; Lherbier et al. 2013). However, this increase of DOS comes from resonant states

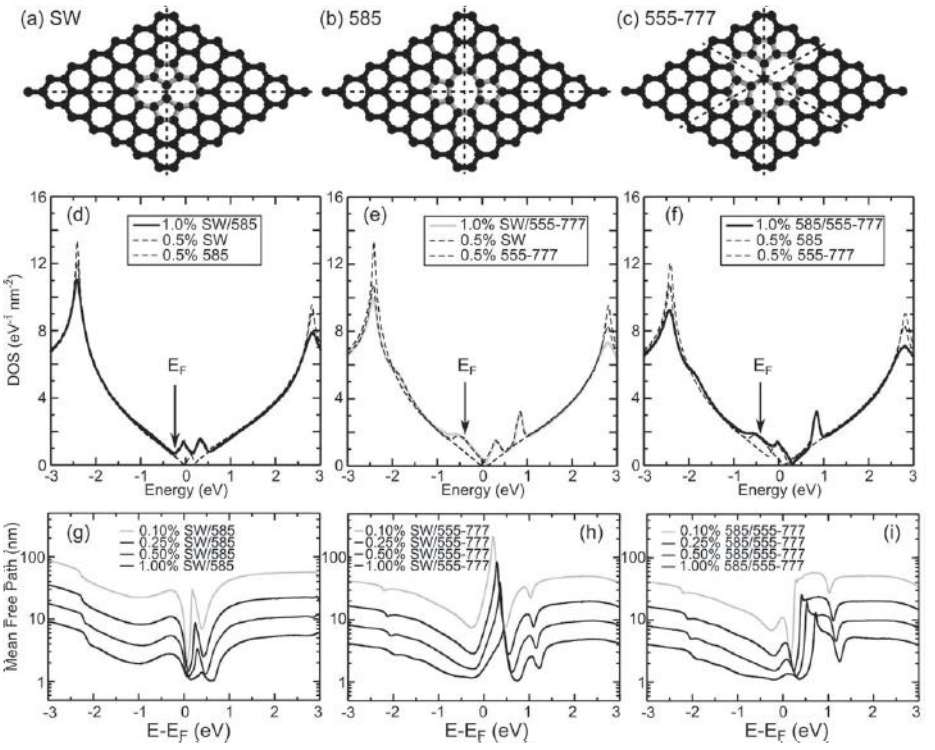

Figure 10.19 Three structural point defects: (a) Stone–Wales, (b) 585, and (c) 555-777 divacancies. The different symmetry axes are outlined in dashed lines. TB densities of states are shown for a large graphene plane containing a defect concentration of 1% (thick solid lines) of (d) SW/585, (e) SW/555-777, and (f) 585/555-777. These DOS are compared with DOS obtained with 0.5% of each defect separately (dashed lines). The position of the Fermi energy is indicated by a vertical arrow. Mean-free paths (ℓ_{el}) for concentrations ranging from 0.1% to 1.0% of (g) SW/585, (h) SW/555-777, and (i) 585/555-777 structural defects. (Adapted from Lherbier et al. (2012). Copyright (2012) by the American Physical Society. Courtesy of Aurélien Lherbier)

mainly localized around the defects, which will therefore not participate in the transport of charge carriers, but will rather degrade it (Lherbier et al. 2013).

The corresponding elastic mean free paths for graphene structures containing varying densities of SW/585 defects, SW/555-777 defects, or 585/555-777 defects (ranging from 0.1% to 1.0%) are illustrated in Fig. 10.19(g–i). The energy dependence of ℓ_{el} exhibits dips associated with the defect resonance energies (or equivalently bumps in the DOS). The mean free path changes by no more than one order of magnitude, regardless of the energy and defect nature. For a defect concentration of ∼0.1%, mean free path ranges within 60–200 nm for the longest values and 2–10 nm for the shortest. For a defect concentration $\geq$ 1%, ℓ_{el} can eventually be shorter than 10 nm for the whole spectrum.

10.5 *Ab Initio* Quantum Transport in 1D Carbon Nanostructures

10.5.1 Introduction

Coherent quantum transport in mesoscopic and low-dimensional systems can be rigorously investigated either with the Kubo–Greenwood (Kubo 1966) or the Landauer–Büttiker formalisms (Büttiker et al. 1985). The first approach, explicitly illustrated in the previous sections, derives from the fluctuation–dissipation theorem. This technique allows evaluation of the intrinsic conduction regimes within the linear response, and gives a direct access to the fundamental transport length scales, such as the elastic mean free path (ℓ_{el}) and the localization length (ξ). While ℓ_{el} results from the elastic backscattering driven by static perturbations (defects, impurities) of an otherwise clean crystalline structure, ξ denotes the scale beyond which quantum conductance decays exponentially with the system length (L), owing to the accumulation of quantum interference effects that progressively drive the electronic system from weak to strong localization.

The coherence length L_ϕ gives the scale beyond which localization effects are fully suppressed owing to decoherence mechanisms, such as electron–phonon (e–ph) or electron–electron (e–e) couplings, treated as perturbations on the otherwise noninteracting electronic gas (weak localization regime). When ℓ_{el} becomes longer than the length of the nanotube in between voltage probes, the carriers propagate ballistically, and contact effects prevail.

In such a situation, the Landauer–Büttiker formalism becomes more appropriate since it rigorously treats transmission properties for open systems and arbitrary interface geometries. Besides, its formal extensions (nonequilibrium Green's functions (NEGF) and Keldysh formalism, see Appendix C) further enable us to investigate quantum transport in situations far from the equilibrium, of relevance for high-bias regimes or situations with a dominating contribution of Coulomb interactions (Datta 1995; Di Ventra 2008).

Interestingly, to investigate coherent quantum transport in a graphene ribbon or a nanotube of length L with reflectionless contacts (ideal contact) to external reservoirs, both transport formalisms are formally fully equivalent. In the following, the Landauer–Büttiker formalism is used and the corresponding conductance $G(E) = 2e^2/h \times T(E)$ is evaluated from the transmission coefficient $T(E) = \mathrm{Tr}\{\hat{\Gamma}_L(E)\hat{G}_S^{(r)}(E)\hat{\Gamma}_R(E)\hat{G}_S^{(a)}(E)\}$, given as a function of the retarded Green function $\hat{G}^{(r)}(E) = \{E\mathbb{I} - \hat{H}_S - \hat{\Sigma}_L(E) - \hat{\Sigma}_R(E)\}^{-1}$ and $\hat{\Sigma}_R(\hat{\Sigma}_L)$ the self-energy accounting for the coupling with the right (left) electrode (Datta 1995; Di Ventra 2008; Pastawski & Medina 2001). The Landauer–Büttiker formula can be implemented with effective models such as a *tight-binding* Hamiltonian fitted on first-principles calculations (as depicted previously) or a fully *ab initio* Hamiltonian. The *ab initio* electronic transport calculations presented in the following sections are performed within the nonequilibrium Green's functions formalism and using the one-particle Hamiltonian obtained from the DFT calculations

as implemented in the TRANSIESTA (Brandbyge et al. 2002) or SMEAGOL codes (Rocha et al. 2006).

When defects in a nanostructure are introduced, the supercells containing the perturbation are connected to perfect nanotube- or ribbon-based leads. To simulate open boundary conditions, the self-energies associated with the leads are included within the self-consistent calculation of the potential. Finally, the electronic transmission functions are evaluated using the Fisher–Lee relation (Fisher & Lee 1981) (see Appendix C). Note that, for the computation of the transmission functions, a convergence study of the supercell size has to be considered in order to obtain a good screening of the perturbed Hartree potential due to the defect. It is then possible to experimentally investigate the energy dependence of the conductance by modulating the density of charge using a capacitive coupling between the nanostructure channel and an external gate.

10.5.2 Carbon Nanotubes

As a reminder, for a carbon nanotube of length L between metallic contact reservoirs, the transport regime is ballistic if the measured conductance is L-independent, and only given by the energy-dependent number of available quantum channels $N(E)$ times the conductance quantum $G_0 = 2e^2/h$, that is $G(E) = 2e^2/h \times N(E)$, including spin degeneracy. Such an ideal situation occurs only in the case of perfect (reflectionless) or ohmic contacts between the CNT and metallic voltage probes. In this regime, the expected energy-dependent conductance spectrum is easily deduced, from band structure calculations, by counting the number of channels at a given energy. For instance, metallic armchair nanotubes present two quantum channels at the Fermi energy $E_F = 0$ or the charge neutrality point, resulting in $G(E_F) = 2G_0$. At higher energies, the conductance increases as more channels become available to conduction. For illustration, the electronic bands and conductance of a (5, 5) metallic tube are displayed in Fig. 10.20 within the symmetric π–π^* *tight-binding* model.

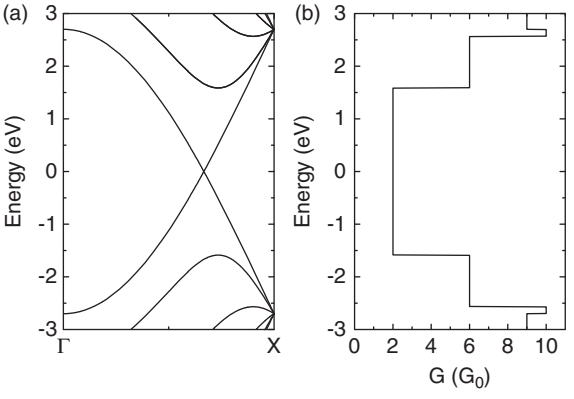

Figure 10.20 Band structure (a) and conductance (b) for (5, 5) armchair nanotube calculated within the nearest neighbor π-orbitals tight-binding model.

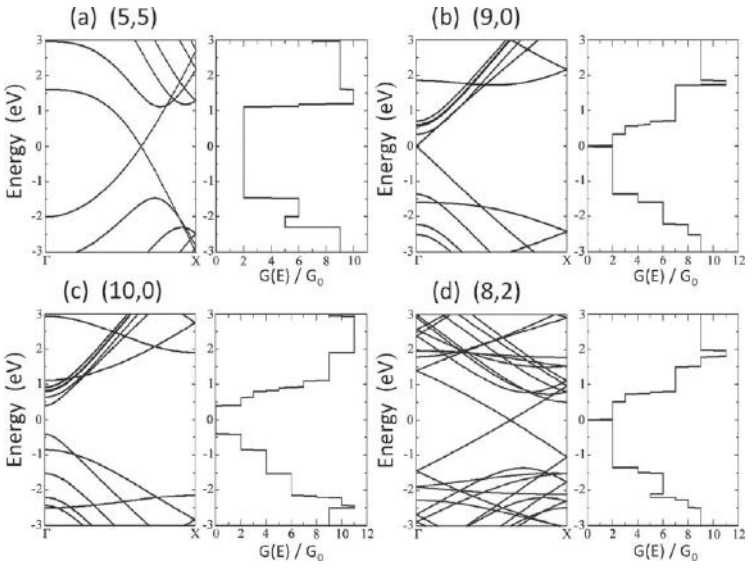

Figure 10.21 *Ab initio* band structures and quantum conductances for (a) (5, 5) armchair; (b) (9, 0); (c) (10, 0) zigzag; and (d) (8, 2) chiral nanotubes. (Reproduced from Dubois et al. (2009), with kind permission from Springer Science and Business Media.)

This quantum conductance of armchair carbon nanotubes within a nearest- neighbor π orbital *tight-binding* Hamiltonian is in good agreement (Fig. 10.21(b)) with *ab initio* calculations (Fig. 10.21(a)). Indeed, the (5, 5) armchair carbon nanotube is found to be a metallic nanowire with two linear electronic energy bands which cross at the Fermi level and contribute two conductance quanta ($=4e^2/h$) to the conductance when the tube is defectless. These two quantum channels at the charge neutrality point also lead to a plateau of conductance over a quite important interval of energies ($\sim$2.5 eV).

In Fig. 10.21(b) and (c), the *ab initio* electronic properties and the corresponding conductance are presented for (9, 0) and (10, 0) zigzag nanotubes, respectively. The first-principles calculations confirm the general features of the electronic structure obtained in the *tight-binding* approach. Indeed, as mentioned in Chapter 2, the opening of a secondary gap (pseudogap) at the Fermi energy produced by the curvature of the graphitic walls in the (9, 0) nanotube can be observed. In the (10, 0) case, predicted to exhibit a semiconducting behavior, a primary gap of 0.8 eV is obtained, leading to a zero transmission for that specific energy window. Finally, in order to be as exhaustive as possible, the *ab initio* electronic properties and the conductance of (8, 2) nanotubes are illustrated in Fig. 10.21(d). Although the single-band model would have proposed a metallic tube, the first-principles calculations predict a semiconducting system with a very small pseudogap related to the curvature of the nanotube, analogous to the (9, 0) nanotube.

Note that all these *ab initio* conductance values are the uppermost theoretical limits that would be experimentally measured. In practical situations, lower values are observed since reflectionless transmission at the interface between the voltage probes (metallic leads) and the nanotubes is fundamentally limited by interface symmetry mismatch, inducing Bragg-type backscattering. Additionally, topological and chemical disorders, as well as intershell coupling, introduce intrinsic backscattering along the tube, which also reduce its transmission capability. To account for both effects, one generally introduces $T_n(E) \leq 1$, the transmission amplitude for a given channel, at energy E, so that $G(E) = G_0 \sum_{n=1,N_\perp} T_n(E)$ (Datta 1995) (see also the discussion in Section 5.2.2), as illustrated in the following for the case of topological defects, doping, and chemical functionalization in carbon nanotubes.

10.5.3 Defective Carbon Nanotubes

The effects of impurities and local structural defects on the conductance of metallic carbon nanotubes have been calculated using *ab initio* techniques within the Landauer–Büttiker formalism (Choi et al. 2000; Dubois et al. 2009). For example, with a point (single-atom) vacancy, the conductance presents one broad dip (valence region) and two narrower dips (conduction region), as illustrated in Fig. 10.22(a). The reduction of conductance at the broad dip is $1G_0$ with approximately half reflection of both π and π^* bands. Because a single impurity breaks the mirror symmetry planes containing the tube axis, an eigenchannel is a mixture of the π and π^* bands. Consequently, an electron in an eigenchannel is either completely reflected or completely transmitted. The location of the broad dip (-1.2 eV with respect to the charge neutrality point) is quite different from the results obtained using a single-band *tight-binding* model, which predicts a single dip exactly at the Fermi level (Chico et al. 1996).

Actually, the electron–hole symmetry is no longer valid in a more realistic *ab initio* calculation, and the dip position moves. Moreover, two other narrower dips are observed closer to E_F and originate from resonant scattering by quasibound states derived from the broken σ bonds around the vacancy (Fig. 10.22(a)). The σ bonds between the removed atom and its neighbors are broken and dangling bonds are produced, which are mainly composed of π orbitals parallel to the tube surface. Since σ bond states are orthogonal to the π valence band states, a very weak coupling is present between them. Among three quasibound states derived from three dangling bonds, one is an *s*-like bonding state, which lies well below the first lower subband (outside the scope of the figure). The other two states are orthogonal to it (i.e., partially anti-bonding) and give rise to the two narrower dips in the conduction region, as shown in Fig. 10.22(a).

The interaction among the dangling σ bonds actually causes substantial atomic relaxations, at the origin of reconstruction of the bare monovacancy (D_{3h} symmetry), into a more stable vacancy structure exhibiting C_s symmetry (Fig. 10.22(b–c), Amara et al., 2007). More specifically, the D_{3h} vacancy undergoes a Jahn–Teller distortion upon relaxation, where two of the atoms near the vacancy move closer, forming a pentagon-like structure while the third atom is slightly displaced out of the plane. In addition,

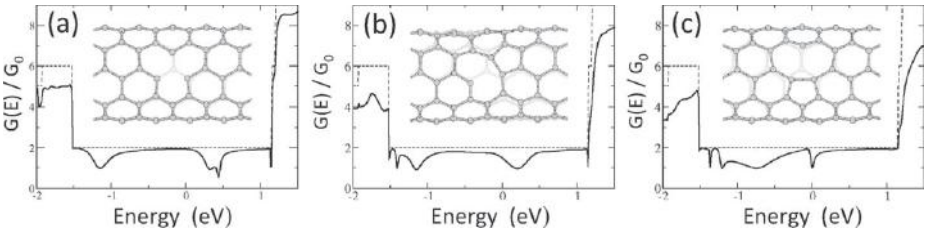

Figure 10.22 *Ab initio* quantum conductance of a (5, 5) armchair nanotube containing a bare D_{3h} monovacancy (a); and a reconstructed C_s vacancy in two different positions: (b) tilted or (c) perpendicular to the axis of the tube. Atomic structures of the corresponding defects are shown in insets. (Reproduced from Dubois et al. (2009), with kind permission from Springer Science and Business Media)

the vacancy can adopt two different positions related to the hexagonal network of the nanotube: a tilted position (Fig. 10.22(b)) or a perpendicular position (Fig. 10.22(c)) regarding the axis of the nanotube. The tilted vacancy is found to be the most stable configuration with a $\Delta E = 1.34\,\text{eV}$ energy difference compared to the perpendicular case (Zanolli and Charlier 2010). Both vacancies have a significant influence on the electronic structure of the tube, at the origin of important backscattering to incoming electrons at resonant energies. In fact, the accurate positions of the vacancy-related quasibound state levels depend on various factors such as atomic configuration, orientation versus the axis of the tube, and the nanotube diameter (Choi et al. 2000; Zanolli & Charlier 2010).

Additionally, since the localized orbitals of unsaturated carbon atoms are expected to behave as magnetic impurities (Lehtinen, Foster, Ayuela et al. 2004; Lehtinen, Foster, Ma et al. 2004; Shibayama et al. 2000), a monovacancy (but not a divacancy) is expected to hold a net magnetic moment. It is worth mentioning that periodic-boundary-condition calculations can lead to results in contradiction with these theoretical predictions. Interestingly, the total magnetic moment of CNTs containing the tilted monovacancy oscillates with the length nd_0 of the $1 \times 1 \times n$ supercell (d_0 being the length of the (5, 5) unit cell), and finally goes to zero as illustrated in Fig. 10.23 (square symbols). It is worth noting that these oscillations are not due to a poor k-point sampling of the Brillouin zone since accurate convergence studies have been performed (Zanolli and Charlier 2010).

In fact, these oscillations of the total magnetic moment are due to a long-range interaction between the periodic images of the magnetic moments mediated by the conduction electrons of the metallic tube, also called indirect exchange coupling (Kirwan et al. 2008). This indirect coupling is defined as the energy required to rotate the magnetic moments from the ferromagnetic to the antiferromagnetic configuration, that is $J = E_{\uparrow\uparrow} - E_{\uparrow\downarrow}$, where $E_{\uparrow\uparrow}$ and $E_{\uparrow\downarrow}$ are the total energies of the ferromagnetic and antiferromagnetic configurations, respectively. The interaction results in an oscillatory behavior of J, whose amplitude decreases as a power law of the distance between the magnetic impurities. Such a power law strongly depends on the nature of the impurity and on the dimensionality of the system.

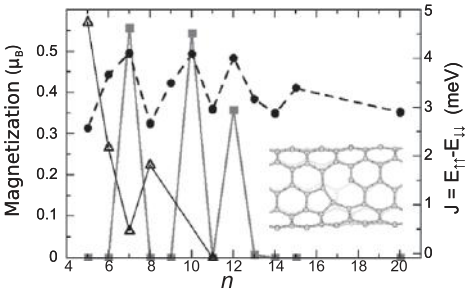

Figure 10.23 Total magnetization (μ_B) for a $1 \times 1 \times n$ supercell containing one monovacancy calculated within the periodic-boundary-condition scheme (gray curve ■—■) and for the open system with $1 \times 1 \times n$ *core* region (black dotted curve ●—●). Indirect exchange coupling (J, meV) for the $1 \times 1 \times 2n$ supercell containing two monovacancies at distance nd_0 (gray curve △—△). All the calculations are performed for a (5, 5) CNT containing a monovacancy reconstructed in the tilted configuration, as illustrated in the inset. (Adapted with permission from Zanolli and Charlier (2010). Copyright (2010) by the American Physical Society)

When the supercell contains a single defect, periodic boundary conditions either allow a non-spin-polarized configuration or a ferromagnetic coupling between the periodically repeated magnetic impurities. Hence, when their distance is such that the antiferromagnetic coupling is the lowest-energy configuration (i.e., $J > 0$), the periodic system is forced into either a non-spin-polarized or a ferromagnetically coupled state, depending on the relative energetic ordering of the three possible magnetic configurations (ferromagnetic, antiferromagnetic and non-spin-polarized) (Venezuela et al. 2009).

To check this assumption, J has been calculated for double supercells of various length, $2nd_0$, containing two monovacancies at nd_0 distance, retrieving the expected damped oscillatory behavior (Fig. 10.23, triangles). Indeed, the single-monovacancy supercells having zero-magnetization (zero values in the "square symbols" gray curve of Fig. 10.23) correspond to a two-monovacancy system where the antiferromagnetic coupling is favored ($J > 0$ in the "triangle symbols" gray curve of Fig. 10.23).

Even though the indirect coupling is quite weak (J is of the order of a few meV), it clearly affects the periodic-boundary-condition computation of the magnetic properties of defected CNTs. Consequently, to accurately describe the local magnetic properties of isolated vacancies, an open system with a single magnetic impurity has to be considered. The defected CNTs are thus modeled as two semi-infinite sections of nanotube and a central region (or *core*) containing a single defect site, as described in Zanolli and Charlier (2009). Using this approach, the magnetization of the tilted monovacancy has always been found to be finite and converges for a core region consisting of $1 \times 1 \times 15$ cells (see Fig. 10.23, black dashed curve).

It can further be noted that both the open system and the periodic-boundary-condition approaches can be considered as first approximations to "real" CNTs with low or high densities of defects, respectively. On the one hand, the open system scheme can approximate the experimental case of low densities of vacancies only when the separation between defects is larger than the interaction range of the indirect exchange coupling.

This interaction is found to depend on the location of the magnetic impurity on the hexagonal network of the host CNT (Kirwan et al. 2008) and can vary substantially from 3 to 10 nm. Consequently, the open system approach can model a "real" defected CNT where vacancies are more than ∼3–10 nm apart.

On the other hand, the periodic-boundary-condition approach presents some intrinsic limitations in describing the opposite limit of a high density of vacancies in CNTs, as recently illustrated for magnetic impurities in graphene (Venezuela et al. 2009). Indeed, a periodic-boundary-condition calculation with one defect per unit cell always forces the periodically repeated magnetic impurities to be in the same spin state (either non-spin-polarized or ferromagnetically coupled).

The antiferromagnetic or noncollinear spin polarization of the magnetic impurities cannot be described within such an approach. Besides, the periodicity of a periodic boundary condition (PBC) calculation is an ideal model, which imposes spurious interactions that are not present in the real system, where the distribution of defects is random. Consequently, the PBC technique cannot model "real" CNTs with a high density of defects, unless the defects are equally and ideally spaced and present either no coupling (no spin polarization) or a ferromagnetic coupling.

After clarification of how to study the magnetic properties of a single defect site in CNTs, the open system scheme is used to predict both the magnetization and the spin-polarized conductance of defected tubes (see Fig. 10.24). From these calculations, it can be seen that the open system scheme makes it possible to recover the expected magnetic behavior of monovacancies. In addition, these results definitely show that the magnetization of defected CNTs can be ascribed to the presence of unsaturated carbon atoms, in agreement with a naive picture of a dangling bond.

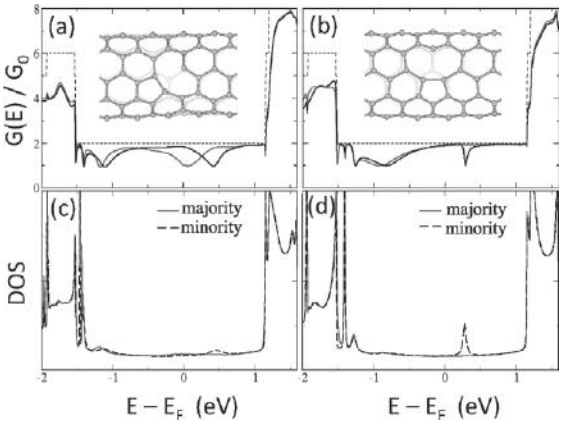

Figure 10.24 *Ab initio* quantum conductance and DOS calculated for a (5, 5) CNT containing a monovacancy reconstructed in its most stable (a, c) and next stable (b, d) configurations, respectively. The DOS allows one to identify the degree of localization of the dips in the transmission curve to facilitate the comparison. (Adapted with permission from Zanolli and Charlier 2010. Copyright (2010) by the American Physical Society)

The analysis of the conductance curves (Fig. 10.24) reveals that a carbon nanotube containing a monovacancy may act as a spin filter within some specific energy windows. For instance, the conductance at E_F of the *tilted* reconstruction of the monovacancy (Fig. 10.24(a)) drops from $2G_0$ to G_0 for one spin channel (*majority* spin carriers) while the *minority* spin conductance is almost unaffected. Consequently, at E_F, half of the electrons with majority spin orientation will be filtered out while minority electrons will be almost fully transmitted. The situation is reversed at 0.4 eV: majority electrons are almost fully transmitted while half the minority electrons are reflected. A similar behavior is predicted for the *parallel* monovacancy (Fig. 10.24(b)).

The conductance dips correspond to states which are quasilocalized (wide dips, Fig. 10.24(a)) or strongly localized (sharp dips, Fig. 10.24(b)) on the under-coordinated carbon, as can be seen from the height of the peaks of the density of states (DOS, Fig. 10.24(c) and (d), respectively) computed from the Green's function of the open system.

The information on the degree of localization of the states on the defect site obtained from the conductance and the DOS computed within the open system scheme helps in better understanding why the range of the exchange coupling is so long and affects the magnetization computed when using periodic boundary conditions. As an example for the monovacancy in the *parallel* configuration, electronic states are seen to be more localized on the defect site (Fig. 10.25(b)) and, hence, little coupling between adjacent cells is found within the periodic-boundary-condition scheme. On the other hand, for the monovacancy in the *tilted* configuration, the electronic states localized on the defect sites are clearly extended over the whole cell (Fig. 10.25(a)), resulting in a strong coupling of the magnetic impurities. The spatial extension of the quasi-localized states is inversely proportional to the tube radius R and the indirect coupling will have the same $1/R$ dependence (Kirwan et al. 2008). For this reason, oscillations in the magnetic moment are less pronounced in the *parallel* case and in the graphene case.

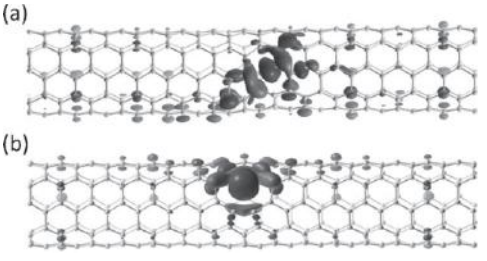

Figure 10.25 Wavefunctions illustrating the degree of localization of the electronic states in a (5,5) CNT containing a monovacancy reconstructed in its most stable (a) and next stable (b) state. The tilted vacancy induces a more extended state (a) than the parallel one (b). (Adapted with permission from Zanolli and Charlier (2010). Copyright (2010) by the American Physical Society)

10.5.4 Doped Carbon Nanotubes

Analogous to point defects, boron or nitrogen impurities, substituting carbon atoms, produce quasibound impurity states of a definite parity and reduce the conductance by a quantum unit $2e^2/h$ via resonant backscattering (Choi et al. 2000), as presented in Fig. 10.26. The conductance of the doped tube is found to be virtually unchanged at E_F, meaning that the impurity potential does not scatter incoming electrons at this energy. On the other hand, two pronounced dips are observed in the conductance below E_F for the boron impurity since it acts as an acceptor dopant. The amount of the conductance reduction at these dips is $1G_0$ (Fig. 10.26(a)). The upper dip is caused by an approximate half reflection from states of both π and π^* bands. Because a single impurity breaks the mirror symmetry planes containing the tube axis, an eigenchannel is a mixture of the π and π^* bands. Consequently, an electron in such an eigen-channel is either completely reflected or completely transmitted. Associated with the two conductance dips, the density of states (DOS) around the boron impurity exhibits two peaks arising from the presence of quasibound states (Fig. 10.26(a)). The lower peak is too close ($\sim$1 meV) to be seen separately from the peak originating from the van Hove singularity of the lower subbands. A nitrogen substitutional impurity has similar effects on the conductance (Choi et al. 2000), but on the opposite site of the charge neutrality point since it acts as a donor dopant (Fig. 10.26(b)). In summary, a substitutional boron or nitrogen impurity produces quasibound states of definite parity (resonant states) made of π orbitals perpendicular to the tube surface below or above E_F, in close analogy to the acceptor or donor levels in semiconductors, and the conductance is reduced at the corresponding quasibound state energies.

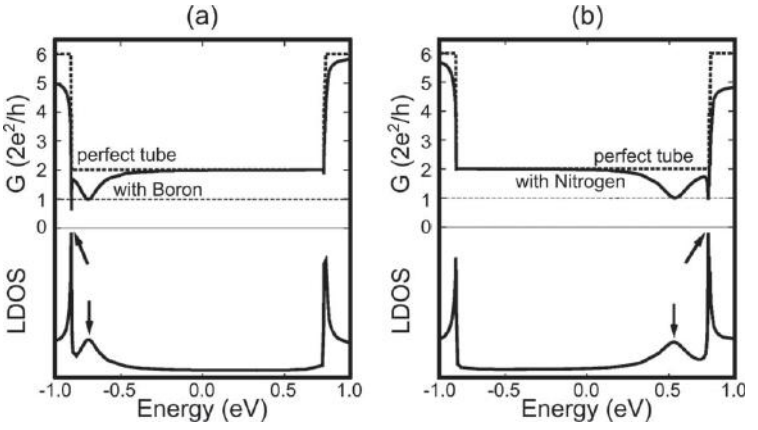

Figure 10.26 Effects of a boron (a) and a nitrogen (b) impurity on the conductance of a (10, 10) carbon nanotube. The conductance as a function of the incident energy exhibits two dips. The local density of states (LDOS) around the impurity presents two peaks (indicated by arrows) and rapid changes, respectively, associated with the dips in the conductance. (Reproduced from Choi et al. (2000). Copyright (2000) by the American Physical Society. Courtesy of Hyoung Joon Choi)

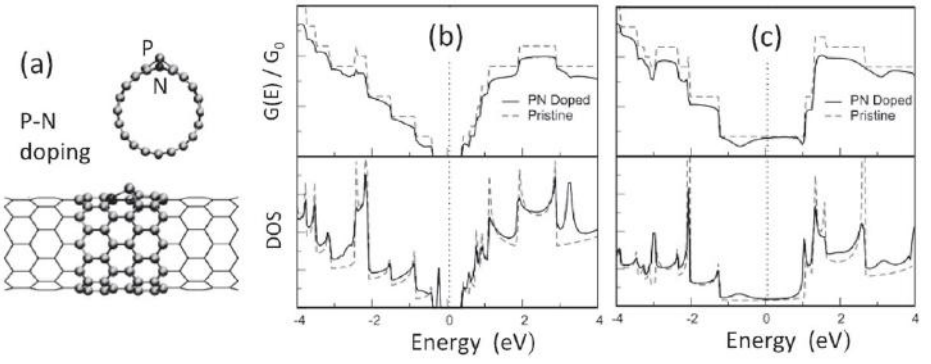

Figure 10.27 (a) Atomic structures of phosphorus–nitrogen-doped (10, 0) nanotube. The phosphorus atom protrudes from the nanotube wall due to the longer P–C bonds. (b, c) Quantum conductance and density of states plots for P–N-doped (b) zigzag (10, 0) and (c) armchair (6, 6) carbon nanotubes (solid line), compared with pristine nanotube values (dashed line). The conductance of the semiconducting tube is almost insensitive to the presence of the dopant. Localized states cause scattering, and hence a reduction of the conductance close to the corresponding energies for the metallic tube. (Adapted from Cruz-Silva et al. (2009))

Experimentally, hetero-doped carbon nanotubes are quite easily synthesized by CVD techniques (Cruz-Silva et al. 2008) using for example benzylamine and triphenylphosphine as nitrogen and phosphorus sources, respectively. These P–N-doped nanotubes are thermodynamically stable, as predicted theoretically when scrutinizing the defect formation energies (Cruz-Silva et al. 2009). Analysis of the relaxed structures confirms that phosphorus maintains an sp^3 hybridization and bonds to the carbon atoms with tetrahedral orbitals, inducing structural strain in the carbon network in order to accommodate the longer P–C bonds and the larger sized P ion (Fig. 10.27(a)). Total energy calculations also confirm that curvature helps to reduce the structural strain caused by the phosphorus, and that the P–N defect is energetically more stable than the phosphorus impurity alone.

The electronic band structure shows the presence of "semi-localized" states around the P–N doping atoms (Cruz-Silva et al. 2009). In contrast to nitrogen, these states do not modify the intrinsic nanotube metallicity. Electronic transport calculations on pristine and P–N-doped nanotubes clarify the different effects of the dopants on their conductance (Fig. 10.27(b, c)). The calculation of the quantum conductance shows that zigzag phosphorus-doped nanotubes do not modify the intrinsic semiconducting behavior (Fig. 10.27(b)), in contrast to what is observed for N-doped nanotubes (Choi et al. 2000). Phosphorus–nitrogen doping in a (10, 0) nanotube only creates bound and quasibound states around the phosphorus atom that are dispersionless giving sharp peaks in the density of states (Fig. 7.27(c)). These states are normal to the nanotube surface and do not contribute to the electronic transport in semiconducting nanotubes, while in the case of a metallic nanotube, these states behave as scatterers, creating small dips in the conductance at specific energies. These electronic properties are also very

useful for fast response and ultrasensitive sensors operating at the molecular level. Such molecular selectivity has been predicted in CO, NH_3, NO_2, and SO_2 adsorbed on P–N-doped nanotubes (Cruz-Silva et al. 2011). In fact, the adsorption of different chemical species onto the doped nanotubes modifies the dopant-induced localized states, which subsequently alter the electronic conductance. Although SO_2 and CO adsorptions cause minor shifts in electronic conductance, NH_3 and NO_2 adsorptions induce the suppression of a conductance dip. Conversely, the adsorption of NO_2 on P–N-doped nanotubes is accompanied by the appearance of an additional dip in conductance, correlated with a shift of the existing values. Overall, these changes in electric conductance provide an efficient way to detect selectively the presence of specific molecules (Cruz-Silva et al. 2011).

10.5.5 Functionalized Carbon Nanotubes

The transport properties of carbon nanotubes can be tailored by molecular functionalization (Balasubramanian et al. 2008; Collins et al. 1998; Star et al. 2003). Indeed, functionalized carbon nanotubes display tunable structural and electronic properties, and promise to become for nanoelectronics what DNA is for the life sciences. For instance, by grafting photoactive molecules onto the nanotube, the resulting nanotube-based devices could be controlled optically (Campidelli et al. 2008; Simmons et al. 2007). The recent development of synthetic methods to attach ligand molecules has been a major breakthrough, and opens the possibility to use molecular self-assembly and nanolithography techniques to arrange nanotubes in a device. An accurate control of the physical properties can also be made possible by target molecular functionalizations that tune the electronic response or the structural conformations.

In order to graft molecules at the nanotube surface, two types of chemical functionalization are usually considered, namely physisorption (non-covalent functionalization) and chemisorption (covalent functionalization). Both methods provide effective pathways for modifying the intrinsic properties of electric transport along CNTs, but a trade-off has to be found to add a new functionality to the tube without excessively damaging its electronic and transport features (Balasubramanian et al. 2008).

Non-covalent Functionalization

In the case of physisorption, the non-covalent adsorption of molecules has the advantage of enabling CNT functionalization while preserving their electronic structure, since the original sp^2 hybridized bonds and conjugation remain unaltered (Tournus et al. 2005). Consequently, the scattering efficiency resulting from molecule deposition remains negligible owing to weak bonding (see, for instance, Latil et al. (2005)) and vanishing charge transfer. Nevertheless, physisorption effects on electronic conduction have been suggested to critically depend on the nature of molecular species and their HOMO-LUMO gap positioning with respect to the Fermi level of the host tube (Latil et al. 2005). For example, benzene molecules yield vanishing modulations of the intrinsic conductance, whereas azulene molecules (with a HOMO-LUMO gap of about ~ 2 eV) produce

substantial elastic backscattering in the nanotube, resulting in mean free paths of the order of a few micrometers for large coverage. Such a possibility of creating/removing a reversible elastic disorder by a simple adsorption/desorption of molecules covering the nanotube surface opens interesting perspectives for experimental studies and potential applications in nanotechnology.

Covalent Functionalization: A Few Examples

In the case of chemisorption, covalent functionalization of CNT involves the formation of saturated sp^3 bonds which markedly breaks the nanotube π conjugation (Zhao et al. 2004). The diazonium addition is a commonly used technique (Cabana & Martel 2007; Lee, Son et al. 2005), but can result in dramatic loss in tube transport capability if too many addends are chemisorbed. The impact of covalent functionalization on tube conductance can, however, be significantly reduced by a suitable choice of the addends. To circumvent such a problem, [2 + 1] cycloaddition reactions have been theoretically proposed (Lee, Son et al. 2005; Lee & Marzari 2006). Such functionalization is driven by grafted carbene (or nitrene) groups that induce bond cleaving between adjacent sidewall carbon atoms, maintaining the sp^2 hybridization and providing sites for further attachment of more complex molecules and related functionalities. A transport study based on a nonorthogonal *tight-binding* Hamiltonian has first reported strong differences between monovalent and divalent additions in short-length nanotubes (Park et al. 2006). Using *ab initio* calculations, Lee and Marzari (Lee, Son et al. 2005; Lee & Marzari 2006) further demonstrated that cycloaddition reactions induce the grafting of dichlorocarbene groups (CCl_2) which preserve most of the conductance in (5, 5) CNT metallic nanotubes, in contrast to phenyl-type functionalization. However, these first-principles calculations have been limited to ultrashort nanotube segments with length below 50 nm. Below, various processes of chemical functionalization are detailed, and their impact on electronic and transport properties in micrometer-long and disordered nanotubes is analyzed following (Lopez-Bezanilla 2009).

Diazonium salts are a group of organic compounds sharing a common functional group with the characteristic structure of $R-N_2^+X^-$, where R can be any organic ligand such alkyl or aryl and X is an anion such as a halogen. Phenyl group (denoted with the formula C_6H_5 and sometimes abbreviated as Φ) is the aryl component of diazonium salts which is widely used in chemistry to functionalize carbon nanotubes to form nanotube composites. Diazonium salts provide a selective chemical reaction that favors the covalent attachment to metallic CNTs. Such a selectivity characteristic is used for sorting nanotubes of different chiralities (Strano et al. 2003). In the grafting process, the aryl diazonium cation gets one electron from the substrate and subsequently becomes an aryl radical by losing an N_2 molecule (see Fig. 10.28). The attachment of a phenyl group onto the nanotube sidewall makes an anchorage point for further grafting of more complex molecules with specific functionalities (Campidelli et al. 2008). Due to the sp^3 rehybridization induced by the grafting of the phenyl group, this new chemical function strongly affects local features of the carbon-based systems.

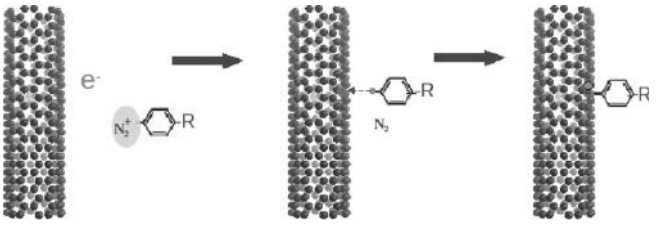

Figure 10.28 Grafting of phenyl groups onto the CNT sidewall. First, an electron is extracted from the nanotube by means of the reaction with diazonium reagents. An N_2 molecule is formed and the aryl group gets chemically attached to the nanotube, resulting in the creation of a stable C–C covalent bond and a radical which is further passivated by another aryl group in a similar process.

Charge transport in metallic single-walled CNTs with random distribution of phenyl and carbene functional groups bonded to the tube sidewalls has been investigated within a first-principles approach (López-Bezanilla et al. 2009; López-Bezanilla, Triozon, Latil et al. 2009). The disorder introduced by the grafted groups breaks both translational and rotational symmetries. The conductance modulations and conduction regimes (from quasiballistic to diffusive) have been investigated as a function of both incident electron energy and functional groups coverage density on long nanotubes from a few hundreds of nanometers to the micron scale. First-principles mesoscopic transport study demonstrates that carbene cycloaddition preserves ballistic conduction up the micron scale, whereas the grafting of phenyl groups yields a mean free path in the nanometer scale, leading to a strong localization regime for commonly studied nanotube lengths.

The computational approach is based on a large set of *ab initio* calculations, which are first performed to get the Hamiltonian and overlap matrix associated with small tube sections functionalized by single groups (see Fig. 10.29(a) and (b)). Such a set of building blocks Hamiltonian is further used to reconstruct a micrometer-long tube Hamiltonian formed by a random mixture of functionalized and pristine tube portions to introduce both rotational and translational disorder (see Fig. 10.29(c)). Upon building the small block Hamiltonian with one defect, periodic boundary conditions are used. The length of the building block is chosen such that geometric and energetic perturbations induced by functional groups vanish as the edges are reached. The renormalization procedure used here takes advantage of the locality of the orbital basis set used in the *ab initio* simulation (SIESTA code), allowing us to consider the system as formed by nearest-neighbors' interacting sections. As depicted in Fig. 10.29 (bottom panel), an armchair CNT is divided in segments, so that H is partitioned in onsite energy diagonal blocks and nearest-neighbor coupling blocks. By coupling, in a random way, functionalized and pristine building blocks, CNTs as long as desired can easily be built up (López-Bezanilla et al. 2009; López-Bezanilla, Triozon, Latil et al. 2009; López-Bezanilla et al. 2010).

The case of a single functional group is first investigated. The effect of a pair of phenyl rings or a carbene group in the electronic structure of an armchair CNT is directly

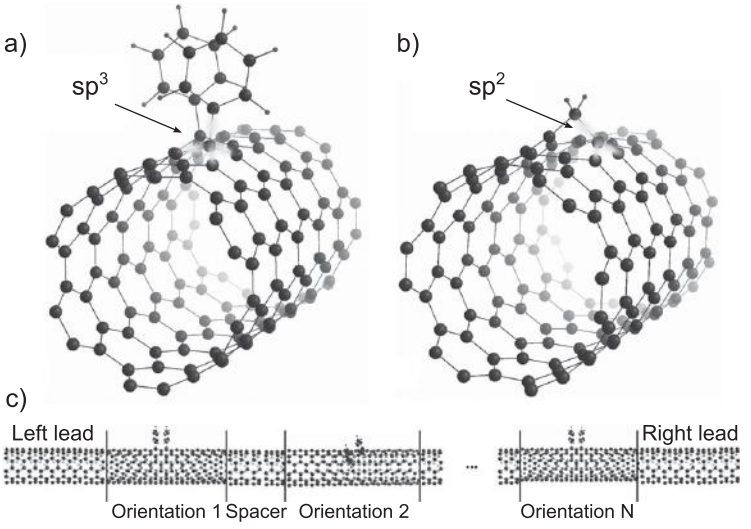

Figure 10.29 sp^2-like and sp^3-like functionalization. Top panel: Atomic structures of the building blocks assembled further in longer structures with both kinds of covalent grafting: (a) sp^3-like functionalization with phenyl groups and (b) sp^2-like functionalization through divalent addition by carbene groups. (c) CNT functionalized with phenyl groups constructed by assembling individual sections. (Adapted with permission from López-Bezanilla, Triozon et al. (2009). Copyright (2009) American Chemical Society)

observable in the band energy diagram. Figure 10.30(a) illustrates the unaltered band structure of a (10, 10) CNT upon functionalization with a carbene group. The bond between neighboring circumferential carbon atoms is broken and new bonds between carbene carbon atom and two nanotube carbon atoms are formed. Figure 10.30(b) and 10.29(c) depict a CNT with a carbene group covalently attached in an orientation that favors a stable configuration. The system CNT-CH_2 reaches its configuration energy minimum by displacing the carbon atoms that serve as an anchorage site to the carbene, which entails a rupture of the original C–C bond of nanotube atoms. If one considers only a nearest-neighbor scheme, every C atom is found to be bonded to three C atoms, preserving the original π orbitals network. In Fig. 10.30(d), the preserved π orbitals centered in the altered nanotube carbon atoms are shown in a representation based on Wannier functions approach (Marzari & Vanderbilt 1997). As seen below, carbene bond orientation in the nanotube plays a key role in electronic transport properties. The orientations depicted in Fig. 10.30(c) and (d) are the most stable configurations for zigzag and armchair CNT, respectively.

As can be seen in Fig. 10.30(b), two flat bands at energy values that coincide with the conductance dips in Fig. 10.31(a) show up in the energy band diagram. These nondispersive bands indicate the presence of molecular states, which have localized the system wavefunction around the phenyl groups, as observed in Fig. 10.30(f) where the local density of states (LDOS) is plotted for the state at energy -0.6 eV. At this

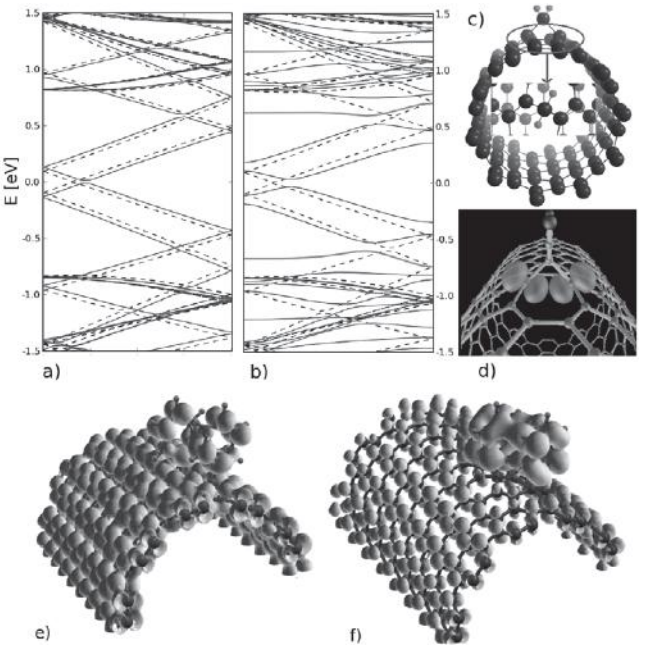

Figure 10.30 Energy bands of a functionalized armchair CNT with a carbene group (a) and with a pair of phenyl rings (b). (c) Ball-and-stick image of a carbene group grafted onto the semiconducting nanotube in a skewed orientation. (d) Carbene functionalization when the C–C bond is perpendicular to nanotube axis (Courtesy of N. Marzari). (e) and (f) The LDOS of the hybrid CNT-pair of phenyl at two energies: in (e) the density of states has been projected over an interval of energy close to the Fermi energy; in (f) the projection is over the localized state at -0.6 eV.

energy, the largest contribution to the DOS comes from the orbitals associated with the functional groups, i.e., system wavefunction is localized over the molecules, unlike Fig. 10.30(e) where the wavefunction is homogeneously spread along the system.

The diameter of such a (10, 10) tube is close to the limit separating the area of stability for closed carbene configurations (larger tubes) and opened geometries (smaller tubes) (Lee & Marzari 2006). Closed configurations introduce significant backscattering and the advantage of cycloaddition is therefore lost for larger diameter tubes. Further, on the basis of activation energy calculations for desorption, carbene is found not to be thermally stable on large tube diameters and graphene. Due to the planar-like geometry of large CNTs, carbene groups do not induce displacement of C atoms from the original structure (as in the case of small–diameter armchair nanotubes), and thus spontaneously desorb at room temperature (Margine et al. 2008). Paired configurations in the 1,4-geometry (para – where two phenyls are grafted as third-nearest neighbors) are investigated keeping intact the conjugation properties of the CNT. Several arguments suggest that such a configuration is the most likely to occur in nanotubes: (a) the grafting of a first radical is known to enhance the reactivity of a carbon atom at an odd

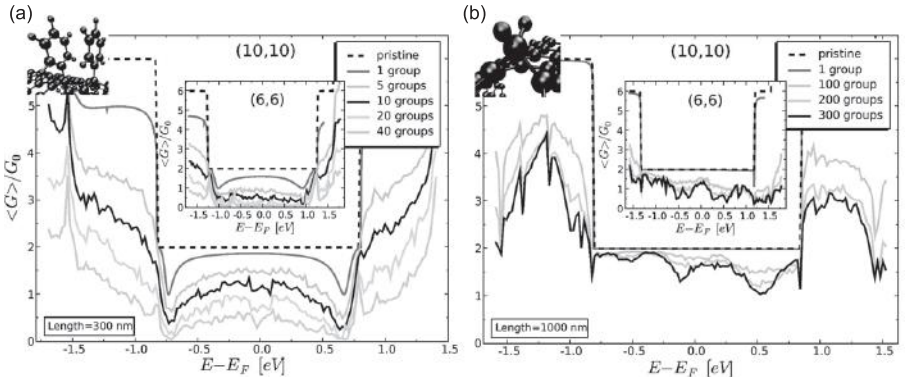

Figure 10.31 Conductance profiles (in units of G_0) for phenyl and carbene functionalization (averaged over 40 different random configurations): (a) Conductance for various molecular coverages of a 300 nm long (10, 10) CNT functionalized with phenyl groups. (b) Same as in (a), but for a 1000 nm long nanotube functionalized with divalent addition of carbene groups. The insets give the same information but for the (6, 6) nanotubes. (Adapted with permission from López-Bezanilla et al. (2009). Copyright (2009) American Chemical Society)

number of bonds away from it, (b) the 1,4-configuration is slightly more stable than the 1,2-configuration (ortho), and (c) isolated phenyls have been shown to spontaneously diffuse or desorb at room temperature on standard diameter tubes (Margine et al. 2008).

Increasing the number of grafted phenyl groups has a strong impact on the conductivity of both 300 nm long (6, 6) and (10, 10) nanotubes, as shown in Fig. 10.31(a). The sp^3 bond between the phenyl and the tube surface reduces the conductance for all energies but with marked suppression of one conduction channel at two symmetric energy resonances for a single grafted group. By increasing the coverage density, a stronger damping of the conductance pattern is observed. For a fixed molecule density, this effect is enhanced for smaller nanotube diameter. The conductance is found to roughly decay inversely proportional to the coverage density (Fig. 10.32). Using a conventional phenomenological law, the disorder average transmission coefficient can be related to the elastic mean free path as $\bar{T} = <G>/G_0 = N_\perp(1 + \frac{L}{\ell_{\rm el}})^{-1}$. This expression allows prediction of some approximated range and scaling behavior of the mean free path (Fig. 10.32).

With simpler disorder models (such as Anderson disorder), analytical forms and scaling behavior of elastic mean free paths have been derived for both carbon nanotubes (White & Todorov 1998) or graphene nanoribbons (Areshkin & White 2007). In particular, $\ell_{\rm el}$ was demonstrated to upscale linearly with tube diameter for a fixed disorder strength. Here, for the 300 nm long (6, 6) nanotube, $\ell_{\rm el}$ quickly decays with coverage density to reach $\ell_{\rm el} \sim 15$ nm when 40 groups are attached to the sidewalls. The same number of functional groups on a larger diameter nanotube (10, 10) will, however, yield $\ell_{\rm el} \sim 100$ nm. The calculated mean free path also presents some upscaling with nanotube diameter, although the scaling behavior cannot be extracted in detail.

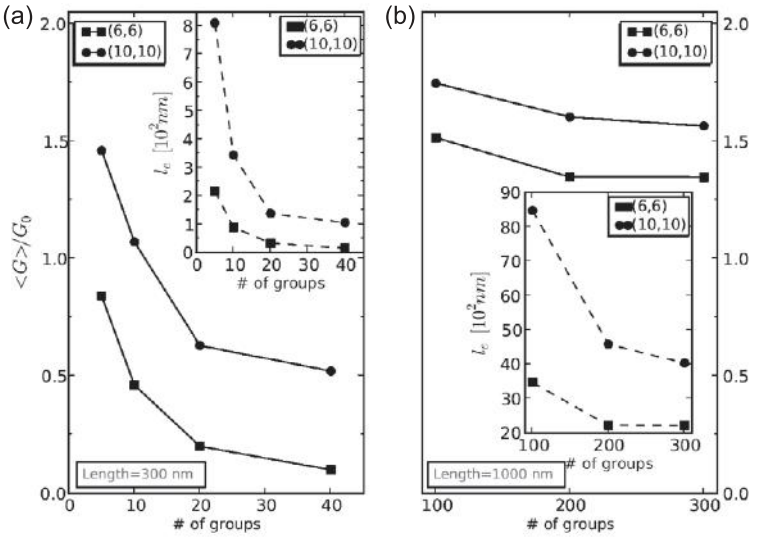

Figure 10.32 (a) Disorder average conductance at the charge neutrality point (main plot) and estimated elastic mean free path (inset) as a function of grafted phenyl groups density for a 300 nm long nanotube. (b) The same for grafted carbene groups for a nanotube length of 1 μm. (Adapted with permission from López-Bezanilla, Triozon, Latil et al. (2009). Copyright (2009) American Chemical Society)

As evidenced by these results, sp^3 bonds are clearly not favorable for good conduction efficiency of hybrid nanotubes, and thus not suitable for applications.

In contrast, the cycloaddition of carbene groups induces only a small downscaling of the conductance in the first plateau, with increase in the coverage density (see Fig. 10.32). In contrast to the phenyl groups, an asymmetry of the conductance decay is already observed for the single molecule case. The much weaker change of conductance indicates a quasiballistic regime. The values of ℓ_{el} are given in the inset to Fig. 10.32(b), and are in the range of $\sim 2-9$ μm, depending on coverage density and nanotube diameter. In this case, a rough linear scaling of ℓ_{el} is observed with tube diameter (López-Bezanilla et al. 2009). Note that the coverage density in the case of carbene groups is larger than for the phenyl case, demonstrating the weak effect of such functionalization on transport properties of pristine nanotubes, which is crucial for further envisioning the use of long hybrid nanotubes. We mention that a recent statistical study of the conductance distributions $P(g)$ in such type of disordered micrometer-long carbon nanotubes has perfectly reproduced the nontrivial, non-Gaussian, crossover to Anderson localization, in full agreement with the Dorokov–Mello–Pereyra–Kumar scaling equation, offering a possible experimental test of such universality (Lopez-Bezanilla et al. 2018).

In summary, by using a fully *ab initio* transport approach, transport regimes in chemically functionalized long carbon nanotubes can be explored, comparing two different and important types of chemical bonding. The results provide evidence of

good conduction ability in the case of carbene cycloadditions, whereas paired phenyl addends are found to yield a strongly diffusive regime, with estimated mean free path ranging from a few tens of nanometers to 1 nm, depending on the coverage density and incident electron energy. Functionalizing is thus an interesting tool to develop novel devices based on modified carbon nanotubes that have specific organic molecules covalently linked to their walls, thus combining the exceptional structural stability and electronic properties of microscopic wires with the diversity and tunability of material properties that come from the molecular attachments.

10.5.6 Carbon Nanotubes Decorated with Metal Clusters

Due to their high surface to volume ratio, CNTs are promising candidates as active elements for extremely sensitive gas-sensing devices since their conductance can be easily perturbed by interaction with gas molecules (Charlier et al. 2009; Goldoni et al. 2010; Zanolli & Charlier 2009). However, the response of pristine CNTs to gases is weak and scarcely selective since the ideal carbon hexagonal network is held together by strong sp^2 bonds characterized by a low chemical reactivity with the molecular environment. Consequently, functionalization of the CNT sidewalls is mandatory to improve both the sensitivity and the selectivity of CNT-based gas sensors (Peng & Cho 2003). In particular, functionalization with metal nanoparticles (NPs) can lead to highly sensitive and selective gas sensors, thanks to the extraordinary catalytic properties of metal NPs (Charlier et al. 2009; Zanolli & Charlier 2012; Zanolli et al. 2011).

Although the sensing ability of CNTs decorated with metal NPs relies on the huge chemical reactivity of the cluster surface, the whole CNT–NP system acts as the detection unit of the device. Indeed, the interaction with gas molecules results in an electronic charge transfer between the molecule and the CNT–NP sensor, which affects the position of the Fermi energy and, hence, the conductivity of the detection unit. Such a conductivity modification can, for instance, be measured by embedding mats of metal-decorated carbon nanotubes in a standard electronic device (Charlier et al. 2009). Since these mats usually behave as p-doped semiconductors, the adsorption of an extra electron coming from molecules exhibiting a donor character will induce a resistance increase. Analogously, the interaction with molecules exhibiting an acceptor character will lead to a reduced resistance. In addition, functionalization of CNTs with metal nanoparticles can be exploited to improve the sensor selectivity, since different metals will present different reactivities toward different molecules. Hence, a gas sensor device can be fabricated by depositing on a microsensor array several sets of CNT mats, each decorated with different types of metallic NPs (Leghrib et al. 2010).

First-principles modeling have been used to investigate sensing responses of CNTs decorated with various NPs in order to deeply understand the detection ability of these nanosystems for specific gas species (Charlier et al. 2009; Zanolli & Charlier 2012; Zanolli et al. 2011), demonstrating that DFT simulations are powerful tools to predict, improve, and design the next generation of gas nano-sensors.

10.5.7 Graphene Nanoribbons

In contrast to carbon nanotubes, quantum transport properties of GNRs are expected to strongly depend on whether their edges exhibit the armchair or the zigzag configuration. Indeed, in the previous sections, the electronic properties of GNRs have been predicted using the single-band model and *ab initio* calculations, revealing a dependence on the edge topology (Nakada et al. 1996). The armchair GNRs are semiconductors with energy gaps, which decrease as a function of increasing ribbon width. As mentioned earlier, the gaps of the *N*-aGNRs depend on the *N* value, separating the ribbons into three different categories (all exhibiting direct bandgaps at Γ). The band structures and the corresponding quantum conductances of two armchair GNRs are illustrated in Fig. 10.33(a, b). The 16-aGNR is a ∼0.8 eV gap semiconductor, thus inducing a quite large energy interval where no transmission is allowed (Fig. 10.33(a)), while the gap of the 17-aGNR is reduced to less than 0.2 eV (Fig. 10.33(b)). The region of zero conductance is also reduced accordingly, and a very small external electric field would induce an electronic transmission through one channel ($1G_0$ for the conductance).

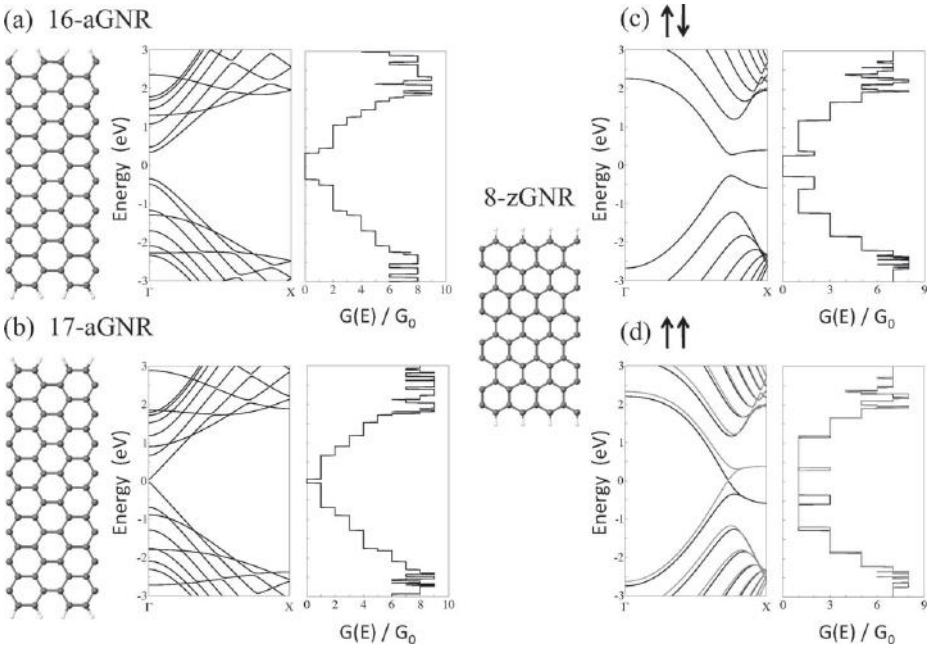

Figure 10.33 Atomic structures, electronic band structures, and quantum conductances (electronic transmission) of various graphene nanoribbons: (a) 16-armchair GNR; (b) 17-armchair GNR. (c, d) 8-zigzag GNR with (c) antiparallel (↑↓) or (d) parallel (↑↑) spin orientations between the two magnetic edges. The spin-dependent transport is evaluated for both magnetic configurations of the 8-zGNR but is only visible for the parallel (↑↑) spin orientations (ferromagnetic). In such a case, one spin orientation is labeled α-spin (in black solid line) while the other is labeled β-spin (in gray solid line). (Reproduced from Dubois et al. (2009), with kind permission from Springer Science and Business Media)

Identically, nanoribbons with zigzag-shaped edges also exhibit direct bandgaps which decrease with increasing width. However, in zGNRs, quantum transport is dominated by edge states, which are expected to be spin polarized owing to their high degeneracy. Indeed, for topological reasons, zigzag-shaped edges give rise to peculiar extended electronic states, which decay exponentially inside the graphene sheet (Nakada et al. 1996). These edge states, which are not reported along the armchair-shaped edges, come with a twofold degenerate band at the Fermi energy over one-third of the Brillouin zone.

The ground state of zGNRs with hydrogen passivated zigzag edges presents finite magnetic moments on each edge with negligible change in atomic structure, thus suggesting zGNRs to be attractive for spintronics (Son et al. 2006a). Indeed, upon inclusion of the spin degrees of freedom within *ab initio* calculations (LSDA), the zGNR are predicted to exhibit a magnetic insulating ground state with ferromagnetic ordering at each zigzag edge and antiparallel spin orientation between the two edges (Son et al. 2006a). The total energy difference between ferromagnetic ($\uparrow\uparrow$) and antiferromagnetic ($\uparrow\downarrow$) couplings between the edges is of the order of $\sim$20 meV per edge atom for an 8-zGNR, but this decreases as the width of the ribbon increases and eventually becomes negligible if this width is significantly larger than the decay length of the spin-polarized edge states (Lee, Son et al. 2005). Because the interaction between spins on opposite edges increases with decreasing width, the total energy of an N-zGNR with antiferromagnetic arrangement across opposite edges is always lower than that of a ferromagnetic arrangement for low values of N ($N \leq 30$).

The band structures and the spin-dependent quantum conductances of an 8-zGNR are illustrated in Fig. 10.33(c, d) in the two respective magnetic configurations ($\uparrow\downarrow$ and $\uparrow\uparrow$) of the ribbon edges. The $\uparrow\downarrow$ spin configuration of the 8-zGNR conserves the semiconducting behavior of the GNR family, and its electronic transmission function displays a gap of 0.5 eV around the Fermi energy (Fig. 10.33(c)). On the contrary, in the $\uparrow\uparrow$ spin configuration, the 8-zGNR becomes metallic, inducing a nonzero electronic transmission function at the Fermi energy (Fig. 10.33(d)). In addition, the spin-dependent conductance calculation also reveals that the transmission of π electrons with one type of spin orientation (α-spin) is favored for an energy region around -0.5 eV below the charge neutrality point. On the contrary, π^* electrons with the other orientation (β-spin) are more easily transmitted around $+0.3$ eV above the Fermi energy.

10.5.8 Graphene Nanoribbons with Point Defects

However, ideal zigzag GNRs are not efficient spin injectors due to the symmetry between the edges with opposite magnetization. In order to obtain net spin injection, this symmetry must be broken (Wimmer et al. 2008). Incorporating defects (such as vacancies or adatoms) in the GNR or imperfections at the edge, which usually cannot be avoided experimentally, breaks the symmetry between the edges and could thus influence the spin conductance of the GNR (Fig. 10.34(a)). In addition, the introduction of magnetic point defects in zGNRs favors a specific spin configuration of the edges. As an example, the $\uparrow\uparrow$ spin configuration is favored when vacancies or

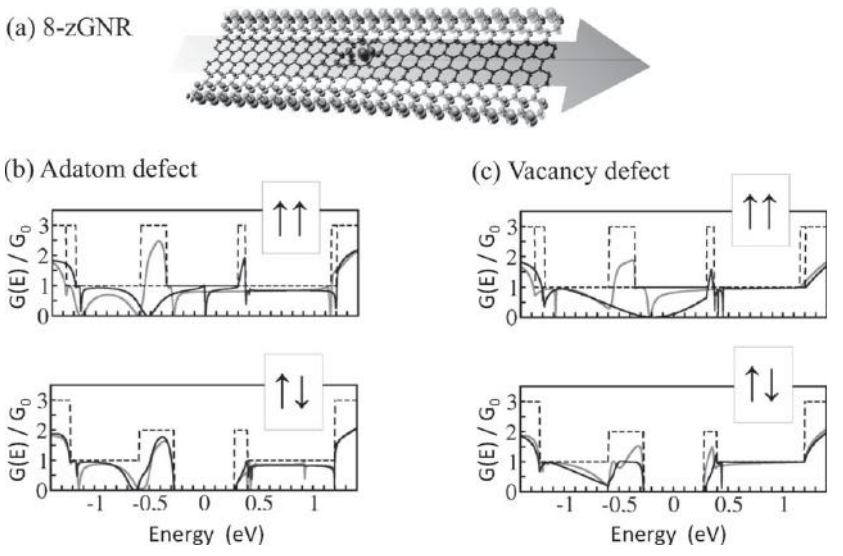

Figure 10.34 Effect of a point defect on the *ab initio* quantum conductance of an 8-zGNR (a). Electronic transmission functions are estimated in the presence of an isolated carbon adatom (b) or an isolated vacancy (c) localized around the ribbon axis, in either the ↑↑ configuration (top panel) or the ↑↓ configuration (bottom panel) of the ribbon edges. The α-spin and β-spin components are shown in dark and light gray, respectively, while the dotted lines indicate the number of π channels in the pristine nanoribbon. (Adapted from Dubois (2009))

adatoms are introduced around the ribbon axis. Consequently, point defects are also expected to play a key role in the transport properties of zGNRs (Dubois et al. 2009). *Ab initio* calculations of the electronic transmission functions have been performed within the Landauer approach using a supercell containing the point defect connected to two leads consisting of a few unit cells of ideal 8-zGNR. Both the (↑↓) semiconducting and the (↑↑) metallic spin configurations of the ribbon are considered (Fig. 10.34).

The main impact of the magnetic point defects on the transport properties is a global reduction of the transmission associated with the π and π^* electrons. This is related to a decrease of the transmission probability of some π–π^* conduction eigenchannels compared to the pristine 8-zGNR. Within the (↑↓) semiconducting configuration (Fig. 10.34(b, c), bottom), the presence of defects essentially reduces the conductance for energies ranging from -0.80 to -0.3 eV (π channels) and from 0.3 to 0.5 eV (π^* channels), inducing a slight breaking of the spin degeneracy. Within the (↑↑) metallic configuration, a similar reduction of the conductance is observed (Fig. 10.34(b, c), top). However, the defects also induce sharp drops in the transmission function around the Fermi level. At these energies, the electronic states localized on the defect are spin polarized and can only mix with one of the two spin conduction channels. Consequently, the spin degeneracy of the electronic transmission function is raised just around the Fermi energy. In summary, when adatoms and vacancies are introduced, the parallel spin orientation may be preferred and the local magnetic moment of the defect adds to

the contributions of the edges. Furthermore, a spin-polarized transmission is observed at the Fermi energy, suggesting a use of defect-doped graphene nanoribbons as a spin-valve device (or spin-filter) in future spin-based electronics.

10.5.9 Graphene Nanoribbons with Edge Reconstruction

In contrast to carbon nanotubes, GNRs exhibit a high degree of edge chemical reactivity, which, for instance, prevents the existence of truly metallic nanoribbons (Barone et al. 2006; Cresti et al. 2008; White et al. 2007). Additionally, the discrepancy between the theoretical electronic confinement gap and the experimentally measured transport gap has been attributed to localized states induced by edge disorder (Evaldsson et al. 2008; Mucciolo et al. 2009; Querlioz et al. 2008). Several experimental studies have also reported the characterization of individual edge defects. To date, several defect topologies of edge disorder (reconstruction and chemistry) have been proposed for GNRs, and *ab initio* calculations have shown the stability of certain types of geometries such as the Stone–Wales reconstruction (Huang et al. 2009; Koskinen et al. 2008; Wassmann et al. 2008). Indeed, at room temperature, the zigzag edge is found to be metastable and a planar reconstruction implying pentagons and heptagons (zz57) spontaneously takes place (Fig. 10.35(a)). Such a zz57-reconstruction self-passivates the edge with respect to adsorption of atomic hydrogen from a molecular atmosphere. Indeed, the formation of triple bonds with alternating single bonds is suggested by the nearly isolated dimers at the ribbon edge, thus removing the dangling bond bands (due to the absence of hydrogen) away from the Fermi level by lifting the degeneracy by almost 5 eV (Koskinen et al. 2008). Because the dangling bond bands shift to elusive energies, the corresponding chemical reactivity is also reduced, stabilizing the zz57 edge. This zz57-reconstruction also modifies the electronic structure of the ribbon.

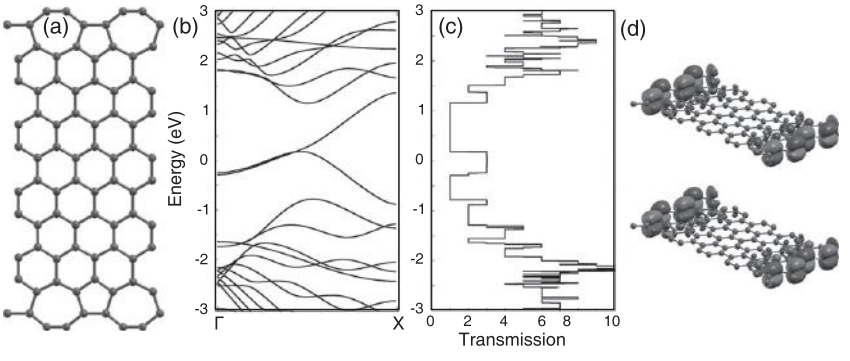

Figure 10.35 Atomic structure model (a), electronic band structure (b), and quantum conductance (c) of an 8-zGNR with a reconstructed edge containing pentagons and heptagons (zz57). The π electronic states surrounding the Fermi energy are represented in (d) and are found to be mainly localized on the zz57-reconstructed edge. (Reproduced from Dubois et al. (2009), with kind permission from Springer Science and Business Media)

The presence of the edge states around the Fermi level (Fig. 10.35(b)) makes this reconstruction ideal for conductance measurements, in contrast to armchair ribbons where the edge state is absent. Indeed, *ab initio* quantum conductance of a zz57-reconstructed 8-zGNR has been calculated (Dubois et al. 2009) and is presented in Fig. 10.35(c). The electronic transmission is predicted to be quite high at the charge neutrality point ($G = 3G_0$), compared to the conventional conductance ($G = 1G_0$) predicted for pristine zGNRs at the Fermi energy (Fig. 10.33(d)). In the zz57-edge reconstruction, π electrons are easily transmitted and these electronic channels are localized at the zz57-reconstructed edge (Fig. 10.33(d)). Consequently, this novel thermodynamically and chemically stable reconstruction could play a key role in the formation of angular joints in nanoribbons (Li, Wang et al. 2008). A knowledge of the atomic structure and the stability of the possible ribbon edges is a crucial issue to control the experimental conditions of the formation of graphene nanoribbons of desired properties for future nanoelectronics.

10.5.10 Graphene Nanoribbons with Edge Disorder

Most of the transport studies of edge-disordered GNRs have assumed simplified defect topologies (Evaldsson et al. 2008; Mucciolo et al. 2009; Querlioz et al. 2008). However, a few *ab initio* calculations have also analyzed a much larger complexity of edge reconstruction and edge chemistry, given the reported stability of certain types of geometries such as the Stone–Wales reconstruction (Huang et al. 2009; Koskinen et al. 2008; Wassmann et al. 2008). Several experimental studies have also reported the characterization of individual edge defects either by means of Raman spectroscopy, scanning tunneling or transmission electron microscopy (Cançado et al. 2004; Girit et al. 2009; Liu et al. 2009). Consequently, it is necessary to investigate the impact of realistic edge-defect topology on the electronic transport properties of long and disordered GNRs.

The electronic and transport properties of aGNRs have been predicted to strongly depend on the geometry of the edge reconstruction (Dubois et al. 2010). Indeed, the transport signature due to a single defect at low energy turns out to range from a full suppression of either hole or electron conduction to a vanishingly small contribution of backscattering. Besides, hydrogenation of the chemically active defects is found to globally restore electron and hole conduction as described below.

Figure 10.36 illustrates various types of possible defect along the ribbon edge using Clar's sextet representation (Clar 1964, 1972). Among all the defects, the reconstructed geometries that preserve the benzenoid structure of pristine aGNRs turn out to weakly affect the electronic transmission. The most striking example is the conductance profile of the D_4 defect (Fig. 10.36(e)). The conductance remains very close to its maximum quantized value as found in the pristine case, with weak backscattering mainly observed in higher subbands. Slightly differently, the double heptagon and pentagon defect (D_3) exhibits two conductance suppression dips (Fig. 10.36(d)), symmetric with respect to the charge neutrality point, recalling the signature of an sp^3-type defect (López-Bezanilla et al. 2009).

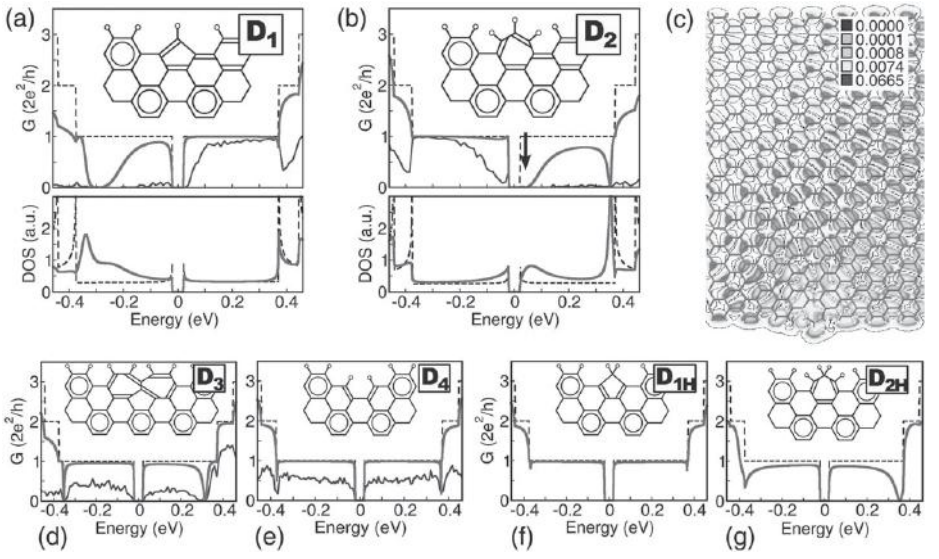

Figure 10.36 Conductance profiles of 35-aGNR for six different edge geometries: pristine ribbon (dashed black lines), single defect (light gray thick solid lines), and average conductance for 500 nm long aGNRs containing 30 defects (dark gray thin noisy lines). TDOS are given for (a) and (b). (Top) Edge-defect topologies containing odd-membered rings: (a) a single pentagon defect – D_1, (b) A single heptagon – D_2. (c) Spatial representation of the transmission eigenchannel at the energy marked by an arrow in panel (b). (Bottom) Edge reconstruction involving only benzenoid defects: (d) two heptagons and one pentagon – D_3, (e) Small hole due to a dimer extraction – D_4. (f) D_{1H} and (g) D_{2H} denote the dihydrogenated pentagon and heptagon, respectively. Insets: Clar's sextet representation for each edge geometry. (Adapted with permission from Dubois et al. (2010). Copyright (2010) American Chemical Society)

Other topologies preserving the benzenoid structure also yield very similar results to those of the D_3 and D_4 defects (not shown here). In marked contrast, edge defects containing monohydrogenated odd-membered rings convey much stronger backscattering efficiency. Conductance fingerprints for single reconstructed pentagon and heptagon defects are illustrated in Fig. 10.36(a) and 10.36(b), respectively. Interestingly, a marked acceptor (donor) character develops for the pentagon (heptagon) defect, as evidenced by the strong electron–hole conductance asymmetry. Such an effect, already observed in nanotube junctions (Charlier et al. 1996), is due to the charge transfer taking place in the π–π^* bands when odd-membered rings are embedded in a perfect hexagonal network. According to the Mulliken decomposition of the electronic density, a slight excess of π electrons ($+0.152$) is found on the pentagonal ring and a small deficit of π electrons (-0.135) is reported on the heptagon. Five-membered rings (D_1) have thus an acceptor character, whereas seven-membered rings (D_2) exhibit a donor character, and even-membered rings (D_3, D_4) are predicted to be neutral in a planar hexagonal network (Tamura & Tsukada 1994).

Total and local DOS have been computed for D_1 and D_2 (Fig. 10.36(a) and (b)) and reveal the energy position of quasibound states, which are responsible for the conductance drops (Choi et al. 2000). The charge density contour plot (Fig. 10.36(c)) represents the electronic state incident from the left and totally reflected by the quasibound state at the energy indicated by an arrow in Fig. 10.36(b). The backscattering associated with quasibound states is a general mechanism. The acceptor, donor, and neutral characteristics reported respectively for the D_1, D_2, and $D_{3/4}$ topologies are actually very robust regardless of the ribbon width. However, the broadening of the conductance dips is expected to decrease for larger ribbon widths. The intensity of the observed electron–hole conductance asymmetry is thus likely to depend on the actual ribbon geometry.

The high chemical reactivity of defects such as D_1 and D_2 is further explored by assuming a dehydrogenation of the carbon atom sitting at the edge. Resulting conductance profiles for the new defects D_{1H} (Fig. 10.36(f)) and D_{2H} (Fig. 10.36(g)) strongly differ from the monohydrogenated cases (D_1 and D_2). Indeed, in the presence of additional passivation, the conductance is fully restored for D_{1H}, whereas the signature for D_{2H} becomes similar to that of D_3. In both cases, the initial strong reduction of electron or hole conductance is markedly suppressed, suggesting a possibility to tune the transport properties from a metallic to a truly insulating state (or vice versa) upon varying the coverage of monatomic hydrogen, as discussed experimentally for 2D graphene (Bostwick et al. 2009).

The Clar's sextet representation (Clar 1964, 1972) (Fig. 10.36 (insets)) provides a pictorial scheme to understand the impact of edge defects (Baldoni et al. 2008) on transport properties. Clar's theory proposes a simplified description of the π electronic structure of hydrocarbons on the basis of the resonance patterns that maximize the number of benzenoid sextets drawn for the system. The benzenoid sextets, depicted as plain circles in the insets of Fig. 10.36, are defined as the carbon hexagons that stem from the resonance between two Kekulé structures with alternating single and double bonds. These are associated with a benzene-like delocalization of the π electrons over the carbon ring. As a consequence, Clar's representation gives direct insights into the aromaticity of the π electronic structure. According to Clar's theory, pristine aGNRs are fully benzenoid (i.e., all π orbitals are involved in a benzenoid sextet). This ideal picture is not preserved in the presence of defects. Upon introduction of the D_1 and D_2 topologies, the bonding of the aGNR can be seen as the superposition of two mirroring Kekulé structures that partially destroy the benzenoid character of the aGNRs (Fig. 10.36(a) and (b)). By increasing the localization of π electrons in carbon–carbon double bonds, such defects destroy the local aromaticity at the ribbon edge and are thus expected to have a large effect on the π–π^* conduction channels. On the contrary, the dihydrogenation of both defects D_1 and D_2 fully restores the benzenoid character of the ribbon, as illustrated by Clar's sextet representations (Fig. 10.36(f) and (g)).

To further substantiate the effect of these topological defects on the mesoscopic transport properties, the behavior of long disordered aGNRs is explored with random distribution of edge defects. In Fig. 10.36, the conductance of 500 nm long disordered aGNRs containing 30 defects (light gray lines) is superimposed onto the single defect

results (dark gray lines). Computed conductances are averaged over 20 different disorder configurations. The original conductance fingerprints of the defects considered are further amplified when longitudinal disorder is introduced, resulting for D_1 (D_2), in an almost fully suppressed hole (electron) conduction for low defect density.

As mentioned earlier, *ab initio* transport calculations are highly computationally demanding, and the development of an accurate *tight-binding* (TB) model is therefore extremely useful for achieving a complete mesoscopic study. Consequently, most studies dedicated to edge disorder in GNRs rely on a simple topological nearest-neighbor TB Hamiltonian. However, when compared to *ab initio* results, this turns out to generally yield a wrong description of transport properties in the case of non-neutral defects.

Figure 10.37 showns the conductance profiles of three defects (D_1, D_2, and D_4) computed either within a topological TB model (black solid lines) or within an adjusted TB model (gray solid lines). Although the agreement between *ab initio* and topological TB results is good for the D_4 defect, strong discrepancies are observed for D_1 and D_2 defects. In the latter cases, the topological model leads to a severe underestimation of the backscattering efficiency. The fitting of the TB parameters from *ab initio* calculations directly by adjusting the conductance profiles for a single defect is definitely more accurate (Avriller et al. 2007).

Within the fitted TB model, the transport properties of disordered aGNRs are investigated by considering lengths varying up to $L = 5$ μm and random distribution of defects

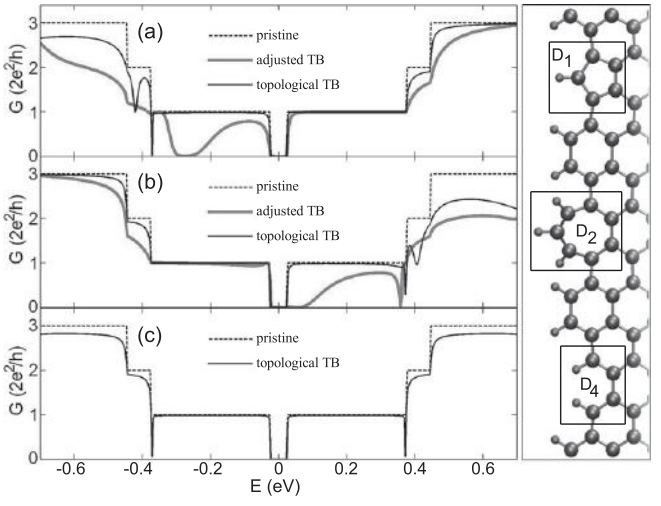

Figure 10.37 Conductance profiles of 35-aGNR for three isolated defects: (a) D_1, (b) D_2, and (c) D_4. Ball-and-stick models of the defects are illustrated on the right. Black dashed lines represent the conductance of the pristine ribbon. The *ab initio* computed curves are shown in light gray solid curve. Black and dark gray lines correspond to the topological and fitted TB models, respectively. (Adapted with permission from Dubois et al. (2010). Copyright (2010) American Chemical Society)

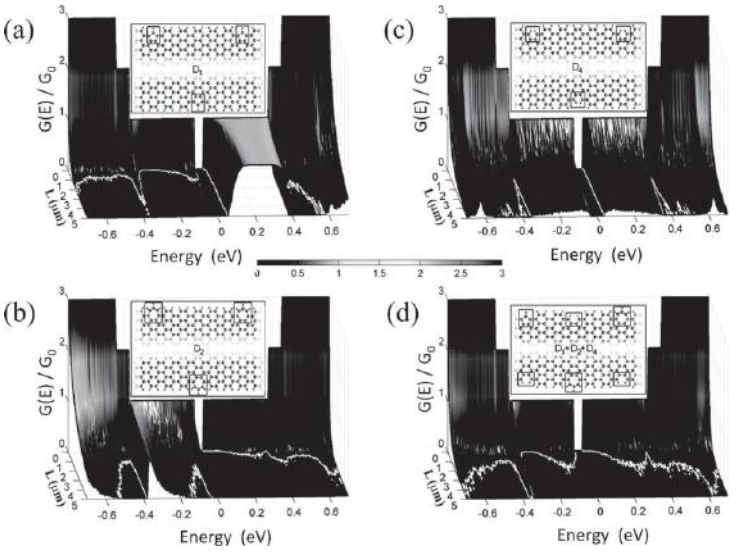

Figure 10.38 Conductance of a 35-aGNR with a 6×10^{-2} nm^{-1} density of (a) D_1 defects, (b) D_2 defects, (c) D_4 defects, and (d) mix of $\{D_1, D_2, D_4\}$ defects. The conductance is given as a function of the carrier energy and the length of the ribbon (L). $G(L, E)$ has been averaged over 100 different defect distributions. The white lines delineate the (L, E) regions for which the conductance value $G \leq 0.01 G_0$ (criterion for the experimental conduction gap). (Adapted with permission from Dubois et al. (2010). Copyright (2010) American Chemical Society)

with a density of 6×10^{-2} nm^{-1}. Figure 10.38 shows the conductance of long disordered aGNRs (averaged over 100 different configurations) as a function of energy and ribbon length. Also, the regions of the (L, E) plane where the conductance is experimentally insignificant (i.e., $G(E) \leq 0.01 G_0$ (Han et al. 2007)) are delineated by white lines, allowing determination of the length-dependent conduction gaps.

In the presence of charged defects (i.e., pentagon (D_1) and heptagon (D_2) defects), the conductance scaling behavior of long disordered aGNRs presents a striking electron–hole asymmetry. Figure 10.38(a) and (b) clearly shows that depending on the energy at which carriers are injected, the electronic transport ranges from ballistic to localized regimes. In D_1-defected aGNRs (Fig. 10.38(a)), the propagation of electrons in the first plateau remains quasiballistic up to a length $L > 5\,\mu$m. As a consequence of the acceptor character of D_1 defects, the hole conduction, in the same energy window, is almost fully suppressed for length $L < 0.5\,\mu$m. In contrast, in the presence of D_2 defects (Fig. 10.38(b)), holes in the first plateau remain conductive up to length $L > 5\,\mu$m, while the donor character of the D_2 defects suppresses electron conduction in the same energy window. Obviously, such disordered edge-defect profiles with a single defect type are rather unlikely, but this example shows however that spectacular fluctuations of transport length scales occur in some specific situations.

The comparison with more realistic defect distributions is rather instructive. Indeed, the conductance scaling in the presence of a random distribution of D_4 defects, and a

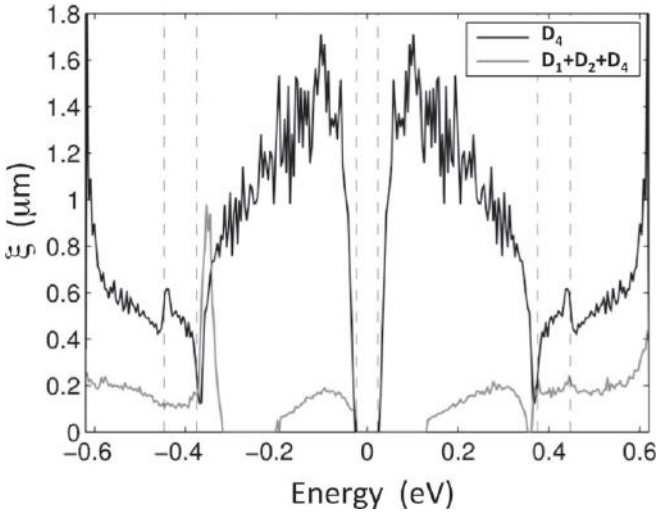

Figure 10.39 Localization length ξ for a 35-aGNR with a 6×10^{-2} nm^{-1} density of D_4 defects (dark gray solid line) and a mix of $\{D_1, D_2, D_4\}$ defects (light gray solid line). The vertical dashed lines correspond to the position of the van Hove singularities. ξ for the D_4 defects is up to almost one order of magnitude longer than in the case of mixed defects. (Adapted with permission from Dubois et al. (2010). Copyright (2010) American Chemical Society)

mix of three types of defects $\{D_1, D_2, D_4\}$ is detailed for the same edge-defect density in Fig. 10.38(c) and Fig. 10.38(d), respectively. For both defect distributions, the conductance decay is rather homogeneous within the first electron and hole plateaus. However, while the marked electron–hole asymmetries associated with the D_1 and D_2 defects compensate each other, the presence of odd-membered rings continues to crucially impact the electron and hole localization. This can be seen by looking at the white line in the (L, E) plane. The presence of defects noncompliant with the benzenoid character of aGNRs (i.e., D_1 and D_2) thus appears to strongly affect the ballistic propagation of carriers, even for low defect concentration (Dubois et al. 2010). This has been further emphasized by the estimated localization lengths that are shown in Fig. 10.39 as a function of the carrier energy.

While the distribution of D_4 defects gives rise to a localization length $\xi \sim 1\,\mu$m for low-energy carriers, the introduction of charged defects strongly reduces the average value in the $[-0.5, 0.5]$ eV energy window. Note that the fluctuations of ξ in correspondence with the van Hove singularities for D_1 defects are due to the increased scattering induced by the high DOS at these points. In the case of the mixed disorder, these fluctuations are absent or considerably reduced owing to the strong smearing effect that disorder produces in the DOS.

At last, recent outbreaks in bottom-up chemical techniques have demonstrated the synthesis of atomically perfect zigzag graphene nanoribbons (zGNRs) (Wang, Talirz et al. 2016) and of their corresponding analogs with phenyl-edge functionalization (Ruffieux et al. 2016). Indeed, as depicted in Fig. 10.40(a), the monomer

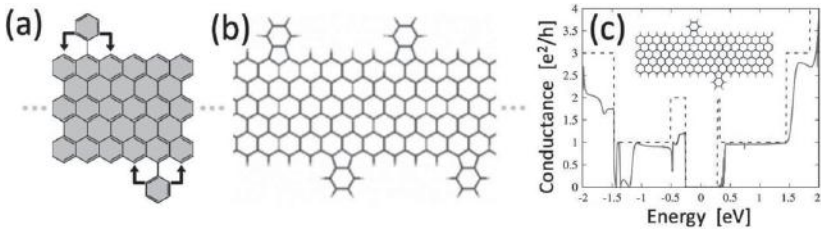

Figure 10.40 (a) Periodic 6-zGNRs with phenyl-edge defects before cyclodehydrogenation as obtained by Ruffieux et al. 2016. This structure is not stable and during the cyclodehydrogenation process, the phenyl groups undergo ring closure, falling either on one or the other side, possibly leading to ideal structures as in (b). (c) Spin-dependent conductance spectra for 6-zGNRs with phenyl groups located on their edges, as illustrated on the inset. (Adapted with permission from Salemi et al. (2018). Copyright (2018) American Physical Society)

used would at first glance yield a perfectly periodic 1D structure. However, during the cyclodehydrogenation process, the phenyl groups undergo ring closure, which can happen toward two directions, inducing either perfectly periodic or also possibly nonperiodic nanoribbons. These phenyl defects are strictly localized along the edges and do not modify the global structure of the ribbon (Fig. 10.40(b)). Since edge-localized states are responsible for magnetic properties of zGNRs, the effect of such phenyl-edge defects might lead to interesting spin-dependent transport properties. Using first-principle calculations and a Landauer-Bttiker approach, the spin-dependent electronic transmissions have been predicted for various phenyl-edge-modified zGNRs (Salemi et al. 2018). Figure 10.40(c) presents the conductance of a 6-zGNR with phenyl groups located at specific positions on both edges. Theoretical results suggest that the control of phenyl decoration at the zigzag edges could accurately tune the spin-polarized currents generated at the edges of the zGNRs (Salemi et al. 2018). Consequently, edge-engineering, with atomically controlled process, could open a new route to tailor the spin-dependent properties of these zGNRs, opening the way to design novel devices for future spintronics applications.

In summary, the electronic and quantum transport properties of edge-disordered graphene nanoribbons have been investigated using both fully *ab initio* techniques and accurately parameterized *tight-binding* models (Dubois et al. 2010). Single topological defects such as pentagons and heptagons have been predicted to induce a strong electron–hole transport asymmetry. Besides, conduction gaps driven by defect-induced localization effects have been found to depend not only on the defect density and ribbon length but also on the geometry and chemical reactivity of edge imperfections. The above analysis is drawn from physical processes that are general in essence. The scope of these results should therefore extend to realistic edge profiles. In particular, similar fluctuations of the conductance have been reported for other GNR topologies whose ground-state π electronic structure is aromatic according to Clar's rule. Note that the GNR topologies that come with partially filled states at the edge are known to break the graphene aromaticity (Wassmann et al. 2008). Therefore, the present

conclusions in terms of Clar's sextet theory are unlikely to apply for such ribbon geometries. In addition, hydrogenation has been identified as a possible new route to tune the robustness of the electronic conductance against edge roughness. As reported experimentally in graphene (Bostwick et al. 2009), the controlled deposition of monatomic hydrogen is a key ingredient in exploring a metal/insulator transition in these 1D materials.

10.5.11 Doped Graphene Nanoribbons

Finally, doping may also be used to tailor the electronic and transport properties of GNRs. In carbon-based materials, *p*-type (*n*-type) chemical doping can be achieved by boron (nitrogen) atom substitution within the carbon matrix, leading to interesting nanodevices, which are crucial for building logic functions and complex circuits (Derycke et al. 2001). As previously mentioned regarding metallic carbon nanotubes, boron (B) and nitrogen (N) impurities yield quasibound states that strongly backscatter propagating charge for specific resonance energies (Choi et al. 2000). In contrast with CNTs, doping in GNRs turns out to display even more complex features depending on the dopant position, ribbon width, and edge symmetry. Indeed, the energies of the quasibound states in GNRs are strongly dependent on the position of the impurity with respect to the ribbon edges (Biel, Triozon, Blase et al. 2009). Binding energies of the bound state associated with the broad drop in conductance are found to increase as the dopant approaches one of the edges of the ribbon. The large variation of resonant energies with dopant position indicates that random distribution of impurities will lead to a rather uniform reduction of conductance over the occupied states as part of the first conduction plateau (Biel, Triozon, Blase et al. 2009). These predictions are in sharp contrast to the case of CNTs where resonant energies do not depend on the position of the dopant around the tube circumference. In addition, doping effects are also found to depend on the ribbon symmetry and width, leading for example to a full suppression of backscattering for symmetry-preserving impurity potentials in armchair ribbons. Finally, chemical doping could be used to enlarge the bandgap of a fixed GNR width, resulting in the enhancement of device performances (Biel, Triozon, Niquet et al. 2009). All these predictions calculated in chemically doped GNRs are illustrated in the following.

The impact of substitutional (boron and nitrogen) doping and edge disorder can be investigated using first-principles methods. A self-consistent calculation (Biel, Triozon, Niquet et al. 2009) provides the profile of the scattering potential around the impurity location, which generally produces quasibound states strongly localized around the defect at a resonance energy. For a boron (nitrogen) impurity, an *ab initio* study can be first performed for the infinite armchair GNR, replacing one of the carbon atoms by the boron (or nitrogen) dopant. In a second step, the onsite and hopping self-consistent Hamiltonian matrix elements (on a localized basis set) are then used to build up the *tight-binding* Hamiltonian.

The *tight-binding* model is developed by adjusting the onsite and hopping self-consistent Hamiltonian matrix elements (on a localized basis set) in order to reproduce

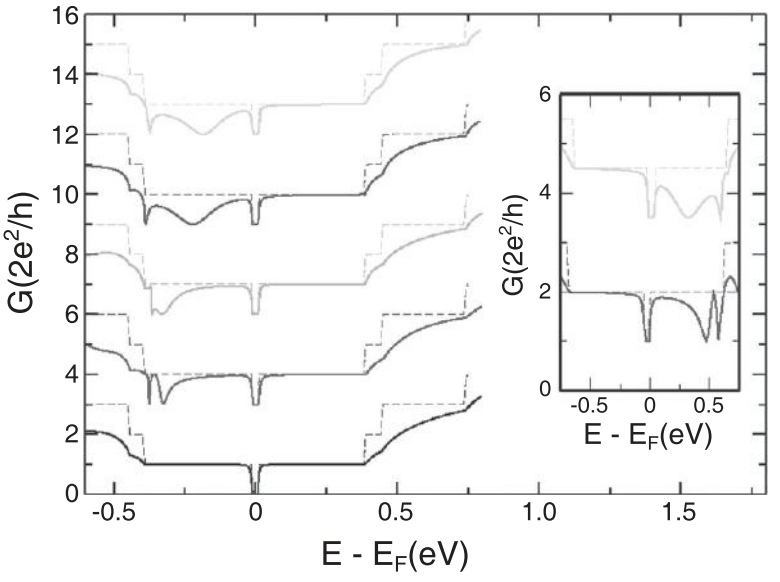

Figure 10.41 Main plot: Conductance for 35-aGNR and a single boron impurity displaced from the center to the ribbon edge (bottom to top). Conductance for the undoped case is given in dashed lines. Except for the bottom curve, all others have been upshifted for clarity. Insets: Same as in main plot for two selected nitrogen dopant positions (at the edge (top), and off-center (bottom) for the 20-aGNR). (Adapted from Biel, Triozon, Niquet et al. (2009))

the *ab initio* conductance fingerprints of a single impurity. This approach turns out to be much more accurate than a simple fit of band structure. Transport calculations based on the Landauer–Büttiker approach are then performed using these TB Hamiltonians, eventually taking into account a random distribution of impurities and disorder average.

Figure 10.41 shows the quantum conductance for a 35-aGNR as a function of energy for different positions of a single boron impurity along the lateral dimension of the ribbon. A large variation of resonant energies with dopant position is observed indicating an increase in binding energy of the bound state, a feature not previously observed in carbon nanotubes owing to rotation symmetry (Biel, Triozon, Blase et al. 2009). This feature also indicates that a random distribution of impurities will lead to a rather uniform reduction of conductance over the lowest energy window of occupied states.

An astonishing feature is the observation of full suppression of backscattering even in the presence of bound states, when the impurities are located exactly at the center of the ribbon. To understand such a symmetry effect, it is worth noting that GNRs do not always present a well-defined parity associated with mirror reflections with respect to their axis. An ideal odd-index aGNR retains a single mirror symmetry plane (perpendicular to the ribbon plane containing the ribbon axis), and its eigenstates thus present well-defined parity with respect to this symmetry plane. The eigenstates of the doped ribbon keep the same parity with respect to this mirror plane, provided that the potential induced by the dopant preserves this symmetry. For the case of an

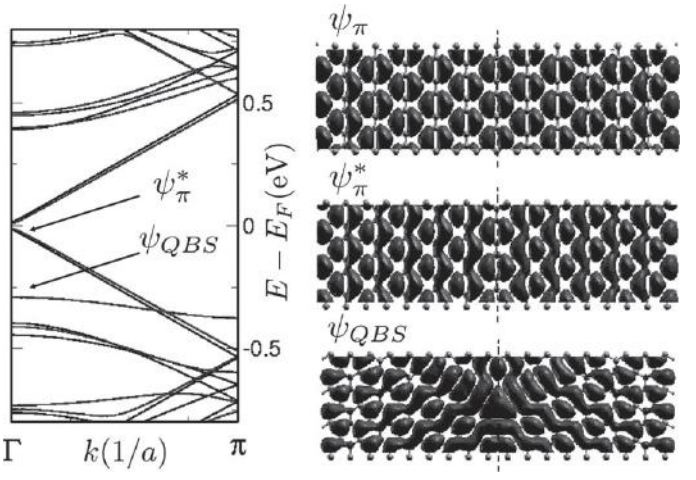

Figure 10.42 Left: Band structure of the 35-aGNR. Black lines correspond to the undoped ribbon; Gray lines correspond to the case of B at the center. Right: Real space projections of several eigenstates at Γ-point (dashed line denotes the ribbon axis). Ψ_π denotes the valence band state for pristine ribbon, Ψ_π^* for same energy but with a single B-defect at center of ribbon, and Ψ_{QSB} the projection of the quasibound state. Corresponding locations of the two latter states are indicated by arrows in the left panel. (Adapted from Biel, Triozon, Blase et al. (2009))

odd-index aGNR, this can only occur when the dopant is located exactly at the central dimer line, as seen in Fig. 10.42. The wavefunctions Ψ_π^*, at the Γ point associated with the first band below the charge neutrality point (CNP), and Ψ_{QSB} do not mix because of opposite parity, which suppress backscattering (Fig. 10.41, bottom curve). For any other position of the dopant, the well-defined parity of the wavefunctions is not preserved, and backscattering develops mainly at the position of the energy resonance of the quasibound state.

Let us examine the impact of different doping rates on ribbons of about 4 nm width, namely the pseudo-metallic 35-aGNR and the semiconducting 34-aGNR. Ribbons with a length up to 1 μm are considered, and impurities are uniformly distributed over the whole ribbon length and width, with a restriction preventing the overlap of the scattering potentials of individual dopants.

Figure 10.43 illustrates conductance as a function of energy for the (a) 35- and (b) 34-aGNRs, for doping rates between ≈0.02% and 0.1%. Here, electrodes are treated as semi-infinite and perfect GNRs, and disorder is included only in the region between the electrodes (channel). As a result of the acceptor-like character of the impurity states induced by the boron dopant, the conductance is affected in a clear asymmetric fashion for energy values below or above the CNP, as evidenced by the opening of a large mobility gap that extends well beyond the first conductance plateau below the small initial electronic bandgap. The mobility gap width reaches almost 1 eV, of the order of the silicon energy gap.

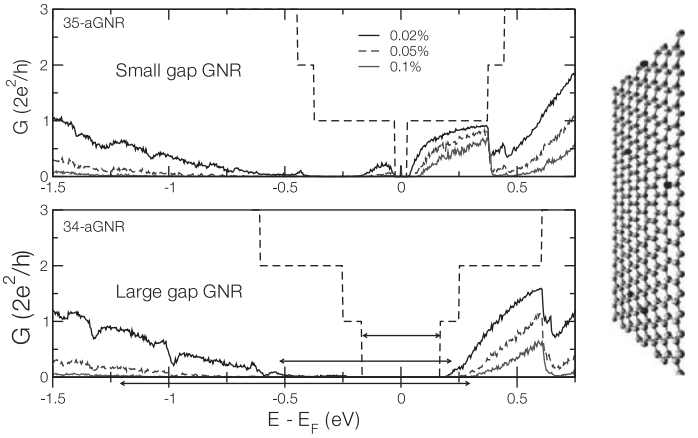

Figure 10.43 Average conductances as a function of energy for the pseudo-metallic 35-aGNR for doping rates ≈0.02%, 0.05%, and 0.1% (from top to bottom). The dashed black line corresponds to the ideal (undoped) case. Averages have been performed over ∼500 disorder realizations with a ribbon length of ≈ 1 μm. Bottom: Same for the semiconducting 34-aGNR. Right: A randomly doped GNR.

The asymmetry of the electron/hole conduction is also spectacularly evidenced by scrutinizing the energy-dependent transport regimes. Figure 10.44 shows the length dependence of the conductance for several configurations of randomly doped 35-aGNRs, with a doping rate of ≈0.05%, at an energy $= 0.25$ eV below (top panel) and above (bottom panel) the CNP. For energy values lying in the conduction band (bottom panel), the conductance for various random configurations is found to slowly decay with ribbon length with values $G \simeq G_0 = 2e^2/h$, indicating the robustness of a quasiballistic regime.

In contrast, for energies lying in the valence band (top panel), a strong exponential decrease of the conductance is observed (inset), with large fluctuations associated with different defect positions (main panel). The exponential decay of the conductance with the length of the ribbon is related to the Anderson localization, which has already been observed experimentally at room temperature in defected metallic carbon nanotubes (Gómez-Navarro et al. 2005), due to their long phase coherence lengths.

Figure 10.44 (inset) shows localization lengths (ξ) extracted from $\langle \ln G/G_0 \rangle = -\xi/L$ (with L the ribbon length) for hole transport at different doping rates. A statistical average over about 500 disorder samples is performed. The value of ξ ranges within 10–300 nm, depending on the ribbon width and doping density, and scales as $1/n_i$. The value of ξ is also observed to further increase with the ribbon width but in a nonlinear fashion, owing to the nonuniformity of the disorder potential with the dopant position.

Since the width of these GNRs is reaching the capability limits of standard lithographic techniques (as, for instance, produced by the IBM group (Chen et al. 2007)), it is interesting to study the case of aGNRs with widths of ≥10 nm, as for instance shown in Fig. 10.45 for an 80- and an 81-aGNR. This figure presents the conductance of a 10 nm

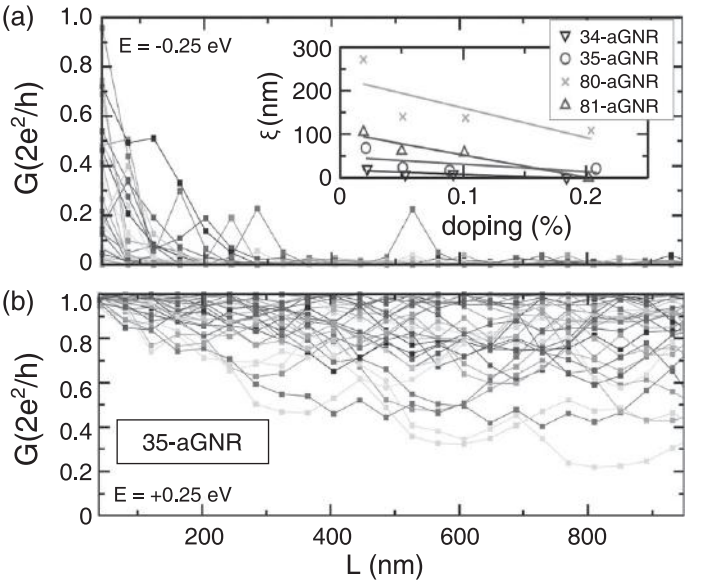

Figure 10.44 Conductances as a function of length for a set of doping realizations of the 35-aGNR at 0.25 eV below (a) and above (b) the CNP for a doping rate of $\approx 0.05\%$. Inset: Localization lengths as a function of doping rate for the 34- and 35-GNRs (at $E = -0.2$ eV), and for 80- and 81-aGNRs (at $E = -0.1$ eV). Solid lines are fits related to calculated values. (Adapted with permission from Biel, Triozon, Niquet et al. (2009). Copyright (2009) American Chemical Society)

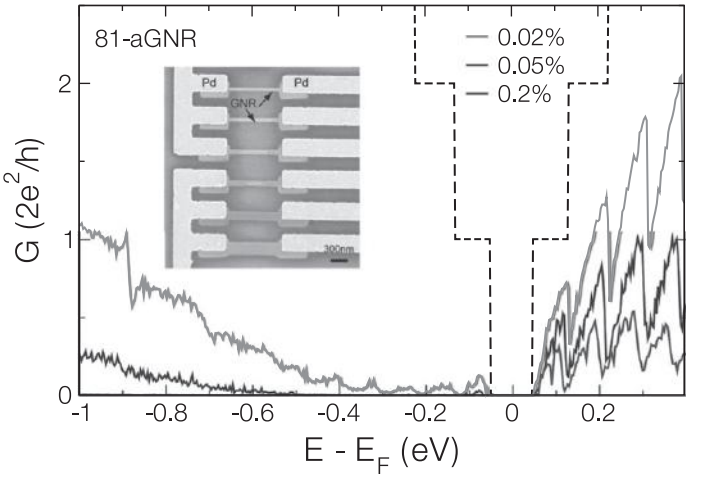

Figure 10.45 Main panel: Same as 10.44 for semiconducting 81-aGNR and three selected doping rates ($\approx$0.02%, 0.05% and 0.2%, from top to bottom). (Adapted with permission from Biel, Triozon, Niquet et al. 2009. Copyright (2009) American Chemical Society) Inset: SEM image of various patterned graphene nanoribbons fabricated by lithography. (Reprinted from Chen et al. (2007). Copyright (2007) with permission from Elsevier)

wide armchair nanoribbon with low boron doping. For a doping density of ≈0.2%, the ribbon manifests a mobility gap of about ∼1 eV. When lowering the doping level to 0.05%, the mobility gap reduces to about 0.5 eV and finally becomes less than 0.1 eV for lower density. The 0.2% case is obtained for a fixed nanoribbon width and length, so that optimization would be required upon upscaling either lateral or longitudinal sizes.

10.5.12 GNR-Based Networks

The controlled formation of narrow graphene strips with well-defined edges has been an intense topic of research. Significant progress in this direction has been achieved recently, as described in recent reviews (Jia et al. 2011; Terrones et al. 2010). Well-defined crystallographic edges displaying zigzag or armchair morphologies are byproducts of CVD-grown graphene inside a TEM after processing using Joule heating (Jia et al. 2009), by scanning tunneling lithography (Tapaszto et al. 2008), or through catalytic cutting (Ci et al. 2008; Datta et al. 2008). Large-scale synthesis of GNRs from the unzipping of carbon nanotubes along their axis has also been demonstrated (Terrones 2009; Terrones et al. 2010). In particular, plasma etching has been used to produce very narrow nanoribbons from single-wall carbon nanotubes (Jiao, Zhang et al. 2010; Ouyang et al. 2010; Wang & Dai 2010). The use of CNTs as starting material to produce GNRs presents the advantage that all the already available technology of CNT production can be exploited. In fact, arrays and networks of CNTs can be used to produce well-aligned arrays and networks of GNRs (Jiao, Zhang et al. 2010). Even though the edges of such nanoribbons are not atomically smooth, devices constructed with arrays of such nanoribbons display relatively high I_{ON} to I_{OFF} ratio. The nanoribbon cross-points have been suggested for use in applications in logic electronic devices. Based on the bottom-up fabrication of GNRs from the dehalogenation of self-assembled polyphenilenes, a controlled synthesis of a GNRs-based nanonetwork has been confirmed (Cai et al. 2010).

Focusing on systems that can be experimentally realized with existing techniques, both in-plane conductance in interconnected graphene nanoribbons and tunneling conductance in out-of-plane nanoribbon intersections have been studied (Botello-Méndez, Cruz-Silva et al. 2011). Both *ab initio* and semiempirical simulations confirm the possibility of designing graphene nanoribbon-based networks capable of guiding electrons along desired and predetermined paths. In addition, some of these intersections exhibit different transmission probability for spin-up and spin-down electrons, suggesting the possible applications of such networks as spin filters (Botello-Méndez, Cruz-Silva et al. 2011). Furthermore, the electron transport properties of out-of-plane nanoribbon cross-points of realistic sizes are described using a combination of first-principles and tight-binding approaches. The stacking angle between individual sheets is found to play a central role in dictating the electronic transmission probability within the networks.

As described in detail in the previous sections, the electronic transport properties of isolated aGNRs are sensitive to the shape of the edges and the ribbon width (Yang et al. 2007). These GNRs exhibit a bandgap E_g that decreases with the width. Con-

sequently, a region of zero conductance is observed in aGNRs due to the absence of conduction channels in the energy window around E_g. Conversely, the electronic band structure of zGNRs exhibits localized edge states close to the Fermi energy (E_F). The states extend along the edges and correspond to nonzero density of states at E_F and a high electronic conductance at the charge neutrality point. Spin-polarized calculations reveal that such edge states carry a finite magnetic moment with a ferromagnetic ordering along the edges but an antiferromagnetic ordering between them (Lee, Son et al. 2005). The interaction between the edges leads to a magnetic insulating ground state. The edge interaction and the bandgap decay with the GNR's width. As the width of the zGNR increases, such interaction weakens, and the difference in energy between the parallel and antiparallel spin ordering along the edges disappears. Therefore, the spin-polarized electron conductance of a narrow zGNR exhibits vanishing conduction around the charge neutrality point, and two sharp peaks of conductance due to the presence of edge states.

The conductance across continuous or in-plane networks of GNRs has already been investigated using a simple single-orbital nearest-neighbor *tight-binding* method (Areshkin & White 2007; Jayasekera & Mintmire 2007). The properties of in-plane cross-points are found to be very sensitive to the geometry of the junction. Notably, under such an approximation, which does not consider spin degrees of freedom, the conductance along a zGNR and across a cross-point exhibits high conductance ($\sim 0.8 G_0$) (Jayasekera & Mintmire 2007). In contrast, *ab initio* simulations (Botello-Méndez, Cruz-Silva et al. 2011) indicate that the electronic transport of GNRs is significantly affected when they are assembled into networks or branches. A notable exception is the cross-point between two zGNR terminals, forming an angle of 60° in which the scattering is minimal, as illustrated in Fig. 10.46 along the (1–4) or (2–3) path, respectively.

First-principles spin-polarized calculations reveal that these 60° intersections have interesting spin transmission behavior. In order to comply with the periodic boundary conditions, the most stable configuration (illustrated in Fig. 10.46(b)) exhibits different spin alignment at the edges of the two 60° turns at the intersection. The existence of the antiferromagnetic state combined with the presence of the junction effectively breaks the left–right symmetry (Fig. 10.46(b)). As a consequence, the transmission probability is different for the two spin channels. For instance, the low-energy spin-up electron conductance along the 1–4 path is significantly higher than the spin-down conductance along this path (compare the light gray lines in Fig. 10.46(c,d)). Opposite behavior is observed for the 2–3 paths. However, note that the symmetric pathways in the total conductance are retrieved (the sum of spin-up and spin-down contribution).

An alternative arrangement for GNR networks is through out-of-plane or bilayer cross-points. In these cases, the interaction between the two GNRs is weak, and the changes in conductance across the GNRs and the conductance between them are driven by tunneling across the GNR cross-point (Botello-Méndez, Cruz-Silva et al. 2011). As illustrated in Fig. 10.47, this hypothesis is confirmed by the *ab initio* quantum conductance along and across two zGNRs. At the cross-point between two 6-zGNRs,

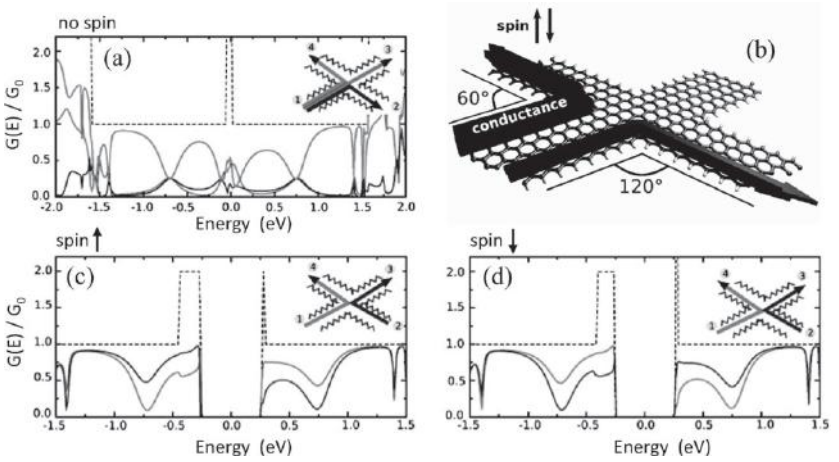

Figure 10.46 (a) *Ab initio* quantum conductance of an in-plane cross-point between two 5-zGNRs for various transmission paths (paramagnetic state–non-spin-polarized calculation). The dark gray and light gray arrows in the inset represent the spin configuration corresponding to the curves shown in (c, d). (b) Ball-and-stick representation of the zGNR intersection. Spin-dependent conductances are found to be higher along specific paths of the cross-point. (c, d) Spin-polarized *ab initio* quantum conductance of a zGNR as represented in (b). Note the different spin-up and spin-down transmission probabilities along the same path (e.g., 1–4). While the total transmission (spin up + spin down) is symmetric along various paths, the spin state effectively breaks the structure's symmetry (i.e., vertical C_2 axis), yielding a spin-dependent conductance. The dashed gray line represents the conductance of an isolated 5-zGNR in the corresponding spin state. (Adapted with permission from Botello-Méndez, Cruz-Silva et al. (2011). Copyright (2009) American Chemical Society)

the conductance along the GNR is mainly preserved. Indeed, the loss of transmitted electrons through tunneling at a cross-point is almost nonexistent, regardless of their spin polarizations (Fig. 10.47(b)). However, there is only very little tunneling for the single electron channel across the two 6-zGNRs. Only the electrons localized at the edges tunnel across the GNRs (Fig. 10.47(c)).

First-principles calculations are frequently limited by computational resources to investigate routinely the transport properties of realistic nanoribbon networks, which include a much larger number of atoms than the systems studied above. For this reason, a single-band *tight-binding* model based on a Slonczewski–Weiss–McClure (SWMC)-like parameterization (Slonczewski & Weiss 1958) has been proposed to investigate larger systems (Botello-Méndez, Cruz-Silva et al. 2011). In order to describe accurately the properties of graphene and GNRs, interactions up to the third-nearest neighbor (White et al. 2007) have to be considered by setting a cutoff interaction of 3.7 Å, and an exponential decay of the hopping parameter of the form $e^{-\eta(d-d_0)}$, where d is the separation between two carbon atoms and d_0 is the C–C equilibrium distance (1.42 Å for in-plane interactions, and 3.35 Å for out-of-plane interactions). Different hopping parameters (γ_0) have been used for the A and B sites of the carbon hexagonal

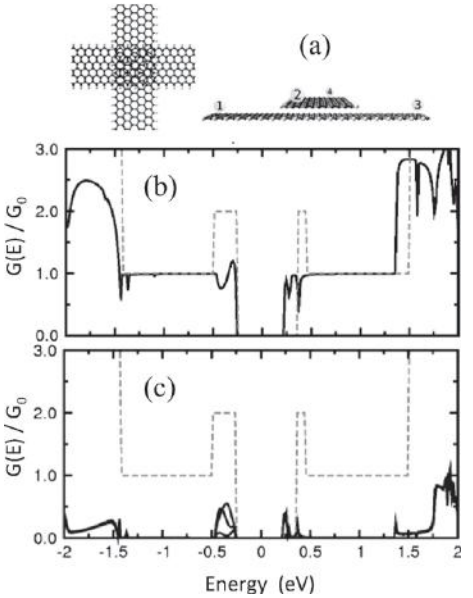

Figure 10.47 (a) Ball-and-stick models of an out-of-plane conducting zGNR network composed of two 6-zGNRs (four terminals are present). *Ab initio* quantum conductance along (b) and across (c) out-of-plane zGNR networks depicted in (a). The dashed lines represent the conductance of isolated GNRs. Note that the small tunneling current (c) between the zGNRs depends on the type of intersection and the localization of the electrons at a particular energy (e.g., edge states). (Adapted with permission from Botello-Méndez, Cruz-Silva et al. (2011). Copyright (2009) American Chemical Society)

lattice in graphene. In order to properly describe the bandgap of GNRs, corrections to the onsite (ε) and hopping parameters of edge atoms (γ_{edge}), and their interaction with other atoms have to be included (Gunlycke & White 2008). One TB parameter has also been used for the out-of-plane interactions (γ_1). Starting from such a model, the numerical values of the onsite and hopping parameters can be fine-tuned using an evolutionary algorithm: the fitness function being defined as a weighted error of the calculated band structure with respect to the first-principles DFT-PBE band structure calculations. The weight has to be chosen in order to minimize the error at low energies. The *ab initio* band structures of graphene, GNRs, bilayer graphene, and GNR networks have been used as references, confirming a satisfactory agreement with the TB model, in the energy region close to the charge neutrality point (Botello-Méndez, Cruz-Silva et al. 2011).

In addition, DFT calculations within the LDA or GGA approximation are known to underestimate the weak attraction between graphene layers (Dion et al. 2004). However, the exponential decay of this TB approach can successfully model the difference of interaction between the *AA* and *AB* stacking within GNR cross-points, fixing a separation distance between the layers to 3.35 Å (which corresponds to the experimental values of the *AB* stacking in graphite). Starting from a cross-point, an armchair nanoribbon can

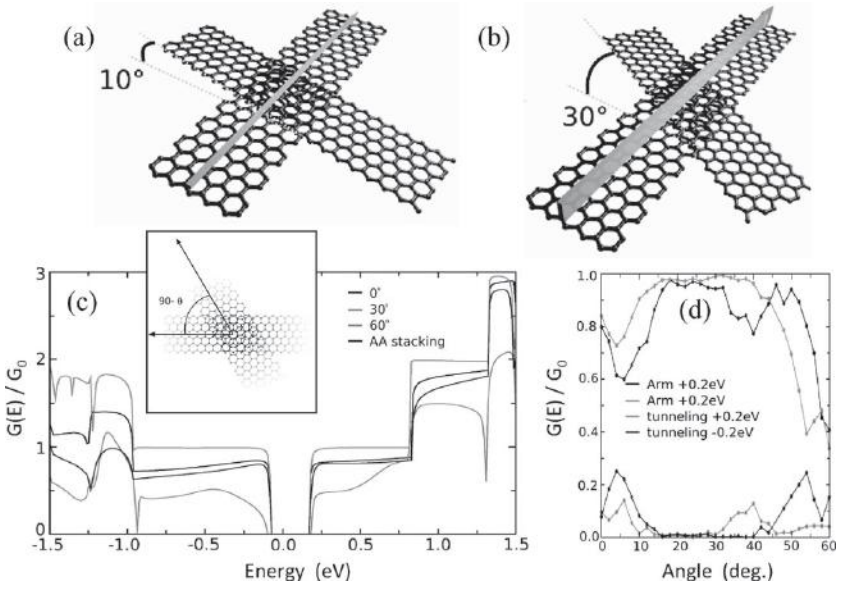

Figure 10.48 Quantum conductance through an aGNR/zGNR out-of-plane cross-point as a function of the stacking angle θ. Atomic models depicting an 11-aGNR and a 6-zGNR intersecting at (a) 10° and (b) 30°. (c) Conductances along the aGNR at the cross-point for various intersection angles compared to *AA* stacking when $\theta = 90°$ (see inset). (d) Quantum conduction as a function of the stacking angle θ for an aGNR/zGNR cross-point with a ∼5 nm width. (Adapted with permission from Botello-Méndez, Cruz-Silva et al. (2011). Copyright (2009) American Chemical Society.)

be rotated by an angle θ, as shown in Fig. 10.48. The conductance along and across the nanoribbons is found to strongly depend on this specific stacking angle θ.

Figure 10.48(d) presents the conductance at ± 0.5 eV as a function of the stacking angle θ both along the 11-aGNR, and across this aGNR through a 6-zGNR each with a width of ∼5 nm. A maximum of conductance along the aGNR is observed for θ values around 30° with almost a 10-fold increase compared to its value at $\theta = 0°$ for -0.5 eV. Such an increase is due to the fact that the interaction between the GNRs is minimal at $\theta = 30°$. Conversely, at $\theta \gg 30°$, the overlap and interaction between the GNRs increase, thus enhancing the tunneling probability and increasing the scattering in the isolated GNR. A similar behavior is observed for different energies for selected stacking angles (Fig. 10.48(c)). A direct comparison between the *AA* and *AB* stacking is also presented in Fig. 10.48(c), for an 11-aGNR/6-zGNR intersection, suggesting that the effect of different stacking orders at $\theta = 0°$ has less impact on the conductance than the stacking angle.

In summary, first-principles and *tight-binding* calculations performed on a number of GNR cross-points (Botello-Méndez, Cruz-Silva et al. 2011) and their quantum transport properties indicate that GNR networks are appealing for potential applications and could play an important role in the development of carbon-based electronics. The quantum

transport through in-plane GNR cross-points has been found to be severely scattered at the intersections, except for 60° zGNR terminals, confirming that patterned graphene and GNRs could be used for functional devices and current flux guides (Romo-Herrera et al. 2008). In addition, the transmission probability at these intersections is different for spin-up and spin-down electrons, suggesting the possibility of their use as spin filters. Furthermore, the tunneling transmission at the intersection of bilayer GNR networks is calculated to be very sensitive to the stacking angle between the ribbons. The edge-state channels are remarkably robust and could be tuned with an external electric field in order to induce tunneling from an aGNR, thus allowing future development in band-to-band tunneling GNR-based transistors (Schwierz 2010).

10.6 Conclusion

In conclusion, the present chapter has overviewed some basics of electronic and quantum transport properties in low-dimensional carbon-based materials including 2D graphene, graphene nanoribbons, and carbon nanotubes. Although CNTs and GNRs share similar electronic confinement properties due to their nanoscale lateral sizes, the effects of boundary conditions in the perpendicular direction with respect to the system axis trigger very different electronic and transport properties. For each nanostructure, a simple *tight-binding* approach (single-band model) has been proposed to describe their specific electronic behavior, and, when necessary, *ab initio* calculations have been used to accurately complete the picture. Both 1D systems have also been perturbed using topological defects (vacancies, adatoms), multi-structures and stacking, chemical doping and functionalization to tailor their electronic structure, etc. The effects of these topological, chemical, structural perturbations on the quantum transport of both CNTs and GNRs have been predicted.

To conclude, because of their remarkable electronic properties and structural physical properties, CNTs or GNRs are expected to play an important role in the future of nanoscale electronics. Not only can nanotubes be metallic, but they are mechanically very stable and strong, and their carrier mobility is equivalent to that of good metals, suggesting that they would make ideal interconnects in nanosized devices. Further, the intrinsic semiconducting character of other tubes, as controlled by their topology, allows us to build logic devices at the nanometer scale, as already demonstrated in many laboratories. Similarly the combination of 2D graphene for interconnects together with graphene nanoribbons for active field-effect transistor devices could allow completely carbon-made nanoelectronics.

The complete understanding of fundamental electronic and transport concepts in low-dimensional carbon-based nanomaterials definitely needs theoretical modeling and advanced quantum simulation, together with joint studies with experiments. Theory has been very important to initiate, validate, and orientate carbon nanotube science, particularly as far as electronic properties are concerned. Yet, in 1992, one year after the discovery of nanotubes by S. Iijima, several groups theoretically predicted their

unique behavior as metals or semiconductors. Similarly, the electronic properties of 2D graphene and graphene ribbons were explored decades before the fabrication of those nanostructures. Since carbon-based nanomaterials have still probably not revealed all their secrets, numerical simulations still have successful days to come in predicting new interesting atomic topologies and their corresponding structural and electronic properties, thus expanding their potential impact in carbon science.

10.7 Further Reading

- See Roche et al. (2006) and Cresti et al. (2008).

Appendix A Electronic Structure Calculations: The Density Functional Theory (DFT)

A.1 Introduction

Over the last few decades, there has been a significant increase in the use of computational simulation within the scientific community. Through a combination of the phenomenal boost in computational processing power and continuing algorithm development, atomistic scale modeling has become a valuable asset, providing a useful insight into the properties of atoms, molecules, and solids on a scale "often inaccessible" to traditional experimental investigation.

Atomistic simulations can be divided into two main categories, quantum mechanical calculations and classical calculations based on empirical parameters. Quantum mechanical simulations (often referred to as *ab initio* or first-principles) aim at solving the many-body Schrödinger equation (Schrödinger 1926). The original reformulation of the Schrödinger equation offered by the DFT provides valuable information on the electronic structure of the system studied.

The very essence of DFT is to deal with noncorrelated single-particle wavefunctions. Many of the chemical and electronic properties of molecules and solids are determined by electrons interacting with each other and with the atomic nuclei. In DFT, the knowledge of the average electron density of the electrons at all points in space is enough to determine the total energy from which other properties of the system can also be deduced. DFT is based on the one-electron theory and shares many similarities with the Hartree–Fock method. DFT is presently the most successful and promising (also the most widely used) approach to computing the electronic structure of matter. In this appendix, the basics of DFT modeling techniques are explained.

A.2 Overview of the Approximations

A.2.1 The Schrödinger Equation

In principle, an exact theory for a system of ions and interacting electrons is based on solving the many-body Schrödinger equation for the corresponding wavefunction (Schrödinger 1926). The wavefunction of a many-body system consisting of interacting electrons and nuclei can be defined as $\Psi(\{\mathbf{r}_i\},\{\mathbf{R}_I\})$, where $\{\mathbf{r}_i\}$ and $\{\mathbf{R}_I\}$ correspond

to the electronic and nuclear coordinates, respectively. In the framework of a nonrelativistic, time-independent approximation, the Schrödinger equation of a system is as follows:

$$\hat{H}\Psi(\{\mathbf{r}_i\},\{\mathbf{R}_I\}) = E\Psi(\{\mathbf{r}_i\},\{\mathbf{R}_I\}), \tag{A.1}$$

where $\hat{H}$ is the time-independent Hamiltonian operator and E is the energy of the system. The Hamiltonian that describes the physics of this many-body system, neglecting the relativistic effects, is given by

$$\begin{aligned}\hat{H} = &-\frac{\hbar^2}{2m_e}\sum_{i}^{N_e}\nabla_i^2 - \frac{\hbar^2}{2M_I}\sum_{I}^{N_n}\nabla_I^2 + \frac{1}{2}\sum_{I\neq J}^{N_n}\frac{Z_I Z_J e^2}{|\mathbf{R}_I - \mathbf{R}_J|}\\ &+\sum_{i}^{N_e}\frac{Z_I e^2}{|\mathbf{r}_i - \mathbf{R}_I|} + \sum_{I}^{N_n}\frac{Z_I e^2}{|\mathbf{r}_i - \mathbf{R}_I|} + \frac{1}{2}\sum_{i\neq j}^{N_e}\frac{e^2}{|\mathbf{r}_i - \mathbf{r}_j|}.\end{aligned} \tag{A.2}$$

Here, the atomic cores and the electrons are referred to by the capital and small indexes, respectively. The index i sums over the number of electrons N_e with mass m_e, and the index I sums over the number of nuclei N_n, with corresponding mass M_I. The first two terms of Eq. (A.2) represent the kinetic energies of all the electrons and nuclei, respectively. The remaining terms represent the electrostatic interactions that occur among the particles of the system: the repulsion between the nuclei, the electron–nucleus, and the repulsive electron–electron Coulomb interactions, respectively. Equation (A.2) can be written in a compact way when considering T and V for kinetic and potential energies, respectively:

$$\begin{aligned}\hat{H} = &\, T_e(\{\mathbf{r}_i\}) + T_n(\{\mathbf{R}_I\}) + V_{\mathrm{n-n}}(\{\mathbf{R}_I\})\\ &+ V_{\mathrm{e-n}}(\{\mathbf{r}_i\},\{\mathbf{R}_I\}) + V_{\mathrm{e-e}}(\{\mathbf{r}_i\}).\end{aligned} \tag{A.3}$$

Ever since the Schrödinger equation was discovered, it has been a dream of researchers to find reasonable approximations to reduce its complexity. The first important approximation is obtained by decoupling the dynamics of the electrons and the nuclei, which is known as the Born–Oppenheimer approximation (Born & Oppenheimer 1927).

A.2.2 The Born–Oppenheimer Approximation

The Born–Oppenheimer approximation exploits the fact that the nuclei are much heavier than the electrons (Born & Oppenheimer 1927). This is true even for the lightest nucleus, a proton whose mass is approximately 1800 times larger than the electron. Hence, in most cases, the timescale of the electron response is a few orders of magnitude faster than that of nuclei, which allows the dynamics of the electrons and nuclei to be decoupled. As a consequence of this approximation, nuclei and electrons can be treated separately. The electrons are evolving in the field of fixed nuclei with Hamiltonian ($\hat{H}_e$) expressed as

$$\hat{H}_e = T_e(\{\mathbf{r}_i\}) + V_{\mathrm{e-n}}(\{\mathbf{r}_i\}, \{\mathbf{R}_I\}) + V_{\mathrm{e-e}}(\{\mathbf{r}_i\}). \tag{A.4}$$

The solution to a Schrödinger equation involving the previous $\hat{H}_e$ is

$$\hat{H}_e \Psi_e(\{\mathbf{r}_i, \sigma_i\}, \{\mathbf{R}_I\}) = E_e \Psi_e(\{\mathbf{r}_i, \sigma_i\}, \{\mathbf{R}_I\}), \tag{A.5}$$

where Ψ_e represents the electronic wavefunction. The latter is a function only of the electronic coordinates $\{\mathbf{r}_i\}$, while it depends parametrically on the set of nuclear coordinates $\{\mathbf{R}_I\}$ for a fixed configuration of the nuclei. Furthermore, for simplicity, the electronic spatial and spin coordinates $\{\mathbf{r}_i, \sigma_i\}$ are placed into one variable $\{\mathbf{x}_i\}$, so that Eq. (A.5) can be rewritten as

$$\hat{H}_e \Psi_e(\{\mathbf{x}_i\}) = E_e \Psi_e(\{\mathbf{x}_i\}). \tag{A.6}$$

The total energy E_{tot}, for given positions of the nuclei, corresponds to the sum of the E_e and the nuclear repulsion energy from the third term in Eq. (A.2), leading to

$$E_{\mathrm{tot}} = E_e + V_{\mathrm{n-n}}(\{\mathbf{R}_I\}). \tag{A.7}$$

In summary, the Born–Oppenheimer approximation allows one to treat separately the nuclear and electronic degrees of freedom in the many-body problem. The major difficulty in solving Eq. (A.6) is the interaction between electrons, where all the many-body quantum effects are hidden. Since the movements of electrons are correlated, the instantaneous coordinates of each electron should be known, which essentially requires the treatment of 3^{N_e} variables for an N_e-electron system. Even after applying this simplification, the many-body problem remains intractable. Hence, further approximations are needed to efficiently solve Eq. (A.6).

A.2.3 The Hartree Approximation

The Hartree approximation (Hartree 1957) provides one way to reduce Eq. (A.6), the many-electron wavefunction problem, to a product of N_e one-electron wavefunctions. Each electron moves independently within its own orbital and sees only the average potential generated by all the other electrons. This Hartree potential can be approximated by an average single-particle potential and is expressed by the Coulomb repulsion between the ith electron and the electron density produced by all other electrons ($n(\mathbf{x}_j)$):

$$V_{\mathrm{H}}(\mathbf{x}_i) = \int \frac{n(\mathbf{x}_j)}{|\mathbf{r}_i - \mathbf{r}_j|} d\mathbf{x}_j, \; n(\mathbf{x}_j) = \sum_{j=1}^{N_e} |\phi_j(\mathbf{x}_j)|^2. \tag{A.8}$$

The solution to the one-particle wave-equation ($\psi_i(\mathbf{x}_i)$) is

$$\left[-\frac{\hbar}{2m} \nabla^2 + V_{\mathrm{ext}}(\mathbf{x}_i) + V_{\mathrm{H}}(\mathbf{x}_i) \right] \psi_i(\mathbf{x}_i) = \epsilon_i \psi_i(\mathbf{x}_i), \tag{A.9}$$

where the first term corresponds to the one-electron kinetic energy. In this equation, the effective potential experienced by the single electron includes two terms: the Hartree potential and the external Coulomb potential, given by

$$V_{\text{ext}}(\mathbf{x}_i) = V_{\text{e-n}}(\{\mathbf{x}_i\}, \{\mathbf{R}_I\}) + V_{\text{n-n}}(\{\mathbf{R}_I\}). \tag{A.10}$$

However, the equations are still nonlinear and the fermionic character of the electrons is ignored. According to the Pauli exclusion principle, two electrons cannot occupy the same quantum state. However, the wavefunction in Hartree theory is

$$\Psi(\mathbf{x}_i) = \prod_{i}^{N_e} \psi_i(\mathbf{x}_i), \tag{A.11}$$

and is not antisymmetric under the interchange of two electrons, which is incompatible with the Pauli principle. This problem is rectified by the Hartree–Fock theory.

A.2.4 The Hartree–Fock Approximation

The Hartree–Fock approach is considered as the fundamental first step in quantum chemistry. Indeed, the Hartree–Fock theory is derived by invoking the variational principle, which states that the expected value of the electronic Hamiltonian ($\hat{H}_e$) for any guessed or trial wavefunction is always greater than or equal to the electronic ground state energy $E_0[\Psi_0]$. This remains true when the wavefunction is in the true ground state Ψ_0, i.e., ($E[\Psi] \geq E_0[\Psi_0]$). The advantage of the variational principle is that the ground state energy $E_0[\Psi_0]$ can be approached by starting with a trial function, and the quality of the wavefunction can be improved variationally in the restricted antisymmetrized space of *single-particle* wavefunctions. The wavefunctions of Eq. (A.11) can be approximately described with a single Slater determinant. A Slater determinant is a linear combination of the product of independent electron wavefunctions ($\psi_i(\mathbf{x}_i)$) with all possible combinations of the permutations of their coordinates. The Slater determinant satisfies the antisymmetric property of the wavefunction, and hence obeys the exclusion principle of Pauli. The wavefunctions of Eq. (A.11) are replaced by

$$\Psi(\{\mathbf{x}_i\}) \approx \Psi_{\text{HF}}(\{\mathbf{x}_i\}) = \frac{1}{\sqrt{N_e!}} \begin{vmatrix} \psi_i(\mathbf{x}_i) & \psi_j(\mathbf{x}_i) & \cdots & \psi_{N_e}(\mathbf{x}_i) \\ \psi_i(\mathbf{x}_j) & \psi_j(\mathbf{x}_j) & \cdots & \psi_{N_e}(\mathbf{x}_j) \\ \vdots & \vdots & \ddots & \vdots \\ \psi_i(\mathbf{x}_{N_e}) & \psi_j(\mathbf{x}_{N_e}) & \cdots & \psi_{N_e}(\mathbf{x}_{N_e}) \end{vmatrix}, \tag{A.12}$$

constructed from a set of one-particle orbitals $\{\psi_i(\mathbf{x}_i)\}$ required to be mutually orthonormal $\langle\psi_i|\psi_j\rangle = \delta_{ij}$. Taking the expectation value of the electronic Hamiltonian $\hat{H}_e$ of Eq. (A.5) with the trial functions defined by the Slater determinant of Eq. (A.12), one gets the total electronic Hartree–Fock energy functional. The Hartree–Fock equation (Marx & Hutter 2000), which comes from an energy-minimization of the Hartree–Fock energy functional, is given by

$$\left[-\frac{\hbar}{2m_e}\nabla^2 + V_{\text{ext}}(\mathbf{x}_i) + V_H(\mathbf{x}_i) + V_X(\mathbf{x}_i)\right]\psi_i(\mathbf{x}_i) = \epsilon_i\psi_i(\mathbf{x}_i), \tag{A.13}$$

where now the exchange term is properly taken into account as

$$V_X(\mathbf{x}_i)\psi_i(\mathbf{x}_i) = -e^2\sum_j \psi_j(\mathbf{x}_i)\int d\mathbf{x}_j \frac{\psi_j^*(\mathbf{x}_j)\psi_i(\mathbf{x}_j)}{\mathbf{r}_i - \mathbf{r}_j}. \tag{A.14}$$

The exchange operator is defined via the action of the electrons on a particular orbital ψ_i. It is noticeable that upon action on orbital ψ_i, the exchange operator of the jth state "exchanges" $\psi_j(\mathbf{x}_j) \rightarrow \psi_i(\mathrm{x}_j)$ in the kernel as well as replaces $\psi_i(\mathbf{x}_i) \rightarrow \psi_j(\mathbf{x}_i)$ in its argument. Thus, the exchange term is a nonlocal operator, and in this sense, the exchange operator does not possess a simple classical interpretation like the Hartree term (Marx & Hutter 2000). A considerable amount of complexity is introduced in this nonlinear exchange operator due to the many-body interactions. This is true even for obtaining the first-order approximation of the total energy (Marx & Hutter 2000).

A.3 Density Functional Theory

DFT differs from other wavefunction-based methods by using the electron density $n(\mathbf{r})$ as the central quantity. An important advantage of using the electron density over the wavefunction is the much reduced dimensionality. Regardless of how many electrons are present in the system, the density is always three-dimensional. This allows DFT to be readily applied to much larger systems; hundreds or even thousands of atoms become possible. This is one among the many reasons why DFT has become the most widely used electronic structure approach today. First, the electron density can be expressed as

$$n(\mathbf{r}) = N_{\text{e}}\int |\Psi(\mathbf{x}_1, \mathbf{x}_2, \ldots, \mathbf{x}_{N_e})|^2 d\sigma_1 d\sigma_2 \ldots d\sigma_{N_e}, \tag{A.15}$$

where $\mathbf{x}_i$ represents both spatial and spin coordinates. $n(\mathbf{r})$ determines the probability of finding any of the N_e electrons within the volume $\mathbf{r}$. The electrons have arbitrary spin and the other $N_e - 1$ electrons have arbitrary positions and spin in the state represented by Ψ. This is a nonnegative simple function integrating the total number of electrons,

$$N_e = \int n(\mathbf{r})d\mathbf{r}. \tag{A.16}$$

A.3.1 The Thomas–Fermi Model

There have been many attempts to reformulate the problem based on the ground state charge density $n(\mathbf{r})$. Thomas and Fermi exploited first the fact that the electronic energy can be expressed in terms of electronic density (Fermi 1927; Thomas 1927). In their model, the kinetic energy of the electrons is derived from the quantum statistical theory

based on the uniform electron gas, whereas the electron–nucleus and electron–electron interactions are treated classically. Within this model, the total energy is a functional of $n(\mathbf{r})$ expressed as

$$E_{\mathrm{TF}}[n(\mathbf{r})] = \frac{3}{10}(2\pi^2)^{2/3}\int n^{3/5}(\mathbf{r})d\mathbf{r} - Z\int \frac{n(\mathbf{r})}{\mathbf{r}}dr + \frac{1}{2}\iint \frac{n_1(\mathbf{r})n_2(\mathbf{r})}{|\mathbf{r}_1 - \mathbf{r}_2|}d\mathbf{r}_1 d\mathbf{r}_2, \tag{A.17}$$

where the first term is the kinetic energy (i.e., the kinetic energy density for a system of noninteracting electrons with density n) while the second and third terms are the electron–nucleus and electron–electron interactions, respectively. Although it is not the most efficient, the Thomas–Fermi model illustrates that the ground state energy can be determined purely using the electron density.

A.3.2 The Hohenberg–Kohn Theorem

The essential role played by the electron density in the search for the electronic ground state was pointed out in 1964 by Hohenberg and Kohn (1964). They derived the fundamentals of DFT, which allows us to express the electronic Hamiltonian as a functional of $n(\mathbf{r})$. This formalism relies on two theorems: (i) there exists a one-to-one correspondence between external potential $\nu(\mathbf{r})$ and electron density $n(\mathbf{r})$, and (ii) the ground state electron density can be obtained by using a variational principle.

The electronic Hamiltonian depends explicitly on the configuration of the nuclei only through $\nu(\mathbf{r})$. Assuming that the first theorem is valid, then from $n(\mathbf{r})$ one can obtain $\nu(\mathbf{r})$ upto a trivial additive constant. The electronic Hamiltonian can be expressed as a functional of n(r). Suppose there is a collection of electrons enclosed in a box influenced by two external potentials $\nu(\mathbf{r})$ and $\nu'(\mathbf{r})$, which differs from $\nu(\mathbf{r})$ by more than a constant in a nondegenerated system (local system). Assuming that these two potentials lead to the same electron density $n(\mathbf{r})$ for the ground state, two different Hamiltonians $\hat{H}$ and $\hat{H}'$, whose ground state electron density is the same, are present. However, their normalized wavefunctions Ψ and Ψ' would be different. As a consequence, the ground state energy E_0 would be

$$E_0 < \langle\Psi'|\hat{H}|\Psi'\rangle = \langle\Psi'|\hat{H}'|\Psi'\rangle + \langle\Psi'|\hat{H} - \hat{H}'|\Psi'\rangle = E_0' + \int n(\mathbf{r})[\nu(\mathbf{r}) - \nu'(\mathbf{r})]d\mathbf{r}, \tag{A.18}$$

where E_0 and E_0' are the ground state energies for $\hat{H}$ and $\hat{H}'$, respectively. Similarly, E_0' would be

$$E_0' < \langle\Psi|\hat{H}|\Psi\rangle = \langle\Psi|\hat{H}'|\Psi\rangle + \langle\Psi|\hat{H}' - \hat{H}|\Psi\rangle = E_0 - \int n(r)[\nu(\mathbf{r}) - \nu'(\mathbf{r})]d\mathbf{r}. \tag{A.19}$$

Summing Eqs. (A.18) and (A.19) leads to $E_0 + E_0' < E_0' + E_0$, which is an obvious contradiction. This demonstrates that it is not possible to find two different external potentials that can give the same electron density $n(\mathbf{r})$. Consequently, $n(\mathbf{r})$ uniquely determines $\nu(\mathbf{r})$ (up to a constant) and all ground state properties.

The energy E_ν can be explicitly written as a function of the electron density $n(\mathbf{r})$ for a given external potential $\nu(\mathbf{r})$:

$$\begin{aligned} E_\nu[n(\mathbf{r})] &= T[n(\mathbf{r})] + V_{\mathrm{n-e}}[n(\mathbf{r})] + V_{\mathrm{e-e}}[n(\mathbf{r})] \\ &= \int n(\mathbf{r})\nu(\mathbf{r})d\mathbf{r} + F_{\mathrm{HK}}[n(\mathbf{r})], \end{aligned} \tag{A.20}$$

where $F_{\mathrm{HK}}[n(\mathbf{r})]$ is dependent only on $n(\mathbf{r})$, independently of any external potential $\nu(\mathbf{r})$. Thus F_{HK} is a universal functional of $n(\mathbf{r})$ and is defined as

$$F_{\mathrm{HK}}[n(\mathbf{r})] = T[n(\mathbf{r})] + V_{\mathrm{e-e}}[n(\mathbf{r})]. \tag{A.21}$$

The second theorem of Hohenberg and Kohn demonstrates that the ground state energy can be obtained variationally from the density. The density that minimizes the total energy is the exact ground state density, thus rationalizing the original intuition of Thomas and Fermi (Fermi 1927; Thomas 1927). This is expressed as

$$E_0[n_0(\mathbf{r})] \leq E_\nu[n(\mathbf{r})]. \tag{A.22}$$

The total energy functional (following the first theorem) given by Eq. (A.20) is calculated for a trial density $\nu(\mathbf{r})$ and is consistent with charge conservation $\int n(\mathbf{r})d\mathbf{r} = N_e$. The total energy functional is always greater than or equal to the true ground state total energy E_0 of the system:

$$E_\nu[n(\mathbf{r})] = \int n(\mathbf{r})\nu(\mathbf{r})d\mathbf{r} + F_{\mathrm{HK}}[n(\mathbf{r})] \geq E_0. \tag{A.23}$$

These two theorems demonstrate that the problem of solving the Schrödinger equation for the ground state can be exactly recast into the variational problem of minimizing the Hohenberg–Kohn functional, Eq. (A.21), with respect to the minimization of a functional of the three-dimensional density function. However, most of the complexities of the many-electron problem are associated with the determination of the universal Hohenberg–Kohn functional $F_{\mathrm{HK}}[n(\mathbf{r})]$.

A.3.3 The Kohn–Sham Equations

Kohn and Sham transformed the DFT into a practical electronic structure theory (Kohn & Sham 1965). They recognized that the failure of the Thomas–Fermi theory mainly resulted from the bad description of the kinetic energy. In order to address this problem, they returned to the picture of noninteracting electrons moving in an effective field.

$F_{\mathrm{HK}}[n(\mathbf{r})]$ is written as a sum of the kinetic energy of noninteracting electrons (T_s), the classical electrostatic Hartree energy (E_H), and all the many-body quantum effects are

put together into the exchange and correlation energy ($E_{\rm xc}$). Thus, the energy functional of the previous section becomes

$$E[n(\mathbf{r})] = \int n(\mathbf{r})v(\mathbf{r})dr + F_{\rm HK}[n(\mathbf{r})]$$
$$= \int n(\mathbf{r})v(\mathbf{r})d\mathbf{r} + T_s[n(\mathbf{r})] + E_H[n(\mathbf{r})] + E_{\rm xc}[n(\mathbf{r})]. \tag{A.24}$$

The constraint minimization of the $F_{\rm HK}[n(\mathbf{r})]$ functional for N_e electrons can be rewritten, introducing the indeterminate multiplier μ as the variational problem:

$$\delta\left\{F_{\rm HK}[n(\mathbf{r})] + \int v(\mathbf{r})n(\mathbf{r})d\mathbf{r} - \mu\left(\int n(\mathbf{r})d\mathbf{r} - N_e\right)\right\} = 0. \tag{A.25}$$

Formally Eq. (A.25) leads to the Euler–Lagrange equation for the charge density:

$$\frac{\delta F_{\rm HK}[n(\mathbf{r})]}{\delta n(\mathbf{r})} + v(\mathbf{r}) = \mu. \tag{A.26}$$

This minimization under the constraint of orthonormality for the one-particle orbitals ψ_i leads to a set of N_e single-particle Schrödinger-like equations, the so-called Kohn–Sham equations, that are expressed as

$$\left[-\frac{\hbar^2}{2m_e}\nabla^2 + v_{\rm KS}[n(\mathbf{r})]\right]\psi_i(\mathbf{r}) = \hat{H}_{\rm KS}\psi_i(\mathbf{r}) = \epsilon_i\psi_i(\mathbf{r}). \tag{A.27}$$

Here, ψ_i are the Kohn–Sham one-electron orbitals and the electron density is defined as

$$n(\mathbf{r}) = \sum_{i=1}^{N_e}|\psi_i|^2, \tag{A.28}$$

where $v_{\rm KS}[n(\mathbf{r})]$ is the effective potential experienced by the electrons and is expressed as

$$v_{\rm KS}[n(\mathbf{r})] = \frac{\delta\int n(\mathbf{r})v(\mathbf{r})d\mathbf{r} + T_s[n(\mathbf{r})] + E_H[n(\mathbf{r})] + E_{\rm xc}[n(\mathbf{r})]}{\delta n(\mathbf{r})}$$
$$= v[n(\mathbf{r})] + \int \frac{n(\mathbf{r}')}{|\mathbf{r}-\mathbf{r}'|}d\mathbf{r}' + v_{\rm xc}[n(\mathbf{r})]. \tag{A.29}$$

The exchange–correlation potential is given by the functional derivative of the exchange–correlation energy:

$$v_{\rm xc}[n(\mathbf{r})] = \frac{\delta E_{\rm xc}[n(\mathbf{r})]}{\delta n(\mathbf{r})}. \tag{A.30}$$

Finally, the total energy can be determined from the resulting equations of density and potentials through

$$E = \sum_{i=1}^{N_e}\epsilon_i - \frac{1}{2}\iint\frac{n(\mathbf{r})n(\mathbf{r}')}{|\mathbf{r}-\mathbf{r}'|} + E_{\rm xc}[n] - \int v_{\rm xc}[n(\mathbf{r})]n(\mathbf{r})d\mathbf{r}. \tag{A.31}$$

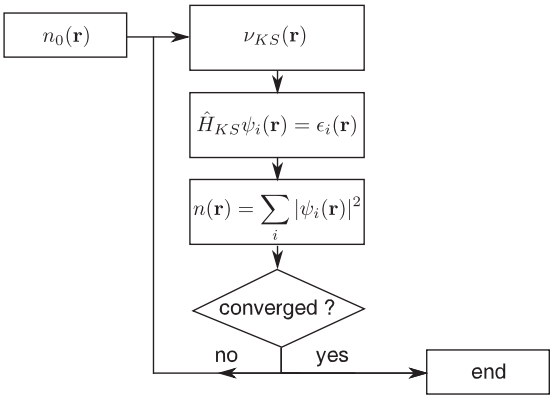

Figure A.1 The self-consistent resolution scheme for the Kohn–Sham equations. (Adapted from Nogueira et al. (2003))

The Kohn–Sham equations, Eq. (A.27), require to be solved self-consistently due to the density dependence on the one-electron Kohn–Sham effective potential ν_{KS}. The general procedure consists in starting with an initial guess of the electron density, and constructing the effective potential $\nu(\mathbf{r})$ from Eq. (A.24) in order to extract the Kohn–Sham orbitals. Based on these orbitals, a new density is obtained from Eq. (A.28) and the process is repeated until convergence is achieved (Payne et al. 1992). Finally, the total energy is calculated from Eq. (A.31) by using the obtained electron density, as illustrated in Fig. A.1.

The exact total energy can be extracted if each term in the Kohn–Sham energy functional is known. This is unfortunately not the case. Indeed, the exchange–correlation (xc) functional (E_{xc}) remains unknown. E_{xc} includes the nonclassical aspects of the electron–electron interaction along with the component of the kinetic energy of the real system, differently from the fictitious noninteracting system. Since E_{xc} cannot be determined exactly, this energy term has to be estimated using different possible approximations.

A.3.4 The Exchange–Correlation Functionals

The simplest way to approximate the exchange–correlation (xc) energy of an electronic system is the local-density approximation (LDA), which was proposed by Kohn and Sham (1965). In this approximation, a real inhomogeneous system is divided into infinitesimal volumes in which the density is assumed to be constant. The exchange–correlation (xc) energy for the system is constructed by assuming that the exchange–correlation energy $\epsilon_{\mathrm{xc}}[n(\mathbf{r})]$ per electron at a point $\mathbf{r}$ in the electron gas is equal to the exchange–correlation energy per electron in a homogeneous electron gas that has the same electron density as the electron gas at point $\mathbf{r}$. Thus, one can write

$$\epsilon_{\mathrm{xc}}[n(\mathbf{r})] = \epsilon_{\mathrm{xc}}^{\mathrm{hom}}[n(\mathbf{r})], \tag{A.32}$$

and the total exchange–correlation energy is written as

$$E_{\mathrm{xc}}^{\mathrm{LDA}}[n(\mathbf{r})] = \int \epsilon_{\mathrm{xc}}^{\mathrm{hom}}[n(\mathbf{r})]n(\mathbf{r})d\mathbf{r}. \tag{A.33}$$

In practice, the exchange and correlation terms are calculated separately. The exchange part is given by the Dirac exchange-energy functional (Dirac 1930):

$$E_{x}^{\mathrm{LDA}}[n(\mathbf{r})] = -\frac{3}{4}\left(\frac{3n(\mathbf{r})}{\pi}\right)^{1/3}. \tag{A.34}$$

Here, the local Wigner–Seitz radius $r_s(\mathbf{r})$ is defined as $r_s(\mathbf{r}) = \left(\frac{3}{4\pi n(\mathbf{r})}\right)^{-1/3}$, which is the radius of the sphere that would contain exactly one electron in the homogeneous electron gas density $n(\mathbf{r})$.

As for the exchange term, the exact correlation term is unknown. However, an approximate expression can be determined by interpolating homogeneous electron gas data obtained by quantum Monte-Carlo calculations as reported by Ceperley and Alder (1980). The parameterization proposed by Perdew and Zunger (1981) is the most commonly used by the scientific community. The LDA ignores corrections to the exchange–correlation energy at a point r due to the nearby inhomogeneities in the electron density. Strictly, the LDA is valid for slowly varying density. However, it is noticeable that calculations performed using the LDA have been remarkably successful (Payne et al. 1992).

However, it was realized very early that only the local uniform density at each given point is not a reasonable approximation for the rapidly varying electron density of many materials. An attempt to improve the LDA consists in taking into account not only the local uniform density $n(\mathbf{r})$, but also the gradient terms ($\nabla n(\mathbf{r})$) of the total charge density in the exchange–correlation energy term. Based on this idea, the exchange–correlation energy of the generalized gradient approximation (GGA) can be written as

$$E_{\mathrm{xc}}^{\mathrm{GGA}}[n(\mathbf{r}), \nabla n(\mathbf{r})] = \int F_{\mathrm{xc}}[n(\mathbf{r}), \nabla n(\mathbf{r})]d\mathbf{r}. \tag{A.35}$$

The GGA functionals are often called "semi-local" functionals due to their dependence on the gradient of the density $\nabla n(\mathbf{r})$. Typically for many properties, such as geometries and ground state energies of molecules and solids, GGA can yield better results than the LDA. The functional F_{xc} is taken as a correction to the LDA exchange and correlation relation, while ensuring again the consistency within exchange–correlation energy as in LDA. Within GGA, the exchange energy is then expressed as

$$E_{x}^{\mathrm{GGA}}[n(\mathbf{r})] = \int \epsilon_x[n(\mathbf{r})]F_{x}^{\mathrm{GGA}}(s)d\mathbf{r}, \tag{A.36}$$

where $F_{x}^{\mathrm{GGA}}(s)$ is the exchange enhanced factor which represents how much exchange energy is over the LDA exchange value for a given $n(\mathbf{r})$. One GGA functional differs from another according to the choice of this exchange enhanced factor F_x, which is a function of s, a dimensionless reduced gradient defined as

$$s = \frac{|\nabla n(\mathbf{r})|}{2(3\pi^2)^{1/3} n(\mathbf{r})^{4/3}}. \tag{A.37}$$

Various approximations have been proposed for the $F_x(s)$ functional, for instance, by Perdew and Wang (Perdew 1991) and by Perdew, Burke, and Ernzerhof (PBE) (Perdew et al. 1996). Generally, when materials properties have to be screened, the PBE functional is used, and the $F_x(s)$ is expressed as

$$F_x^{\mathrm{PBE}}(s) = 1 + k - \frac{\kappa}{1 + \frac{\mu s^2}{\kappa}}. \tag{A.38}$$

In PBE, κ and μ are parameters obtained from (nonempirical) physical constraints (Perdew et al. 1996). The functional form of the gradient-corrected correlation energy E_c^{GGA} is also expressed as a complex function of s. For more details on PBE parameterizations, see Perdew et al. (1996).

A.4 Practical Calculations

For practical reasons, it is necessary to introduce crystal lattices (which exhibit a periodical symmetry) to solve numerically large periodic systems using DFT. The crystal lattice is typically used to reduce the amount of atoms (thus, of interacting particles) when using only the unit cell. In addition to this, the equations derived in the previous section need to be projected onto a complete basis set. This basis set should be of finite size in order to allow us to perform computer calculations. Finally, band structures and **k**-point grids are introduced, followed by the pseudopotentials.

A.4.1 Crystal Lattice and Reciprocal Space

A solid material is composed of many electrons and ionic cores per cm^3. In principle, all these positions should be taken into account to construct the Kohn–Sham Hamiltonian. Fortunately, the periodic symmetry of the crystal lattice allows us to reduce the interaction problem to only electrons and ionic cores that are present in the unit cell. A crystal is determined by its atoms' positions and follows the rules of symmetry (repeating them by performing translations). The set of translations that generates the complete crystal is called the Bravais lattice. This set of translations forms a group, as the sum of two translations is again a translation. Other symmetries (e.g., a rotation) leaving the crystal unchanged can also exist. These form a group called a point group which is a group of geometric symmetries (isometries) that keep at least one point fixed. The space group of a crystal is given by the sum of the translation group and the point group.

The set of all translations forms a lattice in space in which each translation can be written as a linear combination of the primitive vectors $\mathbf{a}_1$, $\mathbf{a}_2$, $\mathbf{a}_3$:

$$\mathbf{t} = i_1\mathbf{a}_1 + i_2\mathbf{a}_2 + i_3\mathbf{a}_3, \tag{A.39}$$

where i_1, i_2, and i_3 are integers. The positions of the atoms in the unit cell can be described with respect to the primitive translation vectors. Due to the periodicity of the lattice, all periodic functions can be Fourier-transformed. The Fourier-transformed space is also called reciprocal space, where the set of reciprocal vectors $\mathbf{b}_i$ of the primitive translations $\mathbf{a}_j$ satisfy

$$\mathbf{b}_i \cdot \mathbf{a}_j = 2\pi\theta_{ij}, \tag{A.40}$$

which is the definition of the reciprocal lattice. A vector in the reciprocal space is usually denoted as $\mathbf{G}$ and is given by

$$\mathbf{G} = i_1\mathbf{b}_1 + i_2\mathbf{b}_2 + i_3\mathbf{b}_3, \tag{A.41}$$

where i_1, i_2, and i_3 are integers. By using this reciprocal lattice, the first Brillouin zone can be defined as the Wigner–Seitz cell of the reciprocal space (Ashcroft & Mermin 1976b). This "minimum representation" of the system to be studied using the periodic boundary conditions of large systems is the basic idea of this approach, to be used for the DFT calculations throughout the various examples of carbon nanostructures investigated in this book.

A.4.2 The Plane Wave Representation

For such periodic systems, the external potential satisfies the relation $V(\mathbf{r}+\mathbf{t}) = V(\mathbf{r})$, imposed by the periodic boundary conditions, and therefore the corresponding effective one-electron Hamiltonian obeys the translation invariance. The Bloch theorem applies to the electronic wavefunctions of the system. The eigenfunctions can be written as a product of a plane wave ($e^{i\mathbf{k}\cdot\mathbf{r}}$) and a function ($u_{n,\mathbf{k}}(\mathbf{r})$) having the same periodicity as the potential $V(\mathbf{r})$:

$$\psi_{n,\mathbf{k}}(\mathbf{r}) = e^{i\mathbf{k}\cdot\mathbf{r}}u_{n,\mathbf{k}}(\mathbf{r}), \qquad \text{where} \qquad u_{n,\mathbf{k}}(\mathbf{r}+\mathbf{t}) = u_{n,\mathbf{k}}(\mathbf{r}). \tag{A.42}$$

Here, $\mathbf{k}$ represents the wave vector, and n is the band index. The Bloch theorem allows us to expand the electronic wavefunction in terms of a discrete set of plane waves to the periodic function $u_{n,\mathbf{k}}(\mathbf{r})$, whose wave vectors are the reciprocal lattice vector ($\mathbf{G}$) of the periodic crystal:

$$u_{n,\mathbf{k}}(\mathbf{r}) = \frac{1}{\sqrt{\Omega}}\sum_{\mathbf{G}} C_{n,\mathbf{k}+\mathbf{G}}\, e^{i\mathbf{G}\cdot\mathbf{r}}, \tag{A.43}$$

where Ω is the volume of the unit cell. The electronic wavefunction can thus be rewritten as

$$\psi_{n,\mathbf{k}}(\mathbf{r}) = \frac{1}{\sqrt{\Omega}}\sum_{\mathbf{G}} C_{n,\mathbf{k}+\mathbf{G}+\mathbf{r}}\, e^{i(\mathbf{k}+\mathbf{G})\cdot\mathbf{r}}. \tag{A.44}$$

Using the above expressions to solve the one-electron Schrödinger-like equation with an effective periodic potential, e.g., the Kohn–Sham potential defined in Eq. (A.29), the

Kohn–Sham wavefunction can be expanded with the plane wave basis sets as described in Eq. (A.44). As a result, Eq. (A.27) can be rewritten as

$$\sum_{\mathbf{G}'}\left[\frac{\hbar^2}{2m}|\mathbf{k}+\mathbf{G}|^2\delta_{\mathbf{G}\mathbf{G}'}+\nu_{\mathrm{n-n}}(\mathbf{G}-\mathbf{G}')+\nu_{\mathrm{H}}(\mathbf{G}-\mathbf{G}')\right.$$
$$\left.+\,\nu_{\mathrm{xc}}(\mathbf{G}-\mathbf{G}')\right]C_{n,\mathbf{k}+\mathbf{G}}=\epsilon_{n,\mathbf{k}}C_{n,\mathbf{k}+\mathbf{G}}, \tag{A.45}$$

where $\nu(\mathbf{G}-\mathbf{G}')$ are the Fourier transforms of the potential in real space (which can exhibit different functional forms depending on the pseudopotential method): here, $\nu_{\mathrm{n-n}}(\mathbf{G}-\mathbf{G}')$ is the nuclei–nuclei interaction Coulomb potential, $\nu_{\mathrm{H}}(\mathbf{G}-\mathbf{G}')$ is the Hartree potential, $\nu_{\mathrm{xc}}(\mathbf{G}-\mathbf{G}')$ is the exchange–correlation potential, $\delta_{\mathbf{G}\mathbf{G}'}$ is the Kronecker symbol δ, and reflects that the kinetic energy is diagonal, whereas ϵ_n are the electronic energies.

The solution of this secular equation is obtained by diagonalizing the Hamiltonian matrix of elements $H_{k+\mathbf{G},k+\mathbf{G}'}$, given by the terms in brackets of Eq. (A.45). The size of the matrix is determined by the choice of the cutoff energy. The plane wave expansion is truncated to include terms with a kinetic energy only up to a certain cutoff value:

$$\frac{\hbar^2}{2m_e}|\mathbf{k}+\mathbf{G}|^2<E_{\mathrm{cutoff}}. \tag{A.46}$$

Employing a finite basis set introduces a new source of inaccuracy, which can be reduced by increasing the number of plane waves or the kinetic energy cutoff (E_{cutoff}). Therefore, appropriate convergence tests have to be performed in order to find an E_{cutoff} that is sufficient to compute the property of interest with the required accuracy. Despite the E_{cutoff}, it is often computationally heavy to determine the size of the matrix for systems that contain both valence and core electrons. This problem can be overcome by using the pseudopotential approximation as discussed in the following sections.

A.4.3 k-Point Grids and Band Structures

In a periodic solid, the number of electrons is of the order of Avogadro's number. Only a set of **k** points is allowed and determined by the periodic boundary conditions or generalized Born–von Karman boundary conditions to the wavefunctions. The latter can be interpreted by saying that a particle that leaves one surface of the crystal simultaneously enters the crystal at the opposite surface. The density of allowed **k** points is proportional to the volume of the solid. The infinite number of electrons in the solid is accounted for by an infinite number of **k** points, and only a finite number of electronic states are occupied. The spacing of the **k** points goes to zero and **k** can be considered as a continuous variable. The occupied states at each **k** point contribute to the ground state properties of the solid such as the electronic potential, electron density, and the total energy. However, the electronic wavefunctions at **k** points that are very close together will be almost identical. Hence, it is possible to represent them by a single **k** point

instead of over a region of **k** space. In order to obtain accurate electronic potential, electron density, and total energy, efficient methods have been used to choose the finite sets of **k** points. Generally, the method proposed by Monkhorst and Pack (1976) is used in which a uniform mesh of **k** points is generated along the three lattice vectors in reciprocal space. The magnitude of any error in the total energy or the total energy difference due to inadequacy of the **k** points sampling can always be reduced to zero by using a denser set of **k** points. Therefore, it is crucial to test the convergence of the results with respect to the number of **k** points in general.

Due to the translational symmetry and to the continuous nature of **k** points, only the first Brillouin zone with its band eigenvalues and energy gaps is taken into account to plot these eigenvalues for the so-called band structures. In order to calculate the electronic density and other properties, it is necessary to integrate (all) over the **k** points in the Brillouin zone. The number of these **k** points necessarily depends on the material: for insulators only a few points are needed as all bands are filled, while for metals more points are needed for the bands that cross the Fermi level. The presence of additional symmetries, such as rotations or mirror reflections, allows one to consider only a part of the Brillouin zone. The smallest possible part that can be mapped to the complete Brillouin zone by applying all symmetries is called the irreducible Brillouin zone (IBZ).

A.4.4 The Pseudopotential Approximation

Most physically interesting properties of solids are largely determined by the valence electrons rather than the core. The valence electrons can be thought of as loosely bound orbitals, delocalized over the crystal, which strongly influence the formation of bands in a solid. In contrast, the core electrons, that are tightly bound around each atomic nucleus and largely unperturbed by the surrounding environment, are essentially not involved in chemical bondings. Moreover, the deeply bound core electrons within plane-wave basis sets require a huge amount of basis functions for their description, which implies a significant computational cost. This can be avoided by using the pseudopotential approximation (Phillips 1958) which replaces the strong ionic potential with a weaker pseudopotential. In general, the pseudopotential formalism is used for two main reasons which are (i) to reduce the number of plane waves to describe the core electrons as a weaker pseudopotential due to their deep potential and (ii) to eliminate the fast oscillations of the wavefunctions of the valence electrons. These two issues are illustrated in Fig. A.2, where the pseudopotential is much weaker than the all-electron potential and where the pseudo wavefunction has no radial node inside the core region. It is essential within the pseudopotential scheme that outside the core region, the pseudopotential and pseudo wavefunction become the same with the corresponding all-electron functions.

The most common form of a pseudopotential is:

$$V^{\mathrm{PS}}(\mathbf{r}) = \sum |Y_{l,\mathrm{m}}\rangle V_l(\mathbf{r}) \langle Y_{l,\mathrm{m}}|, \tag{A.47}$$

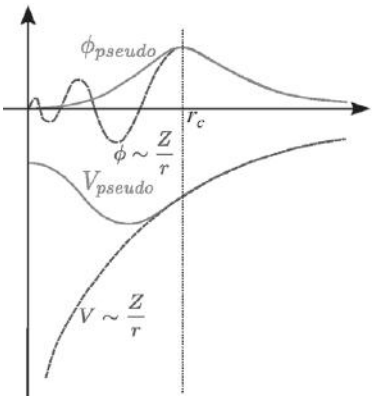

Figure A.2 All-electron potential (dashed line) and pseudopotential (solid line) and their corresponding wavefunctions. The radius at which the all-electron and pseudo-electron values match is designated r_c. (Adapted from Rignanese (1998))

where $|Y_{\mathrm{l,m}}\rangle$ are the spherical harmonics and V_l are the angular momentum dependent components of the pseudopotential. A pseudopotential that uses the same potential in each angular momentum is called a local pseudopotential, i.e., it only depends on the distance from the nucleus. A fundamental requirement for the pseudopotential is the ability to accurately describe the valence electrons in different chemical environments. Such a property is called the transferability of the pseudopotential.

Based on this idea, a systematic and successful procedure for the development of accurate and transferable pseudopotentials has been developed, where the added constraint of norm-conservation is introduced (Bachelet et al. 1982; Hamann et al. 1979). Modern norm-conserving pseudopotentials are obtained by inverting the free atom Schrödinger equation for a given electronic configuration of reference and forcing the pseudo wavefunctions to match the true valence wavefunctions beyond a certain chosen distance from the nucleus. In summary, a norm-conserving pseudopotential is built on a given reference atomic configuration, to meet the following conditions:

(1) The pseudo energy-eigenvalues should match the true (all-electron) valence eigenvalues.
(2) The pseudo wavefunctions ϕ_l^{PS} should be nodeless, and the functions and their first derivatives must be differentiable.
(3) The pseudo wavefunctions should match the all-electron wavefunctions beyond a chosen core radius r_c^l:

$$\phi_l^{\mathrm{PS}}(\mathbf{r}) = \phi_l^{\mathrm{AE}}(\mathbf{r}), \qquad \text{for } r > r_c^l. \tag{A.48}$$

(4) The total integrated pseudo-charge density from a given $\phi_l^{PS}(\mathbf{r})$ and the corresponding all-electron charge density are identical inside the core radius r_c^l:

$$\int_{r<r_c^l} |\phi_l^{\mathrm{PS}}|^2 r^2 dr = \int_{r<r_c^l} |\phi_l^{\mathrm{AE}}|^2 r^2 dr. \tag{A.49}$$

Various parameterization schemes exist to generate the norm-conserving pseudopotentials (e.g., Troullier and Martins (1991) parameterizations). Note that in the original formulations, the pseudopotentials are semi-local but they can easily be transformed into a separable form using the Kleinmann–Bylander scheme (Kleinman & Bylander 1982). The nonlocal pseudopotential is used to accurately represent the combined effect of the nucleus and the core electrons, since different angular momenta can be scattered differently. The pseudopotential can be conventionally rewritten in a form that separates the long- and short-range components, where the long-range component is local and corresponds to the Coulomb tail.

The norm-conserving requirement ensures that the logarithmic derivative of ϕ_l^{PS} (related to the phase shifts in the scattering) has the same behavior (up to the first order changes in energy) as in the all-electron case, which is often related to the transferability. For elements with strongly localized orbitals (i.e., $3d$ elements) the norm-conserving pseudopotentials require a large basis set of plane waves. To overcome this limitation, one usually increases the cutoff radius, but this is in general not a good solution because the transferability is always considerably affected when r_c is increased. Many attempts to improve the norm-conserving pseudopotentials have been centered around the logarithmic derivative of the atomic and pseudo wavefunctions (Rignanese 1998).

Vanderbilt proposed a radically new concept based on relaxing the norm-conserving constraint, introducing a so-called ultrasoft pseudopotential (USPP) (Vanderbilt 1990). As with norm-conserving pseudopotentials, the all-electron and pseudo wavefunctions are required to be equal outside r_c, but inside r_c they are allowed to be as smooth as possible. As a consequence, the pseudo wavefunctions are not normalized inside r_c, resulting in a charge deficit. This problem is solved by introducing a localized atom-centered augmentation charge in which the correct pseudo-charge density accounts for the part of the charge (in the core region) that is not described by the pseudo wavefunctions ψ_i (Rignanese 1998). The augmentation of the pseudo-density with appropriate functions (denoted $Q^I_{\mathrm{nm}}(\mathbf{r})$) localized in the core region is defined as

$$n(\mathbf{r}) = \sum_i [\psi_i^*(\mathbf{r})\psi_i(\mathbf{r}) + \sum_{I,\mathrm{lm}} Q^I_{\mathrm{nm}} \langle \psi_i | \beta^I_n \rangle \langle \beta^I_m | \psi_i \rangle], \tag{A.50}$$

where the functions β^I_n are strictly localized in the core region and are also used to define the nonlocal pseudopotential. The functions β^I_n and $Q^I_{\mathrm{nm}}(\mathbf{r})$ are related to the atomic functions β_n and Q_{nm} by

$$\beta^I_n(\mathbf{r}) = \beta_n(\mathbf{r} - \mathbf{R}_I), \tag{A.51}$$

$$Q^I_{\mathrm{nm}}(\mathbf{r}) = Q_{\mathrm{nm}}(\mathbf{r} - \mathbf{R}_I). \tag{A.52}$$

The Q_{nm} are constructed in the atomic "pseudization" procedure in such way that, at the reference energies, the electron density of the pseudo wavefunctions as defined by Eq. (A.50) is the same as the all-electron density. The functions β_n and Q_{nm} are obtained from first principles in the USPP scheme, and characterize the atomic species (Rignanese 1998).

Although the pseudopotential approach has worked reliably for three decades, a new method called projector-augmented wavefunctions (PAW) has been introduced by Blöchl (1994) to replace these pseudopotentials. In principle, this PAW approach is more accurate compared to others such as USPP for two main reasons. First, the cutoff distance or the extension in space of the pseudopotential is smaller in PAW than in USPP. Second, the PAW approach reconstructs the real wavefunction with all its nodes in the core region, while the USPP do not.

The central idea in the PAW method is to express the all-electron valence states ψ_i in terms of a smooth pseudo wavefunction $\tilde{\psi}_n$, which is augmented by a local basis set expansion and restricted to a small region, called the augmentation sphere, around each atom (Blöchl 1994). The core states of the atoms are considered frozen. Given a smooth pseudo wavefunction, the corresponding all-electron wavefunction (i.e., orthogonal to the set of core orbitals) can be obtained through a linear transformation operator $\hat{\tau}$:

$$\psi_i(\mathbf{r}) = \hat{\tau}\tilde{\psi}_i(\mathbf{r}), \text{ with } \hat{\tau} = 1 + \sum_i |\phi_i^{\mathrm{AE}}\rangle\langle\tilde{p}_i|\tilde{\psi}_n - \sum_i |\tilde{\phi}_i^{\mathrm{PS}}\rangle\langle\tilde{p}_i|\tilde{\psi}_n, \tag{A.53}$$

where $\tilde{p}_i$ are atom specific but system independent functions, which are only nonzero inside the augmentation sphere. The index i refers to the sum over the atomic sites, the angular momentum and reference energies. ϕ_i^{AE} and $\tilde{\phi}_i^{\mathrm{PS}}$ are the all-electron and pseudo-partial waves that match at the core radius. Finally, $\tilde{p}_i$ are the projector functions that have to be created in such a way as to be dual to the partial waves:

$$\langle\tilde{p}_i|\tilde{\psi}_j = \sigma_{ij}. \tag{A.54}$$

A radial cutoff distance, r_c^{AE}, that defines the atomic augmentation sphere is selected, similarly to a cutoff radius for a pseudopotential. The larger is the augmentation sphere, the smoother are the pseudo wavefunctions. However, the overlap with neighboring augmentation spheres should be avoided. For the all-electron valence states, smooth partial waves are constructed for $r > r_c^{\mathrm{AE}}$ and one smooth projector is defined for each of the partial waves. In principle, an infinite number of projectors and partial waves are required for the PAW method to be exact (Blöchl 1994). For practical calculations, an accurate dataset will need only one or two projection functions for each angular momentum. From the atomic frozen-core electron density $n_c^{\mathrm{AE}}(r)$, a new smooth electron density $\tilde{n}_c^{\mathrm{AE}}(\vec{r})$ is obtained. The latter must be identical to $n_c^{\mathrm{AE}}(r)$ for radii larger than r_c^{AE}. The wavefunction and the atom-centered smooth-core electron density contribute to the whole pseudo-electron density. The true all-electron density is obtained from the pseudo-electron density. Finally, the PAW total energy is a function of the pseudo wavefunctions and of the occupation numbers (Blöchl 1994).

A.4.5 Available DFT Codes

Up to this point, the discussion has basically focused on the description of the DFT and its practical calculation to determine the electronic ground-state of an atomic system.

Improvements in computer hardware and software allow simulations of materials with an increasing number of atoms. The computational load scales linearly (or with a higher power) with the number of atoms present in the simulation cells. It is thus of prime importance to choose the right software to be used in this context. Among the several existing DFT approaches, the choice of software is made according to the trade-off between numerical accuracy and system size. Several main DFT codes currently on the market are listed below as examples of software frequently used to predict the electronic and transport properties of carbon-based nanostructures:

(1) ABINIT (Gonze 2005; Gonze et al. 2009) is a GPL licensed DFT package used worldwide. ABINIT is a package whose main program allows one to find the total energy, charge density and electronic structure of systems made of electrons and nuclei (molecules and periodic solids) within DFT, using pseudopotentials and a planewave or wavelet basis. Valence and core electrons are treated on different footings: the core electrons are frozen, and either replaced by norm-conserving pseudopotentials or treated by the augmentation of plane waves by projectors (PAW method). The code also includes options to optimize the geometry according to the DFT forces and stresses, to perform molecular dynamics simulations using these forces, to generate dynamical matrices, Born effective charges, dielectric tensors based on density-functional perturbation theory (DFTP), and many more properties. Excited states can be computed within the many-body perturbation theory (the *GW* approximation and the Bethe–Salpeter equation), and time-dependent density functional theory (for molecules). More details are available on the website: www.abinit.org.

(2) QUANTUM ESPRESSO (Giannozzi et al. 2009) is an integrated suite of open-source computer codes for electronic-structure calculations and materials modeling at the nanoscale. It is based on DFT, plane waves, and pseudopotentials. The main program allows one to compute the ground-state properties within DFT using the pseudopotentials (norm-conserving and ultrasoft) and the PAW method. Several exchange–correlation functionals and some hybrid functionals are included in this code. More details and the code are available at: www.quantum-espresso.org/.

(3) SIESTA (Spanish initiative for electronic simulations with thousands of atoms) (Soler et al. 2002) is both a method and its computer program implementation, to perform electronic structure calculations and *ab initio* molecular dynamics simulations of molecules and solids. This code uses the standard DFT with LDA and GGA together with the norm-conserving pseudopotentials (in the form of Kleinman–Bylander). Atomic orbitals are used as a basis set, allowing unlimited multiple-zeta and angular momenta, polarization, and off-site orbitals. SIESTA uses a finite 3D grid for the calculation of some integrals and the representation of charge densities and potentials. More details are available at: www.icmab.es/dmmis/leem/siesta/.

(4) CASTEP (Clark et al. 2005; Segall et al. 2002) is a leading code for calculating the properties of materials from first principles. Using density functional theory, it can simulate a wide range of materials properties including energetics, structure

at the atomic level, vibrational properties, electronic response properties, etc. In particular, it has a wide range of spectroscopic features that link directly to experiment, such as infrared and Raman spectroscopies, NMR, and core-level spectra. This software is a full-featured materials modeling code based on a first-principles quantum mechanical description of electrons and nuclei. It uses the robust methods of a plane-wave basis set and pseudopotentials. More details are available at: www.castep.org.

(5) VASP (The Vienna *ab initio* simulation package) (Kresse & Furthmüller 1996a, 1996b) is a computer program for atomic scale materials modeling, e.g., electronic structure calculations and quantum mechanical molecular dynamics, from first principles. It computes an approximate solution to the many-body Schrödinger equation, either within density functional theory (DFT), solving the Kohn–Sham equations, or within the Hartree–Fock (HF) approximation. Hybrid functionals that mix the Hartree–Fock approach with density functional theory are implemented as well. In VASP, central quantities, like the one-electron orbitals, the electronic charge density, and the local potential are expressed in plane-wave basis sets. The interactions between the electrons and ions are described using norm-conserving or ultrasoft pseudopotentials, or the projector-augmented-wave method. More details are available at: www.vasp.at.

Appendix B Electronic Structure Calculations: The Many-Body Perturbation Theory (MBPT)

B.1 Introduction

In Appendix A, a detailed description of the electronic structure calculation techniques based on the so-called density functional theory (DFT) was presented. As mentioned and illustrated in that section, DFT is widely used to investigate the electronic properties of materials, their defects, interfaces, etc. Unfortunately, the semi-local approximations of DFT, such as the local density approximation (LDA) and gradient generalized approximation (GGA), suffer from a well-known substantial underestimation of the bandgap. This may be interpreted as a result of the fact that DFT does not properly describe excited states of a system. This failure of DFT may also induce a wrong estimation of the position of the electronic defect/dopant levels in the bandgap.

Some empirical solutions exist to overcome the problem of DFT bandgap underestimation. For example, the "scissor" technique consists in correcting the LDA/GGA gap error by shifting the conduction band up so as to match the gap relative to the experiment. However, such a method is not accurate enough for defining the accurate position of defect/dopant levels occurring in the bandgap.

Another solution to the underestimation of the bandgap in DFT consists in using the so-called hybrid functionals which have recently become very popular. Indeed, these functionals incorporate a fraction of Hartree–Fock (HF) exchange, which leads to improvement of the bandgap compared to LDA/GGA (Curtiss et al. 1998; Muscat et al. 2001; Paier et al. 2006). Yet, the fraction of HF exchange cannot be known in advance for all materials, and its optimal value is material dependent (Ernzerhof et al. 1997; Ernzerhof & Scuseria 1999). Therefore, the reliability of hybrid functionals cannot be assessed *a priori* (Kümmel & Kronik 2008). Indeed, a recent theoretical work (Jain et al. 2011) demonstrates that the orbital energies from various existing hybrid functionals are not reliable in predicting the bandgaps of all materials, either the optical or the quasiparticle gap. Even if a specific functional may give a good value for the bulk bandgaps, the same functional in general does not yield accurate gap values for the same material in different configurations, such as at its surfaces or in nanostructures (Jain et al., 2011).

A more successful approximation for the determination of excited states is based on the many-body perturbation theory (MBPT) (Abrikosov et al. 1975; Fetter & Walecka 1971; Hedin & Lundqvist 1970; Landau & Lifschitz 1980; Onida et al. 2002). Within the

DFT scheme, the response of a system of interacting electrons to an external potential V_{ext} is that of independent particles responding to an "effective" potential. A similar idea is that the long-range, and relatively strong, Coulomb forces could screen the individual electrons, with a surrounding charge cloud of the other electrons. This leads to defining the quasiparticle as an electron plus its screening cloud. Thus, the response of strongly interacting particles can be described in terms of weakly interacting quasiparticles. Hence, MBPT offers an approach for obtaining quasiparticle (QP) energies in solids which is controlled and amenable to systematic improvements. The principal results of MBPT, as well as its practical use, are summarized in the following.

B.2 Many-Body Perturbation Theory (MBPT)

B.2.1 Hedin's Equations

In MBPT, the QP energies E_i^{QP} and wavefunctions ψ_i^{QP} are determined by solving the quasiparticle equation:

$$\left[-\frac{1}{2}\nabla^2 + V_{\text{ext}}(\mathbf{r}) + V_{\text{H}}(\mathbf{r})\right]\psi_i^{\text{QP}}(\mathbf{r}) + \int \Sigma(\mathbf{r},\mathbf{r}';E_i^{\text{QP}})\psi_i^{\text{QP}}(\mathbf{r}')d\mathbf{r}' = E_i^{\text{QP}}\psi_i^{\text{QP}}(\mathbf{r}), \tag{B.1}$$

where V_{ext} and V_{H} are the external and Hartree potentials, respectively. In this equation, the exchange and correlation effects are described by the electron self-energy operator $\Sigma(\mathbf{r},\mathbf{r}',E_i^{\text{QP}})$, which is nonlocal, energy dependent, and non-Hermitian. Hence, the eigenvalues E_i^{QP} are generally complex: their real part is the energy of the quasiparticle, while their imaginary part gives its lifetime.

The main difficulty resides in finding an adequate approximation for the self-energy operator Σ. Another key quantity is Green's function (Hedin & Lundqvist 1970) $G(\mathbf{r},\mathbf{r}',t,t')$. It describes the probability of finding an electron with spin σ at time t and position $\mathbf{r}$, if another electron with spin σ' is added (or removed) at position $\mathbf{r}'$ at time t'. Considering the condition $\Sigma = 0$, the noninteracting (which still contains the Hartree potential) Green's function G_0 can be constructed from the one-particle wavefunctions ψ_i and energies E_i of the "zeroth-order" Hamiltonian as

$$G_0(\mathbf{r},\mathbf{r}',E) = \sum_i \frac{\psi_i(\mathbf{r})\psi_i^*(\mathbf{r}')}{E - E_i + i\eta\,\text{sgn}(E_i - \mu)}, \tag{B.2}$$

where μ is the chemical potential and η is a positive infinitesimal. Hedin (1965) proposed a systematic way to approximate the self-energy Σ by including a perturbation series expansion in the fully screened Coulomb interaction. The exact one-body Green's function G is thus written using the Dyson equation:

$$G(12) = G_0(12) + \int G_0(13)\Sigma(34)G(42)d(34). \tag{B.3}$$

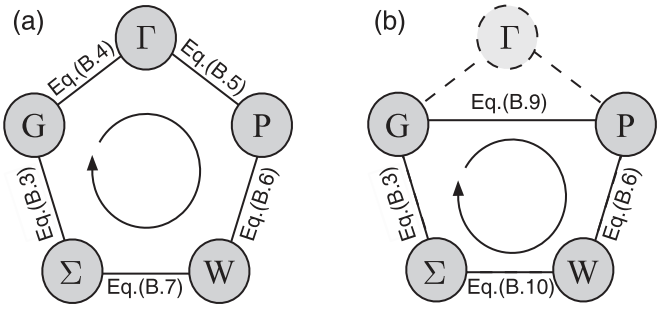

Figure B.1 (a) The self-consistent process for solving the complete Hedin's equations resulting from *GW* approximation. (b) Four coupled integro-differential equations resulting from the *GW* approximation. The so-called G_0W_0 approximation consists in performing the loop only once starting from $G = G_0$. (Adapted from Giantomassi et al. (2011))

Here, $1 \equiv (r_1, \sigma_1, t_1)$ is used to denote space, spin, and time variables and the integral sign stands for summation or integration of all these where appropriate. 1^+ denotes $t_1 + \eta$, where η is a positive infinitesimal. The self-energy Σ is obtained by solving self-consistently Hedin's closed set of coupled integro-differential equations:

$$\Gamma(12;3) = \delta(12)\delta(13) + \int \frac{\delta\Sigma(12)}{\delta G(45)} G(46)G(75)\Gamma(67;3)d(4567), \tag{B.4}$$

$$P(12) = -i\int G(23)G(42^+)\Gamma(34;1)d(34), \tag{B.5}$$

$$W(12) = v(12) + \int W(13)P(34)v(42)d(34), \tag{B.6}$$

$$\Sigma(12) = i\int G(14)W(1^+3)\Gamma(42;3)d(34), \tag{B.7}$$

where P is the polarizability, and W and v are the screened and the unscreened Coulomb interaction, respectively. Γ is the *vertex* function, which describes higher-order corrections to the interaction between quasiholes and quasielectrons. The self-consistent iterative process is illustrated in Fig. B.1(a). The most complicated term in these equations is Γ, which contains a functional derivative and hence cannot in general be evaluated numerically.

B.2.2 *GW* Approximation

In order to solve Hedin's equation, a possible strategy is to start with $\Sigma = 0$ and neglect the variation of the self-energy with respect to the Green's function $\delta\Sigma(12)/\delta G(45) = 0$ in Eq. (B.4). This leads to the Green's function G (at this step, the Hartree independent-particle G_0) and the vertex function is set to a delta function as

$$\Gamma(12;3) = \delta(12)\delta(13). \tag{B.8}$$

Thus, the polarizability in Eq. (B.5) writes

$$P(12) = -iG(12^+)G(21), \tag{B.9}$$

which corresponds to the random phase approximation (RPA) for the dielectric matrix. The screening also corresponds to RPA screening (W_0). The self-energy Σ in Eq. (B.7) is then a product of Green's function and of a screened Coulomb interaction:

$$\Sigma(12) = iG(12)W(1^+2), \tag{B.10}$$

where the Green's function is the one consistent with the Dyson's equation. In principle, this process should continue until self-consistency is reached (until the input Green's function equals the output one). However, in practice it has never been pursued. Instead, calculations usually stop once the self-energy $\Sigma = G_0W_0$ (i.e., after one round) or by searching for the self-consistency of a reduced set of equations is obtained (see Fig. B.1(b)), short-cutting the vertex function. These approximations are called non-self-consistent (one-shot GW or G_0W_0) and self-consistent GW approximation (GWA), respectively. More details can be found in Onida et al. (2002), and Giantomassi et al. (2011).

B.3 Practical Implementation of G_0W_0

B.3.1 Perturbative Approach

In practical calculations, one needs a starting point for the independent-particle Green's function. The quasiparticle energies are more efficiently obtained from Eq. (B.1) than by solving the Dyson equation, Eq. (B.4). The approach consists in treating the difference of the self-energy and the Kohn–Sham potential (see Appendix A) as a perturbation. Despite some fundamental differences, the formal similarity is striking between the quasiparticle equation, Eq. (B.1), and the Kohn–Sham equation, Eq. (A.27):

$$\left[-\frac{1}{2}\nabla^2 + V_{\text{ext}}(\mathbf{r}) + V_{\text{H}}(\mathbf{r})\right]\psi_i^{\text{DFT}}(\mathbf{r}) + V_{\text{xc}}(\mathbf{r})\psi_i^{\text{DFT}}(\mathbf{r}) = E_i^{\text{DFT}}\psi_i^{\text{DFT}}(\mathbf{r}), \tag{B.11}$$

where V_{xc} is the DFT exchange–correlation potential and E_i^{DFT} is the DFT energy. It turns out that the quasiparticle and the DFT wavefunctions are typically similar, at least for many simple bulk materials. For example, in silicon, the overlap between the quasiparticle and the DFT wavefunctions has been reported to be close to 99.9% (Rohlfing et al. 2003; White et al. 1998). Hence, E_i^{DFT} and ψ_i^{DFT} for the ith state are used as a zeroth-order approximation for their quasiparticle counterparts. The QP energy E_i^{QP} is then calculated by adding to E_i^{DFT} the first-order perturbation correction, which comes from substituting the DFT exchange–correlation potential V_{xc} with the self-energy operator Σ:

$$E_i^{\text{QP}} = E_i^{\text{DFT}} + \langle\psi_i^{\text{DFT}}|\Sigma(E_i^{\text{QP}}) - V_{\text{xc}}|\psi_i^{\text{DFT}}\rangle. \tag{B.12}$$

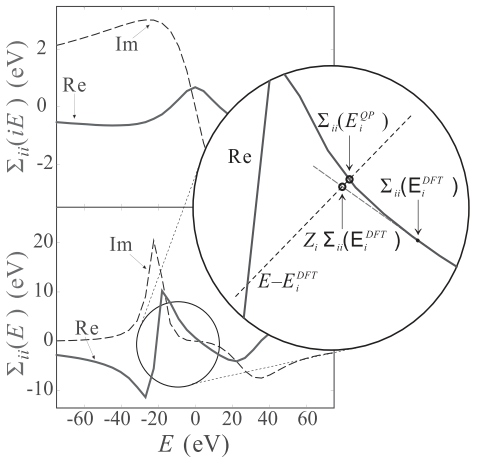

Figure B.2 The perturbative approach for finding the quasiparticle correction. In principle, the self-energy matrix element $\Sigma_{ii}(E) = \langle\psi_i^{\mathrm{DFT}}|\Sigma(E) - V_{\mathrm{xc}}|\psi_i^{\mathrm{DFT}}\rangle$ and the true quasiparticle correction $\Sigma(E_i^{\mathrm{QP}})$ are found from the solution of $E - E_i^{\mathrm{DFT}} = \Sigma_{ii}(E)$, i.e., at the crossing of the dashed black line and $\Sigma_{ii}(E)$ in the circular zoom-in. In practice, the perturbative approach exploits the fact that it is computationally feasible to use the Taylor expansion around $\Sigma(E_i^{\mathrm{DFT}})$ [Eqs (B.14) and (B.15)] and to find an approximate value for the QP correction at the crossing of the gray and black dashed lines. (Extracted from Giantomassi et al. (2011))

To solve Eq. (B.12), the energy dependence of Σ must be known analytically, which is usually not the case. Under the assumption that the difference between QP and DFT energies is relatively small, the matrix elements of the self-energy operator can be Taylor-expanded to the first-order around E_i^{DFT} to be evaluated at E_i^{QP}:

$$\Sigma(E_i^{\mathrm{QP}}) \approx \Sigma(E_i^{\mathrm{DFT}}) + (E_i^{\mathrm{QP}} - E_i^{\mathrm{DFT}}) \left.\frac{\partial\Sigma(E)}{\partial E}\right|_{E=E_i^{\mathrm{DFT}}}. \tag{B.13}$$

In this expression, the QP energy E_i^{QP} can be solved for

$$E_i^{\mathrm{QP}} = E_i^{\mathrm{DFT}} + Z_i\langle\psi_i^{\mathrm{DFT}}|\Sigma(E_i^{\mathrm{DFT}}) - V_{\mathrm{xc}}|\psi_i^{\mathrm{DFT}}\rangle, \tag{B.14}$$

where Z_i is the *renormalization factor* defined by

$$Z_i^{-1} = 1 - \left\langle\psi_i^{\mathrm{DFT}}\right| \left.\frac{\partial\Sigma(E)}{\partial E}\right|_{E=E_i^{\mathrm{DFT}}} \left|\psi_i^{\mathrm{DFT}}\right\rangle. \tag{B.15}$$

The principle is illustrated in Fig. B.2.

B.3.2 Plasmon Pole

Another approximation that is often used concerns the screened Coulomb interaction W. In the calculation of $W = \epsilon^{-1}v$, the inverse dielectric function is a frequency-dependent

matrix. The so-called plasmon-pole model of Godby–Needs (1989) consists in substituting the frequency dependence of the imaginary part of every element of the matrix with just a narrow Lorentzian peak, which is related to the plasmon excitations of the system, since $\Im\left[\epsilon^{-1}_{\mathbf{GG'}}\right]$ is the loss function. This loss function is expressed as

$$\Im\left[\epsilon^{-1}_{\mathbf{GG'}}\right] = A_{\mathbf{GG'}}(\mathbf{q}) \times \left[\delta(\omega - \tilde{\omega}_{\mathbf{GG'}}(\mathbf{q})) - \delta(\omega + \tilde{\omega}_{\mathbf{GG'}}(\mathbf{q}))\right], \tag{B.16}$$

where $A_{\mathbf{GG'}}$ is the amplitude of a delta function centered at the plasmon frequency $\tilde{\omega}_{\mathbf{GG'}}(\mathbf{q})$. Using the Kramers–Kronig relations, the resulting dielectric function is then, in reciprocal space,

$$\Re\left[\epsilon^{-1}_{\mathbf{GG'}}\right] = \delta_{\mathbf{GG'}} + \frac{\Omega^2_{\mathbf{GG'}}(\mathbf{q})}{\omega^2 - \tilde{\omega}^2_{\mathbf{GG'}}(\mathbf{q})}, \tag{B.17}$$

where **G** is a reciprocal lattice vector and **q** a vector in the first Brillouin zone together with Ω and $\tilde{\omega}$, which are parameters giving the strength and the position of the poles, respectively. They can be obtained, for example, using the static screening and sum rules (Godby & Needs 1989), or fitted to a full calculation along the imaginary energy axis. The exact formulation of the plasmon pole model is far beyond the scope of the present appendix. Note that other plasmon pole models have been proposed in the literature (Giantomassi et al. 2011).

In summary, the theoretical bases of MBPT and Hedin's equations have been presented leading to the GW and G_0W_0 approximations. The perturbative approach, which is the most commonly used for obtaining the quasiparticle energies, is introduced together with the frequency dependence of the self-energy operator based on the plasmon pole model. This MBPT within the G_0W_0 approximation is frequently used in various chapters to model more accurately the electronic structures of various carbon-based nanostructures.

Appendix C Green's Functions and *Ab Initio* Quantum Transport in the Landauer–Büttiker Formalism

The Landauer–Büttiker (LB) formalism is widely used to simulate transport properties at equilibrium. The applications range from 1D conductors such as nanowires, nanotubes, nanoribbons to 3D conductors such as molecular junctions with two or more contacts. At the *ab initio* level, this LB formalism is quite practical thanks to the Fisher–Lee relation, which connects the Landauer expression to the Green's function formalism. The transport properties of a given material can be simulated by finding the Green's function of the system within DFT (or even MBPT).

In this appendix, the Green's function formalism is briefly reviewed. Section C.1 provides an introduction with a derivation of the trace formula starting from the Lippmann–Schwinger equations, then Section C.2 discusses recursive Green's function techniques, while Dyson's equation is introduced and applied to the case of a disordered system in Section C.3. Finally, Section C.4 is devoted to the implementation of LB formalism in conventional *ab initio* codes in order to investigate coherent electronic transport in nanoscale devices.

C.1 Phase-Coherent Quantum Transport and the Green's Function Formalism

Green's functions are one of the most useful tools (Economou 2006) for calculation of different physical quantities of interest such as the density of states or the quantum conductance and conductivity. In the context of phase-coherent quantum transport, they play a crucial role because their relation with the scattering matrix can be exploited to compute the quantum transmission probabilities as needed within the Landauer–Büttiker formalism presented in Section 4.3.

Although the real power of the Green's functions (GFs) appears when many-body effects such as electron–electron or electron–phonon interactions are taken into account, the subjects addressed in the present appendix are limited to a description of noninteracting systems. In the following, a brief reminder to Green's functions (GFs) techniques is provided. Our focus will be on lattice models.

From the time-evolution operator to the Green's function in the energy domain. Given the (time-dependent) Schrödinger equation

$$i\hbar\frac{\partial}{\partial t}|\psi(t)\rangle = \mathcal{H}|\psi(t)\rangle \tag{C.1}$$

with the initial condition $|\psi(t = t_0)\rangle = |\psi_0\rangle$, the time-evolution operator $U(t, t_0)$ is defined as

$$|\psi(t)\rangle = U(t, t_0)|\psi(t_0)\rangle. \tag{C.2}$$

This operator is unitary, thereby ensuring that the probability is conserved, $\langle\psi(t)|\psi(t)\rangle = \langle\psi(t_0)|\psi(t_0)\rangle$ and satisfies:

$$i\hbar\frac{\partial U(t, t_0)}{\partial t} = \mathcal{H}U(t, t_0). \tag{C.3}$$

When the Hamiltonian is time-independent, the time-evolution operator is a function of the time difference $t - t_0$, $U(t, t_0) = U(t - t_0)$. If we are interested in the causal propagation of an initial state, then it makes sense to restrict the domain to $t - t_0 \geq 0$. Let us choose for simplicity $t_0 = 0$. One can see that the operator defined by

$$G^r(t) = -\frac{i}{\hbar}\Theta(t)U(t), \tag{C.4}$$

($\Theta(t)$ is the Heaviside step function) satisfies the inhomogeneous equation,

$$\left(i\hbar\frac{\partial}{\partial t} - \mathcal{H}\right)G^r(t) = \delta(t). \tag{C.5}$$

(By now, the delta term on the right-hand side should give a clue to readers that this function $G(t)$ is a Green's function!) For the case of a time-independent Hamiltonian, we have

$$G^r(t) = -\frac{i}{\hbar}\Theta(t)\sum_\alpha e^{-\frac{i}{\hbar}E_\alpha t}|\psi_\alpha\rangle\langle\psi_\alpha| \tag{C.6}$$

where E_α are the Hamiltonian eigenvalues.

Our next step is to Fourier transform the last equation from time to the energy domain:

$$G^r(\varepsilon) = -\frac{i}{\hbar}\sum_\alpha\int_{-\infty}^{\infty} dt\Theta(t)e^{\frac{i}{\hbar}(\varepsilon - E_\alpha)t}|\psi_\alpha\rangle\langle\psi_\alpha|. \tag{C.7}$$

By using the integral representation of the Heaviside function $\Theta(t) = \lim_{\eta\to 0^+} i\int_{-\infty}^{\infty}\frac{d\omega}{2\pi}\frac{e^{-i\omega t}}{\omega + i\eta}$, we get:

$$G^r(\varepsilon) = \lim_{\eta\to 0^+}\sum_\alpha\frac{|\psi_\alpha\rangle\langle\psi_\alpha|}{\varepsilon + i\eta - E_\alpha}. \tag{C.8}$$

This last expression is very useful as it is a representation of the energy domain Green's function in terms of the eigenstates and eigenvalues of the Hamiltonian. The eigenvalues of $\mathcal{H}$ correspond to the poles on the real axis of $G^r(\varepsilon)$, while the residues are related to the eigenfunctions. By using the closure relation, one can also write it in a more compact form:

$$G^r(\varepsilon) = \lim_{\eta\to 0^-}\frac{1}{\varepsilon + i\eta - E_\alpha}. \tag{C.9}$$

This Green's functions is called the *retarded* GF, to be distinguished from the advanced GF denoted as G^a,

$$G^a(\varepsilon) = \lim_{\eta \to 0^-} \frac{1}{\varepsilon + i\eta - E_\alpha}. \tag{C.10}$$

Choosing the retarded or the advanced Green's function implies a choice on the boundary conditions on the eigenfunctions (Messiah 1999). The sign of the imaginary part η is related to the sign of the time that we want to observe (past or future). In particular, we are interested in the retarded Green's function which gives the causal response. Hereafter, we will simply call it the Green's function and for the sake of brevity, we will sometimes omit the $\lim_{\eta \to 0^+}$ limit.

Interpretation. The Green's functions in the energy domain provide the response of the system to a source term (f) added to the time-independent Schrödinger equation:

$$(\mathcal{H} - (\varepsilon + i\eta))\,|\psi(\varepsilon)\rangle = |f\rangle. \tag{C.11}$$

Indeed,

$$|\psi(\varepsilon)\rangle = -G^r(\varepsilon)\,|f\rangle \tag{C.12}$$

where $G^r = \lim_{\eta \to 0^+}[(\varepsilon + i\eta) - \mathcal{H}]^{-1}$ is an operator defining the retarded (r) Green's functions. This allows for a straightforward interpretation of the GFs.

Fisher–Lee relation. The Fisher–Lee relation allows us to connect the scattering matrix element from electrode β to electode α, $S_{\alpha,\beta}$ with the Green's function (Fisher & Lee 1981). For the simple case where the electrodes contain a single channel each, we have:

$$S_{\alpha,\beta}(\varepsilon) = \delta_{\alpha,\beta} - 2i\sqrt{\Gamma_\alpha(\varepsilon)\Gamma_\beta(\varepsilon)}G^r_{\alpha,\beta}(\varepsilon) \tag{C.13}$$

where $\Gamma_\alpha = \hbar v_\alpha / a$, with v_α the group velocity in the corresponding channel and a the lattice constant. The components of S give the probability amplitudes for transmission ($\alpha \neq \beta$) and reflection ($\alpha = \beta$).

Matrix form. One can also formulate the problem in a discrete basis, say $\{|i\rangle\}$ (for example, think of a localized basis set in a crystal structure). Given the Schrödinger equation in matrix form,

$$(\varepsilon \mathbf{I} - \mathbf{H})\mathbf{u} = 0,$$

formally, we define the retarded Green's function (in this matrix form also called the resolvent operator),

$$\mathbf{G}^r(\varepsilon) = \lim_{\eta \to 0^+}((\varepsilon + i\eta)\mathbf{I} - \mathbf{H})^{-1}. \tag{C.14}$$

Each element of this matrix can be written as:

$$G^r_{i,j} = \lim_{\eta \to 0^+} \sum_\alpha \frac{\psi^*_{\alpha,i}\psi_{\alpha,j}}{(\varepsilon + i\eta) - E_\alpha} \tag{C.15}$$

where $\psi_{\alpha,i}$ is the ith component of the eigenvector $\boldsymbol{\psi}_\alpha$ corresponding to the Hamiltonian in matrix form ($\mathbf{H}$), E_α is the corresponding eigenvalue.

Analogously, one can define the advanced Green's function in matrix form.

Relation with the density of states. Another quantity of interest is the local density of states at site i, denoted as $N_i(\varepsilon)$. From the expression for the Green's functions in basis set, one can see that the total density of states $N(\varepsilon)$ is given by

$$N(\varepsilon) = -\frac{1}{\pi}\sum_i \operatorname{Im} G^r_{i,i} = -\frac{1}{\pi}\operatorname{Tr}[\operatorname{Im}\mathbf{G}^r] = \sum_i N_i(\varepsilon). \tag{C.16}$$

$N(\varepsilon)d\varepsilon$ gives the number of states in the energy interval $[\varepsilon, \varepsilon + d\varepsilon]$. One can verify that when the system is finite, the density of states is a sum of delta functions.

Lippmann-Schwinger equations. Another interesting property arises when considering a perturbation V. Assuming that the solutions of the unperturbed Schrödinger equation are known, ($\mathcal{H}^0\,|\psi_n^0\rangle = E_n\,|\psi_n^0\rangle$), the solutions of the perturbed Schrödinger equation,

$$\Big(\mathcal{H}^0 + V - (E + i\eta)\Big)\,|\psi(\mathbf{r})\rangle = 0 \tag{C.17}$$

are given by

$$|\psi(E)\rangle = |\psi^0(E)\rangle + G^0(E)\,V|\psi(E)\rangle \tag{C.18}$$

or equivalently

$$|\psi(E)\rangle = |\psi^0(E)\rangle + G(E)\,V|\psi^0(E)\rangle \tag{C.19}$$

where the $G^0(E)$ and $G(E)$ functions are respectively the retarded GFs of the unperturbed and perturbed system. These relations are called the Lippmann-Schwinger equations and can be applied to the scattering problem. Indeed, this procedure allows to straightforwardly connect the bulk propagating states of the isolated leads ($|\phi^L_{k_j}\rangle$) to the stationary scattering states of the complete system ($|\psi^L_{k_j}\rangle$). Assuming that the perturbation of the system V corresponds to the coupling between the leads and the central region (i.e., $V = H_{\mathrm{LD}} + H_{\mathrm{DL}} + H_{\mathrm{DR}} + H_{\mathrm{RD}}$, the Lippmann-Schwinger Eq. (C.19) is rewritten as

$$|\psi^L_{k_j}\rangle = |\phi^L_{k_j}\rangle + G(E_{k_j})\,V|\phi^L_{k_j}\rangle. \tag{C.20}$$

Dyson equations. Following the same idea as before, if $\mathcal{H} = \mathcal{H}^0 + \mathcal{H}^1$, one can find the so-called Dyson equations:

$$G = G^0 + G^0\mathcal{H}^1 G \tag{C.21}$$

and

$$G = G^0 + G\mathcal{H}^1 G^0 \tag{C.22}$$

where G^0 is the GF associated to $\mathcal{H}^0$ and G is the GF associated to $\mathcal{H}$.

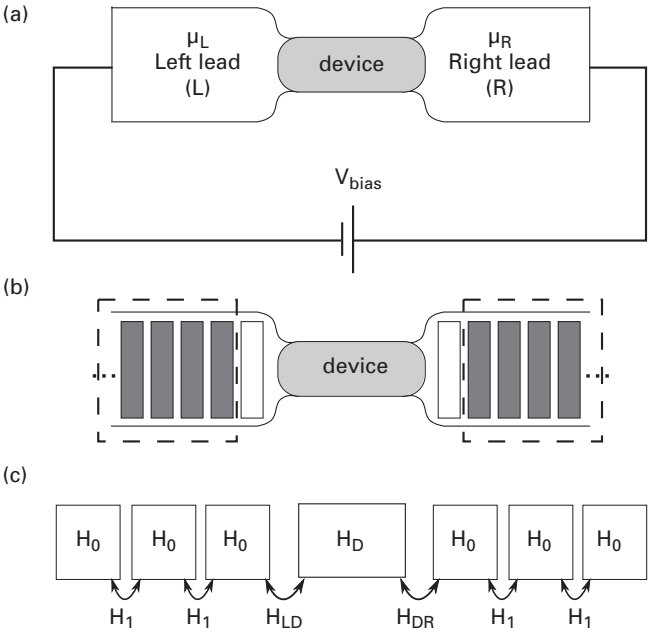

Figure C.1 Schematic representation of the two-terminal transport setup: (a) connected to an external battery. (b) The device is contacted to two semi-infinite bulk electrodes assumed to be at thermal equilibrium. (c) Block-decomposition of the Hamiltonian into sub-matrices associated with the central region and the principal layers of the semi-infinite leads. H_D contains all the interactions inside the central region. H_{LD} and H_{DR} describe the coupling between the central region and the leads. H_0 accounts for all interactions inside the principal layers (PLs) of the leads. H_1 describes the coupling between nearest-neighbor PLs.

Formulation of the problem in a typical transport setup. Hereafter, the typical transport setup depicted in Fig. C.1 is considered in a general scattering approach. This system is conveniently divided into three parts: (i) the left and (ii) right leads that are assumed to be made of perfect, defect-free crystalline materials, and (iii) a central region that can be any kind of set of atoms. This region, which potentially corresponds to the active part of the device, could thus be a single atom, a molecule, a section of carbon nanotubes, a finite-size graphene nanoribbon, or even a bulk slab. Besides, the central part and the leads may either have the same cross section dimensionality or not (e.g., a single molecule stretched between two massive gold electrodes). In summary, the system consists of two semi-infinite, defect-free, electrodes that are coupled to a central region where all the scattering processes take place.

This system can also be conveniently described by means of *principal layers*. A principal layer (PL) is the smallest set of atoms that represents a unit cell of the semi-infinite crystal forming the leads and which interacts only with the nearest-neighbor PLs. Therefore, owing to the decomposition onto a set of localized basis functions, the Hamiltonian of the system under consideration can be written in matrix form as

$$\mathcal{H} = \begin{pmatrix} \cdots & \cdots & \cdots & \cdots & & & \\ H_{-1} & H_0 & H_1 & 0 & \cdots & & \\ 0 & H_{-1} & H_0 & H_{\mathrm{LD}} & 0 & \cdots & \\ \cdots & 0 & H_{\mathrm{DL}} & H_D & H_{\mathrm{DR}} & 0 & \cdots \\ & \cdots & 0 & H_{\mathrm{RD}} & H_0 & H_1 & 0 \\ & & \cdots & 0 & H_{-1} & H_0 & H_1 \\ & & & \cdots & \cdots & \cdots & \cdots \end{pmatrix} \tag{C.23}$$

where H_0 is the $[n \times n]$ matrix that describes all the interactions within the principal layers. Similarly (H_D) is the $[m \times m]$ matrix describing the interactions within the central region. Here, n and m are the dimensions of the basis set localized within a principal layer and the central region, respectively. Finally, the interaction between nearest-neighboring PLs are contained in the $[n \times n]$ H_1 matrix, and the interaction between the central part and the left (right) lead is described in the $[n \times m]$ ($[m \times n]$) H_{LD} (H_{DR}) matrix. In the case of non-orthogonal localized orbitals, the overlap matrix (S) adopts the same block matrix form as the Hamiltonian ($\mathcal{H}$).

Such a transport setup imposes to deal with an infinite hermitian problem whose solutions are not accessible by application of the Bloch theorem owing to the central region that breaks the translational symmetry. However, the problem can be solved by computing the retarded Green's function of the single-particle Schrödinger equation. Roughly speaking, this function gives the response at any point of the system due to a particular excitation at any other. The retarded Green's function of the full system ($G^r(E)$) satisfies,

$$[(E + i\eta)S - \mathcal{H}]\, G^r(E) = \mathbb{I} \tag{C.24}$$

where $\mathbb{I}$ is an infinite-dimensional identity matrix and $(E + i\eta)$ is the energy complemented with an infinitesimal positive imaginary part in order to insure the causality (otherwise, if one takes $\eta \to 0^-$ one gets the advanced GF G^a). $\mathcal{H}$ and S are the infinite dimensional matrix Hamiltonian and overlap matrix.

Let us now apply the Green's function formalism to the transport problem illustrated in Fig. C.1. Though the matrix that has to be inverted is infinite-dimensional, the Green's function formalism allows to account naturally for the open boundary conditions that rule the asymptotic behavior of the transport problem. In the following, the Green's function of the central part is shown to be easily calculated separately, without calculating the whole Green's function. Using the definition of the retarded Green's function, Eq. (C.24) reads

$$\begin{pmatrix} \varepsilon^+ S_L - H_L & \varepsilon^+ S_{\mathrm{LD}} - H_{\mathrm{LD}} & 0 \\ \varepsilon^+ S_{\mathrm{DL}} - H_{\mathrm{DL}} & \varepsilon^+ S_D - H_D & \varepsilon^+ S_{\mathrm{DR}} - H_{\mathrm{DR}} \\ 0 & \varepsilon^+ S_{\mathrm{RD}} - H_{\mathrm{RD}} & \varepsilon^+ S_R - H_R \end{pmatrix} \cdot \begin{pmatrix} G_L & G_{\mathrm{LD}} & G_{\mathrm{LR}} \\ G_{\mathrm{DL}} & G_D & G_{\mathrm{DR}} \\ G_{\mathrm{RL}} & G_{\mathrm{RD}} & G_R \end{pmatrix} = \mathbb{I} \tag{C.25}$$

where $\varepsilon^+ = (E + i\eta)$ and the Hamiltonian overlap, and Green's matrices have been divided into sub-matrices corresponding to the left/right leads and the central region.

The $H_{L/R}$ sub-matrices account for all interaction inside the left and right leads. These blocks are thus infinite-dimensional $[\infty \times \infty]$, as well as $S_{L/R}$ and $G_{L/R}$. On the contrary, the interesting sub-matrices (i.e., S_D, H_D, and G_D) have the dimension $[m \times m]$, where m is the number of degrees of freedom (i.e., orbitals) in the central region. Finally, the sub-matrices H_{LD}, and H_{DR} that represent the interactions between the leads and the central region have the dimension $[\infty \times m]$ and $[m \times \infty]$, respectively. However, these sub-matrices (H_{LD} and H_{DR}) are actually zero with the exception of the bottom/top n lines that represent the coupling between the last PL and the central region (i.e., the H_{LD} and H_{DR} matrices introduced in Eq. (C.23)). Here, n is the number of degrees of freedom (i.e., orbitals) in the PL.

With selection of the three block-equations that involve G_D, the following system of equations is readily derived

$$\left(\varepsilon^{+} S_L - H_L\right) G_{\mathrm{LD}} + \left(S_{\mathrm{LD}} - H_{\mathrm{LD}}\right) G_D = 0 \tag{C.26}$$

$$\left(S_{\mathrm{DL}} - H_{\mathrm{DL}}\right) G_{\mathrm{LD}} + \left(\varepsilon^{+} S_D - H_D\right) G_D + \left(S_{\mathrm{DR}} - H_{\mathrm{DR}}\right) G_{\mathrm{RD}} = 0 \tag{C.27}$$

$$\left(S_{\mathrm{RD}} - H_{\mathrm{RD}}\right) G_D + \left(S_R - H_R\right) \cdot G_{\mathrm{RD}} = 0 \tag{C.28}$$

With substitution of the Eqs. C.26 and C.27 into Eq. (C.28), an explicit expression for the sub-matrix G_D is obtained, and has the following form

$$G_D^r(E) = \left[\varepsilon^{+} S_D - H_D^{\mathrm{eff}}(E)\right]^{-1} \tag{C.29}$$

with

$$H_D^{\mathrm{eff}}(E) = \left[H_D - \Sigma_L^r(E) - \Sigma_R^r(E)\right] \tag{C.30}$$

where the concept of the retarded self-energies associated with the left and right leads is introduced

$$\begin{aligned} \Sigma_L^r(E) &= \left[\varepsilon^{+} S_{\mathrm{DL}} - H_{\mathrm{DL}}\right] G_L^{0r} \left[\varepsilon^{+} S_{\mathrm{LD}} - H_{\mathrm{LD}}\right] \\ \Sigma_R^r(E) &= \left[\varepsilon^{+} S_{\mathrm{DR}} - H_{\mathrm{DR}}\right] G_R^{0r} \left[\varepsilon^{+} S_{\mathrm{RD}} - H_{\mathrm{RD}}\right]. \end{aligned} \tag{C.31}$$

Here, G_α^{0r} are the retarded Green's function associated with the isolated leads $\alpha = L, R$,

$$G_\alpha^{0r} = \left[\varepsilon^{+} S_\alpha - H_\alpha\right]^{-1}. \tag{C.32}$$

Although this last equation still contains infinite matrices, the self-energy can be computed easily by exploiting the fact that the interaction between the central region and the leads only involves a finite number of atoms close to the interface. Besides, owing to the sparsity of $\{H_{\mathrm{DL}}, S_{\mathrm{LD}}, \mathcal{H}_{\mathrm{DR}}, S_{\mathrm{RD}}\}$, only the n lines of $G_{L/R}^{0r}$ that correspond to the surface PL are actually needed in Eq. (C.31). This sub-matrix $G_{L/R}^{0r}$ has the finite dimension $[n \times n]$ and can be computed either semi-analytically or by recursion methods (see Fig. C.2).

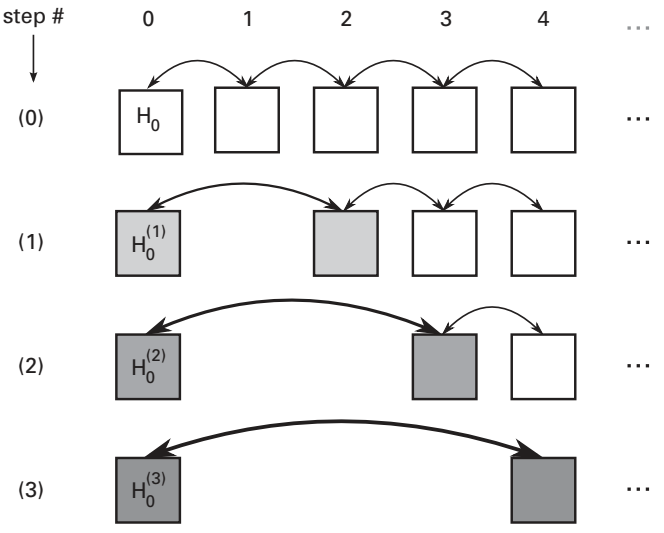

Figure C.2 Scheme representing the recursive procedure described in the text for the calculation of the surface Green's functions. At each step, one layer is eliminated and its effects included through a renormalization of the adjacent's layer Hamiltonian and the matrix elements between them.

In summary, the Green's function expressed in Eq. (C.29) is defined within the central region only while the effect of the contact are mapped into complex self-energies. The imaginary part of the self-energies accounts from the finite lifetime of the electronic states inside the central region. Indeed, due to the interactions with the contact, eigenstates can leak out from the central region.

The connection with the transmission probability $\mathcal{T}$ (from left to right) is given by the so-called trace formula:

$$\mathcal{T}(\varepsilon) = 4\mathrm{Tr}\left[\Gamma_L G_D^{r\dagger} \Gamma_R G_D^r\right], \tag{C.33}$$

where we have introduced the the broadening $\Gamma_{L/R} = \frac{i}{2}\left[\Sigma_{L/R}^r - \Sigma_{L/R}^{r\dagger}\right]$ (which accounts for the non-hermicity of the self-energy operators). We note that in the literature, it is also usual to define these broadenings without the factor $\frac{1}{2}$ (in such a case the factor 4 in the previous equation needs to be removed).

The expression for the electric current through the junction is (Meir & Wingreen 1992),

$$I = \frac{2e}{h} \int 4\mathrm{Tr}\left[\Gamma_L G_D^{r\dagger} \Gamma_R G_D^r\right]\left[f(E-\mu_L) - f(E-\mu_R)\right] dE, \tag{C.34}$$

the factor 2 on the right-hand side takes into account the spin degeneracy. Expression (Eq. (C.34)) is the Landauer formula (Landauer 1957) for a two-terminal system where the transmission probability is written as a trace over the transmission matrix $[\Gamma_L G_D^{r\dagger} \Gamma_R G_D^r]$.

C.2 Self-Energy Corrections and Recursive Green's Functions Techniques

Recursive Green's functions techniques must be in your toolbox as they offer an efficient way to compute the self-energy corrections due to the semi-infinite leads and the Green's functions for the sample region (Guinea et al. 1983; Lopez Sancho et al. 1985; Pastawski et al. 1983). This is specially the case for tight-binding Hamiltonians where their sparse nature can be fully exploited with these techniques.

In the previous section, we considered a tripartite system and expressed the GFs of the central region in terms of an effective $[m \times m]$ Hamiltonian. The other two parts of the system are taken into account exactly through the self-energy corrections. If these two parts consisted, let's say, of only one layer, then Eq. (C.31) together with Eq. (C.32) would provide closed expressions for the self-energy corrections.

For the semi-infinite leads, further work is needed. One may take advantage of the fact that the layers are coupled following a nearest-neighbor structure. Indeed, the Hamiltonian has a tridiagonal block-matrix form that can be exploited to iteratively incorporate the effect of the leads layer by layer following each time the procedure described before for the tripartite system. This is schematically represented in Fig. C.2. The upper line, step (0), represents the principal layers of the semi-infinite lead's Hamiltonian numerated from 0 on, H_0 is the intralayer block-matrix Hamiltonian while $H_{1(-1)}$ is the interlayer Hamiltonian connecting with the next layer to the left (right). Throughout this section, an orthonormal basis will be considered, the case when the overlap matrix is different from the identity matrix can be worked out easily provided that it preserves the block tridiagonal structure.

At step (j), layer j is eliminated, thereby renormalizing the adjacent block Hamiltonian matrices. Their updated values are denoted by $H_0{}^{(j)}$ (marked with shaded gray in Fig. C.2), the effective Hamiltonian is written as:

$$\mathcal{H}_{\text{lead}}^{\text{eff}(n)} = \begin{pmatrix} H_0^{(j)} & H_1^{(j)} & 0 & \cdots & & \\ H_{-1}^{(j)} & H_0^{(j)} & H_1 & 0 & \cdots & \\ 0 & H_{-1} & H_0 & H_1 & 0 & \cdots \\ & & \cdots & \cdots & \cdots & \cdots \end{pmatrix}, \tag{C.35}$$

where

$$H_0^{(j)}(E) = H_0^{(j-1)} + H_{-1}^{(j-1)} G_{(j-1)}^{0r}(E) H_1^{(j-1)}, \tag{C.36}$$

$$H_{\pm 1}^{(j)}(E) = H_{\pm 1}^{(j-1)} G_{(j-1)}^{0r}(E) H_{\pm 1}^{(j-1)}, \tag{C.37}$$

$$G_{(j-1)}^{0r}(E) = ((E + i\eta)\mathbb{I} - H_0^{(j-1)}(E))^{-1}, \tag{C.38}$$

$$H_0^{(0)} = H_0, H_{\pm 1}^{(0)} = H_{\pm 1}. \tag{C.39}$$

By setting a small imaginary part η, after a large enough number of decimation steps $H_0^{(n)}(E)$ will converge and the associated surface GFs can be computed. This closes the loop for the calculation of the self-energy corrections Eq. (C.31). For N decimation

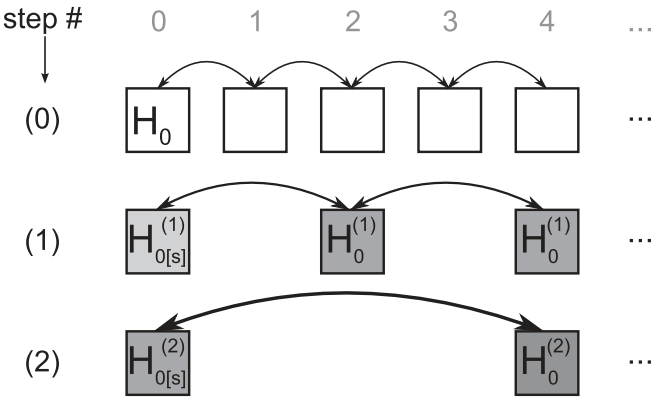

Figure C.3 An alternative and more efficient scheme for the calculation of the surface Green's functions. In contrast to the procedure shown in Fig. C.2, at each step, half of the layers is eliminated.

steps, the computational cost will scale like $N \times n^3$ (since matrix inversions at each step require n^3 operations).

An alternative and much faster scheme (Lopez Sancho et al. 1985) that fully exploits the translational invariance within the leads is represented in Fig. C.3. Here, at each step instead of one, half of the layers are eliminated. The effective block-matrix Hamiltonian are not uniform but distinguish the surface layer from the bulk ones, and after j iteration steps it is given by

$$\mathcal{H}_{\text{lead}}^{\text{eff}(n)} = \begin{pmatrix} H_{0[s]}^{(j)} & H_1^{(j)} & 0 & \cdots & & \\ H_{-1}^{(j)} & H_0^{(j)} & H_1^{(j)} & 0 & \cdots & \\ 0 & H_{-1}^{(j)} & H_0^{(j)} & H_1 & 0 & \cdots \\ & & \cdots & \cdots & \cdots & \cdots \end{pmatrix}, \tag{C.40}$$

where

$$H_{0[s]}^{(j)}(E) = H_{0[s]}^{(j-1)} + \Sigma_+(E), \tag{C.41}$$

$$H_0^{(j)}(E) = H_0^{(j-1)} + \Sigma_+(E) + \Sigma_-(E), \tag{C.42}$$

$$H_{\pm 1}^{(j)}(E) = H_{\pm 1}^{(j-1)} G_{(j-1)}^{0r}(E) H_{\pm 1}^{(j-1)}, \tag{C.43}$$

$$\Sigma_\pm(E) = H_{\mp 1}^{(j-1)} G_{(j-1)}^{0r}(E) H_\pm^{(j-1)}, \tag{C.44}$$

$$G_{(j-1)}^{0r}(E) = ((E + i\eta)\mathbb{I} - H_0^{(j-1)}(E))^{-1}, \tag{C.45}$$

$$H_0^{(0)} = H_{0[s]}^{(0)} = H_0, H_{\pm 1}^{(0)} = H_{\pm 1}. \tag{C.46}$$

After N steps, the surface layer Hamiltonian $H_{0[s]}^{(N)}$ incorporates the effect of $2^N - 1$ neighboring layers (to be compared with N in the previous scheme). The schemes

presented here can be used as well to compute the Green's functions for the sample as needed for the calculation of the conductance using the trace formula. In that case, one must note that only GFs between the first and last layer in the device region are needed because of the sparsity of the self-energies that only have nonvanishing elements on the sites of the device that are connected to the leads as discussed in the paragraph after Eq. (C.32). Furthermore, when a mode decomposition such as the one explained in Section 5.2.2 is feasible, the reduction in the computational cost is enormous.

In cases where the layer dimensions are irregular across the sample or when additional leads are connected to it, the schemes above may fail or just be inefficient. A generalization for such cases called *knitting algorithm* was presented in Kazymyrenko & Waintal (2008) and associated resources are also available on the web (http://inac.cea.fr/Pisp/xavier.waintal/KNIT.php). A more recent project for transport calculations called KWANT (Groth et al. 2014) is also available (https://kwant-project.org/).

C.3 Dyson's Equation and an Application to Treatment of Disordered Systems

The expansion of the Green's function in terms of the eigenstates provides a very elegant representation. The trouble is that most of the time, those eigenstates are unknown. However, if the eigenstates of a given Hamiltonian $\mathcal{H}_0$ are known, then one expects that if an extra term $\mathbf{V}_{\text{dis}}$, describing for example the disorder strength, remains weak enough to be treated as a perturbation, its effect can be captured (to a first approximation) through the induced elastic transition between states of the otherwise clean system. The exact GF for the system is

$$((E + \mathrm{i}\eta)\mathbb{I} - \hat{\mathcal{H}}_0 - \mathbf{V}_{\text{dis}})G^r(E) = \mathbb{I}, \tag{C.47}$$

or

$$((E + \mathrm{i}\eta)\mathbb{I} - \hat{\mathcal{H}}_0)G^r(E) = (\mathbb{I} + \mathbf{V}_{\text{dis}})G^r(E), \tag{C.48}$$

which can be recast in the so-called Dyson equation,

$$G^r(E) = G_0^r(E) + G_0^r(E)\mathbf{V}_{\text{dis}}G^r(E), \tag{C.49}$$

which is a recursive equation valid whatever the strength of the potential $\mathbf{V}_{\text{dis}}$. Given its form, the Dyson equation can be expanded to make explicit all multiple scattering events as

$$\begin{aligned} G^r(\varepsilon) &= G_0^r(E) + G_0^r(E)\mathbf{V}_{\text{dis}}G_0^r(E) + G_0^r(E)\mathbf{V}_{\text{dis}}G_0^r(E)\mathbf{V}_{\text{dis}}G_0^r(E) + \cdots \\ &= G_0^r(E)\Big(\mathbb{I} + \mathbf{V}_{\text{dis}}G_0^r(E) + (\mathbf{V}_{\text{dis}}G_0^r(E))^2 + (\mathbf{V}_{\text{dis}}G_0^r(\varepsilon))^3 + \cdots\Big). \end{aligned} \tag{C.50}$$

In the presence of the disorder potential, the eigenstates of H_0 acquire a finite lifetime due to elastic scattering. To compute such a new timescale, one can consider the propagation probability amplitudes $\langle k|G^r(E)|k'\rangle$, given by

$$\langle k|G^r(E)|k'\rangle = G_0^r(E,k)\delta_{k,k'} + G_0^r(E,k)\langle k|\mathbf{V}_{\rm dis}|k'\rangle G_0^r(E,k) + \int \frac{d^dq}{(2\pi)^d} G_0^r(E,k)\langle k|\mathbf{V}_{\rm dis}|q\rangle G_0^r(E,q)\langle q|\mathbf{V}_{\rm dis}|k'\rangle G_0^r(E,k') + \cdots, \tag{C.51}$$

where the expansion should be made to all orders of the multiple scattering events (see Roche et al. (2006)). There are plenty of possible sources of disorder, such as a random distribution (with density n_i) of structural defects or charged impurities for instance, described by a screened Coulomb potential of the type $V(r-R_i) \sim -e^2/|r-R_i|^2 \times e^{-|r-R_i|/\lambda}$.

In practice, such a calculation for a particular disorder configuration is analytically and numerically out of reach without further approximation. Fortunately, when dealing with transport properties in disordered materials, one is first mainly interested by some disorder-average property, and if existing, some universalities of transport features. Transport coefficients can be generally computed from disorder-averaged Green function elements such as $\langle k|G^r(E)|k'\rangle_{\rm dis}$, where an average over a disorder statistics is performed. Disorder averaging turns out to restore translational invariance of the computed quantity, an essential point to evaluate how averaged Green functions are renormalized in the presence of a weak disorder (treated perturbatively). The Dyson equation (also expressed using Feynman diagrams as illustrated in Fig. C.4) is essentially rewritten as (we take $k' = k$ for simplicity without loss of generality)

$$\langle k|G^r(E)|k\rangle_{\rm dis} = G_0^r(E,k) + G_0^r(E,k)\Sigma_k(E)\langle k|G^r(E)|k\rangle_{\rm dis}, \tag{C.52}$$

where $\Sigma_k(E)$ encompasses the whole ensemble of so-called irreducible Feynman diagrams of $\langle k|G^r(E)|k\rangle_{\rm dis}$, which cannot be decomposed into another subset of diagrams (see Fig. C.5). Equation (C.52) is solved easily and gives

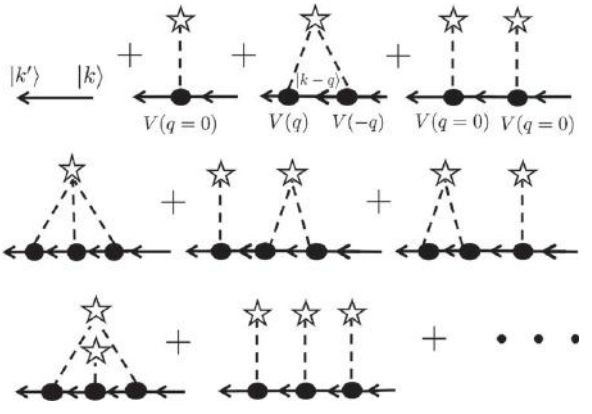

Figure C.4 Feynman diagrams representing probability amplitude $\langle k|G^r(E)|k'\rangle_{\rm dis}$ up to the third order of perturbation. Star symbols denote the averaged scattering impurity potential, the number of stars giving the order of the perturbation. Filled circles pinpoint changes of the momentum direction upon scattering.

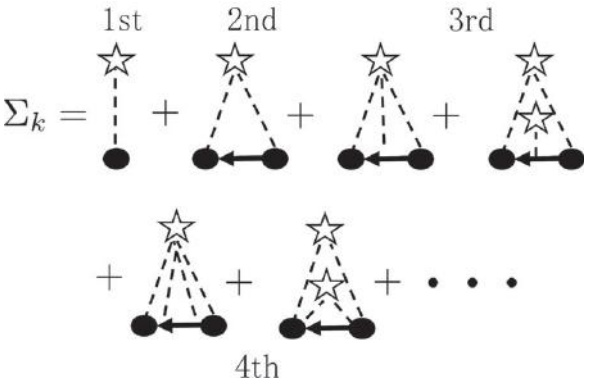

Figure C.5 Irreducible Feynman diagrams in the self-energy $\Sigma_k(\varepsilon)$ up to third order plus two fourth-order diagrams for illustration.

$$\langle k|G^r(E)|k\rangle_{\text{dis}} = \frac{1}{E - \varepsilon_k - \Sigma_k(E)}. \tag{C.53}$$

The calculation of $\Sigma_k(E)$ can be achieved to a given order of perturbation theory, which obviously depends on the disorder strength compared to the energy scale defining the unperturbed structure ($\pi - \pi$ hopping term in sp^2 carbon structures). At the lowest order of the so-called Born approximation, $\Sigma_k(E) = n_i V_0 = n_i \int d\mathbf{r} V(\mathbf{r})$ (the first diagram in Fig. C.5), the average Green function is just modified by a constant shift of all energy levels with no dynamical consequence. In contrast, at the first order of the Born approximation (second diagram of Fig. C.5), $\Sigma_k(E) = \sum_q |V(k-q)|^2 \frac{1}{E-\varepsilon_q+i\eta}$ (note that $V(k-q) = 1/\Omega \int d\mathbf{r} e^{(\mathbf{k}-\mathbf{q})\cdot\mathbf{r}} V(\mathbf{r})$, which has real and imaginary parts, $\Im m \Sigma_k(E)$ moves the poles of the Green function away from the real axis, and is related to the finite lifetime of propagating states conveyed by the initial eigenstates of unperturbed Hamiltonian). In the Born approximation, to the second order of perturbation theory, $\Sigma_k(E)$ is derived as

$$\Re e \Sigma_k(E) = n_i V(q=0) + \sum_q \frac{|V(q)|^2}{\varepsilon_k - \varepsilon_q}, \tag{C.54}$$

$$\Im m \Sigma_k(E) = -\pi n_i \sum_q |V(k-q)|^2 \delta(\varepsilon_k - \varepsilon_q) = \frac{\hbar}{\tau_k}, \tag{C.55}$$

which is also known as the Fermi golden rule (τ_k is the elastic relaxation time). Using such an expression for the self-energy, the impurity average Green function in energy becomes

$$\langle k|G^r(E)|k\rangle_{\text{dis}} = \frac{1}{E - (\varepsilon_k + \Re e \Sigma_k(E)) + \frac{i\hbar}{\tau_k}}. \tag{C.56}$$

By Fourier-transforming such a Green function, one obtains the time- and space-dependent propagators as

$$\langle k|G^r(t)|k\rangle_{\rm dis} = \int \frac{dE}{2\pi} \frac{{\rm e}^{-{\rm i}(E+{\rm i}\eta)t}}{E-(\varepsilon_k + \Re{\rm e}\,\Sigma_k(E)) + \frac{i\hbar}{\tau_k}} = -i\theta(t){\rm e}^{-i\varepsilon_k t}{\rm e}^{-t/\tau_k},$$

$$\langle k|G^r(\mathbf{r})|k\rangle_{\rm dis} = -\frac{\pi\rho(E)}{k_F.r}{\rm e}^{ik|r|}{\rm e}^{-|r|/\ell_{k_F}},$$

with $\ell_{k_F} = v_k\tau_{k_F}$. The impurity scattering transforms the free electrons into quasiparticles with a finite lifetime given by scattering time and a finite elastic mean free path. When dealing with transport coefficients, one needs to evaluate the impurity-average of two-particle Green functions. Indeed, the Kubo–Greenwood formula (in d dimensions) for the quantum conductivity can be rewritten in terms of Green functions as (Kubo 1966)

$$\sigma_{xx} = e^2 \int \frac{d^dk}{(2\pi)^d}\frac{dE}{2\pi}v_x^2(k)\frac{f(E)-f(E+\hbar\omega)}{\hbar\omega}G^r(k,E)G^a(k,E+\hbar\omega), \tag{C.57}$$

developed on the basis of eigenstates of the unperturbed Hamiltonian. The perturbation introduced by a weak disorder potential yields a finite dissipation, which guarantees a finite conductivity. Similar to the one-particle Green function case, the calculation of the propagator $G^r(k,E)G^a(k,E+\hbar\omega)$ is achieved using impurity-averaging and restored translational invariance. The Dyson equation generalized to the two-particles Green function is named the Bethe–Salpeter equation, which gives

$$\begin{aligned}\langle G^r(k,E)G^a(k',E+\hbar\omega)\rangle_{\rm dis} &= \delta(k,k')\langle G^r(k,E)\rangle_{\rm dis}\langle G^a(k',E+\hbar\omega)\rangle_{\rm dis}\\ &+ \langle G^r(k,E)\rangle_{\rm dis}\langle G^a(k,E+\hbar\omega)\rangle_{\rm dis}\mathcal{C}(k,k',\omega)\langle G^r(k',E)\rangle_{\rm dis}\\ &\times \langle G^a(k,E+\hbar\omega)\rangle_{\rm dis}.\end{aligned} \tag{C.58}$$

The first term is the classical (diffusion) term, which excludes all quantum interferences and obeys a classical diffusion equation. The second term contains all constructive quantum interferences that survive to the impurity-averaging process, and which are condensed in the so-called Cooperon term $\mathcal{C}(k,k',\omega)$, which contains all irreducible Feynman diagrams describing such interferences. This is the foundation of weak localization theory, and by developing the perturbation series for the two-particle Green function, the general form of $\mathcal{C}(k,k',\omega)$ is derived and shown to obey the equation

$$\begin{aligned}\mathcal{C}(k,k',\omega) &= \langle G^r(k,E)\rangle_{\rm dis}V(q=0)\langle G^a(k',E+\hbar\omega)\rangle_{\rm dis}\\ &+ \sum_q |V(q)|^2\langle G^r(k-q,E)\rangle_{\rm dis}\langle G^a(k'+q,E+\hbar\omega)\rangle_{\rm dis}|V(-q)|^2+\cdots\end{aligned}$$

Assuming isotropic scattering, $|V(q)|^2 = \mathcal{C}_0 = \hbar/(2\pi\rho(E)\tau)$, and defining

$$\Pi = \sum_q \langle G^r(k-q,E)\rangle_{\rm dis}\langle G^a(k'+q,E+\hbar\omega)\rangle_{\rm dis}, \tag{C.59}$$

the infinite series rewrites $\mathcal{C}(k,k',\omega) = \mathcal{C}_0 + \mathcal{C}_0\Pi\mathcal{C}_0 + \mathcal{C}_0\Pi\mathcal{C}_0\Pi\mathcal{C}_0 + \cdots$, or $\mathcal{C}(k,k',\omega) = \mathcal{C}_0(1 + \Pi\mathcal{C}_0 + (\Pi\mathcal{C}_0)^2 + \cdots) = \mathcal{C}_0/(1 - \Pi\mathcal{C}_0)$, which finally simplifies to

$$\mathcal{C}(k,k',\omega) = \frac{\hbar}{2\pi\rho(E)\tau^2}\frac{1}{D(k+k') - i\omega}. \tag{C.60}$$

It is clear that such a Cooperon term presents a divergence when $k' = -k$, which pinpoints a mathematical pole of the interferences when considering the backscattering probability. The quantum correction of the conductivity is then given by

$$\delta\sigma(\omega) = -\frac{2e^2}{\pi\hbar}D\tau\int\frac{d^dq}{(2\pi)^d}\frac{1}{Dq^2\tau - i\omega\tau}. \tag{C.61}$$

The integral remains finite owing to the physical cutoff (elastic τ_{el} and coherence times τ_φ) that need to be introduced. In two dimensions, a straightforward integral calculation yields

$$\delta\sigma(\omega) = -\frac{e^2}{2\pi^2\hbar}\ln\frac{\tau_\varphi}{\tau_{\mathrm{el}}}, \tag{C.62}$$

which is the basis of the scaling analysis of the localization theory. Equation (C.62) is used when applying the Kubo method in disordered graphene-based materials.

C.4 Computing Transport Properties within *Ab Initio* Simulations

In Section C.1, the computation of the Green's functions for the central region is shown to rely on a proper evaluation of the self-energies associated with the left and right electrodes. In Section C.2, we had an overview of some of the most common recursive Green functions methods as typically used for tight-binding Hamiltonians. Here, we revisit this issue and then present the main steps involved in *ab initio* simulations of quantum transport within a self-consistent Landauer–Büttiker scheme.

Since these self-energies have to be computed for each transverse **k**-vector, and at several energies, a stable and efficient computational algorithm is crucial for the code performance. The main computational cost in calculating the self-energies of the contacts is related to evaluation of the retarded Green's function of the isolated leads. Within several packages (SMEAGOL, TRANSIESTA, etc.; see below), these Green's functions are constructed following a semi-analytical scheme (Rocha 2007) globally composed of three steps. First, the Bloch states of the infinite system are derived. Second, these Bloch states are used to build the retarded Green's function corresponding to the infinite leads. Then, appropriate boundary conditions are applied in order for the Green's function to vanish at the free surface of the semi-infinite leads. The three steps are described in more detail below.

(1) Owing to the division of the leads into "principal layers" (PLs – see Fig. C.1), the Hamiltonian and the overlap matrices are arranged in the trigonal form described in Eq. (C.23). In this formulation, H_0 and S_0 account for all the interactions and overlap

integrals inside one PL. H_1 and S_1 are the off-diagonal blocks that correspond to the interactions and overlap integrals between the nearest-neighbor PLs. In order to simplify the notation, the matrices $K_\alpha = H_\alpha - ES_\alpha$ with $(\alpha = 0, 1, -1)$ are introduced. In the case of an infinite periodic lead, the Bloch theorem applies along the transport direction (z-axis) and the bulk electronic states can be mapped into Bloch states $\Psi_z = \mathrm{e}^{ikz}\phi_k$, where $z = n*d$ is an integer multiple of the PL length (d) and k is the wave-vector along the transport axis. Within this PL notation, the time-independent Schrödinger equation of the isolated contact $[H|\psi\rangle = E\,S|\psi\rangle]$ assumes the following form:

$$K_{-1}\,C_{\alpha-1} + K_0\,C_\alpha + K_1\,C_{\alpha+1} = 0, \tag{C.63}$$

where C_m is a vector of length n, and α labels the successive PLs. The different K matrices are thus defined as

$$\begin{aligned} K_0 &= H_0 - ES_0, \\ K_1 &= H_1 - ES_1, \\ K_{-1} &= H_{-1} - ES_{-1}. \end{aligned} \tag{C.64}$$

Note that, for some applications, it is also common to write Eq. (C.63) in the so-called transfer-matrix form (Sanvito et al. 1999),

$$\begin{pmatrix} -(K_1)^{-1}K_0 & -(K_1)^{-1}K_{-1} \\ 1 & 0 \end{pmatrix} \cdot \begin{pmatrix} C_\alpha \\ C_{\alpha+1} \end{pmatrix} = \mathcal{T} \cdot \begin{pmatrix} C_\alpha \\ C_{\alpha+1} \end{pmatrix}, \tag{C.65}$$

$$= \begin{pmatrix} C_{\alpha-1} \\ C_\alpha \end{pmatrix}, \tag{C.66}$$

where $\mathcal{T}$ is the transfer matrix.

Since deep inside the contacts, the leads are periodic along the transport direction, the electronic scattering states of the system have to obey the asymptotic behavior of propagating Bloch states. The Schrödinger equation (Eq. C.63) inside the contact can therefore be reexpressed into the following eigenvalue problem:

$$\begin{pmatrix} -(K_1)^{-1}K_0 & -(K_1)^{-1}K_{-1} \\ 1 & 0 \end{pmatrix} \cdot \begin{pmatrix} C_\alpha \\ C_{\alpha+1} \end{pmatrix} = \mathrm{e}^{ikd} \begin{pmatrix} C_\alpha \\ C_{\alpha+1} \end{pmatrix}, \tag{C.67}$$

where d is the length of the PLs along the direction of transport. Solving this equation for both leads yields two sets of $2n$ complex wave-vectors ($k_j^{L/R} : j = 1, \ldots, 2m$) and their associated bulk complex state-vectors ($\phi_{k_j}^{L/R}$). These propagating (and decaying) Bloch states are the basis functions on which the transport problem is developed. For convenience, the wave-vectors are ordered such that the first m states are incoming to the scattering region, and the other m outgoing from the scattering region. Finally, the open boundary conditions of the original transport problem can be described in terms of

the bulk states $\phi_{k_j}^{L/R}$ by imposing the proper asymptotic form on the stationary scattering states of $\mathcal{H}$:

$$\Psi_{k_j}^{L}(\mathbf{r}) = \begin{cases} \phi_{k_j}^{L} + \sum_{i=m+1}^{2m} r_{ij}\, \phi_{k_i}^{L}, & r_z \in L, \\ \sum_{i=m+1}^{2m} t_{ij}\, \phi_{k_i}^{R}, & r_z \in R, \end{cases} \tag{C.68}$$

where t_{ij} and r_{ij} are the transmission and the reflection amplitudes, respectively. Here, $\Psi_{k_j}^{L}$ are the scattering states that are incident from the left contact and are characterized by k_j in an asymptotic sense, i.e., these originate from the bulk states ϕ_{k_j}. A similar expression is easily derived for the scattering states $\Psi_{k_j}^{R}$ that are incident from the right contact. The transmission and reflection amplitudes found here are the usual quantities of the scattering theory and can be computed using transfer matrix techniques (Sanvito et al. 1999).

As mentioned earlier, the Schrödinger equation (C.63) can be conveniently mapped into an eigenvalue calculation with the aid of the transfer matrix (Sanvito et al. 1999):

$$\mathcal{T} = \begin{pmatrix} -(K_1)^{-1}K_0 & -(K_1)^{-1}K_{-1} \\ 1 & 0 \end{pmatrix}. \tag{C.69}$$

The eigenvalues of $\mathcal{T}$ are the $2n$ roots $\mathrm{e}^{\mathrm{i}k_l d}$ that define the complex wave-vectors of the Bloch states at energy E. The upper part (i.e., the n first elements) of the $2n$ eigenvectors are the expansion components of the Bloch electronic functions over the localized basis functions. In order to simplify the discussion, the eigenvectors are ordered such that the electronic states with indices ranging from 1 to n correspond to Bloch waves propagating/decaying in the right direction. On the contrary, the indices ranging from $n+1$ to $2n$ are associated with Bloch waves propagating/decaying in the left direction. Finally, it is worth mentioning that the solution of the eigenvalue problem (Eq. (C.69)) assumes that K_1 is invertible. Moreover, the stability of the algorithm requires that K_1 is not ill-defined. Therefore, a regularization procedure for K_1 is highly desirable, though this point is crucial for the accuracy and stability of the code (Rocha 2007; Sanvito et al. 1999).

(2) In order to construct the retarded Green's function of the infinite leads, one notes that the Green's function ($G_{zz'}$) is a simple wave-function for all $z \leq z'$. Since it has to be retarded, and continuous at $z = z'$, one may assume the following form:

$$G_{zz'} = \begin{cases} \sum_{l=1}^{n} \phi_{k_l} \mathrm{e}^{\mathrm{i}k_l(z-z')}\, \alpha_{k_l}, & z \geq z', \\ \sum_{l=n+1}^{2n} \phi_{k_l} \mathrm{e}^{\mathrm{i}k_l(z-z')}\, \alpha_{k_l}, & z \leq z', \end{cases} \tag{C.70}$$

where the α_{k_l} coefficients have to be determined. Folding these expressions into the Schrödinger equation (C.63), the coefficients present the following form:

$$\alpha_{k_l} = \tilde{\phi}_{k_l}^{\dagger} V^{-1}, \tag{C.71}$$

with

$$V = (H_1^\dagger - ES_1^\dagger)\left[\sum_{l=1}^{n} \phi_{k_l} e^{ik_l(z-z')} \tilde{\phi}_{k_l}^\dagger - \sum_{l=n+1}^{2n} \phi_{k_l} e^{ik_l(z-z')} \tilde{\phi}_{k_l}^\dagger\right], \tag{C.72}$$

where the set of $\tilde{\phi}_{k_l}^\dagger$ is made from the duals of ϕ_{k_l} (i.e., $\tilde{\phi}_{k_l}^\dagger \phi_{k_m} = \delta_{lm}$).

(3) Finally, the Green's function of the semi-infinite leads can be obtained from the Green's function of the infinite leads by subtracting from $G_{zz'}$ a linear combination of eigenvectors that ensure the annihilation of the Green's function at the free surface. Considering, for example, the left lead which extends from $z = -\infty$ to $z = z_0 - 1$, subtraction of the term

$$\Delta_z(z' - z_0) = \sum_{l=1}^{n} \sum_{h=n+1}^{2n} \left(\phi_{k_h} e^{ik_l(z-z_0)} \tilde{\phi}_{k_l}^\dagger\right) \cdot \left(\phi_{k_l} e^{ik_l(z_0-z')} \tilde{\phi}_{k_l}^\dagger\right) V^{-1} \tag{C.73}$$

from $G_{zz'}$ gives a new retarded Green's function, which vanishes at the principal layer $z = z_0$ taken as the surface. In this way, the retarded Green's functions of the semi-infinite leads have been computed, and all the ingredients are gathered for calculation of the self-energies.

Finally, note that the derivation of the self-energies proposed above assumes that the entire leads are undisturbed by the central region. This means that the interfaces at which the surface Green's functions are computed have to be sufficiently far away from the scattering region in order for the scattering potential to be zero into the leads. Upon this assumption, the lead self-energies have to be computed only once and remain valid throughout the self-consistent determination of the scattering potential.

Before summarizing, the self-consistent procedure used for calculation of the out-of-equilibrium scattering potential, calculation of the out-of-equilibrium density matrix should be briefly mentioned:

$$\rho = \frac{1}{2\pi} \int_{-\infty}^{\infty} [f_L(E - \mu_L) A_L(E) + f_R(E - \mu_R) A_R(E)]\, dE, \tag{C.74}$$

where $f(E)$ is the equilibrium Fermi electronic distribution, and $\mu_{L/R}$ are the chemical potentials inside the left and right leads, respectively. It is worth noting that the integration in Eq. (C.74) is not a trivial computational task since the integral is unbound and the spectral functions $A_{L/R}$ are not analytical. However, the computational cost of the integration can be significantly reduced by rewriting the integral in Eq. (C.74) as the sum of two contributions, ρ_{equ} and ρ_Δ:

$$\begin{aligned}
\rho &= \frac{1}{2\pi} \int_{-\infty}^{\infty} \Big[f(E - \mu_L) A_L(E) + f(E - \mu_R) A_R(E)\Big] \\
&\quad + \Big[f(E - \mu_L) A_R(E) - f(E - \mu_L) A_R(E)\Big]\, dE \\
&= \frac{1}{2\pi} \int_{-\infty}^{\infty} A_D f(E - \mu_L)\, dE + \frac{1}{2\pi} \int_{-\infty}^{\infty} A_R(E)\Big[f(E - \mu_R) - f(E - \mu_L)\Big]\, dE \\
&= \rho_{\text{equ}} + \rho_\Delta.
\end{aligned} \tag{C.75}$$

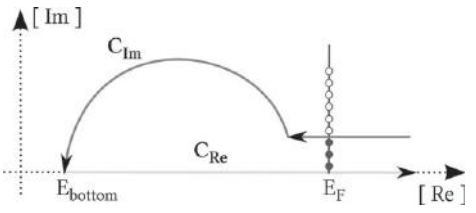

Figure C.6 The closed contour ($C_{\mathrm{Im}} + C_{\mathrm{Re}}$) used to compute the equilibrium component of the electronic density matrix. Filled dots account for the poles of the Fermi distribution function enclosed in the complex integration part.

The first term (ρ_{equ}) accounts for the "equilibrium" component of the electronic density. Indeed, it corresponds to what should be obtained if both leads have the same chemical potential ($\mu_L = \mu_R$). All poles of the spectral function A_D are lying on the real axis, and the function is analytical elsewhere. Therefore, though unbound, the integration of A_D can be performed in the complex plane using contour integral techniques. The contour used conventionally is depicted in Fig. C.6, where E_{bottom} is chosen below the deepest valence electronic state. For finite temperatures, the contour encloses some poles of the Fermi distribution function located at $\{z_\alpha = i(2\alpha + 1)\pi k_B T$, with $\alpha = 1, \ldots, n_\alpha\}$. Finally, the integral is computed as

$$\frac{1}{2\pi}\int_{-\infty}^{\infty} A_D(E) f_L(E-\mu_L)\,dE = -\int_{C_{\mathrm{Im}}} A_D(z) f_L(z-\mu_L)\,dz - 2\pi k_B T \sum_{\alpha=1}^{n_\alpha} A_D(z_\alpha). \tag{C.76}$$

The second term in Eq. (C.76) accounts for the corrections induced by the out-of-equilibrium conditions. The spectral functions $A_{L/R}$ are not analytical and the integration cannot be obtained using complex contours techniques. However, the integration is bounded by the two Fermi distribution functions and can be evaluated on a dense energy grid. Note that the formula (C.76) does not account for the contribution to the density of the electronic states that are localized within the scattering device and do not couple with the leads. In the presence of such states, (C.76) is not valid anymore and additional information has to be supplied.

Finally, the self-consistent procedure related to calculation of the out-of-equilibrium electronic density and electric current is described, as implemented in several *ab initio* transport packages (SMEAGOL, TRANSIESTA, etc.; see below). The main feature of the Green's function DFT-based schemes is to extend the scope of the standard DFT codes based on localized basis sets, by calculating the out-of-equilibrium density matrix. As such, though the out-of-equilibrium electronic density does not minimize the density functional, these schemes rely on the Kohn–Sham Hamiltonian as the single-particle Hamiltonian. Therefore, the self-consistency is very similar to the one encountered in standard DFT codes. The self-consistent procedure can be summarized in the diagram in Fig. C.7.

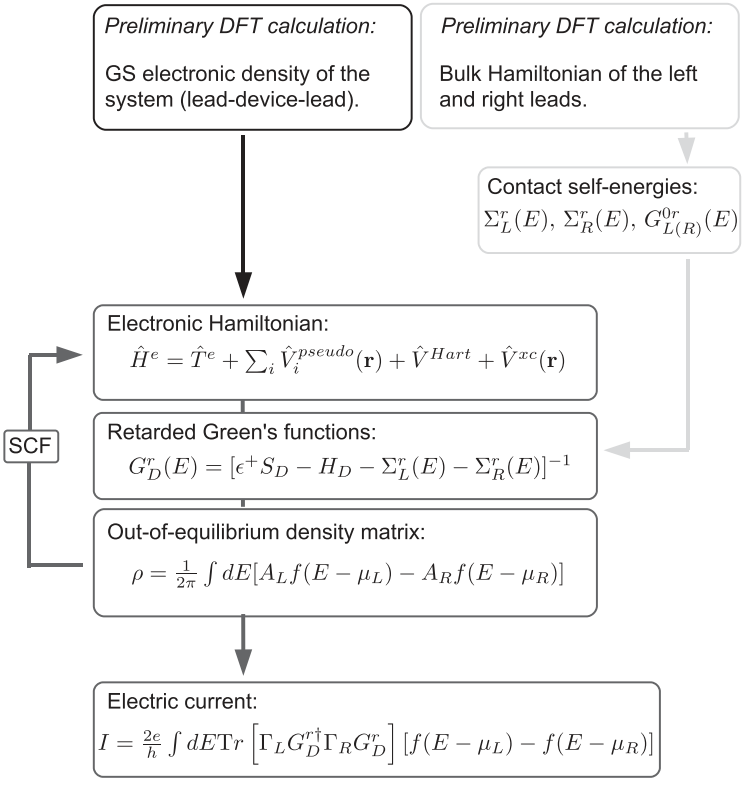

Figure C.7 Self-consistent cycle for computation of the out-of-equilibrium density matrix and electric current. Dark gray frame (top left) corresponds to the preliminary DFT calculation aiming at producing a good initial guess for the out-of-equilibrium electronic density. Light gray frames (top right) describe the preliminary calculation of the self-energies of the leads. Medium gray frames (bottom) correspond to the main step of the actual self-consistent cycle.

In many situations, the nonequilibrium condition brings only small corrections to the ground-state electronic density. Therefore, it is good practice to use a DFT-computed ground-state electronic density as the guess input density for the nonequilibrium calculations. Then, the latter proceed in two steps. First, the electronic structure corresponding to the infinite leads is computed, in order for the contact self-energies to be built over the proper range of energies (i.e., the full bandwidth of the material). This step has to be performed only once, since the leads are assumed to remain in their equilibrium states. Second, the out-of-equilibrium density matrix is computed in a self-consistent way. The self-consistent cycle is accomplished by determining the Hartree (electrostatic) potential as a solution of Poisson's equation with appropriate boundary conditions. Though Poisson's equation can be solved in real space, it is common to use fast-Fourier transform algorithms that are computationally efficient. Actually, the electrostatic potential is calculated for a virtual periodic system obtained by repeating the effective Hamiltonian $H_D^{\mathrm{eff}}(E)$ along the transport direction. Besides, a saw-like

term, whose drop is identical to the bias applied, is added to the Hartree potential in order to recover the correct voltage drop across the device. Finally, when convergence is reached, the electric current is computed as a by-product of the retarded Green's function.

The Green's function formalism outlined in the present appendix has been implemented in several simulation codes. In the following, we list some of these codes and their main features as specified by their developers:

1. SMEAGOL (Rocha et al. 2006) has been designed to calculate transport properties of atomic scale devices. SMEAGOL is an *ab initio* electronic transport code based on a combination of density functional theory (DFT) and nonequilibrium Green's function transport methods (NEGF). The Kohn–Sham equations for an open nonperiodic system are solved in the NEGF scheme, and the current is then extracted from the Landauer formula. The code has been designed to describe two terminal nanoscale devices for which the potential drop must be calculated accurately. It has been specifically created to deal also with magnetic systems, since the code is fully spin-polarized and includes the possibility of performing noncollinear spin calculations (Rocha et al. 2005). More details are available at: www.smeagol.tcd.ie.
2. TRANSIESTA (Brandbyge et al. 2002): the present SIESTA release (Soler et al. 2002) includes the possibility of performing calculations of electronic transport properties using the TRANSIESTA method, which is a procedure to solve the electronic structure of an open system formed by a finite structure sandwiched between two semi-infinite metallic leads. A finite bias can be applied between both leads, to drive a finite current. In practical terms, calculations using TRANSIESTA involve the solution of the electronic density from the DFT Hamiltonian using Green's functions techniques, instead of the usual diagonalization procedure. Therefore, TRANSIESTA calculations involve a SIESTA run in which a set of routines is invoked to solve the Green's functions and the charge density for the open system. These routines are packed in a set of modules, referred to as the "TRANSIESTA module." More details are available at: www.icmab.es/dmmis/leem/siesta/.
3. WANT (Calzolari et al. 2004) is an open-source, GNU General Public License suite of codes that provides an integrated approach for the study of coherent electronic transport in nanostructures. The core methodology combines state-of-the-art DFT, plane-wave, norm-conserving, pseudopotential calculations with a Green's function method based on the Landauer formalism to describe quantum conductance. The essential connection between the two, and a crucial step in the calculation, is use of the maximally localized Wannier function representation to introduce naturally the ground-state electronic structure into the lattice Green's function approach at the basis of the evaluation of the quantum conductance. Moreover, knowledge of the Wannier functions of the system allows direct linking between the electronic transport properties of the device and the nature of the chemical bonds, providing insight into the mechanisms that govern electron flow at the nanoscale. More details are available at: www.wannier-transport.org.

4. ONETEP (Skylaris et al. 2005) (order-*N* electronic total energy package) is a linear-scaling code for quantum-mechanical calculations based on DFT. ONETEP uses a reformulation of the plane-wave pseudopotential method, which exploits the electronic localization that is inherent in systems with a nonvanishing bandgap. Direct optimization of strictly localized quantities expressed in terms of a delocalized plane-wave basis allows division of the computational effort among many processors to allow calculations to be performed efficiently on parallel supercomputers. More details are available at: www2.tcm.phy.cam.ac.uk/onetep/.

Appendix D Recursion Methods for Computing the Density of States (DOS) and Wavepacket Dynamics

The Lanczos tridiagonalization method orthogonally transforms a real symmetric matrix A to symmetric tridiagonal form. Traditionally, this very simple algorithm is suitable when one needs only a few of the lower eigenvalues and the corresponding eigenvectors of very large Hermitian matrices, whose full diagonalization is technically impossible. We introduce here the basic ingredients of the recursion method based on the Lanczos tridiagonalization, and explain how calculation of the DOS as well as the dynamics of wavepackets (and related conductivity) can be performed efficiently.

D.1 Lanczos Method for the Density of States

The Lanczos method is a highly efficient recursive approach for calculation of the electronic structure (Lanczos 1950). This method, first developed by Haydock et al. (1972, 1975), is based on an eigenvalue approach due to Lanczos. It relies on computation of Green functions matrix elements by continued fraction expansion, which can be implemented either in real or reciprocal space. These techniques are particularly well suited for treating disorder and defect-related problems, and were successfully implemented to tackle impurity-level calculations in semiconductors using a tight-binding approximation (Lohrmann 1989), and for electronic structure investigations for amorphous semiconductors, transition metals, and metallic glasses based on linear-muffin-tin orbitals (Bose et al. 1988). Recent developments include the exploration of a degenerated orbital extended Hubbard Hamiltonian of system size up to 10 millions atoms, with the Krylov subspace method (Hoshi et al. 2012; Takayama et al. 2004).

The recursion method is said to be of order N since the computational cost scales linearly with the total number of atoms defining the (disordered) system (Grosso & Parravicini 2006). The key idea of the recursion method is to construct iteratively a Lanczos (or Krylov) basis, which tridiagonalizes the Hamiltonian (initially defined in a localized basis set), and then to compute diagonal matrix elements of the Green function (to access the density of states) by using the continued fraction expansion method.

The recursion method is thus a basis transformation, which turns out to be very suitable for dealing with tight-binding Hamiltonians for which strong disorder limits the use of diagonalization methods and perturbative treatments. The Lanczos method allows simulation of electronic (and transport as discussed in Section D.2) behavior of

disordered systems up to the scale of 100 millions of orbitals using high-performance computing resources. The limit is actually not really the total number of atoms, but rather the necessary computational time to access the transport regimes of interest. As shown below, a very efficient computational trick is to compute the trace of any operator related to electronic and transport properties on a reduced number of random phase states (N_{RP}) instead of a fully complete and orthogonal basis:

$$\mathrm{Tr}\big[\delta(E-\hat{\mathcal{H}})\big]=\sum_{J=1}^{M}\langle\varphi_J|\delta(E-\hat{\mathcal{H}})|\varphi_J\rangle=\frac{M}{N_{\mathrm{RP}}}\times\sum_{i=1}^{N_{\mathrm{RP}}}\langle\varphi_{\mathrm{RP}}^{i}|\delta(E-\hat{\mathcal{H}})|\varphi_{\mathrm{RP}}^{i}\rangle, \tag{D.1}$$

where M is the dimension of $\hat{\mathcal{H}}$ in the TB basis and $|\varphi_{\mathrm{RP}}\rangle$ is defined by

$$|\varphi_{\mathrm{RP}}\rangle=\frac{1}{\sqrt{M}}\sum_{J=1}^{M}\mathrm{e}^{\mathrm{i}2\pi\theta_J}|\varphi_J\rangle, \tag{D.2}$$

with θ_J, a random number between 0 and 1. This state $|\varphi_{\mathrm{RP}}\rangle$ has a random phase on each orbital of the TB basis. Numerically, with only about 10 of such states, a high-energy resolution can be obtained, even though the starting dimension M can be as high as several tens or hundreds of millions of orbitals. Concerning the Lanczos method, the basic algorithm is described as follows:

- The first step starts with $|\psi_1\rangle=|\varphi_{\mathrm{RP}}\rangle$:

$$a_1=\langle\psi_1|\hat{\mathcal{H}}|\psi_1\rangle, \tag{D.3}$$

$$|\tilde{\psi}_2\rangle=\hat{\mathcal{H}}|\psi_1\rangle-a_1|\psi_1\rangle, \tag{D.4}$$

$$b_1=\||\tilde{\psi}_2\rangle\|=\sqrt{\langle\tilde{\psi}_2|\tilde{\psi}_2\rangle}, \tag{D.5}$$

$$|\psi_2\rangle=\frac{1}{b_1}|\tilde{\psi}_2\rangle. \tag{D.6}$$

- All other recursion steps ($\forall n\geq 2$) are identical and given through

$$a_n=\langle\psi_n|\hat{\mathcal{H}}|\psi_n\rangle, \tag{D.7}$$

$$|\tilde{\psi}_{n+1}\rangle=\hat{\mathcal{H}}|\psi_n\rangle-a_n|\psi_n\rangle-b_{n-1}|\psi_{n-1}\rangle, \tag{D.8}$$

$$b_n=\sqrt{\langle\tilde{\psi}_{n+1}|\tilde{\psi}_{n+1}\rangle}, \tag{D.9}$$

$$|\psi_{n+1}\rangle=\frac{1}{b_n}|\tilde{\psi}_{n+1}\rangle. \tag{D.10}$$

The coefficients a_n and b_n are named recursion coefficients and are respectively, the diagonal and off-diagonal of the matrix representation of $\hat{\mathcal{H}}$ in the Lanczos basis (that we write $\tilde{\hat{\mathcal{H}}}$):

$$\tilde{\hat{\mathcal{H}}} = \begin{pmatrix} a_1 & b_1 & & & \\ b_1 & a_2 & b_2 & & \\ & b_2 & \ddots & \ddots & \\ & & \ddots & \ddots & b_N \\ & & & b_N & a_N \end{pmatrix}. \tag{D.11}$$

Simple linear algebra shows that

$$\begin{aligned} \langle \varphi_{\mathrm{RP}} | \delta(E - \hat{\mathcal{H}}) | \varphi_{\mathrm{RP}} \rangle &= \langle \psi_1 | \delta(E - \hat{\mathcal{H}}) | \psi_1 \rangle \\ &= \lim_{\eta \mapsto 0} -\frac{1}{\pi} \Im_m \left(\langle \psi_1 | \frac{1}{E + i\eta - \hat{\mathcal{H}}} | \psi_1 \rangle \right), \end{aligned}$$

while

$$\langle \psi_1 | \frac{1}{E + \mathrm{i}\eta - \tilde{\hat{\mathcal{H}}}} | \psi_1 \rangle = \cfrac{1}{E + \mathrm{i}\eta - a_1 - \cfrac{b_1^2}{E + \mathrm{i}\eta - a_2 - \cfrac{b_2^2}{E + \mathrm{i}\eta - a_3 - \cfrac{b_3^2}{\ddots}}}} \tag{D.12}$$

which is termed a continued fraction. To compute Eq. (D.12), however, in practice we must introduce a cutoff, or termination (named TERM), typically after $N \sim 1000$ recursion steps. Then $\langle \psi_1 | (E + \mathrm{i}\eta - \tilde{\hat{\mathcal{H}}})^{-1} | \psi_1 \rangle$ becomes

$$\cfrac{1}{E + \mathrm{i}\eta - a_1 - \cfrac{b_1^2}{\ddots \cfrac{}{\ddots \cfrac{}{E + \mathrm{i}\eta - a_{N-1} - \cfrac{b_{N-1}^2}{E + \mathrm{i}\eta - a_N - b_N^2 \times \mathrm{TERM}}}}}}$$

Several types of terminations can be employed depending on the spectrum of the system under study (and mainly depending on the number of gaps and energy resolution that is needed). The energy resolution on the computed density of states depends on the total number of recursion steps and the stability of the orthogonality of the constructed Lanczos basis set. Additionally, to evaluate $\delta(E - \hat{\mathcal{H}})$, a Lorentzian function $(E + \mathrm{i}\eta - \hat{\mathcal{H}})^{-1}$ is usually employed, although it is not suitable for a one-dimensional system because of the large number of van Hove singularities (for instance, for studying carbon nanotubes or semiconducting nanowires (Persson et al. 2008)). Another method, the kernel polynomials method (KPM) can cure these problems, and we refer to Weisse et al. (2006) and to the Ph.D. thesis of Aurélien Lherbier (2008) for

further details, and applications to complex materials (such as semiconducting silicon nanowires).

D.1.1 Termination of the Continued Fraction

Let us now show how one can concretely compute the diagonal matrix element from the continued fraction. The general form of the tridiagonalized Hamiltonian after the Lanczos algorithm reads

$$\tilde{\hat{\mathcal{H}}} = \begin{pmatrix} a_1 & b_1 & & & \\ b_1 & a_2 & b_2 & & \\ & b_2 & \ddots & \ddots & \\ & & \ddots & \ddots & b_N \\ & & & b_N & a_N \end{pmatrix}. \tag{D.13}$$

The total density of states can then be computed as a continued fraction. In the tight-binding basis, one has

$$\langle \psi_{\mathrm{RP}} | \delta(E - \hat{\mathcal{H}}) | \psi_{\mathrm{RP}} \rangle = \lim_{\eta \to 0} -\frac{1}{\pi} I_m \left(\langle \psi_{\mathrm{RP}} | \frac{1}{E + \mathrm{i}\eta - \hat{\mathcal{H}}} | \psi_{\mathrm{RP}} \rangle \right), \tag{D.14}$$

while in the Lanczos basis one gets (with $|\psi_{\mathrm{RP}}\rangle$ becoming $|\psi_1\rangle$, the seed vector of the Lanczos procedure),

$$\langle \psi_1 | \delta(E - \tilde{\hat{\mathcal{H}}}) | \psi_1 \rangle = \lim_{\eta \to 0} -\frac{1}{\pi} \mathrm{Im} \cfrac{1}{E + i\eta - a_1 - \cfrac{b_1^2}{E + i\eta - a_2 - \cfrac{b_2^2}{E + i\eta - a_3 - \cfrac{b_3^2}{\ddots}}}}. \tag{D.15}$$

We name G_1 the continued fraction and define G_n as

$$G_1 = \cfrac{1}{E + \mathrm{i}\eta - a_1 - \cfrac{b_1^2}{E + \mathrm{i}\eta - a_2 - \cfrac{b_2^2}{E + \mathrm{i}\eta - a_3 - \cfrac{b_3^2}{\ddots}}}}, \tag{D.16}$$

$$G_1 = \frac{1}{E + \mathrm{i}\eta - a_1 - b_1^2 G_2}, \tag{D.17}$$

$$G_n = \frac{1}{E + \mathrm{i}\eta - a_n - b_n^2 G_{n+1}}. \tag{D.18}$$

Since we compute a finite number of recursion coefficients, the subspace of Lanczos is of finite dimension (N), so it is crucial to terminate the continued fraction by an appropriate choice of the last $\{a_{n=N}, b_{n=N}\}$ elements. Let us rewrite the continued fraction as

$$G_1 = \cfrac{1}{E + \mathrm{i}\eta - a_1 - \cfrac{b_1^2}{E + \mathrm{i}\eta - a_2 - \cfrac{b_2^2}{E + \mathrm{i}\eta - a_3 - \cfrac{b_3^2}{\ddots \cfrac{}{E + \mathrm{i}\eta - a_N - b_N^2 G_{N+1}}}}}}, \tag{D.19}$$

where G_{N+1} denotes such a termination. The simplest case is when all the spectrum is contained in a finite bandwidth $[a - 2b; a + 2b]$, a is the spectrum center and $4b$ its bandwidth. Recursion coefficients a_n and b_n oscillate around their average value a and b, and the damping is usually fast after a few hundreds of recursion steps. The termination then satisfies

$$G_{N+1} = \frac{1}{E + \mathrm{i}\eta - a - b^2 G_{N+2}} = \frac{1}{E + \mathrm{i}\eta - a - b^2 G_{N+1}}, \tag{D.20}$$

from which a polynomial of second degree is found,

$$-(b^2) G_{N+1}^2 + (E + \mathrm{i}\eta - a) G_{N+1} - 1 = 0, \tag{D.21}$$

and straightforwardly solved

$$\Delta = (E + \mathrm{i}\eta - a)^2 - (2b)^2, \tag{D.22}$$

$$G_{N+1} = \frac{(E + \mathrm{i}\eta - a) \mp i\sqrt{-\Delta}}{2b^2}, \tag{D.23}$$

$$G_{N+1} = \frac{(E + \mathrm{i}\eta - a) - \mathrm{i}\sqrt{(2b)^2 - (E + \mathrm{i}\eta - a)^2}}{2b^2}. \tag{D.24}$$

Figure D.1 shows $b(n)$ for the case of pristine graphene. The value of b_n is seen to quickly tend toward $b \sim 4$ eV. As seen in Fig. D.1, a closed form of the termination term can be typically introduced after a few hundreds of recursion steps ($N \sim 100-1000$) depending on the spectrum complexity.

D.2 Wavepacket Propagation Method

We have shown here how to apply the Lanczos method to compute the wavepacket spreading in an arbitrary complex disordered material. This is the central technical ingredient of the (real space and order N) computational implementation of the Kubo–Greenwood method used throughout this book. It has been pioneered by Roche and

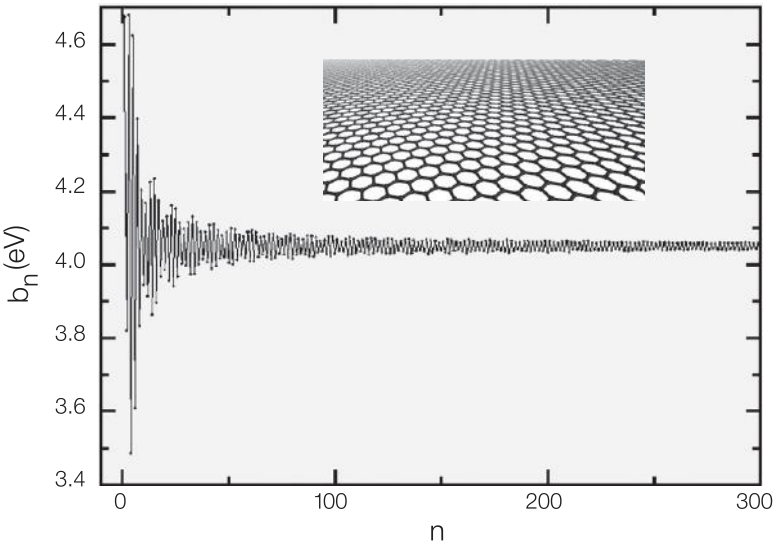

Figure D.1 Recursion coefficient b_n for pristine graphene with bandwith $\sim[-8; 8]$ eV.

Mayou for studying quantum transport in quasicrystals (Roche 1996, 1999; Roche & Mayou 1997), and then further improved for achieving higher energy resolution and optimized computational cost (Lherbier 2008; Triozon 2002). The most recent review of its applicability to graphene -related systems has been provided in Roche et al. (2012).

The main quantity to compute is the mean square spread ($\Delta X^2(E,t)$) introduced in Section 4.4.4. First, starting from Eq. (4.58), we have

$$\Delta X^2(E,t) = \langle \left|\hat{X}(t) - \hat{X}(0)\right|^2 \rangle_E, \tag{D.25}$$

with $\hat{X}(t)$ the position operator in the Heisenberg representation. In Section 4.4, the average of any operator Eq. (4.46) was introduced, which we can rewrite as

$$\Delta X^2(E,t) = \frac{\mathrm{Tr}\left[\delta(E-\hat{\mathcal{H}})\left|\hat{X}(t) - \hat{X}(0)\right|^2\right]}{\mathrm{Tr}\left[\delta(E-\hat{\mathcal{H}})\right]}, \tag{D.26}$$

$$\Delta X^2(E,t) = \frac{\mathrm{Tr}\left[(\hat{X}(t) - \hat{X}(0))^\dagger \delta(E-\hat{\mathcal{H}})(\hat{X}(t) - \hat{X}(0))\right]}{\mathrm{Tr}\left[\delta(E-\hat{\mathcal{H}})\right]}. \tag{D.27}$$

We then use several identities and definitions to rewrite $(\hat{X}(t) - \hat{X}(0))$:

$$\hat{X}(t) = \mathrm{e}^{\frac{\mathrm{i}\hat{\mathcal{H}}t}{\hbar}} \hat{X}(0) \mathrm{e}^{\frac{-\mathrm{i}\hat{\mathcal{H}}t}{\hbar}}, \tag{D.28}$$

$$\hat{U}(t) = \mathrm{e}^{\frac{-\mathrm{i}\hat{\mathcal{H}}t}{\hbar}}, \tag{D.29}$$

where $\hat{U}(t)$ is the evolution operator,

$$\hat{X}(t) - \hat{X}(0) = \hat{U}^{\dagger}(t)\hat{X}\hat{U}(t) - \hat{X}, \tag{D.30}$$

$$\hat{X}(t) - \hat{X}(0) = \hat{U}^{\dagger}(t)\hat{X}\hat{U}(t) - \hat{U}^{\dagger}(t)\hat{U}(t)\hat{X}, \tag{D.31}$$

$$\hat{X}(t) - \hat{X}(0) = \hat{U}^{\dagger}(t)[\hat{X}, \hat{U}(t)], \tag{D.32}$$

using $\hat{U}^{\dagger}(t)\hat{U}(t) = \mathbb{I}$, and $[\cdots, \cdots]$ the commutator. Then by replacing these quantities in Eq. (D.27), one gets

$$\Delta X^2(E,t) = \frac{\mathrm{Tr}\big[[\hat{X}, \hat{U}(t)]^{\dagger}\hat{U}(t)\delta(E-\hat{\mathcal{H}})\hat{U}^{\dagger}(t)[\hat{X}, \hat{U}(t)]\big]}{\mathrm{Tr}\big[\delta(E-\hat{\mathcal{H}})\big]}, \tag{D.33}$$

$$\Delta X^2(E,t) = \frac{\mathrm{Tr}\big[[\hat{X}, \hat{U}(t)]^{\dagger}\delta(E-\hat{\mathcal{H}})[\hat{X}, \hat{U}(t)]\big]}{\mathrm{Tr}\big[\delta(E-\hat{\mathcal{H}})\big]}. \tag{D.34}$$

Using the random phase states as initial states, we find

$$\Delta X^2(E,t) = \frac{\langle\varphi_{\mathrm{RP}}|[\hat{X}, \hat{U}(t)]^{\dagger}\delta(E-\hat{\mathcal{H}})[\hat{X}, \hat{U}(t)]|\varphi_{\mathrm{RP}}\rangle}{\langle\varphi_{\mathrm{RP}}|\delta(E-\hat{\mathcal{H}})|\varphi_{\mathrm{RP}}\rangle}, \tag{D.35}$$

$$\Delta X^2(E,t) = \frac{\langle\varphi'_{\mathrm{RP}}(t)|\delta(E-\hat{\mathcal{H}})|\varphi'_{\mathrm{RP}}(t)\rangle}{\langle\varphi_{\mathrm{RP}}|\delta(E-\hat{\mathcal{H}})|\varphi_{\mathrm{RP}}\rangle}. \tag{D.36}$$

The techniques used for the computation of the density of states can thus also be employed for the computation of $\Delta X^2(E,t)$, provided that one first evaluates $|\varphi'_{\mathrm{RP}}(t)\rangle$. The evaluation of $|\varphi'_{\mathrm{RP}}(t)\rangle$ needs $\hat{U}(t)|\varphi_{\mathrm{RP}}\rangle$ together with $[\hat{X}, \hat{\mathcal{H}}]$. Let us start by explaining the calculation of $[\hat{X}, \hat{\mathcal{H}}]$. By definition $[\hat{X}, \hat{\mathcal{H}}] = \hat{X}\hat{\mathcal{H}} - \hat{\mathcal{H}}\hat{X}$, given that $\hat{X}$ is diagonal:

$$[\hat{X}, \hat{\mathcal{H}}] = \begin{pmatrix} 0 & & & \\ & \ddots & \mathcal{H}_{ij}(X_i - X_j) & \\ & & \ddots & \\ & \mathcal{H}_{ij}(X_i - X_j) & & \ddots \\ & & & 0 \end{pmatrix}, \tag{D.37}$$

where $(X_i - X_j)$ is the distance between orbitals $|\varphi_i\rangle$ and $|\varphi_j\rangle$. We now focus on the calculation of $\hat{U}(t)|\varphi_{\mathrm{RP}}\rangle = |\varphi_{\mathrm{RP}}(t)\rangle$. The time evolution of the random phase wavepacket is followed through use of the evolution operator $\hat{U}(t)$, which can be efficiently approximated using a basis of orthogonal polynomials, with the Chebyshev polynomials as the most computationally efficient choice. For a given time step (T), we can write such a decomposition as

$$\hat{U}(T) = \mathrm{e}^{\frac{-\mathrm{i}\hat{\mathcal{H}}T}{\hbar}} = \sum_{n=0}^{\infty} c_n(T) Q_n(\hat{\mathcal{H}}), \tag{D.38}$$

where Q_n is a Chebyshev polynomial of order n. The Chebyshev polynomials (T_n) usually act on the interval $[-1 : 1]$, whereas the Hamiltonians considered here have larger bandwidths $[-1 : 1]$ so some rescaling of the polynomials needs to be performed to use their recurrent properties. Some useful equations are

$$T_n(\cos(\theta)) = \cos(n\theta), \tag{D.39}$$

$$T_n(\tilde{E}) = \frac{n}{2}\sum_{k=0}^{Pi(\frac{n}{2})}(-1)^k\frac{(n-k-1)!}{k!\,(n-2k)!}(2\tilde{E})^{n-2k}\ (\forall n \neq 0), \tag{D.40}$$

where Pi denotes the integer part and $\tilde{E} \in [-1 : 1]$. Then

$$T_0(\tilde{E}) = 1, \tag{D.41}$$

$$T_1(\tilde{E}) = \tilde{E}, \tag{D.42}$$

$$T_2(\tilde{E}) = 2\tilde{E}^2 - 1, \tag{D.43}$$

$$\vdots$$

additionally for $n \geq 1$,

$$T_{n+1}(\tilde{E}) = 2\tilde{E}\ T_n(\tilde{E}) - T_{n-1}(\tilde{E}), \tag{D.44}$$

while for the rescaled Chebyshev polynomials ($\forall E \in [a - 2b : a + 2b]$) we get

$$Q_n(E) = \sqrt{2}T_n\left(\frac{E-a}{2b}\right)(\forall n \geq 1), \tag{D.45}$$

$$Q_0(E) = 1, \tag{D.46}$$

$$Q_1(E) = \sqrt{2}\frac{E-a}{2b}, \tag{D.47}$$

$$Q_2(E) = 2\sqrt{2}\left(\frac{E-a}{2b}\right)^2 - \sqrt{2}, \tag{D.48}$$

$$\vdots$$

with the recurrence relation $n \geq 2$,

$$Q_{n+1}(E) = 2\left(\frac{E-a}{2b}\right)Q_n(E) - Q_{n-1}(E). \tag{D.49}$$

Once the Q_n polynomials are well defined, one can compute the related $c_n(T)$ coefficients:

$$c_n(T) = \int dE\, p_Q(E)Q_n(E)\mathrm{e}^{\frac{-iET}{\hbar}}, \tag{D.50}$$

$$\text{or } p_Q(E) = \frac{1}{2b\sqrt{1-\left(\frac{E-a}{2b}\right)^2}}, \tag{D.51}$$

introducing the weight $p_Q(E)$ to get an orthonormalized basis. Practically, $c_n(T)$ are computed starting from a fictitious tridiagonal Hamiltonian ($\hat{\mathcal{H}}_f$), where all diagonal elements are identical and taken as a, while all identical off-diagonal elements are b except the first one, being $\sqrt{2}b$, so that

$$\hat{\mathcal{H}}_f = \begin{pmatrix} a & \sqrt{2}b & & & \\ \sqrt{2}b & a & b & & \\ & b & \ddots & & \\ & & & \ddots & b \\ & & & b & a \end{pmatrix}. \tag{D.52}$$

Using this fictitious Hamiltonian in Eq. (D.50),

$$c_n(T) = \int dE\, p_Q(E) Q_n(\hat{\mathcal{H}}_f) \mathrm{e}^{\frac{-\mathrm{i}ET}{\hbar}}, \tag{D.53}$$

$$c_n(T) = \int dE\, \langle 0|\delta(E - \hat{\mathcal{H}}_f)|0\rangle Q_n(\hat{\mathcal{H}}_f) \mathrm{e}^{\frac{-\mathrm{i}ET}{\hbar}}, \tag{D.54}$$

$$c_n(T) = \int dE\, \langle n|\delta(E - \hat{\mathcal{H}}_f)|0\rangle \mathrm{e}^{\frac{-\mathrm{i}ET}{\hbar}}, \tag{D.55}$$

$$c_n(T) = \langle n|\mathrm{e}^{\frac{-\mathrm{i}\hat{\mathcal{H}}_f T}{\hbar}}|0\rangle, \tag{D.56}$$

$$c_n(T) = \sum_{i=0}^{N} \langle n|E_i\rangle \mathrm{e}^{\frac{-\mathrm{i}E_i T}{\hbar}} \langle E_i|0\rangle, \tag{D.57}$$

where we have used $Q_n(\hat{\mathcal{H}}_f)|0\rangle = |n\rangle$ and where E_i and $|E_i\rangle$ are the eigenvalues and eigenvectors of $\hat{\mathcal{H}}_f$. We can now calculate $|\varphi_{\mathrm{RP}}(T)\rangle$:

$$|\varphi_{\mathrm{RP}}(T)\rangle = \hat{U}(T)|\varphi_{\mathrm{RP}}\rangle, \tag{D.58}$$

$$|\varphi_{\mathrm{RP}}(T)\rangle \simeq \sum_{n=0}^{N} c_n(T) Q_n(\hat{\mathcal{H}})|\varphi_{\mathrm{RP}}\rangle = \sum_{n=0}^{N} c_n(T)|\alpha_n\rangle, \tag{D.59}$$

where $|\alpha_n\rangle = Q_n(\hat{\mathcal{H}})|\varphi_{\mathrm{RP}}\rangle$. With the definitions introduced in Eqs. (D.46–D.48) and the recurrence relation Eq. (D.49), we obtain

$$|\alpha_0\rangle = |\varphi_{\mathrm{RP}}\rangle, \tag{D.60}$$

$$|\alpha_1\rangle = \left(\frac{\hat{\mathcal{H}} - a}{\sqrt{2}b}\right)|\alpha_0\rangle, \tag{D.61}$$

$$|\alpha_2\rangle = \left(\frac{\hat{\mathcal{H}} - a}{b}\right)|\alpha_1\rangle - \sqrt{2}|\alpha_0\rangle, \tag{D.62}$$

$$|\alpha_{n+1}\rangle = \left(\frac{\hat{\mathcal{H}} - a}{b}\right)|\alpha_n\rangle - |\alpha_{n-1}\rangle \ (\forall n \geq 2). \tag{D.63}$$

Following the same reasoning as for $|\varphi_{\mathrm{RP}}(T)\rangle, |\varphi'_{\mathrm{RP}}(T)\rangle$ can be evaluated first, and written as

$$|\varphi'_{\mathrm{RP}}(T)\rangle = [\hat{X}, \hat{U}(T)]|\varphi_{\mathrm{RP}}\rangle, \tag{D.64}$$

$$|\varphi'_{\mathrm{RP}}(T)\rangle \simeq \sum_{n=0}^{N} c_n(T)[\hat{X}, Q_n(\hat{\mathcal{H}})]|\varphi_{\mathrm{RP}}\rangle = \sum_{n=0}^{N} c_n(T)|\beta_n\rangle, \tag{D.65}$$

with $|\beta_n\rangle = [\hat{X}, Q_n(\hat{\mathcal{H}})]|\varphi_{\mathrm{RP}}\rangle$. Using Eq. (D.49), we deduce

$$[\hat{X}, Q_{n+1}(\hat{\mathcal{H}})] = \left[\hat{X}, \left(\frac{\hat{\mathcal{H}} - a}{b}\right) Q_n(\hat{\mathcal{H}})\right] - [\hat{X}, Q_{n-1}(\hat{\mathcal{H}})], \tag{D.66}$$

which is rewritten using $[A, BC] = B[A, C] + [A, B]C$,

$$[\hat{X}, Q_{n+1}(\hat{\mathcal{H}})] = \left(\frac{\hat{\mathcal{H}} - a}{b}\right) [\hat{X}, Q_n(\hat{\mathcal{H}})] - [\hat{X}, Q_{n-1}(\hat{\mathcal{H}})] + \left[\hat{X}, \left(\frac{\hat{\mathcal{H}} - a}{b}\right)\right] Q_n(\hat{\mathcal{H}}). \tag{D.67}$$

Multiplying the right term by $|\varphi_{\mathrm{RP}}\rangle$ using $|\beta_n\rangle$ and $|\alpha_n\rangle$ we get

$$|\beta_{n+1}\rangle = \left(\frac{\hat{\mathcal{H}} - a}{b}\right) |\beta_n\rangle - |\beta_{n-1}\rangle + \left[\hat{X}, \left(\frac{\hat{\mathcal{H}} - a}{b}\right)\right] |\alpha_n\rangle. \tag{D.68}$$

The commutator is rewritten as $[\hat{X}, \left(\frac{\hat{\mathcal{H}}-a}{b}\right)]$,

$$\begin{aligned}\left[\hat{X}, \left(\frac{\hat{\mathcal{H}} - a}{b}\right)\right] &= \frac{1}{b}\left[\hat{X}, \left(\hat{\mathcal{H}} - a\right)\right] = \frac{1}{b}\left(\hat{X}(\hat{\mathcal{H}} - a) - (\hat{\mathcal{H}} - a)\hat{X}\right) \\ &= \frac{1}{b}\left(\hat{X}\hat{\mathcal{H}} - \hat{\mathcal{H}}\hat{X} + a\left(\hat{X} - \hat{X}\right)\right) = \frac{1}{b}[\hat{X}, \hat{\mathcal{H}}].\end{aligned} \tag{D.69}$$

So we finally obtain the recurrence relation for $|\beta_n\rangle$:

$$|\beta_{n+1}\rangle = \left(\frac{\hat{\mathcal{H}} - a}{b}\right) |\beta_n\rangle - |\beta_{n-1}\rangle + \frac{1}{b}[\hat{X}, \hat{\mathcal{H}}]|\alpha_n\rangle. \tag{D.70}$$

One notes that computation of $|\beta_n\rangle$ requires evaluation of $|\alpha_n\rangle$ and the commutator $[\hat{X}, \hat{\mathcal{H}}]$. Using such a real-space approach, simulations of charge mobility in disordered graphene samples can be achieved for systems with several tens of millions of atomic orbitals (typical graphene area of 1 μm^2).

Note that a similar methodology has also been developed for following phonon propagation in the harmonic approximation and computing the associated thermal conductivity of material of any complexity (Li et al. 2010, 2011; Sevincli et al. 2011).

D.3 Lanczos Method for Computing Off-Diagonal Green's Functions

One inconvenient feature of the Lanczos approach presented so far is its restriction to calculation of diagonal Green function matrix elements. Although some generalization is possible, as recently proposed by Ortmann and Roche (2013), for calculation of the Hall Kubo conductivity, the situation of transport through open systems (heterojunctions) becomes more problematic.

A similar order-N method for calculation of Landauer–Büttiker conductance has been achieved, however, by Triozon and Roche (2005). This formula has the advantages of being general, and independent of the dimensionality of the system and its eventual geometrical complications.

To implement the recursion approach in the Landauer framework (Imry & Landauer 1999), a generalization of the Lanczos approach to *nonsymmetric matrices* is necessary. The Green's function is obtained from an effective Hamiltonian, $\mathcal{H} = \mathcal{H}_0 + \Sigma_L + \Sigma_R$ (with $\mathcal{H}_0$ the Hamiltonian of the system connected to electrodes left (L) and right (R)), which is nonsymmetric, because of the presence of complex self-energy matrix elements ($\Sigma_{L,R}$) describing the finite system coupled to the electrodes. This requires us to implement a so-called bi-orthogonalization process as summarized below. The basic principle of the algorithm is to start from the normalized vector $|\psi\rangle$ and from the non-Hermitian matrix $\mathcal{H}$ from which a bi-orthogonal basis $\{|\psi_n\rangle, \langle\phi_n|\}$ is constructed following

$$|\psi_{n+1}\rangle = \mathcal{H}|\psi_n\rangle - a_{n+1}|\psi_n\rangle - b_n|\psi_{n-1}\rangle, \tag{D.71}$$

$$\langle\phi_{n+1}| = \langle\phi_n|\mathcal{H} - \langle\phi_n|a_{n+1} - \langle\phi_{n-1}|b_n, \tag{D.72}$$

with the initial conditions $|\psi_{-1}\rangle = |\phi_{-1}\rangle = 0, |\psi_0\rangle = |\phi_0\rangle = |\psi\rangle$ and the bi-orthogonality condition $\langle\phi_n|\psi_m\rangle = 0$ if $n \neq m$. This last condition is equivalent to the following relations for a_n and b_n:

$$a_n = \frac{\langle\phi_n|\mathcal{H}|\psi_n\rangle}{\langle\phi_n|\psi_n\rangle}, \tag{D.73}$$

$$b_n = \frac{\langle\phi_{n-1}|\mathcal{H}|\psi_n\rangle}{\langle\phi_{n-1}|\psi_{n-1}\rangle} = \frac{\langle\phi_n|\psi_n\rangle}{\langle\phi_{n-1}|\psi_{n-1}\rangle}. \tag{D.74}$$

The four Eqs. (D.71–D.74) allow a recursive determination of the bi-orthogonal basis and of the coefficients a_n, b_n. Note that in "ket" notation, Eq. D.72 must be understood as $|\phi_{n+1}\rangle = \mathcal{H}^\dagger|\phi_n\rangle - a^*_{n+1}|\phi_n\rangle - b^*_n|\phi_{n-1}\rangle$. One starts from $|\phi_0\rangle = |\psi_0\rangle = |\psi\rangle$. At step 0, one computes $\mathcal{H}|\psi_0\rangle$ and $a_1 = \langle\phi_0|\mathcal{H}|\psi_0\rangle/\langle\phi_0|\psi_0\rangle$ by expanding all the amplitudes within the tight-binding localized basis.

Values of $|\psi_1\rangle$ and $|\phi_1\rangle$ are then obtained by computing $\mathcal{H}|\psi_0\rangle - a_1|\psi_0\rangle$ and $\mathcal{H}^\dagger|\phi_0\rangle - a^*_1|\phi_0\rangle$, while the first coefficient b_1 is subsequently deduced from Eq. (D.74). At step 1, $\mathcal{H}|\psi_1\rangle$ is computed together with $a_2 = \langle\phi_1|\hat{\mathcal{H}}|\psi_1\rangle/\langle\phi_1|\psi_1\rangle$.

Then $|\psi_2\rangle$ and $|\phi_2\rangle$ result from the computation of vectors $\mathcal{H}|\psi_1\rangle - a_2|\psi_1\rangle - b_1|\psi_0\rangle$ and $\mathcal{H}^\dagger|\phi_1\rangle - a_2^*|\phi_1\rangle - b_1^*|\phi_0\rangle$. Finally, the coefficient b_2 is deduced from Eq. (D.74). Steps $n \geq 2$ are fully similar to step 1. In the basis $\{|\psi_n\rangle\}$, $\mathcal{H}$ thus has a tridiagonal form:

$$\mathcal{H} = \begin{pmatrix} a_1 & b_1 & & & \\ 1 & a_2 & b_2 & & \\ & 1 & a_3 & b_3 & \\ & & 1 & . & . \\ & & & . & . \end{pmatrix}. \tag{D.75}$$

Hence the recurrence relations (D.71) and (D.72) lead to a nonsymmetric matrix and to a nonnormalized bi-orthogonal basis. With the choice of a different convention, a symmetric tridiagonal matrix and/or a normalized basis could be obtained. The quantity $\langle\psi|G^r(z = E \pm 0^+)|\psi\rangle = \langle\phi_0|\frac{1}{z-\mathcal{H}}|\psi_0\rangle$ can then be computed by the continued fraction method.

This quantity is actually equal to the first diagonal element of $(z - \mathcal{H})^{-1}$ where $\mathcal{H}$ is the tridiagonal matrix (D.75). Let us call $G_0(z)$ this matrix element and define $G_n(z)$, the first diagonal element of the matrix $(z - \mathcal{H}_n)^{-1}$, with $\mathcal{H}_n$ the matrix $\mathcal{H}$ without its n first lines and columns:

$$\mathcal{H}_n = \begin{pmatrix} a_n & b_n & & & \\ 1 & a_{n+1} & b_{n+1} & & \\ & 1 & a_{n+2} & b_{n+2} & \\ & & 1 & . & . \\ & & & . & . \end{pmatrix}. \tag{D.76}$$

From standard linear algebra, it can be shown that

$$G_0(z) = \frac{1}{z - a_1 - b_1 G_1(z)}, \tag{D.77}$$

and replicating such an algorithm, one gets a continued fraction of $G_0(z)$:

$$G_0(z) = \cfrac{1}{z - a_1 - \cfrac{b_1}{z - a_2 - \cfrac{b_2}{\cdots}}}. \tag{D.78}$$

In contrast with the standard recursion method, the recursion coefficients a_n and b_n do not show any simple behavior for large n. Simple truncation of the continued fraction at sufficiently large n has been shown to yield reasonably good convergence. This method was tested on carbon nanotube-based heterojunctions (Triozon & Roche 2005), with perfect agreement with the decimation techniques presented in Appendix C.

References

Abanin, D. A., Lee, P. A., & Levitov, L. S. (2006), "Spin-filtered edge states and quantum Hall effect in graphene," *Phys. Rev. Lett.* **96**, 176803.

Abanin, D. A., Novoselov, K. S., Zeitler, U., et al. (2007), "Dissipative quantum Hall effect in graphene near the dirac point," *Phys. Rev. Lett.* **98**(19), 196806.

Abergel, D. S. L. & Chakraborty, T. (2009), "Generation of valley polarized current in bilayer graphene," *Appl. Phys. Lett.* **95**(6), 062107.

Abrahams, E., Anderson, P. W., Licciardello, D. C., & Ramakrishnan, T. V. (1979), "Scaling theory of localization: Absence of quantum diffusion in two dimensions," *Phys. Rev. Lett.* **42**, 673–676.

Abrikosov, A., Gorkov, L., & Dzyaloshinskii, E. (1975), *Methods of Quantum Field Theory in Statistical Physics*, Dover, New York.

Adam, S., Hwang, E. H., Galitski, V. M., & Sarma, S. D. (2007), "A self-consistent theory for graphene transport," *PNAS* **104**, 18392.

Adam, S., Jung, S., Klimov, N. N., et al. (2011), "Mechanism for puddle formation in graphene," *Phys. Rev. B* **84**, 235421.

Adessi, C., Roche, S., & Blase, X. (2006), "Reduced backscattering in potassium-doped nanotubes: Ab initio and semiempirical simulations," *Phys. Rev. B* **73**(12), 125414.

Aharonov, Y. & Bohm, D. (1959), "Significance of electromagnetic potentials in the quantum theory," *Phys. Rev.* **115**(3), 485–491.

Ahn, S. J., Moon, P., Kim, T.-H., et al. (2018), "Dirac electrons in a dodecagonal graphene quasicrystal," *Science* **361**(6404), 782–786.

Ajiki, H. & Ando, T. (1993), "Electronic states of carbon nanotubes," *J. Phys. Soc. Jpn.* **62**(4), 1255–1266.

Ajiki, H. & Ando, T. (1996), "Energy bands of carbon nanotubes in magnetic fields," *J. Phys. Soc. Jpn.* **65**(2), 505–514.

Akhmerov, A. (2011), Dirac and Majorana edge states in graphene and topological superconductors, PhD thesis, Leiden University.

Akhmerov, A. R. & Beenakker, C. W. J. (2008), "Boundary conditions for dirac fermions on a terminated honeycomb lattice," *Phys. Rev. B* **77**, 085423.

Akkermans, E. & Montambaux, G. (2007), *Mesoscopic Physics of Electrons and Photons*, Cambridge University Press, Cambridge, UK.

Aleiner, I. L. & Efetov, K. B. (2006), "Effect of disorder on transport in graphene," *Phys. Rev. Lett.* **97**, 236801.

Alexandrov, A. S. & Capellmann, H. (1991), "Orbital diamagnetism of two-dimensional electrons," *PRL* **66**(3), 365–368.

Alhassid, Y. (2000), "The statistical theory of quantum dots," *Rev. Mod. Phys.* **72**, 895–968.

Allain, P. & Fuchs, J. (2011), "Klein tunneling in graphene: Optics with massless electrons," **83**(3), 301–317.

Allen, M. T., Martin, J., & Yacoby, A. (2012), "Gate-defined quantum confinement in suspended bilayer graphene," *Nat. Commun.* **3**, 934–936.

Alos-Palop, M. & Blaauboer, M. (2011), "Adiabatic quantum pumping in normal-metal-insulator-superconductor junctions in a monolayer of graphene," *Phys. Rev. B* **84**(7), 073402.

Altland, A. (2006), "Low-energy theory of disordered graphene," *Phys. Rev. Lett.* **97**, 236802.

Altshuler, B., Aronov, A., Efros, A. L., & Pollak., M., eds (1985), *Electron–Electron Interaction in Disordered Conductors*, Elsevier, Amsterdam, pp. 1–153.

Altshuler, B. L., Aronov, A. G., & Spivak, B. Z. (1981), "The Aharonov-Bohm effect in disordered conductors," *JETP Lett.* **33**, 94.

Altshuler, B. L. & Glazman, L. I. (1999), "Pumping electrons," *Science* **283**(5409), 1864–1865.

Amara, H., Latil, S., Meunier, V., Lambin, P., & Charlier, J.-C. (2007), "Scanning tunneling microscopy fingerprints of point defects in graphene: A theoretical prediction," *Phys. Rev. B* **76**(11), 115423.

Amorim, R. G., Fazzio, A., Antonelli, A., Novaes, F. D., & da Silva, A. J. R. (2007), "Divacancies in graphene and carbon nanotubes," *Nano Lett.* **7**(8), 2459–2462.

An, J., Voelkl, E., Suk, J. W., et al. (2011), "Domain (grain) boundaries and evidence of 'twinlike' structures in chemically vapor deposited grown graphene," *ACS Nano* **5**, 2433.

Anantram, M. P. (2000), "Current-carrying capacity of carbon nanotubes," *Phys. Rev. B* **62**, R4837–R4840.

Anantram, M. P. & Léonard, F. (2006), "Physics of carbon nanotube electronic devices," *Rep. Progr. Phys.* **69**(3), 507.

Anasori, B., Xie, Y., Beidaghi, M., et al. (2015), "Two-dimensional, ordered, double transition metals carbides (MXenes)," *ACS Nano* **9**(10), 9507–9516.

Anda, E. V., Makler, S., Pastawski, H. M., & Barrera, R. G. (1994), "Electron-phonon effects on transport in mesoscopic heterostructures," *Braz. J. Phys.* **24**, 330.

Anderson, P. W. (1958), "Absence of diffusion in certain random lattices," *Phys. Rev.* **109**(5), 1492–1505.

Anderson, P. W., Thouless, D. J., Abrahams, E., & Fisher, D. S. (1980), "New method for a scaling theory of localization," *Phys. Rev. B* **22**(8), 3519–3526.

Ando, T. (1991), "Quantum point contacts in magnetic fields," *Phys. Rev. B* **44**, 8017.

Ando, T., Nakanishi, T., & Saito, R. (1998), "Berry's phase and absence of back scattering in carbon nanotubes," *J. Phys. Soc. Jpn.* **67**(8), 2857–2862.

Andrei, E. Y., Li, G., & Du, X. (2012), "Electronic properties of graphene: A perspective from scanning tunneling microscopy and magnetotransport," *Rep. Progr. Phy.* **75**(5), 056501.

Appenzeller, J., Radosavljević, M., Knoch, J., & Avouris, P. (2004), "Tunneling versus thermionic emission in one-dimensional semiconductors," *Phys. Rev. Lett.* **92**, 048301.

Areshkin, D. A., Gunlycke, D., & White, C. T. (2007), "Ballistic transport in graphene nanostrips in the presence of disorder: Importance of edge effects," *Nano Lett.* **7**(1), 204–210.

Areshkin, D. A. & White, C. T. (2007), "Building blocks for integrated graphene circuits," *Nano Lett.* **7**(11), 3253–3259.

Arrachea, L. & Moskalets, M. (2006), "Relation between scattering-matrix and Keldysh formalisms for quantum transport driven by time-periodic fields," *Phys. Rev. B* **74**(24), 245322.

Ashcroft, N. W. & Mermin, N. D. (1976a), *Solid State Physics*, Holt, Rinehart and Winston, New York.

Ashcroft, N. W. & Mermin, N. D. (1976b), *Solid State Physics*, Holt Saunders, Philadelphia.

Ast, C. R. & Gierz, I. (2012), "sp-Band tight-binding model for the Bychkov-Rashba effect in a two-dimensional electron system including nearest-neighbor contributions from an electric field," *Phys. Rev. B* **86**, 085105.

Avouris, P., Heinz, T., & Low, T., eds (2017), *2D Materials: Properties and Devices*, Cambridge University Press, Cambridge, UK.

Avriller, R. (2008), Contribution à la modélisation théorique et à l'étude du transport quantique dans les dispositifs à base de nanotubes de carbone, PhD thesis, Université Joseph-Fourier.

Avriller, R., Latil, S., Triozon, F., Blase, X., & Roche, S. (2006), "Chemical disorder strength in carbon nanotubes: Magnetic tuning of quantum transport regimes," *Phys. Rev. B* **74**(12), 121406.

Avriller, R., Roche, S., Triozon, F., Blase, X., & Latil, S. (2007), "Low-dimensional quantum transport properties of chemically-disordered carbon nanotubes: From weak to strong localization regimes," *Mod. Phys. Lett. B* **21**, 1955.

Avsar, A., Lee, J. H., Koon, G. K. W., & Özyilmaz, B. (2015), "Enhanced spin-orbit coupling in dilute fluorinated graphene," *2D Mater.* **2**(4), 044009.

Avsar, A., Tan, J. Y., Taychatanapat, T., et al. (2014), "Spin-orbit proximity effect in graphene," *Nat. Commun.* **5**, 4875.

Avsar, A., Yang, T.-Y., Bae, S., et al. (2011), "Toward wafer scale fabrication of graphene based spin valve devices," *Nano Lett.* **11**(6), 2363–2368.

Babic, B. & Schönenberger, C. (2004), "Observation of Fano resonances in single-wall carbon nanotubes," *Phys. Rev. B* **70**, 195408.

Bachelet, G. B., Hamann, D. R., & Schlüter, M. (1982), "Pseudopotentials that work: From H to Pu," *Phys. Rev. B* **26**, 4199–4228.

Bachilo, S. M., Strano, M. S., Kittrell, C., et al. (2002), "Structure-assigned optical spectra of single-walled carbon nanotubes," *Science* **298**(5602), 2361–2366.

Bachtold, A., Strunk, C., Salvetat, J.-P., et al. (1999), "Aharonov-Bohm oscillations in carbon nanotubes," *Nature* **397**(6721), 673–675.

Bae, S., Kim, H., Lee, Y., et al. (2010), "Roll-to-roll production of 30-inch graphene films for transparent electrodes," *Nat. Nanotechnol.* **5**(8), 574–578.

Baibich, M. N., Broto, J. M., Fert, A., et al. (1988), "Giant magnetoresistance of (001)Fe/(001)Cr magnetic superlattices," *Phys. Rev. Lett.* **61**, 2472–2475.

Bajpai, U., Popescu, B. S., Plechác, P., et al. (2019), "Spatio-temporal dynamics of shift current quantum pumping by femtosecond light pulse," *J. Phys.: Mater.* **2**(2), 025004.

Balakrishnan, J., Gavin, K. W., Jaiswal, M., Neto, A. H. C., & Özyilmaz, B. (2013), "Colossal enhancement of spin-orbit coupling in weakly hydrogenated graphene," *Nat. Phys.* **9**, 284–287.

Balakrishnan, J., Koon, G. K. W., Avsar, A., et al. (2014), "Giant spin Hall effect in graphene grown by chemical vapour deposition," *Nat. Commun.* **5**, 4748.

Balasubramanian, K., Lee, E. J. H., Weitz, R. T., Burghard, M., & Kern, K. (2008), "Carbon nanotube transistors: Chemical functionalization and device characterization," *Phys. Status Solidi (a)* **205**(3), 633–646.

Baldoni, M., Sgamellotti, A., & Mercuri, F. (2008), "Electronic properties and stability of graphene nanoribbons: An interpretation based on Clar sextet theory," *Chem. Phys. Lett.* **464**(4–6), 202–207.

Banhart, F., Kotakoski, J., & Krasheninnikov, A. V. (2011), "Structural defects in graphene," *ACS Nano* **5**(1), 26–41.

Banszerus, L., Schmitz, M., Engels, S., et al. (2015), "Ultrahigh-mobility graphene devices from chemical vapor deposition on reusable copper," *Sci. Adv.* **1**(6), e1500222.

Baranger, H. U. & Stone, A. D. (1989), "Electrical linear-response theory in an arbitrary magnetic field: A new Fermi-surface formation," *Phys. Rev. B* **40**(12), 8169–8193.

Bardarson, J. H., Tworzydło, J., Brouwer, P. W., & Beenakker, C. W. J. (2007), "One-parameter scaling at the dirac point in graphene," *Phys. Rev. Lett.* **99**, 106801.

Barone, V., Hod, O., & Scuseria, G. E. (2006), "Electronic structure and stability of semiconducting graphene nanoribbons," *Nano Lett.* **6**(12), 2748–2754.

Barsoum, M. W. (2000), "The MN+1AXN phases: A new class of solids: Thermodynamically stable nanolaminates," *Prog. Solid State Chem.* **28**(1), 201–281.

Beenakker, C. W. J. (1991), "Theory of Coulomb-blockade oscillations in the conductance of a quantum dot," *Phys. Rev. B* **44**, 1646–1656.

Beenakker, C. W. J. (1997), "Random-matrix theory of quantum transport," *Rev. Mod. Phys.* **69**, 731–808.

Beenakker, C. W. J. (2008), "Colloquium: Andreev reflection and Klein tunneling in graphene," *Rev. Mod. Phys.* **80**(4), 1337–1354.

Begliarbekov, M., Sasaki, K.-I., Sul, O., Yang, E.-H., & Strauf, S. (2011), "Optical control of edge chirality in graphene," *Nano Lett.* **11**(11), 4874–4878.

Benitez, L., Sierra, J., Savero Torres, W., et al. (2018), "Strongly anisotropic spin relaxation in graphene-transition metal dichalcogenide heterostructures at room temperature," *Nat. Phys.* **14**(3), 303–308.

Benítez, L. A., Sierra, J. F., Torres, W. S., et al. (2018), "Strongly anisotropic spin relaxation in graphene-transition metal dichalcogenide heterostructures at room temperature," *Nat. Phys.* **14**(3), 303.

Benítez, L. A., Torres, W. S., Sierra, J. F., et al. (2019), arXiv 1908.07868.

Berdakin, M., Vargas, J. E. B., & Torres, L. E. F. (2018), "Directional control of charge and valley currents in a graphene-based device," *Phys. Chem. Chem. Phys.* **20**(45), 28720–28725.

Berger, C., Song, Z., Li, X., et al. (2006), "Electronic confinement and coherence in patterned epitaxial graphene," *Science* **312**(5777), 1191–1196.

Bergman, G. (1984), "Weak localization in thin films: A time-of-flight experiment with conduction electrons," *Phys. Rep.* **107**(1), 1–58.

Bernal, J. D. (1924), "The structure of graphite," *Proc. R. Soc.of Lond. Ser. A* **106**(740), 749–773.

Berry, M. V. (1984), "Quantal phase factors accompanying adiabatic changes," *Proc. R. Soc. Lond. A* **392**(1802), 45–57.

Berry, M. V. & Mondragon, R. J. (1987), "Neutrino billiards: Time-reversal symmetry-breaking without magnetic fields," *Proc. R. Soc. Lond. A Math. Phys. Sci.* **412**(1842), 53–74.

Bethune, D. S., Klang, C. H., de Vries, M. S., et al. (1993), "Cobalt-catalysed growth of carbon nanotubes with single-atomic-layer walls," *Nature* **363**(6430), 605–607.

Biel, B., Triozon, F., Blase, X., & Roche, S. (2009), "Chemically induced mobility gaps in graphene nanoribbons: A route for upscaling device performances," *Nano Lett.* **9**(7), 2725–2729.

Biel, B., Triozon, F., Niquet, Y., & Roche, S. (2009), "Anomalous doping effects on charge transport in graphene nanoribbons," *Phys. Rev. Lett.* **102**, 096803.

Binasch, G., Grünberg, P., Saurenbach, F., & Zinn, W. (1988), "Enhanced magnetoresistance in layered magnetic structures with antiferromagnetic interlayer exchange," *Phys. Rev. B* **39**, 4828.

Biró, L. P., Márk, G. I., Koós, A. A., Nagy, J., & Lambin, P. (2002), "Coiled carbon nanotube structures with supraunitary nonhexagonal to hexagonal ring ratio," *Phys. Rev. B* **66**, 165405.

Blanter, Y. & Büttiker, M. (2000), "Shot noise in mesoscopic conductors," *Phys. Rep.* **336**(1–2), 1–166.

Blase, X., Benedict, L. X., Shirley, E. L., & Louie, S. G. (1994), "Hybridization effects and metallicity in small radius carbon nanotubes," *Phys. Rev. Lett.* **72**, 1878–1881.

Blase, X., Rubio, A., Louie, S. G., & Cohen, M. L. (1995), "Quasiparticle band structure of bulk hexagonal boron nitride and related systems," *Phys. Rev. B* **51**(11), 6868–6875.

Blöchl, P. E. (1994), "Projector augmented-wave method," *Phys. Rev. B* **50**, 17953–17979.

Bockrath, M., Cobden, D. H., Lu, J., et al. (1999), "Luttinger-liquid behaviour in carbon nanotubes," *Nature* **397**(6720), 598–601.

Boehm, H. P., Clauss, A., Fischer, G. O., & Hofmann, U. (1962), "Das adsorptionsverhalten sehr dünner kohlenstoff-folien," *Z. Anorg. Allg. Chem.* **316**(3-4), 119–127.

Boettger, J. C. & Trickey, S. B. (2007), "Erratum: First-principles calculation of the spin-orbit splitting in graphene," *Phys. Rev. B* **75**, 121402(R).

Bolotin, K. I., Sikes, K. J., Hone, J., Stormer, H. L., & Kim, P. (2008), "Temperature-dependent transport in suspended graphene," *Phys. Rev. Lett.* **101**(9), 096802.

Bonaccorso, F., Sun, Z., Hasan, T., & Ferrari, A. C. (2010), "Graphene photonics and optoelectronics," *Nat. Photonics* **4**(9), 611–622.

Bonča, J. & Trugman, S. A. (1995), "Effect of inelastic processes on tunneling," *Phys. Rev. Lett.* **75**(13), 2566–2569.

Born, M. & Oppenheimer, M. (1927), "Zur quantentheorie der molekeln," *Ann. Phys.* **84**, 457.

Bose, S. K., Winer, K., & Andersen, O. K. (1988), "Electronic properties of a realistic model of amorphous silicon," *Phys. Rev. B* **37**, 6262.

Bostwick, A., McChesney, J. L., Emtsev, K. V., et al. (2009), "Quasiparticle transformation during a metal-insulator transition in graphene," *Phys. Rev. Lett.* **103**(5), 056404.

Botello-Méndez, A. R., Cruz-Silva, E., Romo-Herrera, J., et al. (2011), "Quantum transport in graphene nanonetworks," *Nano Lett.* **11**(8), 3058–3064.

Botello-Mendez, A. R., Declerck, X., Terrones, M., Terrones, H., & Charlier, J.-C. (2011), "One-dimensional extended lines of divacancy defects in graphene," *Nanoscale* **3**(7), 2868–2872.

Bourrellier, R., Meuret, S., Tararan, A., et al. (2016), "Bright UV single photon emission at point defects in h-BN," *Nano Lett.* **16**(7), 4317–4321.

Boykin, T. B., Bowen, R. C., & Klimeck, G. (2001), "Electromagnetic coupling and gauge invariance in the empirical tight-binding method," *PRB* **63**(24), 245314.

Brandbyge, M., Mozos, J.-L., Ordejón, P., Taylor, J., & Stokbro, K. (2002), "Density-functional method for nonequilibrium electron transport," *Phys. Rev. B* **65**(16), 165401.

Brenner, D. W. (1990), "Empirical potential for hydrocarbons for use in simulating the chemical vapor deposition of diamond films," *Phys. Rev. B* **42**, 9458–9471.

Brey, L. & Fertig, H. A. (2006), "Electronic states of graphene nanoribbons studied with the dirac equation," *Phys. Rev. B* **73**, 235411.

Britnell, L., Gorbachev, R. V., Jalil, R., et al. (2012), "Field-effect tunneling transistor based on vertical graphene heterostructures," *Science* **335**(6071), 947–950.

Britnell, L., Ribeiro, R. M., Eckmann, A., et al. (2013), "Strong light-matter interactions in heterostructures of atomically thin films," *Science* **340**(6138), 1311–1314.

Brouwer, P. W. (1998), "Scattering approach to parametric pumping," *Phys. Rev. B* **58**, R10135–R10138.

Bunch, J. S., Yaish, Y., Brink, M., Bolotin, K., & McEuen, P. L. (2005), "Coulomb oscillations and Hall effect in quasi-2D graphite quantum dots," *Nano Lett.* **5**(2), 287–290.

Buscema, M., Groenendijk, D. J., Blanter, S. I., et al. (2014), "Fast and broadband photoresponse of few-layer black phosphorus field-effect transistors," *Nano Lett.* **14**(6), 3347–3352.

Busl, M., Platero, G., & Jauho, A.-P. (2012), "Dynamical polarizability of graphene irradiated by circularly polarized AC electric fields," *Phys. Rev. B* **85**(15), 155449.

Büttiker, M. (1988a), "Absence of backscattering in the quantum Hall effect in multiprobe conductors," *Phys. Rev. B* **38**, 9375–9389.

Büttiker, M. (1988b), "Symmetry of electrical conduction," *IBM J. Res. Dev.* **32**(3), 317–334.

Büttiker, M., Imry, Y., Landauer, R., & Pinhas, S. (1985), "Generalized many-channel conductance formula with application to small rings," *Phys. Rev. B* **31**, 6207–6215.

Büttiker, M. & Moskalets, M. (2006), "Scattering theory of dynamic electrical transport," in J. Asch & A. Joye, eds, *Mathematical Physics of Quantum Mechanics*, Vol. 690 of Lecture Notes in Physics, Springer Berlin/Heidelberg, Berlin, pp. 33–44, doi:10.1007/3-540-34273-75.

Büttiker, M., Thomas, H., & Pretre, A. (1994), "Current partition in multiprobe conductors in the presence of slowly oscillating external potentials," *Z. Phys. B Condens. Matter* **94**, 133–137.

Bychov, Y. A. & Rashba, E. I. (1984), "Properties of a 2D electron gas with lifted spectral degeneracy," *Pis'ma Eksp. Teor. Fiz.* **39**, 66.

Cabana, J. & Martel, R. (2007), "Probing the reversibility of sidewall functionalization using carbon nanotube transistors," *J. Am. Chem. Soc.* **129**(8), 2244–2245.

Cahangirov, S., Topsakal, M., Aktürk, E., Şahin, H., & Ciraci, S. (2009), "Two- and one-dimensional honeycomb structures of silicon and germanium," *Phys. Rev. Lett.* **102**(23), 236804.

Cai, J., Ruffieux, P., Jaafar, R., et al. (2010), "Atomically precise bottom-up fabrication of graphene nanoribbons," *Nature* **466**(7305), 470–473.

Cai, Y., Zhang, G., & Zhang, Y.-W. (2014), "Layer-dependent band alignment and work function of few-layer phosphorene," *Sci. Rep.* **4**, 6677.

Calandra, M. & Mauri, F. (2007), "Electron-phonon coupling and electron self-energy in electron-doped graphene: Calculation of angular-resolved photoemission spectra," *Phys. Rev. B* **76**, 205411.

Calvo, H. L., Pastawski, H. M., Roche, S., & Foa Torres, L. E. F. (2011), "Tuning laser-induced band gaps in graphene," *Appl. Phys. Lett.* **98**(23), 232103.

Calvo, H. L., Perez-Piskunow, P. M., Pastawski, H. M., Roche, S., & Foa Torres, L. E. F. (2013), "Non-perturbative effects of laser illumination on the electrical properties of graphene nanoribbons," *J. Phys.: Condens. Matter* **25**(14), 144202.

Calvo, H. L., Perez-Piskunow, P. M., Roche, S., & Foa Torres, L. E. F. (2012), "Laser-induced effects on the electronic features of graphene nanoribbons," *Appl. Phys. Lett.* **101**(25), 253506.

Calzolari, A., Marzari, N., Souza, I., & Buongiorno Nardelli, M. (2004), "Ab initio transport properties of nanostructures from maximally localized Wannier functions," *Phys. Rev. B* **69**(3), 035108.

Campidelli, S., Ballesteros, B., Filoramo, A., et al. (2008), "Facile decoration of functionalized single-wall carbon nanotubes with phthalocyanines via click chemistry," *J. Am. Chem. Soc.* **130**(34), 11503–11509.

Campos-Delgado, J., Romo-Herrera, J. M., Jia, X., et al. (2008), "Bulk production of a new form of sp^2 carbon: Crystalline graphene nanoribbons," *Nano Lett.* **8**(9), 2773–2778.

Cançado, L. G., Pimenta, M. A., Neves, B. R. A., Dantas, M. S. S., & Jorio, A. (2004), "Influence of the atomic structure on the Raman spectra of graphite edges," *Phys. Rev. Lett.* **93**(24), 247401.

Cao, Y., Fatemi, V., Demir, A., et al. (2018), "Correlated insulator behaviour at half-filling in magic-angle graphene superlattices," *Nature* **556**(7699), 80–84.

Cao, Y., Fatemi, V., Fang, S., et al. (2018), "Unconventional superconductivity in magic-angle graphene superlattices," *Nature* **556**(7699), 43–50.

Castellanos-Gomez, A. (2015), "Black phosphorus: Narrow gap, wide applications," *J. Physi. Chem. Lett.* **6**(21), 4280–4291.

Castellanos-Gomez, A. (2016), "Why all the fuss about 2D semiconductors?," *Nat. Photonics* **10**, 202–204.

Castro, E. V., Novoselov, K. S., Morozov, S. V., et al. (2007), "Biased bilayer graphene: Semiconductor with a gap tunable by the electric field effect," *Phys. Rev. Lett.* **99**, 216802.

Cataldo, F., ed. (2005), *Polyynes: Synthesis, Properties, and Applications*, Taylor & Francis, London.

Cayssol, J., Dlóra, B., Simon, F., & Moessner, R. (2013), "Floquet topological insulators," *Physica Status Solidi (RRL) - Rapid Res. Lett.* **7**, 101.

Cazalilla, M. A., Iucci, A., Guinea, F., & Neto, A. H. C. (2012), "Local moment formation and kondo effect in defective graphene," *(unpublished) arXiv:1207.3135 [cond-mat.str-el]*.

Ceperley, D. M. & Alder, B. J. (1980), "Ground state of the electron gas by a stochastic method," *Phys. Rev. Lett.* **45**, 566–569.

Chakravarty, S. & Schmid, A. (1986), "Weak localization: The quasiclassical theory of electrons in a random potential," *Phys. Rep.* **140**(4), 193–236.

Champagne, A., Shi, L., Ouisse, T., Hackens, B., & Charlier, J.-C. (2018), "Electronic and vibrational properties of V_2C-based MXenes: From experiments to first-principles modeling," *Phys. Rev. B* **97**(11), 115439.

Chang, A. M., Baranger, H. U., Pfeiffer, L. N., West, K. W., & Chang, T. Y. (1996), "Non-Gaussian distribution of Coulomb blockade peak heights in quantum dots," *Phys. Rev. Lett.* **76**, 1695.

Chappert, C., Fert, A., & Nguyen Van Dau, F. (2007), "The emergence of spin electronics in data storage," *Nat. Mater.* **6**, 813–823.

Charlier, J.-C., Arnaud, L., Avilov, I. V., et al. (2009), "Carbon nanotubes randomly decorated with gold clusters: From nano 2 hybrid atomic structures to gas sensing prototypes," *Nanotechnology* **20**(37), 375501.

Charlier, J.-C., Blase, X., & Roche, S. (2007), "Electronic and transport properties of nanotubes," *Rev. Mod. Phys.* **79**, 677–732.

Charlier, J.-C., Ebbesen, T. W., & Lambin, P. (1996), "Structural and electronic properties of pentagon-heptagon pair defects in carbon nanotubes," *Phys. Rev. B* **53**, 11108–11113.

Charlier, J.-C., Gonze, X., & Michenaud, J.-P. (1994a), "First-principles study of the stacking effect on the electronic properties of graphite(s)," *Carbon* **32**(2), 289–299.

Charlier, J.-C., Gonze, X., & Michenaud, J.-P. (1994b), "Graphite interplanar bonding: Electronic delocalization and van der Waals interaction," *EPL (Europhysics Letters)* **28**(6), 403.

Charlier, J.-C., Gonze, X., & Michenaud, J.-P. (1995), "First-principles study of carbon nanotube solid-state packings," *EPL (Europhysics Letters)* **29**(1), 43.

Charlier, J.-C. & Lambin, P. (1998), "Electronic structure of carbon nanotubes with chiral symmetry," *Phys. Rev. B* **57**, R15037–R15039.

Charlier, J.-C., Michenaud, J.-P., & Gonze, X. (1992), "First-principles study of the electronic properties of simple hexagonal graphite," *Phys. Rev. B* **46**, 4531–4539.

Charlier, J.-C., Michenaud, J.-P., Gonze, X., & Vigneron, J.-P. (1991), "Tight-binding model for the electronic properties of simple hexagonal graphite," *Phys. Rev. B* **44**, 13237–13249.

Checkelsky, J. G., Li, L., & Ong, N. P. (2008), "Zero-energy state in graphene in a high magnetic field," *Phys. Rev. Lett.* **100**(20), 206801.

Cheianov, V. V. & Fal'ko, V. I. (2006), "Selective transmission of dirac electrons and ballistic magnetoresistance of n-p junctions in graphene," *Phys. Rev. B* **74**(4), 041403(R).

Chen, J., Badioli, M., Alonso-Gonzalez, P., et al. (2012), "Optical nano-imaging of gate-tunable graphene plasmons," *Nature* **487**(7405), 77–81.

Chen, J.-H., Cullen, W. G., Jang, C., Fuhrer, M. S., & Williams, E. D. (2009), "Defect scattering in graphene," *Phys. Rev. Lett.* **102**, 236805.

Chen, J.-H., Jang, C., Adam, S., et al. (2008), "Charged-impurity scattering in graphene," *Nat. Phys.* **4**(5), 377–381.

Chen, J.-H., Li, L., Cullen, W. G., Williams, E. D., & Fuhrer, M. S. (2011), "Tunable Kondo effect in graphene with defects," *Nat. Phys.* **7**(7), 535–538.

Chen, Z., Lin, Y.-M., Rooks, M., & Avouris, P. (2007), "Graphene nanoribbon electronics," *Physica E: Low Dimens. Syst. Nanostruct.* **40**(2), 228–232.

Chenaiov, V., Falko, V., Altshuler, B. I., & Aleiner, I. (2007), "Random resistor network model of minimal conductivity in graphene," *Phys. Rev. Lett.* **99**, 176801.

Chico, L., Crespi, V. H., Benedict, L. X., Louie, S. G., & Cohen, M. L. (1996), "Pure carbon nanoscale devices: Nanotube heterojunctions," *Phys. Rev. Lett.* **76**, 971–974.

Choi, H., Ihm, J., Louie, S., & Cohen, M. (2000), "Defects quasibound states, and quantum conductance in metallic carbon nanotubes," *Phys. Rev. Lett.* **84**, 2917–2920.

Churchill, H. O. H. & Jarillo-Herrero, P. (2014), "Two-dimensional crystals: Phosphorus joins the family," *Nat. Nanotechnol.* **9**(5), 330–331.

Chuvilin, A., Kaiser, U., Bichoutskaia, E., Besley, N. A., & Khlobystov, A. N. (2010), "Direct transformation of graphene to fullerene," *Nat. Chem.* **2**(6), 450–453.

Chuvilin, A., Meyer, J. C., Algara-Siller, G., & Kaiser, U. (2009), "From graphene constrictions to single carbon chains," *New J. Phy.* **11**(8), 083019.

Ci, L., Xu, Z., Wang, L., et al. (2008), "Controlled nanocutting of graphene," *Nano Res.* **1**, 116–122.

Clar, E. (1964), *Polycyclic Hydrocarbons*, Academic Press, London.

Clar, E. (1972), *The Aromatic Sextet*, Wiley, New York.

Clark, S. J., Segall, M. D., Pickard, C. J., et al. (2005), "First principles methods using castep," *Z. Kristallog. - Cryst. Mater.* **220**, 567–570.

Chappert, C., Fert, A., & Van Dau, F. N. (2007), "The emergence of spin electronics in data storage," *Nat. Mater.* **6**, 813.

Cockayne, E., Rutter, G. M., Guisinger, N. P., et al. (2011), "Grain boundary loops in graphene," *Phys. Rev. B* **83**, 195425.

Collins, A., Kanda, H., Isoya, J., & van Wyk, C. A. J. (1998), "Correlation between optical absorption and EPR in high-pressure diamond grown from a nickel solvent catalyst," *Diam. Relat. Mater.* **7**, 333–338.

Colomés, E. & Franz, M. (2018), "Antichiral edge states in a modified haldane nanoribbon," *Phys. Rev. Lett.* **120**, 086603.

Connétable, D., Rignanese, G.-M., Charlier, J.-C., & Blase, X. (2005), "Room temperature peierls distortion in small diameter nanotubes," *Phys. Rev. Lett.* **94**, 015503.

Connolly, M. R., Chiu, K. L., Giblin, S. P., et al. (2013), "Gigahertz quantised charge pumping in graphene quantum dots," *Nat. Nanotechnol.* **8**, 417–420.

Constantinescu, G. C. & Hine, N. D. M. (2016), "Multipurpose black-phosphorus/hBN heterostructures," *Nano Lett.* **16**(4), 2586–2594.

Cornaglia, P. S., Usaj, G., & Balseiro, C. A. (2009), "Localized spins on graphene," *Phys. Rev. Lett.* **102**(4), 046801.

Crespi, A., Corrielli, G., Valle, G. D., Osellame, R., & Longhi, S. (2013), "Dynamic band collapse in photonic graphene," *New J. Phys.* **15**(1), 013012.

Crespi, V. H., Benedict, L. X., Cohen, M. L., & Louie, S. G. (1996), "Prediction of a pure-carbon planar covalent metal," *Phys. Rev. B* **53**(20), R13303–R13305.

Cresti, A., Grosso, G., & Parravicini, G. (2007), "Numerical study of electronic transport in gated graphene ribbons," *Phys. Rev. B* **76**, 205433.

Cresti, A., Lopez-Bezanilla, A., Ordejon, P., & Roche, S. (2011), "Oxygen surface functionalization of graphene nanoribbons for transport gap engineering," *ACS Nano* **5**(11), 9271–9277.

Cresti, A., Louvet, T., Ortmann, F., et al. (2013), "Impact of vacancies on diffusive and pseudodiffusive electronic transport in graphene," *Crystals* **3**, 289–305.

Cresti, A., Nemec, N., Biel, B., et al. (2008), "Charge transport in disordered graphene-based low dimensional materials," *Nano Res.* **1**, 361–394.

Cresti, A., Nikolic, B. K., Garcia, J. H., & Roche, S. (2016), "Charge, spin and valley Hall effects in disordered graphene," *Rivista del Nuovo Cimento* **12**, 587–667.

Cresti, A., Ortmann, F., Louvet, T., Van Tuan, D., & Roche, S. (2013), "Broken symmetries, zero-energy modes, and quantum transport in disordered graphene: From supermetallic to insulating regimes," *Phys. Rev. Lett.* **110**, 196601.

Cresti, A. & Roche, S. (2009), "Edge-disorder-dependent transport length scales in graphene nanoribbons: From Klein defects to the superlattice limit," *Phys. Rev. B* **79**(23), 233404.

Cruz-Silva, E., Cullen, D. A., Gu, L., et al. (2008), "Heterodoped nanotubes: Theory, synthesis, and characterization of phosphorus-nitrogen doped multiwalled carbon nanotubes," *ACS Nano* **2**(3), 441–448.

Cruz-Silva, E., López-Urías, F., Mun oz-Sandoval, E., et al. (2009), "Electronic transport and mechanical properties of phosphorus- and phosphorus-nitrogen-doped carbon nanotubes," *ACS Nano* **3**(7), 1913–1921.

Cruz-Silva, E., Lopez-Urias, F., Munoz-Sandoval, E., et al. (2011), "Phosphorus and phosphorus-nitrogen doped carbon nanotubes for ultrasensitive and selective molecular detection," *Nanoscale* **3**(3), 1008–1013.

Cui, X., Lee, G.-H., Kim, Y. D., et al. (2015), "Multi-terminal transport measurements of MoS_2 using a van der Waals heterostructure device platform," *Nat. Nanotechnol.* **10**(6), 534–540.

Cummings, A. W., Cresti, A., & Roche, S. (2014), "Quantum Hall effect in polycrystalline graphene: The role of grain boundaries," *Phys. Rev. B* **90**, 161401.

Cummings, A. W., Duong, D. L., Nguyen, V. L., et al. (2014), "Charge transport in polycrystalline graphene: Challenges and opportunities," *Adv. Mater.* **26**(30), 5079–5094.

Cummings, A. W., Garcia, J. H., Fabian, J., & Roche, S. (2017), "Giant spin lifetime anisotropy in graphene induced by proximity effects," *Phys. Rev. Lett.* **119**, 206601.

Cummings, A. W. & Roche, S. (2016), "Effects of dephasing on spin lifetime in ballistic spin-orbit materials," *Phys. Rev. Lett.* **116**, 086602.

Curtiss, L. A., Raghavachari, K., Redfern, P. C., Rassolov, V., & Pople, J. A. (1998), "Gaussian-3 (g3) theory for molecules containing first and second-row atoms," *J. Chem. Phys.* **109**(18), 7764–7776.

Dai, S., Fei, Z., Ma, Q., et al. (2014), "Tunable phonon polaritons in atomically thin van der Waals crystals of boron nitride," *Science* **343**(6175), 1125–1129.

Dai, S., Ma, Q., Liu, M. K., et al. (2015), "Graphene on hexagonal boron nitride as a tunable hyperbolic metamaterial," *Nat. Nanotechnol.* **10**(8), 682–686.

Dal Lago, V., Suárez Morell, E., & Foa Torres, L. E. F. (2017), "One-way transport in laser-illuminated bilayer graphene: A Floquet isolator," *Phy. Rev. B* **96**(23), 235409.

D'Amato, J. L. & Pastawski, H. M. (1990), "Conductance of a disordered linear chain including inelastic scattering events," *Phys. Rev. B* **41**, 7411–7420.

D'Amato, J. L., Pastawski, H. M., & Weisz, J. F. (1989), "Half-integer and integer quantum-flux periods in the magnetoresistance of one-dimensional rings," *Phys. Rev. B* **39**(6), 3554–3562.

Dankert, A. & Dash, S. P. (2017), "Electrical gate control of spin current in van der Waals heterostructures at room temperature," *Nat. Commun.* **8**, 16093.

Das Sarma, S., Adam, S., Hwang, E. H., & Rossi, E. (2011), "Electronic transport in two-dimensional graphene," *Rev. Mod. Phys.* **83**, 407–470.

Das Sarma, S., Hwang, E. H., & Li, Q. (2012), "Disorder by order in graphene," *Phys. Rev. B* **85**(19), 195451.

Datta, S. (1995), *Electronic Transport in Mesoscopic Systems*, Cambridge University Press, Cambridge, UK.

Datta, S. S., Strachan, D. R., Khamis, S. M., & Johnson, A. T. C. (2008), "Crystallographic etching of few-layer graphene," *Nano Lett.* **8**(7), 1912–1915.

Dean, C. R., Wang, L., Maher, P., et al. (2013), "Hofstadter's butterfly and the fractal quantum Hall effect in moiré superlattices," *Nature* **497**(7451), 598–602.

Dean, C. R., Young, A. F., Meric, I., et al. (2010), "Boron nitride substrates for high-quality graphene electronics," *Nat. Nanotechnol.* **5**(10), 722–726.

Dehghani, H., Oka, T., & Mitra, A. (2015), "Out-of-equilibrium electrons and the Hall conductance of a Floquet topological insulator," *Phys. Rev. B* **91**(15), 155422.

Delaney, P., Choi, H. J., Ihm, J., Louie, S. G., & Cohen, M. L. (1998), "Broken symmetry and pseudogaps in ropes of carbon nanotubes," *Nature* **391**(6666), 466–468.

Dery, H., Wu, H., Ciftcioglu, B., et al. (2012), "Nanospintronics based on magnetologic gates," *IEEE Trans. Electron Devices* **59**, 259–262.

Derycke, V., Martel, R., Appenzeller, J., & Avouris, P. (2001), "Carbon nanotube inter- and intramolecular logic gates," *Nano Lett.* **1**(9), 453–456.

Di Ventra, M. (2008), *Electrical Transport in Nanoscale Systems*, Cambridge University Press, Cambridge, UK.

Dion, M., Rydberg, H., Schróder, E., Langreth, D. C., & Lundqvist, B. I. (2004), "Van der Waals density functional for general geometries," *Phys. Rev. Lett.* **92**(24), 246401.

Dirac, P. (1928), "The quantum theory of the electron," *Proc. R. Soc. Londn. Ser. A* **117**, 610.

Dirac, P. A. M. (1930), "Note on exchange phenomena in the Thomas atom," *Math. Proc. Cambr. Philos. Soc.* **26**(03), 376–385.

Dlubak, B., Martin, M.-B., Deranlot, C., et al. (2012), "Highly efficient spin transport in epitaxial graphene on SiC," *Nat. Phys.* **8**, 557.

Dresselhaus, G., Pimenta, M., Saito, R., et al. (2000), "On the '$\pi - \pi$' overlap energy in carbon nanotubes," *Science and Application of Nanotubes*, Kluwer Academic/Plenum Publishers, New York, pp. 275–295.

Dresselhaus, M., Dresselhaus, G., & Eklund, P. (1996), *Science of Fullerenes and Carbon Nanotubes: Their Properties and Applications*, Academic Press, San Diego, CA.

Dresselhaus, M. S. (2011), "On the past and present of carbon nanostructures," *Phys. Status Solidi B* **248**(7), 1566–1574.

Dresselhaus, M. S. & Dresselhaus, G. (2002), "Intercalation compounds of graphite," *Adv. Phys.* **51**(1), 1–186.

Dresselhaus, M. S., Dresselhaus, G., & Avouris, P., eds (2001), *Carbon Nanotubes: Synthesis, Structure, Properties, and Applications*. Topics in Applied Physics, Vol. 80, Springer, Heidelberg.

Drexler, C., Tarasenko, S. A., Olbrich, P., et al. (2013), "Magnetic quantum ratchet effect in graphene," *Nat. Nanotechnol.* **8**, 104–107.

Drogeler, M., Franzen, C., Volmer, F., et al. (2016), "Spin lifetimes exceeding 12 ns in graphene nonlocal spin valve devices," *Nano Lett.* **16**, 3533.

Drogeler, M., Volmer, F., Wolter, M., et al. (2014), "Nanosecond spin lifetimes in single- and few-layer graphene-hBN heterostructures at room temperature," *Nano Lett.* **14**(11), 6050–6055.

Du, X., Skachko, I., Barker, A., & Andrei, E. Y. (2008), "Approaching ballistic transport in suspended graphene," *Nat. Nanotechnol.* **3**(8), 491–495.

Dubois, S. M.-M. (2009), Quantum transport in graphene-based nanostructures, PhD thesis, Université catholique de Louvain.

Dubois, S. M.-M., Lopez-Bezanilla, A., et al. (2010), "Quantum transport in graphene nanoribbons: Effects of edge reconstruction and chemical reactivity," *ACS Nano* **4**(4), 1971–1976.

Dubois, S. M.-M., Zanolli, Z., Declerck, X., & Charlier, J.-C. (2009), "Electronic properties and quantum transport in graphene-based nanostructures," *Eur. Phys. J. B* **72**, 1–24.

Dunlap, B. I. (1994), "Relating carbon tubules," *Phys. Rev. B* **49**, 5643–5651.

Dvila, M. E., Xian, L., Cahangirov, S., Rubio, A., & Lay, G. L. (2014), "Germanene: A novel two-dimensional germanium allotrope akin to graphene and silicene," *New J. Phy.* **16**(9), 095002.

D'yakonov, M. I. & Perel, V. I. (1971a), "Spin orientation of electrons associated with interband absorption of light in semiconductors," *Zh. Eksp. Teor. Fiz.* **60**, 1954.

D'yakonov, M. I. & Perel, V. I. (1971b), *Sov. Phys. Solid State* **13**, 3023.

D'yakonov, M. I. & Perel, V. I. (1971c), "Current-induced spin orientation of electrons in semiconductors," *Phys. Lett. A* **35**(6), 459–460.

D'yakonov, M. I. & Perel, V. I. (1971d), "Possibility of orienting electron spins with current," *Sov. J. Exp. Theor. Phys. Lett.* **13**(11), 467–469.

Economou, E. N. (2006), *Green's Functions in Quantum Physics*, Springer-Verlag, Berlin/Heidelberg.

Egger, R. (1999), "Luttinger liquid behavior in multiwall carbon nanotubes," *Phys. Rev. Lett.* **83**(26), 5547–5550.

Egger, R. & Gogolin, A. O. (1997), "Effective low-energy theory for correlated carbon nanotubes," *Phys. Rev. Lett.* **79**(25), 5082–5085.

Ehlen, N., Senkovskiy, B. V., Fedorov, A. V., et al. (2016), "Evolution of electronic structure of few-layer phosphorene from angle-resolved photoemission spectroscopy of black phosphorous," *Phys. Rev. B* **94**(24), 245410.

Ehlert, M., Song, C., Ciorga, M., et al. (2014), "All-electrical detection of spin Hall effect in semiconductors," *Phys. Status Solidi B* **251**, 1725.

Elias, D. C., Gorbachev, R. V., Mayorov, A. S., et al. (2011), "Dirac cones reshaped by interaction effects in suspended graphene," *Nat. Phys.* **7**(9), 701–704.

Elias, D. C., Nair, R. R., Mohiuddin, T. M. G., et al. (2009), "Control of graphene's properties by reversible hydrogenation: Evidence for graphane," *Science* **323**(5914), 610–613.

Elliot, R. J. (1954), "Theory of the effect of spin-orbit coupling on magnetic resonance in some semiconductors," *Phys. Rev.* **96**, 266.

Enoki, T., Kobayashi, Y., & Fukui, K.-I. (2007), "Electronic structures of graphene edges and nanographene," *Int. Rev. Phys. Chem.* **26**(4), 609–645.

Entin-Wohlman, O., Aharony, A., & Levinson, Y. (2002), "Adiabatic transport in nanostructures," *Phys. Rev. B* **65**, 195411.

Ernzerhof, M., Perdew, J. P., & Burke, K. (1997), "Coupling-constant dependence of atomization energies," *Int. J. Quantum Chem.* **64**(3), 285–295.

Ernzerhof, M. & Scuseria, G. E. (1999), "Assessment of the Perdew–Burke–Ernzerhof exchange-correlation functional," *J. Chem. Phys.* **110**(11), 5029–5036.

Ertler, C., Konschuh, S., Gmitra, M., & Fabian, J. (2009), "Electron spin relaxation in graphene: The role of the substrate," *Phys. Rev. B* **80**, 041405.

Evaldsson, M., Zozoulenko, I. V., Xu, H., & Heinzel, T. (2008), "Edge-disorder-induced Anderson localization and conduction gap in graphene nanoribbons," *Phys. Rev. B* **78**, 161407.

Ezawa, M. (2006), "Peculiar width dependence of the electronic properties of carbon nanoribbons," *Phys. Rev. B* **73**, 045432.

Fabian, J., Matos-Abiague, A., Ertler, C., Stano, P., & Žutić, I. (2007), "Semiconductor spintronics," *Acta Phys. Slovaca* **57**, 565.

Falko, V. I., Kechedzhi, K., McCann, E., et al. (2007), "Weak localization in graphene," *Solid State Commun.* **143**, 3338.

Fan, Z., Garcia, J. H., Cummings, A., et al. (2019), "Linear scaling quantum transport methodologies," *Rev. Mod. Phys*. (submitted), arXiv:1811.07387

Fan, Z., Uppstu, A., & Harju, A. (2014), "Anderson localization in two-dimensional graphene with short-range disorder: One-parameter scaling and finite-size effects," *Phys. Rev. B* **89**, 245422.

Fang, H., Battaglia, C., Carraro, C., et al. (2014), "Strong interlayer coupling in van der Waals heterostructures built from single-layer chalcogenides," *Proc. Natl. Acad. Sci.* **111**(17), 6198–6202.

Fano, U. (1935), "Sullo spettro di assorbimento dei gas nobili presso il limite dello spettro d'arco," *Il Nuovo Cimento* 12, 154–161.

Farhat, H., Son, H., Samsonidze, G. G., et al. (2007), "Phonon softening in individual metallic carbon nanotubes due to the Kohn anomaly," *Phys. Rev. Lett.* **99**(14), 145506.

Favron, A., Gaufrès, E., Fossard, F., et al. (2015), "Photooxidation and quantum confinement effects in exfoliated black phosphorus," *Nat. Mater.* **14**(8), 826–832.

Fedorov, G., Tselev, A., Jiménez, D., et al. (2007), "Magnetically induced field effect in carbon nanotube devices," *Nano Lett.* **7**(4), 960–964.

Feng, B., Ding, Z., Meng, S., et al. (2012), "Evidence of silicene in honeycomb structures of silicon on Ag(111)," *Nano Lett.* **12**(7), 3507–3511.

Feng, B., Zhang, J., Zhong, Q., et al. (2016), "Experimental realization of two-dimensional boron sheets," *Nat. Chem.* **8**(6), 563–568.

Fermi, E. (1927), "Un metodo statistico per la determinazione di alcune prioprietà dell'atomo," *Rend. Accad. Naz. Lincei* **6**, 602–607.

Ferreira, A. & Mucciolo, E. R. (2015), "Critical delocalization of chiral zero energy modes in graphene," *Phys. Rev. Lett.* **115**, 106601.

Ferreira, A., Xu, X., Tan, C.-L., et al. (2011), "Transport properties of graphene with one-dimensional charge defects," *EPL (Europhysics Letters)* **94**, 28003.

Fert, A. (2008), "Nobel lecture: Origin, development, and future of spintronics," *Rev. Mod. Phys.* **80**, 1517–1530.

Fetter, A. & Walecka, J. (1971), *Quantum Theory of Many-Particle Systems*, McGraw-Hill, New York.

Fisher, D. S. & Lee, P. A. (1981), "Relation between conductivity and transmission matrix," *Phys. Rev. B* **23**(12), 6851–6854.

Floquet, G. (1883), "Sur les équations différentielles linéaires à coefficients périodiques," *Annales scientifiques de l'École Normale Supérieure, S'er. 2* **12**, 47–88.

Foa Torres, L. E. F. (2005), "Mono-parametric quantum charge pumping: Interplay between spatial interference and photon-assisted tunneling," *Phys. Rev. B* **72**(24), 245339.

Foa Torres, L. E. F., Avriller, R., & Roche, S. (2008), "Nonequilibrium energy gaps in carbon nanotubes: Role of phonon symmetries," *Phys. Rev. B* **78**(3), 035412.

Foa Torres, L. E. F., Calvo, H. L., Rocha, C. G., & Cuniberti, G. (2011), "Enhancing single-parameter quantum charge pumping in carbon-based devices," *Appl. Phys. Lett.* **99**(9), 092102.

Foa Torres, L. E. F. & Cuniberti, G. (2009), "Controlling the conductance and noise of driven carbon-based Fabry–Pérot devices," *Appl. Phys. Lett.* **94**(22), 222103.

Foa Torres, L. E. F., Dal Lago, V., & Suárez Morell, E. (2016), "Crafting zero-bias one-way transport of charge and spin," *Phys. Rev. B* **93**(7), 075438.

Foa Torres, L. E. F., Lewenkopf, C. H., & Pastawski, H. M. (2003), "Coherent versus sequential electron tunneling in quantum dots," *Phys. Rev. Lett.* **91**, 116801.

Foa Torres, L. E. F., Perez-Piskunow, P. M., Balseiro, C. A., & Usaj, G. (2014), "Multiterminal conductance of a Floquet topological insulator," *Phys. Rev. Lett.* **113**, 266801.

Foa Torres, L. E. F. & Roche, S. (2006), "Inelastic quantum transport and Peierls-like mechanism in carbon nanotubes," *Phys. Rev. Lett.* **97**(7), 076804.

Fogler, M. M., Butov, L. V., & Novoselov, K. S. (2014), "High-temperature superfluidity with indirect excitons in van der Waals heterostructures," *Nat. Commun.* **5**, 4555.

Franklin, A. D. & Chen, Z. (2010), "Length scaling of carbon nanotube transistors," *Nat. Nanotechnol.* **5**(12), 858–862.

Fujita, T., Jalil, M. B. A., & Tan, S. G. (2010), "Valley filter in strain engineered graphene," *Appl. Phy. Lett.* **97**(4), 043508.

Furchi, M. M., Pospischil, A., Libisch, F., Burgdörfer, J., & Mueller, T. (2014), "Photovoltaic effect in an electrically tunable van der Waals heterojunction," *Nano Lett.* **14**(8), 4785–4791.

Gabor, N. M., Song, J. C. W., Ma, Q., et al. (2011), "Hot carrier-assisted intrinsic photoresponse in graphene," *Science* **334**(6056), 648–652.

Gao, B., Komnik, A., Egger, R., Glattli, D. C., & Bachtold, A. (2004), "Evidence for Luttinger-liquid behavior in crossed metallic single-wall nanotubes," *Phys. Rev. Lett.* **92**(21), 216804.

Garcia, J. H., Cummings, A. W., & Roche, S. (2017), "Spin Hall effect and weak antilocalization in graphene/transition metal dichalcogenide heterostructures," *Nano Lett.* **17**(8), 5078–5083.

Garcia, J. H., Vila, M., Cummings, A. W., & Roche, S. (2018), "Spin transport in graphene/transition metal dichalcogenide heterostructures," *Chem. Soc. Rev.* **47**, 3359–3379.

Garello, K., Yasin, F., Couet, S., et al. (2018), "SOT-MRAM 300mm integration for low power and ultrafast embedded memories," *VLSI2018 Session C8-2*, 81–82.

Geim, A. K. (2011), "Nobel lecture: Random walk to graphene," *Rev. Mod. Phys.* **83**(3), 851–862.

Geim, A. K. & Grigorieva, I. V. (2013), "Van der Waals heterostructures," *Nature* **499**(7459), 419–425.

Geim, A. K. & Novoselov, K. S. (2007), "The rise of graphene," *Nat. Mater.* **6**(3), 183–191.

Georgiou, T., Jalil, R., Belle, B. D., et al. (2013), "Vertical field-effect transistor based on graphene-WS_2 heterostructures for flexible and transparent electronics," *Nat. Nanotechnol.* **8**(2), 100–103.

Gerlach, W. & Stern, O. (1922), "Der experimentelle nachweis der richtungsquantelung im magnetfeld," *Z. Phys.* **9**(1), 349–352.

Gheorghe, M., Gutiérrez, R., Ranjan, N., et al. (2005), "Vibrational effects in the linear conductance of carbon nanotubes," *EPL (Europhysics Letters)* **71**(3), 438.

Ghiasi, T. S., Ingla-Aynés, J., Kaverzin, A. A., & van Wees, B. J. (2017), "Large proximity-induced spin lifetime anisotropy in transition-metal dichalcogenide/graphene heterostructures," *Nano Lett.* **17**(12), 7528–7532.

Ghidiu, M., Lukatskaya, M. R., Zhao, M.-Q., Gogotsi, Y., & Barsoum, M. W. (2014), "Conductive two-dimensional titanium carbide clay with high volumetric capacitance," *Nature* **516**(7529), 78–81.

Giaever, I. & Zeller, H. R. (1968), "Superconductivity of small tin particles measured by tunneling," *Phys. Rev. Lett.* **20**(26), 1504–1507.

Giannozzi, P., Baroni, S., Bonini, N., et al. (2009), "Quantum espresso: A modular and open-source software project for quantum simulations of materials," *J. Phys.: Condens. Matter* **21**(39), 395502.

Giantomassi, M., Stankovski, M., Shaltaf, R., et al. (2011), "Electronic properties of interfaces and defects from many-body perturbation theory: Recent developments and applications," *Phys. Status Solidi (b)* **248**(2), 275–289.

Giesbers, A. J. M., Ponomarenko, L. A., Novoselov, K. S., et al. (2009), "Gap opening in the zeroth Landau level of graphene," *Phys. Rev. B* **80**(20), 201403.

Girit, C., Meyer, J. C., Erni, R., et al. (2009), "Graphene at the edge: Stability and dynamics," *Science* **323**(5922), 1705–1708.

Glazov, M. M. & Ganichev, S. D. (2014), "High frequency electric field-induced nonlinear effects in graphene," *Phys. Rep.* **535**, 101–138.

Gmitra, M. & Fabian, J. (2015), "Graphene on transition-metal dichalcogenides: A platform for proximity spin-orbit physics and optospintronics," *Phys. Rev. B* **92**(15), 155403.

Gmitra, M., Kochan, D., Högl, P., & Fabian, J. (2016), "Trivial and inverted Dirac bands and the emergence of quantum spin Hall states in graphene on transition-metal dichalcogenides," *Phys. Rev. B* **93**, 155104.

Gmitra, M., Konschuh, S., Ertler, C., Ambrosch-Draxl, C., & Fabian, J. (2009), "Band-structure topologies of graphene: Spin-orbit coupling effects from first principles," *Phys. Rev. B* **80**(23), 235431.

Godby, R. W. & Needs, R. J. (1989), "Metal-insulator transition in Kohn-Sham theory and quasiparticle theory," *Phys. Rev. Lett.* **62**, 1169–1172.

Goerbig, M. (2011), "Electronic properties of graphene in a strong magnetic field," *Rev. Mod. Phys.* **83**, 1193.

Goldoni, A., Petaccia, L., Lizzit, S., & Larciprete, R. (2010), "Sensing gases with carbon nanotubes: A review of the actual situation," *J. Phys.: Condens. Matter* **22**(1), 013001.

Gómez-Navarro, C., de Pablo, P., Biel, B., et al. (2005), "Tuning the conductance of single-walled carbon nanotubes by ion irradiation in the Anderson localization regime," *Nat. Mater.* **4**, 534.

Gonze, X. (2005), "A brief introduction to the ABINIT software package," *Z. Kristallogr. - Cryst. Mater.* **220**, 558–562.

Gonze, X., Amadon, B., Anglade, P.-M., et al. (2009), "ABINIT: First-principles approach to material and nanosystem properties," *Comput. Phys. Commun.* **180**(12), 2582–2615.

Gorbachev, R. V., Geim, A. K., Katsnelson, M. I., et al. (2012), "Strong Coulomb drag and broken symmetry in double-layer graphene," *Nat. Phys.* **8**(12), 896–901.

Gorbachev, R. V., Song, J. C. W., Yu, G. L., et al. (2014), "Detecting topological currents in graphene superlattices," *Science* **346**(6208), 448–451.

Grazianetti, C., Cinquanta, E., & Molle, A. (2016), "Two-dimensional silicon: The advent of silicene," *2D Mater.* **3**(1), 012001.

Grichuk, E. & Manykin, E. (2010), "Quantum pumping in graphene nanoribbons at resonant transmission," *EPL (Europhysics Letters)* **92**(4), 47010.

Grigorenko, A. N., Polini, M., & Novoselov, K. S. (2012), "Graphene plasmonics," *Nat. Photonics* **6**(11), 749–758.

Grossmann, F., Dittrich, T., Jung, P., & Hänggi, P. (1991), "Coherent destruction of tunneling," *Phys. Rev. Lett.* **67**, 516–519.

Grosso, G. & Parravicini, G. P. (2006), *Solid State Physics*, Elsevier, Amsterdam.

Groth, C. W., Wimmer, M., Akhmerov, A. R., & Waintal, X. (2014), "Kwant: A software package for quantum transport," *New J. Phys.* **16**(6), 063065.

Grüneis, A., Attaccalite, C., Wirtz, L., et al. (2008), "Tight-binding description of the quasiparticle dispersion of graphite and few-layer graphene," *Phys. Rev. B* **78**(20), 205425.

Grushina, A. L. & Morpurgo, A. F. (2013) "A ballistic pn junction in suspended graphene with split bottom gates," *Appl. Phys. Lett.* 102, 223102.

Gu, Z., Fertig, H. A., Arovas, D. P., & Auerbach, A. (2011), "Floquet spectrum and transport through an irradiated graphene ribbon," *Phys. Rev. Lett.* **107**(21), 216601.

Guan, J., Zhu, Z., & Tománek, D. (2014), "Phase coexistence and metal-insulator transition in few-layer phosphorene: A computational study," *Phys. Rev. Lett.* **113**(4), 046804.

Guimarães, M. H. D., Veligura, A., Zomer, P. J., et al. (2012), "Spin transport in high-quality suspended graphene devices," *Nano Lett.* **12**, 3512–3517.

Guimarães, M. H. D., Zomer, P. J., Ingla-Aynés, J., et al. (2014), "Controlling spin relaxation in hexagonal BN-encapsulated graphene with a transverse electric field," *Phys. Rev. Lett.* **113**, 086602.

Guinea, F. (2010), "Spin-orbit coupling in a graphene bilayer and in graphite," *New J. Phys.* **12**, 083063.

Guinea, F., Tejedor, C., Flores, F., & Louis, E. (1983), "Effective two-dimensional hamiltonian at surfaces," *Phys. Rev. B* **28**(8), 4397–4402.

Guinea, F. & Vergés, J. A. (1987), "Localization and topological disorder," *Phys. Rev. B* **35**(3), 979–986.

Gunlycke, D. & White, C. T. (2008), "Tight-binding energy dispersions of armchair-edge graphene nanostrips," *Phys. Rev. B* **77**, 115116.

Gunlycke, D. & White, C. T. (2011), "Graphene valley filter using a line defect," *Phys. Rev. Lett.* **106**(13), 136806.

Güttinger, J., Molitor, F., Stampfer, C., et al. (2012), "Transport through graphene quantum dots," *Rep. Progr. Phys.* **75**(12), 126502.

Haeckel, E. (1862), *Die Radiolarien*, Georg Reimer, Berlin.

Haering, R. R. (1958), "Band structure of rhombohedral graphite," *Canad. J. Phys.* **36**(3), 352–362.

Haigh, S. J., Gholinia, A., Jalil, R., et al. (2012), "Cross-sectional imaging of individual layers and buried interfaces of graphene-based heterostructures and superlattices," *Nat. Mater.* **11**(9), 764–767.

Haldane, F. D. M. (1988), "Model for a quantum Hall effect without Landau levels: Condensed-matter realization of the 'parity anomaly'," *Phys. Rev. Lett.* **61**(18), 2015–2018.

Hallal, A., Ibrahim, F., Yang, H., Roche, S., & Chshiev, M. (2017), "Tailoring magnetic insulator proximity effects in graphene: First-principles calculations," *2D Mater.* **4**(2), 025074.

Hamada, N., Sawada, S.-I., & Oshiyama, A. (1992), "New one-dimensional conductors: Graphitic microtubules," *Phys. Rev. Lett.* **68**, 1579–1581.

Hamann, D. R., Schlüter, M., & Chiang, C. (1979), "Norm-conserving pseudopotentials," *Phys. Rev. Lett.* **43**, 1494–1497.

Han, M. Y., Özyilmaz, B., Zhang, Y., & Kim, P. (2007), "Energy band-gap engineering of graphene nanoribbons," *Phys. Rev. Lett.* **98**, 206805.

Han, W. & Kawakami, R. K. (2011), "Spin relaxation in single-layer and bilayer graphene," *Phys. Rev. Lett.* **107**, 047207.

Han, W., Kawakami, R. K., Gmitra, M., & Fabian, J. (2014), "Graphene spintronics," *Nat. Nanotechnol.* **9**(10), 794–807.

Han, W., Pi, K., McCreary, K. M., et al. (2010), "Tunneling spin injection into single layer graphene," *Phys. Rev. Lett.* **105**, 167202.

Hankiewicz, E. M., Li, J., Jungwirth, T., et al. (2005), "Charge Hall effect driven by spin-chemical potential gradients and onsager relations in mesoscopic systems," *Phys. Rev. B* **72**, 155305.

Harris, P. (1999), *Carbon Nanotubes and Related Structures: New Materials for the Twenty-first Century*, Cambridge University Press, Cambridge, UK.

Harrison, W. (1989), *Electronic Structure and the Properties of Solids: The Physics of the Chemical Bond*, Dover Publications, New York.

Hartree, D. R. (1957), *The Calculation of Atomic Structures*, John Wiley & Sons, New York.

Hasan, M. Z. & Kane, C. L. (2010), "*Colloquium*: Topological insulators," *Rev. Mod. Phys.* **82**, 3045–3067.

Haydock, R., Heine, V., & Kelly, M. J. (1972), "Electronic structure based on the local atomic environment for tight-binding bands," *J. Phys. C: Solid State Phys.* **5**(20), 2845.

Haydock, R., Heine, V., & Kelly, M. J. (1975), "Electronic structure based on the local atomic environment for tight-binding bands: II," *J. Phys. C: Solid State Phys.* **8**(20), 2591.

Haydock, R., Heine, V., & Kelly, M. J. (2016), "Determination of the spin-lifetime anisotropy in graphene using oblique spin precession," *Nat. Commun*. **7**, 11444.

Hedin, L. (1965), "New method for calculating the one-particle Green's function with application to the electron-gas problem," *Phys. Rev.* **139**, A796–A823.

Hedin, L. & Lundqvist, S. (1970), "Effects of electron-electron and electron-phonon interactions on the one-electron states of solids," *Solid State Physics*, Vol. 23, Academic Press, New York, pp. 1–181.

Heimann, R., Evsyukov, S., & Kavan, L. (1999), *Carbyne and Carbynoid Structures*, Kluwer Academic, Dordrecht.

Heinze, S., Tersoff, J., Martel, R., et al. (2002), "Carbon nanotubes as Schottky barrier transistors," *Phys. Rev. Lett.* **89**, 106801.

Hemstreet, Louis A., J., Fong, C. Y., & Cohen, M. L. (1970), "Calculation of the band structure and optical constants of diamond using the nonlocal-pseudopotential method," *Phys. Rev. B* **2**(6), 2054–2063.

Herrmann, L. G., Delattre, T., Morfin, P., et al. (2007), "Shot noise in Fabry-Perot interferometers based on carbon nanotubes," *Phys. Rev. Lett.* **99**, 156804.

Hikami, S., Larkin, A. I., & Nagaoka, Y. (1980), "Spin-orbit interaction and magnetoresistance in the two dimensional random system," *Progr. Theor. Phys.* **63**(2), 707–710.

Hirsch, J. E. (1999), "Spin Hall effect," *Phys. Rev. Lett.* **83**, 1834–1837.

Hirvonen, P., Ervasti, M. M., Fan, Z., et al. (2016), "Multiscale modeling of polycrystalline graphene: A comparison of structure and defect energies of realistic samples from phase field crystal models," *Phys. Rev. B* **94**, 035414.

Hjort, M. & Stafström, S. (2001), "Disorder-induced electron localization in metallic carbon nanotubes," *Phys. Rev. B* **63**(11), 113406.

Hoffmann, A. (2013), "Spin Hall effects in metals," *IEEE Trans. Magn.* **49**, 5172.

Hofstadter, D. R. (1976), "Energy levels and wave functions of Bloch electrons in rational and irrational magnetic fields," *Phys. Rev. B* **14**, 2239–2249.

Hohenberg, P. & Kohn, W. (1964), "Inhomogeneous electron gas," *Phys. Rev.* **136**, B864–B871.

Holmström, E., Fransson, J., Eriksson, O., et al. (2011), "Disorder-induced metallicity in amorphous graphene," *Phys. Rev. B* **84**(20), 205414.

Hong, X., Kim, J., Shi, S.-F., et al. (2014), "Ultrafast charge transfer in atomically thin MoS_2/WS_2 heterostructures," *Nat. Nanotechnol.* **9**(9), 682–686.

Horsell, D. W., Tikhonenko, F. V., Gorbachev, R. V., & Savchenko, A. K. (2008), "Weak localization in monolayer and bilayer graphene," *Philos. Trans. R. Soc. A* **366**, 245.

Hoshi, T., Yamamoto, S., Zhang, S.-L., & Fujiwara, T. (2012), "An order-n electronic structure theory with generalized eigenvalue equations and its application to a ten-million-atom system," *J. Phys.: Condens. Matter* **24**, 165502.

Hossain, M. Z., Johns, J. E., Bevan, K. H., et al. (2012), "Chemically homogeneous and thermally reversible oxidation of epitaxial graphene," *Nat. Chem.* **4**(4), 305–309.

Hu, T., Wang, J., Zhang, H., et al. (2015), "Vibrational properties of Ti3C2 and Ti3C2T2 (T = O, F, OH) monosheets by first-principles calculations: A comparative study," *Phys. Chem. Chem. Phys.* **17**(15), 9997–10003.

Huang, B., Clark, G., Klein, D., et al. (2018), "Electrical control of 2D magnetism in bilayer CrI3," *Nat Nanotechnol*. **13**(7), 544–548.

Huang, B., Clark, G., Navarro-Moratalla, E., et al. (2017), "Layer-dependent ferromagnetism in a van der Waals crystal down to the monolayer limit," *Nature* **546**, 270–273.

Huang, B., Liu, M., Su, N., et al. (2009), "Quantum manifestations of graphene edge stress and edge instability: A first-principles study," *Phys. Rev. Lett.* **102**(16), 166404.

Huang, L., Lai, Y.-C., & Grebogi, C. (2010), "Relativistic quantum level-spacing statistics in chaotic graphene billiards," *Phys. Rev. E* **81**(5), 055203.

Huang, P., Ruiz-Vargas, C. S., van der Zande, A. M., et al. (2011), "Grains and grain boundaries in single-layer graphene atomic patchwork quilts," *Nature* **469**, 389–392.

Huang, Y., Shirodkar, S. N., & Yakobson, B. I. (2017), "Two-dimensional boron polymorphs for visible range plasmonics: A first-principles exploration," *J. Am. Chem. Soc.* **139**(47), 17181–17185.

Huertas-Hernando, D., Guinea, F., & Brataas, A. (2006), "Spin-orbit coupling in curved graphene, fullerenes, nanotubes, and nanotube caps," *Phys. Rev. B* **74**, 155426.

Huertas-Hernando, D., Guinea, F., & Brataas, A. (2009), "Spin-orbit-mediated spin relaxation in graphene," *Phys. Rev. Lett.* **103**, 146801.

Hwang, C., Park, C.-H., Siegel, D. A., et al. (2011), "Direct measurement of quantum phases in graphene via photoemission spectroscopy," *Phys. Rev. B* **84**, 125422.

Hwang, E. H. & Sarma, S. D. (2008), "Acoustic phonon scattering limited carrier mobility in two-dimensional extrinsic graphene," *Phys. Rev. B* **77**, 115449.

Iijima, S. (1991), "Helical microtubules of graphitic carbon," *Nature* **354**(6348), 56–58.

Iijima, S. & Ichihashi, T. (1993), "Single-shell carbon nanotubes of 1-nm diameter," *Nature* **363**(6430), 603–605.

Iijima, S., Yudasaka, M., Yamada, R., et al. (1999), "Nano-aggregates of single-walled graphitic carbon nano-horns," *Chem. Phys. Lett.* **309**(3–4), 165–170.

Imry, Y. & Landauer, R. (1999), "Conductance viewed as transmission," *Rev. Mod. Phys.* **71**, S306–S312.

Ingaramo, L. H. & Foa Torres, L. E. F. (2013), "Defect assisted adiabatic quantum charge pumping in graphene-based devices," *Appl. Phys. Lett.* **103**, 123508.

Ingaramo, L. H. & Foa Torres, L. E. F. (2016), "Valley filtering by a line-defect in graphene: Quantum interference and inversion of the filter effect," *J. Phys.: Condens. Matter* **28**(48), 485302.

Isacsson, A., Cummings, A. W., Colombo, L., et al. (2017), "Scaling properties of polycrystalline graphene: A review," *2D Mater.* **4**(1), 012002.

Ishii, H., Roche, S., Kobayashi, N., & Hirose, K. (2010), "Inelastic transport in vibrating disordered carbon nanotubes: Scattering times and temperature-dependent decoherence effects," *Phys. Rev. Lett.* **104**, 116801.

Ishii, H., Triozon, F., Kobayashi, N., Hirose, K., & Roche, S. (2009), "Charge transport in carbon nanotubes based materials, a Kubo-Greenwood computational approach," *C. R. Phys.* **10**(4), 283–296.

Isobe, H., Yuan, N. F., & Fu, L. (2018), "Unconventional superconductivity and density waves in twisted bilayer graphene," *Phys. Rev. X* **8**(4), 041041.

Jacob, Z. (2014), "Nanophotonics: Hyperbolic phonon-polaritons," *Nat. Mater.* **13**(12), 1081–1083.

Jain, M., Chelikowsky, J. R., & Louie, S. G. (2011), "Reliability of hybrid functionals in predicting band gaps," *Phys. Rev. Lett.* **107**, 216806.

Jalabert, R. A., Stone, A. D., & Alhassid, Y. (1992), "Statistical theory of Coulomb blockade oscillations: Quantum chaos in quantum dots," *Phys. Rev. Lett.* **68**(23), 3468–3471.

Janssen, T. J. B. M., Tzalenchuk, A., Lara-Avila, S., Kubatkin, S., & Fal'leko, V. I. (2013), "Quantum resistance metrology using graphene," *Rep. Prog. Phys.* **76**(10), 104501.

Jariwala, D., Marks, T. J., & Hersam, M. C. (2017), "Mixed-dimensional van der Waals heterostructures," *Nat. Mater.* **16**(2), 170–181.

Jariwala, D., Sangwan, V. K., Lauhon, L. J., Marks, T. J., & Hersam, M. C. (2014), "Emerging device applications for semiconducting two-dimensional transition metal dichalcogenides," *ACS Nano* **8**(2), 1102–1120.

Javey, A., Guo, J., Paulsson, M., et al. (2004), "High-field quasiballistic transport in short carbon nanotubes," *Phys. Rev. Lett.* **92**, 106804.

Javey, A., Guo, J., Wang, Q., Lundstrom, M., & Dai, H. (2003), "Ballistic carbon nanotube field-effect transistors," *Nature* **424**(6949), 654–657.

Jayasekera, T. & Mintmire, J. W. (2007), "Transport in multiterminal graphene nanodevices," *Nanotechnology* **18**(42), 424033.

Jeong, H. Y., Kim, J. Y., Kim, J. W., et al. (2010), "Graphene oxide thin films for flexible nonvolatile memory applications," *Nano Lett.* **10**(11), 4381–4386.

Ji, J., Song, X., Liu, J., et al. (2016), "Two-dimensional antimonene single crystals grown by van der Waals epitaxy," *Nature Commun.* **7**, 13352.

Jia, X., Campos-Delgado, J., Terrones, M., Meunier, V., & Dresselhaus, M. S. (2011), "Graphene edges: A review of their fabrication and characterization," *Nanoscale* **3**(1), 86–95.

Jia, X., Goswami, P., & Chakravarty, S. (2008), "Dissipation and criticality in the lowest Landau level of graphene," *Phys. Rev. Lett.* **101**(3), 036805.

Jia, X., Hofmann, M., Meunier, V., et al. (2009), "Controlled formation of sharp zigzag and armchair edges in graphitic nanoribbons," *Science* **323**(5922), 1701–1705.

Jiang, J., Dong, J., & Xing, D. Y. (2003), "Quantum interference in carbon-nanotube electron resonators," *Phys. Rev. Lett.* **91**(5), 056802.

Jiang, Z., Zhang, Y., Stormer, H. L., & Kim, P. (2007), "Quantum Hall states near the charge-neutral dirac point in graphene," *Phys. Rev. Lett.* **99**, 106802.

Jiao, L., Wang, X., Diankov, G., Wang, H., & Dai, H. (2010), "Facile synthesis of high-quality graphene nanoribbons," *Nat. Nanotechnol.* **5**(5), 321–325.

Jiao, L., Zhang, L., Ding, L., Liu, J., & Dai, H. (2010), "Aligned graphene nanoribbons and crossbars from unzipped carbon nanotubes," *Nano Res.* **3**(6), 387–394.

Jiao, L., Zhang, L., Wang, X., Diankov, G., & Dai, H. (2009), "Narrow graphene nanoribbons from carbon nanotubes," *Nature* **458**(7240), 877–880.

Jin, C., Lan, H., Peng, L., Suenaga, K., & Iijima, S. (2009), "Deriving carbon atomic chains from graphene," *Phys. Rev. Lett.* **102**(20), 205501.

Johnson, M. & Silsbee, R. H. (1985), "Interfacial charge-spin coupling: Injection and detection of spin magnetization in metals," *Phys. Rev. Lett.* **55**, 1790–1793.

Jonson, M. & Grincwajg, A. (1987), "Effect of inelastic scattering on resonant and sequential tunneling in double barrier heterostructures," *Appl. Phys. Lett.* **51**(21), 1729–1731.

Jorio, A., Dresselhaus, M. S., Saito, R., & Dresselhaus, G. (2011), *Raman Spectroscopy in Graphene Related Systems*, Wiley-VCH, Weinheim.

Jorio, A., Souza Filho, A. G., Dresselhaus, G., et al. (2001), "Joint density of electronic states for one isolated single-wall carbon nanotube studied by resonant raman scattering," *Phys. Rev. B* **63**, 245416.

Jotzu, G., Messer, M., Desbuquois, R., et al. (2014), "Experimental realization of the topological Haldane model with ultracold fermions," *Nature* **515**(7526), 237–240.

Kaestner, B., Kashcheyevs, V., Amakawa, S., et al. (2008), "Single-parameter nonadiabatic quantized charge pumping," *Phys. Rev. B* **77**(15), 153301.

Kane, C. L. & Mele, E. J. (1997), "Size, shape, and low energy electronic structure of carbon nanotubes," *Phys. Rev. Lett.* **78**, 1932–1935.

Kane, C. L. & Mele, E. J. (2005a), "Quantum spin hall effect in graphene," *Phys. Rev. Lett.* **95**, 226801.

Kane, C. L. & Mele, E. J. (2005b), "z_2 topological order and the quantum spin Hall effect," *Phys. Rev. Lett.* **95**, 146802.

Karch, J., Drexler, C., Olbrich, P., et al. (2011), "Terahertz radiation driven chiral edge currents in graphene," *Phys. Rev. Lett.* **107**(27), 276601.

Karplus, R. & Luttinger, J. M. (1954), "Hall effect in ferromagnetics," *Phys. Rev.* **95**, 1154–1160.

Kashcheyevs, V., Aharony, A., & Entin-Wohlman, O. (2004), "Resonance approximation and charge loading and unloading in adiabatic quantum pumping," *Phys. Rev. B* **69**, 195301.

Kastner, M. A. (1992), "The single-electron transistor," *Rev. Mod. Phys.* **64**(3), 849–858.

Kato, T. & Hatakeyama, R. (2012), "Site- and alignment-controlled growth of graphene nanoribbons from nickel nanobars," *Nat. Nanotechnol.* **7**(10), 651–656.

Kato, Y. K., Myers, R. C., Gossard, A. C., & Awschalom, D. D. (2004), "Observation of the spin Hall effect in semiconductors," *Science* **306**(5703), 1910–1913.

Katsnelson, M. I. (2012), *Graphene: Carbon in Two Dimensions*, Cambridge University Press, Cambridge, UK.

Katsnelson, M. I., Novoselov, K. S., & Geim, A. K. (2006), "Chiral tunnelling and the Klein paradox in graphene," *Nat. Phys.* **2**(9), 620–625.

Kavan, L. & Kastner, J. (1994), "Carbyne forms of carbon: Continuation of the story," *Carbon* **32**(8), 1533–1536.

Kaverzin, A. A. & van Wees, B. J. (2015), "Electron transport nonlocality in monolayer graphene modified with hydrogen silsesquioxane polymerization," *Phys. Rev. B* **91**, 165412.

Kawai, T., Miyamoto, Y., Sugino, O., & Koga, Y. (2000), "Graphitic ribbons without hydrogen-termination: Electronic structures and stabilities," *Phys. Rev. B* **62**, R16349–R16352.

Kazymyrenko, K. & Waintal, X. (2008), "Knitting algorithm for calculating green functions in quantum systems," *Phys. Rev. B* **77**(11), 115119.

Kechedzhi, K., McCann, E., I., F. Fal'ko, V. I., et al. (2007), "Weak localization in monolayer and bilayer graphene," *Eur. Phys. J. Spec. Top.* **148**, 39.

Khokhriakov, D., Cummings, A. W., Song, K., et al. (2018), "Tailoring emergent spin phenomena in dirac material heterostructures," *Sci. Adv.* **4**(9).

Kibis, O. V. (2010), "Metal-insulator transition in graphene induced by circularly polarized photons," *Phys. Rev. B* **81**(16), 165433.

Kim, K., Lee, Z., Regan, W., et al. (2011), "Grain boundary mapping in polycrystalline graphene," *ACS Nano* **5**, 2142.

Kim, K. S., Walter, A. L., Moreschini, L., Seyller, T., Horn, K., Rotenberg, E., & Bostwick, A. (2013), "Coexisting massive and massless Dirac fermions in symmetry-broken bilayer graphene," *Nat. Mater.* **12**, 887–892.

Kim, N. Y., Recher, P., Oliver, W. D., et al. (2007), "Tomonaga-Luttinger liquid features in ballistic single-walled carbon nanotubes: Conductance and shot noise," *Phys. Rev. Lett.* **99**, 036802.

Kim, W., Javey, A., Tu, R., et al. (2005), "Electrical contacts to carbon nanotubes down to 1 nm in diameter," *Appl. Phys. Lett.* **87**(17), 173101.

Kirwan, D. F., Rocha, C. G., Costa, A. T., & Ferreira, M. S. (2008), "Sudden decay of indirect exchange coupling between magnetic atoms on carbon nanotubes," *Phys. Rev. B* **77**(8), 085432.

Kitagawa, T., Oka, T., Brataas, A., Fu, L., & Demler, E. (2011), "Transport properties of nonequilibrium systems under the application of light: Photoinduced quantum Hall insulators without Landau levels," *Phys. Rev. B* **84**(23), 235108.

Klein, D. R., MacNeill, D., Lado, J. L., et al. (2018), "Probing magnetism in 2D van der Waals crystalline insulators via electron tunneling," *Science* **360**(6394), 1218–1222.

Klein, O. (1929), "Die reflexion von elektronen an einem potentialsprung nach der relativistischen dynamik von dirac," *Z. Phys. A: Hadrons Nuclei* **53**, 157–165.

Kleinman, L. & Bylander, D. M. (1982), "Efficacious form for model pseudopotentials," *Phys. Rev. Lett.* **48**, 1425–1428.

Klimeš, J. & Michaelides, A. (2012), "Perspective: Advances and challenges in treating van der Waals dispersion forces in density functional theory," *J. Chem. Phys.* **137**(12), 120901.

Klos, J. W. & Zozoulenko, I. V. (2010), "Effect of short- and long-range scattering in the conductivity of graphene: Boltzmann approach vs tight-binding calculations," *Phys. Rev. B* **82**, 081414.

Kobayashi, Y., Fukui, K.-i., Enoki, T., Kusakabe, K., & Kaburagi, Y. (2005), "Observation of zigzag and armchair edges of graphite using scanning tunneling microscopy and spectroscopy," *Phys. Rev. B* **71**, 193406.

Kochan, D., Gmitra, M., & Fabian, J. (2014), "Spin relaxation mechanism in graphene: Resonant scattering by magnetic impurities," *Phys. Rev. Lett.* **112**, 116602.

Kochan, D., Irmer, S., & Fabian, J. (2017), "Model spin-orbit coupling Hamiltonians for graphene systems," *Phys. Rev. B* **95**, 165415.

Kohler, S., Lehmann, J., & Hänggi, P. (2005), "Driven quantum transport on the nanoscale," *Phys. Rep.* **406**(6), 379–443.

Kohmoto, M. (1985), "Topological invariant and the quantization of the Hall conductance," *Ann. Phys.* **160**(2), 343–354.

Kohn, W. (1959a), "Image of the Fermi surface in the vibration spectrum of a metal," *Phys. Rev. Lett.* **2**(9), 393–394.

Kohn, W. (1959b), "Theory of bloch electrons in a magnetic field: The effective Hamiltonian," *PR* **115**(6), 1460–1478.

Kohn, W. & Luttinger, J. M. (1957), "Quantum theory of electrical transport phenomena," *Phys. Rev.* **108**, 590–611.

Kohn, W. & Sham, L. J. (1965), "Self-consistent equations including exchange and correlation effects," *Phys. Rev.* **140**, A1133–A1138.

Komatsu, K., Morita, Y., Watanabe, E., et al. (2018), "Observation of the quantum valley Hall state in ballistic graphene superlattices," *Sci. Adv.* **4**(5), eaaq0194.

Konschuh, S., Gmitra, M., & Fabian, J. (2010), "Tight-binding theory of the spin-orbit coupling in graphene," *Phys. Rev. B* **82**(24), 245412.

Konstantatos, G., Badioli, M., Gaudreau, L., et al. (2012), "Hybrid graphene-quantum dot phototransistors with ultrahigh gain," *Nat. Nanotechnol.* **7**(6), 363–368.

Koppens, F. H. L., Chang, D. E., & Garcia de Abajo, F. J. (2011), "Graphene plasmonics: A platform for strong light-matter interactions," *Nano Lett.* **11**(8), 3370–3377.

Koppens, F. H. L., Mueller, T., Avouris, P., et al. (2014), "Photodetectors based on graphene, other two-dimensional materials and hybrid systems," *Nat. Nanotechnol.* **9**(10), 780–793.

Koskinen, P., Malola, S., & Häkkinen, H. (2008), "Self-passivating edge reconstructions of graphene," *Phys. Rev. Lett.* **101**, 115502.

Kostyrko, T., Bartkowiak, M., & Mahan, G. D. (1999), "Localization in carbon nanotubes within a tight-binding model," *Phys. Rev. B* **60**(15), 10735–10738.

Kosynkin, D. V., Higginbotham, A. L., Sinitskii, A., et al. (2009), "Longitudinal unzipping of carbon nanotubes to form graphene nanoribbons," *Nature* **458**(7240), 872–876.

Kotakoski, J., Krasheninnikov, A. V., Kaiser, U., & Meyer, J. C. (2011), "From point defects in graphene to two-dimensional amorphous carbon," *Phys. Rev. Lett.* **106**, 105505.

Kotakoski, J. & Meyer, J. C. (2012), "Mechanical properties of polycrystalline graphene based on a realistic atomistic model," *Phys. Rev. B* **85**, 195447.

Kouwenhoven, L. & Glazman, L. (2001), "Revival of the Kondo effect," *Phys. World* **January**, 33–38.

Kouwenhoven, L. P., Marcus, C. M., McEuen, P. L., et al. (1997), "Electron transport in quantum dots," in *Nato ASI Conference Proceedings*, Kluwer Academic, Dordrecht, pp. 105–214.

Kowalczyk, P., Holyst, R., Terrones, M., & Terrones, H. (2007), "Hydrogen storage in nanoporous carbon materials: Myth and facts," *Phys. Chem. Chem. Phys.* **9**(15), 1786–1792.

Kramer, B. & MacKinnon, A. (1993), "Localization: Theory and experiment," *Rep. Progr. Phys.* **56**(12), 1469–1564.

Krasheninnikov, A. V. & Banhart, F. (2007), "Engineering of nanostructured carbon materials with electron or ion beams," *Nat. Mater.* **6**(10), 723–733.

Kresse, G. & Furthmüller, J. (1996a), "Efficiency of ab-initio total energy calculations for metals and semiconductors using a plane-wave basis set," *Comput. Mater. Sci.* **6**(1), 15–50.

Kresse, G. & Furthmüller, J. (1996b), "Efficient iterative schemes for ab initio total-energy calculations using a plane-wave basis set," *Phys. Rev. B* **54**(16), 11169–11186.

Krishnan, A., Dujardin, E., Treacy, M. M. J., et al. (1997), "Graphitic cones and the nucleation of curved carbon surfaces," *Nature* **388**(6641), 451–454.

Kroto, H. W., Heath, J. R., O'Brien, S. C., Curl, R. F., & Smalley, R. E. (1985), "C60: Buckminsterfullerene," *Nature* **318**(6042), 162–163.

Kroto, H. W. & McKay, K. (1988), "The formation of quasi-icosahedral spiral shell carbon particles," *Nature* **331**(6154), 328–331.

Kubo, R. (1966), "The fluctuation-dissipation theorem," *Rep. Progr. Phys.* **29**(1), 255.

Kümmel, S. & Kronik, L. (2008), "Orbital-dependent density functionals: Theory and applications," *Rev. Mod. Phys.* **80**, 3–60.

Kundu, A., Fertig, H. A., & Seradjeh, B. (2014), "Effective theory of Floquet topological transitions," *Phys. Rev. Lett.* **113**(23), 236803.

Kurasch, S., Kotakoski, J., Lehtinen, O., et al. (2012), "Atom-by-atom observation of grain boundary migration in graphene," *Nano Lett.* **12**(6), 3168–3173.

Kurganova, E. V., van Elferen, H. J., McCollam, A., et al. (2011), "Spin splitting in graphene studied by means of tilted magnetic-field experiments," *Phys. Rev. B* **84**(12), 121407.

Kwon, Y.-K. & Tománek, D. (1998), "Electronic and structural properties of multiwall carbon nanotubes," *Phys. Rev. B* **58**, R16001–R16004.

Lagow, R. J., Kampa, J. J., Wei, H.-C., et al. (1995), "Synthesis of linear acetylenic carbon: The 'sp' carbon allotrope," *Science* **267**(5196), 362–367.

Lahiri, J., Lin, Y., Bozkurt, P., Oleynik, I. I., & Batzill, M. (2010), "An extended defect in graphene as a metallic wire," *Nat. Nanotechnol.* **5**(5), 326–329.

Lambin, P., Fonseca, A., Vigneron, J., Nagy, J., & Lucas, A. (1995), "Structural and electronic properties of bent carbon nanotubes," *Chem. Phys. Lett.* **245**(1), 85–89.

Lambin, P., Philippe, L., Charlier, J., & Michenaud, J. (1994), "Electronic band structure of multilayered carbon tubules," *Comput. Mater. Sci.* **2**(2), 350–356.

Lanczos, C. (1950), "Solution of systems of linear equations by minimized iterations," *J. Res. Natl. Bur. Stand.* **45**, 255.

Landau, L. & Lifschitz, E. (1980), *Statistical Physics Part II*, Pergamon, Oxford.

Landauer, R. (1957), "Spatial variation of currents and fields due to localized scatterers in metallic conduction," *IBM J. Res. Dev.* **1**, 223.

Landauer, R. (1970), "Electrical resistance of disordered one-dimensional lattices," *Philos. Mag.* **21**, 863–867.

Latil, S. & Henrard, L. (2006), "Charge carriers in few-layer graphene films," *Phys. Rev. Lett.* **97**, 036803.

Latil, S., Meunier, V., & Henrard, L. (2007), "Massless fermions in multilayer graphitic systems with misoriented layers: *Ab initio* calculations and experimental fingerprints," *Phys. Rev. B* **76**, 201402.

Latil, S., Roche, S., & Charlier, J.-C. (2005), "Electronic transport in carbon nanotubes with random coverage of physisorbed molecules," *Nano Lett.* **5**(11), 2216–2219.

Latil, S., Roche, S., Mayou, D., & Charlier, J.-C. (2004), "Mesoscopic transport in chemically doped carbon nanotubes," *Phys. Rev. Lett.* **92**, 256805.

Laughlin, R. B. (1983), "Anomalous quantum Hall effect: An incompressible quantum fluid with fractionally charged excitations," *Phys. Rev. Lett.* **50**(18), 1395–1398.

Lazzeri, M. & Mauri, F. (2006), "Coupled dynamics of electrons and phonons in metallic nanotubes: Current saturation from hot-phonon generation," *Phys. Rev. B* **73**, 165419.

Lazzeri, M., Piscanec, S., Mauri, F., Ferrari, A. C., & Robertson, J. (2006), "Phonon linewidths and electron-phonon coupling in graphite and nanotubes," *Phys. Rev. B* **73**, 155426.

Leconte, N., Lherbier, A., Varchon, F., et al. (2011), "Quantum transport in chemically modified two-dimensional graphene: From minimal conductivity to Anderson localization," *Phys. Rev. B* **84**, 235420.

Leconte, N., Moser, J., Ordejon, P., et al. (2010), "Damaging graphene with ozone treatment: A chemically tunable metal-insulator transition," *ACS Nano* **4**(7), 4033–4038.

Leconte, N., Ortmann, F., Cresti, A., & Roche, S. (2016), "Unconventional features in the quantum Hall regime of disordered graphene: Percolating impurity states and Hall conductance quantization," *Phys. Rev. B* **93**, 115404.

Lee, C.-H., Lee, G.-H., van der Zande, A. M., et al. (2014), "Atomically thin p-n junctions with van der Waals heterointerfaces," *Nat. Nanotechnol.* **9**(9), 676–681.

Lee, G.-D., Wang, C. Z., Yoon, E., et al. (2005), "Diffusion, coalescence, and reconstruction of vacancy defects in graphene layers," *Phys. Rev. Lett.* **95**, 205501.

Lee, H., Son, Y.-W., Park, N., Han, S., & Yu, J. (2005), "Magnetic ordering at the edges of graphitic fragments: Magnetic tail interactions between the edge-localized states," *Phys. Rev. B* **72**, 174431.

Lee, P. A. & Ramakrishnan, T. V. (1985), "Disordered electronic systems," *Rev. Mod. Phys.* **57**, 287–337.

Lee, P. A. & Stone, A. D. (1985), "Universal conductance fluctuations in metals," *Phys. Rev. Lett.* **55**(15), 1622–1625.

Lee, Y.-S. & Marzari, N. (2006), "Cycloaddition functionalizations to preserve or control the conductance of carbon nanotubes," *Phys. Rev. Lett.* **97**(11), 116801.

Leek, P. J., Buitelaar, M. R., Talyanskii, V. I., et al. (2005), "Charge pumping in carbon nanotubes," *Phys. Rev. Lett.* **95**, 256802.

Lefebvre, J., Homma, Y., & Finnie, P. (2003), "Bright band gap photoluminescence from unprocessed single-walled carbon nanotubes," *Phys. Rev. Lett.* **90**, 217401.

Leghrib, R., Felten, A., Demoisson, F., et al. (2010), "Room-temperature, selective detection of benzene at trace levels using plasma-treated metal-decorated multiwalled carbon nanotubes," *Carbon* **48**(12), 3477–3484.

Lehtinen, P. O., Foster, A. S., Ayuela, A., Vehviläinen, T. T., & Nieminen, R. M. (2004), "Structure and magnetic properties of adatoms on carbon nanotubes," *Phys. Rev. B* **69**(15), 155422.

Lehtinen, P. O., Foster, A. S., Ma, Y., Krasheninnikov, A. V., & Nieminen, R. M. (2004), "Irradiation-induced magnetism in graphite: A density functional study," *Phys. Rev. Lett.* **93**(18), 187202.

Leonard, F. & Talin, A. A. (2011), "Electrical contacts to one- and two-dimensional nanomaterials," *Nat. Nanotechnol.* **6**(12), 773–783.

Léonard, F. & Tersoff, J. (1999), "Novel length scales in nanotube devices," *Phys. Rev. Lett.* **83**, 5174–5177.

Léonard, F. & Tersoff, J. (2000a), "Negative differential resistance in nanotube devices," *Phys. Rev. Lett.* **85**, 4767–4770.

Léonard, F. & Tersoff, J. (2000b), "Role of fermi-level pinning in nanotube schottky diodes," *Phys. Rev. Lett.* **84**, 4693–4696.

Léonard, F. & Tersoff, J. (2002), "Multiple functionality in nanotube transistors," *Phys. Rev. Lett.* **88**, 258302.

Lepro, X., Vega-Cantu, Y., Rodriguez-Macias, F., et al. (2007), "Production and characterization of coaxial nanotube junctions and networks of CNx/CNT," *Nano Lett.* **7**(8), 2220–2226.

Leutenantsmeyer, J. C., Ingla-Aynés, J., Fabian, J., & van Wees, B. J. (2018), "Observation of spin-valley-coupling-induced large spin-lifetime anisotropy in bilayer graphene," *Phys. Rev. Lett.* **121**, 127702.

Leutenantsmeyer, J. C., Kaverzin, A. A., Wojtaszek, M., & van Wees, B. J. (2017), "Proximity induced room temperature ferromagnetism in graphene probed with spin currents," *2D Mater.* **4**, 014001.

Lherbier, A. (2008), Étude des propriétés électroniques et des propriétés de transport de nanofils semiconducteurs et de plans de graphène, PhD thesis, Université Joseph-Fourier.

Lherbier, A., Biel, B., Niquet, Y.-M., & Roche, S. (2008), "Transport length scales in disordered graphene-based materials: Strong localization regimes and dimensionality effects," *Phys. Rev. Lett.* **100**, 036803.

Lherbier, A., Blase, X., Niquet, Y. M., Triozon, F., & Roche, S. (2008), "Charge transport in chemically doped 2D graphene," *Phys. Rev. Lett.* **101**(3), 036808.

Lherbier, A., Botello-Méndez, A. R., & Charlier, J.-C. (2016), "Electronic and optical properties of pristine and oxidized borophene," *2D Mater.* **3**(4), 045006.

Lherbier, A., Dubois, S. M.-M., Declerck, X., et al. (2012), "Transport properties of graphene containing structural defects," *Phys. Rev. B* **86**(7), 075402.

Lherbier, A., Dubois, S. M. M., Declerck, X., et al. (2011), "Two-dimensional graphene with structural defects: Elastic mean free path, minimum conductivity, and Anderson transition," *Phys. Rev. Lett.* **106**(4), 046803.

Lherbier, A., Roche, S., Restrepo, O. A., et al. (2013), "Highly defective graphene: A key prototype of two-dimensional Anderson insulators," *Nano Res.* **6**, 326.

Li, D., Muller, M. B., Gilje, S., Kaner, R. B., & Wallace, G. G. (2008), "Processable aqueous dispersions of graphene nanosheets," *Nat. Nanotechnol.* **3**(2), 101–105.

Li, G., Luican, A., & Andrei, E. Y. (2009), "Scanning tunneling spectroscopy of graphene on graphite," *Phys. Rev. Lett.* **102**(17), 176804.

Li, G., Luican, A., Lopes dos Santos, J. M. B., et al. (2010), "Observation of Van Hove singularities in twisted graphene layers," *Nat. Phys.* **6**(2), 109–113.

Li, L., Yu, Y., Ye, G. J., et al. (2014), "Black phosphorus field-effect transistors," *Nat. Nanotechnol.* **9**(5), 372–377.

Li, W., Sevincli, H., Roche, S., & Cuniberti, G. (2011), "Efficient linear scaling method for computing the thermal conductivity of disordered materials," *Phys. Rev. B* **83**, 155416.

Li, W., Sevinçli, H., Cuniberti, G., & Roche, S. (2010), "Phonon transport in large scale carbon-based disordered materials: Implementation of an efficient order-*n* and real-space Kubo methodology," *Phys. Rev. B* **82**, 041410.

Li, X., Wang, X., Zhang, L., Lee, S., & Dai, H. (2008), "Chemically derived, ultrasmooth graphene nanoribbon semiconductors," *Science* **319**(5867), 1229–1232.

Liang, W., Bockrath, M., Bozovic, D., et al. (2001), "Fabry-Perot interference in a nanotube electron waveguide," *Nature* **411**(6838), 665–669.

Libisch, F., Stampfer, C., & Burgdörfer, J. (2009), "Graphene quantum dots: Beyond a dirac billiard," *Phys. Rev. B* **79**(11), 115423.

Lieb, E. H. (1989), "Two theorems on the hubbard model," *Phys. Rev. Lett.* **62**, 1201–1204.

Lin, Y.-C., Ghosh, R. K., Addou, R., et al. (2015), "Atomically thin resonant tunnel diodes built from synthetic van der Waals heterostructures," *Nat. Commun.* **6**, 7311.

Lindner, N. H., Refael, G., & Galitski, V. (2011), "Floquet topological insulator in semiconductor quantum wells," *Nat. Phys.* **7**(6), 490–495.

Lipson, H. & Stokes, A. R. (1942), "The structure of graphite," *Proc. R. Soc. Lond. Ser. A: Math. Phys. Sci.* **181**(984), 101–105.

Liu, H., Neal, A. T., Zhu, Z., et al. (2014), "Phosphorene: An unexplored 2D semiconductor with a high hole mobility," *ACS Nano* **8**(4), 4033–4041.

Liu, J., Dai, H., Hafner, J. H., et al. (1997), "Fullerene 'crop circles'," *Nature* **385**(6619), 780–781.

Liu, K., Avouris, P., Martel, R., & Hsu, W. K. (2001), "Electrical transport in doped multiwalled carbon nanotubes," *Phys. Rev. B* **63**(16), 161404.

Liu, X., Oostinga, J. B., Morpurgo, A. F., & Vandersypen, L. M. K. (2009), "Electrostatic confinement of electrons in graphene nanoribbons," *Phys. Rev. B* **80**(12), 121407.

Liu, Y., Bian, G., Miller, T., & Chiang, T.-C. (2011), "Visualizing electronic chirality and berry phases in graphene systems using photoemission with circularly polarized light," *Phys. Rev. Lett.* **107**(16), 166803.

Liu, Z., Suenaga, K., Harris, P. J. F., & Iijima, S. (2009), "Open and closed edges of graphene layers," *Phys. Rev. Lett.* **102**, 015501.

Locatelli, N., Cros, V., & Grollier, J. (2014), "Spin-torque building blocks," *Nat. Mater.* **13**, 11–20.

Lohrmann, D. (1989), "Shallow and deep impurity levels in multivalley semiconductors: A green-function study of a cubic model by the recursion method," *Phys. Rev. B* **40**, 8404.

Lopez-Bezanilla, A. (2009), Étude à partir des premiers principes de l'effet de la fonctionnalisat-iron sur le transport de charge dans les systèmes à base de carbone à l'échelle mésoscopique, PhD thesis, Université Joseph Fourier.

López-Bezanilla, A., Blase, X., & Roche, S. (2010), "Quantum transport properties of chemically functionalized long semiconducting carbon nanotubes," *Nano Res.* **3**, 288–295.

Lopez-Bezanilla, A., Froufe-Pérez, L. S., Roche, S., & Sáenz, J. J. (2018), "Unequivocal signatures of the crossover to Anderson localization in realistic models of disordered quasi-one-dimensional materials," *Phys. Rev. B* **98**, 235423.

López-Bezanilla, A., Triozon, F., & Roche, S. (2009), "Chemical functionalization effects on armchair graphene nanoribbons transport," *Nano Lett.* **9**, 2527.

López-Bezanilla, A., Triozon, F., Latil, S., Blase, X., & Roche, S. (2009), "Effect of the chemical functionalization on charge transport in carbon nanotubes at the mesoscopic scale," *Nano Lett.* **9**(3), 940–944.

Lopez-Sanchez, O., Lembke, D., Kayci, M., Radenovic, A., & Kis, A. (2013), "Ultrasensitive photodetectors based on monolayer MoS_2," *Nat. Nanotechnol.* **8**(7), 497–501.

Lopez Sancho, M. P., Sancho, J. M. L., Sancho, J. M. L., & Rubio, J. (1985), "Highly convergent schemes for the calculation of bulk and surface green functions," *J. Phys. F: Metal Phys.* **15**(4), 851.

Low, T., Jiang, Y., Katsnelson, M., & Guinea, F. (2012), "Electron pumping in graphene mechanical resonators," *Nano Lett.* **12**(2), 850–854.

Lukatskaya, M. R., Mashtalir, O., Ren, C. E., et al. (2013), "Cation intercalation and high volumetric capacitance of two-dimensional titanium carbide," *Science* **341**(6153), 1502–1505.

Luryi, S. (1989), "Coherent versus incoherent resonant tunneling and implications for fast devices," *Superlattice. Microstruct.* **5**(3), 375–382.

Luttinger, J. M. (1951), "The effect of a magnetic field on electrons in a periodic potential," *Phys. Rev.* **84**(4), 814–817.

Luttinger, J. M. (1963), "An exactly soluble model of a many-fermion system," *J. Math. Phys.* **4**(9), 1154–1162.

Ma, R., Huan, Q., Wu, L., et al. (2017), "Direct four-probe measurement of grain-boundary resistivity and mobility in millimeter-sized graphene," *Nano Lett.* **17**(9), 5291–5296.

Maassen, J., Zahid, F., & Guo, H. (2009), "Effects of dephasing in molecular transport junctions using atomistic first principles," *Phys. Rev. B* **80**, 125423.

Maassen, T., van den Berg, J. J., Huisman, E. H., et al. (2013), "Localized states influence spin transport in epitaxial graphene," *Phys. Rev. Lett.* **110**, 067209.

Maassen, T., van den Berg, J. J., Ijbema, N., et al. (2012), "Long spin relaxation times in wafer scale epitaxial graphene on SiC(0001)," *Nano Lett.* **12**(3), 1498–1502.

MacKinnon, A. & Kramer, B. (1981), "One-parameter scaling of localization length and conductance in disordered systems," *Phys. Rev. Lett.* **47**, 1546–1549.

Mak, K. F., Lee, C., Hone, J., Shan, J., & Heinz, T. F. (2010), "Atomically thin MoS_2: A new direct-gap semiconductor," *Phys. Rev. Lett.* **105**(13), 136805.

Mak, K. F., Lui, C. H., Shan, J., & Heinz, T. F. (2009), "Observation of an electric-field-induced band gap in bilayer graphene by infrared spectroscopy," *Phys. Rev. Lett.* **102**, 256405.

Mannix, A. J., Zhang, Z., Guisinger, N. P., Yakobson, B. I., & Hersam, M. C. (2018), "Borophene as a prototype for synthetic 2D materials development," *Nat. Nanotechnol.* **13**(6), 444.

Mannix, A. J., Zhou, X.-F., Kiraly, B., et al. (2015), "Synthesis of borophenes: Anisotropic, two-dimensional boron polymorphs," *Science* **350**(6267), 1513–1516.

Marconcini, P. & Macucci, M. (2011), "The k·p method and its application to graphene, carbon nanotubes and graphene nanoribbons: The dirac equation," *La Rivista del Nuovo Cimento* **34**, 489–584.

Margine, E. R., Bocquet, M.-L., & Blase, X. (2008), "Thermal stability of graphene and nanotube covalent functionalization," *Nano Lett.* **8**(10), 3315–3319.

Marmolejo-Tejada, J. M., García, J. H., Petrović, M. D., et al. (2018), "Deciphering the origin of nonlocal resistance in multiterminal graphene on hexagonal-boron-nitride with ab initio quantum transport: Fermi surface edge currents rather than Fermi sea topological valley currents," *J. Phys.: Mater.* **1**(1), 015006.

Martel, R., Derycke, V., Lavoie, C., et al. (2001), "Ambipolar electrical transport in semiconducting single-wall carbon nanotubes," *Phys. Rev. Lett.* **87**, 256805.

Martinez, D. F. (2003), "Floquet-green function formalism for harmonically driven Hamiltonians," *J. Phys. A: Math. Gen.* **36**(38), 9827.

Marx, D. & Hutter, J. (2000), "Ab initio molecular dynamics: Theory and Implementation," *Modern Methods and Algorithms of Quantum Chemistry, Proceedings*, 2nd edn, NIC Series, Vol. 3, John von Neumann Institute for Computing, Jülich, pp. 329–477.

Marzari, N. & Vanderbilt, D. (1997), "Maximally localized generalized wannier functions for composite energy bands," *Phys. Rev. B* **56**(20), 12847–12865.

Matsumura, H. & Ando, T. (2001), "Conductance of carbon nanotubes with a stone-wales defect," *J. Phys. Soc. Jpn.* **70**(9), 2657–2665.

Mayorov, A. S., Gorbachev, R. V., Morozov, S. V., et al. (2011), "Micrometer-scale ballistic transport in encapsulated graphene at room temperature," *Nano Lett.* **11**(6), 2396–2399.

McCann, E., Abergel, D. S., & Fal'ko, V. I. (2007), "The low energy electronic band structure of bilayer graphene," *Eur. Phys. J. Spec. Top.* **148**(1), 91–103.

McCann, E. & Falko, V. I. (2006), "Landau-level degeneracy and quantum Hall effect in a graphite bilayer," *Phys. Rev. Lett.* **96**(8), 086805.

McCann, E. & Fal'ko, V. I. (2012), "$z \rightarrow -z$ Symmetry of spin-orbit coupling and weak localization in graphene," *Phys. Rev. Lett.* **108**, 166606.

McCann, E., Kechedzhi, K., Fal'ko, V. I., et al. (2006), "Weak-localization magnetoresistance and valley symmetry in graphene," *Phys. Rev. Lett.* **97**, 146805.

McClure, J. (1969), "Electron energy band structure and electronic properties of rhombohedral graphite," *Carbon* **7**(4), 425–432.

McClure, J. W. (1956), "Diamagnetism of graphite," *Phys. Rev.* **104**(3), 666–671.

McClure, J. W. (1957), "Band structure of graphite and de Haas-van Alphen effect," *Phys. Rev.* **108**, 612–618.

McCreary, K. M., Swartz, A. G., Han, W., Fabian, J., & Kawakami, R. K. (2012), "Magnetic moment formation in graphene detected by scattering of pure spin currents," *Phys. Rev. Lett.* **109**(18), 186604.

McIver, J. W., Schulte, B., Stein, F.-U., et al. (2018), "Light-induced anomalous Hall effect in graphene," *arXiv:1811.03522 [cond-mat]*. arXiv: 1811.03522.

Meir, Y. & Wingreen, N. S. (1992), "Landauer formula for the current through an interacting electron region," *Phys. Rev. Lett.* **68**(16), 2512–2515.

Mello, P. A., Pereyra, P., & Kumar, N. (1988), "Macroscopic approach to multichannel disordered conductors," *Ann. Phys. (N.Y.)* **181**, 290–317.

Mermin, N. D. & Wagner, H. (1966), "Absence of ferromagnetism or antiferromagnetism in one- or two-dimensional isotropic heisenberg models," *Phys. Rev. Lett.* **17**, 1133–1136.

Messiah, A. (1999), *Quantum Mechanics* (2 Volumes in 1), Dover Publications, Mineola.

Meyer, J. C., Girit, C. O., Crommie, M. F., & Zettl, A. (2008), "Imaging and dynamics of light atoms and molecules on graphene," *Nature* **454**(7202), 319–322.

Meyer, J. C., Kisielowski, C., Erni, R., et al. (2008), "Direct imaging of lattice atoms and topological defects in graphene membranes," *Nano Lett.* **8**(11), 3582–3586.

Miao, F., Wijeratne, S., Zhang, Y., et al. (2007), "Phase-coherent transport in graphene quantum billiards," *Science* **317**(5844), 1530–1533.

Min, H., Hill, J. E., Sinitsyn, N. A., et al. (2006), "Intrinsic and Rashba spin-orbit interactions in graphene sheets," *Phys. Rev. B* **74**, 165310.

Mingo, N. & Han, J. (2001), "Conductance of metallic carbon nanotubes dipped into metal," *Phys. Rev. B* **64**, 201401.

Mingo, N., Yang, L., Han, J., & Anantram, M. (2001), "Resonant versus anti-resonant tunneling at carbon nanotube ABA heterostructures," *Phys. Status Solidi (b)* **226**(1), 79–85.

Mintmire, J. W., Dunlap, B. I., & White, C. T. (1992), "Are fullerene tubules metallic?," *Phys. Rev. Lett.* **68**, 631–634.

Mintmire, J. W. & White, C. T. (1998), "Universal density of states for carbon nanotubes," *Phys. Rev. Lett.* **81**, 2506–2509.

Miroshnichenko, A. E., Flach, S., & Kivshar, Y. S. (2010), "Fano resonances in nanoscale structures," *Rev. Mod. Phys.* **82**(3), 2257–2298.

Mishchenko, A., Tu, J. S., Cao, Y., et al. (2014), "Twist-controlled resonant tunnelling in graphene/boron nitride/graphene heterostructures," *Nat. Nanotechnol.* **9**(10), 808–813.

Miyake, T. & Saito, S. (2003), "Quasiparticle band structure of carbon nanotubes," *Phys. Rev. B* **68**, 155424.

Miyamoto, Y., Nakada, K., & Fujita, M. (1999), "First-principles study of edge states of h-terminated graphitic ribbons," *Phys. Rev. B* **59**, 9858–9861.

Miyamoto, Y., Saito, S., & Tománek, D. (2001), "Electronic interwall interactions and charge redistribution in multiwall nanotubes," *Phys. Rev. B* **65**, 041402.

Molle, A., Goldberger, J., Houssa, M., et al. (2017), "Buckled two-dimensional Xene sheets," *Nat. Mater.* **16**(2), 163–169.

Monkhorst, H. J. & Pack, J. D. (1976), "Special points for Brillouin-zone integrations," *Phys. Rev. B* **13**, 5188–5192.

Monteverde, M., Ojeda-Aristizabal, C., Weil, R., et al. (2010), "Transport and elastic scattering times as probes of the nature of impurity scattering in single-layer and bilayer graphene," *Phys. Rev. Lett.* **104**, 126801.

Moon, P., Koshino, M., & Son, Y.-W. (2019), "Quasicrystalline electronic states in 30° rotated twisted bilayer graphene," *Phys. Rev. B* **99**, 165430.

Moore, A. (1974), "Highly oriented pyrolytic graphite," P. L. Walker and P. A. Thrower, eds, *Chemistry and Physics of Carbon*, Vol. 11, Marcel Dekker Inc., New York.

Morita, A. (1986), "Semiconducting black phosphorus," *Appl. Phys. A* **39**(4), 227–242.

Moser, J., Tao, H., Roche, S., et al. (2010), "Magnetotransport in disordered graphene exposed to ozone: From weak to strong localization," *Phys. Rev. B* **81**, 205445.

Moskalets, M. & Büttiker, M. (2002), "Floquet scattering theory of quantum pumps," *Phys. Rev. B* **66**(20), 205320.

Mott, N. F. (1990), *Metal-insulator Transitions*, 2nd edn, Taylor & Francis, London.

Mounet, N., Gibertini, M., Schwaller, P., et al. (2018), "Two-dimensional materials from high-throughput computational exfoliation of experimentally known compounds," *Nat. Nanotechnol.* **13**(3), 246.

Mucciolo, E. R., Castro Neto, A. H., & Lewenkopf, C. H. (2009), "Conductance quantization and transport gaps in disordered graphene nanoribbons," *Phys. Rev. B* **79**, 075407.

Munoz, E. (2012), "Phonon-limited transport coefficients in extrinsic graphene," *J. Phys.: Condens. Matter* **24**, 195302.

Muscat, J., Wander, A., & Harrison, N. (2001), "On the prediction of band gaps from hybrid functional theory," *Chem. Phys. Lett.* **342**(34), 397–401.

Naguib, M., Mochalin, V. N., Barsoum, M. W., & Gogotsi, Y. (2014), "25th anniversary article: MXenes: A new family of two-dimensional materials," *Adv. Mater.* **26**(7), 992–1005.

Nakada, K., Fujita, M., Dresselhaus, G., & Dresselhaus, M. S. (1996), "Edge state in graphene ribbons: Nanometer size effect and edge shape dependence," *Phys. Rev. B* **54**, 17954–17961.

Nam, Y., Sun, J., Lindvall, N., et al. (2013), "Quantum Hall effect in graphene decorated with disordered multilayer patches," *Appl. Phys. Lett.* **103**(23), 233110.

Naumis, G. G., Barraza-Lopez, S., Oliva-Leyva, M., & Terrones, H. (2017), "Electronic and optical properties of strained graphene and other strained 2D materials: A review," *Rep. Progr. Phys.* **80**(9), 096501.

Nemec, N., Tománek, D., & Cuniberti, G. (2006), "Contact dependence of carrier injection in carbon nanotubes: An *ab initio* study," *Phys. Rev. Lett.* **96**, 076802.

Nogueira, F., Castro, A., & Marques, M. A. L. (2003), "A tutorial on density functional theory," *A Primer in Density-Functional Theory*, Lecture Notes in Physics, Vol. 620, Springer, Berlin, pp. 218–256.

Nomura, K. & MacDonald, A. H. (2006), "Quantum Hall ferromagnetism in graphene," *Phys. Rev. Lett.* **96**, 256602.

Nomura, K. & MacDonald, A. H. (2007), "Quantum transport of massless dirac fermions," *Phys. Rev. Lett.* **98**, 076602.

Novoselov, K. S., Geim, A. K., Morozov, S. V., et al. (2005), "Two-dimensional gas of massless dirac fermions in graphene," *Nature* **438**(7065), 197–200.

Novoselov, K. S., Geim, A. K., Morozov, S. V., et al. (2004), "Electric field effect in atomically thin carbon films," *Science* **306**(5696), 666–669.

Novoselov, K. S., Jiang, D., Schedin, F., et al. (2005), "Two-dimensional atomic crystals," *Proc. Natl. Acad. Sci. U.S.A.* **102**(30), 10451–10453.

Novoselov, K. S., Jiang, Z., Zhang, Y., et al. (2007), "Room-temperature quantum Hall effect in graphene," *Science* **315**(5817), 1379.

Novoselov, K. S., Mishchenko, A., Carvalho, A., & Neto, A. H. C. (2016), "2D materials and van der Waals heterostructures," *Science* **353**(6298), aac9439.

Nozaki, D., Girard, Y., & Yoshizawa, K. (2008), "Theoretical study of long-range electron transport in molecular junctions," *J. Phy. Chem. C* **112**(44), 17408–17415.

Oberlin, A., Endo, M., & Koyama, T. (1976), "Filamentous growth of carbon through benzene decomposition," *J. Cryst. Growth* **32**(3), 335–349.

Ochoa, H., Castro Neto, A. H., & Guinea, F. (2012), "Elliot-Yafet mechanism in graphene," *Phys. Rev. Lett.* **108**(20), 206808.

O'Connell, M. J., Bachilo, S. M., Huffman, C. B., et al. (2002), "Band gap fluorescence from individual single-walled carbon nanotubes," *Science* **297**(5581), 593–596.

Odom, T. W., Huang, J.-L., Kim, P., & Lieber, C. M. (1998), "Atomic structure and electronic properties of single-walled carbon nanotubes," *Nature* **391**(6662), 62–64.

Odom, T. W., Huang, J.-L., & Lieber, C. M. (2002), "STM studies of single-walled carbon nanotubes," *J. Phys.: Condens. Matter* **14**(6), R145.

Oezyilmaz, B., Jarillo-Herrero, P., Efetov, D., et al. (2007), "Electronic transport and quantum Hall effect in bipolar graphene *p-n-p* junctions," *Phys. Rev. Lett.* **99**, 166804.

Offidani, M. & Ferreira, A. (2018), "Microscopic theory of spin relaxation anisotropy in graphene with proximity-induced spin-orbit coupling," *Phys. Rev. B* **98**(24), 245408.

Oganov, A. R., Chen, J., Gatti, C., et al. (2009), "Ionic high-pressure form of elemental boron," *Nature* **457**(7231), 863–867.

Oka, T. & Aoki, H. (2009), "Photovoltaic Hall effect in graphene," *Phys. Rev. B* **79**(8), 081406.

Okada, S. & Oshiyama, A. (2001), "Magnetic ordering in hexagonally bonded sheets with first-row elements," *Phys. Rev. Lett.* **87**, 146803.

Oksanen, M., Uppstu, A., Laitinen, A., Cox, D. J., et al. (2014), "Single-mode and multimode Fabry-Pérot interference in suspended graphene," *Phys. Rev. B* **89**, 121414(R).

Omar, S. & van Wees, B. J. (2017), "Graphene-WS_2 heterostructures for tunable spin injection and spin transport," *Phys. Rev. B* **95**, 081404.

Onida, G., Reining, L., & Rubio, A. (2002), "Electronic excitations: Density-functional versus many-body Green's-function approaches," *Rev. Mod. Phys.* **74**, 601–659.

Orellana, P. A. & Pacheco, M. (2007), "Photon-assisted transport in a carbon nanotube calculated using Green's function techniques," *Phys. Rev. B* **75**, 115427.

Ortmann, F., Cresti, A., Montambaux, G., & Roche, S. (2011), "Magnetoresistance in disordered graphene: The role of pseudospin and dimensionality effects unraveled," *EPL (Europhysics Letters)* **94**(4), 47006.

Ortmann, F. & Roche, S. (2011), "Polaron transport in organic crystals: Temperature tuning of disorder effects," *Phys. Rev. B* **84**(18), 180302.

Ortmann, F. & Roche, S. (2013), "Splitting of the zero-energy Landau level and universal dissipative conductivity at critical points in disordered graphene," *Phys. Rev. Lett.* **110**(8), 086602.

Ostrovsky, P. M., Gornyi, I. V., & Mirlin, A. D. (2006), "Electron transport in disordered graphene," *Phys. Rev. B* **74**, 235443.

Ostrovsky, P. M., Gornyi, I. V., & Mirlin, A. D. (2008), "Theory of anomalous quantum Hall effects in graphene," *Phys. Rev. B* **77**(19), 195430.

Ostrovsky, P. M., Titov, M., Bera, S., Gornyi, I. V., & Mirlin, A. D. (2010), "Diffusion and criticality in undoped graphene with resonant scatterers," *Phys. Rev. Lett.* **105**, 266803.

Ouyang, M., Huang, J.-L., Cheung, C. L., & Lieber, C. M. (2001a), "Atomically resolved single-walled carbon nanotube intramolecular junctions," *Science* **291**(5501), 97–100.

Ouyang, M., Huang, J.-L., Cheung, C. L., & Lieber, C. M. (2001b), "Energy gaps in 'metallic' single-walled carbon nanotubes," *Science* **292**(5517), 702–705.

Ouyang, Y., Dai, H., & Guo, J. (2010), "Projected performance advantage of multilayer graphene nanoribbons as a transistor channel material," *Nano Res.* **3**(1), 8–15.

Paier, J., Marsman, M., Hummer, K., et al. (2006), "Screened hybrid density functionals applied to solids," *J. Chem. Phy.* **124**(15), 154709.

Palacios, J. J., Pérez-Jiménez, A. J., Louis, E., SanFabián, E., & Vergés, J. A. (2003), "First-principles phase-coherent transport in metallic nanotubes with realistic contacts," *Phys. Rev. Lett.* **90**(10), 106801.

Park, H., Zhao, J., & Lu, J. P. (2006), "Effects of sidewall functionalization on conducting properties of single wall carbon nanotubes," *Nano Lett.* **6**(5), 916–919.

Park, J.-Y., Rosenblatt, S., Yaish, Y., et al. (2004), "Electron-phonon scattering in metallic single-walled carbon nanotubes," *Nano Lett.* **4**(3), 517–520.

Pastawski, H. M. (1991), "Classical and quantum transport from generalized Landauer-Büttiker equations," *Phys. Rev. B* **44**(12), 6329–6339.

Pastawski, H. M. & Medina, E. (2001), "Tight binding methods in quantum transport through molecules and small devices: From the coherent to the decoherent description," *Rev. Mex. Fis.* **47**(S1), 1–23.

Pastawski, H. M., Weisz, J. F., & Albornoz, S. (1983), "Matrix continued-fraction calculation of localization length," *Phys. Rev. B* **28**(12), 6896–6903.

Patel, S. R., Stewart, D. R., Marcus, C. M., et al. (1998), "Non-Gaussian distribution of Coulomb blockade peak heights in quantum dots," *Phys. Rev. Lett.* **81**, 5900.

Payne, M. C., Teter, M. P., Allan, D. C., Arias, T. A., & Joannopoulos, J. D. (1992), "Iterative minimization techniques for ab initio total-energy calculations: Molecular dynamics and conjugate gradients," *Rev. Mod. Phys.* **64**(4), 1045–1097.

Peierls, R. (1933), "On the theory of the diamagnetism of conduction electrons," *Z. Phys.* **80**, 763.

Peltonen, T. J., Ojajärvi, R., & Heikkilä, T. T. (2018), "Mean-field theory for superconductivity in twisted bilayer graphene," *Phys. Rev. B* **98**(22), 220504.

Penev, E. S., Bhowmick, S., Sadrzadeh, A., & Yakobson, B. I. (2012), "Polymorphism of two-dimensional boron," *Nano Lett.* **12**(5), 2441–2445.

Peng, S. & Cho, K. (2003), "Ab initio study of doped carbon nanotube sensors," *Nano Lett.* **3**(4), 513–517.

Perdew, J. P. (1991), *Electronic Structure of Solids '91*, Akademie Verlag, Berlin, p. 11.

Perdew, J. P., Burke, K., & Ernzerhof, M. (1996), "Generalized gradient approximation made simple," *Phys. Rev. Lett.* **77**, 3865–3868.

Perdew, J. P. & Zunger, A. (1981), "Self-interaction correction to density-functional approximations for many-electron systems," *Phys. Rev. B* **23**, 5048–5079.

Pereira, V. M., dos Santos, L., & Neto, A. H. C. (2008), "Modeling disorder in graphene," *Phys. Rev. B* **77**(11), 115109.

Perez-Piskunow, P. M., Foa Torres, L. E. F., & Usaj, G. (2015), "Hierarchy of Floquet gaps and edge states for driven honeycomb lattices," *Phys. Rev. A* **91**(4), 043625.

Perez-Piskunow, P. M., Usaj, G., Balseiro, C. A., & Foa Torres, L. E. F. (2014), "Floquet chiral edge states in graphene," *Phys. Rev. B* **89**(12), 121401(R).

Perfetto, E., Stefanucci, G., & Cini, M. (2010), "Time-dependent transport in graphene nanoribbons," *Phys. Rev. B* **82**(3), 035446.

Persson, M. P., Lherbier, A., Niquet, Y.-M., Triozon, F., & Roche, S. (2008), "Orientational dependence of charge transport in disordered silicon nanowires," *Nano Lett.* **8**(12), 4146–4150.

Phillips, J. C. (1958), "Energy-band interpolation scheme based on a pseudopotential," *Phys. Rev.* **112**, 685–695.

Pi, K., Han, W., McCreary, K. M., et al. (2010), "Manipulation of spin transport in graphene by surface chemical doping," *Phys. Rev. Lett.* **104**, 187201.

Piquemal-Banci, M., Galceran, R., Caneva, S., et al. (2016), "Magnetic tunnel junctions with monolayer hexagonal boron nitride tunnel barriers," *Appl. Phys. Lett.* **108**(10), 102404.

Piquemal-Banci, M., Galceran, R., Godel, F., et al. (2018), "Insulator-to-metallic spin-filtering in 2D-magnetic tunnel junctions based on hexagonal boron nitride," *ACS Nano* **12**(5), 4712–4718.

Pisana, S., Lazzeri, M., Casiraghi, C., et al. (2007), "Breakdown of the adiabatic Born-Oppenheimer approximation in graphene," *Nat. Mater.* **6**(3), 198–201.

Platero, G. & Aguado, R. (2004), "Photon-assisted transport in semiconductor nanostructures," *Phys. Rep.* **395**(12), 1–157.

Po, H. C., Zou, L., Vishwanath, A., & Senthil, T. (2018), "Origin of Mott insulating behavior and superconductivity in twisted bilayer graphene," *Phys. Rev. X* **8**(3), 031089.

Poncharal, P., Berger, C., Yi, Y., Wang, Z. L., & de Heer, W. A. (2002), "Room temperature ballistic conduction in carbon nanotubes," *J. Phys. Chem. B* **106**(47), 12104–12118.

Ponomarenko, L. A., Geim, A. K., Zhukov, A. A., et al. (2011), "Tunable metal-insulator transition in double-layer graphene heterostructures," *Nat. Phys.* **7**(12), 958–961.

Ponomarenko, L. A., Gorbachev, R. V., Yu, G. L., et al. (2013), "Cloning of Dirac fermions in graphene superlattices," *Nature* **497**(7451), 594–597.

Ponomarenko, L. A., Schedin, F., Katsnelson, M. I., et al. (2008), "Chaotic Dirac billiard in graphene quantum dots," *Science* **320**(5874), 356–358.

Poumirol, J.-M., Cresti, A., Roche, S., et al. (2010), "Edge magnetotransport fingerprints in disordered graphene nanoribbons," *Phys. Rev. B* **82**(4), 041413.

Prada, E., San-Jose, P., & Schomerus, H. (2009), "Quantum pumping in graphene," *Phys. Rev. B* **80**, 245414.

Pumera, M. & Sofer, Z. (2017), "2D monoelemental arsenene, antimonene, and bismuthene: Beyond black phosphorus," *Adv. Mater.* **29**(21), 1605299.

Purewal, M. S., Hong, B. H., Ravi, A., et al. (2007), "Scaling of resistance and electron mean free path of single-walled carbon nanotubes," *Phys. Rev. Lett.* **98**, 186808.

Qiao, Z., Jiang, H., Li, X., Yao, Y., & Niu, Q. (2012), "Microscopic theory of quantum anomalous Hall effect in graphene," *Phys. Rev. B* **85**, 115439.

Qiu, D. Y., da Jornada, F. H., & Louie, S. G. (2017), "Environmental screening effects in 2D materials: Renormalization of the bandgap, electronic structure, and optical spectra of few-layer black phosphorus," *Nano Lett.* **17**(8), 4706–4712.

Querlioz, D., Apertet, Y., Valentin, A., et al. (2008), "Suppression of the orientation effects on bandgap in graphene nanoribbons in the presence of edge disorder," *Appl. Phys. Lett.* **92**(4), 042108.

Radchenko, T. M., Shylau, A. A., & Zozoulenko, I. V. (2012), "Influence of correlated impurities on conductivity of graphene sheets: Time-dependent real-space Kubo approach," *Phys. Rev. B* **86**, 035418.

Radisavljevic, B., Radenovic, A., Brivio, J., Giacometti, V., & Kis, A. (2011), "Single-layer MoS_2 transistors," *Nat. Nanotechnol.* **6**(3), 147–150.

Raes, B., Cummings, A. W., Bonell, F., et al. (2017), "Spin precession in anisotropic media," *Phys. Rev. B* **95**, 085403.

Ralph, D. C. & Stiles, M. D. (2008), "Spin transfer torques," *J. Magn. Magn. Mater.* **320**(7), 1190–1216.

Raquet, B., Avriller, R., Lassagne, B., et al. (2008), "Onset of Landau-level formation in carbon-nanotube-based electronic Fabry-Perot resonators," *Phys. Rev. Lett.* **101**(4), 046803.

Rashba, E. I. (2009), "Graphene with structure-induced spin-orbit coupling: Spin-polarized states, spin zero modes, and quantum Hall effect," *Phys. Rev. B* **79**, 161409(R).

Ravagnan, L., Piseri, P., Bruzzi, M., et al. (2007), "Influence of cumulenic chains on the vibrational and electronic properties of sp-sp^2 amorphous carbon," *Phys. Rev. Lett.* **98**(21), 216103.

Ravagnan, L., Siviero, F., Lenardi, C., et al. (2002), "Cluster-beam deposition and in situ characterization of carbyne-rich carbon films," *Phys. Rev. Lett.* **89**(28), 285506.

Rechtsman, M. C., Zeuner, J. M., Plotnik, Y., et al. (2013), "Photonic Floquet topological insulators," *Nature* **496**(7444), 196–200.

Reich, S., Maultzsch, J., Thomsen, C., & Ordejón, P. (2002), "Tight-binding description of graphene," *Phys. Rev. B* **66**, 035412.

Reis, F., Li, G., Dudy, L., et al. (2017), "Bismuthene on a SiC substrate: A candidate for a high-temperature quantum spin Hall material," *Science* **357**(6348), 287–290.

Resta, R. (2000), "Manifestations of berry phase in molecules and condensed matter," *J. Phys.: Condens. Matter* **12**(9), R107–R143.

Ribeiro-Palau, R., Lafont, F., Brun-Picard, J., et al. (2015), "Quantum Hall resistance standard in graphene devices under relaxed experimental conditions," *Nat. Nanotechnol.* **10**(11), 965–971.

Ribeiro-Palau, R., Zhang, C., Watanabe, K., et al. (2018), "Twistable electronics with dynamically rotatable heterostructures," *Science* **361**(6403), 690–693.

Ribeiro, R., Poumirol, J.-M., Cresti, A., et al. (2011), "Unveiling the magnetic structure of graphene nanoribbons," *Phys. Rev. Lett.* **107**(8), 086601.

Ribeiro-Soares, J., Almeida, R. M., Barros, E. B., et al. (2014), "Group theory analysis of phonons in two-dimensional transition metal dichalcogenides," *Phys. Rev. B* **90**(11), 115438.

Rickhaus, P., Maurand, R., Liu, M.-H., et al. (2013), "Ballistic interferences in suspended graphene," *Nat. Commun.* **4**, 2342.

Rignanese, G.-M. (1998), First-principles molecular dynamics study of SiO_2: Surface and interface with Si, PhD thesis, Université Catholique de Louvain.

Ritter, K. A. & Lyding, J. W. (2009), "The influence of edge structure on the electronic properties of graphene quantum dots and nanoribbons," *Nat. Mater.* **8**(3), 235–242.

Rivera, P., Schaibley, J. R., Jones, A. M., et al. (2015), "Observation of long-lived interlayer excitons in monolayer $MoSe_2WSe_2$ heterostructures," *Nat. Commun.* **6**, 6242.

Rocha, A. R. (2007), Theoretical and computational aspects of electronic transport at the nanoscale, PhD thesis, University of Dublin, Trinity College.

Rocha, A. R., García-Suárez, V. M., Bailey, S., et al. (2006), "Spin and molecular electronics in atomically generated orbital landscapes," *Phys. Rev. B* **73**(8), 085414.

Rocha, A. R., Garcia-Suarez, V. M., Bailey, S. W., et al. (2005), "Towards molecular spintronics," *Nat. Mater.* **4**(4), 335–339.

Rocha, C. G., Foa Torres, L. E. F., & Cuniberti, G. (2010), "ac transport in graphene-based Fabry-Pérot devices," *Phys. Rev. B* **81**(11), 115435.

Roche, S. (1996), Contribution à l'étude théorique du transport électronique dan les quasicristaux, PhD thesis, Université Joseph-Fourier.

Roche, S. (1999), "Quantum transport by means of o(n) real-space methods," *Phys. Rev. B* **59**(3), 2284–2291.

Roche, S. (2011), "Nanoelectronics: Graphene gets a better gap," *Nat. Nanotechnol.* **6**(1), 8–9.

Roche, S., Akerman, J., Beschoten, B., et al. (2015), "Graphene spintronics: The European flagship perspective," *2D Mater.* **2**(3), 030202.

Roche, S., Akkermans, E., Chauvet, O., et al. (2006), "Transport properties," *Understanding Carbon Nanotubes, from Basics to Application*, Lecture Notes on Physics, Berlin, Heidelberg, Springer-Verlag, pp. 335–437.

Roche, S., Dresselhaus, G., Dresselhaus, M. S., & Saito, R. (2000), "Aharonov-Bohm spectral features and coherence lengths in carbon nanotubes," *Phys. Rev. B* **62**, 16092–16099.

Roche, S., Jiang, J., Triozon, F., & Saito, R. (2005), "Quantum dephasing in carbon nanotubes due to electron-phonon coupling," *Phys. Rev. Lett.* **95**(7), 076803.

Roche, S., Leconte, N., Ortmann, F., et al. (2012), "Quantum transport in disordered graphene: A theoretical perspective," *Solid State Commun.* **152**(15), 1404–1410.

Roche, S. & Mayou, D. (1997), "Conductivity of quasiperiodic systems: A numerical study," *Phys. Rev. Lett.* **79**, 2518–2521.

Roche, S. & Saito, R. (2001), "Magnetoresistance of carbon nanotubes: From molecular to mesoscopic fingerprints," *Phys. Rev. Lett.* **87**, 246803.

Roche, S., Triozon, F., Rubio, A., & Mayou, D. (2001), "Conduction mechanisms and magneto-transport in multiwalled carbon nanotubes," *Phys. Rev. B* **64**(12), 121401.

Roche, S. & Valenzuela, S. O. (2014), "Graphene spintronics: Puzzling controversies and challenges for spin manipulation," *J. Phys. D: Appl. Phys.* **47**, 094011.

Rodriguez-Vega, M., Schwiete, G., Sinova, J., & Rossi, E. (2017), "Giant Edelstein effect in topological-insulator–graphene heterostructures," *Phys. Rev. B* **96**, 235419.

Rohlfing, M., Wang, N.-P., Krüger, P., & Pollmann, J. (2003), "Image states and excitons at insulator surfaces with negative electron affinity," *Phys. Rev. Lett.* **91**, 256802.

Romo-Herrera, J. M., Terrones, M., Terrones, H., Dag, S., & Meunier, V. (2006), "Covalent 2D and 3D networks from 1D nanostructures: Designing new materials," *Nano Lett.* **7**(3), 570–576.

Romo-Herrera, J. M., Terrones, M., Terrones, H., & Meunier, V. (2008), "Guiding electrical current in nanotube circuits using structural defects: A step forward in nanoelectronics," *ACS Nano* **2**(12), 2585–2591.

Ross, J. S., Klement, P., Jones, A. M., et al. (2014), "Electrically tunable excitonic light-emitting diodes based on monolayer WSe_2 p-n junctions," *Nat. Nanotechnol.* **9**(4), 268–272.

Rudner, M. S., Lindner, N. H., Berg, E., & Levin, M. (2013), Anomalous edge states and the bulk-edge correspondence for periodically-driven two dimensional systems. *Phys. Rev. X* **3**, 031005.

Ruffieux, P., Wang, S., Yang, B., et al. (2016), "On-surface synthesis of graphene nanoribbons with zigzag edge topology," *Nature* **531**(7595), 489–492.

Rycerz, A., Tworzydlo, J., & Beenakker, C. (2007a), "Valley filter and valley valve in graphene," *Nat. Phys.* **3**, 172–175.

Rycerz, A., Tworzydo, J., & Beenakker, C. W. J. (2007b), "Anomalously large conductance fluctuations in weakly disordered graphene," *Europhys. Lett.* **79**, 57003.

Safeer, C. K., Ingla-Aynés, J., Herling, F., et al. (2019), "Room-temperature spin Hall effect in graphene/MoS_2 van der Waals heterostructures," *Nano Lett.* **19**(2), 1074–1082.

Saito, R., Dresselhaus, G., & Dresselhaus, M. (1998), *Physical Properties of Carbon Nanotubes*, Imperial College Press, London.

Saito, R., Dresselhaus, G., & Dresselhaus, M. S. (1994), "Magnetic energy bands of carbon nanotubes," *Phys. Rev. B* **50**(19), 14698–14701.

Saito, R., Dresselhaus, G., & Dresselhaus, M. S. (1996), "Tunneling conductance of connected carbon nanotubes," *Phys. Rev. B* **53**, 2044–2050.

Saito, R., Dresselhaus, G., & Dresselhaus, M. S. (2000), "Trigonal warping effect of carbon nanotubes," *Phys. Rev. B* **61**, 2981–2990.

Saito, R., Fujita, M., Dresselhaus, G., & Dresselhaus, M. S. (1992a), "Electronic structure of chiral graphene tubules," *Appl. Phys. Lett.* **60**(18), 2204–2206.

Saito, R., Fujita, M., Dresselhaus, G. & Dresselhaus, M. S. (1992b), "Electronic structure of graphene tubules based on C_{60}," *Phys. Rev. B* **46**(3), 1804–1811.

Salemi, L., Lherbier, A., & Charlier, J.-C. (2018), "Spin-dependent properties in zigzag graphene nanoribbons with phenyl-edge defects," *Phys. Rev. B* **98**(21), 214204.

Sambe, H. (1973), "Steady states and quasienergies of a quantum-mechanical system in an oscillating field," *Phys. Rev. A* **7**, 2203–2213.

San-Jose, P., Prada, E., Kohler, S., & Schomerus, H. (2011), "Single-parameter pumping in graphene," *Phys. Rev. B* **84**(15), 155408.

San-Jose, P., Prada, E., Schomerus, H., & Kohler, S. (2012), "Laser-induced quantum pumping in graphene," *Appl. Phys. Lett.* **101**, 153506.

Sanvito, S., Lambert, C. J., Jefferson, J. H., & Bratkovsky, A. M. (1999), "General Green's-function formalism for transport calculations with spd Hamiltonians and giant magnetoresistance in Co- and Ni-based magnetic multilayers," *Phys. Rev. B* **59**(18), 11936–11948.

Sasaki, K., Murakami, S., & Saito, R. (2006), "Stabilization mechanism of edge states in graphene," *Appl. Phys. Lett.* **88**(11), 113110.

Savelev, S. E. & Alexandrov, A. S. (2011), "Massless dirac fermions in a laser field as a counterpart of graphene superlattices," *Phys. Rev. B* **84**(3), 035428.

Savelev, S. E., Häusler, W., & Hänggi, P. (2012), "Current resonances in graphene with time-dependent potential barriers," *Phys. Rev. Lett.* **109**(22), 226602.

Scholz, A., López, A., & Schliemann, J. (2013), "Interplay between spin-orbit interactions and a time-dependent electromagnetic field in monolayer graphene," *Phys. Rev. B* **88**(4), 045118.

Schrödinger, E. (1926), "An undulatory theory of the mechanics of atoms and molecules," *Phys. Rev.* **28**, 1049–1070.

Schwierz, F. (2010), "Graphene transistors," *Nat. Nanotechnol.* **5**(7), 487–496.

Segall, M. D., Lindan, P. J. D., Probert, M. J., et al. (2002), "First-principles simulation: Ideas, illustrations and the CASTEP code," *J. Phys.: Condens. Matter* **14**(11), 2717.

Seifert, M., Vargas, J. E. B., Bobinger, M., et al. (2015), "Role of grain boundaries in tailoring electronic properties of polycrystalline graphene by chemical functionalization," *2D Mater.* **2**(2), 024008.

Sela, I. & Cohen, D. (2008), "Quantum stirring in low-dimensional devices," *Phys. Rev. B* **77**(24), 245440.

Semenoff, G. W. (1984), "Condensed-matter simulation of a three-dimensional anomaly," *Phys. Rev. Lett.* **53**, 2449–2452.

Seneor, P., Dlubak, B., Martin, M.-B., et al. (2012), "Spintronics with graphene," *MRS Bull.* **37**(12), 1245–1254.

Sergeeva, A. P., Popov, I. A., Piazza, Z. A., et al. (2014), "Understanding Boron through size-selected clusters: Structure, chemical bonding, and fluxionality," *Acc. Chem. Res.* **47**(4), 1349–1358.

Settnes, M., Garcia, J. H., & Roche, S. (2018), "Valley-polarized quantum transport generated by gauge fields in graphene," *2D Mater.* **4**(3), 031006.

Sevincli, H., Li, W., Mingo, N., Cuniberti, G., & Roche, S. (2011), "Effects of domains in phonon conduction through hybrid boron nitride and graphene sheets," *Phys. Rev. B* **84**, 205444.

Sheng, D. N., Sheng, L., & Weng, Z. Y. (2006), "Quantum Hall effect in graphene: Disorder effect and phase diagram," *Phys. Rev. B* **73**(23), 233406.

Shevtsov, O., Carmier, P., Petitjean, C., et al. (2012), "Graphene-based heterojunction between two topological insulators," *Phys. Rev. X* **2**(3), 031004.

Shibayama, Y., Sato, H., Enoki, T., & Endo, M. (2000), "Disordered magnetism at the metal-insulator threshold in nano-graphite-based carbon materials," *Phys. Rev. Lett.* **84**(8), 1744–1747.

Shimazaki, Y., Yamamoto, M., Borzenets, I. V., et al. (2015), "Generation and detection of pure valley current by electrically induced Berry curvature in bilayer graphene," *Nat. Phys.* **11**(12), 1032–1036.

Shimizu, T., Haruyama, J., Marcano, D., et al. (2011), "Large intrinsic energy bandgaps in annealed nanotube-derived graphene nanoribbons," *Nat. Nanotechnol.* **6**(1), 45–50.

Shirley, J. H. (1965), "Solution of the Schrödinger equation with a Hamiltonian periodic in time," *Phys. Rev.* **138**, B979–B987.

Shon, N. H. & Ando, T. (1998), "Quantum transport in two-dimensional graphite system," *J. Phys. Soc. Jpn.* **67**(7), 2421–2429.

Shytov, A. V., Rudner, M. S., & Levitov, L. S. (2008), "Klein backscattering and Fabry-Perot interference in graphene heterojunctions," *Phys. Rev. Lett.* **101**(15), 156804.

Siegel, D. A., Park, C.-H., Hwang, C., et al. (2011), "Many-body interactions in quasi-freestanding graphene," *Proc. Natl. Acad. Sci.* **108**(28), 11365–11369.

Simmons, J. M., In, I., Campbell, V. E., et al. (2007), "Optically modulated conduction in chromophore-functionalized single-wall carbon nanotubes," *Phys. Rev. Lett.* **98**(8), 086802.

Sinova, J., Valenzuela, S. O., Wunderlich, J., Back, C. H., & Jungwirth, T. (2015), "Spin Hall effects," *Rev. Mod. Phys.* **87**, 1213–1260.

Skylaris, C.-K., Haynes, P. D., Mostofi, A. A., & Payne, M. C. (2005), "Introducing ONETEP: Linear-scaling density functional simulations on parallel computers," *J. Chem. Phys.* **122**(8), 084119.

Slonczewski, J. C. & Weiss, P. R. (1958), "Band structure of graphite," *Phys. Rev.* **109**, 272–279.

Sluiter, M. H. F. & Kawazoe, Y. (2003), "Cluster expansion method for adsorption: Application to hydrogen chemisorption on graphene," *Phys. Rev. B* **68**(8), 085410.

Smith, B. W., Monthioux, M., & Luzzi, D. E. (1998), "Encapsulated C60 in carbon nanotubes," *Nature* **396**(6709), 323–324.

Sofo, J. O., Chaudhari, A. S., & Barber, G. D. (2007), "Graphane: A two-dimensional hydrocarbon," *Phys. Rev. B* **75**(15), 153401.

Soler, J. M., Artacho, E., Gale, J. D., et al. (2002), "The SIESTA method for ab initio order-n materials simulation," *J. Phys.: Condens. Matter* **14**(11), 2745.

Son, Y.-W., Cohen, M. L., & Louie, S. G. (2006a), "Energy gaps in graphene nanoribbons," *Phys. Rev. Lett.* **97**, 216803.

Son, Y.-W., Cohen, M. L., & Louie, S. G. (2006b), "Half-metallic graphene nanoribbons," *Nature* **444**(7117), 347–349.

Song, K., Soriano, D., Cummings, A. W., et al. (2018), "Spin proximity effects in graphene/topological insulator heterostructures," *Nano Lett.* **18**(3), 2033–2039.

Soriano, D., Leconte, N., Ordejón, P., et al. (2011), "Magnetoresistance and magnetic ordering fingerprints in hydrogenated graphene," *Phys. Rev. Lett.* **107**, 016602.

Soriano, D., Tuan, D. V., Dubois, S. M.-M., et al. (2015), "Spin transport in hydrogenated graphene," *2D Mater.* **2**(2), 022002.

Spataru, C. D., Ismail-Beigi, S., Benedict, L. X., & Louie, S. G. (2004), "Excitonic effects and optical spectra of single-walled carbon nanotubes," *Phys. Rev. Lett.* **92**, 077402.

Splendiani, A., Sun, L., Zhang, Y., et al. (2010), "Emerging photoluminescence in monolayer MoS2," *Nano Lett.* **10**(4), 1271–1275.

Sponza, L., Amara, H., Attaccalite, C., et al. (2018), "Direct and indirect excitons in boron nitride polymorphs: A story of atomic configuration and electronic correlation," *Phys. Rev. B* **98**(12), 125206.

Sprinkle, M., Ruan, M., Hu, Y., et al. (2010), "Scalable templated growth of graphene nanoribbons on SiC," *Nat. Nanotechnol.* **5**(10), 727–731.

Stampfer, C., Güttinger, J., Hellmüller, S., et al. (2009), "Energy gaps in etched graphene nanoribbons," *Phys. Rev. Lett.* **102**, 056403.

Stampfer, C., Guttinger, J., Molitor, F., et al. (2008), "Tunable Coulomb blockade in nanostructured graphene," *Appl. Phys. Lett.* **92**(1), 012102.

Stander, N., Huard, B., & Goldhaber-Gordon, D. (2009), "Evidence for Klein tunneling in graphene *p–n* junctions," *Phys. Rev. Lett.* **102**, 026807.

Star, A., Gabriel, J.-C. P., Bradley, K., & Grüner, G. (2003), "Electronic detection of specific protein binding using nanotube fet devices," *Nano Lett.* **3**(4), 459–463.

Stauber, T., Peres, N. M. R., & Guinea, F. (2007), "Electronic transport in graphene: A semiclassical approach including midgap states," *Phys. Rev. B* **76**, 205423.

Stefanucci, G., Kurth, S., Rubio, A., & Gross, E. K. U. (2008), "Time-dependent approach to electron pumping in open quantum systems," *Phys. Rev. B* **77**, 075339.

Stegmann, T. & Szpak, N. (2016), "Current flow paths in deformed graphene: From quantum transport to classical trajectories in curved space," *New J. Phys.* **18**(5), 053016.

Stegmann, T. & Szpak, N. (2018), "Current splitting and valley polarization in elastically deformed graphene," *2D Mater.* **6**(1), 015024.

Stern, A., Aharonov, Y., & Imry, Y. (1990), "Phase uncertainty and loss of interference: A general picture," *Phys. Rev. A* **41**(7), 3436–3448.

Stojetz, B., Miko, C., Forró, L., & Strunk, C. (2005), "Effect of band structure on quantum interference in multiwall carbon nanotubes," *Phys. Rev. Lett.* **94**(18), 186802.

Stone, A. & Wales, D. (1986), "Theoretical studies of icosahedral C60 and some related species," *Chem. Phys. Lett.* **128**(56), 501–503.

Strano, M. S., Dyke, C. A., Usrey, M. L., et al. (2003), "Electronic structure control of single-walled carbon nanotube functionalization," *Science* **301**(5639), 1519–1522.

Strunk, C., Stojetz, B., & Roche, S. (2006), "Quantum interference in multiwall carbon nanotubes," *Semicond. Sci. Technol.* **21**(11), S38.

Suárez Morell, E. & Foa Torres, L. E. F. (2012), "Radiation effects on the electronic properties of bilayer graphene," *Phys. Rev. B* **86**(12), 125449.

Suárez Morell, E., Correa, J. D., Vargas, P., Pacheco, M., & Barticevic, Z. (2010), "Flat bands in slightly twisted bilayer graphene: Tight-binding calculations," *Phys. Rev. B* **82**(12), 121407.

Suenaga, K., Wakabayashi, H., Koshino, M., et al. (2007), "Imaging active topological defects in carbon nanotubes," *Nat. Nanotechnol.* **2**(6), 358–360.

Sun, J., Lee, H.-W., Pasta, M., et al. (2015), "A phosphorenegraphene hybrid material as a high-capacity anode for sodium-ion batteries," *Nat. Nanotechnol.* **10**(11), 980–985.

Sun, X., Lin, L., Sun, L., et al. (2018), "Low-temperature and rapid growth of large single-crystalline graphene with ethane," *Small* **14**(3), 1702916.

Suzuura, H. & Ando, T. (2002), "Crossover from symplectic to orthogonal class in a two-dimensional honeycomb lattice," *Phys. Rev. Lett.* **89**, 266603.

Svensson, J. & Campbell, E. E. B. (2011), "Schottky barriers in carbon nanotube-metal contacts," *J. Appl. Phys.* **110**(11), 111101.

Switkes, M., Marcus, C. M., Campman, K., & Gossard, A. C. (1999), "An adiabatic quantum electron pump," *Science* **283**(5409), 1905–1908.

Syzranov, S. V., Fistul, M. V., & Efetov, K. B. (2008), "Effect of radiation on transport in graphene," *Phys. Rev. B* **78**(4), 045407.

Takayama, R., Hoshi, T., & Fujiwara, T. (2004), "Krylov subspace method for molecular dynamics simulation based on large-scale electronic structure theory," *J. Phys. Soc. Jpn* **73**, 1519.

Tamura, R. & Tsukada, M. (1994), "Disclinations of monolayer graphite and their electronic states," *Phys. Rev. B* **49**(11), 7697–7708.

Tan, Y.-W., Zhang, Y., Bolotin, K., et al. (2007), "Measurement of scattering rate and minimum conductivity in graphene," *Phys. Rev. Lett.* **99**, 246803.

Tang, Z. K., Zhang, L., Wang, N., et al. (2001), "Superconductivity in 4 angstrom single-walled carbon nanotubes," *Science* **292**(5526), 2462–2465.

Tao, L., Cinquanta, E., Chiappe, D., et al. (2015), "Silicene field-effect transistors operating at room temperature," *Nat. Nanotechnol* **10**(3), 227–231.

Tapaszto, L., Dobrik, G., Lambin, P., & Biro, L. P. (2008), "Tailoring the atomic structure of graphene nanoribbons by scanning tunnelling microscope lithography," *Nat. Nanotechnol.* **3**(7), 397–401.

Tarnopolsky, G., Kruchkov, A. J., & Vishwanath, A. (2019), "Origin of magic angles in twisted bilayer graphene," *Phys. Rev. Lett.* **122**(10), 106405.

Terrones, H. & Terrones, M. (2003), "Curved nanostructured materials," *New J. Phys.* **5**(1), 126.

Terrones, H., Terrones, M., Hernández, E., et al. (2000), "New metallic allotropes of planar and tubular carbon," *Phys. Rev. Lett.* **84**, 1716–1719.

Terrones, M. (2009), "Materials science: Nanotubes unzipped," *Nature* **458**(7240), 845–846.

Terrones, M., Banhart, F., Grobert, N., et al. (2002), "Molecular junctions by joining single-walled carbon nanotubes," *Phys. Rev. Lett.* **89**, 075505.

Terrones, M., Botello-Méndez, A. R., Campos-Delgado, J., et al. (2010), "Graphene and graphite nanoribbons: Morphology, properties, synthesis, defects and applications," *Nano Today* **5**(4), 351–372.

Terrones, M., Terrones, H., Banhart, F., Charlier, J.-C., & Ajayan, P. M. (2000), "Coalescence of single-walled carbon nanotubes," *Science* **288**(5469), 1226–1229.

Tersoff, J. (2003), "Nanotechnology: A barrier falls," *Nature* **424**(6949), 622–623.

Thess, A., Lee, R., Nikolaev, P., et al. (1996), "Crystalline ropes of metallic carbon nanotubes," *Science* **273**(5274), 483–487.

Thomas, L. (1927), "On the capture of electrons by swiftly moving electrified particles," *Proc. R. Soc. Lond. Ser. A* **114**, 561–576.

Thomas, L. H. (1926), "The motion of the spinning electron," *Nature* **117**, 514.

Thouless, D. (1998), *Topological Quantum Numbers in Nonrelativistic Physics*, World Scientific, Singapore.

Thouless, D. J. (1973), "Localization distance and mean free path in one-dimensional disordered systems," *J. Phys. C: Solid State Phys.* **6**(3), L49.

Thouless, D. J. (1977), "Maximum metallic resistance in thin wires," *Phys. Rev. Lett.* **39**, 1167–1169.

Thouless, D. J. (1983), "Quantization of particle transport," *Phys. Rev. B* **27**, 6083–6087.

Tielrooij, K. J., Song, J. C. W., Jensen, S. A., et al. (2013), "Photoexcitation cascade and multiple hot-carrier generation in graphene," *Nat. Phys.* **9**, 248–252.

Tien, P. K. & Gordon, J. P. (1963), "Multiphoton process observed in the interaction of microwave fields with the tunneling between superconductor films," *Phys. Rev.* **129**, 647–651.

Tikhonenko, F. V., Horsell, D. W., Gorbachev, R. V., & Savchenko, A. K. (2008), "Weak localization in graphene flakes," *Phys. Rev. Lett.* **100**, 056802.

Tikhonenko, F. V., Kozikov, A. A., Savchenko, A. K., & Gorbachev, R. V. (2009), "Transition between electron localization and antilocalization in graphene," *Phys. Rev. Lett.* **103**, 226801.

Todd, K., Chou, H.-T., Amasha, S., & Goldhaber-Gordon, D. (2009), "Quantum dot behavior in graphene nanoconstrictions," *Nano Lett.* **9**(1), 416–421.

Tombros, N., Jozsa, C., Popinciuc, M., Jonkman, H. T., & van Wees, B. J. (2007), "Electronic spin transport and spin precession in single graphene layers at room temperature," *Nature (London)* **448**, 571.

Torres, W. S., Sierra, J. F., Benitez, L. A., Bonell, F., Costache, M. V., & Valenzuela, S. O. (2017), "Spin precession and spin Hall effect in monolayer graphene/Pt nanostructures," *2D Mater.* **4**(4), 041008.

Tournus, F., Latil, S., Heggie, M. I., & Charlier, J.-C. (2005), "π-stacking interaction between carbon nanotubes and organic molecules," *Phys. Rev. B* **72**(7), 075431.

Trambly de Laissardière, G. & Mayou, D. (2013), "Conductivity of graphene with resonant and nonresonant adsorbates," *Phys. Rev. Lett.* **111**, 146601.

Trevisanutto, P. E., Giorgetti, C., Reining, L., Ladisa, M., & Olevano, V. (2008), "*Ab initio* GW many-body effects in graphene," *Phys. Rev. Lett.* **101**, 226405.

Triozon, F. (2002), Diffusion quantique et conductivité dans les systèmes apériodiques, PhD thesis, Université Joseph-Fourier.

Triozon, F., Lambin, P., & Roche, S. (2005), "Electronic transport properties of carbon nanotube based metal/semiconductor/metal intramolecular junctions," *Nanotechnology* **16**(2), 230.

Triozon, F., Roche, S., Rubio, A., & Mayou, D. (2004), "Electrical transport in carbon nanotubes: Role of disorder and helical symmetries," *Phys. Rev. B* **69**, 121410.

Triozon, F. & Roche, S. (2005), "Efficient linear scaling method for computing the Landauer-Büttiker conductance," *Eur. Phys. J. B - Condens. Matter Complex Syst.* **46**, 427–431.

Troullier, N. & Martins, J. L. (1991), "Efficient pseudopotentials for plane-wave calculations," *Phys. Rev. B* **43**, 1993–2006.

Tsen, A. W., Brown, L., Levendorf, M. P., et al. (2012), "Tailoring electrical transport across grain boundaries in polycrystalline graphene," *Science* **336**, 1143.

Tsui, D. C., Stormer, H. L., & Gossard, A. C. (1982), "Two-dimensional magnetotransport in the extreme quantum limit," *Phys. Rev. Lett.* **48**(22), 1559–1562.

Tworzydło, J., Trauzettel, B., Titov, M., Rycerz, A., & Beenakker, C. W. J. (2006), "Sub-poissonian shot noise in graphene," *Phys. Rev. Lett.* **96**, 246802.

Ugarte, D. (1992), "Curling and closure of graphitic networks under electron-beam irradiation," *Nature* **359**(6397), 707–709.

Ugeda, M. M., Brihuega, I., Guinea, F., & Rodríguez, J. M. G. (2010), "Missing atom as a source of carbon magnetism," *Phys. Rev. Lett.* **104**, 096804.

Ugeda, M. M., Brihuega, I., Hiebel, F., et al. (2012), "Electronic and structural characterization of divacancies in irradiated graphene," *Phys. Rev. B* **85**, 121402.

Usaj, G. (2009), "Edge states interferometry and spin rotations in zigzag graphene nanoribbons," *Phys. Rev. B* **80**(8), 081414.

Usaj, G., Perez-Piskunow, P. M., Foa Torres, L. E. F., & Balseiro, C. A. (2014), "Irradiated graphene as a tunable Floquet topological insulator," *Phys. Rev. B* **90**(11), 115423.

Valenzuela, S. O. (2009), "Nonlocal electronic spin detection, spin accumulation and the spin Hall effect," *Int. J. Mod. Phys. B* **23**(11), 2413–2438.

Valenzuela, S. O. & Tinkham, M. (2006), "Direct electronic measurement of the spin hall effect," *Nature* **442**, 176–179.

Van Troeye, B., Lherbier, A., Charlier, J.-C., & Gonze, X. (2018), "Large phosphorene in-plane contraction induced by interlayer interactions in graphene-phosphorene heterostructures," *Phys. Rev. Mater.* **2**(7), 074001.

Van Tuan, D. (2016), *Charge and Spin Transport in Disordered Graphene-Based Materials*, Springer International Publishing, Cham.

Van Tuan, D., Kotakoski, J., Louvet, T., et al. (2013), "Scaling properties of charge transport in polycrystalline graphene," *Nano Lett.* **13**(4), 1730–1735.

Van Tuan, D., Ortmann, F., Cummings, A. W., Soriano, D., & Roche, S. (2016), "Spin dynamics and relaxation in graphene dictated by electron-hole puddles," *Sci. Rep.* **6**, 21046.

Van Tuan, D., Ortmann, F., Soriano, D., Valenzuela, S., & Roche, S. (2014), "Pseudospin-driven spin relaxation mechanism in graphene," *Nat. Phys.* **10**, 857.

Vanderbilt, D. (1990), "Soft self-consistent pseudopotentials in a generalized eigenvalue formalism," *Phys. Rev. B* **41**, 7892–7895.

Varchon, F., Feng, R., Hass, J., et al. (2007), "Electronic structure of epitaxial graphene layers on SiC: Effect of the substrate," *Phys. Rev. Lett.* **99**, 126805.

Venema, L. C., Wildöer, J. W. G., Janssen, J. W., et al. (1999), "Imaging electron wave functions of quantized energy levels in carbon nanotubes," *Science* **283**(5398), 52–55.

Venezuela, P., Muniz, R. B., Costa, A. T., et al. (2009), "Emergence of local magnetic moments in doped graphene-related materials," *Phys. Rev. B* **80**(24), 241413.

Vila, M., Hung, N., Roche, S., & Saito, R. (2019), "Tunable circular dichroism and valley polarization in the modified haldane model," *Phys. Rev. R (Rapid Comm.)* **99**, 161404(R).

Vogt, P., De Padova, P., Quaresima, C., et al. (2012), "Silicene: Compelling experimental evidence for graphenelike two-dimensional silicon," *Phys. Rev. Lett.* **108**(15), 155501.

Völkl, T., Kochan, D., Ebnet, T., et al. (2019), "Absence of a giant spin Hall effect in plasma-hydrogenated graphene," *Phys. Rev. B* **99**, 085401.

Völkl, T., Rockinger, T., Drienovsky, M., et al. (2017), "Magnetotransport in heterostructures of transition metal dichalcogenides and graphene," *Phys. Rev. B - Condens. Matter Mater. Phys.* **96**(12), 125405.

von Klitzing, K. (2005), "Chapter 25: Years of quantum Hall effect (QHE): A personal view on the discovery, physics and applications of this quantum effect," in *The Quantum Hall Effect*, New York, Springer, pp. 1–21.

von Klitzing, K., Dorda, G., & Pepper, M. (1980), "New method for high-accuracy determination of the fine-structure constant based on quantized Hall resistance," *Phys. Rev. Lett.* **45**(6), 494–497.

Wakabayashi, K., Fujita, M., Ajiki, H., & Sigrist, M. (1999), "Electronic and magnetic properties of nanographite ribbons," *Phys. Rev. B* **59**, 8271–8282.

Wakamura, T., Reale, F., Palczynski, P., et al. (2018), "Strong anisotropic spin-orbit interaction induced in graphene by monolayer WS2," *Phys. Rev. Lett.* **120**, 106802.

Wallace, P. R. (1947), "The band theory of graphite," *Phys. Rev.* **71**, 622–634.

Wallbank, J. R., Patel, A. A., Mucha-Kruczynski, M., Geim, A. K., & Fal'ko, V. I. (2013), "Generic miniband structure of graphene on a hexagonal substrate," *Phys. Rev. B* **87**(24), 245408.

Wang, G., Chernikov, A., Glazov, M. M., et al. (2018), "Colloquium: Excitons in atomically thin transition metal dichalcogenides," *Rev. Mod. Phys.* **90**(2), 021001.

Wang, N., Tang, Z. K., Li, G. D., & Chen, J. S. (2000), "Materials science: Single-walled 4 A carbon nanotube arrays," *Nature* **408**(6808), 50–51.

Wang, Q. H., Kalantar-Zadeh, K., Kis, A., Coleman, J. N., & Strano, M. S. (2012), "Electronics and optoelectronics of two-dimensional transition metal dichalcogenides," *Nat. Nanotechnol.* **7**(11), 699–712.

Wang, S., Talirz, L., Pignedoli, C. A., et al. (2016), "Giant edge state splitting at atomically precise graphene zigzag edges," *Nat. Commun.* **7**, 11507.

Wang, X. & Dai, H. (2010), "Etching and narrowing of graphene from the edges," *Nat. Chem.* **2**(8), 661–665.

Wang, X., Ouyang, Y., Jiao, L., et al. (2011), "Graphene nanoribbons with smooth edges behave as quantum wires," *Nat. Nanotechnol.* **6**(9), 563–567.

Wang, X., Ouyang, Y., Li, X., et al. (2008), "Room-temperature all-semiconducting sub-10-nm graphene nanoribbon field-effect transistors," *Phys. Rev. Lett.* **100**, 206803.

Wang, Y., Cai, X., Reutt-Robey, J., & Fuhrer, M. S. (2015), "Neutral-current Hall effects in disordered graphene," *Phys. Rev. B* **92**, 161411.

Wang, Y. H., Steinberg, H., Jarillo-Herrero, P., & Gedik, N. (2013), "Observation of Floquet-Bloch states on the surface of a topological insulator," *Science* **342**(6157), 453–457.

Wang, Z., Ki, D.-K., Chen, H., et al. (2015), "Strong interface-induced spin-orbit interaction in graphene on WS_2," *Nat. Commun.* **6**, 8339.

Wang, Z., Ki, D.-K., Khoo, J. Y., et al. (2016), "Origin and magnitude of 'designer' spin-orbit interaction in graphene on semiconducting transition metal dichalcogenides," *Phys. Rev. X* **6**, 041020.

Wassmann, T., Seitsonen, A. P., Saitta, A. M., Lazzeri, M., & Mauri, F. (2008), "Structure, stability, edge states, and aromaticity of graphene ribbons," *Phys. Rev. Lett.* **101**, 096402.

Watanabe, K., Taniguchi, T., Niiyama, T., Miya, K., & Taniguchi, M. (2009), "Far-ultraviolet plane-emission handheld device based on hexagonal boron nitride," *Nature Photonics* **3**(10), 591–594.

Weil, T. & Vinter, B. (1987), "Equivalence between resonant tunneling and sequential tunneling in double-barrier diodes," *Appl. Phys. Lett.* **50**(18), 1281–1283.

Weisse, A., Wellein, G., Alvermann, A., & Fehske, H. (2006), "The kernel polynomial method," *Rev. of Mod. Phys.* **78**, 275.

White, C. T., Li, J., Gunlycke, D., & Mintmire, J. W. (2007), "Hidden one-electron interactions in carbon nanotubes revealed in graphene nanostrips," *Nano Lett.* **7**(3), 825–830.

White, C. T. & Mintmire, J. W. (1998), "Density of states reflects diameter in nanotubes," *Nature* **394**(6688), 29–30.

White, C. T. & Todorov, T. N. (1998), "Carbon nanotubes as long ballistic conductors," *Nature* **393**(6682), 240–242.

White, I. D., Godby, R. W., Rieger, M. M., & Needs, R. J. (1998), "Dynamic image potential at an Al(111) surface," *Phys. Rev. Lett.* **80**, 4265–4268.

Wilder, J. W. G., Venema, L. C., Rinzler, A. G., Smalley, R. E., & Dekker, C. (1998), "Electronic structure of atomically resolved carbon nanotubes," *Nature* **391**(6662), 59–62.

Wilson, J. A. & Yoffe, A. D. (1969), "The transition metal dichalcogenides discussion and interpretation of the observed optical, electrical and structural properties," *Adv. Phys.* **18**(73), 193–335.

Wimmer, M. (2009), Quantum transport in nanostructures: From computational concepts to spintronics in graphene and magnetic tunnel junctions, PhD thesis, Universität Regensburg.

Wimmer, M., Adagideli, I., Berber, S., Tománek, D., & Richter, K. (2008), "Spin currents in rough graphene nanoribbons: Universal fluctuations and spin injection," *Phys. Rev. Lett.* **100**, 177207.

Withers, F., Del Pozo-Zamudio, O., Mishchenko, A., et al. (2015), "Light-emitting diodes by band-structure engineering in van der Waals heterostructures," *Nat. Mater.* **14**(3), 301–306.

Woessner, A., Lundeberg, M. B., Gao, Y., et al. (2015), "Highly confined low-loss plasmons in graphene-boron nitride heterostructures," *Nat. Mater.* **14**(4), 421–425.

Wu, F., MacDonald, A., & Martin, I. (2018), "Theory of phonon-mediated superconductivity in twisted bilayer graphene," *Phys. Rev. Lett.* **121**(25), 257001.

Wu, F., Queipo, P., Nasibulin, A., et al. (2007), "Shot noise with interaction effects in single-walled carbon nanotubes," *Phys. Rev. Lett.* **99**, 156803.

Wu, Y., Perebeinos, V., Lin, Y.-m., et al. (2012), "Quantum behavior of graphene transistors near the scaling limit," *Nano Lett.* **12**(3), 1417–1423.

Wunderlich, J., Kaestner, B., Sinova, J., & Jungwirth, T. (2005), "Experimental observation of the spin-Hall effect in a two-dimensional spin-orbit coupled semiconductor system," *Phys. Rev. Lett.* **94**, 047204.

Xia, F., Farmer, D. B., Lin, Y.-m., & Avouris, P. (2010), "Graphene field-effect transistors with high on/off current ratio and large transport band gap at room temperature," *Nano Lett.* **10**(2), 715–718.

Xia, F., Mueller, T., Lin, Y.-m., Valdes-Garcia, A., & Avouris, P. (2009), "Ultrafast graphene photodetector," *Nat. Nanotechnol.* **4**(12), 839–843.

Xia, F., Perebeinos, V., Lin, Y.-m., Wu, Y., & Avouris, P. (2011), "The origins and limits of metal-graphene junction resistance," *Nat. Nanotechnol.* **6**(3), 179–184.

Xiao, D., Chang, M.-C., & Niu, Q. (2010), "Berry phase effects on electronic properties," *Rev. Mod. Phys.* **82**, 1959–2007.

Xiao, D., Liu, G.-B., Feng, W., Xu, X., & Yao, W. (2012), "Coupled spin and valley physics in monolayers of MoS_2 and other group-VI dichalcogenides," *Phys. Rev. Lett.* **108**(19), 196802.

Xiao, D., Yao, W., & Niu, Q. (2007), "Valley-contrasting physics in graphene: Magnetic moment and topological transport," *Phys. Rev. Lett.* **99**, 236809.

Xu, C. & Balents, L. (2018), "Topological superconductivity in twisted multilayer graphene," *Phys. Rev. Lett.* **121**(8), 087001.

Xu, J., Zhu, T., Luo, Y. K., Lu, Y.-M., & Kawakami, R. K. (2018), "Strong and tunable spin-lifetime anisotropy in dual-gated bilayer graphene," *Phys. Rev. Lett.* **121**, 127703.

Yacoby, A. (2011), "Graphene: Tri and tri again," *Nat. Phys.* **7**(12), 925–926.

Yan, J. & Fuhrer, M. S. (2011), "Correlated charged impurity scattering in graphene," *Phys. Rev. Lett.* **107**, 206601.

Yan, W., Txoperena, O., Llopis, R., et al. (2016), "A two-dimensional spin field-effect switch," *Nat. Commun.* **7**, 13372.

Yang, B., Lohmann, M., Barroso, D., et al. (2017), "Strong electron-hole symmetric Rashba spin-orbit coupling in graphene/monolayer transition metal dichalcogenide heterostructures," *Phys. Rev. B - Condens. Matter Mater. Phys.* **96**(4), 041409.

Yang, B., Tu, M.-F., Kim, J., et al. (2016), "Tunable spin-orbit coupling and symmetry-protected edge states in graphene/WS_2," *2D Mater.* **3**, 031012.

Yang, H. X., Hallal, A., Terrade, D., et al. (2013), "Proximity effects induced in graphene by magnetic insulators: First-principles calculations on spin filtering and exchange-splitting gaps," *Phys. Rev. Lett.* **110**, 046603.

Yang, L., Park, C.-H., Son, Y.-W., Cohen, M. L., & Louie, S. G. (2007), "Quasiparticle energies and band gaps in graphene nanoribbons," *Phys. Rev. Lett.* **99**, 186801.

Yang, T.- Y., Balakrishnan, J., Volmer, F., et al. (2011), "Observation of long spin-relaxation times in Bilayer Graphene at Room Temperature," *Phys. Rev. Lett.* **107**, 047206.

Yankowitz, M., Chen, S., Polshyn, H., et al. (2019), "Tuning superconductivity in twisted bilayer graphene," *Science* **363**(6431), 1059–1064.

Yao, Y., Ye, F., Qi, X.-L., Zhang, S.-C., & Fang, Z. (2007), "Spin-orbit gap of graphene: First-principles calculations," *Phys. Rev. B* **75**, 041401.

Yao, Z., Kane, C. L., & Dekker, C. (2000), "High-field electrical transport in single-wall carbon nanotubes," *Phys. Rev. Lett.* **84**, 2941–2944.

Yao, Z., Postma, H. W. C., Balents, L., & Dekker, C. (1999), "Carbon nanotube intramolecular junctions," *Nature* **402**(6759), 273–276.

Yazyev, O. & Louie, S. (2010a), "Electronic transport in polycrystalline graphene," *Nat. Mater.* **9**, 806.

Yazyev, O. V. (2008), "Magnetism in disordered graphene and irradiated graphite," *Phys. Rev. Lett.* **101**, 037203.

Yazyev, O. V. (2010), "Emergence of magnetism in graphene materials and nanostructures," *Rep. Progr. Phys.* **73**(5), 056501.

Yazyev, O. V. & Helm, L. (2007), "Defect-induced magnetism in graphene," *Phys. Rev. B* **75**(12), 125408.

Yazyev, O. V. & Louie, S. G. (2010b), "Topological defects in graphene: Dislocations and grain boundaries," *Phys. Rev. B* **81**(19), 195420.

Young, A. F. & Kim, P. (2009), "Quantum interference and Klein tunnelling in graphene heterojunctions," *Nat. Phys.* **5**(3), 222–226.

Young, A. F. & Kim, P. (2011), "Electronic transport in graphene heterostructures," *Ann. Rev. Condens. Matter Phys.* **2**(1), 101–120.

Young, A. F., Zhang, Y., & Kim, P. (2014), *Experimental Manifestation of Berry Phase in Graphene*, Springer International Publishing, Cham, pp. 3–27.

Yu, Q., Jauregui, L. A., Wu, W., et al. (2011), "Control and characterization of individual grains and grain boundaries in graphene grown by chemical vapour deposition," *Nat. Mater.* **10**(6), 443–449.

Yuan, S., De Raedt, H., & Katsnelson, M. I. (2010), "Modeling electronic structure and transport properties of graphene with resonant scattering centers," *Phys. Rev. B* **82**(11), 115448.

Zak, J. (1989), "Berry's phase for energy bands in solids," *Phys. Rev. Lett.* **62**(23), 2747–2750.

Zanolli, Z. & Charlier, J.-C. (2009), "Defective carbon nanotubes for single-molecule sensing," *Phys. Rev. B* **80**(15), 155447.

Zanolli, Z. & Charlier, J.-C. (2010), "Spin transport in carbon nanotubes with magnetic vacancy-defects," *Phys. Rev. B* **81**(16), 165406.

Zanolli, Z. & Charlier, J.-C. (2012), "Single-molecule sensing using carbon nanotubes decorated with magnetic clusters," *ACS Nano* **6**(12), 10786–10791.

Zanolli, Z., Leghrib, R., Felten, A., et al. (2011), "Gas sensing with Au-decorated carbon nanotubes," *ACS Nano* **5**(6), 4592–4599.

Zaric, S., Ostojic, G. N., Kono, J., et al. (2004), "Optical signatures of the Aharonov-Bohm phase in single-walled carbon nanotubes," *Science* **304**(5674), 1129–1131.

Zhang, C., Li, M.-Y., Tersoff, J., et al. (2018), "Strain distributions and their influence on electronic structures of WSe_2-MoS_2 laterally strained heterojunctions," *Nat. Nanotechnol.* **13**(2), 152.

Zhang, L., Zhang, Y., Khodas, M., Valla, T., & Zaliznyak, I. A. (2010), "Metal to insulator transition on the N = 0 Landau level in graphene," *Phys. Rev. Lett.* **105**(4), 046804.

Zhang, P. & Wu, M. (2012), "Electron spin relaxation in graphene with random Rashba field: Comparison of the D'yakonov-Perel' and Elliott-Yafet-like mechanisms," *New J. Phys.* **14**(3), 033015.

Zhang, S. (2000), "Spin Hall effect in the presence of spin diffusion," *Phys. Rev. Lett.* **85**, 393–396.

Zhang, S., Yan, Z., Li, Y., Chen, Z., & Zeng, H. (2015), "Atomically thin arsenene and antimonene: Semimetal-semiconductor and indirect-direct band-gap transitions," *Angew. Chem. Int. Ed.* **54**(10), 3112–3115.

Zhang, Y., Jiang, Z., Small, J. P., et al. (2006), "Landau-level splitting in graphene in high magnetic fields," *Phys. Rev. Lett.* **96**, 136806.

Zhang, Y., Rubio, A., & Lay, G. L. (2017), "Emergent elemental two-dimensional materials beyond graphene," *J. Phys. D: Appl. Phys.* **50**(5), 053004.

Zhang, Y., Tan, Y.-W., Stormer, H. L., & Kim, P. (2005), "Experimental observation of the quantum Hall effect and Berry's phase in graphene," *Nature* **438**(7065), 201–204.

Zhang, Y., Tang, T.-T., Girit, C., et al. (2009), "Direct observation of a widely tunable bandgap in bilayer graphene," *Nature* **459**(7248), 820–823.

Zhang, Y.-Y., Hu, J., Bernevig, B. A., et al. (2009), "Localization and the Kosterlitz-Thouless transition in disordered graphene," *Phys. Rev. Lett.* **102**, 106401.

Zhao, J., Park, H., Han, J., & Lu, J. P. (2004), "Electronic properties of carbon nanotubes with covalent sidewall functionalization," *J. Phys. Chem. B* **108**(14), 4227–4230.

Zhao, M., Ye, Y., Han, Y., Xia, Y., et al. (2016), "Large-scale chemical assembly of atomically thin transistors and circuits," *Nat. Nanotechnol.* **11**(11), 954–959.

Zhao, P. & Guo, J. (2009), "Modeling edge effects in graphene nanoribbon field-effect transistors with real and mode space methods," *J. Appl. Phys.* **105**, 034503.

Zhao, Y., Cadden-Zimansky, P., Ghahari, F., & Kim, P. (2012), "Magnetoresistance measurements of graphene at the charge neutrality point," *Phys. Rev. Lett.* **108**(10), 106804.

Zheng, L. X., O'Connell, M. J., Doorn, S. K., et al. (2004), "Ultralong single-wall carbon nanotubes," *Nat. Mater.* **3**(10), 673–676.

Zhou, S. Y., Gweon, G.-H., Fedorov, A. V., et al. (2007), "Substrate-induced bandgap opening in epitaxial graphene," *Nat. Mater.* **6**(10), 770–775.

Zhou, X.-F., Dong, X., Oganov, A. R., et al. (2014), "Semimetallic two-dimensional boron allotrope with massless Dirac fermions," *Phys. Rev. Lett.* **112**(8), 085502.

Zhou, Y. & Wu, M. W. (2011), "Optical response of graphene under intense terahertz fields," *Phys. Rev. B* **83**(24), 245436.

Zhou, Y. & Wu, M. W. (2012), "Single-parameter quantum charge and spin pumping in armchair graphene nanoribbons," *Phys. Rev. B* **86**, 085406.

Zhu, F.-F., Chen, W.-J., Xu, Y., et al. (2015), "Epitaxial growth of two-dimensional stanene," *Nat. Mater.* **14**(10), 1020–1025.

Zhu, R. & Chen, H. (2009), "Quantum pumping with adiabatically modulated barriers in graphene," *Appl. Phys. Lett.* **95**(12), 122111.

Zhu, W., Li, W., Shi, Q. W., et al. (2012), "Vacancy-induced splitting of the dirac nodal point in graphene," *Phys. Rev. B* **85**, 073407.

Zhu, Z., Cai, X., Yi, S., et al. (2017), "Multivalency-driven formation of Te-based monolayer materials: A combined first-principles and experimental study," *Phys. Rev. Lett.* **119**(10), 106101.

Zhu, Z. & Tománek, D. (2014), "Semiconducting layered blue phosphorus: A computational study," *Phys. Rev. Lett.* **112**(17), 176802.

Zihlmann, S., Cummings, A. W., Garcia, J. H., et al. (2018), "Large spin relaxation anisotropy and valley-Zeeman spin-orbit coupling in WSe_2/graphene/*h*-BN heterostructures," *Phys. Rev. B* **97**, 075434.

Zomer, P. J., Guimaraes, M. H. D., Tombros, N., & van Wees, B. J. (2012), "Long-distance spin transport in high-mobility graphene on hexagonal boron nitride," *Phys. Rev. B* **86**, 161416(R).

Zurek, W. H. (2003), "Decoherence and the transition from quantum to classical – Revisited," *arXiv:quant-ph/0306072*.

Index